

Electronic Structure and Substrate Binding of the Water-Oxidizing Manganese Cluster in Photosystem II as Studied by Pulse EPR and ENDOR Spectroscopy

vorgelegt von
Master of Science
Thomas Frank Lohmiller
geb. in Herrenberg

von der Fakultät II - Mathematik und Naturwissenschaften
der Technischen Universität Berlin
zur Erlangung des akademischen Grades

Doktor der Naturwissenschaften
Dr. rer. nat.

genehmigte Dissertation

Promotionsausschuss:

Vorsitzender: Prof. Dr. Andreas Grohmann
Berichter/Gutachter: Prof. Dr. Wolfgang Lubitz
Berichter/Gutachter: Prof. Dr. Peter Hildebrandt

Tag der wissenschaftlichen Aussprache: 13. Juni 2014

Berlin 2016

D 83

Abstract

Oxygenic photosynthesis is the biochemical process by which plants, algae and cyanobacteria convert solar into chemical energy, fixing carbon from CO₂ in the form of carbohydrates. As such, it produces almost all biomass and biological primary energy on Earth and is the origin of our oxygen atmosphere, essential for all aerobic life. Oxygen is generated from light-driven oxidation of water by the oxygen-evolving complex (OEC), a Mn₄O₅Ca cofactor of photosystem II (PSII). Understanding this catalytic reaction is not only of great interest in a biological and ecological context, but also with respect to sustainable energy production.

In the present work, an array of multifrequency EPR methods was employed to characterize the OEC in defined states of the catalytic S_i cycle (*i* = 0-4). This includes the identification of the oxidation states of the individual Mn ions and sites and modes of substrate binding, as well as of the effects of structural perturbations and the function of the Ca²⁺ ion, specifically:

- (i) The current state of research on the OEC and oligonuclear Mn model compounds is reviewed focusing on concepts and potentials of and recent advances from (pulsed) EPR experiments and their combination with theoretical (DFT) calculations.
- (ii) An EPR/⁵⁵Mn-ENDOR-based investigation of the OEC inhibited by Ca²⁺-depletion has been conducted. It is shown that the Ca²⁺ ion is not crucial for its electronic and spatial structure, but instead is possibly essential for proton-coupled electron transfer from the Mn ions to the nearby tyrosine Y_Z and/or substrate binding and activation.
- (iii) A combined EPR/DFT study of the electronic structures and ligand binding results in a common general model for native, Ca²⁺/Sr²⁺-exchanged and NH₃-modified S₂ state variants. On this basis, perturbation of the interactions with ¹⁷O ligands allows for an unambiguous assignment of the only exchangeable μ-oxo bridge to a specific oxygen in the cluster, next to the Ca²⁺/Sr²⁺ site and probably the early binding substrate.
- (iv) An EPR/⁵⁵Mn-ENDOR analysis characterizes the regenerated catalyst immediately after O₂ release (S₀ state). It represents a Mn^{III}₃Mn^{IV} complex, in which the position of the Mn^{IV} is assigned via the ¹⁴N coupling of the histidine ligand of the OEC and DFT modelling. ¹⁷O and ²H spectra identify a single, exchangeable μ-hydroxo bridge, consistent with the DFT model and the S₂ state, and thus the early binding substrate water.

The combined outcome is a conclusive mechanistic description of the first half of the reaction cycle of photosynthetic water oxidation, starting from catalyst reactivation after oxygen release and including Mn oxidation state changes, substrate binding and deprotonation events.

Abstract

Zusammenfassung

Mittels der oxygenen Photosynthese wandeln Pflanzen, Algen und Cyanobakterien Sonnenenergie in chemische Energie um und speichern Kohlenstoff aus CO_2 in Form von Kohlenhydraten. Sie erzeugt fast die gesamte Biomasse und biologische Primärenergie auf der Erde sowie die für aerobes Leben essentielle Sauerstoffatmosphäre. O_2 entsteht bei der lichtgetriebenen Oxidation von Wasser durch den $\text{Mn}_4\text{O}_5\text{Ca}$ -Kofaktor OEC des Enzyms Photosystem II (PSII). Diese katalytische Reaktion ist daher im biologischen und ökologischen Kontext wie auch für eine nachhaltige Energieerzeugung von größtem Interesse.

In der vorliegenden Arbeit wurden EPR-Methoden zur Charakterisierung des OEC in mehreren Zuständen des S_i -Katalysezyklus ($i = 0-4$) verwendet. Dies umfasst die Bestimmung der Oxidationszustände der einzelnen Mn-Ionen, der Bindungsstellen und -formen der Wasser-Substrate, der Auswirkungen struktureller Modifikationen und der Funktion des Ca^{2+} -Ions.

- (i) Der derzeitige Forschungsstand zum OEC und oligonuklearen Mn-Modellverbindungen wird zusammengefasst, mit Schwerpunkt auf der EPR-Methodik, kombiniert mit DFT-Rechnungen. Konzepte, Potential sowie neueste Erkenntnisse werden vorgestellt.
- (ii) Eine EPR/ ^{55}Mn -ENDOR-basierte Untersuchung des durch Entfernung des Ca^{2+} -Ions inhibierten OEC zeigt, dass das Ca^{2+} nicht entscheidend ist für die elektronische und räumliche Struktur, sondern wahrscheinlich für den Protonen-gekoppelten Elektronentransfer zum benachbarten Tyrosin Y_Z und/oder für Substratbindung und -aktivierung.
- (iii) Eine EPR/DFT-Studie ihrer Strukturen und Ligandenbindungen führt zu einem allgemeinen Modell für den nativen und die $\text{Ca}^{2+}/\text{Sr}^{2+}$ - und NH_3 -modifizierten S_2 -Zustände. Dadurch ermöglicht die Variation von ^{17}O -Ligandensignalen die Zuordnung der einzigen austauschbaren μ -Oxo-Brücke zu einem Sauerstoff, der an das $\text{Ca}^{2+}/\text{Sr}^{2+}$ -Ion koordiniert. Er resultiert wahrscheinlich vom zuerst bindenden Substratwasser.
- (iv) Eine EPR/ ^{55}Mn -ENDOR-Analyse charakterisiert den Katalysator direkt nach der O_2 -Freisetzung (S_0 -Zustand) als $\text{Mn}^{\text{III}}_3\text{Mn}^{\text{IV}}$ -Komplex. Das Mn^{IV} -Ion lässt sich über die ^{14}N -Kopplung eines Histidins im OEC und DFT-Modellierung zuordnen. ^{17}O - und ^2H -Spektren identifizieren eine einzelne μ -Hydroxo-Brücke, übereinstimmend mit DFT-Modell und S_2 -Zustand, als austauschbar und somit als das zuerst bindende Substrat.

Zusammen führt dies zu einer mechanistischen Beschreibung der ersten Hälfte des katalytischen Zyklus der Wasseroxidation, beginnend mit der Reaktivierung des OEC durch Substratbindung, einschließlich der Änderungen der Mn-Oxidationszustände und Deprotonierungen.

Zusammenfassung

Table of Contents

Chapter 1

Motivation:

Chemical Energy Conversion and Storage and Nature's Water-Oxidizing Complex..... 1

1.1 References 4

Chapter 2

Photosynthesis and Photosystem II 7

2.1 Overview 7

2.2 The Light Reactions in Oxygenic Photosynthesis..... 9

2.3 Photosystem II 12

2.3.1 Structure 12

2.3.2 Charge Separation and Electron Transfer 13

2.3.3 The Tyrosines Y_Z and Y_D 15

2.3.4 The Oxygen-Evolving Complex (OEC) 15

2.4 References 17

Chapter 3

Electron Paramagnetic Resonance 21

3.1 The Spin Hamiltonian..... 21

3.1.1 The Electron and Nuclear Zeeman Interactions..... 22

3.1.2 The Fine Structure or Zero-Field Splitting 23

3.1.3 The Electron Exchange Interaction..... 24

3.1.4 The Hyperfine Interaction..... 25

3.1.5 The Nuclear Quadrupole Interaction 26

3.2 EPR Spectroscopy 27

3.2.1 The Continuous-Wave (CW) EPR Experiment 28

3.2.2 Pulse EPR Experiments 29

3.2.2.1 Electron Spin Echo (ESE)-detected EPR 30

3.2.2.2 Two- and Three-Pulse ESE Envelope Modulation (ESEEM) and Hyperfine Sublevel Correlation (HYSCORE)..... 32

3.2.2.3 Multi-Resonance Spin-Polarization-Transfer Experiments: Davies Electron-Nuclear Double Resonance (ENDOR) and Electron-Electron Double Resonance (ELDOR)-detected NMR (EDNMR) 34

3.3 References 36

Chapter 4

EPR Spectroscopy and the Electronic Structure of the Oxygen-Evolving Complex of Photosystem II 37

Table of Contents

Chapter 5	
The Basic Properties of the Electronic Structure of the Oxygen-Evolving Complex of Photosystem II Are Not Perturbed by Ca²⁺ Removal.....	77
Chapter 6	
Structure, Ligands and Substrate Coordination of the Oxygen-Evolving Complex of Photosystem II in the S₂ State: a Combined EPR and DFT Study.....	91
Chapter 7	
The First Substrate Water of Nature’s Water-Oxidizing Cofactor Binds as a μ-Hydroxo Bridge during Catalyst Regeneration.....	109
Chapter 8	
Summary and Outlook.....	125
8.1 References.....	128
Appendices	129
A Supporting Information for Chapter 4.....	131
B Supporting Information for Chapter 5.....	143
C Supporting Information for Chapter 6.....	155
D Supporting Information for Chapter 7.....	197
Abbreviations.....	229
Acknowledgments.....	231
Publications.....	233

Chapter 1

Motivation: Chemical Energy Conversion and Storage and Nature's Water-Oxidizing Complex

Access to and storage of energy is an essential requirement to power physiological processes for all forms of life, from bacteria to algae, fungi, plants and animals. The by far largest fraction of energy utilized both by phototrophic and chemotrophic organisms on Earth originates from the conversion of incident solar energy into chemical energy in oxygenic photosynthesis.

Throughout history, humans have been using an ever-increasing amount of energy from the biosphere also for non-physiological purposes, starting from basic needs such as lighting and preparation of food. Today, the human world energy consumption amounts to 5.5×10^{17} kJ/a or 1.5×10^{14} kWh/a, of which 82 % stem from fossil fuels (as of 2011)¹, which represent ancient, accumulated photosynthetic biomass. The combustion of these fuels yields as a by-product carbon dioxide, a greenhouse gas that represents the largest contributor to global warming.² To offset the negative impact of anthropogenic climate change, renewable energy technologies are sort to cease our dependence on fossil oil, coal and natural gas. It would at the same time bypass the problem of their limited supply and accessibility and concomitant environmental and political issues. One such technology to directly utilize solar light is the generation of electricity by photovoltaics. However, it comes with the disadvantage that, to account for its dependence on daylight and to make it usable in mobile applications such as powering vehicles, it relies on batteries for storage, the energy densities of which are inherently low.

Artificial photosynthesis in contrast is a technology that converts sunlight into chemical energy stored in solar fuels. High energy density, facile storage and already established infrastructure make especially liquid solar fuels a more practical option to replace fossil fuels than photovoltaics. Thus, the development of efficient and cheap catalysts for generating solar fuels is highly desirable.³ Many approaches in this direction involve as an oxidation reaction the splitting of water to yield electrons. These highly energetic reducing equivalents can then be employed to convert low-energy substrates into oxidizable small-molecule fuels of higher energy, such as: hydrogen by reduction of protons; methane, methanol or formic acid by reduction of CO₂; or ammonia by reduction of nitrogen.^{4,5} Besides utilizing it by combustion or in fuel cells, H₂ gas can also be used as a reductant to produce (carbon-based) fuels that are easier to handle, which allows for improved storability and higher energy densities. Water oxidation is preferably conducted via a more efficient direct photo(electro)chemical process instead of driven by photovoltaic electricity due to inherent losses by an additional energy conversion step. Such a no-risk technology has the potential to solve the energy question, which, in face of the rapid population increase and intimately linked to global warming, is the biggest challenge of our time.

A synthetic photo-driven water-oxidizing device would have the same basic function as the enzymatic water-splitting system that has developed in nature, photosystem II (PSII) in oxygenic photosynthesis, introduced in Chapter 2. Therein, the site of water-oxidation catalysis is an inorganic Mn₄O₅Ca cofactor, constituting what is often referred to as the oxygen-evolving complex (OEC). The OEC exhibits a high turnover frequency (TOF $\geq 10^3$ s⁻¹)⁶ and a high maximum turnover number (TON $\leq 10^6$)⁷ limited by protein degradation due to reactive oxygen species (ROS) formed. As it employs only cheap, earth-abundant and non-toxic elements, it can be viewed as a blueprint for an ideal synthetic catalyst, which is extensively investigated.⁸ Hence, the study of the natural system and process is of utmost importance. A complete understanding of its chemical function involves resolving (i) the catalyst structure throughout its reaction cycle, (ii) structure and function of the surrounding matrix, (iii) the mechanism of substrate transport/delivery and (iv) its subsequent binding and activation, as well as (v) oxidation state changes, (vi) deprotonation processes and (vii) O-O bond formation.

Multifrequency electron paramagnetic resonance (EPR) spectroscopy^{9,10} provides a toolbox of versatile techniques, described in Chapter 3, that are suited for addressing these questions. Its applicability to the OEC results from the electron spins S originating from the unpaired electrons of the four Mn ions. The strong interaction of the individual Mn spins results in effective

total spin states S_T with characteristic EPR signals in all metastable valence states of the cluster, of which the $S_T = \frac{1}{2}$ states are most readily observable by EPR. EPR spectroscopy can provide information about this coupling and the spin state ladder. Moreover, different nuclear spins in the OEC can be probed via their coupling to the electron spin by several EPR experiments, such as electron spin echo envelope modulation (ESEEM), hyperfine sublevel correlation (HYSCORE), electron-nuclear double resonance (ENDOR) and electron-electron double resonance (ELDOR)-detected nuclear magnetic resonance (EDNMR). Analysis of the ^{55}Mn resonances provides information about oxidation states and the local (coordination) symmetries of the Mn ions. The $^{14}\text{N}/^{15}\text{N}$ and ^{13}C nuclei of ligating amino acids allow the coordination mode of these residues to be identified and provide information on the ligated Mn ion, such as valence and spin density. Interacting $^1\text{H}/^2\text{H}$ and ^{17}O nuclei from (exchangeable) bridges and $\text{H}_2\text{O}/\text{OH}^-$ serve to characterize substrate binding. The interpretation of spectroscopic results can be greatly aided by theory at the density functional theory (DFT) level. The broken-symmetry (BS) formalism now allows systems of magnetically interacting open-shell transition-metal ions, such as the OEC, to be reliably computed, relating spectroscopic observables to structural constraints.^{11,12} This combined experimental-theoretical approach is presented in detail in Chapter 4.

PSII samples with the OEC in well-defined states can be obtained as core complex preparations or alternatively as membrane preparations from thermophilic cyanobacteria and higher plants. The desired S states can be generated by various illumination procedures. The preparations allow for specific modifications of the OEC, such as the depletion of the Ca^{2+} ion,¹³ its substitution for Sr^{2+} ¹⁴ or the binding of NH_3 ¹⁵. Furthermore, the sample buffer can be exchanged to isotopically enriched D_2O or H_2^{17}O in order to introduce spin-labelled water and derivatives (OH^- , O^{2-}) into the OEC.

The OEC cycles through five valence states, the so-called S states S_0 to S_4 , by sequential oxidation to convert H_2O to dioxygen, protons and electrons. In this work, the above described techniques were applied in combination to study the total spin $S_T = \frac{1}{2}$ conformations of the S_2 and S_0 states. Detailed knowledge of the early S states immediately following O_2 release and prior to O-O bond formation is essential for understanding the successive steps and the catalytic mechanism as a whole. The combination of sample modification and directed perturbation of the inorganic cluster together with spectroscopic and theoretical methods is a key element for the characterization of the respective electronic structures, individual Mn oxidation states and substrate binding. Chapter 5 investigates the Ca^{2+} -depleted OEC in PSII prepara-

tions isolated from spinach. The role of the Ca^{2+} ion in water oxidation catalysis is scrutinized via the effect of its removal on the electronic structure of the S_2/S_2' state as characterized by EPR and ^{55}Mn -ENDOR spectroscopy. Additionally, previously proposed Mn^{2+} binding to a site in Ca^{2+} -depleted PSII is quantitatively analyzed by Q-band ^{55}Mn -ENDOR. Chapter 6 gives a comprehensive EPR/BS-DFT description of the S_2 state, which is achieved by comparison of the native form with the $\text{Ca}^{2+}/\text{Sr}^{2+}$ -exchanged and the NH_3 -binding variant. Refined electronic and spatial models form the basis for analyzing substrate interaction. For this, the effects of the structural perturbations in the different S_2 state variants on ^{17}O resonances from exchanged water-derived species are measured by W-band EDNMR. Finally, Chapter 7 focuses on the S_0 state, *i.e.* the regenerated catalyst, investigating its valence state pattern and substrate binding. BS-DFT models are developed and tested for feasibility by comparison with experimental results from EPR, ^{55}Mn -ENDOR and ^{14}N -ESEEM/-HYSCORE. On this basis, both by means of ^{17}O and ^2H interactions, the question about the presence and identity of an early binding, slowly exchanging substrate W_s in the S_0 state is approached. In Chapter 8, the combined results are summarized and integrated into the bigger picture of photosynthetic water oxidation discussing the consequences of the outcome of this work for the mechanism of photosynthetic water oxidation.

1.1 References

- (1) IEA - Report. <http://www.iea.org/statistics/statisticssearch/report/?&country=WORLD&year=2011&product=Balances> (accessed Apr 20, 2014).
- (2) IPCC *Climate Change 2013: The Physical Science Basis. Contribution of Working Group I to the Fifth Assessment Report of the Intergovernmental Panel on Climate Change* Cambridge University Press: Cambridge, United Kingdom and New York, NY, USA, 2013.
- (3) *Chemical Energy Storage*; Schlögl, R., Ed.; De Gruyter: Berlin, 2012.
- (4) Dubois, M. R.; Dubois, D. L. *Acc. Chem. Res.* **2009**, *42*, 1974.
- (5) Kalyanasundaram, K.; Graetzel, M. *Curr. Opin. Biotechnol.* **2010**, *21*, 298.
- (6) Joliot, P.; Barbieri, G.; Chabaud, R. *Photochem. Photobiol.* **1969**, *10*, 309.
- (7) Lubitz, W.; Reijerse, E. J.; Messinger, J. *Energy Environ. Sci.* **2008**, *1*, 15.
- (8) Cox, N.; Lubitz, W. In *Chemical Energy Storage*; Schlögl, R., Ed.; De Gruyter: Berlin, 2012, p 185.

- (9) Schweiger, A.; Jeschke, G. *Principles of pulse electron paramagnetic resonance*; Oxford University Press: Oxford, 2001.
- (10) Weil, J. A.; Bolton, J. R. *Electron paramagnetic resonance : elementary theory and practical applications*; 2nd ed.; John Wiley & Sons, Inc.: Hoboken, NJ, 2007.
- (11) Neese, F. *Coord. Chem. Rev.* **2009**, *253*, 526.
- (12) Pantazis, D. A.; Orio, M.; Petrenko, T.; Zein, S.; Bill, E.; Lubitz, W.; Messinger, J.; Neese, F. *Chem.-Eur. J.* **2009**, *15*, 5108.
- (13) Ono, T.-a.; Inoue, Y. *FEBS Lett.* **1988**, *227*, 147.
- (14) Boussac, A.; Rappaport, F.; Carrier, P.; Verbavatz, J. M.; Gobin, R.; Kirilovsky, D.; Rutherford, A. W.; Sugiura, M. *J. Biol. Chem.* **2004**, *279*, 22809.
- (15) Beck, W. F.; De Paula, J. C.; Brudvig, G. W. *J. Am. Chem. Soc.* **1986**, *108*, 4018.

Chapter 1

Chapter 2

Photosynthesis and Photosystem II

2.1 Overview

Photosynthesis is the main biochemical process of conversion of light, *i.e.* electromagnetic energy into chemical energy as performed by most phototrophs, organisms that use light as their source of energy, such as plants, most algae and several types of bacteria. It comprises two stages to synthesize high-energy organic molecules from low-energy substrates. In the primary, light(-dependent) reactions, absorbed photons drive an electron transfer from an initial donor to generate the energy currencies of the cell reduced nicotinamide adenine dinucleotide phosphate (NADPH) and adenosine triphosphate (ATP). These are then used in the secondary, light-independent reactions for carbon assimilation yielding carbohydrates via the Calvin cycle¹ or pyruvate in some bacteria^{2,3}. Carbon dioxide serves as the carbon source in plants, algae and photoautotrophic microorganisms, while simple organic molecules are only assimilated by photoheterotrophic heliobacteria.⁴ In the most common form of photosynthesis, performed by plants, algae and most cyanobacteria, the electron donor for carbon reduction is water, which is oxidized to molecular oxygen (Figure 1.1). In contrast, other photosynthetic bacteria perform anoxygenic photosynthesis, using a wider range of reductants, inorganic molecules, such as hydrogen sulfide, sulfur, hydrogen, nitrite or Fe^{2+} ions (see Ref. ⁵), or small organic compounds, that do not result in the formation of O_2 .

There are two types of pigments involved in photosynthesis, which are part of protein-cofactor supercomplexes: (i) non-redox-active chromophores that harvest light energy and funnel it to the so-called reaction centers of the complexes and (ii) redox-active pigments within the reaction centers capable of stabilizing a charge-separated state, analogous to a photovoltaic cell. The spectral range of light that can be absorbed to provide the energy for

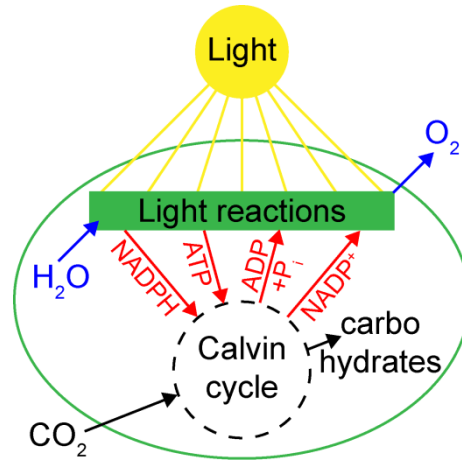
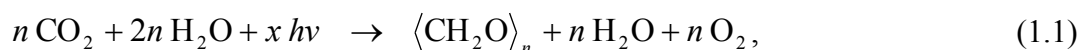


Figure 1.1. General scheme of oxygenic photosynthesis. NADPH and ATP, the energy currencies of the cell, are regenerated by the light-driven oxidation of H₂O in the primary reactions. They thereby provide the energy for fixation of carbon from CO₂ in the form of carbohydrates via the Calvin cycle.

driving the photosynthetic processes is determined by the type of pigments, mostly chlorins and carotenoids, present in the different organisms. The light-harvesting pigment-protein complexes are arranged as antenna systems around reaction-center protein complexes to increase the absorption cross section and broaden the energy range. This allows efficient funneling of captured quanta (excitons) to the reaction center to excite the primary photochemical redox event. In plants and green algae, they are also involved in a protective mechanism (non-photochemical quenching) regulating the energy supply to the reaction centers by dissipating excess energy as heat. In contrast to reaction centers, antenna complexes show a considerable variety in composition and size among photosynthetic species, for the purpose of evolutionary adaptation to diverse environments and adjustment of energy input to the reaction centers. A green sulfur bacterium that absorbs weak far-red and infrared geothermal radiation at a deep-sea hydrothermal vent is the only species found so far that uses radiation other than sunlight to perform photosynthesis.⁶

The net reaction of oxygenic photosynthesis can be written as:



with $\langle \text{CH}_2\text{O} \rangle$ representing the carbohydrate formed. Since mixtures of H₂O and CO₂ under illumination do not undergo this reaction spontaneously, a complex machinery is necessary to accomplish numerous single reaction steps. In cyanobacteria, they take place in the cellular

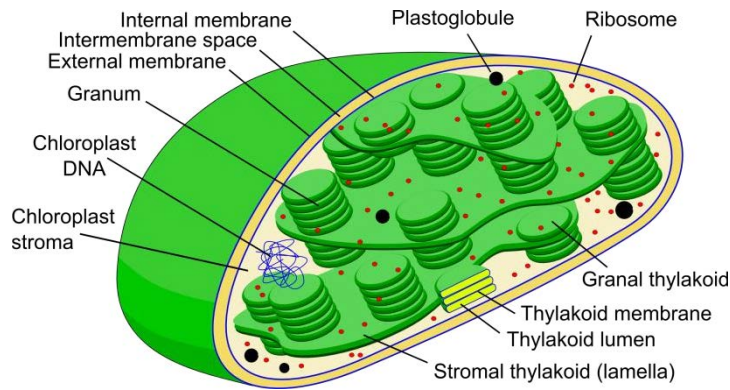


Figure 1.2. Organization of chloroplast membranes. Chloroplasts are surrounded by an inner and an outer membrane and feature large interconnected membrane systems, the thylakoids, within their aqueous phase called the stroma. To a great extent, thylakoid membranes are arranged in stacks resembling coins, named grana. The space confined by the thylakoid membranes is called lumen. The light reactions take place in the thylakoid membrane, the light-independent reactions in the stroma. Modified from http://commons.wikimedia.org/wiki/File:Scheme_Chloroplast-en.svg, CC BY-SA 3.0.

membrane (light reactions) and the cytosol (light-independent reactions). In contrast, in plant and algal cells, the photosynthetic apparatus is contained in chloroplasts (Figure 1.2), organelles separated from the cytosol by two lipid-bilayer membranes, thought to have originated from endosymbiotic cyanobacteria.

Oxygenic photosynthesis is the main source of oxygen in today's atmosphere, essential for the evolution of complex, aerobic life employing cellular respiration. While both the anoxygenic and later the oxygenic photosynthesis evolved in a nearly anoxic atmosphere, cyanobacteria enriched the atmosphere with oxygen during the Great Oxidation Event ≈ 2.4 billion years ago.⁷ By conversion of inorganic substrates to carbohydrates, such as glucose, sucrose, starch and cellulose, which enter biogeochemical cycles, photosynthesis also supplies almost the entire biosphere with organic compounds as an energy source and building material for organisms.

2.2 The Light Reactions in Oxygenic Photosynthesis

In oxygenic photosynthesis, the light reactions oxidize H_2O and convert light into chemical energy, stored in the high-energy molecules NADPH and ATP. They take place in specialized compartmented membrane formations of the cyanobacterial cell or of the chloroplast in plant

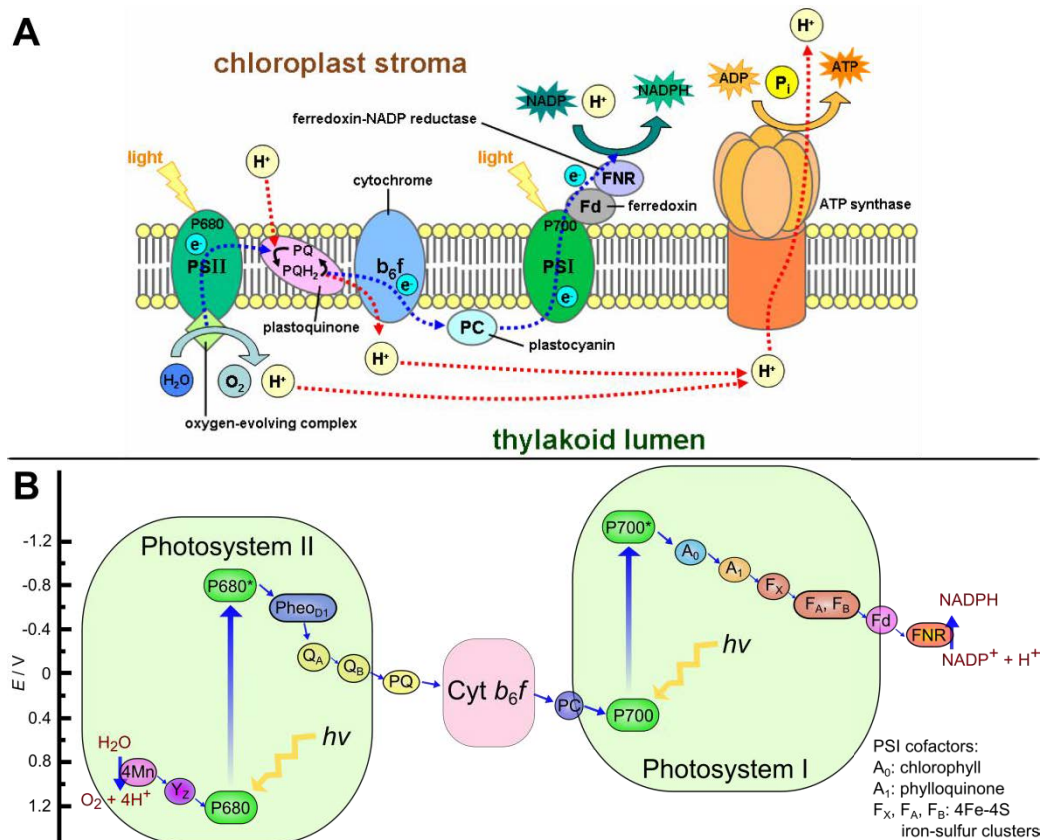
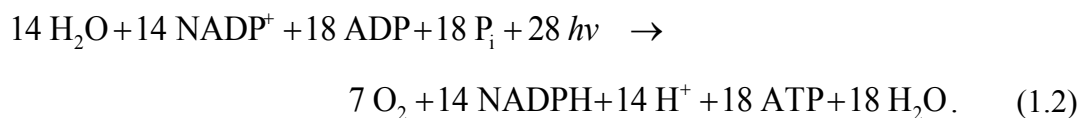


Figure 1.3. Schematic representation of the light reactions. **A:** Components of the light reactions. The distinct orientation of the photosynthetic protein complexes in the thylakoid membrane allows for vectorial electron transport through PS II, *cyt b₆f* and PSI. This is accompanied by proton translocation across the membrane generating an electrochemical gradient driving photophosphorylation by ATP synthase. **B:** Z scheme of photosynthetic electron flow from H_2O to $NADP^+$. Redox-active components are arranged according to their reduction potential E and their position in the electron transport chain. Modified from http://commons.wikimedia.org/wiki/File:Z-scheme_%28pl%29.svg, CC BY-SA 3.0.

cells named thylakoids and involve uniquely oriented membrane proteins, including the integral multisubunit complexes PSII, cytochrome (*cyt*) *b₆f*, photosystem I (PSI) and ATP synthase (Figure 1.3 A). PSII and PSI absorb visible light, powering electron transport within the photosynthetic membrane via a number of electron donors and acceptors, including *cyt b₆f*. The initial donor is H_2O in the lumen, the inner thylakoid space, whereas the final acceptor is $NADP^+$ in the space surrounding the thylakoids, *i.e.* the cytosol in cyanobacteria or the chloroplast stroma in plants and green algae. The electron transport is coupled to proton translocation across the membrane resulting in a proton gradient, which drives the regeneration of ATP by ATP synthase.

The electron transport chain can be illustrated by the so-called Z scheme, in which the involved redox components are arranged according to their position in the sequence and reduction potential (Figure 1.3 B). The two distinct functional units PSII and PSI, which comprise antenna complexes and reaction centers, operate in series to power linear electron flow. The solar-to-chemical energy conversion itself takes place as the primary photochemical event at a coupled multi-pigment assembly, called P₆₈₀ in PSII and P₇₀₀ in PSI reaction centers with absorption maxima at 680 and 700 nm, respectively. Light energy conveyed from the antennae excites these primary electron donors to an excited state. These exhibit significantly decreased redox potentials, such that they instantaneously reduce the primary acceptors, generating a short-lived charge-separated radical-pair state. From there, the electrons are shuttled energetically downhill, and the electron holes formed are rapidly filled by electrons from secondary donors. These cascades of charge separation events occur on a ps-to-ns timescale, fast enough to efficiently minimize wasteful charge recombination events. In this way, PSII provides a strong oxidant, the Mn₄O₅Ca cluster of the OEC, to split water and PSI produces a strong reductant, the water-soluble iron-sulfur protein ferredoxin, to generate NADPH. Electron transport in between them is accomplished by mobile carriers, membrane-soluble plastoquinone and the water-soluble blue-copper protein plastocyanin (PC), via the cyt *b₆f* complex.

As mentioned above, water splitting, electron flow and NADP⁺ reduction entail H⁺ translocation across the thylakoid membrane (Figure 1.3 A). Due to the asymmetric nature of the photosynthetic membrane, this is a directed transport from the cytosol or stroma to the lumen. The result is a pH gradient of 2-3 units with a luminal pH of 5-6 and a stromal pH ≈ 8 in chloroplasts, and an electric potential difference. Together, these parameters constitute the proton electrochemical potential, which represents the free energy stored in the photochemically generated H⁺ gradient. Its proton-motive force drives the synthesis of ATP from adenosine diphosphate (ADP) and inorganic phosphate (P_i) by ATP synthase (Figure 1.3 A), a process known as photophosphorylation. The principle of using the energy of a transmembrane gradient to power a thermodynamically unfavorable reaction is called chemiosmosis.⁸ Since with each reduction of a NADPH molecule, 6 H⁺ are effectively translocated across the membrane, and a minimum of 14 H⁺ are required for the coupled formation of three molecules of ATP, the net equation of the light reactions with an idealized quantum yield of 1 is:



For a comprehensive introduction into photosynthesis, see Refs. ^{9,10}.

2.3 Photosystem II

2.3.1 Structure

The most detailed description of the structure of the PSII complex has been obtained from X-ray diffraction of protein crystals from the thermophilic cyanobacteria *Thermosynechococcus elongatus/vulcanus* (Figure 1.4),¹¹⁻¹³ as well as biochemical experiments and electron microscopy^{14,15} of the enzyme isolated from higher plants. In cyanobacteria and plants PSII, which exhibit a broad homology, it is a homodimer with each monomer comprising the reaction center, three associated light-harvesting complexes II (LHCII) and three different minor chlorophyll *a/b*-binding proteins.

Each reaction center consists of ≈ 20 polypeptides, which are characterized by a pseudotwofold axis along the membrane normal. This relates the protein subunits D1 and D2, a heterodimer of respectively 32 kDa and 34 kDa molecular weight, as well as the inner light-harvesting antenna proteins CP43 and CP47. Together with the *cyt b₅₅₉* subunit, they make up the core of the PSII supercomplex. A few smaller integral membrane proteins associated with

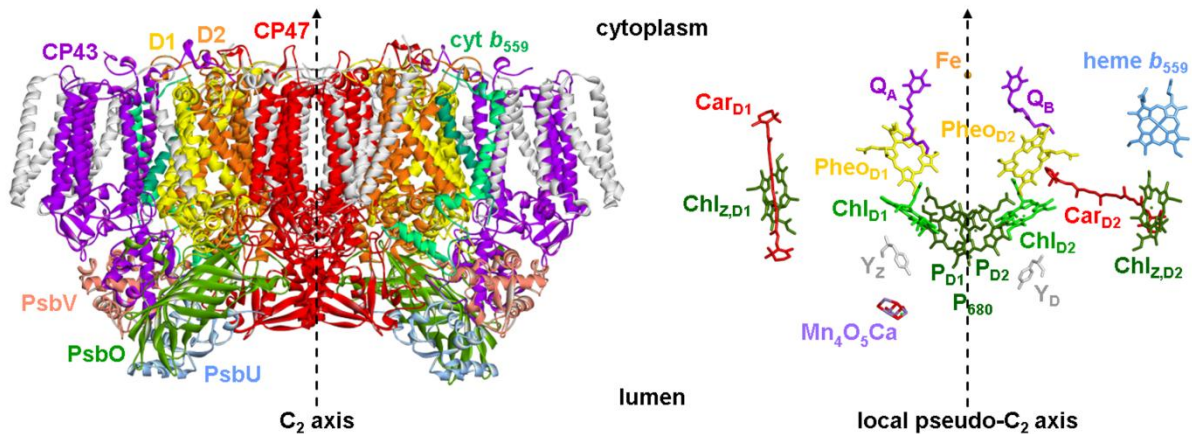


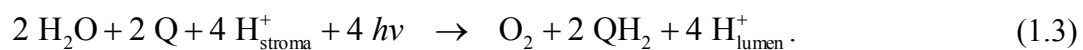
Figure 1.4. X-ray crystallographic structure of the reaction center of dark-adapted PSII isolated from *Thermosynechococcus vulcanus* at 1.9 Å resolution (Protein Data Bank accession number 3ARC).¹³ The symmetry axes are aligned along the normal of the thylakoid membrane oriented as indicated. **Left:** Cartoon representation of homodimeric PSII reaction centers with the most prominent protein subunits highlighted. **Right:** Redox-active sites of a single reaction center. P_{D1} , P_{D2} , Chl_{D1} and Chl_{D2} are the Chl *a* pigment molecules that form part of P_{680} , the coupled entity of the primary photochemical event.

the core complete the reaction center. A total of ≈ 250 chlorophylls are associated with each PSII monomer in a Chl *a* to Chl *b* ratio of about 2 to 1, of which the LHCII antennae contain ≈ 200 the others being located in the reaction center. PSII also hosts ≈ 110 carotenoid molecules, of which 11-12 are associated with the core complex. The redox-active components that are part of the reaction center include the $\text{Mn}_4\text{O}_5\text{Ca}$ cluster of the OEC, the tyrosines Y_Z (D1-Tyr161) and Y_D (D2-Tyr160 in cyanobacteria, D2-Tyr161 in higher plants), the four Chl *a* molecules P_{D1} and P_{D2} , both from the primary donor P_{680} , and Chl_{D1} and Chl_{D2} , two pheophytin *a* molecules (Pheo_{D1} , Pheo_{D2}), two plastoquinones (Q_A on D2 and Q_B on D1) and a non-heme Fe between Q_A and Q_B (Figure 1.4 right). All redox-active components of PSII involved in linear electron transport are bound to D1 and D2. The D1/D2 heterodimer, primarily D1, and CP43 are involved in the binding of the luminal $\text{Mn}_4\text{O}_5\text{Ca}$ cluster of the OEC.

Additionally, several water-soluble peripheral proteins bind to the luminal side of intrinsic PSII subunits (Figure 1.4, left) with high affinity (2 – 10 nM):¹⁶ PsbO (33kDa), also called the Mn stabilizing protein, as well as PsbP (23 kDa) and PsbQ (17 kDa) in higher plants and PsbU (12 kDa) and PsbV, a *cyt c*₅₅₀, in cyanobacteria. Although they do not provide the major binding site of the OEC, the extrinsic subunits play an important role for its stabilization and the regulation of the binding of the metal ions and a nearby Cl^- ion. Besides stabilizing the inorganic cluster, they protect it against chemical attack, especially against reduction of the Mn ions. PsbO also affects the binding of PsbP and PsbQ in higher plants. PsbP prevents Ca^{2+} from being released during the catalysis of water splitting and, together with PsbQ, provides a high affinity Cl^- binding site. The Cl^- ion is essential for oxygen evolution, probably relevant for a H-bonding network involved in transport of the generated H^+ to the lumen.¹⁷ However, it can be replaced by Br^- , NO_3^- and I^- , yet reducing enzymatic activity, but not by F^- .¹⁶ For a review of the extrinsic polypeptides see Ref.¹⁸.

2.3.2 Charge Separation and Electron Transfer

The LHCII complexes capture light energy in the range of 400-700 nm and funnel it towards the reaction center, driving water oxidation on the luminal side and transfer of the electrons to reduce plastoquinone Q_B near the stroma or cytosol, respectively. This results in the following net reaction:



Remarkably, the light-driven water:plastoquinone oxidoreductase PSII combines three redox cycles: (i) the four-electron chemistry of water oxidation, coupled to (ii) the two-electron chemistry of Q_B reduction via (iii) one-electron transfer steps of light-induced charge separation.

The initial step in this chain is the light-induced charge separation by fast oxidation (a few ps)¹⁹ of the excited P_{680}^* by $Pheo_{D1}$ (see Ref. ²⁰). Within 100-200 ps, $Pheo_{D1}$ is oxidized by the tightly bound Q_A , slowing the recombination reaction. Q_A forwards an electron to Q_B , which, at the same time, binds a stromal or cytosolic H^+ , respectively, within ≈ 1 ms. Q_B becomes fully reduced and protonated after a second photochemical turnover, yielding a neutral and hydrophobic plastoquinol Q_BH_2 , which is more weakly bound and diffuses into the membrane. There, it becomes part of the plastoquinone pool, which supplies electrons to the cyt *b₆f* complex. It is replaced by another plastoquinone molecule previously bound at a third plastoquinone site on D1, Q_C , which in turn is replenished by the pool.¹² The Q_B site is the site of competitive binding of inhibitors of photosynthetic electron flow, such as the high affinity herbicide 3-(3,4-dichlorophenyl)-1,1-dimethylurea (DCMU).²¹ As such, it can be used to limit electron transfer from Q_A to Q_B in PSII to one turnover during sample illumination at 0 °C.

The oxidized $P_{680}^{\bullet+}$ cation radical, exhibiting the highest oxidation potential $E = +1.2-1.3$ V²² found in nature, is rapidly reduced by the nearby redox-active Y_Z , the electron relay to the Mn_4O_5Ca cluster, by which Y_Z^\bullet is reduced in return. After four consecutive oxidations,²³ accompanied by the release of four protons to the lumen, the Mn_4O_5Ca cluster is re-reduced instantaneously recovering four electrons from two oxidized water molecules in a single step.²⁴

Compared to the reaction center chemistry of electron transport, the oxidation steps in the OEC, involving substrate binding, H^+ translocation and O-O bond formation, are relatively slow. Depending on the specific processes associated with the S-state transitions, their rates increase with each oxidation step from 30-40 μ s for the transition from S_0 to S_1 up to 1-2 ms for that from S_3 via the transient S_4 state back to S_0 (see Ref. ²⁵) However, the rate limiting step of the overall reaction catalyzed by PSII is the exchange of plastoquinone molecules with the membrane pool. The fast electron shuttling away from P_{680} and its fast re-reduction leads to a high quantum yield $\Phi > 0.9$ for the entire process.

2.3.3 The Tyrosines Y_Z and Y_D

Y_Z , as discussed above, acts as the primary electron donor to $P_{680}^{\bullet+}$, while Y_D , having a lower redox potential than Y_Z ²⁶ and lacking a nearby donor, does not actively take part in linear electron transfer. In their oxidized state, both tyrosines can be probed by EPR spectroscopy, reviewed in Refs.^{27,28}. Electron transfer from Y_Z to $P_{680}^{\bullet+}$ is coupled to transfer of protons (proton-coupled electron transport, PCET) from Y_Z to the neighboring histidine D1-His190, stabilizing the Y_Z^{\bullet} radical, see Refs.²⁷⁻²⁹. The subsequent oxidation of the Mn_4O_5Ca cluster by Y_Z^{\bullet} is coupled to previous H^+ release from substrate water in the majority of the S-state transitions. Y_D plays a role in the protection of PS II against photoinhibition,³⁰ being able to donate an electron to $P_{680}^{\bullet+}$. The Y_D^{\bullet} radical formed is stable for days at room temperature and for months at liquid nitrogen temperature. It can also oxidize the Mn_4O_5Ca cluster in its lowest oxidation state S_0 ,³¹ a reaction that is relatively slow compared to the other electron transfer processes in PSII. This results in the dark-stable resting state of the OEC being the S_1 state.

2.3.4 The Oxygen-Evolving Complex (OEC)

The term OEC generally refers to the inorganic Mn_4O_5Ca cofactor including its first coordination sphere of water(-derived) and amino acid ligands. The at present most detailed crystal structure by Umena *et al.*¹³ at 1.9 Å resolution provided for the first time a picture of the OEC at an atomic level (Figure 1.5). The Mn_4O_5Ca scaffold is arranged in the form of a ‘distorted chair’. It consists of a distorted μ -oxo-bridged Mn_3O_4Ca cube, to which the fourth, dangling Mn_{A4}^{\dagger} is attached via a further oxo bridge (O4). However, the oxygen of the cube closest to Mn_{A4} (O5) exhibits distances to its neighboring Mn centers ≥ 2.4 Å, which are clearly longer than those measured by EXAFS on PSII³³ and Mn-O bond lengths reported for other Mn complexes throughout the literature(see Ref.³⁴). This is thought to be induced by X-ray radiation damage of the cluster, leading to a reduction of the high-valent Mn ions to Mn^{II} and increasing bond lengths.³⁵ Thus, the structure is thought to represent an S_n state with $n < 1$,³⁶ which must not necessarily be catalytically relevant. Without subsequent spectroscopic investigation of irradiated crystals, an assignment to an overall valence and/or spin state remains speculative. For the S_2 state, a recent combined DFT/EPR study by Pantazis *et al.*³⁷ has revealed the O5 position to be variable. The oxygen is able to form either a μ -oxo bridge bet-

[†] The notation used for the Mn ions combines the lettering used by Yano *et al.*³² in polarized EXAFS models and the numbering in the PSII crystal structure of Umena *et al.*¹³.

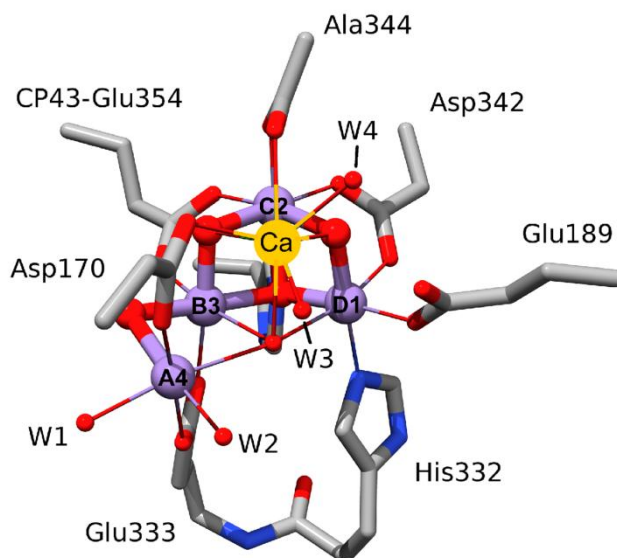


Figure 1.5. The oxygen-evolving complex as found in the X-ray crystallographic PSII structure 3ARC¹³, including all amino acid residues and H₂O/OH⁻ (W1-W4) that are ligands to the Mn and Ca²⁺ ions. Amino acids, except CP43-Glu354, are part of the D1 protein. Mn, Ca, N, O, and C atoms are colored purple, yellow, blue, red, and gray, respectively.

ween Mn_{A4} and Mn_{B3} in the $S_T = 1/2$ open, ‘fused twist’ conformation. This is in equilibrium with O5 representing a coordinating ligand of Mn_{D1} and thus a vertex of the cuboidal Mn trimer moiety in the $S_T = 5/2$ closed, cubane-like structure.

The high-resolution X-ray structure allows for an unambiguous identification of all amino acid ligands to the individual Mn and Ca ions and of four first-coordination sphere H₂O/OH⁻ ligands, as depicted in Figure 1.5. Some of these interactions can also be detected by Fourier transform infrared (FTIR) and EPR spectroscopy,³⁸⁻⁴¹ and it is the combination of crystallographic and spectroscopic information that greatly advances the knowledge on electronic structure. The electron density map obtained from X-ray crystallography itself does neither allow to draw conclusions about the oxidation states of the Mn ions, nor about protonation states, especially relevant for waters/substrates. However, it has been of great value for spectroscopic and theoretical studies, serving as an initial point to tackle these matters. The surrounding protein matrix is of high relevance for the water-splitting reaction, thought to tune critical properties such as redox levels and pK_a values in the different states of the cluster. It also provides channels for substrate (H₂O) and product (H⁺ and O₂) delivery or transport, pathways of which are suggested by the crystal structures.^{12,13,42} The site of water oxidation catalysis is described in greater detail in Chapter 4, as well as in the Introduction sections of Chapters 5 to 7 and in Refs.⁴³⁻⁴⁷

2.4 References

- (1) Calvin, M.; Benson, A. A. *Science* **1948**, *107*, 476.
- (2) Evans, M. C. W.; Buchanan, B. B.; Arnon, D. I. *Proc. Natl. Acad. Sci. U. S. A.* **1966**, *55*, 928.
- (3) Herter, S.; Fuchs, G.; Bacher, A.; Eisenreich, W. *J. Biol. Chem.* **2002**, *277*, 20277.
- (4) Heinnickel, M.; Golbeck, J. H. *Photosynth. Res.* **2007**, *92*, 35.
- (5) Madigan, M. T.; Martinko, J. M.; Stahl, D.; Clark, D. P. *Brock Biology of Microorganisms*; Benjamin Cummings: San Francisco, 2010.
- (6) Beatty, J. T.; Overmann, J.; Lince, M. T.; Manske, A. K.; Lang, A. S.; Blankenship, R. E.; Van Dover, C. L.; Martinson, T. A.; Plumley, F. G. *Proc. Natl. Acad. Sci. U. S. A.* **2005**, *102*, 9306.
- (7) Buick, R. *Phil. Trans. R. Soc. B* **2008**, *363*, 2731.
- (8) Mitchell, P. *Nature* **1961**, *191*, 144.
- (9) Blankenship, R. E. *Molecular Mechanisms of Photosynthesis*; Blackwell Science Ltd.: Oxford, 2002.
- (10) Taiz, L.; Zeiger, E. *Plant Physiology*; Sinauer Associates, Inc.: Sunderland, MA, 2010.
- (11) Ferreira, K. N.; Iverson, T. M.; Maghlaoui, K.; Barber, J.; Iwata, S. *Science* **2004**, *303*, 1831.
- (12) Guskov, A.; Kern, J.; Gabdulkhakov, A.; Broser, M.; Zouni, A.; Saenger, W. *Nat. Struct. Mol. Biol.* **2009**, *16*, 334.
- (13) Umena, Y.; Kawakami, K.; Shen, J.-R.; Kamiya, N. *Nature* **2011**, *473*, 55.
- (14) Nield, J.; Orlova, E. V.; Morris, E. P.; Gowen, B.; van Heel, M.; Barber, J. *Nat. Struct. Biol.* **2000**, *7*, 44.
- (15) Boekema, E. J.; van Breemen, J. F. L.; van Roon, H.; Dekker, J. P. *J. Mol. Biol.* **2000**, *301*, 1123.
- (16) Yocum, C. F. In *Manganese Redox Enzymes*; Pecoraro, V. L., Ed.; VCH: Weinheim, 1992, p pp. 71.
- (17) Olesen, K.; Andreasson, L. E. *Biochemistry* **2003**, *42*, 2025.
- (18) Seidler, A. *Biochim. Biophys. Acta, Bioenerg.* **1996**, *1277*, 35.
- (19) Holzwarth, A. R.; Muller, M. G.; Reus, M.; Nowaczyk, M.; Sander, J.; Rogner, M. *Proc. Natl. Acad. Sci. U. S. A.* **2006**, *103*, 6895.

- (20) Renger, G.; Holzwarth, A. R. In *Photosystem II: The Light-Driven Water:Plastoquinone Oxidoreductase*; Wydrzynski, T. J., Satoh, K., Freeman, J. A., Eds.; Springer: Dordrecht, 2005; Vol. 1, p 139.
- (21) Metz, J. G.; Pakrasi, H. B.; Seibert, M.; Arntzen, C. J. *FEBS Lett.* **1986**, *205*, 269.
- (22) Rappaport, F.; Guergova-Kuras, M.; Nixon, P. J.; Diner, B. A.; Lavergne, J. *Biochemistry* **2002**, *41*, 8518.
- (23) Joliot, P.; Barbieri, G.; Chabaud, R. *Photochem. Photobiol.* **1969**, *10*, 309.
- (24) Kok, B.; Forbush, B.; McGloin, M. *Photochem. Photobiol.* **1970**, *11*, 457.
- (25) Dau, H.; Haumann, M. *Coord. Chem. Rev.* **2008**, *252*, 273.
- (26) Vass, I.; Styring, S. *Biochemistry* **1991**, *30*, 830.
- (27) Diner, B. A.; Britt, R. D. In *Photosystem II: The Light-Driven Water:Plastoquinone Oxidoreductase*; Wydrzynski, T. J., Satoh, K., Freeman, J. A., Eds.; Springer: Dordrecht, 2005; Vol. 1, p 207.
- (28) Havelius, K. G. V.; Sjöholm, J.; Ho, F. M.; Mamedov, F.; Styring, S. *Appl. Magn. Reson.* **2010**, *37*, 151.
- (29) Meyer, T. J.; Huynh, M. H. V.; Thorp, H. H. *Angew. Chem., Int. Ed.* **2007**, *46*, 5284.
- (30) Magnuson, A.; Rova, M.; Mamedov, F.; Fredriksson, P. O.; Styring, S. *Biochim. Biophys. Acta, Bioenerg.* **1999**, *1411*, 180.
- (31) Styring, S.; Rutherford, A. W. *Biochemistry* **1987**, *26*, 2401.
- (32) Yano, J.; Kern, J.; Sauer, K.; Latimer, M. J.; Pushkar, Y.; Biesiadka, J.; Loll, B.; Saenger, W.; Messinger, J.; Zouni, A.; Yachandra, V. K. *Science* **2006**, *314*, 821.
- (33) Pushkar, Y.; Yano, J.; Glatzel, P.; Messinger, J.; Lewis, A.; Sauer, K.; Bergmann, U.; Yachandra, V. K. *J. Biol. Chem.* **2007**, *282*, 7198.
- (34) Ames, W.; Pantazis, D. A.; Krewald, V.; Cox, N.; Messinger, J.; Lubitz, W.; Neese, F. *J. Am. Chem. Soc.* **2011**, *133*, 19743.
- (35) Yano, J.; Kern, J.; Irrgang, K. D.; Latimer, M. J.; Bergmann, U.; Glatzel, P.; Pushkar, Y.; Biesiadka, J.; Loll, B.; Sauer, K.; Messinger, J.; Zouni, A.; Yachandra, V. K. *Proc. Natl. Acad. Sci. U. S. A.* **2005**, *102*, 12047.
- (36) Galstyan, A.; Robertazzi, A.; Knapp, E. W. *J. Am. Chem. Soc.* **2012**, *134*, 7442.
- (37) Pantazis, D. A.; Ames, W.; Cox, N.; Lubitz, W.; Neese, F. *Angew. Chem., Int. Ed.* **2012**, *51*, 9935.
- (38) Debus, R. J. *Coord. Chem. Rev.* **2008**, *252*, 244.

- (39) Stull, J. A.; Stich, T. A.; Service, R. J.; Debus, R. J.; Mandal, S. K.; Armstrong, W. H.; Britt, R. D. *J. Am. Chem. Soc.* **2010**, *132*, 446.
- (40) Stich, T. A.; Yeagle, G. J.; Service, R. J.; Debus, R. J.; Britt, R. D. *Biochemistry* **2011**, *50*, 7390.
- (41) Rapatskiy, L.; Cox, N.; Savitsky, A.; Ames, W. M.; Sander, J.; Nowaczyk, M. M.; Rögner, M.; Boussac, A.; Neese, F.; Messinger, J.; Lubitz, W. *J. Am. Chem. Soc.* **2012**, *134*, 16619.
- (42) Ho, F. M.; Styring, S. *Biochim. Biophys. Acta, Bioenerg.* **2008**, *1777*, 140.
- (43) McEvoy, J. P.; Brudvig, G. W. *Chem. Rev.* **2006**, *106*, 4455.
- (44) Cox, N.; Lubitz, W. In *Chemical Energy Storage*; Schlögl, R., Ed.; De Gruyter: Berlin, 2012, p 185.
- (45) Cox, N.; Messinger, J. *Biochim. Biophys. Acta, Bioenerg.* **2013**, *1827*, 1020.
- (46) Cox, N.; Pantazis, D. A.; Neese, F.; Lubitz, W. *Acc. Chem. Res.* **2013**, *46*, 1588.
- (47) Yano, J.; Yachandra, V. *Chem. Rev.* **2014**, *114*, 4175.

Chapter 3

Electron Paramagnetic Resonance

This Chapter introduces basic theoretical and methodological aspects of EPR, the main technique employed in this work. Detailed descriptions including technical considerations and applications of EPR spectroscopy can be found in Refs. ¹⁻⁵. The treatment of systems with multiple exchange-coupled spins by means of an effective spin Hamiltonian and the spin projection formalism are described in detail in the following chapters, particularly in Chapter 4, with emphasis on its application to EPR experiments on oligomeric Mn complexes, such as in the OEC; see also Ref. ⁶.

3.1 The Spin Hamiltonian

EPR spectroscopy can provide detailed information on the electronic structure of systems that exhibit an electron spin S , such as radicals or paramagnetic transition-metal ions, since the respective magnetic parameters are encoded in the electronic wave function. The energy of all states of a quantum-mechanical system can be described using the Hamiltonian formalism, which can be employed for the analysis of EPR spectra. For a system of electronic and nuclear spins, as investigated in this work, the spin Hamiltonian \hat{H} , first formulated by Abragam and Pryce,⁷ operates on the wave function of the bound electrons. It comprises the following operators for the interactions of the electronic and nuclear spins with an applied magnetic field and with each other:

$$\hat{H} = \hat{H}_{EZ} + \hat{H}_{ZFS} + \hat{H}_{EE} + \hat{H}_{HF} + \hat{H}_{NZ} + \hat{H}_{NQ}. \quad (2.1)$$

The individual terms for (i) the electron Zeeman interaction \hat{H}_{EZ} , (ii) the fine structure interaction or zero-field splitting \hat{H}_{ZFS} , (iii) the electron exchange interaction \hat{H}_{EE} , (iv) the hyperfine

interaction \hat{H}_{HF} , (v) the nuclear Zeeman interaction \hat{H}_{NZ} and (vi) the nuclear quadrupole interaction \hat{H}_{NQ} are detailed in the following sections.

A basis set that describes a system of n spins of unpaired electrons and k nuclear spins can be built as the product of the eigenstates of the interacting spins, *i.e.* their uncoupled wave functions, and takes the form:

$$|S_1 \dots S_n M_{S,1} \dots M_{S,n} I_1 \dots I_k M_{I,1} \dots M_{I,k}\rangle, \quad (2.2)$$

with S_i being the electron spin quantum numbers, $M_{S,i} = S_i, S_i-1, \dots, 1-S_i, -S_i$ the corresponding magnetic sublevel quantum numbers, *i.e.* their projection on the axis of a static magnetic field, and I_i representing the nuclear spins and $M_{I,i} = -I_i, 1-I_i, \dots, I_i-1, I_i$ their magnetic sublevels. For the coupled spin system, it is inconvenient to use the basis set described above. A second basis, which describes the eigenstates of the coupled spin manifold, represents a linear combination of the original basis yielding weights corresponding to the eigenfunctions. This is obtained by diagonalization of the spin Hamiltonian matrix, *i.e.* the spin Hamiltonian applied to the original basis.

3.1.1 The Electron and Nuclear Zeeman Interactions

The Zeeman interaction is the interaction between the magnetic (dipole) moment $\vec{\mu}$ of an electron or a nuclear spin and an external static magnetic field \vec{B}_0 . The Hamiltonian describing the electron Zeeman interaction is:

$$\hat{H}_{\text{EZ}} = \beta_e \vec{B}_0 \cdot \hat{g} \cdot \vec{S}, \quad (2.3)$$

where β_e is the Bohr magneton. A magneton is a proportionality constant in units of $\vec{\mu}$. \hat{g} represents the interaction matrix, which describes the magnetic moment associated with a given spin and is dimensionless. As $\vec{\mu}$ in the most general case depends on the specific spatial orientation of the molecule considered, the corresponding \hat{g} is an anisotropic 3×3 matrix in the laboratory frame. Same as the other matrices for the different interactions (see below), the \hat{g} matrix can be converted by rotation into a form in which all non-diagonal elements are 0, termed the principal axes coordinate system or, especially in case of the \hat{g} matrix, the molecular frame. It is defined by its diagonal elements g_x , g_y and g_z , called principal components, and the three Euler angles α , β and γ of the rotation.

For a free electron, the \hat{g} matrix represents its isotropic, *i.e.* scalar g factor $g_e \approx 2.0023$. However, for bound electrons, the ground state, of which the orbital angular momentum \vec{L} is usually quenched, interacts with excited states. This leads to admixing of the excited-state orbital angular momentum \vec{L} , described in the resulting Hamiltonian in equation 2.4. As a consequence, the g factor deviates from g_e and, unless the spatial distribution of contributing orbitals is symmetric, it becomes anisotropic.

$$\hat{H}_{\text{EZ}} = \beta_e \vec{B}_0 \cdot (\vec{L} + g_e \cdot \vec{S}) + \lambda \vec{L} \cdot \vec{S}. \quad (2.4)$$

$\lambda \vec{L} \cdot \vec{S}$ is the spin-orbit coupling term with λ being the effective spin-orbit coupling constant. The relativistic nature of the spin-orbit interaction results in non-linearly increasing λ with elementary mass of the spin carrying center. While it is comparatively small for elements of the first and second row, and thus for organic radicals, it becomes increasingly significant for transition metals and lanthanides. Since this perturbation is inversely proportional to the energy difference between the interacting orbitals, its contribution gets significantly larger with increasing degeneracy of the orbitals.

The Hamiltonian for the nuclear Zeeman interaction is:

$$\hat{H}_{\text{NZ}} = -\beta_n \vec{B}_0 \cdot \hat{g}_n \cdot \vec{I} = -g_n \beta_n \vec{B}_0 \cdot \vec{I}, \quad (2.5)$$

where β_n is the nuclear magneton. Since this is ≈ 1800 times smaller than the Bohr magneton, the deviation from the nuclear g_n factor and the anisotropy of the interaction are not resolved in EPR experiments, such that the isotropic g_n can be used throughout.

3.1.2 The Fine Structure or Zero-Field Splitting

In spin systems with several unpaired electrons, *e.g.* molecules in a triplet state, transition-metal ions or lanthanides, a strong interaction of the magnetic dipole moments of the individual electron spins allows them to be described by means of a single effective total spin S . The interaction breaks the degeneracy of the total spin states S and their magnetic sublevels M_S in the energy ladder. This splitting is independent of an external magnetic field; *i.e.*, it is present also at zero field. The energy of the interaction for a spin $S > 1/2$ state can be expressed by the following Hamiltonian. Its form is analogous to the Hamiltonian describing the through-space dipolar coupling of two different spins:

$$\hat{H}_{\text{ZFS}} = \vec{S} \cdot \hat{d} \cdot \vec{S}. \quad (2.6)$$

\hat{d} is a second-rank tensor, which is symmetric and can be diagonalized in its principal axes system. Since the fine structure interaction has no isotropic component, the diagonalized tensor is traceless. Thus, the principal components d_x , d_y and d_z , which define the energy splitting of the M_S sublevels of the spin manifold S at zero field, are not independent and can be expressed in terms of two parameters D and E :

$$d_x = \frac{1}{3}D + E, \quad d_y = \frac{1}{3}D - E, \quad d_z = -\frac{2}{3}D, \quad (2.7)$$

respectively:

$$D = \frac{3}{2}d_z, \quad E = \frac{1}{2}(d_x - d_y). \quad (2.8)$$

The fine structure splitting can also be conceived as the interaction between the electric quadrupole moment, associated with spins $> 1/2$, and the electric-field gradient, thus as the electronic quadrupole interaction. As for the deviations of the \hat{g} matrix from g_e , it originates predominantly from spin-orbit coupling. To first order, it does not affect the energy difference between levels $+M_S$ and $-M_S$, thus also not the energy of the allowed transition between $M_S = 1/2$ and $-1/2$. Thus, for half-integer spin systems, there is always an allowed transition that is not affected by the fine structure term to first order and, as such, readily observable by EPR. In contrast, for transitions involving sublevels of increasing $|M_S|$, the anisotropic broadening increases. With decreasing symmetry of the ligand sphere, the fine structure term can become the dominant interaction at commonly used microwave (mw) frequencies. Thus, EPR experiments at high field/high frequency can be required in order to resolve the signals of such systems over their entire range, especially for integer spin species.

3.1.3 The Electron Exchange Interaction

Quantum-mechanics require the electronic wave function to be anti-symmetric with respect to the exchange of electrons in overlapping orbitals. This results in a difference in the average electrostatic or Coulomb interaction for states with parallel and antiparallel spins and thus in their respective energies. The interaction can be described by the Heisenberg exchange Hamiltonian of the following form:

$$\hat{H}_{EE} = -2J\vec{S}_1 \cdot \vec{S}_2. \quad (2.9)$$

The exchange interaction has an often dominant isotropic and an anisotropic part, the latter of which results from spin-orbit coupling and cannot be distinguished from the anisotropic dipole-dipole interaction in experiments. Thus, it is usually not considered, such that the interaction matrix \hat{J} can be expressed by a scalar coupling constant J , and the exchange interaction is generally conceived as the isotropic component of spin-spin interactions.

A negative J represents the case of antiferromagnetic interaction in a weak bonding situation, while ferromagnetic coupling in a weak antibonding situation is represented by a positive J . Since the exchange energy generally decreases exponentially with increasing distance r , and thus faster than the dipole-dipole energy with r^3 , at longer distances, usually above 1.5 nm, the latter will dominate. In addition to direct Heisenberg exchange, indirect super-exchange interaction, described by the same Heisenberg-exchange term, can also proceed via an orbital overlap of a common binding partner of the spin-carrying centers. In most cases, direct exchange, often the dominant contribution, is antiferromagnetic, whereas super-exchange contributions can be either antiferromagnetic or ferromagnetic, depending on the specific bonding situation. If the spin coupling is strong enough, the system is more conveniently described by an effective total spin.

3.1.4 The Hyperfine Interaction

The hyperfine interaction comprises the isotropic and the anisotropic interactions between an electron and a nuclear spin. Hence, in the corresponding Hamiltonian, the resulting hyperfine interaction matrix \hat{a} can be separated into a coupling constant a_{iso} for the isotropic part and an interaction matrix \hat{a}_{aniso} for the anisotropic component:

$$\hat{H}_{\text{HF}} = \vec{S} \cdot \hat{a} \cdot \vec{I} = \vec{S} \cdot (a_{\text{iso}} + \hat{a}_{\text{aniso}}) \cdot \vec{I} = \hat{H}_{\text{FC}} + \hat{H}_{\text{DD}}. \quad (2.10)$$

The anisotropic component is the electron-nuclear dipole-dipole interaction, described by the Hamiltonian:

$$\hat{H}_{\text{DD}} = \vec{S} \cdot \hat{a}_{\text{aniso}} \cdot \vec{I} = \frac{\mu_0}{4\pi\hbar} g_e \beta_e g_n \beta_n \left[\frac{3(\vec{S} \cdot \vec{r})(\vec{r} \cdot \vec{I})}{r^5} - \frac{\vec{S} \cdot \vec{I}}{r^3} \right], \quad (2.11)$$

in which μ_0 is the vacuum permeability, h the Planck constant, and the vector \vec{r} is the difference between the position vectors of the point dipoles. The interaction matrix \hat{a}_{aniso} is traceless and symmetric in its principal axes system.

For spin density located in s orbitals, due to its spherical symmetry, the average dipole-dipole interaction is expected to cancel out and the resulting hyperfine coupling to be zero. However, at the nucleus, the equation 2.11 is not valid as $r = 0$. The spherical average of the magnetic field it experiences is not zero, resulting in an isotropic hyperfine splitting of the magnetic sublevels, termed Fermi contact interaction, the energy of which is defined by the Hamiltonian:

$$\hat{H}_{\text{FC}} = a_{\text{iso}} \vec{S} \cdot \vec{I} = \frac{2\mu_0}{3h} g_e \beta_e g_n \beta_n |\Psi_0(0)|^2 \vec{S} \cdot \vec{I} = \frac{1}{3} \text{trace}(\hat{a}), \quad (2.12)$$

In the case of a spin originating primarily from an unpaired electron in a p, d or f orbital, non-zero spin density at the nucleus arises due to spin polarization, resulting in the presence of an isotropic hyperfine component, as well.

3.1.5 The Nuclear Quadrupole Interaction

Nuclei with a spin $I > \frac{1}{2}$ exhibit a charge distribution of non-spherical symmetry, which gives rise to a nuclear electric quadrupole moment Q . It interacts with the electric field gradient, which originates from the electrons and nuclei in close vicinity. In analogy to the fine structure term (the quadrupole interaction of electron spins), the Hamiltonian for the electric quadrupole interaction of nuclei can be expressed as:

$$\hat{H}_{\text{NQ}} = \vec{I} \cdot \hat{P} \cdot \vec{I}, \quad (2.13)$$

Typically, the nuclear quadrupole interaction is parameterized in its principal axes system, in which the nuclear quadrupole interaction matrix \hat{P} is traceless, as:

$$\hat{H}_{\text{NQ}} = P_x \hat{I}_x^2 + P_y \hat{I}_y^2 + P_z \hat{I}_z^2 = P_z \left[\left(3\hat{I}_z^2 - I(I+1) \right) + \eta \left(\hat{I}_x^2 - \hat{I}_y^2 \right) \right], \quad (2.14)$$

with the convention $|P_z| \geq |P_y| \geq |P_x|$ and the asymmetry parameter defined as:

$$\eta = \frac{P_x - P_y}{P_z}, \quad (2.15)$$

such that $0 \leq \eta \leq 1$. The principal component of largest absolute value is given by:

$$P_z = \frac{e^2 Q q}{2I(2I-1)\hbar}. \quad (2.16)$$

eq is the largest component of the electric field gradient at the nucleus.

To describe a nuclear quadrupole interaction, generally, the parameters $\frac{e^2Qq}{h}$ and η are given, which thus relate to the diagonal matrix by:

$$\hat{P} = \frac{P_z}{2} \begin{pmatrix} -(1-\eta) & 0 & 0 \\ 0 & -(1+\eta) & 0 \\ 0 & 0 & 2 \end{pmatrix} = \frac{e^2Qq}{4I(2I-1)h} \begin{pmatrix} -(1-\eta) & 0 & 0 \\ 0 & -(1+\eta) & 0 \\ 0 & 0 & 2 \end{pmatrix}. \quad (2.17)$$

3.2 EPR Spectroscopy

Transitions between spin states of different energies according to the spin Hamiltonian, described in the above section, can be induced by the absorption of photons associated with an oscillating magnetic field the energy of which equals the transition energy. In EPR spectroscopy, linearly polarized mw or radio frequency (rf) radiation are applied to excite electron and nuclear spin transitions, respectively (Figure 2.1A). In a basic EPR experiment, the spectrum is mostly obtained employing mw radiation at a constant frequency, as a function of an external magnetic field B_0 . This comes about from technological aspects of mw sources and the use of resonators of constant size, in which the samples are placed, for sensitivity enhancement. The absorption of mw power is detected when the mw energy $h\nu$ matches the field-dependent energy difference ΔE between the states, which can be expressed by the resonance condition:

$$h\nu = \Delta E = g_{\text{eff}} \beta_e B_0, \quad (2.18)$$

where g_{eff} is the effective g value at which the transition appears in the spectrum. (Since interactions other than the Zeeman term are independent of B_0 , the resonance condition can only be applied at high fields where the Zeeman energy is the dominant contribution to ΔE .) The condition results from the selection rule $\Delta M_S = 1$, $\Delta M_I = 0$ for allowed transitions in effect for the EPR experiment. The absorption gives rise to a line, which displays homogenous broadening due to transverse (T_2) relaxation processes besides possible other broadening mechanisms (inhomogenous, heterogenous). The most commonly employed mw frequency bands are X- (≈ 9 GHz), Q- (≈ 35 GHz) and W-band (≈ 94 GHz), with a tendency over the last decades of going towards increasing frequencies, which allow better resolution of the g tensor and thus also an improvement of orientation selectivity.

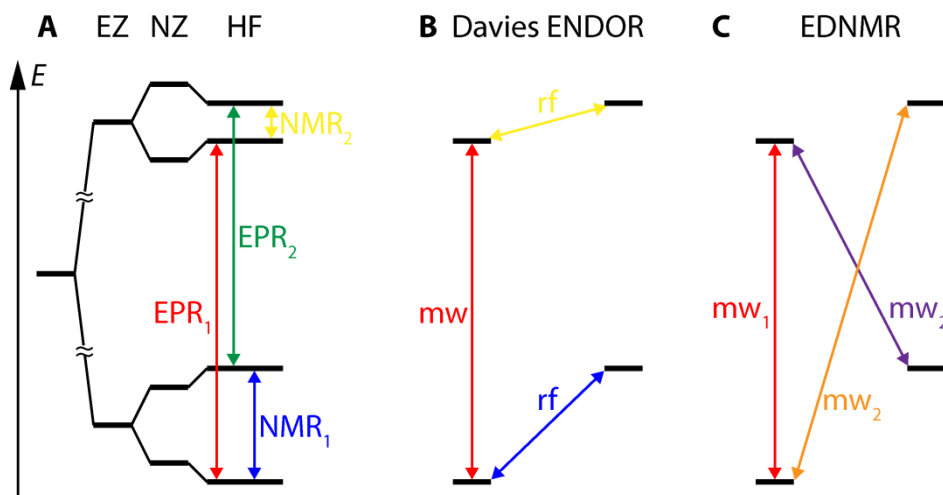


Figure 2.1. Schematics of the energies (E) of and transitions between spin state sublevels in a system with an electron spin $S = \frac{1}{2}$ and a nuclear spin $I = \frac{1}{2}$. **A:** Splitting of the spin state multiplets due to the electron Zeeman (EZ), nuclear Zeeman (NZ) and hyperfine (HF) interactions along with the allowed EPR and nuclear magnetic resonance (NMR) transitions between the sublevels. The splitting of the electron Zeeman levels in relation to the nuclear Zeeman energy is larger than depicted in the diagram. **B:** Spin state transitions in a Davies ENDOR experiment (section 3.2.2.3, Figure 2.2). The selective mw preparation pulse inverts the populations of the states associated with the excited EPR transition, the mixing rf pulse drives a spin polarization transfer via the NMR transitions, and the mw Hahn echo sequence probes the magnetization in the z direction. **C:** Spin state transitions in an EDNMR experiment (section 3.2.2.3, Figure 2.2). The mixing mw_2 pulse induces a spin polarization transfer by pumping allowed and forbidden transitions, probed by the mw_1 Hahn echo sequence.

3.2.1 The Continuous-Wave (CW) EPR Experiment

The CW EPR experiment owes its name to the continuous irradiation of the sample to drive EPR transitions. In order to suppress noise and enhance the sensitivity of the measurement, sinusoidal field modulation combined with phase-selective detection of the modulated signal is employed. As a consequence, a CW EPR spectrum is recorded and usually presented in the form of the first derivative of the mw absorption signal.

Absorption of mw power by the spin ensemble requires a difference of populations in spin multiplet sublevels of lower and higher energy, to which the signal is proportional. In a two-level system, these would be the states α ($M_S = +\frac{1}{2}$) and β ($M_S = -\frac{1}{2}$), respectively. The population difference ΔN and thus the signal intensity are then related to the absolute temperature T according to the following equation, thus diminishing with increasing T :

$$\Delta N = N \cdot \frac{1 - \exp\left(-\frac{\Delta E}{k_B T}\right)}{1 + \exp\left(-\frac{\Delta E}{k_B T}\right)}, \quad (2.19)$$

where k_B is the Boltzmann constant. At high temperatures and weak magnetic fields, where ΔN is inversely proportional to T , this can be approximated by Curie's Law as:

$$\Delta N = \frac{\Delta E}{2k_B T}. \quad (2.20)$$

The amplitude of the oscillating magnetic field B_1 of the mw radiation is proportional to the square root of the mw power P_{mw} . Thus, the EPR signal is expected to increase linearly with the square root of P_{mw} , which is indeed the case at low powers and high temperatures at which longitudinal T_1 relaxation is fast enough. However, at too high powers, the transition becomes saturated, such that the signal intensity does not show this proportionality anymore and eventually decreases linearly with increasing power. For maximum intensity, and to obtain unbiased line shapes, one aims to conduct the CW experiment in the unsaturated regime. For spins relaxing too slowly, the unsaturated regime can also be reached by raising the sample temperature, lowering T_1 . However, this happens at the expense of signal intensity, according to equation 2.19. Hence, these effects have to be balanced when choosing the experimental settings.

3.2.2 Pulse EPR Experiments

In the pulse EPR mode, instead of continuous irradiation, short mw and rf pulses of ns to μ s length and high power of several hundred W up to several kW are applied to the samples to induce spin transitions. For a broad description of the technique including a quantum mechanical explanation, see for example Ref. ². The spin dynamics induced by the pulses can be visualized using the vector model, which describes the evolution of the net magnetization vector \vec{M} in time. The macroscopic magnetization of a spin ensemble represents the summed vectors of their individual magnetic moments in a sample. At thermal equilibrium, \vec{M} is aligned along the applied static magnetic field \vec{B}_0 , generally defined as the z axis. A mw pulse that introduces a second magnetic field \vec{B}_1 perpendicular to \vec{B}_0 and oscillating with the frequency of the transition, the Larmor frequency, can be applied. Thereby, \vec{M} is transiently reorientated away from its equilibrium orientation and precesses at the Larmor frequency around the z

axis. The system then evolves, recovering its original state due to T_1 spin-lattice relaxation processes. In pulse EPR mode, the transverse magnetization in the xy plane is detected as the signal. In the simplest pulse EPR experiment, \vec{M} is rotated 90° and the evolution of its transverse component, the free induction decay (FID), is monitored. By choosing sequences of pulses of appropriate lengths and powers, defined quantum coherences can be created, resulting in the separation of magnetic interactions to probe them selectively. This represents a great advantage over conventional EPR experiments and their inherent limitations with respect to resolution. The respective experiments, as described below, are especially helpful for systems, in which the interactions of nuclear spins are not resolved in their EPR spectra. Such superposition can be due to split lines that are present in too large number and/or lie within the EPR linewidth, defined by the comparatively short spin-spin relaxation time T_2 , and/or due to the anisotropy of an interaction. This is mostly the case for metal complexes in frozen solution, which due to their fast spin-lattice relaxation T_1 need to be measured at low temperatures, such as the OEC in PSII. Selective probing of nuclear transitions presented in a frequency-domain spectrum tremendously reduces the number of lines and, depending on the experiment, can be accompanied by their linewidth being governed by T_1 instead of the shorter T_2 . Basically, such spectra of a $S = \frac{1}{2}$ system display resonances at transition frequencies $\nu_{\alpha/\beta}$ according to:

$$|\nu_{\alpha/\beta}| = \nu_n \pm \frac{a}{2}. \quad (2.21)$$

Thus, they are centered at half the absolute hyperfine coupling $|a|$ and split by twice the Larmor frequency ν_n in the low-field limit ($2\nu_n < |a|$), and are centered at ν_n and split by $|a|$ in the high-field limit ($|a| < 2\nu_n$). However, this pattern can be further complicated by the presence of a perturbation due to the nuclear quadrupole interaction for nuclei of $I > \frac{1}{2}$.

3.2.2.1 Electron Spin Echo (ESE)-detected EPR

An EPR spectrum can be obtained by employing mw pulses according to the Hahn echo sequence of pulses,⁸ generating an electron spin echo (Figure 2.2). A 90° or $\pi/2$ pulse of the respective length and power rotates the magnetization vector \vec{M} into the xy plane. There, it dephases due to local field inhomogeneities or magnetic interactions entailing slightly different Larmor frequencies of the individual spins. After a time interval τ , a second pulse π of twice the length and same relative direction reverses this inhomogeneous dephasing of the spin packet such that the magnetic moments are refocused after 2τ , resulting in a detectable

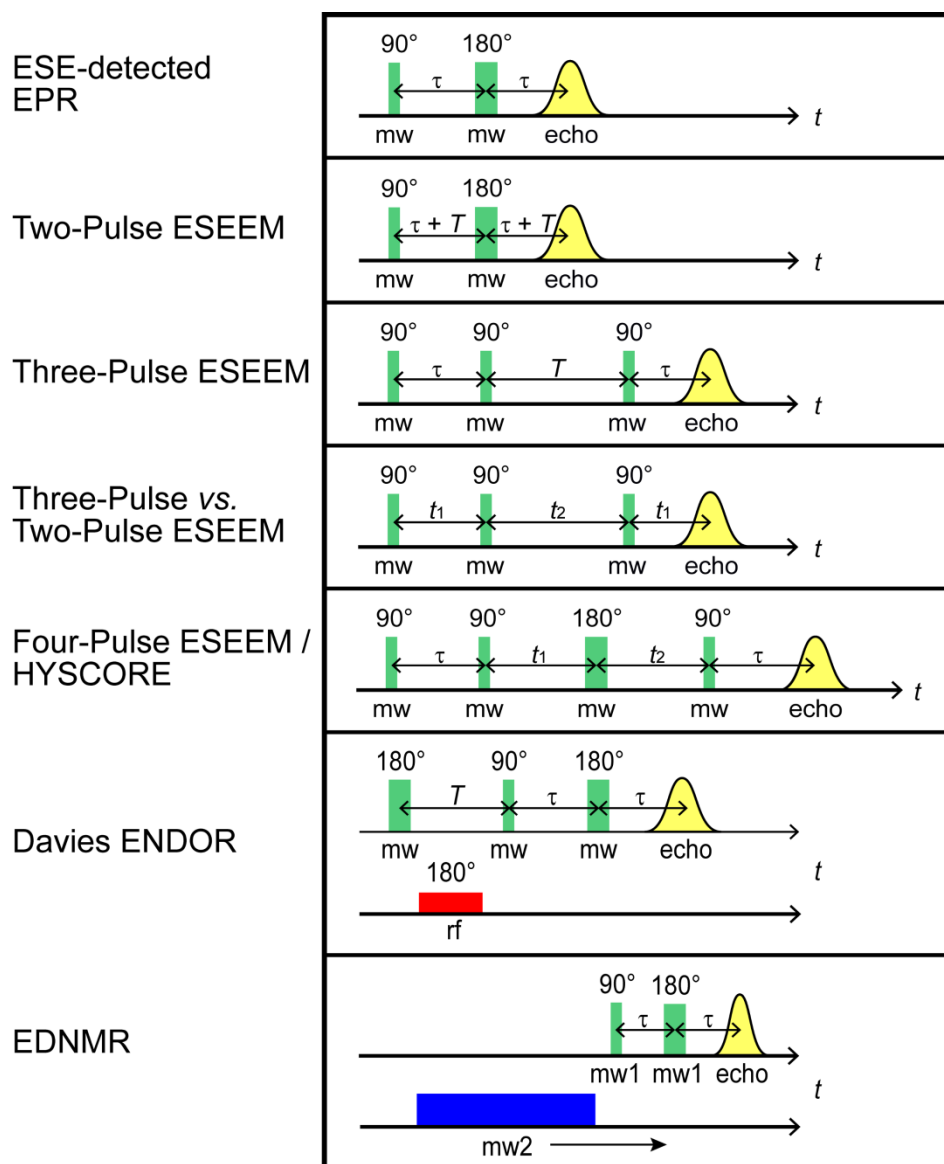


Figure 2.2. Pulse sequences for the experiments employed in this work and described in the sections below. By these, spectra are generated via variation of the strength of the magnetic field B_0 (field-swept electron spin echo, FS-ESE), by incrementing the evolution times T , t_1 and t_2 in the respective ESEEM experiments or the frequencies of the rf or mw2 pulses (ENDOR, EDNMR), or by combinations thereof (e.g. field-dependent ENDOR or EDNMR). In the sequence diagrams, the vertical dimension corresponds to pulse power and echo signal, respectively

echo. The pulse sequence $\pi/2$ - τ - π - τ -echo can be applied at multiple field positions B_0 over a chosen range, such that the integrated echo intensities represent the signal intensity in the field-swept EPR absorption spectrum. Echo decay occurs due to transverse dephasing processes that cannot be restored by the refocussing π pulse, such as T_2 spin-spin relaxation be-

sides others. The time constant thereof, the phase memory time T_2' , determines the homogeneous spectral line-width.

3.2.2.2 Two- and Three-Pulse ESE Envelope Modulation (ESEEM) and Hyperfine Sublevel Correlation (HYSCORE)

The ESEEM technique represent a class of experiments to probe transition frequencies of nuclear spins via their coupling to an electron spin, in particular weakly interacting nuclei, *i.e.* mainly such of low nuclear g_n factor. The general principle of the method is based upon the fact that the relaxation-induced decay of an ESE over time is superimposed by modulations with transition frequencies of interacting nuclear spins. The modulation depth scales with the dipolar component of the electron-nuclear coupling, hence with the anisotropy of the hyperfine tensor. For nuclei exhibiting only small hyperfine anisotropy, this can hamper the application of the ESEEM technique and make it necessary to take advantage of other experiments. The modulations comprise besides the allowed also forbidden transitions due to a possible coherence transfer as a result of the mixing of states by the pulse pattern. A frequency-domain spectrum can be obtained by Fourier transformation of the modulations of the time-domain traces after subtraction of the relaxation decay curves. It contains resonances at frequencies encoding information on the nuclear Zeeman energy, *i.e.* on the type of nuclide, the hyperfine interaction and the nuclear quadrupole interaction.

An echo decay, modulated by the nuclear transition frequencies, is generated by recording the integrated echo intensity as a function of increasing evolution times, which are periods between applied pulses. The simplest method is the two-pulse ESEEM experiment, in which the inter-pulse delay τ in a Hahn echo sequence is varied (Figure 2.2).⁹ Along with the basic nuclear transition frequencies, also the sums and differences of these are observed. The time-domain signal decays with the phase memory time T_2' of the electron spin, which thus governs the linewidth, as well as the signal intensity. The resolution is therefore usually distinctly lower than in experiments that directly excite nuclear magnetic resonance (NMR) transitions, such as ENDOR, as these are limited by the normally significantly longer $T_{2,n}'$ of the nuclear spin itself.

This limitation can be overcome by the three-pulse ESEEM experiment.¹⁰, which follows the decay of a stimulated echo⁸ instead of a Hahn echo over time. This is generated by a sequence of three $\pi/2$ pulses, of which the first and third are followed by a constant inter-pulse delay τ and the varying evolution time T lies between the second and the third pulse (Figure 2.2). As a

consequence, dephasing only occurs during a shorter time 2τ , when \vec{M} precesses in the xy plane, but not during the evolution period, when \vec{M} is aligned longitudinally along the z axis. The encoded information is preserved and then recovered by the third $\pi/2$ pulse. During T , the magnetization and thus the detected echo decays with T_1 , which is usually significantly longer than T_2' , *i.e.* on the order of the $T_{2,n}'$ time of nuclear spins. Hence, the linewidth is clearly smaller and the signal-to-noise ratio increased as compared to two-pulse ESEEM spectra, improving the applicability of three-pulse ESEEM also for systems with short T_2' relaxation times. A further effect is that the spectra are simplified due to the absence of sum and difference frequencies. However, three-pulse ESEEM inherently suffers from blind spotting, suppressing modulations of frequencies that are integer multiples of $1/\tau$. Therefore, the experiments are typically conducted at several values for τ to identify and minimize artifacts from blind spots. On the other hand, this effect can also be used advantageously to suppress interfering transitions from background signals, such as large proton signals stemming from (matrix) water or as a source of additional information on the transition frequencies.

This information is most readily accessible in the two-dimensional three-pulse *vs.* two-pulse experiment.¹¹ In the three-pulse ESEEM sequence, the inter-pulse distances $\tau = t_1$ and $T = t_2$ are incremented independently in two dimensions (Figure 2.2), in a way that the traces of incrementing T represent three-pulse ESEEM experiments in t_2 , the τ value of which is varied in the other dimension t_1 . Fourier transformation in both dimensions yields the two-dimensional frequency-domain spectrum containing cross-peaks at the correlated frequencies, which simplifies peak assignments considerably.

HYSCORE is a two-dimensional four-pulse ESEEM experiment based on the three-pulse ESEEM sequence.^{12,13} A mixing pulse is inserted between the second and the third $\pi/2$ pulse (Figure 2.2) to create correlations between the NMR transitions of the electron spin manifolds M_S , between which the coherences of the nuclear spins are switched. To acquire the two-dimensional time-domain modulation signal, the stimulated echo amplitude is observed as a function of the independently varied evolution times t_1 and t_2 employing a constant τ . The quadrant in the two-dimensional frequency-domain spectrum in which cross peaks are observed depends on their nuclear Larmor frequency ν_n and hyperfine coupling constant a . For the weak coupling case ($\nu_n > |a|/2$), where the nuclear transition frequencies associated with the different electron spin manifolds have the same sign, the cross peaks appear in the second quadrant (+,+). In contrast, in the strong coupling case ($\nu_n < |a|/2$), where the frequencies have opposite signs, the peaks appear in the first quadrant (-,+). As a result of a non-ideal π inver-

sion pulse, additional autocorrelation peaks can appear along the diagonal of the (+,+) quadrant. Same as the three-pulse ESEEM experiment, HYSCORE is subject to blind spotting.

3.2.2.3 Multi-Resonance Spin-Polarization-Transfer Experiments: Davies Electron-Nuclear Double Resonance (ENDOR) and Electron-Electron Double Resonance (ELDOR)-detected NMR (EDNMR)

In contrast to ESEEM, a coherence transfer technique, other EPR methods, such as ENDOR and EDNMR, utilize the transfer of spin polarization between sublevels split by Zeeman and hyperfine interactions to probe nuclear spin interactions. The induced altering of the populations of these states is detected by a change in electron spin echo intensity as a function of incident radiation energies. In this way, spectra in the frequency domain are measured directly.

The ENDOR technique makes use of rf irradiation of the sample to excite allowed NMR transitions according to the selection rule $\Delta M_S = 0$, $\Delta M_I = 1$ as a function of the rf frequency. It is noted that continuously sweeping the rf frequency can introduce heating artifacts in the ENDOR spectra; hence, it is ideally varied stochastically. In the Davies ENDOR experiment (Figures 2.1B and 2.2),¹⁴ a selective preparation mw pulse inverts the spin population of the EPR transitions within a limited spin packet, which can be regarded as burning a hole into the EPR envelope. During the following mixing period, the magnetization aligned along the z-axis is subject to T_1 relaxation. At this time, a selective rf pulse of several μs length is applied to drive NMR transitions. Only in case the rf frequency is on resonance with an NMR transition, it inverts the magnetization of nuclear spin states within the coupled M_S spin manifold. This results in the leveling of the population difference of the excited EPR transition. During the following detection period, the magnetization in z direction is probed by a Hahn echo sequence. For on-resonant rf frequencies, ideally, the echo integral becomes zero. However, the gain in resolution as compared to EPR is at the expense of sensitivity, as the ENDOR effect is distinctly less intense than the EPR effect. It is limited (i) because the achievable rf pulse is usually insufficient to excite the entire nuclear spin ensemble, and (ii) by its dependence on the T_1 relaxation time.

The power of the oscillating magnetic field component of the rf pulse can exhibit variations with frequency, depending on the rf setup, which requires powerful amplifiers for the rf radiation. In general, the ENDOR intensity varies with the size of the hyperfine interactions, as well as the size of the nuclear spin, suppressing resonances from small couplings in favor of

larger ones. Furthermore, detection of small hyperfine interactions affords a highly selective inversion pulse as the technique is insensitive to couplings within the linewidth of the spectral hole created. Thus, the Davies ENDOR experiment is most applicable for nuclei with significant hyperfine interactions, rendering it highly suited for the study of the strong couplings from the ^{55}Mn ions of the OEC. The Mims ENDOR experiment¹⁵ in contrast is superior for the detection of smaller hyperfine couplings. However, as it is based on a stimulated echo, same as three-pulse ESEEM experiments, it suffers from blind spotting.

In the EDNMR experiment, nuclear transition frequencies are measured indirectly.¹⁶ For this, a soft and thus highly selective pulse $\text{mw}2$ in the second channel is swept around the resonance frequency $\nu_{\text{mw}1}$ to pump transitions, both allowed EPR and forbidden $\Delta M_S = 1$, $\Delta M_I = 1$ ones, by the latter of which both the electron and nuclear spin states are altered (Figures 2.1C and 2.2). This is followed by a Hahn echo sequence in the first channel $\text{mw}1$ at the resonance frequency $\nu_{\text{mw}1}$. On-resonance, the mixing mw pulse causes a depolarization of the probed EPR transition and thus a decrease of echo intensity. In the frequency spectrum, this appears as the central hole of Lorentzian lineshape around $\nu_{\text{mw}1}$, along with smaller side holes from the excited forbidden transitions, with the corresponding $\Delta M_I = 1$ transition frequencies required to be smaller than the homogeneous EPR linewidth, positioned symmetrically around $\nu_{\text{mw}1}$. Their distance $\Delta\nu = \nu_{\text{mw}2} - \nu_{\text{mw}1}$ to the resonance frequency corresponds to the nuclear transition frequencies.

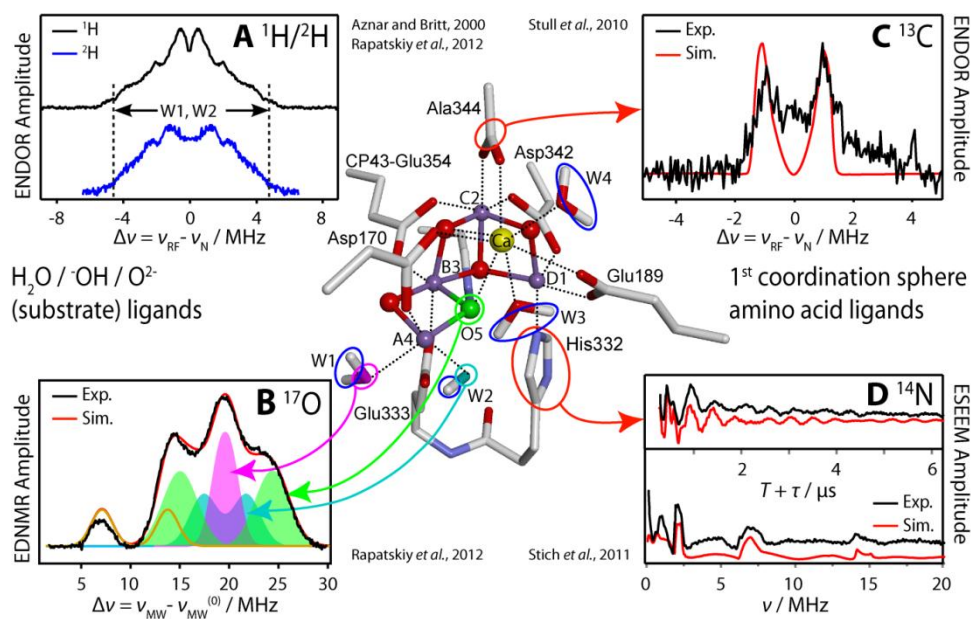
By performing the EDNMR experiment at high field/high frequency, even signals from nuclei of low nuclear g_n factor that, in addition, are weakly interacting with the electron spin ($a/2 < \nu_n$) can be resolved from the central hole. Furthermore, a high field leads to spectral separation of nuclides with similar nuclear g_n factors and thus reduces complications due to signal overlap. On the other hand, in three-pulse ESEEM and ENDOR, blind spotting or different optimal rf pulse lengths, respectively, may prevent the simultaneous detection of nuclear species. Altogether, W-band EDNMR is thus particularly helpful for the study of ^{17}O interactions in metal complexes.^{17,18} For nuclei of $I > 1/2$, exhibiting a nuclear quadrupole moment, also multiple-quantum transitions are excited and observed. They are centered around the respective scalar multiple of the Larmor frequency and split by the same multiple of the hyperfine coupling. Especially for systems that suffer from short T_1 times, EDNMR is more sensitive than ESEEM or ENDOR, which are more significantly restrained by T_1 relaxation.^{17,18}

3.3 References

- (1) Abragam, A.; Bleaney, B. *Electron Paramagnetic Resonance of Transition Metal Ions*; Clarendon Press: Oxford, 1970.
- (2) Schweiger, A.; Jeschke, G. *Principles of pulse electron paramagnetic resonance*; Oxford University Press: Oxford, 2001.
- (3) Weil, J. A.; Bolton, J. R. *Electron paramagnetic resonance : elementary theory and practical applications*; 2nd ed.; John Wiley & Sons, Inc.: Hoboken, NJ, 2007.
- (4) Möbius, K.; Savitsky, A. *High-Field EPR Spectroscopy on Proteins and their Model Systems: Characterization of Transient Paramagnetic States*; Royal Society of Chemistry: Cambridge, UK, 2008.
- (5) *Multifrequency Electron Paramagnetic Resonance: Theory and Applications*; Misra, S. K., Ed.; Wiley-VCH Verlag & Co. KGaA: Weinheim, 2011.
- (6) Bencini, A.; Gatteschi, D. *EPR of Exchange Coupled Systems*; Springer: Berlin, 1990.
- (7) Abragam, A.; Pryce, M. H. L. *Proc. R. Soc. Lond. A* **1951**, *205*, 135.
- (8) Hahn, E. L. *Phys. Rev.* **1950**, *80*, 580.
- (9) Rowan, L. G.; Hahn, E. L.; Mims, W. B. *Phys. Rev.* **1965**, *137*, A61.
- (10) Mims, W. B. *Phys. Rev. B: Solid State* **1972**, *5*, 2409.
- (11) Merks, R. P. J.; Beer, R. D. *J. Phys. Chem.* **1979**, *83*, 3319.
- (12) Höfer, P.; Grupp, A.; Nebenführ, H.; Mehring, M. *Chem. Phys. Lett.* **1986**, *132*, 279.
- (13) Shane, J. J.; Höfer, P.; Reijerse, E. J.; Deboer, E. *J. Magn. Reson.* **1992**, *99*, 596.
- (14) Davies, E. R. *Phys. Lett. A* **1974**, *A 47*, 1.
- (15) Mims, W. B. *Proc. R. Soc. Lond. A* **1965**, *283*, 452.
- (16) Schosseler, P.; Wacker, T.; Schweiger, A. *Chem. Phys. Lett.* **1994**, *224*, 319.
- (17) Rapatskiy, L.; Cox, N.; Savitsky, A.; Ames, W. M.; Sander, J.; Nowaczyk, M. M.; Rögner, M.; Boussac, A.; Neese, F.; Messinger, J.; Lubitz, W. *J. Am. Chem. Soc.* **2012**, *134*, 16619.
- (18) Cox, N.; Lubitz, W.; Savitsky, A. *Mol. Phys.* **2013**, *111*, 2788.

Chapter 4

EPR Spectroscopy and the Electronic Structure of the Oxygen-Evolving Complex of Photosystem II



Lohmiller, T.; Ames, W.; Lubitz, W.; Cox, N.; Misra, S. K.

Appl. Magn. Reson. **2013**, *44* (6), 691-720.

© Springer-Verlag Wien 2013; with kind permission from Springer Science and Business Media. The final publication is available at Springer via <http://dx.doi.org/10.1007/s00723-012-0437-3>.

EPR Spectroscopy and the Electronic Structure of the Oxygen-Evolving Complex of Photosystem II

Thomas Lohmiller, William Ames, Wolfgang Lubitz, Nicholas Cox

Max-Planck-Institut für Chemische Energiekonversion, Stiftstrasse 34-36, D-45470 Mülheim an der Ruhr, Germany

49-208-306-3552

49-208-306-3955

nicholas.cox@cec.mpg.de

Present Address:

William Ames

Department of Chemistry & Biochemistry, Middlebury College, McCardell Bicentennial Hall, 276 Bicentennial Way, Middlebury, VT 05753, USA

Sushil K. Misra

Physics Department, Concordia University, 1455 de Maisonneuve Boulevard West, Montreal, QC H3G 1M8, Canada

Abstract This article provides an overview of the application of electron paramagnetic resonance (EPR) and related hyperfine spectroscopies for the investigation of the electronic and geometric structure of the tetramanganese cluster that constitutes the oxygen-evolving complex (OEC) of photosystem II. Starting from the spin physics of Mn ions, a quantum-mechanical description of exchange-coupled oligonuclear Mn systems is given. Then, the focus shifts to the characterization of the OEC with emphasis on the two half-integer spin states of its catalytic cycles, namely the S_0 and S_2 . The development of electronic models based on EPR and related spectroscopies, such as electron nuclear double resonance (ENDOR), is described in detail. The role of broken-symmetry density functional theory (BS-DFT) is also outlined. The characterization of Mn ligands and bound substrate waters, via electron nuclear magnetic interactions is also described. Implications for the mechanism of water oxidation catalysis are discussed.

1 Introduction

Light driven water oxidation is achieved by a single enzyme in nature, photosystem II (PS II). Despite its importance and recent advancements in structural characterization, critical details about the molecular mechanism of water oxidation by the catalytic center of PS II, the oxygen-evolving complex (OEC) are still not resolved. In view of increasing demands for clean, cheap and renewable energy, understanding nature's unique water oxidizing catalyst will be of invaluable use for the development of synthetic biomimetic water splitting catalysts (see Refs. [1-3]).

Electron paramagnetic resonance (EPR) spectroscopy is a powerful tool for the elucidation of the electronic structure and function of biomacromolecules that contain metal cofactors, e.g. metalloproteins. Manganese-containing cofactors provide a particularly rich playground as the naturally abundant nucleus (^{55}Mn , 100%) has an intrinsic magnetic moment (nuclear spin $I = 5/2$, nuclear g factor $g_n = +1.3819$). Thus, spectroscopies that probe the hyperfine interaction, such as electron nuclear double resonance (ENDOR), electron spin echo envelope modulation (ESEEM) and electron-electron double resonance (ELDOR)-detected nuclear magnetic resonance (NMR), are well suited to study these systems. In this article, we review the evolution of the electronic model of the tetramanganese core of the OEC. As a starting point, we introduce the structure and function of the OEC, leading to a description of relevant simpler (model) Mn spin systems and their EPR-spectroscopic investigations. Then, the review focuses on current electronic models of the OEC as determined from the most recent multi-frequency EPR and hyperfine spectroscopic studies combined with density functional theory (DFT) calculations. The subsequent identification of magnetically coupled exchangeable substrate waters provides information on the possible mechanism of the photosynthetic water oxidation reaction.

2 The Oxygen-Evolving Complex

2.1 Photosystem II

PS II is a multi-subunit pigment-protein super-complex found in the thylakoid membrane of organisms that perform oxygenic photosynthesis. It uses visible light (400-700 nm) to drive the oxidation of water, transferring its electrons to bound plastoquinone, reducing it to plastoquinol. Concomitant H^+ translocation across the membrane results in a proton gradient.

Plastoquinol and the H^+ gradient are further used to generate the energy carriers that are used in carbon fixation, nicotinamide adenine dinucleotide phosphate in its reduced form (NADPH) and adenosine triphosphate (ATP), respectively. Four main processes constitute PS II function: (i) Light harvesting and exciton transfer from its antenna complexes to the reaction center of PS II, (ii) excitation and charge separation of the reaction center, (iii) reduction and protonation of acceptor side plastoquinone and (iv) accumulation of oxidizing equivalents on the donor side and H_2O oxidation by the tetramanganese core of the OEC. For further details, see Refs. [4, 5].

2.2 The Catalytic Reaction Cycle of the Oxygen-Evolving Complex: the S State Cycle

As outlined above, the OEC is driven by the PS II reaction center. Photon absorption leads to an excited pigment state ($P680^*$), which initiates charge separation across the membrane. The first radical pair state $P680^+/Pheo_{D1}^-$ rapidly undergoes further electron/hole migration, leading to a cascade of subsequent radical pair states that act to stabilize the charge separated system and thus allow the comparably slow water oxidation chemistry of the OEC to occur. The oxidation of water to dioxygen is a four-electron process,



whereas photooxidation of P680 is a one-electron process. Thus, the role of the OEC can be thought of as that of an electron hole accumulator. $P680^+$ oxidizes the OEC repeatedly, one electron at a time, until the OEC has been oxidized four times. The OEC then converts water to dioxygen and resets itself to its most reduced state [6, 7]. Each net oxidation states of the Mn_4O_5Ca core of the OEC are known as the S_n states, where the index $n = 0, 1, 2, 3, 4$ represents the number of stored oxidizing equivalents in the ligated metal cluster proper (Fig. 1). S_0 represents the most reduced state, whereas the S_4 state is the most oxidized in the catalytic cycle. S_1 is the dark-stable state. The S_0 state is of sufficient reduction potential that it can be slowly oxidized via a redox-active tyrosine residue of the D2 protein, Y_D (D2-Tyr160) [8]. Y_D does not participate further in the S state cycle. Apart from the spontaneous $[S_4] \rightarrow S_0$ reaction step, all of the $S_n \rightarrow S_{n+1}$ transitions are induced by the photochemical oxidation of $P680^+$, which in turn oxidizes the OEC via the redox-active tyrosine Y_Z residue of the D1 protein (D1-Tyr161); each $S_n \rightarrow S_{n+1}$ transition passes through an intermediate $S_n Y_Z^{\bullet}$ state, wherein the oxidized tyrosine is poised to oxidize the metal cluster of the OEC.

An $[S_4]$ state different from the S_3YZ^{\bullet} state has not yet been identified. For further information, see Refs. [4, 5].

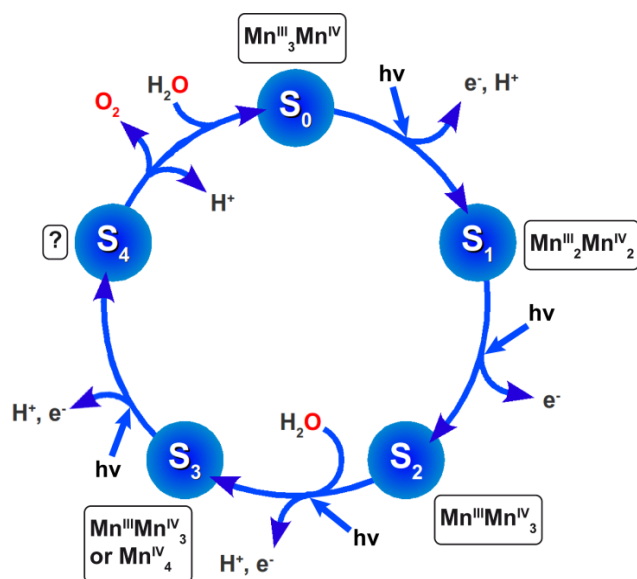


Fig. 1 The light ($h\nu$)-driven catalytic reaction cycle of the OEC with the putative valence state configurations of the Mn ions in the individual S states [9]. S_1 is stable in the dark, while S_4 decays spontaneously into S_0 , under the release of O_2 , allowing (a) new water molecule(s) to bind. Arrows indicate abstraction of an electron by YZ^{\bullet} and proton release from the OEC

2.3 The Mn_4O_5Ca core

The OEC is comprised of four manganese ions and one calcium ion [10-12]. Historically, extended X-ray absorption fine structure (EXAFS) spectroscopy was the first structural technique to provide robust structural constraints for the cluster, including Mn-Mn and Mn-Ca interatomic distances and angles (for a review, see [13]). X-ray crystallography followed these initial studies, taking a decade of effort before a atomic resolution structure was obtained. The first X-ray crystallographic were of insufficient resolution (3.8 [14] and 3.7 Å [15]) to provide a detailed picture, they nevertheless, allowed many structural motifs to be discarded. These structures resolved a ‘Y-shaped’ electron density map of the tetramanganese cluster, three Mn ions where placed in the corners around one central Mn ion, while the Ca^{2+} ion and bridging atoms could not be identified. This basic model was refined in the subsequent ‘London’ structure, at a resolution of 3.5 Å [16]. Here, a trinuclear cubane-like Mn_3O_4Ca cluster was proposed with the forth, outer Mn attached directly to one of the O vertices, similar to the cubane-like Mn_4O_4 core suggested by Brudvig and Crabtree [17]; in

the cubane proper the four Mn ions form the corners of the cuboid forming a tetramer. Subsequent structures from the Berlin groups, at 3.0 [18] and 2.9 Å [19] resolution, confirmed a '3+1' topology, but still did not allow for an assignment of the precise Mn and Ca positions and their connectivity. The same PS II crystals were also studied by polarized EXAFS which led to the development of models based on a common motif of Mn₄ connectivity, later termed the 'fused twist' topology. Finally in 2011 after more than ten years of crystallographic effort, that a PS II X-ray structure with atomic (1.9 Å) resolution, was reported [20]. Its Mn₄O₅Ca cluster clearly resolves the four Mn ions being linked via a network of five μ-oxo bridges. The cluster exhibits a distorted cuboidal topology with three Mn ions and the Ca²⁺ cofactor as well as four bridging oxygens forming the eight vertices (Fig. 2a, b). The fourth, outer Mn ion is connected to the cuboidal unit via another μ-oxo bridge to one of the Mn corners ('distorted chair'). The crystal structure allowed for an unambiguous identification of ligating amino acid residues and surrounding H₂O/OH⁻ molecules (Fig. 2a). However, corresponding X-ray absorption spectroscopy (XAS) measurements suggest the X-ray radiation dose the PS II crystal experiences during X-ray crystallographic measurement is sufficient to lead to reduction of the high-valent Mn ions and a distortion of the catalytic core [21, 22]. It is therefore, not entirely clear what S state the crystal structure represents. While the group of Pace suggests it to be in the S₁ state [23], with an overall valence state Mn^{III}₄, which in average, is 0.5 units lower than generally assumed [9, 13, 24-27], most theoretical work supports a non-physiological oxidation state below S₀ [28-30]. As a consequence, geometric models of the physiological states of the OEC have been developed by means of density functional theory (DFT) [31-33], also based on the crystal structure [28, 34, 35]. These optimized structures of the OEC poised in the S₂ state are more compact, displaying shorter Mn-Mn and Mn-O distances, consistent with earlier EXAFS results. The models typically contain either 4:1 (fused twist) or 3:2 (cubane-like) ratios of μ₂-oxo to μ₃-oxo bridges, rendering one of the Mn ions of the tetramer, the Mn^{III}, pentacoordinate (Fig. 2c, d). Both the X-ray crystallographic and DFT structures exhibit two H₂O/OH⁻ ligands bound to the remote Mn and two H₂O ligands bound to the Ca²⁺ ion.

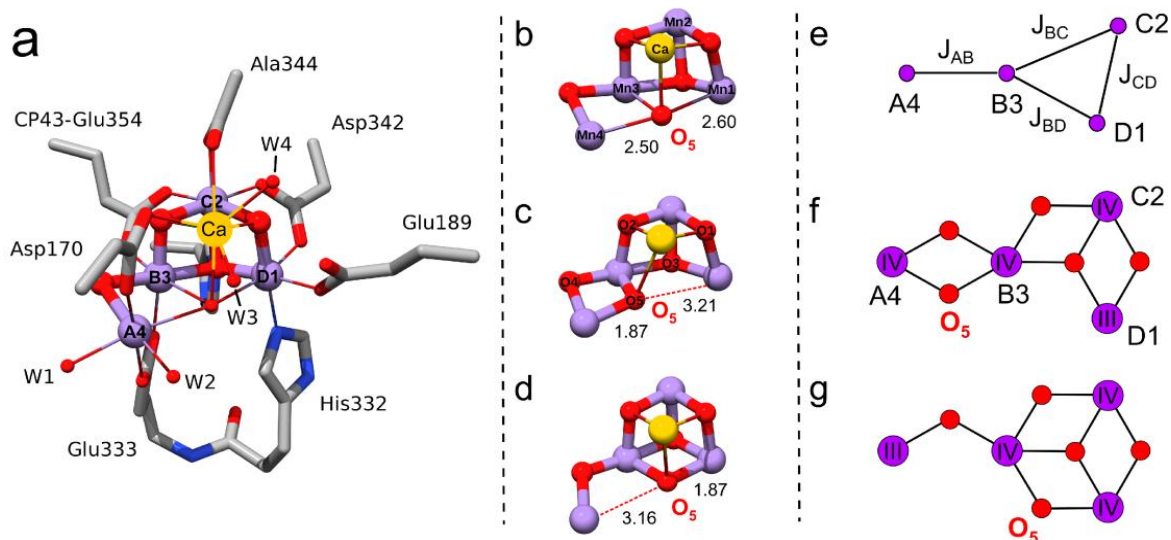


Fig. 2 **a** The X-ray crystallographic structure of the OEC in dark-adapted PS II at 1.9 Å resolution [20]. **b** The $\text{Mn}_4\text{O}_5\text{Ca}$ inorganic cluster from the crystal structure [20], as in panel a. **c** Fused twist geometry-optimized DFT structure of the $\text{Mn}_4\text{O}_5\text{Ca}$ core in the S_2 state [35]. **d** Cubane-like geometry-optimized DFT structure of the $\text{Mn}_4\text{O}_5\text{Ca}$ core in the S_2 state [35]. Structures c and d both reproduce the Mn-Mn distance constraints from EXAFS and the magnetic resonance data; see Refs. [32, 34, 35] for further details. **e** The ‘Y coupling’ scheme for the S_2 state developed from EPR/ ^{55}Mn ENDOR [9, 36, 37] (see Section 5.2.2). **f, g** Mn_4O_5 connectivities of the fused twist (c) and the cubane-like (d) core topologies. The nomenclature of the Mn ions in a, e and f combines the lettering used in earlier EPR and EXAFS spectroscopic work and the numbering from the crystal structures, as in b. W1-W4 represent $\text{H}_2\text{O}/\text{OH}^-$ ligands. Amino acids, except CP43-Glu354, are from PS II subunit D1. Mn, Ca, N, O, and C atoms are depicted in purple, yellow, blue, red, and gray, respectively.

Ca^{2+} is an essential cofactor in oxygen evolution [38-42]; its removal inhibits water splitting by blocking the OEC early in its reaction cycle and leads to a perturbed EPR signal. It has been hypothesized that (i) calcium acts in water splitting by binding a substrate water molecule [43-46], as evidenced by the mass spectroscopic measurements of ^{18}O -labeled dioxygen release [47, 48], and (ii) it modifies the redox potential of the OEC, perhaps by controlling proton-coupled electron transfer to Y_Z^* [13, 49, 50]. Sr^{2+} is the only surrogate that is capable of restoring water splitting after Ca^{2+} removal [38, 51-53]. This may be due to a combination of two important requirements that the surrogate must match: (i) the approximate size and (ii) the Lewis acidity [54] of Ca^{2+} . Chloride ions are also essential for photosynthetic oxygen evolution [48, 55, 56]. Two Cl^- binding sites have been identified at, or near, the site of water splitting. The Cl^- ions, however, do not directly coordinate the OEC [57-61]. Cl^- depletion blocks OEC turnover, just as Ca^{2+} depletion does [59, 62-64]. Cl^- , like Ca^{2+} , has been proposed to influence proton transfer from the OEC as part of a hydrogen-

bonding network, based on oxygen evolution activity measurements and EPR spectroscopy [65-67].

Two substrate water molecules must bind to the OEC during its reaction cycle. Currently, the sites of substrate binding are unknown. ESEEM and hyperfine correlation spectroscopy (HYSCORE) measurements have demonstrated that the OEC interacts with numerous exchangeable hydrogens, most probably belonging to waters and/or hydroxide groups [68-70]. EPR data [71-76] have indicated that substrate analogues, such as small alcohols and ammonia, are also able to bind to the OEC. In addition, non-EPR techniques have confirmed the presence of water at the OEC, too, e.g. near-infrared (IR) Raman spectroscopy [77], Fourier transform IR (FTIR) spectroscopy [78-80] and mass spectrometric measurements of ^{18}O -labeled dioxygen evolution [81, 82].

2.4 EPR Signals of the Oxygen-Evolving Complex

The four Mn ions that make up the OEC are magnetically coupled in all S states that have been isolated thus far (S_0 - S_3) and all display characteristic EPR signals [74, 83-95]. The S_2 state, which has a ground spin state of total spin $S_t = 1/2$, is the best characterized in current literature and gives rise to the well-known S_2 state EPR multiline signal [83]. It is centered at $g \approx 2$ and contains 18-21 spectral lines with a peak-to-peak spacing of ~ 7.5 -9 mT (Fig. 3a). Depending on the conditions used, the S_2 state of higher plant PS II also exhibits broad EPR signals, centered at $g \geq 4.1$, which have been assigned to an $S_t = 5/2$ spin state [35, 96-100]. The $g \geq 4.1$ signals can also be induced by near-IR illumination of the S_2 multiline state at temperatures ≤ 160 K [96, 97]. Similarly, high spin state ($g \geq 4.1$) signals have been observed in the S_2 state OEC from cyanobacterial PS II [101, 102]. In plant PS II, the presence of small alcohols prevents the formation of the $g \geq 4.1$ signal [103-105]. Amongst all the alcohols, methanol (MeOH) has a specific effect in that it modifies the S_2 multiline signal [104-106], which is then also no longer sensitive to near-IR illumination [105, 107]. The modified S_2 multiline signal is narrower than that seen for the non-treated plant PS II preparation, resolving fewer spectral lines. MeOH also affects the other S states. None of these effects are observed in cyanobacteria; for a comparison see Su *et al.* [108].

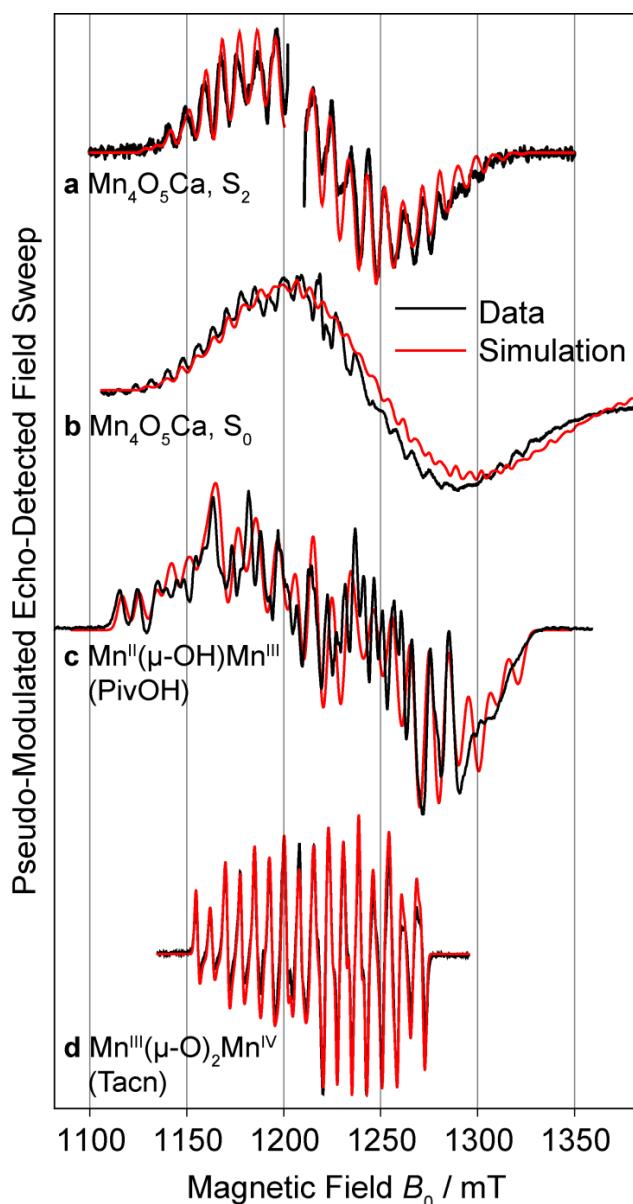


Fig. 3 Q-band EPR spectra of the OEC and related model systems. **a** S_2 state of the OEC in PS II from spinach (4% MeOH) [9]. **b** S_0 state of the OEC in PS II from spinach (4% MeOH) [9]. **c** $Mn^{II}-(\mu-OH)-Mn^{III}$ (PivOH) $[Mn^{II}Mn^{III}(\mu-OH)-(\mu-piv)_2(Me_3tacn)_2](ClO_4)_2$ (piv = $(CH_3)_3CCO_2$) [109]. **d** $Mn^{III}-(\mu-O)_2-Mn^{IV}$ (Tacn) $[(tacn)_2Mn^{III}Mn^{IV}(\mu-O)_2\mu-OAc](BPh_4)_2$ (tacn = 1,4,7-triazacyclononane) [110]. The black solid lines represent the data, the red solid lines represent simulations based on the spin Hamiltonian formalism (see Eqs. 3 and 14)

A similar multiline signal centered at $g \approx 2$ is observed for the S_0 state of the OEC; it contains up to 26 spectral lines with a peak-to-peak spacing of ~ 8 mT (Fig. 3b) [88, 90, 111]. To observe this signal in spinach, 3-5% MeOH must be added to the PS II sample. In contrast, an S_0 signal in cyanobacteria does not require the addition of MeOH [112].

Parallel mode signals from integer total spin states have been identified for the S_1 and S_3 states: in S_1 at $g \approx 4.9$ [84, 86] and $g \approx 12$ [89] and in S_3 at $g \approx 4$, $g \approx 8$ and $g \approx 12$ [91, 95].

The temperature dependence of the $g \approx 4.9$ signal indicates that it arises from an excited state of effective spin $S_t = 1$, and the S_1 state to have a ground spin state with $S_t = 0$ [86]. Recent simulations of the S_3 state signals indicated they originate from an $S_t = 3$ state [95].

‘Split’ EPR signals, which arise from the weak magnetic interaction between the Mn_4O_5Ca cluster and the Y_Z^\bullet radical are visible in all $S_n Y_Z^\bullet$ states [113-120]. This coupling on the order of 10^{-2} cm^{-1} results in a broadening of the tetramanganese signals and a splitting of the $S = 1/2$ Y_Z^\bullet signal.

3 The Mn oxidation states relevant to the OEC

3.1 Mononuclear Mn^{II} , Mn^{III} , Mn^{IV}

3.1.1 Mononuclear Mn^{II} complexes

Mn^{II} is a d^5 ion ($S = 5/2$). Its half occupied valence electron shell (3d) often engenders low g and hyperfine anisotropy and a small fine structure term D . In the circumstance where the fine structure parameter D is significantly smaller than $h\nu$ ($D \ll h\nu$ where h is Planck’s constant and ν is the frequency of the source resonance radiation), only the allowed $\Delta M_S = \pm 1$ transitions, where M_S is the electronic magnetic quantum number, are observed in an EPR experiment. The central transitions $M_S = 1/2 \leftrightarrow -1/2$, appear at $g \approx 2.0$ and manifest as six sharp lines due to the ^{55}Mn hyperfine interaction. When $D \gg h\nu$, the spin manifold splits into three Kramers doublets with $M_S = \pm 5/2, \pm 3/2$ and $\pm 1/2$. The large fine structure term acts to spread the EPR spectrum across a large magnetic field range. These systems typically display much faster spin-lattice relaxation times than for the case $D \ll h\nu$, leading to a broadening of EPR lines especially to the non-central outer transitions. Their resonance positions may coincide with magnetic field positions that exceed the sweep range of the magnet. At room temperature, the outer transitions are broadened beyond detection and only the central transitions are observed. This submanifold is effectively a spin $S = 1/2$ system, with the resonant line being anisotropic due to the zero-field splitting term. For axial symmetry (symmetry parameter $E = 0$), one observes the effective g values to be: $g_{\parallel} = 2.0$, $g_{\perp} = 6.0$. That is, when there is large zero-field splitting, there are turning points in the angular variation of line position at $g = 6$ and 2 . A listing of the spin Hamiltonian parameters – g tensor, D , E , higher order fine structure parameters b_4^m ($m = 0, 2, 4$), and hyperfine tensor \mathbf{a} – has been previously tabulated by Misra [121].

3.1.2 Mononuclear Mn^{III} complexes

Mn^{III} is a d⁴ ion ($S = 2$). Unlike Mn^{II}, Mn^{III} has an inherently asymmetric electron configuration and thus often displays a large fine structure splitting, of the order of 2-5 cm⁻¹. As a consequence, Mn^{III} is usually not detected at low frequencies (X-, Q-, W-band). The EPR of Mn^{III} has only been detected at very high frequency (VHF) [122]. In principle, the strictly forbidden $\Delta M_S = 0$ transition of the Mn^{III} spin manifold can be detected at low frequencies in highly axial systems, i.e. $E \approx 0$, by using parallel polarization EPR, wherein $\mathbf{B}_1 \parallel \mathbf{B}$, such as for the S₁ state signals [84, 86]. (\mathbf{B}_1 is the radiation field inducing transitions and \mathbf{B} is the external magnetic field.) The fine structure interaction splits the levels into two doublets ($M_S = \pm 1, \pm 2$) and a singlet ($M_S = 0$). In addition, the lines are expected to be quite broad. An overview of spin Hamiltonian parameters of monomeric Mn^{III} complexes is listed in Supplementary Table S1 [53].

3.1.3 Mononuclear Mn^{IV} complexes

Mn^{IV} is a d³ ion ($S = 3/2$). Depending on its symmetry, it can display large or small g and hyperfine anisotropy and fine structure terms. In octahedral ligand fields, Mn^{IV} ions are characterized by half-filled t_{2g} orbitals and thus usually display small fine structure splittings D , whereas in tetragonal ligand fields D tends to be larger. As seen for Mn^{II}, when D is small, the overlapping electronic transitions are seen at about $g \approx 2$. In contrast, when D is large, the spin manifold splits into two Kramers doublets $M_S = \pm 1/2, \pm 3/2$. The transition $1/2 \leftrightarrow -1/2$ is observed even with large D , the effective g values being $g_{\parallel} = 2.0, g_{\perp} = 4.0$. Supplementary Table S2 lists spin Hamiltonian parameters of monomeric Mn^{IV} complexes [53].

3.2 Binuclear Mn Complexes

3.2.1 Exchange-Coupled Mn Dimers

The EPR spectra of antiferromagnetically exchange-coupled mixed valence Mn dimers (Mn^{II}Mn^{III}, Mn^{III}Mn^{IV}, Fig. 3c, d) bear characteristics similar to the S₂ and S₀ multiline signals described above in Section 2.4 (Fig. 3a, b). The spin Hamiltonian \mathbf{H} for a coupled

system consisting of two Mn electron spins \mathbf{S}_i ($i = 1,2$) contains terms representing the electronic exchange interaction $-2J \mathbf{S}_1 \cdot \mathbf{S}_2$, the dipolar (through-space) term $\mathbf{S}_1 \mathbf{T} \mathbf{S}_2$ between the electron spins \mathbf{S}_1 and \mathbf{S}_2 of the two Mn ions, electronic Zeeman terms $\mu_B \mathbf{S}_i \mathbf{g}_i \mathbf{B}$ for each Mn ion with μ_B being the Bohr magneton, hyperfine interaction terms for each Mn ion with their respective nuclei $\mathbf{S}_i \mathbf{a}_i \mathbf{I}_i$ and the zero-field or fine structure term $\mathbf{S}_i \mathbf{d}_i \mathbf{S}_i$ [110, 123, 124]:

$$\mathbf{H} = -2J\mathbf{S}_1\mathbf{S}_2 + \mathbf{S}_1\mathbf{T}\mathbf{S}_2 + \mu_B\mathbf{S}_1\mathbf{g}_1\mathbf{B} + \mu_B\mathbf{S}_2\mathbf{g}_2\mathbf{B} + \mathbf{S}_1\mathbf{a}_1\mathbf{I}_1 + \mathbf{S}_2\mathbf{a}_2\mathbf{I}_2 + \mathbf{S}_1\mathbf{d}_1\mathbf{S}_1 + \mathbf{S}_2\mathbf{d}_2\mathbf{S}_2 \quad (2)$$

In Eq. 2, J is the isotropic electronic exchange coupling constant, which is negative for antiferromagnetic coupling and positive for ferromagnetic coupling. The magnitude of J depends on the degree of orbital overlap between the two ions and is strongly influenced by the bridging ligand(s). The elements of the dipolar tensor \mathbf{T} depend on the orientation of the two Mn ions with the magnitude $\mu_0\mu_B^2g^2/R^3$, with μ_0 being the permeability of the free space, and R the inter-spin distance. \mathbf{d}_i are the fine structure tensors, \mathbf{g}_i are the \mathbf{g} tensors and \mathbf{a}_i are the hyperfine tensors. \mathbf{S}_i and \mathbf{I}_i are the electron and nuclear spin operators, respectively, for the two Mn ions.

The magnitude of J relative to \mathbf{T} , \mathbf{d}_1 and \mathbf{d}_2 predominantly determines the EPR spectrum of a binuclear Mn complex. (Note that the magnitudes of \mathbf{a}_1 and \mathbf{a}_2 are of the order of hundreds of MHz and thus can always be considered small relative to the magnitudes of J , \mathbf{T} , \mathbf{d}_1 and \mathbf{d}_2 .) The EPR spectrum becomes very complex when these terms are of the same order of magnitude. In contrast, when J is large and \mathbf{T} , \mathbf{d}_1 and \mathbf{d}_2 are relatively small, the EPR spectrum is fairly simple to interpret. In the following discussion it is assumed that J is indeed large. In this case, the resultant spin $S = S_1 + S_2$ is obtained by the vector coupling rule, and the exchange-coupled system is described by the use of the vector projection model. Thus, $S = |S_1 - S_2|, |S_1 - S_2| + 1, \dots, |S_1 + S_2| - 1, |S_1 + S_2|$. For $\text{Mn}^{\text{II}}\text{Mn}^{\text{III}}$ and $\text{Mn}^{\text{III}}\text{Mn}^{\text{IV}}$ exchange-coupled systems, the coupling leads to electronic states of total spin $S_t = 1/2, 3/2, 5/2, 7/2$ (and $9/2$ in case of $\text{Mn}^{\text{II}}\text{Mn}^{\text{III}}$) in increasing order of energies when the coupling is antiferromagnetic. However, this order reverses when the coupling is ferromagnetic, as shown in Fig. 4 for an exchange-coupled $\text{Mn}^{\text{III}}\text{Mn}^{\text{IV}}$ dimer. For a variety of μ -oxo-bridged dimanganese model compounds, the electronic exchange coupling is typically antiferromagnetic. When such a dimer is in a mixed valence state in which the Mn ions differ by one oxidation state, it is usually characterized by a ground state with $S_t = 1/2$. If an antiferromagnetically exchange-coupled dimer is not in a mixed valence state, then the

ground state is usually $S_t = 0$. Thus, in strongly antiferromagnetically exchange-coupled Mn dimers, EPR signals are normally observed only for mixed-valence states. The energy levels for an exchange-coupled $\text{Mn}^{\text{III}}\text{Mn}^{\text{IV}}$ dimer are shown in Fig. 4.

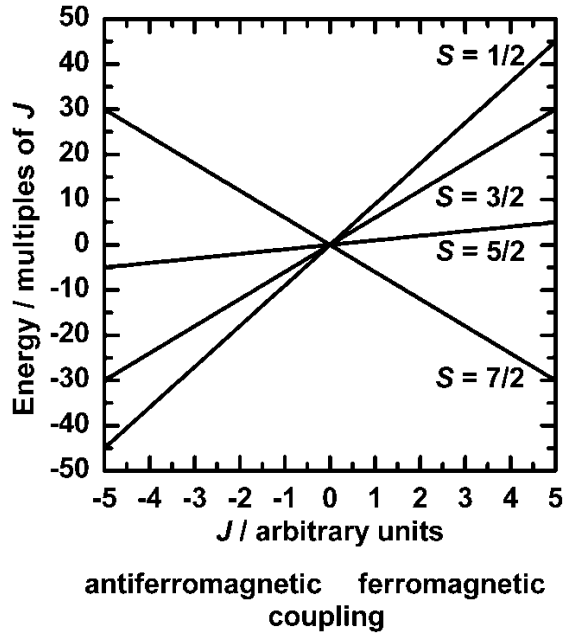


Fig. 4 Energy level diagram for the resulting effective spin states S of an exchange-coupled $\text{Mn}^{\text{III}}\text{Mn}^{\text{IV}}$ dimer as a function of the strength and sign of the J coupling ($J < 0$: antiferromagnetic, $J > 0$: ferromagnetic), according to the Heisenberg exchange term $-2J \mathbf{S}_1 \mathbf{S}_2$

3.2.2 Exchange-Coupled Dimer States for Large J

In case of a large and negative J , as described in the previous section, the spin Hamiltonian \mathbf{H} for the exchange-coupled $S_t = 1/2$ resulting ground state is [110, 124-126]:

$$\mathbf{H} = \mu_B \mathbf{S} \mathbf{G} \mathbf{B} + \mathbf{S} \mathbf{A}_1 \mathbf{I}_1 + \mathbf{S} \mathbf{A}_2 \mathbf{I}_2 \quad (3)$$

The effective \mathbf{G} tensor of the coupled system is expressed in terms of \mathbf{g}_1 and \mathbf{g}_2 for the isolated systems as

$$\mathbf{G} = \rho_1 \mathbf{g}_1 + \rho_2 \mathbf{g}_2 + \frac{\rho_1 \rho_2}{5J} (\mathbf{g}_1 - \mathbf{g}_2) [(3\rho_1 + 1)\mathbf{d}_1 - (3\rho_2 + 1)\mathbf{d}_2] \quad (4)$$

where

$$\rho_1 = \frac{S(S+1) + S_1(S_1+1) - S_2(S_2+1)}{2S(S+1)}, \quad (5)$$

$$\rho_2 = \frac{S(S+1) - S_1(S_1+1) + S_2(S_2+1)}{2S(S+1)} \quad (6)$$

ρ_1 and ρ_2 are referred to as spin projection factors, which can be interpreted as the contributions of the individual electronic spins to the total spin state. For coupled Mn^{III}Mn^{IV} systems ($S(\text{Mn}^{\text{III}}) = 2$, $S(\text{Mn}^{\text{IV}}) = 3/2$), $\rho(\text{Mn}^{\text{III}}) = 2$ and $\rho(\text{Mn}^{\text{IV}}) = -1$. The third term of Eq. 4 is usually neglected in Mn^{III}Mn^{IV} complexes, since $J \gg D_i$ ($i = 1,2$). The effective Mn hyperfine coupling tensors \mathbf{A}_1 and \mathbf{A}_2 of the coupled system can be expressed in a similar way in terms of the intrinsic (on-site) hyperfine coupling tensors \mathbf{a}_1 and \mathbf{a}_2 :

$$\mathbf{A}_1 = \rho_1 \mathbf{a}_1 - \frac{\mathbf{a}_1 \rho_1 \rho_2}{5J} [(3\rho_1 + 1)\mathbf{d}_1 - (3\rho_2 + 1)\mathbf{d}_2] \quad (7)$$

$$\mathbf{A}_2 = \rho_2 \mathbf{a}_2 + \frac{\mathbf{a}_2 \rho_1 \rho_2}{5J} [(3\rho_1 + 1)\mathbf{d}_1 - (3\rho_2 + 1)\mathbf{d}_2] \quad (8)$$

It is seen that the measured hyperfine anisotropy is in part dependent on the energy spacing of the spin manifold, i.e. on J , \mathbf{d}_1 and \mathbf{d}_2 . This can lead to interesting cases where anisotropy is effectively transferred from one Mn nucleus to the other. Supplementary Table S3 contains a listing of the spin Hamiltonian parameters for Mn^{III}Mn^{IV} mixed-valence complexes [53], as these complexes are of relevance to the recent models for the tetramanganese cluster of the OEC.

3.2.3 Magnetic Coupling of Ligands (e.g. ¹H, ¹³C, ¹⁴N, ¹⁷O) to a Mn Dimer

The interaction of a ligand nucleus with the electron spin of the Mn dimer is typically small, less than the intrinsic EPR linewidth. As such, it does not need to be explicitly considered when analyzing EPR spectra of these systems. This coupling can, however, be probed by continuous wave (CW) and pulsed EPR techniques (ESEEM, ENDOR, ELDOR-detected NMR). When measured at the center field, these spectra can be rationalized by considering

only the ligand terms of the spin Hamiltonian (hyperfine, quadrupole terms) coupled to an isotropic spin $S_t = 1/2$ state with an effective g value as all power pattern position are sampled equally, i.e. ^{55}Mn hyperfine terms etc. do not need to be explicitly included. The ligand hyperfine interaction is typically made up of two components: (i) a through-bond component, the Fermi contact term, which approximates the isotropic hyperfine coupling A_{iso} and (ii) a through-space component, the dipolar coupling \mathbf{A}_{dip} , which approximates the anisotropic hyperfine coupling. As the system contains two metals, this latter term is made up of two contributions, representing the interaction of the ligand with each metal center (see Eqs. 9-11), referred to in the literature as the extended point-dipole model [69, 127, 128]. Eq. 9 below gives the general expression describing this interaction and, on the right side, gives the product of the constants if the coupling nucleus is ^1H .

$$\mathbf{A}_{dip} = \frac{\mu_B \mu_n g_e g_n}{h} \mathbf{T}_h = 79.2 \text{ MHz } \text{\AA}^3 \mathbf{T}_h \quad (9)$$

Here, \mathbf{T}_h is the 3×3 diagonal tensor with the diagonal elements $-\delta$, $-I + \delta/2$, $I + \delta/2$, with δ and I defined by the parameters \mathbf{r}_1 , \mathbf{r}_2 and θ as follows:

$$\delta = 2|\mathbf{r}_1|^{-3} - |\mathbf{r}_2|^{-3} \quad (10)$$

$$I = \frac{3}{2} \sqrt{4|\mathbf{r}_1|^{-6} - 4|\mathbf{r}_1|^{-3}|\mathbf{r}_2|^{-3} \cos 2\theta + |\mathbf{r}_2|^{-6}} \quad (11)$$

Here, for the $\text{Mn}^{\text{III}}-\text{Mn}^{\text{IV}}$ dimer, \mathbf{r}_1 , \mathbf{r}_2 , \mathbf{d} are the Mn^{III} nucleus, Mn^{IV} nucleus, $\text{Mn}^{\text{III}}-\text{Mn}^{\text{IV}}$ inter-spin vectors, respectively; and θ , ϕ are the angles between $(\mathbf{r}_1, \mathbf{r}_2)$ and $(\mathbf{r}_1, \mathbf{d})$, respectively, as shown in Fig. 5a.

Although, in general, \mathbf{A}_{dip} is a non-axial tensor, it becomes axial when the proton is located on the line joining the two Mn ions ($\theta = 0$ or π , $I = \frac{3}{2} \delta$, Fig. 5b), with the diagonal elements being $-\delta$, $-\delta$, 2δ . One can modify Eq. 9 for practical use. The parameters \mathbf{r}_2 and θ in Eqs. 10 and 11 can be expressed as

$$|\mathbf{r}_2| = \sqrt{|\mathbf{d}|^2 - 2|\mathbf{d}||\mathbf{r}_1| \cos \phi + |\mathbf{r}_1|^2} \quad (12)$$

$$\theta = \arcsin \left[\left(\frac{|d|}{|r_2|} \right) \sin \phi \right] \quad (13)$$

This extended point-dipole model is applicable only if the distances between the magnetic moments are large compared to the size of the spin density distribution. Nevertheless, this model is very helpful in correlating hyperfine tensors to nuclear positions. ^1H , ^{13}C , ^{14}N , and ^{17}O couplings in the Mn model complexes $[(2\text{-OH-}3,5\text{-Cl}_2\text{-salpn})_2\text{Mn}^{\text{III}}\text{Mn}^{\text{IV}}]$ (salpn = N,N'-bissalicylidene-1,3-diamino-2-hydroxypropane) [128], $[\text{R}_4\text{dtneMn}^{\text{III}}\text{Mn}^{\text{IV}}(\mu\text{-O})_2(\mu\text{-OAc})](\text{BPh}_4)_2$ (R = H, CH₃, dtne = 1,2-bis(1,4,7-triazacyclonon-1-yl)ethane), $[(\text{tacn})_2\text{Mn}^{\text{III}}\text{Mn}^{\text{IV}}(\mu\text{-O})_2\mu\text{-OAc}](\text{BPh}_4)_2$, $[\text{bpy}_4\text{Mn}^{\text{III}}\text{Mn}^{\text{IV}}(\mu\text{-O})_2](\text{ClO}_4)_3$ (bpy = 2,2'-bipyridyl) and $[(\text{phen})_4\text{Mn}^{\text{III}}\text{Mn}^{\text{IV}}(\mu\text{-O})_2](\text{ClO}_4)_3$ (phen = 1,10-phenanthroline) [110, 124, 129-131] were successfully analyzed using this concept. These same concepts can be applied to systems with more than two paramagnetic centers and oligonuclear sites in proteins, such as the $\text{Mn}_4\text{O}_5\text{Ca}$ cluster of the OEC [69, 127], which we will discuss in the following section.

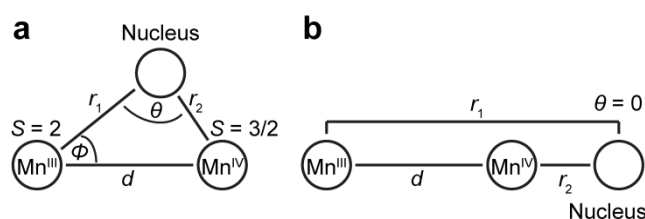


Fig. 5 Geometric representation of the point-dipole model [69, 127, 128] describing the configuration of the various constituents, as shown in Ref. [124]. Here, the nucleus could for example be a proton (^1H , $I = 1/2$), carbon (^{13}C , $I = 1/2$), nitrogen (^{14}N , $I = 1$), or oxygen (^{17}O , $I = 5/2$). **a** Bridging ligand with non-axial \mathbf{A}_{dip} . **b** Terminal ligand in the extension of the $\text{Mn}^{\text{III}}\text{-Mn}^{\text{IV}}$ axis exhibiting an axial \mathbf{A}_{dip}

4 The Exchange-Coupled Tetranuclear Manganese Complex

4.1 Effective Spin Hamiltonian and Spin Projection Formalism

A spin Hamiltonian analogous to the dimer system can be built to describe the tetramanganese cluster of the OEC. For example, when poised in the S_2 or the S_0 state, the four Mn ions couple together to give a ground electronic configuration of total spin $S_t = 1/2$.

The oxidation states of the individual Mn ions that make up the OEC in the S_2 state is generally considered to be $Mn^{III}Mn^{IV}_3$ [9, 13, 24-27]. The effective spin Hamiltonian of the ground state can thus be expressed as the sum of Zeeman and hyperfine interactions as [132]:

$$\mathbf{H} = \mu_B \mathbf{S} \mathbf{G} \mathbf{B} + \mathbf{S} \mathbf{A}_1 \mathbf{I}_1 + \mathbf{S} \mathbf{A}_2 \mathbf{I}_2 + \mathbf{S} \mathbf{A}_3 \mathbf{I}_3 + \mathbf{S} \mathbf{A}_4 \mathbf{I}_4 \quad (14)$$

In Eq. 14, (analogous to Eq. 3,) \mathbf{G} is the effective tensor for the coupled state with the total spin $S = S_1 + S_2 + S_3 + S_4$, as determined using the vector coupling rule, and \mathbf{A}_i ($i = 1 \dots 4$) are the effective hyperfine tensors of the four manganese nuclei. The properties are to be evaluated within the subspace of \mathbf{S} because here, the interionic exchange interaction is dominant, i.e. $|J| \gg D_i$, as observed in $Mn^{III}Mn^{IV}$ complexes. With this coupling, each \mathbf{S}_i can be replaced by a product of a constant spin projection factor times the total spin operator, i.e. $\mathbf{S}_i = \rho_i \mathbf{S}$, when the Wigner-Eckart theorem is applied. More details of spin projection are given in the Supplementary Sections S2 and S3, where the related list of basis vectors and calculation of spin projections is found [53]. The factors ρ_i can be expressed as

$$\rho_i = \frac{\langle |\mathbf{S}_i \mathbf{S}| \rangle}{\mathbf{S}^2} \quad (15)$$

where the bra-ket notation $|\ \rangle$, stands for any state within the $S_t = 1/2$ ground state wave function given by the Heisenberg-Dirac-van Vleck term $-2 \sum_{i < j} J_{ij} \mathbf{S}_i \mathbf{S}_j$.

Then, in Eq. 14, \mathbf{G} becomes

$$\mathbf{G} = \rho_1 \mathbf{g}_1 + \rho_2 \mathbf{g}_2 + \rho_3 \mathbf{g}_3 + \rho_4 \mathbf{g}_4 \quad (16)$$

Eq. 14 is then transformed, by substituting $A_i = \rho_i a_i$, into the readily usable form

$$\mathbf{H} = \mu_B \mathbf{S} \mathbf{G} \mathbf{B} + \rho_1 \mathbf{S} \mathbf{a}_1 \mathbf{I}_1 + \rho_2 \mathbf{S} \mathbf{a}_2 \mathbf{I}_2 + \rho_3 \mathbf{S} \mathbf{a}_3 \mathbf{I}_3 + \rho_4 \mathbf{S} \mathbf{a}_4 \mathbf{I}_4 \quad (17)$$

Eq. 17 can be subjected to different approaches to account for the magnetic properties. The obvious approach is to treat each $\rho_i a_i$ as a single parameter, evaluated by a spectral-fitting procedure, and then find a physical explanation for it. This is, however, a very tedious

procedure as it involves four nuclei. There can be as many as 15 principal values for the \mathbf{g} and the four ^{55}Mn hyperfine tensors \mathbf{a}_i , requiring 12 Euler angles for their relative orientations. Instead, this problem can be handled by treating ρ_i and \mathbf{a}_i separately, making full use of the intrinsic Mn hyperfine tensors and their orientations obtained from simulation of model complexes and proteins. The spin projection factors ρ_i are used to scale the intrinsic hyperfine parameters \mathbf{a}_i in order to obtain effective hyperfine parameters for the Mn tetramer system. Expressions for ρ_i can be derived from an electronic exchange interaction model as a set of pairwise J coupling constants describing the respective spin system, such as the models in Fig. 2e and presented below [9, 32, 133-135]. These can be used to simulate EPR and hyperfine (ENDOR, ESEEM-type, ELDOR-detected NMR) spectra for the different states of the Mn tetramer; only the relative orientations of the tensor axes need to be established. For this, one makes use of the observation that, for $(\mu\text{-O})_2$ -bridged $\text{Mn}^{\text{III}}\text{Mn}^{\text{IV}}$ dimer systems, the hyperfine and \mathbf{g} matrices are essentially axial and nominally collinear. This approach has been successfully applied both in theoretical and experimental studies on the electronic structure and spectroscopic properties of exchange-coupled tetramanganese complexes, such as $[\text{Mn}^{\text{III}}\text{Mn}^{\text{IV}}_3\text{O}_6(\text{bpy})_6]^{3+}$ [134] and $[\text{Mn}^{\text{IV}}_3\text{Ca}_2\text{O}_4(\text{O}_2\text{CBu}')_8(\text{Bu}'\text{CO}_2\text{H})_4]$ [136].

4.2 Inclusion of the Fine Structure Term of One or Several Mn Ions

The spin projections calculated above can be corrected for the fine structure terms of the spin Hamiltonian, analogous to the Mn dimer systems. In practice, the fine structure tensor \mathbf{d} of only one sort of Mn ions, that of Mn^{III} , is of a relevant size to be considered. Its valence electron configuration leads to a large Jahn-Teller distortion, described in greater detail in the Supplementary Section S4. Mn^{III} always possesses a fine structure constant of significant magnitude $D = 1\text{-}4\text{ cm}^{-1}$, whereas Mn^{IV} in octahedral environments typically displays fine structure constants an order of magnitude smaller than this [126] (see Supplementary Tables S1 and S2 and the references given therein). For the calculation of anisotropic spin projections, the spin Hamiltonian, which describes the zero-field splitting of the spin states, includes the electronic exchange interaction and the fine structure term of the complex:

$$\mathbf{H} = -\sum_{i<j} 2J\mathbf{S}_i\mathbf{S}_j + \mathbf{S}_j\mathbf{d}_j\mathbf{S}_j \quad (18)$$

In Eq. 18, the j^{th} spin operator \mathbf{S}_j refers to the Mn^{III} ion, with \mathbf{d}_j being its fine structure tensor, which is assumed to be axial and can thus be expressed in terms of a single parameter D (see [53]):

$$\mathbf{d} = \begin{bmatrix} -\frac{1}{3}D & 0 & 0 \\ 0 & -\frac{1}{3}D & 0 \\ 0 & 0 & \frac{2}{3}D \end{bmatrix} \quad (19)$$

Inclusion of the fine structure term of the Mn^{III} ion renders the spin projections ρ_i as tensors rather than scalars. Since all pairwise exchange couplings J_{ij} have here been assumed to be isotropic, and the fine structure tensor \mathbf{d}_j of the Mn^{III} is axial, the spin projection tensor of the i^{th} Mn can be expressed as a diagonal matrix of the form:

$$\rho_i = \begin{bmatrix} \rho_{\perp,i} & 0 & 0 \\ 0 & \rho_{\perp,i} & 0 \\ 0 & 0 & \rho_{\parallel,i} \end{bmatrix} \quad (20)$$

5 Electronic Exchange Coupling Models for the Tetramanganese Cluster of the Oxygen-Evolving Complex

In this section, we give an overview of the development of electronic structural models for the $\text{Mn}_4\text{O}_5\text{Ca}$ cluster of the OEC, and the key role EPR spectroscopy played in this exercise. EPR spectroscopy was the first technique to show that the PS II super-complex contained a Mn-cofactor that was intimately linked to photosynthetic oxygen evolution. A key finding was the identification of an intermediate displaying an $S = 1/2$ EPR signal, the so-called multiline signal of the S_2 state, first observed in spinach chloroplasts [83, 137]. Based on comparison to Mn model complexes, the S_2 state was assigned to either a binuclear $\text{Mn}^{\text{II}}\text{Mn}^{\text{III}}$ site or a tetranuclear $\text{Mn}^{\text{III}}\text{Mn}^{\text{VI}}_3$ cluster. The four-flash periodicity of the S_2 multiline signal (maximum intensity yield on every fourth light flash in accordance with a four-electron process), together with inhibition studies confirmed that enzymatic water oxidation catalysis was Mn-centered, as had been suggested before (reviewed in [138]). Early proposals for the electronic structure of the oligo-Mn center were developed from spectroscopic data in

combination with biochemical experiments already at a time when the geometric structure of the OEC was not known. Outdated models that studies have proven to be physically not relevant are not reviewed here. A description of such earlier models, such as the tetramanganese ‘cubane-like’ core [17], the ‘dimer of dimers’ [132] and the ‘butterfly’ core models possessing simplified electronic exchange coupling schemes, and their quantum-mechanical treatment have been reviewed by Misra [139].

Meanwhile, the progress in the X-ray crystallographic structure determination of PS II up to the 1.9 Å structure by Umena *et al.* [20] in conjunction with new or enhanced spectroscopic methodologies, such as X-ray absorption spectroscopy (XAS) [140-142], electron paramagnetic resonance (EPR/ENDOR) spectroscopy [9, 53, 133], and vibrational spectroscopy [143], now provide a robust picture of the electronic structure of the OEC in its low oxidation states (S_0 - S_2). Just as critical to this process are recent advances in the computational treatment of the OEC, in particular developments in the calculation of EPR-spectroscopic observables using broken-symmetry (BS) DFT [144], providing a connection between the electronic structure as probed by EPR and the molecular structure. The current model of the Mn_4O_5Ca cluster in the S_2 state is described below, with particular emphasis on the role that combined EPR and ^{55}Mn ENDOR spectroscopy along with BS-DFT played in its development.

5.1 Calculations of EPR Parameters from Density Functional Theory

5.1.1 Electronic Exchange Coupling and the Heisenberg–Dirac–van Vleck Hamiltonian

For systems containing multiple Mn ions wherein the transition metal centers are antiferromagnetically coupled, the application of the BS formalism is necessary for the correct calculation of the exchange coupling and other EPR parameters from DFT[145-147]. By means of the BS-DFT approach, the exchange coupling constants J and hyperfine coupling constants A_{iso} can be calculated with reasonable accuracy for Mn dimer, trimer and tetramer model systems [134, 148-150]. The pairwise magnetic interactions J_{ij} between the electron spins of the manganese centers are assumed to be described by the isotropic Heisenberg–Dirac–van Vleck (HDvV) Hamiltonian:

$$\mathbf{H}_{\text{HDvV}} = -2 \sum_{i < j} J_{ij} \mathbf{S}_i \mathbf{S}_j \quad (21)$$

The OEC consists of four coupled Mn ions, resulting in six possible exchange coupling pathways J_{ij} . Within the BS-DFT framework, the exact problem is solved without making any assumptions for the magnitude of non-nearest-neighbor interactions. A system of four coupled spin centers contains eight single-determinant representations; one high spin along with seven BS single-determinant representations from the remaining parallel/antiparallel spin combinations. For example, in the case of one Mn^{III} and three Mn^{IV} centers, as in the S_2 state, with fixed atomic high-spin d^4 or d^3 electronic configurations, there are three BS solutions with total $M_S = 7/2$, one BS solution with total $M_S = 5/2$ and three BS solutions with total $M_S = 1/2$. It is noted that the BS energies for each single-determinant solution are not of significance when considered individually. However, considered together, the BS solutions, along with the high-spin solution, allow for the extraction of the exchange coupling constants from the HDvV Hamiltonian. It is only once the analysis of the exchange coupling constants has been made that the energies, spin states, and molecular properties can be related to the experiment [134]. Additionally, it should be noted that individual pairwise exchange couplings are not observables; it is the identity, ordering and spacing of the spin levels derived from a given set of J values that determine the observable energy level spin ladder of a system.

The over-determined equation space from the high-spin and the seven BS solutions for the calculation of the six exchange coupling constants (see Section 5.2.3) can be solved using the technique of singular value decomposition. This method gives the best solution, in the least-squares sense, for the six exchange interactions between four Mn spin centers. Having the six exchange coupling constants for each structure, it is then straightforward to diagonalize the HDvV Hamiltonian in order to obtain the complete energy level spin ladder, identifying the true ground spin state, and to calculate the associated properties of a given system. The application of the BS-DFT methodology to the calculation of exchange coupling constants has been discussed in previous studies of manganese systems [32, 134, 144, 149, 150].

5.1.2 Hyperfine Coupling Constants from Broken-Symmetry Density Functional Theory

The calculation of hyperfine coupling constants A_{iso} from BS-DFT has been made possible from recent advances in theory, previously described in detail [134]. A meaningful comparison of experimental and calculated results can be achieved using this new methodology. It has been used to discriminate between different cluster topologies and ligand environments of Mn ions in oligonuclear clusters [134], and has already been applied to several models of the OEC [32, 34, 35, 135]. For exchange-coupled multinuclear paramagnetic systems, an exact quantum-mechanical treatment would computationally be too demanding for systems of such high complexity. BS-DFT, in combination with the spin projection formalism, described in Section 4.1, represents a pragmatic, efficient alternative. For a complete in-depth description of the theory and methodology for the calculation of hyperfine couplings from BS-DFT, the reader is referred to Ref. [134]. In the present article, only the main concepts will be highlighted and discussed.

For a system composed of metal-centered spin subsystems, with nucleus K belonging to subsystem A, the general equations that directly connect the BS calculation to the observable effective hyperfine coupling constant $A_{\text{iso}}^{(\text{K})}$ are as follows

$$a_{\text{iso,site}}^{(\text{K})} = \pm a_{\text{iso,BS}}^{(\text{K})} \left(\frac{\langle \mathbf{S}_z \rangle_{\text{BS}}}{S_A} \right) \quad (22)$$

$$A_{\text{iso}}^{(\text{K})} = \pm a_{\text{iso,site}}^{(\text{K})} \left(\frac{\langle \mathbf{S}_z^{(\text{A})} \rangle}{S_t} \right) \quad (23)$$

In Eq. 22, S_A is the site spin of subsystem A, and the positive or negative sign depends on whether the fragment carries majority (α) or minority (β) spin. $a_{\text{iso,BS}}^{(\text{K})}$ is the ‘raw’ hyperfine coupling constant calculated directly from the BS formalism, and $\langle \mathbf{S}_z \rangle_{\text{BS}}$ is the total electronic magnetic quantum number M_S of the appropriate BS wavefunction. In Eq. 23, S_t is the fictitious effective total ground state spin, $\langle \mathbf{S}_z^{(\text{A})} \rangle$ is the on-site spin expectation value, and $a_{\text{iso,site}}^{(\text{K})}$ is the on-site isotropic coupling constant. To correctly determine the final projection of the on-site hyperfine coupling constants to a calculated hyperfine constant comparable to

experiment, the determination of the site spin expectation value $\langle \mathbf{S}_z^{(A)} \rangle$ is required. For a subsystem A in a system consisting of subsystems A...N, the site spin expectation value used for the isotropic spin projection coefficients, is given by

$$\langle \mathbf{S}_z^{(A)} \rangle = \sum_{S_A M_{S_A} \dots S_N M_{S_N}} \left| C_1^{S_A M_{S_A} \dots S_N M_{S_N}} \right|^2 M_{S_A} \quad (24)$$

where $\left| C_1^{S_A M_{S_A} \dots S_N M_{S_N}} \right|^2$ is the weight of the basis state $|S_A M_{S_A}, \dots, S_N M_{S_N}\rangle$ in the ground state eigenfunction describing the lowest-energy Kramers doublet of lowest energy.

5.2 Current Electronic Model of the Oxygen Evolving Complex in the S₂ State

5.2.1 The EPR Experiment

As described above, the four Mn ions that make up the OEC are magnetically coupled in the various S_n states; each S_n state of the Mn₄O₅Ca cluster exhibits characteristic EPR signals. Of these, the S₂ state, which has a ground state of total spin S_t = 1/2, is the best characterized in the current literature, giving rise to the well-known S₂ state multiline EPR signal. The S₂ multiline signal as observed at 9 GHz (X-band) is centered at g~2 and contains 18-21 spectral lines with a peak-to-peak spacing of ~7.5-9 mT (Fig. 3a). The multiline is spectrally sparse, since not all of the potential 1296 allowed transitions within the ground state S₂ manifold are resolved. Thus, no unique fitting of the spectrum can be obtained with the spin Hamiltonian formalism described above. Although multi-frequency EPR (9-94 GHz) provides more details on the spin Hamiltonian parameters, especially with regard to the **g** matrix, it does not lead to an improved understanding of the hyperfine couplings. This is because of the inhomogeneous linewidth characterizing the multiline spectrum at all these frequencies, in other words, the spectral breadth, which is determined by the ⁵⁵Mn hyperfine couplings, is such that all powder pattern orientations contribute significantly to all line positions across the spectral envelope in the resultant spectrum, with the exception of those on the extreme edges. Furthermore, the linewidth increases with increasing magnetic field due to strain effects, hampering further the analysis of the hyperfine structure. As a consequence, additional, independent spectroscopic data are required to correctly interpret the multiline

spectrum. To this end, ^{55}Mn ENDOR becomes the particular method of choice. More details are described below.

5.2.2 The ^{55}Mn ENDOR Experiment

The ^{55}Mn ENDOR experiment for the $S_t = 1/2$ OEC, or for that matter, for all Mn complexes, is a challenging experiment as the ^{55}Mn -ENDOR spectrum for the OEC is expected to be spread over a large radio frequency range of ~ 100 - 300 MHz. The technology to perform such experiments was developed initially in 1994 in the Britt laboratory at the University of California, Davis at X-band [36, 133, 151, 152], and thereafter, in 1995, in the Lubitz laboratory at the Technische Universität, Berlin and subsequently at the Max-Planck Institute for Bioinorganic Chemistry, Mülheim an der Ruhr, where an extension to higher frequency bands was accomplished [9, 53, 124, 127, 153-157].

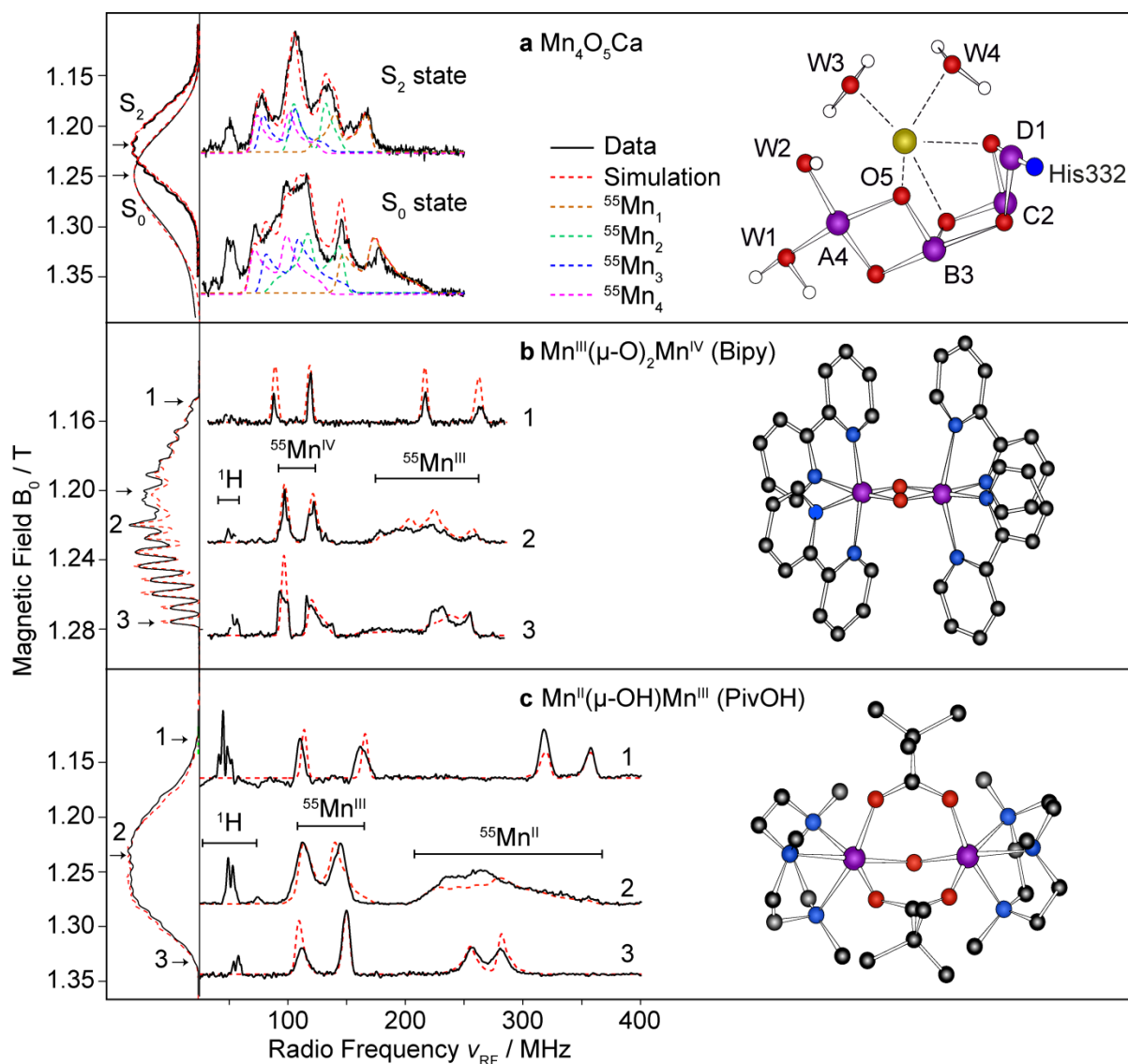


Fig. 6 Q-band EPR (vertical) and ^{55}Mn ENDOR (horizontal) spectra of the OEC and related model systems (left) and their atomic structures (right). **a** The S_2 and S_0 states of the OEC of in spinach PS II (4% MeOH) [9]. **b** $\text{Mn}^{\text{III}}-(\mu\text{-O})_2\text{-Mn}^{\text{IV}}$ (Bipy). **c** $\text{Mn}^{\text{II}}-(\mu\text{-OH})\text{-Mn}^{\text{III}}$ (PivOH) [109]. The black solid lines represent the data, the red dashed lines represent simulations based on the spin Hamiltonian formalism (see Eqs. 3 and 14). In the structural models, manganese, calcium, oxygen, nitrogen and hydrogen atoms are shown in purple, yellow, red, blue and white, respectively

Table 1 Principal values of the effective \mathbf{G} and ^{55}Mn hyperfine matrices \mathbf{A}_i ($i = 1-4$) for the simulations of the S_2 spectra of *T. elongatus* and spinach PS II as published in Ref. [108]

		\mathbf{G}	$\mathbf{A}_i / \text{MHz}$			
			\mathbf{A}_1	\mathbf{A}_2	\mathbf{A}_3	\mathbf{A}_4
<i>T.</i>	x	1.971	350	249	202	148
	y	1.948	310	227	182	162

<i>elongatus</i>	\perp ^a	1.960	330	238	192	155
	$z(\parallel)$ ^a	1.985	275	278	240	263
	iso ^b	1.968	312	251	208	191
	aniso ^c	-0.025	55	-40	-48	-108
Spinach	X	1.997	310	235	185	170
	Y	1.970	310	235	185	170
	\perp ^a	1.984	310	235	185	170
	$z(\parallel)$ ^a	1.965	275	275	245	240
	iso ^b	1.977	298	248	205	193
	aniso ^c	0.019	35	-40	-60	-70

^a The equatorial and axial \mathbf{G} and \mathbf{A}_i values are defined as: $G_{\perp} = (G_x + G_y)/2$, $G_{\parallel} = G_z$ and $A_{\perp, i} = (A_{x, i} + A_{y, i})/2$, $A_{\parallel, i} = A_{z, i}$. ^b The isotropic \mathbf{G} and \mathbf{A}_i values are the average of the individual values: $G_{\text{iso}} = (G_x + G_y + G_z)/3$ and $A_{\text{iso}, i} = (A_{x, i} + A_{y, i} + A_{z, i})/3$. ^c The anisotropy of the \mathbf{G} and \mathbf{A}_i tensors is expressed as the difference between the equatorial and axial components of the tensor: $G_{\text{aniso}} = G_{\parallel} - G_{\perp}$ and $A_{\text{aniso}, i} = A_{\parallel, i} - A_{\perp, i}$

The Q-band ⁵⁵Mn ENDOR spectrum of the S₂ state multiline spectrum of spinach PS II, shown in Fig. 6a, basically resolves four peaks (with additional shoulders) spread over a range of 80-200 MHz. The line shape is virtually invariant when measured at different positions within the spectral envelope. As seen with the multiline spectrum, it also has poor spectral resolution. In contrast to the spectra of the dinuclear model complexes depicted in Fig. 6b, c, the eigenvalues of the individual ⁵⁵Mn hyperfine matrices (\mathbf{A}_1 - \mathbf{A}_4) are not distinctly resolved for the Mn₄O₅Ca cluster, but rather overlap each other, such that the turning points in the powder spectrum are not clearly identified. Nevertheless, this experiment readily yields an important result. As all the eigenvalues of the ⁵⁵Mn hyperfine matrices are only spread over ~100 MHz, they all have approximately of the same magnitude (Table 1). This then requires all four Mn ions to carry significant electron spin, i.e. possess large spin projection coefficients: $|\rho_i| \sim 1$ to reproduce both the ENDOR and EPR spectral envelopes simultaneously. This same feature is not observed in mixed valence model complexes (Fig. 6b, c). Here, the two Mn ions carry significantly different spin projections (see Section 3.2 about Mn^{III}Mn^{IV} and Mn^{II}Mn^{III} dimers). In these systems, the eigenvalues of the two ⁵⁵Mn hyperfine matrices (\mathbf{A}_1 , \mathbf{A}_2) are spectrally resolved, and thus can be determined by inspection (Fig. 6b, c). While this is not achievable for the OEC, simulations that reproduce satisfactorily both multi-frequency Q- and X-band EPR and ENDOR spectra can be considered to provide a unique solution for the effective spin Hamiltonian parameters (\mathbf{G}

and the eigenvalues of the ^{55}Mn hyperfine matrices \mathbf{A}_i), within the assumption that the principal directions of the \mathbf{G} and \mathbf{A}_i matrices are collinear.

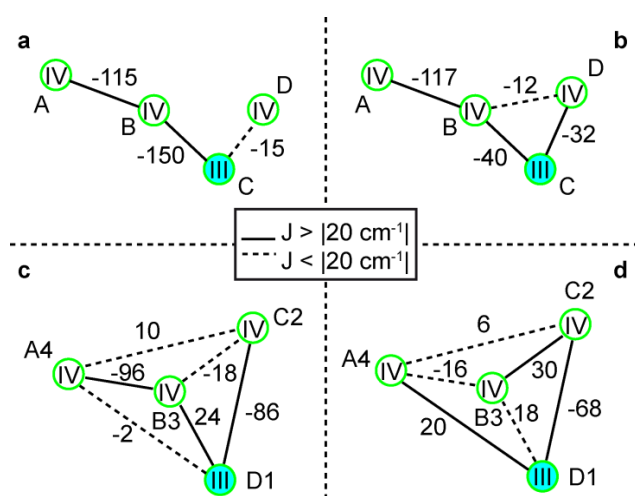


Fig. 7 Models for the electronic exchange coupling of the Mn ions in the S_2 state of the $\text{Mn}_4\text{O}_5\text{Ca}$ cluster with pairwise J_{ij} couplings given in cm^{-1} . **a** The original 3+1 / dangler model of Peloquin *et al.* [133]; **b** Y coupling scheme 3 by Kulik *et al.* [9]; **c** Pantazis model 1, [32] based on EXAFS core I [32, 140], and **d** Pantazis model 11, [32] based on the structure by Siegbahn [33, 158, 159]. In models a and b, the individual Mn spin centers are not assigned to specific Mn positions in a structural model of the OEC; thus, the nomenclature does not contain numbers from X-ray crystallographic structures. In models a and b, the only Mn^{III} ion is Mn_C , whereas in models c and d, this is Mn_{D1} . Models a-c require $\text{Mn}_{A/A4}$ to be strongly coupled to $\text{Mn}_{B/B3}$. Models b-d require $\text{Mn}_{C/C2}$ to be strongly coupled to $\text{Mn}_{D/D1}$. The topologies of models a and b on the one hand, and models c and d on the other differ by their connectivity of $\text{Mn}_{A/A4}$ to the trimer unit

The eigenvalues of the four ^{55}Mn \mathbf{A}_i matrices can then be used to evaluate and develop electronic exchange coupling models (J coupling schemes), which define their individual spin projection tensors $\boldsymbol{\rho}_i$. The computed $\boldsymbol{\rho}_i$ matrices map the effective \mathbf{A}_i matrices to the intrinsic (on-site) hyperfine coupling matrices \mathbf{a}_i according to the relation $\mathbf{A}_i = \boldsymbol{\rho}_i \mathbf{a}_i$. For a certain scheme to be valid, the calculated isotropic and anisotropic intrinsic values a_{iso} and a_{aniso} are required to match the known characteristic ranges of Mn^{III} and Mn^{IV} ions (see Supplementary Tables S1-S3). For more detailed information, see Refs. [32, 37, 53, 123, 133]. In the case of the strongly coupled tetramanganese cluster, in which the electronic exchange coupling is the dominant interaction, the J coupling scheme also determines the energy level spin ladder. Therefore, a further observable to relate a J coupling model to experimental data is the energy difference Δ between the ground spin state and the first excited spin state [32, 34]. Δ can be estimated from temperature-dependent EPR experiments on the signal of the ground spin state. One method is to measure the temperature dependence of the CW EPR signal intensity

[86, 106, 160]. In case an Orbach process is the dominant spin-lattice relaxation mechanism, the temperature dependence of the T_1 relaxation time, which can be determined using the pulse EPR inversion recovery experiment, can be related to Δ [161, 162]. For the $S_t = 1/2$ states of the OEC, the ground-to-first state energy difference has been found to be 3-37 cm^{-1} in S_2 [53, 106, 108, 163, 164] and 22 cm^{-1} to $\geq 30 \text{ cm}^{-1}$ in S_0 [90, 165], depending on sample treatment, such as the addition of MeOH or modifications at the Ca^{2+} site.

In the original work of Peloquin *et al.* [133], four fitted ^{55}Mn hyperfine tensors, which nominally yield experimental spin projection coefficients (see Section 4), were used to develop J coupling schemes for the $\text{Mn}_4\text{O}_5\text{Ca}$ cluster in the S_2 state. They proposed a tetramer topology for the $\text{Mn}^{\text{III}}(\text{Mn}^{\text{IV}})_3$ complex, the ‘3 + 1’ model, where three of the four Mn ions are strongly coupled together ($J \geq 50 \text{ cm}^{-1}$), with the fourth, outer Mn ion being more weakly coupled (Fig. 7a), similar to previous theoretical evaluation of EPR and EXAFS data [166]. This ‘dangler’ model was subsequently refined by Charlot *et al.* [37] and Kulik *et al.* [9] who favored a Y coupling scheme, where three of the four Mn ions form a trimer unit, with the fourth Mn ion being strongly coupled to one Mn ion of the triangle (Fig. 7b). The position of the only Mn^{III} of the S_2 state within the Y-shaped core remained ambiguous. Two consistent coupling schemes were developed by Kulik *et al.* [9], in which the Mn^{III} is assigned to either the monomeric Mn_A or Mn_C in the triangle. The position of the Mn^{III} as part of the trimer unit is supported by the large ^{14}N coupling from the coordinating histidine D1-His332 (see Section 5.3) and orientation-dependent EPR/ ^{55}Mn ENDOR on PS II single crystals [167].

5.2.3 The Density Functional Approach

The advancement of DFT as a tool to reliably calculate magnetic resonance observables has fundamentally changed the development of OEC models. The interpretation of EPR/ ^{55}Mn ENDOR data can now be achieved theoretically on the basis of detailed geometric models. First, an atomic structure of the OEC, e.g. based on X-ray crystallographic information, is proposed. BS-DFT then allows one to estimate the theoretical exchange pathways within the specific model of interest. The exchange coupling constants allow the spin projection coefficients/hyperfine couplings to be calculated and compared against the EPR/ ^{55}Mn ENDOR experiment. Thus, the EPR/ ^{55}Mn ENDOR experiment now acts as a filter via which OEC structural candidates are differentiated.

DFT calculations of ^{55}Mn hyperfine coupling constants performed by Pantazis *et al.* [32] for two groups of models of the OEC (Fig. 7c, d), the experimental, polarized EXAFS-based models [140] and the energy-minimized computational model of Siegbahn [33, 159], established for the first time relations between structural, magnetic and spectroscopic properties. Recent work by Cox *et al.* [53] has shown that only two models are satisfactory with regard to the calculated ^{55}Mn hyperfine coupling constants, one generated from polarized EXAFS core I and the other being a model of Siegbahn [32, 53]. Additional spin projection analysis indicated that the latter model [33] was the most consistent with all spectroscopic EPR/ ^{55}Mn ENDOR data to date [53]. These findings agree with those of Schinzel *et al.* [135] for a similar J coupling scheme derived from this structure. Furthermore, the model has proven to be very robust in that it can be adapted to be valid for several variants of the OEC, such as originating from different species like cyanobacteria and higher plants [108], and explain modifications, such as addition of MeOH [108], substitution of Ca^{2+} for Sr^{2+} [53] or removal of Ca^{2+} [164]. These modifications could all be rationalized on the basis of a modulation of the electronic exchange coupling between Mn_{A4} and the Mn ions of the $\text{Mn}_{\text{B3}}\text{Mn}_{\text{C2}}\text{Mn}_{\text{D1}}$ moiety and suggest that small molecules, such as small organic alcohols and NH_3 [70, 73, 76, 102, 168], bind in the vicinity of the monomer-trimer junction. Similarly, as Ca^{2+} coordinates one of the oxo-bridges that connects Mn_{A4} with the $\text{Mn}_{\text{B3}}\text{Mn}_{\text{C2}}\text{Mn}_{\text{D1}}$ moiety, its replacement by Sr^{2+} or its removal should also perturb the Mn monomer-trimer exchange interaction.

This basic picture for electronic structure perturbation of the OEC can be further extended to include the $S > 1/2$ spin state configurations. In a very recent DFT study [35], Pantazis *et al.* identified a second low energy conformation for the S_2 state $\text{Mn}_4\text{O}_5\text{Ca}$ cluster, besides the ‘open’ cuboid or fused twist structure. This second form represents a ‘proper’ $\text{Mn}_3\text{O}_4\text{Ca}$ cuboid with Mn_{A4} attached as a dangling Mn via a mono- μ -oxo bridge being the unique Mn^{III} ion. Thus, it resembles a revised model of the original ‘London’ structure [16] proposed by Barber and Murray [169]. It possesses a ground spin $S_t = 5/2$ and supposedly gives rise to the $g \geq 4.1$ signals, while the $S_t = 1/2$ open cuboid conformation is the origin of the $g \approx 2$ multiline signal.

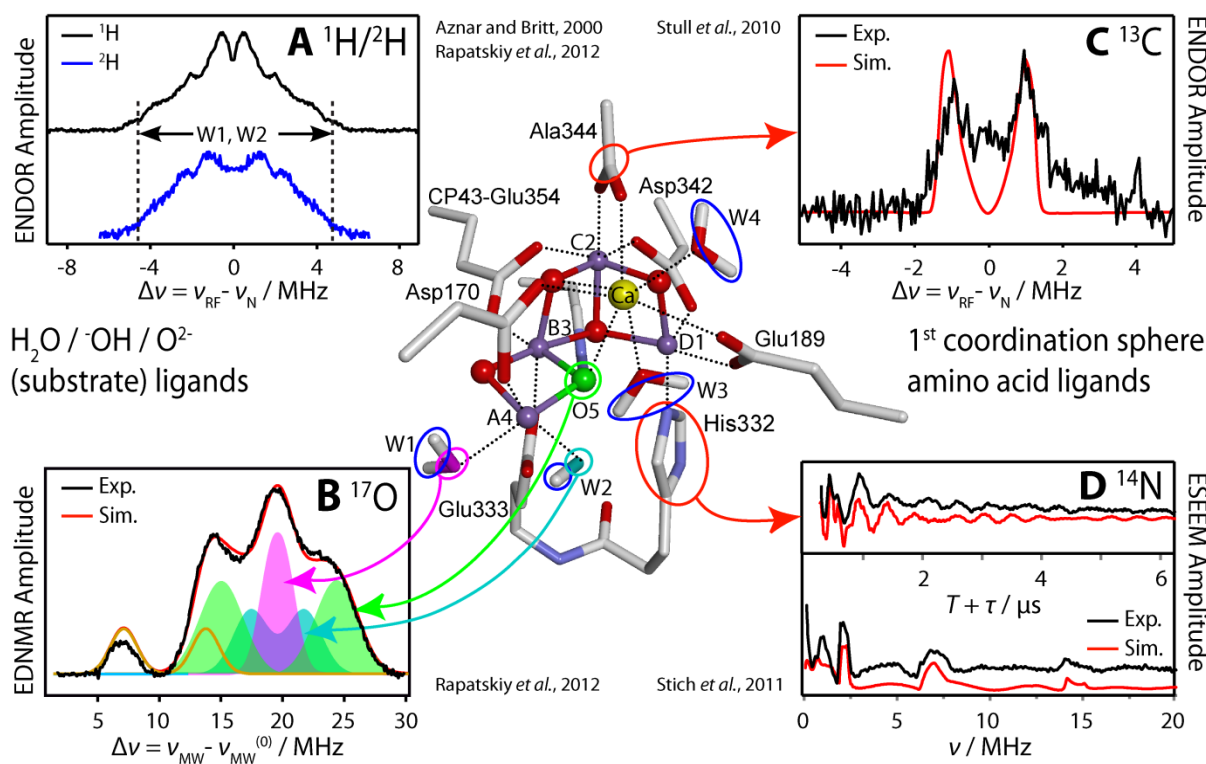


Fig. 8 Detection of various electron nuclear interactions of ligand nuclei with the $\text{Mn}_4\text{O}_5\text{Ca}$ cluster in the S_2 state (center, model 1d2' from Ames *et al.* [34]) via different spectroscopic techniques. **a** ^1H Davies ENDOR [131]; **b** $^{14}\text{N}/^{17}\text{O}$ ELDOR-detected NMR [131]; **c** ^{13}C Mims ENDOR, adapted from [130]; **d** ^{14}N 3-pulse ESEEM, adapted from [170]. Mn, Ca, N, O, C and H atoms are shown in purple, yellow, blue, red gray, and white respectively. Exchangeable O atoms are depicted in magenta, turquoise, and green. For reasons of clarity, only water-derived H atoms are shown. Colored circles indicate contributions from individual nuclei to the respective spectra. Black and blue solid traces represent the data, red and orange solid traces and colored areas represent simulations based on the spin Hamiltonian formalism

5.3 Magnetic Coupling of Ligands (e.g. ^1H , ^{13}C , ^{14}N , ^{17}O) in the S_2 State of the $\text{Mn}_4\text{O}_5\text{Ca}$ cluster

The EPR-spectroscopic investigation of the magnetic interaction between the $\text{Mn}_4\text{O}_5\text{Ca}$ cluster and its ligands, comprising ^1H , ^{13}C , ^{14}N , and ^{17}O nuclei, is another experimental handle that has further helped in the development of electronic and structural models of the OEC and to locate potential substrate sites (Fig. 8). Here, the spin projection coefficient of a specific Mn ion can be assessed from the magnitude of ligand couplings to it compared to those measured in model complexes and to DFT calculations.

This basic approach was applied for the imidazole ^{14}N ligand of histidine D1-His332 to the Mn_{D1} ion. In the S_2 state, an effective ^{14}N hyperfine coupling constant $A_{\text{iso}} \approx 7$ MHz was determined by ESEEM (Fig. 8d) [170, 171] and ELDOR-detected NMR measurements [131]

and assigned to D1-His332 by mutagenesis experiments [170, 172]. It is considerably larger than those seen for Mn^{IV}-bound histidine ligands in dimeric Mn^{III}Mn^{IV}-complexes, such as in dimanganese-containing catalase ($A_{\text{iso}} = 2\text{-}3$ MHz) [173], suggesting that Mn_{D1} is not a Mn^{IV} but instead must represent the Mn^{III} ion. The coupling for a nitrogen ligand to the Mn^{III} ion is expected to be larger as it carries a considerably larger spin projection factor ($|\rho| \approx 1.6$) compared to the Mn^{IV} ions ($|\rho| \approx 1$). Within this framework, the intrinsic hyperfine coupling constant a_{iso} is of the order of 4-5 MHz, midway between on-site couplings seen for equatorial (2-4 MHz) and axial (6 MHz) Mn^{III} ligands. This result compares well to ¹⁴N hyperfine and nuclear quadrupole coupling estimates from the BS-DFT studies of Schinzel *et al.* [135] and Ames *et al.* [34] for several models of the S₂ state of the OEC. Thus, the D1-His332 ¹⁴N electron nuclear interaction fixes the oxidation state of the Mn_{D1} ion to Mn^{III} with a spin projection $|\rho_{\text{D1}}| > 1.5$.

¹³C hyperfine spectroscopy on selectively labeled PS II mutants can identify the binding of amino acid residues to the tetramanganese core. Mims ENDOR experiments on PS II samples with a ¹³C-labeled C-terminal carboxylate carbon of the D1 protein, from alanine D1-Ala344, revealed an effective isotropic ¹³C hyperfine coupling constant A_{iso} on the order of 1 MHz (Fig. 8c) [130]. By comparison to the ¹³C hyperfine coupling of the Mn^{III}-(μ -O)₂-Mn^{IV} Taccn complex, the COO⁻ group of D1-Ala344 was assigned to be directly Mn-bound, to a Mn^{IV} ion carrying a spin projection $|\rho|$ of 1. Taking into account recent X-ray crystallographic (Fig. 2a) [20] and computational structures (Fig. 8) [32-34, 135], which show the carboxylate group to be ligated to Mn_{C2} and Ca²⁺, requires Mn_{C2} to have a $|\rho_{\text{C2}}| \approx 1$ and be a Mn^{IV} ion. Thus, the D1-His332 ¹⁴N and D1-Ala344 ¹³C electron nuclear couplings both support the tetramer model for the electronic structure of the S₂ state of the OEC derived from ⁵⁵Mn ENDOR described in detail above (Fig. 7d) [32, 34, 53].

Substrate binding to the OEC can be probed using either the ¹H (or ²H) or ¹⁷O isotopes. Analysis of the coupling model of ¹H/²H nuclei to the Mn₄O₅Ca core is relatively straightforward as they represent more distant nuclei. Thus, their hyperfine interaction with the electronic spin of the tetramanganese cluster can be treated as being dominated by the through-space dipolar mechanism, which can be calculated from geometric constraints (see Section 3.2.3). The ¹H/²H couplings as inferred from CW and pulse (Mims, Davies) ENDOR (Fig. 8a), ESEEM or HYSCORE [68, 69, 76, 131, 174, 175] extend to 8 MHz (A_{\parallel}). This coupling magnitude is similar to those from terminal water/hydroxo ligands of Mn^{IV} ions seen in model complexes, including the dimanganese complexes in Refs. [124, 128]. Within the tetramer spin projection model for the electronic structure of the S₂ state [32, 34, 53], this

result can then be readily understood. The largest $^1\text{H}/^2\text{H}$ hyperfine couplings observed represent the terminal $\text{H}_2\text{O}/\text{OH}^-$ ligands (W1, W2) of the Mn_{A4} ion ($|\rho_{\text{A4}}| \approx 1$, $\text{Mn}_{\text{A4}}\text{-H}$ distance $\approx 2.5\text{-}3$ Å) [131, 174, 175]. Protons from Ca^{2+} -bound water (W3, W4) are expected to exhibit smaller couplings as these protons are 1-2 Å further from any Mn spin center. The absence of any larger coupling precludes the presence of a protonated (μ -hydroxo) bridge in the S_2 state [131].

The same approach can be used for ^{17}O nuclei. Recently, Rapatskiy *et al.* performed W-band ELDOR-detected NMR experiments on PS II (Fig. 8b) [131] and interpreted the measured spectra on the basis of the spin coupling model developed by Pantazis *et al.* [32] (see Fig. 7d). In ^{17}O -exchanged PS II samples, three distinguishable signals originating from oxygen ligands could be detected. Weakly ($A_{\text{iso}} \approx 1$ MHz) and intermediately ($A_{\text{iso}} \approx 5$ MHz) coupling ^{17}O species were assigned to terminal $\text{H}_2\text{O}/\text{OH}^-$ ligands of Mn_{A4} (W1, W2) and the Ca^{2+} ion (W3, W4). These results are also consistent with a fused twist core model [131] and the surrounding $\text{H}_2\text{O}/\text{OH}^-$ ligands present in the structure by Siegbahn [33], which are similar to those in the Umena crystal structure [20]. Additionally, a strongly coupling ^{17}O species with $A_{\text{iso}} \approx 10$ MHz was identified. By comparison to the μ -oxo bridged $\text{Mn}^{\text{III}}\text{-(}\mu\text{-O)}_2\text{-Mn}^{\text{IV}}$ BIPY complex (see Fig. 6b), it was assigned to one of the μ -oxo bridges within the cluster. As this putative bridge exchanges with solvent water on a seconds timescale, it was proposed to serve as one of the two substrates. Based on a comparative analysis of the principal directions of the hyperfine matrices of this ^{17}O and the ^{14}N from D1-His332, it was concluded that, in a fused twist core, this μ -oxo bridge represents one of the two μ -oxo atoms bridging Mn_{A4} and Mn_{B3} . This has immediate consequences for the possible mechanism of O-O bond formation in the higher oxidation states. According to these findings, the μ -oxo bridge is attacked by a nucleophilic oxygen atom or, after being oxidized, undergoes a radical coupling with the other substrate. As proposed by Siegbahn [33], this second substrate would be a water molecule binding in its designated site, supposedly the open coordination site of Mn_{D1} , past the S_2 state. Both, in the latter case and also if the other substrate is one of the Ca^{2+} -bound water molecules, spatial considerations render O5 to be most likely the exchangeable substrate detected (Fig. 1). Unique properties of the O5 μ -oxo bridge are its specific coordination environment, created by direct ligation of the strong Lewis acid Ca^{2+} , and its flexibility, inferred by the structural equilibrium between μ -oxo bridge and cuboidal corner [35]. These features serve as an explanation for its unusually facile exchangeability, at rates much faster than those observed in μ -oxo bridged model complexes.

6 Concluding remarks

This review article summarizes the necessary theoretical background and the relevant studies making use of EPR and related (hyperfine) spectroscopies to investigate the OEC and the water splitting reaction. The basic spin physics approach employed to analyze EPR results was introduced, first in terms of manganese models and subsequently with regard to the Mn tetramer of the OEC proper. It is shown how these complicated systems can be treated within the spin Hamiltonian formalism as a coupled entity, with the help of spin projection factors. To obtain these factors, knowledge of a valid electronic model that reproduces the electronic exchange coupling topology effective in the particular system is crucial. State-of-the-art theoretical methodology, namely the BS-DFT formalism, which can be used to relate spectroscopic observables and structural properties has been described. Through a combination of these techniques, the picture of the OEC in low oxidation states, especially S_2 and S_0 , has been advanced over the last years to an electronic model consistent with an increasing amount of experimental data. These results have helped refine the X-ray crystallography model, which, although having provided an improved structure at near-atomic resolution, still suffers from reductive radiation damage. EPR-based techniques not only help to discriminate between proposed models and improve these structures, but provide a number of experiments to directly probe ligand interactions and the binding of substrate molecules. Knowledge of the substrates, their identity, position and binding kinetics, is key to understanding the mechanism of photosynthetic water oxidation. Further investigation of the higher oxidized S states of the Mn_4O_5Ca cluster, when the O-O bond is formed, will be crucial for its elucidation.

Acknowledgments S.K.M. is grateful to the Natural Sciences and Engineering Research Council (NSERC) of Canada for partial financial support, and to Professor Wolfgang Lubitz for inviting him to spend three months of his sabbatical leave at the Max Planck Institute for Bioinorganic Chemistry, Mülheim an der Ruhr, Germany. T.L. is supported by the Federal Ministry of Education and Research of Germany (BMBF) in the framework of the Bio-H2 project (03SF0355C).

References

[1] A. Magnuson, M. Anderlund, O. Johansson, P. Lindblad, R. Lomoth, T. Polivka, S. Ott, K. Stensjo, S. Styring, V. Sundstrom, L. Hammarstrom, *Acc. Chem. Res.* 42(12), 1899-1909 (2009)

- [2] I. McConnell, G.H. Li, G.W. Brudvig, *Chem. Biol.* 17(5), 434-447 (2010)
- [3] S. Styring, *Faraday Discuss.* 155(357-376 (2012)
- [4] T. Wydrzynski, S. Satoh, *Photosystem II: The Light-Driven Water:Plastoquinone Oxidoreductase*, (Springer, Dordrecht, 2005),
- [5] W. Lubitz, E.J. Reijerse, J. Messinger, *Energy Environ. Sci.* 1(1), 15-31 (2008)
- [6] P. Joliot, G. Barbieri, R. Chabaud, *Photochem. Photobiol.* 10(5), 309-329 (1969)
- [7] B. Kok, B. Forbush, M. McGloin, *Photochem. Photobiol.* 11(6), 457-475 (1970)
- [8] S. Styring, A.W. Rutherford, *Biochemistry* 26(9), 2401-2405 (1987)
- [9] L.V. Kulik, B. Epel, W. Lubitz, J. Messinger, *J. Am. Chem. Soc.* 129(44), 13421-13435 (2007)
- [10] G.M. Cheniae, I.F. Martin, *Biochim. Biophys. Acta, Bioenerg.* 197(2), 219-239 (1970)
- [11] K. Sauer, *Acc. Chem. Res.* 13(8), 249-256 (1980)
- [12] C.F. Yocum, C.T. Yerkes, R.E. Blankenship, R.R. Sharp, G.T. Babcock, *Proc. Natl. Acad. Sci. U. S. A.* 78(12), 7507-7511 (1981)
- [13] V.K. Yachandra, K. Sauer, M.P. Klein, *Chem. Rev.* 96(7), 2927-2950 (1996)
- [14] A. Zouni, H.T. Witt, J. Kern, P. Fromme, N. Krauss, W. Saenger, P. Orth, *Nature* 409(6821), 739-743 (2001)
- [15] N. Kamiya, J.R. Shen, *Proc. Natl. Acad. Sci. U. S. A.* 100(1), 98-103 (2003)
- [16] K.N. Ferreira, T.M. Iverson, K. Maghlaoui, J. Barber, S. Iwata, *Science* 303(5665), 1831-1838 (2004)
- [17] G.W. Brudvig, R.H. Crabtree, *Proc. Natl. Acad. Sci. U. S. A.* 83(13), 4586-4588 (1986)
- [18] B. Loll, J. Kern, W. Saenger, A. Zouni, J. Biesiadka, *Nature* 438(7070), 1040-1044 (2005)
- [19] A. Guskov, J. Kern, A. Gabdulkhakov, M. Broser, A. Zouni, W. Saenger, *Nat. Struct. Mol. Biol.* 16(3), 334-342 (2009)
- [20] Y. Umena, K. Kawakami, J.-R. Shen, N. Kamiya, *Nature* 473(7345), 55-60 (2011)
- [21] J. Yano, J. Kern, K.D. Irrgang, M.J. Latimer, U. Bergmann, P. Glatzel, Y. Pushkar, J. Biesiadka, B. Loll, K. Sauer, J. Messinger, A. Zouni, V.K. Yachandra, *Proc. Natl. Acad. Sci. U. S. A.* 102(34), 12047-12052 (2005)
- [22] M. Grabolle, M. Haumann, C. Müller, P. Liebisch, H. Dau, *J. Biol. Chem.* 281(8), 4580-4588 (2006)
- [23] S. Petrie, P. Gatt, R. Stranger, R.J. Pace, *Phys. Chem. Chem. Phys.* 14(32), 11333-11343 (2012)
- [24] U. Bergmann, M.M. Grush, C.R. Horne, P. DeMarois, J.E. Penner-Hahn, C.F. Yocum, D.W. Wright, Dube, W.H. Armstrong, G. Christou, H.J. Eppley, S.P. Cramer, *J. Phys. Chem. B* 102(42), 8350-8352 (1998)
- [25] M. Haumann, C. Müller, P. Liebisch, L. Iuzzolino, J. Dittmer, M. Grabolle, T. Neisius, W. Meyer-Klaucke, H. Dau, *Biochemistry* 44(6), 1894-1908 (2005)
- [26] J. Messinger, J.H. Robblee, U. Bergmann, C. Fernandez, P. Glatzel, H. Visser, R.M. Cinco, K.L. McFarlane, E. Bellacchio, S.A. Pizarro, S.P. Cramer, K. Sauer, M.P. Klein, V.K. Yachandra, *J. Am. Chem. Soc.* 123(32), 7804-7820 (2001)
- [27] T.A. Roelofs, W. Liang, M.J. Latimer, R.M. Cinco, A. Rompel, J.C. Andrews, K. Sauer, V.K. Yachandra, M.P. Klein, *Proc. Natl. Acad. Sci. U. S. A.* 93(8), 3335-3340 (1996)
- [28] S. Lubner, I. Rivalta, Y. Umena, K. Kawakami, J.R. Shen, N. Kamiya, G.W. Brudvig, V.S. Batista, *Biochemistry* 50(29), 6308-6311 (2011)
- [29] A. Grundmeier, H. Dau, *Biochim. Biophys. Acta, Bioenerg.* 1817(1), 88-105 (2012)
- [30] A. Galstyan, A. Robertazzi, E.W. Knapp, *J. Am. Chem. Soc.* 134(17), 7442-7449 (2012)

- [31] M. Kusunoki, *Biochim. Biophys. Acta, Bioenerg.* 1767(6), 484-492 (2007)
- [32] D.A. Pantazis, M. Orio, T. Petrenko, S. Zein, W. Lubitz, J. Messinger, F. Neese, *Phys. Chem. Chem. Phys.* 11(31), 6788-6798 (2009)
- [33] P.E.M. Siegbahn, *Acc. Chem. Res.* 42(12), 1871-1880 (2009)
- [34] W. Ames, D.A. Pantazis, V. Krewald, N. Cox, J. Messinger, W. Lubitz, F. Neese, *J. Am. Chem. Soc.* 133(49), 19743-19757 (2011)
- [35] D. Pantazis, W. Ames, N. Cox, W. Lubitz, F. Neese, *Angew. Chem., Int. Ed.* 51(39), 9935-9940 (2012)
- [36] J.M. Peloquin, K.A. Campbell, R.D. Britt, *J. Am. Chem. Soc.* 120(27), 6840-6841 (1998)
- [37] M.-F. Charlot, A. Boussac, G. Blondin, *Biochim. Biophys. Acta, Bioenerg.* 1708(1), 120-132 (2005)
- [38] D.F. Ghanotakis, G.T. Babcock, C.F. Yocum, *FEBS Lett.* 167(1), 127-130 (1984)
- [39] T.-a. Ono, Y. Inoue, *FEBS Lett.* 227(2), 147-152 (1988)
- [40] M. Sivaraja, J. Tso, G.C. Dismukes, *Biochemistry* 28(24), 9459-9464 (1989)
- [41] A. Boussac, J.L. Zimmermann, A.W. Rutherford, *Biochemistry* 28(23), 8984-8989 (1989)
- [42] A. Boussac, J.-L. Zimmermann, A.W. Rutherford, *FEBS Lett.* 277(1-2), 69-74 (1990)
- [43] A.W. Rutherford, *Trends Biochem. Sci.* 14(6), 227-232 (1989)
- [44] V.L. Pecoraro, M.J. Baldwin, M.T. Caudle, W.-Y. Hsieh, N.A. Law, *Pure Appl. Chem.* 70(4), 925-929 (1998)
- [45] J. Limburg, V.A. Szalai, G.W. Brudvig, *J. Chem. Soc., Dalton Trans.* 9, 1353-1361 (1999)
- [46] J.S. Vrettos, J. Limburg, G.W. Brudvig, *Biochim. Biophys. Acta, Bioenerg.* 1503(1-2), 229-245 (2001)
- [47] G. Hendry, T. Wydrzynski, *Biochemistry* 42(20), 6209-6217 (2003)
- [48] H.J. van Gorkom, C.F. Yocum, in *Photosystem II: The Light-Driven Water:Plastoquinone Oxidoreductase*, ed. By T. Wydrzynski, K. Satoh (Springer, Dordrecht, 2005), pp. 285-305
- [49] P.J. Riggs-Gelasco, R. Mei, D.F. Ghanotakis, C.F. Yocum, J.E. Penner-Hahn, *J. Am. Chem. Soc.* 118(10), 2400-2410 (1996)
- [50] W. Junge, M. Haumann, *Biochim. Biophys. Acta, Bioenerg.* 1411(1), 121-133 (1999)
- [51] A. Boussac, A.W. Rutherford, *Biochemistry* 27(9), 3476-3483 (1988)
- [52] A. Boussac, F. Rappaport, P. Carrier, J.M. Verbavatz, R. Gobin, D. Kirilovsky, A.W. Rutherford, M. Sugiura, *J. Biol. Chem.* 279(22), 22809-22819 (2004)
- [53] N. Cox, L. Rapatskiy, J.-H. Su, D.A. Pantazis, M. Sugiura, L. Kulik, P. Dorlet, A.W. Rutherford, F. Neese, A. Boussac, W. Lubitz, J. Messinger, *J. Am. Chem. Soc.* 133(10), 3635-3648 (2011)
- [54] J.S. Vrettos, D.A. Stone, G.W. Brudvig, *Biochemistry* 40(26), 7937-7945 (2001)
- [55] C.F. Yocum, in *Manganese Redox Enzymes*, ed. By V.L. Pecoraro (VCH Publishers, New York, 1992), pp. 71-84
- [56] P.H. Homann, *Photosynth. Res.* 73(1-3), 169-175 (2002)
- [57] S. Izawa, R.L. Heath, G. Hind, *Biochim. Biophys. Acta, Bioenerg.* 180(2), 388-398 (1969)
- [58] H. Wincencjusz, H.J. van Gorkom, C.F. Yocum, *Biochemistry* 36(12), 3663-3670 (1997)
- [59] H. Wincencjusz, C.F. Yocum, H.J. van Gorkom, *Biochemistry* 37(23), 8595-8604 (1998)
- [60] K. Hasegawa, Y. Kimura, T.A. Ono, *Biochemistry* 41(46), 13839-13850 (2002)
- [61] K. Hasegawa, Y. Kimura, T. Ono, *Biophys. J.* 86(2), 1042-1050 (2004)
- [62] M. Baumgarten, J.S. Philo, G.C. Dismukes, *Biochemistry* 29(48), 10814-10822 (1990)

- [63] A. Boussac, P. Setif, A.W. Rutherford, *Biochemistry* 31(4), 1224-1234 (1992)
- [64] N. Lydakis-Simantiris, P. Dorlet, D.F. Ghanotakis, G.T. Babcock, *Biochemistry* 37(18), 6427-6435 (1998)
- [65] K. Olesen, L.E. Andreasson, *Biochemistry* 42(7), 2025-2035 (2003)
- [66] R. Pokhrel, I.L. McConnell, G.W. Brudvig, *Biochemistry* 50(14), 2725-2734 (2011)
- [67] I. Rivalta, M. Amin, S. Lubner, S. Vassiliev, R. Pokhrel, Y. Umena, K. Kawakami, J.R. Shen, N. Kamiya, D. Bruce, G.W. Brudvig, M.R. Gunner, V.S. Batista, *Biochemistry* 50(29), 6312-6315 (2011)
- [68] A. Kawamori, T. Inui, T. Ono, Y. Inoue, *FEBS Lett.* 254(1-2), 219-224 (1989)
- [69] R. Fiege, W. Zweggart, R. Bittl, N. Adir, G. Renger, W. Lubitz, *Photosynth. Res.* 48(1-2), 227-237 (1996)
- [70] R.D. Britt, K.A. Campbell, J.M. Peloquin, M.L. Gilchrist, C.P. Aznar, M.M. Dicus, J. Robblee, J. Messinger, *Biochim. Biophys. Acta, Bioenerg.* 1655(158-171) (2004)
- [71] W.F. Beck, G.W. Brudvig, *Biochemistry* 25(21), 6479-6486 (1986)
- [72] W.F. Beck, J.C. De Paula, G.W. Brudvig, *J. Am. Chem. Soc.* 108(14), 4018-4022 (1986)
- [73] D.A. Force, D.W. Randall, G.A. Lorigan, K.L. Clemens, R.D. Britt, *J. Am. Chem. Soc.* 120(51), 13321-13333 (1998)
- [74] R.D. Britt, J.M. Peloquin, K.A. Campbell, *Annu. Rev. Biophys. Biomol. Struct.* 29(463-495) (2000)
- [75] M.C.W. Evans, R.J. Ball, J.H.A. Nugent, *FEBS Lett.* 579(14), 3081-3084 (2005)
- [76] K.A. Åhring, M.C.W. Evans, J.H.A. Nugent, R.J. Ball, R.J. Pace, *Biochemistry* 45(23), 7069-7082 (2006)
- [77] A. Cua, D.H. Stewart, M.J. Reifler, G.W. Brudvig, D.F. Bocian, *J. Am. Chem. Soc.* 122(9), 2069-2077 (2000)
- [78] T. Noguchi, M. Sugiura, *Biochemistry* 39(36), 10943-10949 (2000)
- [79] T. Noguchi, M. Sugiura, *Biochemistry* 41(52), 15706-15712 (2002)
- [80] Y. Kimura, A. Ishii, T. Yamanari, T.A. Ono, *Biochemistry* 44(21), 7613-7622 (2005)
- [81] K. Burda, K.P. Bader, G.H. Schmid, *FEBS Lett.* 491(1-2), 81-84 (2001)
- [82] K. Burda, K.P. Bader, G.H. Schmid, *Biochim. Biophys. Acta, Bioenerg.* 1557(77-82) (2003)
- [83] G.C. Dismukes, Y. Siderer, *Proc. Natl. Acad. Sci. U. S. A.* 78(1), 274-278 (1981)
- [84] S.L. Dexhemier, M.P. Klein, *J. Am. Chem. Soc.* 114(8), 2821-2826 (1992)
- [85] H. Levanon, K. Möbius, *Annu. Rev. Biophys. Biomol. Struct.* 26(495-540) (1997)
- [86] T. Yamauchi, H. Mino, T. Matsukawa, A. Kawamori, T. Ono, *Biochemistry* 36(24), 7520-7526 (1997)
- [87] J. Messinger, J.H.A. Nugent, M.C.W. Evans, *Biochemistry* 36(37), 11055-11060 (1997)
- [88] J. Messinger, J.H. Robblee, W.O. Yu, K. Sauer, V.K. Yachandra, M.P. Klein, *J. Am. Chem. Soc.* 119(46), 11349-11350 (1997)
- [89] K.A. Campbell, J.M. Peloquin, D.P. Pham, R.J. Debus, R.D. Britt, *J. Am. Chem. Soc.* 120(2), 447-448 (1998)
- [90] K.A. Åhring, S. Peterson, S. Styring, *Biochemistry* 37(22), 8115-8120 (1998)
- [91] T. Matsukawa, H. Mino, D. Yoneda, A. Kawamori, *Biochemistry* 38(13), 4072-4077 (1999)
- [92] K.A. Campbell, D.A. Force, P.J. Nixon, F. Dole, B.A. Diner, R.D. Britt, *J. Am. Chem. Soc.* 122(15), 3754-3761 (2000)
- [93] J.P. McEvoy, G.W. Brudvig, *Chem. Rev.* 106(11), 4455-4483 (2006)
- [94] A. Haddy, *Photosynth. Res.* 92(3), 357-368 (2007)
- [95] A. Boussac, M. Sugiura, A.W. Rutherford, P. Dorlet, *J. Am. Chem. Soc.* 131(14), 5050-5051 (2009)

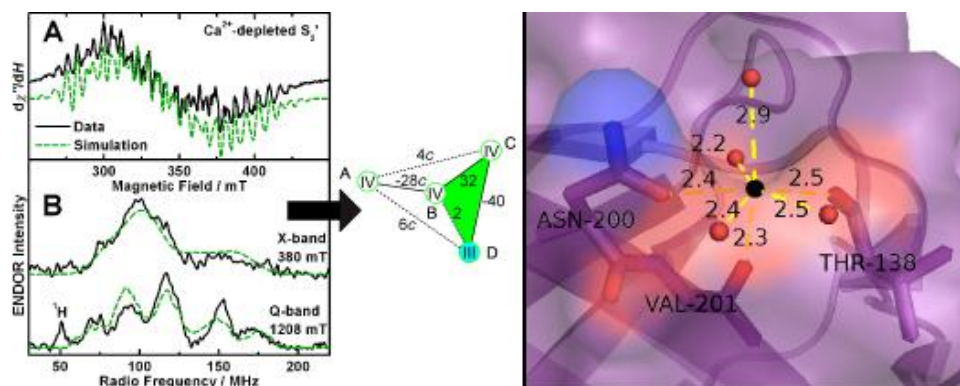
- [96] A. Boussac, J.J. Girerd, A.W. Rutherford, *Biochemistry* 35(22), 6984-6989 (1996)
- [97] A. Boussac, S. Un, O. Horner, A.W. Rutherford, *Biochemistry* 37(12), 4001-4007 (1998)
- [98] O. Horner, E. Rivière, G. Blondin, S. Un, A.W. Rutherford, J.-J. Girerd, A. Boussac, *J. Am. Chem. Soc.* 120(31), 7924-7928 (1998)
- [99] A. Boussac, A.W. Rutherford, *Biochim. Biophys. Acta, Bioenerg.* 1457(3), 145-156 (2000)
- [100] A. Haddy, K.V. Lakshmi, G.W. Brudvig, H.A. Frank, *Biophys. J.* 87(4), 2885-2896 (2004)
- [101] A. Boussac, H. Kuhl, S. Un, M. Rogner, A.W. Rutherford, *Biochemistry* 37(25), 8995-9000 (1998)
- [102] A. Boussac, M. Sugiura, Y. Inoue, A.W. Rutherford, *Biochemistry* 39(45), 13788-13799 (2000)
- [103] J.L. Zimmermann, A.W. Rutherford, *Biochemistry* 25(16), 4609-4615 (1986)
- [104] Z. Deák, S. Peterson, P. Geijer, K.A. Åhring, S. Styring, *Biochim. Biophys. Acta, Bioenerg.* 1412(3), 240-249 (1999)
- [105] P. Geijer, S. Peterson, K.A. Åhring, Z. Deák, S. Styring, *Biochim. Biophys. Acta, Bioenerg.* 1503(1-2), 83-95 (2001)
- [106] R.J. Pace, P.J. Smith, R. Bramley, D. Stehlik, *Biochim. Biophys. Acta, Bioenerg.* 1058(2), 161-170 (1991)
- [107] A. Boussac, *J. Biol. Inorg. Chem.* 2(5), 580-585 (1997)
- [108] J.H. Su, N. Cox, W. Ames, D.A. Pantazis, L. Rapatskiy, T. Lohmiller, L.V. Kulik, P. Dorlet, A.W. Rutherford, F. Neese, A. Boussac, W. Lubitz, J. Messinger, *Biochim. Biophys. Acta, Bioenerg.* 1807(7), 829-840 (2011)
- [109] N. Cox, W. Ames, B. Epel, L.V. Kulik, L. Rapatskiy, F. Neese, J. Messinger, K. Wieghardt, W. Lubitz, *Inorg. Chem.* 50(17), 8238-8251 (2011)
- [110] K.O. Schäfer, Exchange Coupled Manganese Complexes: Model Systems for the Active Centres of Redoxproteins Investigated with EPR Techniques, Doctoral Thesis, Technische Universität Berlin, 2002
- [111] K.A. Åhring, S. Peterson, S. Styring, *Biochemistry* 36(43), 13148-13152 (1997)
- [112] A. Boussac, H. Kuhl, E. Ghibaudi, M. Rogner, A.W. Rutherford, *Biochemistry* 38(37), 11942-11948 (1999)
- [113] J.H.A. Nugent, S. Turconi, M.C.W. Evans, *Biochemistry* 36(23), 7086-7096 (1997)
- [114] J.H.A. Nugent, I.P. Muhiuddin, M.C.W. Evans, *Biochemistry* 41(12), 4117-4126 (2002)
- [115] D. Koulougliotis, J.R. Shen, N. Ioannidis, V. Petrouleas, *Biochemistry* 42(10), 3045-3053 (2003)
- [116] D. Koulougliotis, C. Teutloff, Y. Sanakis, W. Lubitz, V. Petrouleas, *Phys. Chem. Chem. Phys.* 6(20), 4859-4863 (2004)
- [117] V. Petrouleas, D. Koulougliotis, N. Ioannidis, *Biochemistry* 44(18), 6723-6728 (2005)
- [118] J.H. Su, K.G.V. Havelius, F. Mamedov, F.M. Ho, S. Styring, *Biochemistry* 45(24), 7617-7627 (2006)
- [119] K.G.V. Havelius, J.H. Su, Y. Feyziyev, F. Mamedov, S. Styring, *Biochemistry* 45(30), 9279-9290 (2006)
- [120] N. Cox, F.M. Ho, N. Pownim, R. Steffen, P.J. Smith, K.G. Havelius, J.L. Hughes, L. Debono, S. Styring, E. Krausz, R.J. Pace, *Biochim. Biophys. Acta, Bioenerg.* 1787(7), 882-889 (2009)
- [121] S.K. Misra, in *Handbook of Electron Spin Resonance*, ed. By C.P. Poole, H.A. Farach (Springer, New York, 1999), pp. 115-150
- [122] D.P. Goldberg, J. Telser, J. Krzystek, A.G. Montalban, L.-C. Brunel, A.G.M. Barrett, B.M. Hoffman, *J. Am. Chem. Soc.* 119(37), 8722-8723 (1997)
- [123] A. Bencini, D. Gatteschi, *EPR of Exchange Coupled Systems*, (Springer-Verlag, Berlin, 1990),

- [124] K.O. Schäfer, R. Bittl, W. Zweggart, F. Lenzian, G. Haselhorst, T. Weyhermuller, K. Wieghardt, W. Lubitz, *J. Am. Chem. Soc.* 120(50), 13104-13120 (1998)
- [125] J.T. Sage, Y.M. Xia, P.G. Debrunner, D.T. Keough, J. Dejersey, B. Zerner, *J. Am. Chem. Soc.* 111(18), 7239-7247 (1989)
- [126] M. Zheng, S.V. Khangulov, G.C. Dismukes, V.V. Barynin, *Inorg. Chem.* 33(2), 382-387 (1994)
- [127] W. Zweggart, ESR- und ENDOR-Untersuchungen an mehrkernigen gemischtvalenten Mangankomplexen als Modelle für das wasseroxidierende Enzymsystem im Photosystem II, Doctoral Thesis, Technische Universität Berlin, 1995
- [128] D.W. Randall, A. Gelasco, M.T. Caudle, V.L. Pecoraro, R.D. Britt, *J. Am. Chem. Soc.* 119(19), 4481-4491 (1997)
- [129] O.M. Usov, V.M. Grigoryants, R. Tagore, G.W. Brudvig, C.P. Scholes, *J. Am. Chem. Soc.* 129(39), 11886-11887 (2007)
- [130] J.A. Stull, T.A. Stich, R.J. Service, R.J. Debus, S.K. Mandal, W.H. Armstrong, R.D. Britt, *J. Am. Chem. Soc.* 132(2), 446-447 (2010)
- [131] L. Rapatskiy, N. Cox, W. Ames, A. Savitsky, J. Sander, M. Nowaczyk, M. Rögner, A. Boussac, F. Neese, J. Messinger, W. Lubitz, *J. Am. Chem. Soc.* (in press)
- [132] M. Zheng, G.C. Dismukes, *Inorg. Chem.* 35(11), 3307-3319 (1996)
- [133] J.M. Peloquin, K.A. Campbell, D.W. Randall, M.A. Evanchik, V.L. Pecoraro, W.H. Armstrong, R.D. Britt, *J. Am. Chem. Soc.* 122(44), 10926-10942 (2000)
- [134] D.A. Pantazis, M. Orio, T. Petrenko, S. Zein, E. Bill, W. Lubitz, J. Messinger, F. Neese, *Chem. Eur. J.* 15(20), 5108-5123 (2009)
- [135] S. Schinzel, J. Schraut, A. Arbuznikov, P. Siegbahn, M. Kaupp, *Chem. Eur. J.* 16(34), 10424-10438 (2010)
- [136] S. Mukherjee, J.A. Stull, J. Yano, T.C. Stamatatos, K. Pringouri, T.A. Stich, K.A. Abboud, R.D. Britt, V.K. Yachandra, G. Christou, *Proc. Natl. Acad. Sci. U. S. A.* 109(7), 2257-2262 (2012)
- [137] G.C. Dismukes, Y. Siderer, *Febs Letters* 121(1), 78-80 (1980)
- [138] R. Radmer, G. Cheniae, in *Primary Processes of Photosynthesis*, ed. By J. Barber (Elsevier, Amsterdam, 1977), 303-349
- [139] S.K. Misra, in *Advanced EPR Applied to Biosciences, Satellite Symposium B in APES'01*, ed. By A. Kawamori (Kwansei Gakuin University, 2002), pp. 47-64
- [140] J. Yano, J. Kern, K. Sauer, M.J. Latimer, Y. Pushkar, J. Biesiadka, B. Loll, W. Saenger, J. Messinger, A. Zouni, V.K. Yachandra, *Science* 314(5800), 821-825 (2006)
- [141] Y. Pushkar, J. Yano, P. Glatzel, J. Messinger, A. Lewis, K. Sauer, U. Bergmann, V.K. Yachandra, *J. Biol. Chem.* 282(10), 7198-7208 (2007)
- [142] Y.L. Pushkar, J. Yano, K. Sauer, A. Boussac, V.K. Yachandra, *Proc. Natl. Acad. Sci. U. S. A.* 105(6), 1879-1884 (2008)
- [143] T. Noguchi, *Coord. Chem. Rev.* 252(3-4), 336-346 (2008)
- [144] F. Neese, *Coord. Chem. Rev.* 253(5-6), 526-563 (2009)
- [145] L. Noodleman, *J. Chem. Phys.* 74(5737-5743 (1981)
- [146] L. Noodleman, E.R. Davidson, *Chem. Phys.* 109(1), 131-143 (1986)

- [147] L. Noodleman, D.A. Case, *Adv. Inorg. Chem.* 38(423-470 (1992)
- [148] S. Sinnecker, F. Neese, L. Noodleman, W. Lubitz, *J. Am. Chem. Soc.* 126(8), 2613-2622 (2004)
- [149] M. Orio, D.A. Pantazis, T. Petrenko, F. Neese, *Inorg. Chem.* 48(15), 7251-7260 (2009)
- [150] C. Baffert, M. Orio, D.A. Pantazis, C. Duboc, A.G. Blackman, G. Blondin, F. Neese, A. Deronzier, M.-N. Collomb, *Inorg. Chem.* 48(21), 10281-10288 (2009)
- [151] B.E. Sturgeon, J.A. Ball, D.W. Randall, R.D. Britt, *J. Phys. Chem.* 98(49), 12871-12883 (1994)
- [152] D.W. Randall, B.E. Sturgeon, J.A. Ball, G.A. Lorigan, M.K. Chan, M.P. Klein, W.H. Armstrong, R.D. Britt, *J. Am. Chem. Soc.* 117(47), 11780-11789 (1995)
- [153] W. Zwegart, R. Bittl, K. Wieghardt, W. Lubitz, *Chem. Phys. Lett.* 261(3), 272-276 (1996)
- [154] K.O. Schafer, R. Bittl, F. Lendzian, V. Barynin, T. Weyhermuller, K. Wieghardt, W. Lubitz, *J. Phys. Chem. B* 107(5), 1242-1250 (2003)
- [155] L.V. Kulik, B. Epel, W. Lubitz, J. Messinger, *J. Am. Chem. Soc.* 127(8), 2392-2393 (2005)
- [156] L. Kulik, B. Epel, J. Messinger, W. Lubitz, *Photosynth. Res.* 84(1-3), 347-353 (2005)
- [157] C. Teutloff, K.O. Schafer, S. Sinnecker, V. Barynin, R. Bittl, K. Wieghardt, F. Lendzian, W. Lubitz, *Magn. Reson. Chem.* 43(S1), S51-S64 (2005)
- [158] Per E.M. Siegbahn, *Chem. Eur. J.* 14(27), 8290-8302 (2008)
- [159] P.E.M. Siegbahn, *J. Am. Chem. Soc.* 131(51), 18238-18239 (2009)
- [160] R.D. Britt, G.A. Lorigan, K. Sauer, M.P. Klein, J.L. Zimmermann, *Biochim. Biophys. Acta, Bioenerg.* 1140(1), 95-101 (1992)
- [161] R. Orbach, *Proc. R. Soc. London, A* 264(1319), 458-484 (1961)
- [162] A. Schweiger, G. Jeschke, *Principles of pulse electron paramagnetic resonance*, (Oxford University Press, Oxford, 2001), p. 225
- [163] G.A. Lorigan, R.D. Britt, *Biochemistry* 33(40), 12072-12076 (1994)
- [164] T. Lohmiller, N. Cox, J.H. Su, J. Messinger, W. Lubitz, *J. Biol. Chem.* 287(29), 24721-24733 (2012)
- [165] L.V. Kulik, W. Lubitz, J. Messinger, *Biochemistry* 44(26), 9368-9374 (2005)
- [166] K. Hasegawa, T. Ono, Y. Inoue, M. Kusunoki, *Bull. Chem. Soc. Jpn.* 72(5), 1013-1023 (1999)
- [167] C. Teutloff, S. Pudollek, S. Kessen, M. Broser, A. Zouni, R. Bittl, *Phys. Chem. Chem. Phys.* 11(31), 6715-6726 (2009)
- [168] R.D. Britt, J.L. Zimmermann, K. Sauer, M.P. Klein, *J. Am. Chem. Soc.* 111(10), 3522-3532 (1989)
- [169] J. Barber, J.W. Murray, *Phil. Trans. R. Soc. B* 363(1494), 1129-1137 (2008)
- [170] T.A. Stich, G.J. Yeagle, R.J. Service, R.J. Debus, R.D. Britt, *Biochemistry* 50(34), 7390-7404 (2011)
- [171] G.J. Yeagle, M.L. Gilchrist, R.M. McCarrick, R.D. Britt, *Inorg. Chem.* 47(6), 1803-1814 (2008)
- [172] R.J. Debus, K.A. Campbell, W. Gregor, Z.L. Li, R.L. Burnap, R.D. Britt, *Biochemistry* 40(12), 3690-3699 (2001)
- [173] T.A. Stich, J.W. Whittaker, R.D. Britt, *J. Phys. Chem. B* 114(45), 14178-14188 (2010)
- [174] C.P. Aznar, R.D. Britt, *Phil. Trans. R. Soc. B* 357(1426), 1359-1365 (2002)
- [175] S. Milikisiyants, R. Chatterjee, C.S. Coates, F.H.M. Koua, J.R. Shen, K.V. Lakshmi, *Energy Environ. Sci.* 5(7), 7747-7756 (2012)

Chapter 5

The Basic Properties of the Electronic Structure of the Oxygen-Evolving Complex of Photosystem II Are Not Perturbed by Ca^{2+} Removal



Lohmiller, T.; Cox, N.; Su, J.-H.; Messinger, J.; Lubitz, W.

J. Biol. Chem. **2012**, 287 (29), 24721-24733. <http://dx.doi.org/10.1074/jbc.M112.365288>

This research was originally published in The Journal of Biological Chemistry. © the American Society for Biochemistry and Molecular Biology.

The Basic Properties of the Electronic Structure of the Oxygen-evolving Complex of Photosystem II Are Not Perturbed by Ca^{2+} Removal^{*[5]}

Received for publication, March 22, 2012, and in revised form, April 25, 2012. Published, JBC Papers in Press, May 1, 2012, DOI 10.1074/jbc.M112.365288

Thomas Lohmiller^{†1}, Nicholas Cox[‡], Ji-Hu Su^{†2}, Johannes Messinger^{§3}, and Wolfgang Lubitz^{†4}

From the [†]Max-Planck-Institut für Bioorganische Chemie, Stiftstrasse 34-36, 45470 Mülheim an der Ruhr, Germany and the [§]Department of Chemistry, Chemical Biological Centre (KBC), Umeå University, S-90187 Umeå, Sweden

Background: EPR/⁵⁵Mn ENDOR spectroscopy of the oxygen-evolving complex (OEC) and Mn^{2+} in Ca^{2+} -depleted photosystem II.

Results: Electronic model of the Ca^{2+} -depleted OEC; characterization of Mn^{2+} binding.

Conclusion: Ca^{2+} is not critical for maintaining the electronic and spatial structure of the OEC. Its removal exposes a Mn^{2+} binding site supposedly in an extrinsic subunit.

Significance: Mechanistic implications for water oxidation; Mn^{2+} in photoassembly/D1 protein repair.

Ca^{2+} is an integral component of the $\text{Mn}_4\text{O}_5\text{Ca}$ cluster of the oxygen-evolving complex in photosystem II (PS II). Its removal leads to the loss of the water oxidizing functionality. The S_2' state of the Ca^{2+} -depleted cluster from spinach is examined by X- and Q-band EPR and ⁵⁵Mn electron nuclear double resonance (ENDOR) spectroscopy. Spectral simulations demonstrate that upon Ca^{2+} removal, its electronic structure remains essentially unaltered, *i.e.* that of a manganese tetramer. No redistribution of the manganese valence states and only minor perturbation of the exchange interactions between the manganese ions were found. Interestingly, the S_2' state in spinach PS II is very similar to the native S_2 state of *Thermosynechococcus elongatus* in terms of spin state energies and insensitivity to methanol addition. These results assign the Ca^{2+} a functional as opposed to a structural role in water splitting catalysis, such as (i) being essential for efficient proton-coupled electron transfer between Y_Z and the manganese cluster and/or (ii) providing an initial binding site for substrate water. Additionally, a novel ⁵⁵Mn²⁺ signal, detected by Q-band pulse EPR and ENDOR, was observed in Ca^{2+} -depleted PS II. Mn^{2+} titration, monitored by ⁵⁵Mn ENDOR, revealed a specific Mn^{2+} binding site with a submicromolar K_D . Ca^{2+} titration of Mn^{2+} -loaded, Ca^{2+} -depleted PS II demonstrated that the site is reversibly made accessible to Mn^{2+} by Ca^{2+} depletion and reconstitution. Mn^{2+} is proposed to bind at one of the extrinsic subunits. This process is possibly relevant for the formation of the $\text{Mn}_4\text{O}_5\text{Ca}$ cluster during photoassembly and/or D1 repair.

The oxygen-evolving complex (OEC)⁵ of photosystem II (PS II) catalyzes the light-driven oxidation of water. The OEC contains an inorganic $\text{Mn}_4\text{O}_5\text{Ca}$ metallocofactor that includes five μ -oxo bridge linkages and is coordinated by a framework of surrounding amino acids (1–6) in a highly defined manner that confers catalytic function. The redox-active tyrosine residue Y_Z (D1-Tyr-161) enables electron transfer from the $\text{Mn}_4\text{O}_5\text{Ca}$ cluster to P_{680}^+ , the radical cation formed upon photon absorption and charge separation. The $\text{Mn}_4\text{O}_5\text{Ca}$ cluster undergoes four successive oxidations, cycling through a series of different net valence states, referred to as the S_i states (where $i = 0-4$ denotes the number of oxidizing equivalents stored in the cluster). The transient state S_4 spontaneously returns to S_0 upon regaining four electrons from the two substrate water molecules, which in the process form molecular oxygen. The release of O_2 is followed by the rebinding of at least one H_2O molecule (for reviews, see Refs. 7–14).

X-ray crystallographic structures of the PS II protein complex provided an atomic picture of the structure of the OEC (1–6), identifying all amino acids that ligate the $\text{Mn}_4\text{O}_5\text{Ca}$ cluster. The metallocofactor resembles a distorted chair, consisting of the cuboidal moiety $\text{Mn}_3\text{O}_3\text{Ca}$ ($\text{Mn}_{\text{B3}}\text{Mn}_{\text{C2}}\text{Mn}_{\text{D1}}$),⁶ with the fourth, outer manganese ion (Mn_{A4}), connected to the cuboid via an additional μ -oxo bridge (O4) to one of the manganese vertices (Mn_{B3}). The reported cluster is likely modified due to photoreduction of the Mn^{III} and Mn^{IV} ions, such that the Mn-Mn and Mn-Ca distances seen in the x-ray structure are all elongated as compared with those derived from extended x-ray absorption fine structure (EXAFS) measurements (15). Allowing for this, the basic topology of the x-ray structure is similar to earlier literature models, including the geometry-optimized

* This work was supported by Max Planck Gesellschaft and the EU/Energy Network project SOLAR-H2 (FP7 Contract 212508).

[5] This article contains supplemental Equation S1, Table S1, and Figs. S1–S4.

¹ Supported by the Federal Ministry of Education and Research of Germany (BMBF) in the framework of the Bio-H2 project (03SF0355C).

² Supported by the National Natural Science Foundation of China (31070211). Present address: Dept. of Modern Physics, University of Science and Technology of China, Hefei, Anhui 230026, China.

³ Supported by Vetenskapsrådet, Umeå University (Solar Fuels Strong Research Environment), the K&A Wallenberg foundation (Artificial Leaf project Umeå), and the Kempe foundation.

⁴ To whom correspondence should be addressed. Tel.: 49-208-306-3614; Fax: 49-208-306-3955; E-mail: wolfgang.lubitz@mpi-mail.mpg.de.

⁵ The abbreviations used are: OEC, oxygen-evolving complex; PS II, photosystem II; EXAFS, extended X-ray absorption fine structure; ENDOR, electron-nuclear double resonance; CW, continuous wave; RC, reaction center; ESE, electron spin echo; RF, radio frequency; HFI, hyperfine interaction; ZFS, zero-field splitting; DFT, density functional theory; mT, millitesla; MW, microwave; a.u., arbitrary units.

⁶ The nomenclature used for the manganese ions combines the lettering/numbering used in polarized EXAFS models (90) and that of Umena *et al.* (6).

Electronic Structure of the Ca^{2+} -depleted OEC of Photosystem II

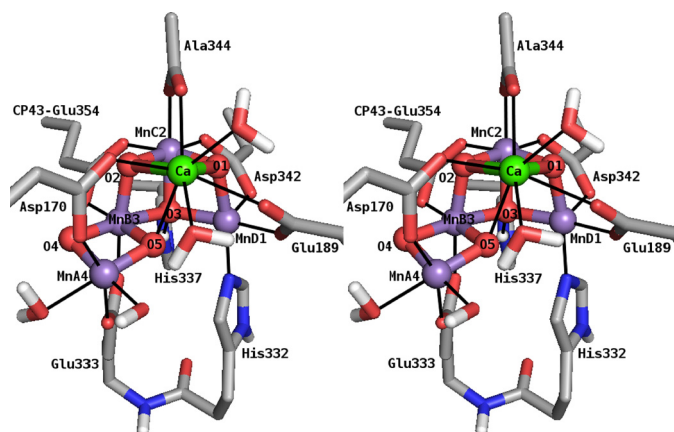


FIGURE 1. Stereo view of a DFT model of the $\text{Mn}_4\text{O}_5\text{Ca}$ cluster in the S_2 state and directly ligating amino acid residues and $\text{H}_2\text{O}/\text{OH}^-$ molecules (18). Amino acids, except CP43-Glu-354, are from PS II subunit D1. Manganese, calcium, nitrogen, oxygen, carbon, and hydrogen atoms are shown in purple, green, blue, red, gray, and white, respectively. Nonpolar H atoms are omitted for clarity.

density functional theory (DFT) models of Kusunoki (16), Siegbahn (17), and the recent model of Ames *et al.* (18), in which the cuboid exhibits an open conformation with $\text{Mn}_{\text{A}4}$ connected to $\text{Mn}_{\text{B}3}$ via a di- μ -oxo bridge (Fig. 1).

The Ca^{2+} ion of the $\text{Mn}_4\text{O}_5\text{Ca}$ cluster, which can be removed from and reconstituted into the OEC (19–21), is essential for catalytic function (19–23). The non-catalytic Ca^{2+} -depleted OEC cannot complete the S state cycle, advancing only to a modified S_2 state, termed S_2' (24, 25). The reason for this remains unclear. However, four basic explanations exist in the current literature based on the proposed role(s) for the Ca^{2+} ion during the S state cycle (for reviews, see Refs. 26–28). These include the following: (i) As an integral component of the OEC (6), the Ca^{2+} ion can be suspected to be of crucial structural importance. However, EXAFS experiments suggest that Ca^{2+} depletion leads to only a small spatial reorganization of the remnant Mn_4O_5 cluster (29). (ii) It facilitates fast one-electron transfer from the OEC to Y_Z^+ (for reviews, see Refs. 11 and 30). The formation of the S_2' state requires long visible light illumination at temperatures $\geq 0^\circ\text{C}$. This is in contrast to the native S_2 state, which can be generated via visible light illumination at -78°C . This apparent increase in the activation energy of OEC turnover upon Ca^{2+} removal may represent a decoupling of the Y_Z^+ from the OEC, such that Ca^{2+} -mediated protein conformational changes and/or H^+ translocations associated with physiological S state transitions are blocked. (iii) It is a binding/staging site for substrate water and its deprotonation (26, 31). The kinetics of substrate water binding to the OEC are affected by biochemical exchange of Ca^{2+} with Sr^{2+} , the only surrogate ion able to confer catalytic activity (19, 23, 32). It can presumably act in place of Ca^{2+} as it has approximately the same size and a similar Lewis acidity (31). This result has been interpreted as evidence for Ca^{2+} binding one of the substrate waters. Inhibition due to Ca^{2+} depletion would then reflect the loss of a substrate binding site. (iv) Although the basic structural arrangement of manganese ions in the cluster is retained upon Ca^{2+} removal, it is uncertain if their magnetic and/or electronic interactions are per-

turbed, which could lead to a decoupling of the cluster or a rearrangement of the manganese valence states. Thus, Ca^{2+} depletion could potentially change the redox properties as well as substrate and/or protein interactions of the complex, inhibiting catalytic function.

The $\text{Mn}_4\text{O}_5\text{Ca}$ cluster in the S_2 state exhibits a characteristic multiline EPR signal centered at $g \approx 2$ (33) that arises from an $S = 1/2$ ground spin state of the cluster. Under certain conditions (illumination, reactants), additional signals are observed at higher g values; in spinach, a second broad signal can be detected at $g \approx 4.1$ (34, 35), attributed to an $S = 5/2$ spin state (36). These signals are affected by the presence of small alcohols, foremost methanol (MeOH) (37–41), which enhance the intensity of the multiline signal at the expense of the $g \approx 4.1$ signal (37) (for a full discussion see Ref. 41). The Mn_4O_5 cluster in the S_2' state also exhibits a multiline signal; however, its hyperfine splitting pattern is perturbed. It contains a larger number of resolved lines as compared with the native S_2 multiline signal, with a smaller average line spacing (5.5–6 versus 8.8 mT). The magnetic interaction between Y_Z^+ and the OEC is also perturbed in Ca^{2+} -depleted PS II as evidenced by changes in the tyrosine split signal of the $S_2'\text{Y}_Z^+$ state (24, 25).

A detailed understanding of the electronic structure of the $\text{Mn}_4\text{O}_5\text{Ca}$ cluster in the S_2 state has been developed from pulse EPR data (42–46), in particular ^{55}Mn electron nuclear double resonance (ENDOR). These experiments demonstrated that the four manganese ions contribute about equally to the ground electronic state of the S_2 state; *i.e.* all four manganese ions carry approximately the same spin density. This requirement allows an assessment of the electronic exchange interactions between the four manganese ions and the development of Mn_4 coupling schemes. These necessarily reflect the geometric structure of the OEC and allow the assignment of the individual manganese oxidation states. Our recently proposed model for the S_2 state (18) is described under “Discussion.” This scheme places the only Mn^{III} ion inside the cuboidal unit ($\text{Mn}_{\text{D}1}$) (see also Ref. 47) and compares favorably with information from complementary spectroscopic measurements (48–50).

Although it has not been directly observed by EPR spectroscopy, the possibility of another paramagnetic manganese species being able to bind to the Ca^{2+} -depleted PS II has been suggested in an earlier study by Booth *et al.* (51). The additional species was suggested to be a Mn^{2+} ion that can bind specifically to a site in the protein complex that is created or becomes accessible via structural changes in the course of Ca^{2+} removal. This was based on the observation that, after equimolar amounts of Mn^{2+} ions had been added to Ca^{2+} -depleted PS II, no Mn^{2+} was observed by X-band continuous wave (CW) EPR. Upon titrating Ca^{2+} ions back into these samples, Mn^{2+} was released as seen from the appearance of the six-line Mn^{2+} EPR signal.

In this work, both the spin system of the Mn_4O_5 cluster in the S_2' state of Ca^{2+} -depleted PS II and the binding of Mn^{2+} ions to this protein were studied by EPR and ENDOR spectroscopy at X- and Q-band frequencies. The results provide new insight into the role of the Ca^{2+} ion in the native OEC.

TABLE 1

Oxygen evolution activities and relative S_2 multiline EPR signal intensities of the Ca^{2+} -containing native, the Ca^{2+} -depleted, and the Ca^{2+} -reconstituted PS II membrane preparations from spinach

Observable	Native	Ca^{2+} -depleted	Ca^{2+} -reconstituted
Enzymatic rates/ $\mu\text{mol O}_2/\text{mg chlorophyll/h}^a$	390 ± 30	27 ± 1	330 ± 30
Relative enzymatic rates	100%	$7 \pm 0\%$	$84 \pm 8\%$
Relative S_2 state multiline signal intensities ^b	100%	$8 \pm 3\%$	$105 \pm 12\%$

^a Determined as an average of at least 8 single measurements at a minimum of 2 different chlorophyll concentrations from 5 to 25 $\mu\text{g/ml}$.

^b Determined from the peak-to-rough distances of four prominent derivative peaks in the CW EPR spectrum (100).

EXPERIMENTAL PROCEDURES

Sample Preparation—PS II-enriched thylakoid membranes were prepared from spinach based on the procedure of Berthold *et al.* (52) using detergent treatment by incubation with Triton X-100 for 15 min. All work was performed in the dark or very dim green light, and the PS II was kept at 4 °C before storage in the dark at -80 °C or in liquid N_2 . Chlorophyll concentrations were determined by assays using aqueous acetone (80%) extracts (53) with updated extinction coefficients (54) using an ATI Unicam UV-visible spectrometer UV2–300.

Ca^{2+} depletion and reconstitution based on the low pH/citrate treatment method (21) was achieved as described previously (55). The final buffer used was 50 mM MES, 15 mM NaCl, 0.4 M sucrose, 1 mM EDTA, pH 6.5. Ca^{2+} removal and, as a proof for the integrity of the OEC, Ca^{2+} rebinding was confirmed both by enzymatic assays and by X-band CW EPR. The O_2 evolution rates of native PS II were ~ 400 $\mu\text{mol O}_2/\text{mg}$ of chlorophyll/h (see the following section). O_2 evolution rates dropped to 5–10% in Ca^{2+} -depleted and were reactivated to >80% in Ca^{2+} -reconstituted samples. Similar percentages of the S_2 multiline signal were observed after white light illumination with a tungsten lamp through an aqueous 5% CuSO_4 IR filter of the respective samples at 200 K for 5 min (Table 1, Fig. 2A). These numbers are consistent with previous literature reports (25, 29, 56).

Advancement of dark-adapted S_1 ' state EPR samples to the S_2' and $S_2'Y_Z$ ' states (25) was done by illumination at 0 °C for 3 min, with 125 μM 3-(3,4-dichlorophenyl)-1,1-dimethylurea (10 mM in dimethyl sulfoxide) added to the samples advanced to the S_2' state, which restricts the acceptor site and, thus, Y_Z to one turnover.

For Ca^{2+} and Mn^{2+} titration experiments, dark-adapted Ca^{2+} -depleted PS II membranes were rebuffed in EDTA-free buffer by three cycles of dilution, centrifugation at $39,000 \times g$ for 15 min, and resuspension using 50 mM MES, 15 mM NaCl, 5 mM MgCl_2 , 0.4 M sucrose, pH 6.5. The final concentration of PS II reaction centers (RCs) in the samples was 28 ± 3 μM based on a chlorophyll concentration of 6.3 ± 0.8 mg ml^{-1} and assuming 250 chlorophylls/RC (57) after 15 min Triton X-100 treatment. The samples were incubated with known amounts of Mn^{2+} ranging from 0 to 4 eq per RC for 2 h. For the Ca^{2+} titration, samples containing 0.8 added eq of Mn^{2+} were incubated with known amounts of Ca^{2+} between 0 and 2400 eq for one additional hour. Mn^{2+} and Ca^{2+} ions were added from stock solutions of their chlorides.

Oxygen Evolution Measurements—Steady state PS II enzyme activity at 25 °C was determined by polarographic measurement of the O_2 concentration in a PS II-containing assay mixture using a Clark-type Hansatech oxygen electrode with a high

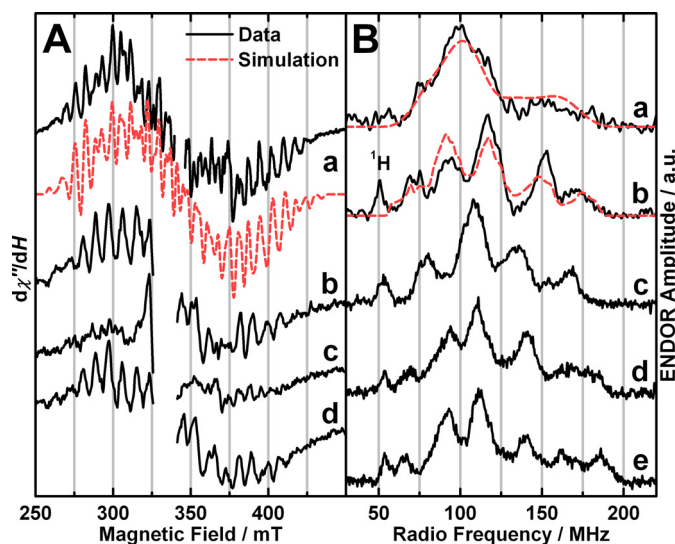


FIGURE 2. EPR and ENDOR experimental spectra (black solid traces) and simulations (red dashed traces). A, X-band CW EPR of PS II isolated from spinach. Shown are the Ca^{2+} -depleted OEC poised in the S_2' state (a) and the native (b), Ca^{2+} -depleted (c), and Ca^{2+} -reconstituted OECs (d) illuminated at 200 K. In the experimental spectrum, the region of the overlapping Y_D ' signal ($g \approx 2$) was omitted for clarity. In a, a fourth order polynomial, and in b–d, a background signal of the resonator cavity were subtracted from the raw data. Experimental parameters: MW frequencies, 9.634 GHz (a), 9.44 GHz (b–d); MW power, 0.5 milliwatt (a), 20 milliwatts (b–d); modulation amplitude, 7.5 G (a), 15 G (b–d); time constant, 82 ms; temperature, 8 K (a), 10 K (b–d). B, X-band (a) and Q-band (b–e) Davies ENDOR of the Ca^{2+} -depleted S_2' state from spinach compared with the native and Sr^{2+} -substituted S_2' states from spinach and *T. elongatus*. Shown are Ca^{2+} -depleted $\text{Mn}_4\text{O}_5 S_2'$, spinach (a and b), native $\text{Mn}_4\text{O}_5\text{Ca}$ S_2' , spinach (taken from Refs. 45 and 46) (c), native $\text{Mn}_4\text{O}_5\text{Ca}$ S_2' , *T. elongatus* (from Ref. 49) (d), and Sr^{2+} -substituted $\text{Mn}_4\text{O}_5\text{Sr}$ S_2' , *T. elongatus* (from Ref. 49) (e). a and b were smoothed using a 9- and 5-point moving average, respectively. b is the difference of an S_2' state spectrum after illumination at 0 °C minus an S_1' state spectrum after dark adaptation (supplemental Fig. S2) to remove an overlapping Mn^{2+} signal. The Mn^{2+} signal is attributed to residual Mn^{2+} ions stemming from a small fraction of damaged manganese clusters. In X-band pulse EPR (not shown) and ENDOR spectra (a), Mn^{2+} contributions were avoided by optimizing the MW pulse lengths for the S_2' state signal of the Mn_4O_5 spin system with an $S = 1/2$ ground spin state. Experimental parameters: a and b, MW frequencies, 9.717 GHz (X-band), 34.033 GHz (Q-band); shot repetition rate, 5 ms; MW pulse lengths π , 12 ns (X-band), 72 ns (Q-band); τ , 200 ns (X-band), 440 ns (Q-band); magnetic fields, 380 mT (X-band), 1208 mT (Q-band); RF pulse length π_{RF} , 4 μs ; temperature, 5 K; c–e, see Refs. 45 and 49.

sensitivity Teflon membrane under continuous illumination with a tungsten lamp through an aqueous 5% CuSO_4 IR filter. The assay medium was the buffer of the samples lacking EDTA and with 5 mM MgCl_2 and 0.2 mM phenyl-*p*-benzoquinone (20 mM in dimethyl sulfoxide) added as an electron acceptor.

EPR/ENDOR Spectroscopy—X-band CW EPR spectra were recorded on a Bruker ELEXSYS E500 spectrometer equipped with an ESR900 liquid helium flow cryostat and an ITC503 helium flow temperature controller (Oxford Instruments Ltd.). X-band pulse experiments were performed with a Bruker ESP

380E spectrometer equipped with a dielectric ring resonator, an Oxford ITC liquid helium flow system, and a temperature controller. Q-band pulse experiments were performed using a Bruker ELEXSYS E580 spectrometer equipped with a laboratory-built cylindrical ENDOR resonator (58), a CF935 cryostat, and an ITC5025 temperature controller (Oxford Instruments Ltd.). Field-swept electron spin echo (ESE)-detected experiments were performed at Q-band frequencies using the pulse sequence $\pi/2-\tau-\pi/2-\tau$ -echo with $\pi = 72$ ns and $\tau = 440$ ns. For ⁵⁵Mn Davies ENDOR, the pulse sequence was $\pi-\pi_{\text{RF}}-T-\pi/2-\tau-\pi/2-\tau$ -echo, with $\pi = 12$ ns (X-band), 72 ns (Q-band), or 16 ns (Q-band Mn²⁺ titration/quantification), $\pi_{\text{RF}} = 4$ μ s (X-, Q-band) or 4.5 μ s (Q-band Mn²⁺ titration/quantification), $T = 3.4$ μ s (X-, Q-band) or 1 μ s (Q-band Mn²⁺ titration/quantification), and $\tau = 200$ ns (X-band), 440 ns (Q-Band), or 320 ns (Q-band Mn²⁺ titration/quantification). The radio frequency (RF) was varied randomly in the desired range, and the RF pulses were amplified by an ENI 5100L amplifier. Except for Mn²⁺ titration/quantification, ⁵⁵Mn Davies ENDOR spectra were collected using a home-built computer console with SpecMan control software (59) coupled to an SMT02 external RF pulse generator.

EPR/ENDOR Spectral Simulations—Simulations of EPR and ⁵⁵Mn ENDOR spectra were performed numerically using the EasySpin software package (60). The fitting procedures employed a least squares minimization routine. All tensors were set to be collinear. The Ca²⁺-depleted Mn₄O₅ cluster in the S₂' state was treated as an effective electronic spin $S = 1/2$ ground state coupled to the four ⁵⁵Mn nuclei, described by the following spin Hamiltonians for the EPR (Equation 1) and ⁵⁵Mn ENDOR (Equation 2) spectra.

$$H_{\text{Mn}_4\text{O}_5,\text{EPR}} = \beta_e B_0 G S + \sum_{i=1}^4 (SA_i I_i) \quad (\text{Eq. 1})$$

$$H_{\text{Mn}_4\text{O}_5,\text{ENDOR}} = \beta_e B_0 G S + \sum_{i=1}^4 (\beta_n B_0 g_n I_i + SA_i I_i) \quad (\text{Eq. 2})$$

The EPR spectrum was calculated using second order perturbation theory, neglecting nuclear Zeeman terms and forbidden transitions. The ⁵⁵Mn ENDOR spectra were calculated exactly, including nuclear Zeeman terms and considering all transitions. For the monomeric Mn²⁺ ion ($S = 5/2, I = 5/2$) bound to the Ca²⁺-depleted PS II, the following spin Hamiltonian was solved exactly both for the ESE and ENDOR spectra:

$$H_{\text{Mn}^{2+}} = \beta_e B_0 G S + D \left[S_z^2 - \frac{1}{3} S(S+1) \right] + E(S_x^2 - S_y^2) + \beta_n B_0 g_n I + SA I \quad (\text{Eq. 3})$$

For details on the simulation procedure and the theoretical background, see Refs. 46, 49, and 61.

Temperature-dependent CW EPR Signal Intensity—The temperature was calibrated using a thermometer in place of the sample in the EPR tube. To guarantee that the actual unsaturated intensity I_1 of the S₂' state modified multiline, as the

ground state signal, was measured at all temperatures, the saturation behavior was studied at the lowest temperature employed. As a result, the non-saturating microwave (MW) power of 0.1 milliwatt was used throughout. The intensities I_1 of the derivative signals were measured by means of the heights of 19 peaks throughout the spectral range, thereby minimizing statistical errors and contributions of underlying broader signals, such as from cytochrome *b*₅₅₉ and the semiquinone-iron complex. How the ground-to-first excited state energy difference Δ is determined from the temperature dependence of I_1 is outlined in the supplemental data.

Quantification of the Relative Concentrations of PS II-bound Mn²⁺ and Hexaquo-Mn²⁺—The Mn²⁺ species in Ca²⁺ and Mn²⁺ titration samples were quantified by means of their Q-band ⁵⁵Mn Davies ENDOR spectra in two ways, and the results were averaged. (i) The relative contributions of the spectra from the pure Mn²⁺ species needed to reproduce the spectra from the various titration points were determined. The spectra from Mn²⁺ already present in the Ca²⁺-depleted PS II samples without the addition of Mn²⁺ ions and from 40 μ M MnCl₂ dissolved in the titration buffer represented PS II-bound and hexaquo-Mn²⁺, respectively. (ii) The relative amplitudes of the ⁵⁵Mn ENDOR $m_S = -3/2$ transitions, which appear in different RF ranges characteristic for the two Mn²⁺ species, were quantified in the regions of 353–376 MHz for PS II-bound Mn²⁺ and 390–395 MHz for hexaquo-Mn²⁺.

RESULTS

EPR and ⁵⁵Mn ENDOR of the Ca²⁺-depleted Mn₄O₅ Cluster in the S₂' State—The characteristic modified multiline CW EPR signal (24, 25) was observed for Ca²⁺-depleted PS II samples poised in the S₂' state. It is centered at $g \approx 2$ and spans the magnetic field range from ~ 260 to ~ 430 mT, resolving at least 27 hyperfine interaction (HFI) lines with an average peak-to-peak spacing of ~ 6 mT (Fig. 2A). The central HFI lines are superimposed by the signal of the stable tyrosyl radical Y_D• centered at $g \approx 2$, which is not depicted for clarity of presentation. The broad underlying signal of the reduced Q_A⁻ Fe²⁺ complex (62) contributes in the 350–375-mT region (24, 25, 29).

Traces *a* and *b* in Fig. 2B show the X- and Q-band Davies ENDOR spectra of the S₂' state recorded at 5 K and magnetic fields of 380 and 1208 mT, respectively. The ⁵⁵Mn ENDOR spectrum of the Mn₄O₅ cluster in the S₂' state is essentially invariant across the corresponding EPR signal envelope (supplemental Fig. S1). It is ~ 130 MHz wide, extending over a range from ~ 60 to ~ 190 MHz. As compared with the ⁵⁵Mn ENDOR spectrum of the native S₂ state (Fig. 2Bc, supplemental Fig. S1), the Ca²⁺-depleted S₂' state spectrum is broader. The edges of the spectrum change up to 10 MHz, resulting in a ~ 20 and ~ 10 MHz increase in the width of the X- and Q-band ⁵⁵Mn ENDOR spectra, respectively, as compared with the Ca²⁺-containing S₂ state of spinach PS II (42, 45, 46). The Q-band spectrum of the S₂' state exhibits five clearly resolved peaks, as also seen for the native S₂ state spectrum from *Thermosynechococcus elongatus* (Fig. 2Bd); however, their positions differ slightly.

The X-band CW EPR and X- and Q-band ⁵⁵Mn Davies ENDOR spectra were simultaneously simulated using the spin Hamiltonian formalism (for details see “Experimental Proce-

TABLE 2

Isotropic and anisotropic values of the effective ^{55}Mn HFI tensors A_i ($i = 1-4$) used for the simulations of the X- and Q-band EPR and ENDOR spectra of the Ca^{2+} -depleted PS II from spinach in the S_2' state (Fig. 2) and for the S_2 states of native spinach PS II (46) and native and Sr^{2+} -substituted PS II from *T. elongatus* (49)

Species	OEC state	Tensor component	A_1	A_2	A_3	A_4
			MHz	MHz	MHz	MHz
Spinach	$-\text{Ca}^{2+} S_2'$	iso ^a	311	234	202	171
		aniso ^b	72	-84	-38	-59
<i>T. elongatus</i>	$\text{Ca}^{2+} S_2$	iso	298	248	205	193
		aniso	35	-40	-60	-70
	$\text{Ca}^{2+} S_2$	iso	312	251	208	191
		aniso	55	-40	-48	-108
$\text{Sr}^{2+} S_2$	iso	332	243	203	173	
	aniso	59	-37	-30	-56	

^a The isotropic $A_{i,\text{iso}}$ ($i = 1-4$) values are the averages of the principal values: $A_{i,\text{iso}} = (A_{i,x} + A_{i,y} + A_{i,z})/3$.

^b The anisotropy in the A_i values is expressed as the difference $A_{i,\text{aniso}} = A_{\perp} - A_{\parallel}$ between the equatorial and axial components of the tensor. The equatorial and axial A_i values are defined as $A_{i,\perp} = (A_{i,x} + A_{i,y})/2$, $A_{i,\parallel} = A_{i,z}$.

dures" and Refs. 46 and 49). In these simulations, the S_2' state Mn_4O_5 cluster is treated as an effective $S = 1/2$ electronic spin state coupled to the four ^{55}Mn nuclei, the same as for the native S_2 state (41, 42, 46, 48, 49, 63–66). This approach requires the ground electronic spin state to be well separated from higher states, as is experimentally observed (see the following section). The simulations reproduce all the major spectral features of the EPR and ^{55}Mn ENDOR spectra (Fig. 2, dashed red traces).

The isotropic and anisotropic values of the fitted effective ^{55}Mn HFI tensors A_i ($i = 1-4$) are given in Table 2. For means of comparison, the numbers for the native S_2 state from spinach (46) and the native and Sr^{2+} -substituted S_2 states from *T. elongatus* (49) are also listed. A full set of G and HFI tensor components is listed in supplemental Table S1. As seen for the $\text{Mn}_4\text{O}_5\text{Ca/Sr}$ clusters, four effective HFI tensors are required to simulate the Mn_4O_5 cluster spectra. Their magnitudes are on the order seen for mono- and dimeric Mn^{3+} and Mn^{4+} complexes. Hence, their individual spin projection coefficients ρ_i must be on the order of 1 (see Ref. 49). In contrast to preliminary simulations of the S_2' spectra (67) or others on the S_2 state from spinach PS II (46), the HFI tensors were not constrained to axial symmetry. However, as was found previously in simulations of the $\text{Mn}_4\text{O}_5\text{Ca/Sr}$ clusters in *T. elongatus* (49), the tensors nevertheless show a considerable degree of axial symmetry. Moreover, these four OEC clusters show the same geometries of their HFI tensors, with larger axial than equatorial tensor components ($A_{\text{aniso}} < 0$) for $A_2 - A_4$ and vice versa for the largest HFI A_1 ($A_{\text{aniso}} > 0$).

Spin State Energies of the Ca^{2+} -depleted Mn_4O_5 Cluster in the S_2' State—The energy difference Δ of the paramagnetic ground spin state and the first excited state was estimated from the temperature dependence of the unsaturated X-band CW modified multiline signal of the Ca^{2+} -depleted S_2' state. The measured intensities I_1 of the derivative signal at a series of temperatures are depicted in a Curie plot versus $1/T$ in Fig. 3. This relation is approximately linear over the measured range from 14.4 to 5.5 K and extrapolates to 0 for $T \rightarrow \infty$. This Curie behavior of the temperature dependence indicates that the Ca^{2+} -depleted S_2' state features an $S = 1/2$ ground spin state energetically well separated from states of higher spin multiplicity. The temperature dependence of the S_2' modified multiline signal can be reproduced reasonably well with $\Delta \geq 35 \text{ cm}^{-1}$ corresponding to $J_{\text{eff}} \geq 12 \text{ cm}^{-1}$ (see "Experimental Procedures"). This relatively large separation from states of higher

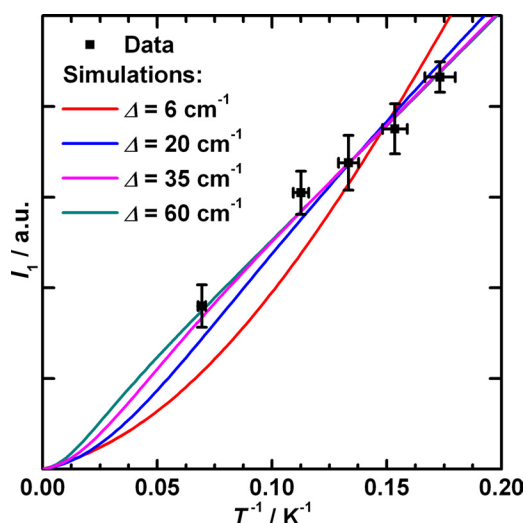


FIGURE 3. Curie plot showing the dependence of the intensity I_1 of the modified multiline derivative signal of the Ca^{2+} -depleted S_2' state on the inverse temperature T . The error of the x-values comes from the calibration of the actual temperature at the sample position (see "Experimental Procedures"). The curves are simulations of the Curie temperature dependence over a range of Δ values on the basis of Equation S1 in the supplemental data and the simplified electron 2-spin coupling scheme for the OEC outlined under "Experimental Procedures." Experimental parameters: MW frequency, 9.437 GHz; MW power, 0.1 milliwatt; modulation amplitude, 0.75 mT; time constant, 82 ms; temperatures, 5.5, 6.3, 7.3, 8.7, and 14.4 K.

spin multiplicity allows the S_2' state Mn_4O_5 spin system to be treated in the strong exchange limit, *i.e.* as an effective $S = 1/2$ spin state, as assumed in the previous section.

EPR and ^{55}Mn ENDOR of a Specifically Bound Mn^{2+} Ion—The Ca^{2+} -depleted PS II preparations exhibit an additional EPR and ENDOR signal in all accessible S' states that is not present in native PS II samples. At 5 K, Q-band ESE-detected field sweep EPR spectra of the dark-adapted Ca^{2+} -depleted PS II preparations (S_1' state), in which the Mn_4O_5 cluster does not show a perpendicular mode EPR signal, displayed a broad EPR signal centered at $g = 1.99$ with a full width at half-maximum of $\sim 63 \text{ mT}$ (Fig. 4, inset). A corresponding signal was not observed using CW X-band EPR spectroscopy; the signal is probably too broad to be discerned from the base-line drift in the CW EPR experiment (51). Q-band Davies ENDOR spectra were recorded at several magnetic fields in the RF frequency range of 30 to 400 MHz (Fig. 4). The ^{55}Mn ENDOR spectra are dominated by two broad peaks between 100–195 MHz and another line centered at $\sim 370 \text{ MHz}$. The two lines at 100–195 MHz are

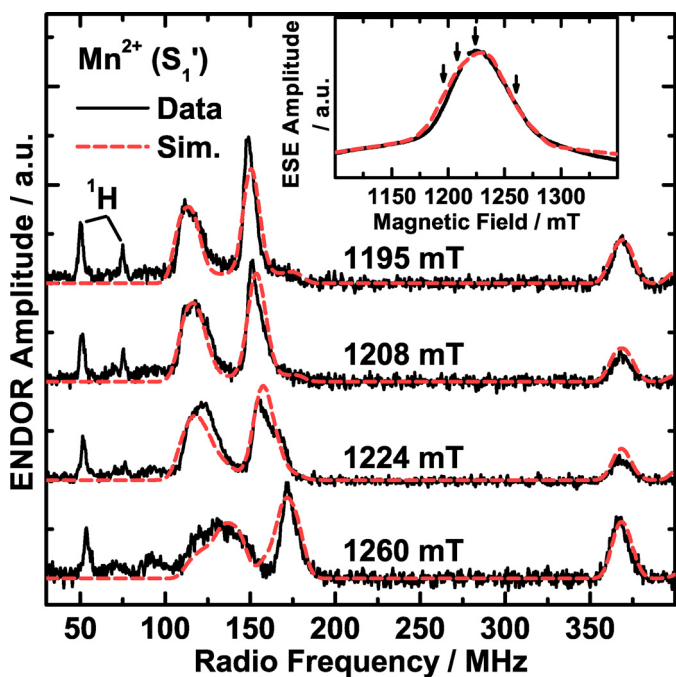


FIGURE 4. Q-band pulse ESE-detected field-swept EPR (inset) and Davies ENDOR experimental spectra (black solid traces) and simulations (Sim.; red dashed traces) of the Mn^{2+} ion bound to Ca^{2+} -depleted PS II isolated from spinach and poised in the S_1' state. In the EPR spectrum, the region of the overlapping Y_D^- EPR signal ($g \approx 2$) is not displayed for clarity and was omitted in the simulations. The arrows indicate the four magnetic fields at which the ENDOR spectra were measured. Experimental parameters: MW frequency, 34.07 GHz; shot repetition rate, 5 ms; MW pulse length π , 72 ns; τ , 440 ns; Davies ENDOR, magnetic fields, 1195, 1208, 1224, 1260 mT (top to bottom); RF pulse length π_{RF} , 4 μs ; temperature, 5 K.

dependent on the magnetic field and shift to higher frequencies with increasing magnetic field. The spectra also contain sharp proton signals, one centered at the ^1H Larmor frequency (~ 50 MHz) and a strongly coupled one at ~ 75 MHz with decreasing amplitude at increasing field positions. Its partner at low frequency (~ 25 MHz) lies outside the spectral range. No further low frequency signals were detected for this species using either ENDOR or electron spin echo envelope modulation (ESEEM).

These EPR and ^{55}Mn ENDOR signals can be readily assigned to high spin Mn^{2+} with $S = 5/2$, although their appearance is different from the spectra typically associated with Mn^{2+} complexes (see Discussion and Fig. 5A). Simultaneous simulations of the EPR and of four ENDOR spectra at different magnetic fields (Fig. 4, dashed red traces) are consistent with this assignment. They reproduce both the spectral breadth and line shape of the EPR absorption signal and the peaks in the four ^{55}Mn ENDOR spectra. Besides a near-isotropic G tensor (principal values 1.983, 1.996, 2.002), the simulations yielded an almost isotropic HFI tensor with the principal components $A_x = 256$ MHz, $A_y = 260$ MHz and $A_z = 257$ MHz, resulting in an isotropic average A_{iso} of 258 MHz. In addition, the simulations required a large fine structure parameter $D = -2355$ MHz with a pronounced rhombicity $\eta = E/D = -0.38$ of the zero-field splitting (ZFS). It is noted that the predominant contribution to the width of the EPR and ENDOR signals is the large and rhombic ZFS interaction (more information on the effect of the ZFS can be found in the supplemental data and Ref. 61). Hence, considering the good agreement of the measured and calcu-

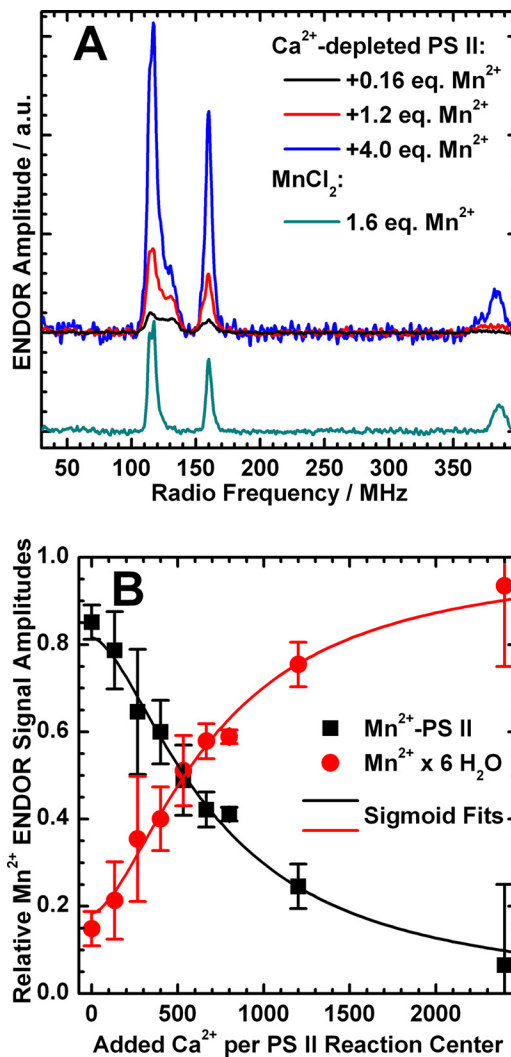


FIGURE 5. Mn^{2+} and Ca^{2+} titrations monitored by Q-band ^{55}Mn ENDOR. A, Q-band ^{55}Mn Davies ENDOR spectra of dark-adapted Ca^{2+} -depleted PS II samples (S_1' state) with 0.16, 1.2, and 4.0 eq (black, red, and blue trace) of Mn^{2+} ions added relative to the number of PS II RCs and of 40 μM MnCl_2 (corresponding to 1.6 eq) dissolved in the same buffer used for the PS II titration experiments. For the titration curve, see supplemental Fig. S3. The spectra were smoothed using a 5-point moving average. B, titration of Ca^{2+} -depleted PS II samples containing 1 eq of Mn^{2+} ions with respect to the PS II RCs with Ca^{2+} . The relative ^{55}Mn ENDOR signal amplitudes of Mn^{2+} ions bound to the PS II protein complex (black squares) and hexaquo- Mn^{2+} in solution (red circles), quantified as described under "Experimental Procedures," are plotted against the equivalents of Ca^{2+} ions added to the samples. The concentrations of both Mn^{2+} species as a function of added Ca^{2+} were reproduced by a sigmoid fit curve (solid lines). The concentration of RCs in the samples was $25 \pm 3 \mu\text{M}$. Experimental parameters: MW frequency, 34.03 GHz; shot repetition rate, 5 ms; MW pulse length π , 16 ns; τ , 320 ns; magnetic field, 1224 mT; RF pulse length π_{RF} , 4.5 μs ; temperature, 5 K.

lated EPR and ENDOR signals (Fig. 4), the optimized fine structure parameter D can be considered robust; *i.e.* a single set of D and E values is sufficient to rationalize the data. The fact that the inclusion of a distribution of the ZFS parameters is not required indicates that there are only small site-to-site inhomogeneities of the Mn^{2+} ligand sphere. Therefore, we propose that the Mn^{2+} ion is bound to one specific site in Ca^{2+} -depleted PS II.

Mn^{2+} and Ca^{2+} Titration Experiments—To further investigate the Mn^{2+} species described in the previous section, Mn^{2+} and Ca^{2+} titration experiments of Ca^{2+} -depleted PS II

were performed, monitoring the CW EPR and ENDOR signal described above.

$\text{Mn}^{2+}/\text{Ca}^{2+}$ Titration Monitored by CW EPR— Mn^{2+} ions were added to Ca^{2+} -depleted PS II samples and the characteristic $\text{S}_2'\text{Y}_Z\cdot$ state split signal, S_2' multiline signal, and hexaquo- Mn^{2+} signal (not shown) were measured. The addition of ≤ 0.8 eq of Mn^{2+} ions relative to the number of PS II RCs did not quantitatively alter the three signals. The Mn^{2+} ions added are CW EPR-silent, as seen in the study of Booth *et al.* (51), which is consistent with a protein-bound Mn^{2+} species. In addition, this species does not cause any line broadening or even splitting of the signals from the OEC or the tyrosyl radicals. The addition of ≥ 0.8 equivalents of Mn^{2+} ions resulted in the appearance of the hexaquo- Mn^{2+} signal. The subsequent addition of Ca^{2+} to Ca^{2+} -depleted, Mn^{2+} -loaded PS II samples led to a loss of the $\text{S}_2'\text{Y}_Z\cdot$ state split signal and of the multiline signal, as the Ca^{2+} -reconstituted $\text{Mn}_4\text{O}_5\text{Ca}$ cluster can proceed beyond the S_2' state upon illumination. A concomitant increase of the Mn^{2+} six-line signal was observed due to the release of the PS II-bound Mn^{2+} into solution (51).

$\text{Mn}^{2+}/\text{Ca}^{2+}$ Titration Monitored by ^{55}Mn ENDOR— Mn^{2+} binding was also directly monitored by Q-band ENDOR. The concentrations of PS II-bound and solubilized Mn^{2+} ions in each sample were quantified by means of the relative amplitudes of their characteristic ^{55}Mn ENDOR signals (Fig. 5A; for the titration curve, see supplemental Fig. S3). Without the addition of MnCl_2 , dark-adapted Ca^{2+} -depleted PS II (S_1' state) always displayed the PS II-bound Mn^{2+} signal shown in Fig. 4. The addition of ~ 0.8 eq of MnCl_2 led to a 4–5-fold increase of this signal with only little free hexaquo- Mn^{2+} ($15 \pm 4\%$) present at the same time. This suggests that $\sim 20\%$ of RCs contain a bound Mn^{2+} before exogenous addition of MnCl_2 so that in the end a total of ~ 1 eq Mn^{2+} is in the sample. The basal Mn^{2+} is likely derived from centers damaged during the Ca^{2+} depletion procedure and nominally corresponds to the loss of $\sim 5\%$ $\text{Mn}_4\text{O}_5(\text{Ca})$ clusters. The high occupancy of the Mn^{2+} site suggests that it is of high affinity, with a dissociation constant K_D that is too small to be determined here. From the employed concentrations of the binding partner, K_D is expected to be in the submicromolar/nanomolar range. It is also noted that the addition of the chelating agent EDTA did not remove or alter the appearance of the bound Mn^{2+} signal, consistent with the protein site having a high affinity for Mn^{2+} .

An additional Ca^{2+} titration was performed on the fully Mn^{2+} -loaded Ca^{2+} -depleted PS II (+0.8 eq of MnCl_2 , *i.e.* a final ratio of 1 Mn^{2+} ion per PS II RC). The Ca^{2+} concentrations ranged from 0 to 2400 eq Ca^{2+} per RC (0–60 mM). In Fig. 5B, the relative concentrations of the two Mn^{2+} species (PS II-bound and solubilized) are plotted against the equivalents of Ca^{2+} ions added. This behavior could be reproduced by a sigmoid curve with a half-saturation value of 700 Ca^{2+} ions per RC. This value is similar to 1200 eq of Ca^{2+} reported in Booth *et al.* (51). The difference may be due to the Ca^{2+} depletion method used, the low pH/citrate treatment in this study *versus* a NaCl salt wash (24) in the study of Booth *et al.* (51). Their differing effects on the extrinsic PS II subunit composition could alter the Ca^{2+} binding kinetics (see Refs. 24 and 51).

DISCUSSION

Location of the Mn^{2+} Binding Site—Based on the observations described above (see “Results”), a preliminary assignment can be made as to where the binding site of the Mn^{2+} ion is located. No strong magnetic interaction was observed between the Mn^{2+} ion and the Ca^{2+} -depleted Mn_4O_5 cluster or the tyrosyl radical $\text{Y}_Z\cdot$ in the form of a broadening or splitting of the corresponding EPR signals. Thus, Mn^{2+} binding directly to the Ca^{2+} site of the OEC can be excluded. This Mn^{2+} ion must be at least 10 Å away not to be detectable via dipolar magnetic interaction. A similar argument holds for $\text{Y}_D\cdot$ (D2-Tyr-160), as it also displays an unperturbed EPR lineshape when Mn^{2+} is bound. These “exclusion zones” are indicated by *green* and *violet spheres* in Fig. 6A. There is, however, a long range dipolar interaction between the Mn^{2+} ion and $\text{Y}_D\cdot$ as evidenced by the relaxation enhancement of its EPR signal (51). Being smaller than the enhancement resulting from the $\text{Mn}_4\text{O}_5\text{Ca}$ cluster in the S_2 state suggests a weaker Mn^{2+} - $\text{Y}_D\cdot$ interaction and thus a longer distance than the 31 Å measured between the cluster and Y_D (6).

The binding and titration behavior can either be rationalized by a significant allosteric effect of Ca^{2+} on the Mn^{2+} site, or Mn^{2+} binding could take place directly at a depleted Ca^{2+} site. The recent crystal structure (6) of PS II from *Thermosynechococcus vulcanus* exhibits three additional Ca^{2+} sites at distances greater than 30 Å from the paramagnetic species monitored, *i.e.* the $\text{Mn}_4\text{O}_5(\text{Ca})$ cluster, $\text{Y}_Z\cdot$, and $\text{Y}_D\cdot$ (Fig. 6A). In the structure of PS II from *T. elongatus*, a different Ca^{2+} site in PsbO has been identified (4, 5, 68), not found in the *T. vulcanus* crystals. All these Ca^{2+} sites are located on the lumenal/donor side of PS II in the subunit CP47, the cytochrome b_{559} subunit β (PsbF), and the extrinsic protein PsbO, and are solvent-accessible. It is not clear, however, whether Ca^{2+} binding at these sites is solely a crystallization artifact under the conditions used or of physiological relevance. With the exception of the two sites in PsbO, the Ca^{2+} sites appear to be of low affinity, as the Ca^{2+} ions are ligated to a large part by H_2O and glycerol. In contrast, the two Ca^{2+} sites seen in the PsbO possess at least three ligands from amino acid side chains (Fig. 6, B and C) and thus are potentially of high affinity. In the homologous PsbO from spinach, which has also been reported to bind Ca^{2+} (69–71), Asn-197 and Val-198 of the binding motif in Fig. 6B correspond to the conserved residues Ser-286 and Val-287, whereas there is no equivalent for Thr-135. Glu-81, Glu-140, and His-257 in the other binding motif (Fig. 6C) correspond to Glu-146, Glu-205, and Glu-317 (for a sequence alignment, see supplemental Fig. S4). Mn^{2+} binding to PsbO has indeed been demonstrated previously in isolated PsbO from higher plants (72–74). As in the present study and Ref. 51, protein-bound Mn^{2+} did not show a CW EPR signal, but a six-line signal was observed after denaturation of the protein (73). PsbO was reported to show carbonic anhydrase activity, which was maximal in the presence of Mn^{2+} (74).

The magnetic properties of the Mn^{2+} ion provide information about the immediate ligand environment in this binding pocket. The D and E values of Mn^{2+} complexes of higher symmetry, such as Mn^{2+} -EDTA and hexaquo- Mn^{2+} , are significantly smaller than those for the PS II-bound Mn^{2+} described

Electronic Structure of the Ca^{2+} -depleted OEC of Photosystem II

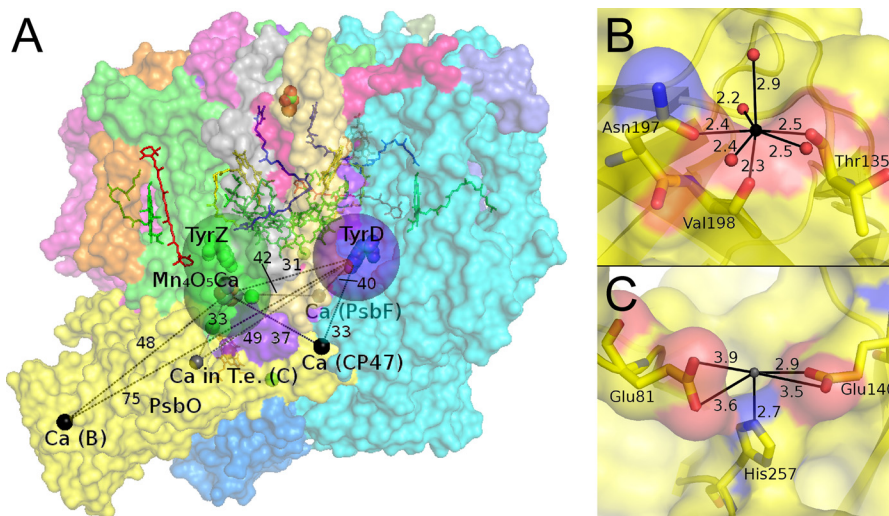


FIGURE 6. Ca^{2+} and potential Mn^{2+} binding sites in cyanobacterial PS II crystals. A, PS II crystal structure from *T. vulcanus* (6) (PDB accession number 3ARC) highlighting the Ca^{2+} ions (black spheres) as well as a Ca^{2+} binding site found in PS II from *T. elongatus* (gray sphere) and their distances to the paramagnetic entities $\text{Mn}_4\text{O}_5\text{Ca}$ cluster, Y_Z , and Y_D . The 10 Å spheres around the latter indicate the approximate region in which a bound Mn^{2+} would cause a splitting of their EPR signals and thus can be excluded to contain the Mn^{2+} binding site. B and C, ligand environments of the Ca^{2+} ions in the extrinsic PsbO proteins from *T. vulcanus* and *T. elongatus* (*T.e.*) (5), respectively. Oxygen, nitrogen, and carbon atoms are shown in red, blue, and yellow, respectively. Differences between the PsbO proteins of these cyanobacterial species and from higher plant spinach are displayed by a sequence alignment in supplemental Fig. S4. All distances are in Å.

here (see supplemental data and Ref. 61). The large and highly rhombic ZFS reflects an asymmetric coordination sphere. Both the 7- and the 5-fold coordination geometries of the Ca^{2+} ions in PsbO from the two cyanobacterial species exhibit considerable asymmetry (Fig. 6, B and C). In addition, the large proton coupling seen also suggests the Mn^{2+} ion to have at least one water ligand. The absence of any smaller coupling, such as from ^{14}N (not shown), indicates that the Mn^{2+} ion does not bind to a N-containing ligand residue like histidine. Thus, the absence of a (visible) water and the presence of His-257 as ligands of the Ca^{2+} ion in *T. elongatus* PsbO (Fig. 6C) favor Mn^{2+} binding to the Ca^{2+} site in PsbO identified in the *T. vulcanus* crystal structure (Fig. 6B).

PS II from higher plants exhibits an extrinsic subunit composition different from that of the cyanobacterial system. Higher plant luminal PsbP has been reported to be capable of binding Mn^{2+} stoichiometrically (75, 76). Similar to Ca^{2+} -depleted PS II in this study and in Ref. 51, isolated PsbP loaded with Mn^{2+} did not show a Mn^{2+} X-band CW EPR signal unless it was denatured. A bound Mn^{2+} could be detected by high field EPR spectroscopy and distinguished from non-specifically attached Mn^{2+} , similar to the present study. It is noted though that the binding constant reported in Bondarava *et al.* (76) is probably incorrect; for a discussion, see Ref. 77. Moreover, the Mn^{2+} ion in PsbP could be (partially) replaced by Ca^{2+} , and Zn^{2+} has been found to bind at one of the two proposed Mn^{2+} sites in PsbP crystals from spinach (PDB accession number 2VU4) and its cyanobacterial homologue CyanoP (78). Mn^{2+} bound to the PsbP would be at least 30 Å from either the OEC or Y_D , again consistent with the distance constraints identified above. Thus, PsbP could also contain the putative site of specific Mn^{2+} binding in Ca^{2+} -depleted higher plant PS II.

The physiological role of the putative Mn^{2+} binding site is the delivery of Mn^{2+} to the OEC during photoassembly and/or the storage of Mn^{2+} during the damage/repair cycle of the D1

protein (see Refs. 79–82). Ca^{2+} is essential for photoactivation of the OEC. It was suggested to bind at a site within the PS II complex, which leads to a conformational change of the protein pocket where the OEC is assembled (*i.e.* the C terminus of D1). Thus, it appears reasonable that in the absence of Ca^{2+} , it is favorable for the PS II supercomplex to sequester in a site Mn^{2+} that can be rapidly delivered upon an increase in Ca^{2+} concentration. In this scenario the luminal Ca^{2+} concentration would be a signaling mechanism for OEC assembly and repair.

Spectral Properties of the Mn_4O_5 Cluster in the S_2' State Compared with Other S_2 State Systems—The appearance of the ^{55}Mn ENDOR spectra, the fitted ^{55}Mn HFI tensors, and the ground-to-first excited state energy separation of the Ca^{2+} -depleted S_2' state all fall within the natural spectral variations observed for the native S_2 states in different species (41). This demonstrates that the basic electronic and thus also spatial structure of the Mn_4O_5 cluster remains intact upon Ca^{2+} removal. This confirms and further refines observations on the interatomic distances of the manganese ions from earlier EXAFS experiments (29).

The Ca^{2+} -depleted S_2' state from spinach resembles the native S_2 state from *T. elongatus* with regard to the spin state energies. Upon removal of the Ca^{2+} ion, Δ increases to $\geq 35 \text{ cm}^{-1}$, which is much larger than for the native spinach S_2 state ($\Delta = 3\text{--}6 \text{ cm}^{-1}$) but more similar to *T. elongatus* ($\Delta = 12\text{--}25 \text{ cm}^{-1}$) (41, 83, 84). In intact spinach PS II, the energy ladder is sensitive to MeOH addition. The mechanism by which MeOH binding perturbs the electronic structure of the S_2 state was recently discussed in Su *et al.* (41). In the model proposed, MeOH binding to the OEC increases the electronic coupling of the pending manganese (Mn_{A4}) to the cuboidal ($\text{Mn}_{B3}, \text{Mn}_{C2}, \text{Mn}_{D1}$) unit. It is this effective coupling that defines the ground-to-first excited state energy difference Δ of the S_2 state. Ca^{2+} depletion appears to have the same effect. However, the addition of MeOH did not modify the appearance of the S_2' state

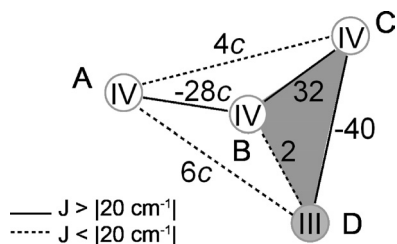


FIGURE 7. Model for the electronic structure of the OEC in the native S_2 and Ca²⁺-depleted S_2' states calculated based on a refined DFT structure of the OEC (18) in the latest crystal structure (6). A–D label the manganese ions in their respective oxidation state, and the numbers give the pair-wise exchange coupling J_{ij} between the electronic spins of the Mn^{III} and Mn^{IV} ions in cm^{-1} . The constant c is 1 in the originally derived model but differs for the various clusters and conditions, such as the presence or absence of MeOH. The S_2' state can be described by the scheme with $c = 1.65$.

ESE and ENDOR spectra (not shown). It is emphasized though that this effect is of the same size as that of the variation between species and thus is unlikely to be of physiological significance.

Electronic Structure/Exchange Coupling Scheme of the Ca²⁺-depleted Mn_4O_5 Cluster in the S_2' State—To further rationalize the spectral results from the Ca²⁺-depleted Mn_4O_5 cluster, a spin coupling scheme for the S_2' state was developed. It was constructed to meet the following requirements: (i) a ground state of spin multiplicity $S = 1/2$, (ii) a ground-to-first excited state energy difference $\Delta \approx 35 \text{ cm}^{-1}$, (iii) spin projection factors $|\rho_i| \approx 1$ for all four manganese electronic spins, and (iv) intrinsic ZFS constants d_i of the manganese ions that lie within the range found for mono- and dimeric model complexes, *i.e.* $1 \text{ cm}^{-1} < |d| < 5 \text{ cm}^{-1}$ for Mn^{III} and $|d| < 0.1 \text{ cm}^{-1}$ for Mn^{IV} ions in an octahedral ligand environment (see Refs. 18, 47, and 49). The inferred structural (29) and spectral similarity of the native and the Ca²⁺-depleted manganese cluster suggest that the spin coupling scheme for the native S_2 state (Fig. 7, $c = 1$) (18), in which Mn_{D1} is the Mn^{III} ion, can be used as a starting point. Calculated on the basis of the refined model of the OEC in the latest crystal structure (6), the basic arrangement of this scheme is in accordance with the spatial organization as described by Siegbahn and our group (17, 18, 47, 85), in which Mn_{B3}, Mn_{C2}, and Mn_{D1} form a trimeric core unit connected to Mn_{A4} by a di- μ -oxo bridge via Mn_{B3} (Fig. 1). Thus, this scheme represents an extension of the (3 + 1)- or Y-coupling schemes, proposed earlier in EPR spectroscopic studies (42, 46, 47, 49), where $J_{A4-C2} = J_{A4-D1} = 0$.

The coupling topology fulfills criteria (i) and (iii) as ground spin state multiplicity and spin projection factors are the same for the two states, S_2 and S_2' . In contrast, their ground-to-first excited state energy differences Δ and effective ⁵⁵Mn HFI tensors A_p , relevant for (ii) and (iv), are different. Thus, the $\Delta = 10.5 \text{ cm}^{-1}$ calculated for the S_2 state coupling scheme also differs from the experimental $\Delta \geq 35 \text{ cm}^{-1}$ determined for the S_2' state. Correlations between the exchange coupling scheme and this energy difference have been investigated in previous studies (41, 47). One mechanism by which Δ is influenced directly was shown to be the strength and the sign of the exchange coupling between Mn_{A4} and the trimeric unit comprising Mn_{B3}, Mn_{C2}, and Mn_{D1}. An increase or decrease in the magnitudes of the coupling constant J_{A4-B3} results in a larger or

TABLE 3

Calculated spin projection tensor components ρ_{\perp} and ρ_{\parallel} , intrinsic ⁵⁵Mn HFI tensor components a_{\perp} and a_{\parallel} , and isotropic and anisotropic intrinsic HFI values a_{iso} and a_{aniso} for the Mn ions of the OEC in the Ca²⁺-depleted S_2' state on the basis of the electronic exchange coupling scheme in Fig. 7 with $c = 1.65$ and intrinsic ZFS values $d_{A4} = d_{B3} = d_{C2} = 0 \text{ cm}^{-1}$ for the Mn^{IV} ions and $d_{D1} = -2.27 \text{ cm}^{-1}$ for the Mn_{D1}^{III} ion

Manganese ion	ρ_{\perp}	ρ_{\parallel}	a_{\perp}^a	a_{\parallel}^a	a_{iso}^b	a_{aniso}^c
			MHz	MHz	MHz	MHz
Mn _{A4} (Mn ^{IV})	1.03	1.25	197	230	208	33
Mn _{B3} (Mn ^{IV})	-0.81	-1.09	187	190	188	3
Mn _{C2} (Mn ^{IV})	-0.87	-1.21	220	188	209	-31
Mn _{D1} (Mn ^{III})	1.66	2.04	202	123	175	-79

^a The equatorial and axial a_i values are defined as: $a_{\perp} = (a_x + a_y)/2$, $a_{\parallel} = a_z$.

^b The isotropic a_{iso} values are the averages of the individual components of the tensor $a_{\text{iso}} = (a_x + a_y + a_z)/3$.

^c The anisotropy of the a tensor is expressed as the difference $a_{\text{aniso}} = a_{\parallel} - a_{\perp}$ between the parallel and perpendicular tensor components.

smaller energy gap, respectively. As the monomer-trimer joint is in the vicinity of a possible binding site of a MeOH molecule, this rationalizes the effect of MeOH on the electronic structure of the Mn_4O_5Ca cluster in the native S_2 state (41). For the Ca²⁺-depleted S_2' state, the coupling of Mn_{A4} to the trimeric unit was varied by multiplying the respective exchange coupling constants J_{A4-B3} , J_{A4-C2} , and J_{A4-D1} by a factor c (Fig. 7). It can be readily calculated that with $c = 1.65$ ($J_{A4-B3} = -46 \text{ cm}^{-1}$, $J_{A4-C2} = 7 \text{ cm}^{-1}$, and $J_{A4-D1} = 10 \text{ cm}^{-1}$), Δ is 35 cm^{-1} and thus in the desired range.

For testing whether the obtained model also reproduces reasonable estimates for the intrinsic ZFS values d_i of the Mn^{III} and Mn^{IV} ions, a brief description on how those can be assessed based on the inferred coupling scheme and the fitted effective HFI tensors is given in the supplemental data. Because of their inherently small ZFSs, the d_i values of the three Mn^{IV} ions can be assumed to be 0 cm^{-1} for the calculations of the intrinsic HFI tensors a_i from the fitted effective A_i and the computed ρ_i tensors. Mn^{III} ions generally exhibit an absolute isotropic HFI value $|a_{\text{iso}}|$ in the range between 165 and 225 MHz and considerable anisotropy defined as the difference $a_{i,\text{aniso}} = |a_{\parallel}| - |a_{\perp}|$ between the absolute values. Mn^{IV} ions tend to exhibit slightly larger isotropic HFI values ($|a_{\text{iso}}| = 187\text{--}253 \text{ MHz}$) and only small intrinsic HFI anisotropies ($|a_{\text{iso}}| \sim 30 \text{ MHz}$) (see Ref. 49). For the Ca²⁺-depleted S_2' state, a ZFS value d_{D1} of the Mn_{D1}^{III} ion in the range of -2.24 to -2.31 cm^{-1} yields a_i tensors consistent with the valence states of the individual manganese ions. An optimized ZFS value $d_{D1} = -2.27 \text{ cm}^{-1}$ leads to the spin projection and intrinsic HFI tensors ρ_i and a_i listed in Table 3. In terms of the intrinsic isotropic and anisotropic HFI values, the calculated numbers match the prerequisites as found in the literature very well. As the ZFS $d_{D1} = -2.24$ to -2.31 cm^{-1} lies in the range usually found for Mn^{III} ions ($1 \text{ cm}^{-1} < |d| < 5 \text{ cm}^{-1}$), the developed model fulfills the four essential criteria imposed.

Structural Implications of the Zero-field Splitting d_{D1} of the Mn_{D1}^{III} Ion—The removal of the Ca²⁺ ion from the spinach OEC is found to result in a significant change of d_{D1} from -1.2 cm^{-1} (41) to -2.2 to -2.3 cm^{-1} . This perturbation is larger than for the Ca²⁺/Sr²⁺ replacement in PS II from *T. elongatus*. For these systems, the intrinsic ZFS values of the Mn_{D1}^{III} ion are relatively similar (Ca²⁺, $d_{D1} = -1.3 \text{ cm}^{-1}$; Sr²⁺, $d_{D1} =$

Electronic Structure of the Ca^{2+} -depleted OEC of Photosystem II

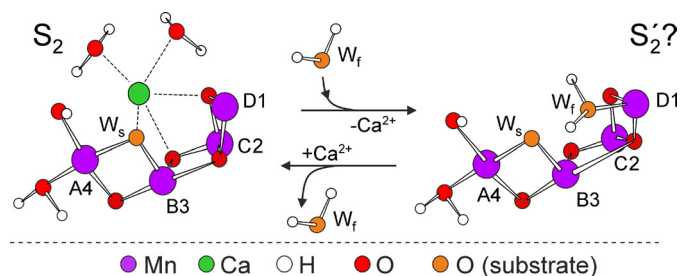


FIGURE 8. Scheme of the native $\text{Mn}_4\text{O}_5\text{Ca}$ cluster in the S_2 state and the Ca^{2+} -depleted S_2' state represented by a hypothesized Mn_4O_5 cluster. In the putative S_2' state, the fast exchanging substrate water is already bound to $\text{Mn}_{\text{D1}}^{\text{III}}$, filling the space of the Ca^{2+} ion. W_s and W_f denote the slowly and fast exchanging substrate waters, respectively (96, 99).

-1.2 cm^{-1}) (49). It is, however, noted that the signs of the d_{D1} and of the HFI anisotropy of the Mn^{III} ion do not change between the Ca^{2+} -depleted S_2' and the Ca^{2+} -containing S_2 state. These parameters can be related to the ligand sphere of the Mn^{III} ion (86–88). Negative numbers for d_{D1} and $a_{\text{D1,anis}}$ correspond to a $^5\text{B}_{1g}$ ground state, obtained in the cases of square pyramidal 5-coordinate or tetragonally elongated 6-coordinate ligand geometries. This suggests the coordination sphere of the $\text{Mn}_{\text{D1}}^{\text{III}}$ for the S_2' and S_2 states to be similar. However, the increase in the magnitude of d_{D1} upon Ca^{2+} removal does indicate modifications of the precise binding mode, e.g. altered ligand distances and angles. One possible mechanism for altering d_{D1} is protonation of one of the μ -oxo bridges ligating the Ca^{2+} ion (Fig. 1) as a means of overall charge compensation of the cluster upon Ca^{2+} removal. It is known from model complexes that Mn–Mn distances are elongated upon protonation of Mn–O–Mn bridges (89). However, within the trimeric cuboidal unit, this lengthening could be strongly impaired for the $\text{Mn}_{\text{C2}}\text{--Mn}_{\text{D1}}$ distance. The fitted averaged distance of the Mn–Mn interactions at 2.7–2.8 Å from EXAFS on Ca^{2+} -depleted PS II samples (29), however, does not allow for a conclusive assessment. Also, glutamate 189 of the D1 protein (D1-Glu-189), which directly coordinates the $\text{Mn}_{\text{D1}}^{\text{III}}$ (6, 17, 47) and potentially also the Ca^{2+} ion (18), could be reoriented upon Ca^{2+} depletion leading to a distortion of the coordination sphere and thus an altered d_{D1} .

In the latest crystal structure, all four manganese ions are 6-coordinate (6). This, however, requires the O5 μ -oxo bridge to be a ligand of Mn_{A4} , Mn_{B3} , and Mn_{D1} , engendering very long Mn–O5 bond distances well outside the range seen in model complexes (see Ref. 18) and by EXAFS spectroscopy of the $\text{Mn}_4\text{O}_5\text{Ca}$ cluster in PS II (90, 91). In most geometry-optimized DFT structures, such as those proposed by Siegbahn and our group (17, 18, 47), the position of O5 is significantly altered (Fig. 1). The O5 shifts toward the Mn_{A4} , forming a genuine μ -oxo bridge between Mn_{A4} and Mn_{B3} , and results in Mn_{D1} having an open coordination site. In this case, in the Ca^{2+} -depleted S_2' state, Glu-189 might function as a bidentate ligand in a then tetragonally elongated 6-coordinate $\text{Mn}_{\text{D1}}^{\text{III}}$ ligand sphere, leading to the observed change of d_{D1} .

Alternatively, the absence of Ca^{2+} may allow this open site to be occupied by a water molecule in the S_2' state (Fig. 8) forming a sixth ligand to Mn_{D1} . The Mn_{D1} -bound water molecule is the second substrate water in the mechanism proposed by Sie-

bahn (17), which potentially binds during the S_2 -to- S_3 transition. Thus, within this model, one of the roles of Ca^{2+} in the active cluster would be to prevent the second substrate from binding too early in the reaction cycle (25, 92). This activity would presumably avoid detrimental side product formation (reactive oxygen species) and lead to single product (O_2) formation. Consistent with this role for the Ca^{2+} ion is the known S state dependence of the affinity of Ca^{2+} to this site (93). It drops significantly in the S_3 state, suggesting that in this state Ca^{2+} is less tightly bound, having a more flexible ligand sphere that potentially allows greater solvent access to the Mn_{D1} ion.

Besides μ -oxo bridge protonation, the loss of two positive charges is likely to be compensated by protonation of amino acid residues ligating the Ca^{2+} ion in the intact cluster. Other possibilities are the replacement of Ca^{2+} by monovalent Na^+ in the samples or the absence of complete charge compensation, leaving the Mn_4O_5 cluster with an additional negative charge. It is evident that any of these modifications could have a critical effect on the catalytic capabilities of the cluster, especially with regard to proton-coupled electron transfer to Y_Z . In light of the proposed deprotonation sequence 1,0,1,2 for the individual oxidation steps starting from S_0 (94), this would explain the Mn_4O_5 cluster being able to advance to S_2' but not from $S_2'Y_Z$ to S_3' .

Conclusions—This study demonstrates that Ca^{2+} is not required for conferring the critical electronic properties to the $\text{Mn}_4\text{O}_5\text{Ca}$ cluster. This also confirms that Ca^{2+} is not essential for structural maintenance of the OEC. Its presence or absence does not affect the position of the only Mn^{III} ion of the cluster in the S_2/S_2' state (Mn_{D1}), and the contribution of the four manganese ions to the electronic states S_2 and S_2' does not differ considerably. Thus, the necessity for Ca^{2+} in water splitting catalysis must be due to another functional role of the Ca^{2+} ion.

Although the exact mechanism of inhibition upon Ca^{2+} removal is still unclear, two models can be considered in terms of the two basic catalytic mechanisms proposed in the literature. (i) For mechanisms that involve O–O bond formation between a Ca^{2+} -bound and a manganese-bound substrate water (be it a terminal ligand $\text{Mn}^{\text{V}} = \text{O}$ or a μ -oxo bridge) (11, 95–97), inhibition due to Ca^{2+} depletion is readily explained. The enzyme is inactive, as it has lost a substrate binding site. It should be noted though that this model provides no rationale for the fact that the catalytic cycle is blocked at the stage of $S_2'Y_Z$. (ii) Instead, O–O bond formation has been proposed to follow a mechanism that results in the coupling of substrates bound to two manganese sites (be it between two terminal bound Mn–O ligands or involving a μ -oxo bridge via oxyl radical coupling) (10, 14, 16, 17, 98). Then, inhibition due to Ca^{2+} removal probably represents a secondary effect where the Ca^{2+} ion is critical for maintaining the H-bond network between Y_Z and the manganese cluster (6, 11, 30) as opposed (or in addition) to perturbation of substrate binding. Thus, Ca^{2+} removal would disable proton-coupled electron transfer during the $S_2'Y_Z$ -to- S_3' transition, preventing substrate deprotonation and concomitant oxidation of $\text{Mn}_{\text{D1}}^{\text{III}}$. Therefore, the elucidation of the mechanistic role of the Ca^{2+} ion in the OEC is tightly linked to understanding the mechanism of photosynthetic water splitting.

REFERENCES

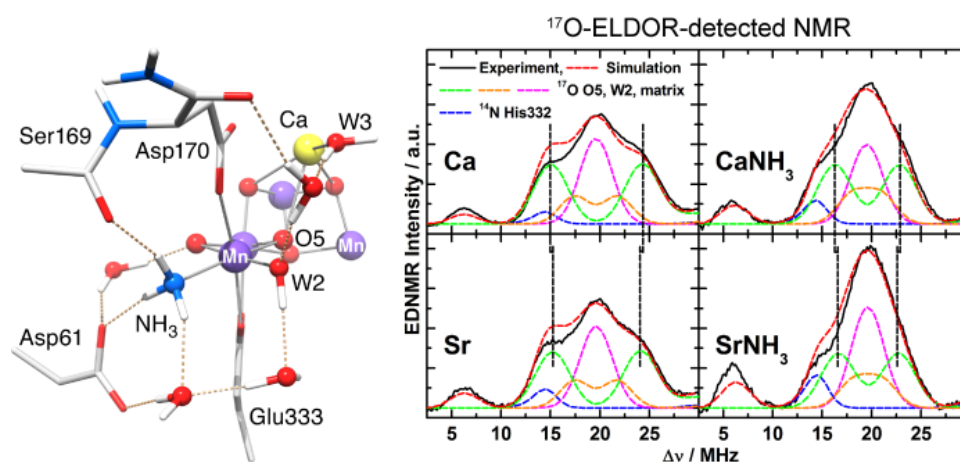
- Zouni, A., Witt, H. T., Kern, J., Fromme, P., Krauss, N., Saenger, W., and Orth, P. (2001) Crystal structure of photosystem II from *Synechococcus elongatus* at 3.8 Å resolution. *Nature* **409**, 739–743
- Kamiya, N., and Shen, J. R. (2003) Crystal structure of oxygen-evolving photosystem II from *Thermosynechococcus vulcanus* at 3.7 Å resolution. *Proc. Natl. Acad. Sci. U.S.A.* **100**, 98–103
- Ferreira, K. N., Iverson, T. M., Maghlaoui, K., Barber, J., and Iwata, S. (2004) Architecture of the photosynthetic oxygen-evolving center. *Science* **303**, 1831–1838
- Loll, B., Kern, J., Saenger, W., Zouni, A., and Biesiadka, J. (2005) Toward complete cofactor arrangement in the 3.0 Å resolution structure of photosystem II. *Nature* **438**, 1040–1044
- Guskov, A., Kern, J., Gabdulkhakov, A., Broser, M., Zouni, A., and Saenger, W. (2009) Cyanobacterial photosystem II at 2.9 Å resolution and the role of quinones, lipids, channels, and chloride. *Nat. Struct. Mol. Biol.* **16**, 334–342
- Umena, Y., Kawakami, K., Shen, J. R., and Kamiya, N. (2011) Crystal structure of oxygen-evolving photosystem II at a resolution of 1.9 Å. *Nature* **473**, 55–60
- Lubitz, W., Reiher, E. J., and Messinger, J. (2008) Solar water-splitting into H₂ and O₂. Design principles of photosystem II and hydrogenases. *Energy Environ. Sci.* **1**, 15
- Dau, H., and Zaharieva, I. (2009) Principles, efficiency, and blueprint character of solar-energy conversion in photosynthetic water oxidation. *Acc. Chem. Res.* **42**, 1861–1870
- Messinger, J., and Renger, G. (2008) in *Primary Processes of Photosynthesis, Part 2: Principles and Apparatus* (Renger, G., ed.) pp. 291–349, Royal Society of Chemistry, Cambridge
- Renger, G., and Renger, T. (2008) Photosystem II. The machinery of photosynthetic water splitting. *Photosynth. Res.* **98**, 53–80
- McEvoy, J. P., and Brudvig, G. W. (2006) Water-splitting chemistry of photosystem II. *Chem. Rev.* **106**, 4455–4483
- Nelson, N., and Yocum, C. F. (2006) Structure and function of photosystems I and II. *Annu. Rev. Plant Biol.* **57**, 521–565
- Hillier, W., and Messinger, J. (2005) in *Photosystem II: The Light-Driven Water:Plastoquinone Oxidoreductase* (Wydrzynski, T. J., and Satoh, K., eds.) pp. 567–608, Springer, Dordrecht
- Messinger, J., Noguchi, T., and Yano, J. (2012) in *Molecular Solar Fuels, RSC Energy and Environment Series* (Wydrzynski, T. J., and Hillier, W., eds.) pp. 163–207, Royal Society of Chemistry, Cambridge
- Yano, J., Kern, J., Irrgang, K. D., Latimer, M. J., Bergmann, U., Glatzel, P., Pushkar, Y., Biesiadka, J., Loll, B., Sauer, K., Messinger, J., Zouni, A., and Yachandra, V. K. (2005) X-ray damage to the Mn₄Ca complex in single crystals of photosystem II. A case study for metalloprotein crystallography. *Proc. Natl. Acad. Sci. U.S.A.* **102**, 12047–12052
- Kusunoki, M. (2007) Mono-manganese mechanism of the photosystem II water splitting reaction by a unique Mn₄Ca cluster. *Biochim. Biophys. Acta* **1767**, 484–492
- Siegbahn, P. E. (2009) Structures and energetics for O₂ formation in photosystem II. *Acc. Chem. Res.* **42**, 1871–1880
- Ames, W., Pantazis, D. A., Krewald, V., Cox, N., Messinger, J., Lubitz, W., and Neese, F. (2011) Theoretical evaluation of structural models of the S₂ state in the oxygen evolving complex of photosystem II. Protonation states and magnetic interactions. *J. Am. Chem. Soc.* **133**, 19743–19757
- Ghanotakis, D. F., Babcock, G. T., and Yocum, C. F. (1984) Calcium reconstitutes high rates of oxygen evolution in polypeptide depleted photosystem II preparations. *FEBS Lett.* **167**, 127–130
- Ghanotakis, D. F., Topper, J. N., Babcock, G. T., and Yocum, C. F. (1984) Water-soluble 17- and 23-kDa polypeptides restore oxygen evolution activity by creating a high affinity binding site for Ca²⁺ on the oxidizing side of photosystem II. *FEBS Lett.* **170**, 169–173
- Ono, T., and Inoue, Y. (1988) Discrete extraction of the Ca²⁺ atom functional for O₂ evolution in higher plant photosystem II by a simple low pH treatment. *FEBS Lett.* **227**, 147–152
- Boussac, A., Maison-Peteri, B., Etienne, A. L., and Vernotte, C. (1985) Reactivation of oxygen evolution of NaCl-washed photosystem II particles by Ca²⁺ and/or the 24-kDa protein. *Biochim. Biophys. Acta Bioenerg.* **808**, 231–234
- Boussac, A., and Rutherford, A. W. (1988) Nature of the inhibition of the oxygen-evolving enzyme of photosystem II induced by NaCl washing and reversed by the addition of Ca²⁺ or Sr²⁺. *Biochemistry* **27**, 3476–3483
- Boussac, A., Zimmermann, J. L., and Rutherford, A. W. (1989) EPR signals from modified charge accumulation states of the oxygen evolving enzyme in Ca²⁺-deficient photosystem II. *Biochemistry* **28**, 8984–8989
- Sivaraja, M., Tso, J., and Dismukes, G. C. (1989) A calcium-specific site influences the structure and activity of the manganese cluster responsible for photosynthetic water oxidation. *Biochemistry* **28**, 9459–9464
- Miqyass, M., van Gorkom, H. J., and Yocum, C. F. (2007) The PSII calcium site revisited. *Photosynth. Res.* **92**, 275–287
- Yocum, C. F. (2008) The calcium and chloride requirements of the O₂ evolving complex. *Coord. Chem. Rev.* **252**, 296–305
- Yachandra, V. K., and Yano, J. (2011) Calcium in the oxygen-evolving complex. Structural and mechanistic role determined by X-ray spectroscopy. *J. Photochem. Photobiol. B* **104**, 51–59
- Latimer, M. J., DeRose, V. J., Yachandra, V. K., Sauer, K., and Klein, M. P. (1998) Structural effects of calcium depletion on the manganese cluster of photosystem II. Determination by x-ray absorption spectroscopy. *J. Phys. Chem. B* **102**, 8257–8265
- Diner, B. A., and Britt, R. D. (2005) in *Photosystem II: The Light-Driven Water:Plastoquinone Oxidoreductase* (Wydrzynski, T. J., and Satoh, K., eds.) pp. 207–233, Springer, Dordrecht
- Vrettos, J. S., Stone, D. A., and Brudvig, G. W. (2001) Quantifying the ion selectivity of the Ca²⁺ site in photosystem II. Evidence for direct involvement of Ca²⁺ in O₂ formation. *Biochemistry* **40**, 7937–7945
- Boussac, A., Rappaport, F., Carrier, P., Verbavatz, J. M., Gobin, R., Kirilovsky, D., Rutherford, A. W., and Sugiura, M. (2004) Biosynthetic Ca²⁺/Sr²⁺ exchange in the photosystem II oxygen-evolving enzyme of *Thermosynechococcus elongatus*. *J. Biol. Chem.* **279**, 22809–22819
- Dismukes, G. C., and Siderer, Y. (1981) Intermediates of a polynuclear manganese center involved in photosynthetic oxidation of water. *Proc. Natl. Acad. Sci. U.S.A.* **78**, 274–278
- Casey, J. L., and Sauer, K. (1984) EPR detection of a cryogenically photo-generated intermediate in photosynthetic oxygen evolution. *Biochim. Biophys. Acta Bioenerg.* **767**, 21–28
- Zimmermann, J. L., and Rutherford, A. W. (1984) EPR studies of the oxygen-evolving enzyme of photosystem II. *Biochim. Biophys. Acta Bioenerg.* **767**, 160–167
- Horner, O., Rivière, E., Blondin, G., Un, S., Rutherford, A. W., Girerd, J. J., and Boussac, A. (1998) SQUID magnetization study of the infrared-induced spin transition in the infrared-induced spin transition in the S₂ state of photosystem II. Spin value associated with the g = 4.1 EPR signal. *J. Am. Chem. Soc.* **120**, 7924–7928
- Boussac, A. (1997) Inhomogeneity of the EPR multiline signal from the S₂ state of the photosystem II oxygen-evolving enzyme. *J. Biol. Inorg. Chem.* **2**, 580–585
- Åhring, K. A., Evans, M. C., Nugent, J. H., and Pace, R. J. (2004) The two forms of the S₂ state multiline signal in photosystem II. Effect of methanol and ethanol. *Biochim. Biophys. Acta* **1656**, 66–77
- Force, D. A., Randall, D. W., Lorigan, G. A., Clemens, K. L., and Britt, R. D. (1998) ESEEM studies of alcohol binding to the manganese cluster of the oxygen-evolving complex of photosystem II. *J. Am. Chem. Soc.* **120**, 13321–13333
- Åhring, K. A., Evans, M. C., Nugent, J. H., Ball, R. J., and Pace, R. J. (2006) ESEEM studies of substrate water and small alcohol binding to the oxygen-evolving complex of photosystem II during functional turnover. *Biochemistry* **45**, 7069–7082
- Su, J. H., Cox, N., Ames, W., Pantazis, D. A., Rapatskiy, L., Lohmiller, T., Kulik, L. V., Dorlet, P., Rutherford, A. W., Neese, F., Boussac, A., Lubitz, W., and Messinger, J. (2011) The electronic structures of the S₂ states of the oxygen-evolving complexes of photosystem II in plants and cyanobacteria in the presence and absence of methanol. *Biochim. Biophys. Acta* **1807**, 829–840
- Peloquin, J. M., Campbell, K. A., Randall, D. W., Evanchik, M. A., Pec-

- oraro, V. L., Armstrong, W. H., and Britt, R. D. (2000) ^{55}Mn ENDOR of the S_2 -state multiline EPR signal of photosystem II. Implications on the structure of the tetranuclear Mn cluster. *J. Am. Chem. Soc.* **122**, 10926–10942
43. Lorigan, G. A., and Britt, R. D. (1994) Temperature-dependent pulsed electron paramagnetic resonance studies of the S_2 state multiline signal of the photosynthetic oxygen-evolving complex. *Biochemistry* **33**, 12072–12076
44. Kulik, L., Epel, B., Messinger, J., and Lubitz, W. (2005) Pulse EPR, ^{55}Mn -ENDOR, and ELDOR-detected NMR of the S_2 -state of the oxygen evolving complex in photosystem II. *Photosynth. Res.* **84**, 347–353
45. Kulik, L. V., Epel, B., Lubitz, W., and Messinger, J. (2005) ^{55}Mn pulse ENDOR at 34 GHz of the S_0 and S_2 states of the oxygen-evolving complex in photosystem II. *J. Am. Chem. Soc.* **127**, 2392–2393
46. Kulik, L. V., Epel, B., Lubitz, W., and Messinger, J. (2007) Electronic structure of the $\text{Mn}_4\text{O}_x\text{Ca}$ cluster in the S_0 and S_2 states of the oxygen-evolving complex of photosystem II based on pulse ^{55}Mn -ENDOR and EPR spectroscopy. *J. Am. Chem. Soc.* **129**, 13421–13435
47. Pantazis, D. A., Orio, M., Petrenko, T., Zein, S., Lubitz, W., Messinger, J., and Neese, F. (2009) Structure of the oxygen-evolving complex of photosystem II. Information on the S_2 state through quantum chemical calculation of its magnetic properties. *Phys. Chem. Chem. Phys.* **11**, 6788–6798
48. Teutloff, C., Pudollek, S., Kessen, S., Broser, M., Zouni, A., and Bittl, R. (2009) Electronic structure of the tyrosine D radical and the water-splitting complex from pulsed ENDOR spectroscopy on photosystem II single crystals. *Phys. Chem. Chem. Phys.* **11**, 6715–6726
49. Cox, N., Rapatskiy, L., Su, J. H., Pantazis, D. A., Sugiura, M., Kulik, L., Dorlet, P., Rutherford, A. W., Neese, F., Boussac, A., Lubitz, W., and Messinger, J. (2011) Effect of $\text{Ca}^{2+}/\text{Sr}^{2+}$ substitution on the electronic structure of the oxygen-evolving complex of photosystem II. A combined multifrequency EPR, ^{55}Mn -ENDOR, and DFT study of the S_2 state. *J. Am. Chem. Soc.* **133**, 3635–3648
50. Stich, T. A., Yeagle, G. J., Service, R. J., Debus, R. J., and Britt, R. D. (2011) Ligation of D1-His-332 and D1-Asp-170 to the manganese cluster of photosystem II from *Synechocystis* assessed by multifrequency pulse EPR spectroscopy. *Biochemistry* **50**, 7390–7404
51. Booth, P. J., Rutherford, A. W., and Boussac, A. (1996) Location of the calcium binding site in photosystem II. A Mn^{2+} substitution study. *Biochim. Biophys. Acta Bioenerg.* **1277**, 127–134
52. Berthold, D. A., Babcock, G. T., and Yocum, C. F. (1981) A highly resolved, oxygen-evolving photosystem II preparation from spinach thylakoid membranes. EPR and electron-transport properties. *FEBS Lett.* **134**, 231–234
53. Arnon, D. I. (1949) Copper enzymes in isolated chloroplasts. Polyphenoloxidase in β -vulgaris. *Plant Physiol.* **24**, 1–15
54. Porra, R. J., Thompson, W. A., and Kriedemann, P. E. (1989) Determination of accurate extinction coefficients and simultaneous equations for assaying chlorophylls *a* and *b* extracted with four different solvents. Verification of the concentration of chlorophyll standards by atomic absorption spectroscopy. *Biochim. Biophys. Acta Bioenerg.* **975**, 384–394
55. Cinco, R. M., Robblee, J. H., Rompel, A., Fernandez, C., Yachandra, V. K., Sauer, K., and Klein, M. P. (1998) Strontium EXAFS reveals the proximity of calcium to the manganese cluster of oxygen-evolving photosystem II. *J. Phys. Chem. B* **102**, 8248–8256
56. Ono, T., and Inoue, Y. (1989) Roles of Ca^{2+} in O_2 evolution in higher plant photosystem II. Effects of replacement of Ca^{2+} site by other cations. *Arch. Biochem. Biophys.* **275**, 440–448
57. Roberts, A. G., Gregor, W., Britt, R. D., and Kramer, D. M. (2003) Acceptor and donor-side interactions of phenolic inhibitors in photosystem II. *Biochim. Biophys. Acta* **1604**, 23–32
58. Reijerse, E., Lendzian, F., Isaacson, R., and Lubitz, W. (2012) A tunable general purpose Q-band resonator for CW and pulse EPR/ENDOR experiments with large sample access and optical excitation. *J. Magn. Reson.* **214**, 237–243
59. Epel, B., Gromov, I., Stoll, S., Schweiger, A., and Goldfarb, D. (2005) Spectrometer manager. A versatile control software for pulse EPR spectrometers *Concepts Magn. Reson. Part B (Magn. Reson. Engineering)* **26B**, 36–45
60. Stoll, S., and Schweiger, A. (2006) EasySpin, a comprehensive software package for spectral simulation and analysis in EPR. *J. Magn. Reson.* **178**, 42–55
61. Sturgeon, B. E., Ball, J. A., Randall, D. W., and Britt, R. D. (1994) ^{55}Mn electron spin echo ENDOR of Mn^{2+} Complexes. *J. Phys. Chem.* **98**, 12871–12883
62. Rutherford, A. W., and Zimmermann, J. L. (1984) A new EPR signal attributed to the primary plastoquinone acceptor in photosystem II. *Biochim. Biophys. Acta Bioenerg.* **767**, 168–175
63. Zheng, M., and Dismukes, G. C. (1996) Orbital configuration of the valence electrons, ligand field symmetry, and manganese oxidation states of the photosynthetic water oxidizing complex. Analysis of the S_2 state multiline EPR signals. *Inorg. Chem.* **35**, 3307–3319
64. Kusunoki, M. (1992) A new paramagnetic hyperfine structure effect in manganese tetramers. The origin of “multiline” EPR signals from an S_2 state of a photosynthetic water-splitting enzyme. *Chem. Phys. Lett.* **197**, 108–116
65. Charlot, M. F., Boussac, A., and Blondin, G. (2005) Toward a spin coupling model for the Mn_4 cluster in photosystem II. *Biochim. Biophys. Acta* **1708**, 120–132
66. Teutloff, C., Kessen, S., Kern, J., Zouni, A., and Bittl, R. (2006) High-field (94 GHz) EPR spectroscopy on the S_2 multiline signal of photosystem II. *FEBS Lett.* **580**, 3605–3609
67. Lohmiller, T., Cox, N., Su, J. H., Messinger, J., and Lubitz, W. (2010) *Proceedings of 15th International Congress on Photosynthesis* Beijing, China, August 22–27, 2010, Zhejiang University Press/Springer, Dordrecht
68. Murray, J. W., and Barber, J. (2006) Identification of a calcium-binding site in the PsbO protein of photosystem II. *Biochemistry* **45**, 4128–4130
69. Zhang, L. X., Liang, H. G., Wang, J., Li, W. R., and Yu, T. Z. (1996) Fluorescence and Fourier-transform infrared spectroscopic studies on the role of disulfide bond in the calcium binding in the 33-kDa protein of photosystem II. *Photosynth. Res.* **48**, 379–384
70. Heredia, P., and De Las Rivas, J. (2003) Calcium-dependent conformational change and thermal stability of the isolated PsbO protein detected by FTIR spectroscopy. *Biochemistry* **42**, 11831–11838
71. Kruk, J., Burda, K., Jemioła-Rzemińska, M., and Strzałka, K. (2003) The 33-kDa protein of photosystem II is a low affinity calcium- and lanthanide-binding protein. *Biochemistry* **42**, 14862–14867
72. Abramowicz, D. A., and Dismukes, G. C. (1984) Manganese proteins isolated from spinach thylakoid membranes and their role in O_2 evolution. II. A binuclear manganese-containing 34-kilodalton protein, a probable component of the water dehydrogenase enzyme. *Biochim. Biophys. Acta* **765**, 318–328
73. Yamamoto, Y., Shinkai, H., Isogai, Y., Matsuura, K., and Nishimura, M. (1984) Isolation of an Mn-carrying 33-kDa protein from an oxygen-evolving photosystem-II preparation by phase partitioning with butanol. *FEBS Lett.* **175**, 429–432
74. Lu, Y. K., Theg, S. M., and Stemler, A. J. (2005) Carbonic anhydrase activity of the photosystem II OEC33 protein from pea. *Plant Cell Physiol.* **46**, 1944–1953
75. Bondarava, N., Beyer, P., and Krieger-Liszka, A. (2005) Function of the 23-kDa extrinsic protein of photosystem II as a manganese-binding protein and its role in photoactivation. *Biochim. Biophys. Acta* **1708**, 63–70
76. Bondarava, N., Un, S., and Krieger-Liszka, A. (2007) Manganese binding to the 23-kDa extrinsic protein of photosystem II. *Biochim. Biophys. Acta* **1767**, 583–588
77. Bricker, T. M., and Frankel, L. K. (2011) Auxiliary functions of the PsbO, PsbP, and PsbQ proteins of higher plant photosystem II. A critical analysis. *J. Photochem. Photobiol. B* **104**, 165–178
78. Michoux, F., Takasaka, K., Boehm, M., Nixon, P. J., and Murray, J. W. (2010) Structure of CyanoP at 2.8 Å. Implications for the evolution and function of the PsbP subunit of photosystem II. *Biochemistry* **49**, 7411–7413
79. Dasgupta, J., Ananyev, G. M., and Dismukes, G. C. (2008) Photoassembly of the water-oxidizing complex in photosystem II. *Coord. Chem. Rev.* **252**, 347–360

80. Mulo, P., Sirpiö, S., Suorsa, M., and Aro, E. M. (2008) Auxiliary proteins involved in the assembly and sustenance of photosystem II. *Photosynth. Res.* **98**, 489–501
81. Grasse, N., Mamedov, F., Becker, K., Styring, S., Rögner, M., and Nowaczyk, M. M. (2011) Role of novel dimeric photosystem II (PSII)-Psb27 protein complex in PSII repair. *J. Biol. Chem.* **286**, 29548–29555
82. Komenda, J., Michoux, F., and Nixon, P. (2011) in *Self-Healing at the Nanoscale*, pp. 3–22, CRC Press
83. Pace, R. J., Smith, P., Bramley, R., and Stehlik, D. (1991) EPR saturation and temperature dependence studies on signals from the oxygen-evolving centre of photosystem II. *Biochim. Biophys. Acta Bioenerg.* **1058**, 161–170
84. Åhrling, K. A., Peterson, S., and Styring, S. (1998) The S_0 state EPR signal from the Mn cluster in photosystem II arises from an isolated $S = 1/2$ ground state. *Biochemistry* **37**, 8115–8120
85. Siegbahn, P. E. (2009) Water oxidation in photosystem II. Oxygen release, proton release, and the effect of chloride. *Dalton Trans.* **45**, 10063–10068
86. Griffith, J. S. (2009) *The Theory of Transition-Metal Ions*, Cambridge University Press, Cambridge, UK
87. Gerritsen, H. J., and Sabisky, E. S. (1963) Paramagnetic resonance of trivalent manganese in rutile (TiO_2). *Phys. Rev.* **132**, 1507–1512
88. Campbell, K. A., Force, D. A., Nixon, P. J., Dole, F., Diner, B. A., and Britt, R. D. (2000) Dual-mode EPR detects the initial intermediate in photoassembly of the photosystem II Mn cluster. The influence of amino acid residue 170 of the D1 polypeptide on Mn coordination. *J. Am. Chem. Soc.* **122**, 3754–3761
89. Baldwin, M. J., Stemmler, T. L., Riggs-Gelasco, P. J., Kirk, M. L., Penner-Hahn, J. E., and Pecoraro, V. L. (1994) Structural and magnetic effects of successive protonations of oxo bridges in high-valent manganese dimers. *J. Am. Chem. Soc.* **116**, 11349–11356
90. Yano, J., Kern, J., Sauer, K., Latimer, M. J., Pushkar, Y., Biesiadka, J., Loll, B., Saenger, W., Messinger, J., Zouni, A., and Yachandra, V. K. (2006) Where water is oxidized to dioxygen: structure of the photosynthetic Mn_4Ca cluster. *Science* **314**, 821–825
91. Pushkar, Y., Yano, J., Glatzel, P., Messinger, J., Lewis, A., Sauer, K., Bergmann, U., and Yachandra, V. (2007) Structure and orientation of the Mn_4Ca cluster in plant photosystem II membranes studied by polarized range-extended x-ray absorption spectroscopy. *J. Biol. Chem.* **282**, 7198–7208
92. Tso, J., Sivaraja, M., and Dismukes, G. C. (1991) Calcium limits substrate accessibility or reactivity at the manganese cluster in photosynthetic water oxidation. *Biochemistry* **30**, 4734–4739
93. Boussac, A., and Rutherford, A. W. (1988) Ca^{2+} binding to the oxygen evolving enzyme varies with the redox state of the Mn cluster. *FEBS Lett.* **236**, 432–436
94. Lavergne, J., and Junge, W. (1993) Proton release during the redox cycle of the water oxidase. *Photosynth. Res.* **38**, 279–296
95. Pecoraro, V. L., Baldwin, M. J., Caudle, M. T., Hsieh, W.-Y., and Law, N. A. (1998) A proposal for water oxidation in photosystem II. *Pure Appl. Chem.* **70**, 925–929
96. Messinger, J., Badger, M., and Wydrzynski, T. (1995) Detection of one slowly exchanging substrate water molecule in the S_3 state of photosystem II. *Proc. Natl. Acad. Sci. U.S.A.* **92**, 3209–3213
97. Dau, H., and Haumann, M. (2008) The manganese complex of photosystem II in its reaction cycle. Basic framework and possible realization at the atomic level. *Coord. Chem. Rev.* **252**, 273–295
98. Yachandra, V. K. (2005) in *Photosystem II: The Light-Driven Water: Plastoquinone Oxidoreductase* (Wydrzynski, T. J., and Satoh, K., eds.) pp. 235–260, Springer, Dordrecht
99. Hillier, W., and Wydrzynski, T. (2008) ^{18}O -water exchange in photosystem II. Substrate binding and intermediates of the water splitting cycle. *Coord. Chem. Rev.* **252**, 306–317
100. Messinger, J., Robblee, J. H., Bergmann, U., Fernandez, C., Glatzel, P., Visser, H., Cinco, R. M., McFarlane, K. L., Bellacchio, E., Pizarro, S. A., Cramer, S. P., Sauer, K., Klein, M. P., and Yachandra, V. K. (2001) Absence of Mn-centered oxidation in the $S_2 \rightarrow S_3$ transition. Implications for the mechanism of photosynthetic water oxidation. *J. Am. Chem. Soc.* **123**, 7804–7820

Chapter 6

Structure, Ligands and Substrate Coordination of the Oxygen-Evolving Complex of Photosystem II in the S_2 State: a Combined EPR and DFT Study



Lohmiller, T.; Krewald, V.; Pérez Navarro, M.; Retegan, M.; Rapatskiy, L.; Nowaczyk, M. M.; Boussac, A.; Neese, F.; Lubitz, W.; Pantazis, D. A.; Cox, N.

Phys. Chem. Chem. Phys. **2014**, *16* (24), 11877-11892. <http://dx.doi.org/10.1039/c3cp55017f>

Reproduced by permission of the PCCP Owner Societies.

Structure, ligands and substrate coordination of the oxygen-evolving complex of photosystem II in the S_2 state: a combined EPR and DFT study†

Cite this: DOI: 10.1039/c3cp55017f

 Thomas Lohmiller,^a Vera Krewald,^a Montserrat Pérez Navarro,^a Marius Retegan,^a Leonid Rapatskiy,^a Marc M. Nowaczyk,^b Alain Boussac,^c Frank Neese,^a Wolfgang Lubitz,^a Dimitrios A. Pantazis*^a and Nicholas Cox*^a

The S_2 state of the oxygen-evolving complex of photosystem II, which consists of a Mn_4O_5Ca cofactor, is EPR-active, typically displaying a multiline signal, which arises from a ground spin state of total spin $S_T = 1/2$. The precise appearance of the signal varies amongst different photosynthetic species, preparation and solvent conditions/compositions. Over the past five years, using the model species *Thermosynechococcus elongatus*, we have examined modifications that induce changes in the multiline signal, i.e. Ca^{2+}/Sr^{2+} -substitution and the binding of ammonia, to ascertain how structural perturbations of the cluster are reflected in its magnetic/electronic properties. This refined analysis, which now includes high-field (W-band) data, demonstrates that the electronic structure of the S_2 state is essentially invariant to these modifications. This assessment is based on spectroscopies that examine the metal centres themselves (EPR, ^{55}Mn -ENDOR) and their first coordination sphere ligands ($^{14}N/^{15}N$ - and ^{17}O -ESEEM, -HYSCORE and -EDNMR). In addition, extended quantum mechanical models from broken-symmetry DFT now reproduce all EPR, ^{55}Mn and ^{14}N experimental magnetic observables, with the inclusion of second coordination sphere ligands being crucial for accurately describing the interaction of NH_3 with the Mn tetramer. These results support a mechanism of multiline heterogeneity reported for species differences and the effect of methanol [*Biochim. Biophys. Acta, Bioenerg.*, 2011, **1807**, 829], involving small changes in the magnetic connectivity of the solvent accessible outer Mn_{A4} to the cuboidal unit Mn_3O_3Ca , resulting in predictable changes of the measured effective ^{55}Mn hyperfine tensors. Sr^{2+} and NH_3 replacement both affect the observed ^{17}O -EDNMR signal envelope supporting the assignment of O5 as the exchangeable μ -oxo bridge and it acting as the first site of substrate inclusion.

Received 28th November 2013,
Accepted 30th January 2014

DOI: 10.1039/c3cp55017f

www.rsc.org/pccp

1 Introduction

In oxygenic photosynthesis, light-driven water oxidation is catalysed by the oxygen-evolving complex (OEC) of the transmembrane protein complex photosystem II (PSII). The OEC

consists of a μ -oxo-bridged tetramanganese-calcium cofactor (Mn_4O_5Ca), embedded in its protein matrix. This matrix includes the redox-active tyrosine residue Y_Z (D1-Tyr161), which couples electron transfer between the Mn_4O_5Ca cluster and $P680^{*+}$, the photooxidant of the PSII reaction centre. The four-electron water oxidation reaction requires four consecutive light-induced charge separation events, driving the catalytic cycle of the OEC.^{1,2} This cycle involves five redox intermediates, the S_n states, where $n = 0-4$ indicates the number of stored oxidizing equivalents. All S-state transitions represent oxidations of the Mn_4O_5Ca cluster by Y_Z^* with the exception of the regeneration of S_0 from S_4 , which proceeds spontaneously under the release of molecular triplet oxygen and the rebinding of at least one substrate water molecule. The rate-limiting step, oxidation of S_3 by Y_Z^* , has prevented the transient, fast-decaying S_4 state from being characterized yet. For a general introduction into water oxidation by the OEC, see ref. 3–8.

The structure of the Mn_4O_5Ca inorganic core⁹ resembles a 'distorted chair' where the base is formed by a μ -oxo-bridged

^a Max-Planck-Institut für Chemische Energiekonversion, Stiftstrasse 34-36, D-45470 Mülheim an der Ruhr, Germany. E-mail: dimitrios.pantazis@cec.mpg.de, nicholas.cox@cec.mpg.de; Fax: +49 208 306 3955; Tel: +49 208 306 3552

^b Ruhr-University Bochum, Universitätsstrasse 150, D-44780 Bochum, Germany

^c iBiTec-S, SB2SM, UMR 8221, CEA Saclay, 91191 Gif-sur-Yvette, France

† Electronic supplementary information (ESI) available: PSII sample preparation; data processing: baseline correction and light-minus-dark subtraction; spectral simulations; theoretical background; DFT calculations: NH_3 binding modes and spatial coordinates of the S_2 state models; Q-band ^{55}Mn -ENDOR: comparison of instrumental settings; electronic structures: exchange couplings and spin states of the BS-DFT models; the Mn_{D1} -His332-imino-N interaction: Q-band three-pulse ESEEM, Q-band HYSCORE, W-band EDNMR and simulations; X-band ^{14}N - and ^{15}N -three pulse ESEEM experiments on the NH_3 -modified S_2 state; exchangeable ^{17}O species: W-band EDNMR and X-band EPR. See DOI: 10.1039/c3cp55017f



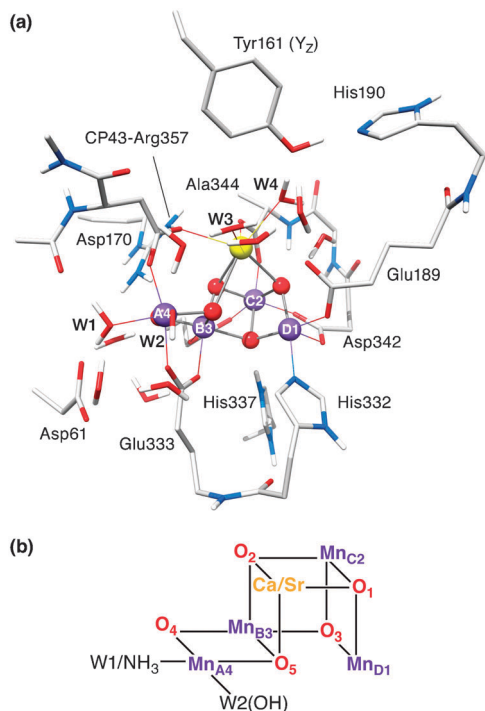


Fig. 1 (a) DFT cluster model of the native OEC and its immediate surroundings in the S_2 ($S_T = 1/2$) state. Mn ions are depicted in purple, O in red, Ca in yellow, C in light grey, N in blue and H in white; most H atoms are omitted for clarity. (b) $Mn_4O_5Ca/Sr-H_2O/NH_3$ cores showing the atom and ligand labels used in this work.

cuboidal Mn_3O_4Ca unit (Fig. 1), while the fourth, 'outer' Mn, Mn_{A4} is attached to this core structure *via* two μ -oxo bridges, O4 and O5. Spectroscopic evidence suggests that all five oxygen bridges are deprotonated in the S_2 state.^{10–15} In addition to the μ -oxo-bridged network, the Mn_4O_5Ca scaffold is held together by six carboxylate ligands, four of which (D1-Asp342, D1-Asp170, D1-Glu333 and CP47-Glu354) form μ -carboxylato bridges between Mn sites. The cluster has only one immediate nitrogen ligand, the imidazole imino-N of D1-His332.

An understanding of the mechanism of water oxidation catalysis is intimately linked to an understanding of the electronic states of the paramagnetic tetranuclear Mn complex. Electron paramagnetic resonance (EPR) spectroscopy represents a powerful methodology in this endeavour.^{16–19} The S_2 state, being readily generated from the dark-stable S_1 state, is the most extensively characterized S state by EPR. It is intrinsically heterogeneous,^{20–22} existing in two ground state configurations. The lowest energy form exhibits a ground state of total spin $S_T = 1/2$. This spin configuration gives rise to the well-known S_2 state EPR multiline signal centred at $g \approx 2.0$, with a hyperfine pattern of at least 24 peaks, with a line spacing around 87 G.²³ Depending on the conditions used, the S_2 state can also exhibit other broad EPR signals, centred at $g \geq 4.1$, which have been assigned to (an) $S_T \geq 5/2$ spin state(s).^{20,24–28} The $g \geq 4.1$ signal can also be induced by near-infrared illumination of the S_2 multiline state at temperatures ≤ 160 K.^{24,25,29} Pulse electron nuclear double resonance (ENDOR) experiments,³⁰ especially at Q-band

frequencies,^{31–34} have enabled a more detailed examination of the electronic structure by uniquely determining four ^{55}Mn hyperfine interactions that give rise to the multiline pattern of the corresponding $S_T = 1/2$ EPR signal. This ENDOR analysis has strongly suggested that the OEC contains one Mn^{III} ion and three Mn^{IV} ions when poised in the S_2 state.^{30–34}

OEC models developed from broken-symmetry (BS) density functional theory (DFT) have been crucial for the interpretation of EPR and related magnetic resonance results.^{12,14,18,33,35–44} These calculations now allow different S-state models to be assessed based on the spin multiplicities and relative energies of their lowest magnetic levels, and, by means of the spin projection formalism (see ref. 18 and 36), the metal and ligand hyperfine couplings. This strategy enables the assignment of individual Mn oxidation states and coordination geometries and represents a method to develop unified models of the OEC that combine constraints from X-ray diffraction, EXAFS and magnetic resonance.

Site perturbation of the OEC provides a means to further characterize the global geometric and electronic structure of the Mn tetramer and obtain information about localized changes associated with the introduced modification. The two best described OEC perturbations in the literature are (i) the replacement of the Ca^{2+} with a Sr^{2+} ion^{33,45–47} and (ii) the binding of NH_3 to the cluster.^{48–55} Both of these perturbations *do not* inhibit functional turnover of the catalyst, but do modify the kinetics of O–O bond formation, substrate water uptake and its subsequent deprotonation. A brief description of these two modified OEC forms is given below:

(i) Sr^{2+} can be introduced into the OEC through chemical removal of the Ca^{2+} ion^{45,46,56} or alternatively by biosynthetic incorporation in cyanobacterial cultures grown in the presence of $SrCl_2$ instead of $CaCl_2$.⁴⁷ Without Ca^{2+} (or Sr^{2+}) the OEC is inhibited,^{56–63} not progressing further than a modified form of the S_2 state, *i.e.* the S_2/Y_Z^* state.^{60–62} Sr^{2+} is unique as it is the only ion which can replace the Ca^{2+} ion while retaining catalytic activity, albeit at a lower enzymatic rate.^{45,47,56} Presumably this is because Sr^{2+} has a similar size and Lewis acidity as Ca^{2+} .⁶⁴ While slowing the turnover rate of the catalyst, Sr^{2+} substitution at the same time enhances the exchange rate with bulk water of at least one of the bound substrates,^{65,66} as observed by time-resolved membrane inlet mass spectrometry (MIMS).^{67,68} This behaviour suggests the Ca^{2+} ion may play an important role in substrate water binding and possibly proton release (for reviews, see ref. 3 and 69).

(ii) Ammonia binding to the Mn cluster (in the presence of high Cl^- concentrations)^{48,50,51,54} only occurs upon formation of the S_2 state. It is subsequently released at some point during the S-state cycle ($S_3 \rightarrow S_0 \rightarrow S_1$), such that it is not bound upon return to S_1 .⁵¹ As with Sr^{2+} replacement, NH_3 binding does not inhibit catalytic function. In the higher plant electron spin echo envelope modulation (ESEEM) study of Britt *et al.*,⁷⁰ NH_3 was shown to bind as a direct ligand of the Mn tetramer. The precise binding site and coordination mode of the NH_3 molecule was the subject of a recent study on cyanobacterial PSII from our laboratory.⁴⁴ By employing electron electron double resonance (ELDOR)-detected NMR (EDNMR), it was concluded that NH_3



replaces the water ligand of Mn_{A4} *trans* to the O5 bridge (W1, Fig. 1b). As the binding of NH_3 was also shown not to affect substrate exchange rates, these results suggest W1 does not represent a substrate water. One or more additional NH_3 binding sites, which are inhibitory, are known but are less well characterized.^{49,50,71}

Here, we present an extension of our earlier multifrequency EPR studies^{33,34,44} of different ‘archetypal’ multiline forms, namely the native ($\text{Mn}_4\text{O}_5\text{Ca}$), Sr^{2+} substituted ($\text{Mn}_4\text{O}_5\text{Sr}$) and NH_3 -treated ($\text{Mn}_4\text{O}_5\text{Ca-NH}_3$) S_2 states, providing a comprehensive analysis of all present X-, Q- and W-band data of ^{55}Mn , $^{14}\text{N}/^{15}\text{N}$ and ^{17}O signals and for the first time including additional data on the doubly modified ($\text{Mn}_4\text{O}_5\text{Sr-NH}_3$) S_2 state. Improved ^{55}Mn ENDOR experimental conditions provide more reliable spectral line shapes than before, confirming our previous general S_2 state model. Extended BS-DFT models are shown to reproduce all EPR, ^{55}Mn and ^{14}N magnetic spectroscopic observables for the native and the modified systems, a feature not achieved previously. The experimental results and calculations for $^{14}\text{N}/^{15}\text{N}$ ligands of the various S_2 state forms serve to prove that the basic electronic structure is not perturbed by these modifications, a result crucial for the interpretation of concomitant perturbations of the ^{17}O EDNMR signal envelope. This combined experimental and theoretical approach supports our qualitative model for multiline heterogeneity, demonstrating that the magnetic connectivity between the two subunits and also within the trimeric moiety governs the structure of the multiline signal.³⁴ This basic structural template also explains the apparent orientations of the ^{55}Mn hyperfine tensors, as inferred from spectral simulations and single crystal measurements,³² and potentially provides a framework to further examine substrate binding. The different OEC forms represent a starting point to examine the energetics of higher S-state transitions, as they differ with regard to substrate binding and the kinetics of O–O bond formation and O_2 release.

2 Materials and methods

2.1 PSII sample preparation

Ca^{2+} - and Sr^{2+} -containing PSII core complex preparations from *T. elongatus*⁷² were isolated as reported before^{47,73,74} with the same modifications for the X-band samples as described in ref. 44. Universal ^{15}N -labelling of the PSII proteins was achieved by growing the cyanobacteria in a modified BG11 or DTN medium that contained $^{15}\text{NH}_4\text{Cl}$ and $^{15}\text{NO}_3^-$ salts as the sole nitrogen source.⁷⁵ PSII preparations were stored at -80°C until use. Dark-adapted samples were placed in X-, Q- or W-band quartz tubes with inner diameters of 3.0, 1.6 and 0.6 mm, respectively, and kept at 77 K (liquid N_2) until use. A sample concentration of 3.0–4.0 mg chlorophyll per ml was used throughout this study. All work was conducted in the dark or under dim green light. NH_3 modification was conducted as described in ref. 44, see also Section S1 of the ESI.† Isotopically enriched H_2^{17}O buffer exchange was achieved as described in ref. 14.

2.2 X-, Q-, and W-band EPR and ENDOR measurements

X-band (≈ 9 GHz) continuous-wave (CW) EPR spectra were recorded at liquid He temperatures on a Bruker ELEXSYS E500 spectrometer, equipped with an ESR 900 liquid helium flow cryostat and an ITC503 helium flow temperature controller (Oxford Instruments Ltd). X-band pulse EPR measurements were carried out at 4.3 K using a Bruker ELEXSYS E580 spectrometer, equipped with a CF935 cryostat and an ITC503 temperature controller. Q-band (≈ 34 GHz) pulse EPR measurements were performed around 5 K using an ELEXSYS E580 spectrometer, equipped with a homebuilt TE_{011} microwave cavity,⁷⁶ a CF935 liquid helium cryostat, an ITC-503 temperature controller and a radiofrequency (RF) amplifier ENI 5100L. W-band (≈ 94 GHz) EPR experiments were performed at 4.8 K using a Bruker ELEXSYS E680 EPR spectrometer. All W-band experiments were carried out using a homebuilt ENDOR microwave cavity, which contained a solenoid of Teflon coated silver wire integrated into a commercial ENDOR probe head (Bruker). In order to ensure broadband microwave excitation and minimize distortions, the loaded quality factor Q_L was lowered to 700 to obtain a microwave frequency bandwidth of 130 MHz.

Electron spin echo-detected (ESE) field-swept EPR spectra were measured using the pulse sequence $t_p-\tau-2t_p-\tau$ -echo,⁷⁷ three-pulse ESEEM spectra by use of $t_p-\tau-t_p-T-t_p-\tau$ -echo⁷⁸ and hyperfine sublevel correlation (HYSCORE) spectra by employing $t_p-\tau-t_p-T_1-2t_p-T_2-t_p-\tau$ -echo.⁷⁹ The lengths of the $\pi/2$ microwave pulses were generally set to $t_p = 16$ ns (X-band), 12 ns (Q-band) and 24 ns (W-band), respectively. For ESE-detected EPR experiments, inter-pulse distances were $\tau = 260$ ns (Q-band) and 300 ns (W-band). For the three-pulse ESEEM measurements, multiple τ values in the ranges $\tau = 136$ –248 ns (X-band) and 200–356 ns (Q-band) and an optimum $\tau = 260$ ns for the HYSCORE experiments were chosen to account for blind-spotting artefacts. Q-band ^{55}Mn -ENDOR spectra were acquired employing the Davies-type pulse sequence $t_{\text{inv}}-t_{\text{RF}}-T-t_p-\tau-2t_p-\tau$ -echo⁸⁰ using a length $t_{\text{inv}} = 24$ ns for the π inversion microwave pulse and a radio frequency π pulse length $t_{\text{RF}} = 3.5$ μs . The length of the $\pi/2$ microwave pulse in the detection sequence was generally set to $t_p = 12$ ns and the inter-pulse delays to $T = 2$ μs and $\tau = 268$ ns. A shot repetition time of 1 ms was used for all measurements. EDNMR measurements were collected using the pulse sequence $t_{\text{HTA}}-T-t_p-\tau-2t_p-\tau$ -echo.⁸¹ The high turning angle (HTA) microwave pulse was applied at microwave frequencies ν_{mw} . The Hahn echo detection pulse sequence $t_p-\tau-2t_p-\tau$ -echo, at a microwave frequency $\nu_{\text{mw}}^{(0)}$ matched to the cavity resonance, was set at a sufficient time T after the HTA pulse to ensure near-complete decay of the electron spin coherencies. The $\pi/2$ pulse length used for detection was $t_p = 200$ ns (^{14}N , ^{17}O) or 80 ns (^{15}N) and an inter-pulse separation of $\tau = 500$ ns was used. The echo was integrated ≈ 600 ns around its maximum. The spectra were acquired *via* continuously sweeping the HTA frequency ν_{mw} at a fixed magnetic field in steps of 78.1 kHz (^{14}N), 128.9 kHz (^{15}N) or 162.1 kHz (^{17}O). A HTA microwave pulse of length $t_{\text{HTA}} = 14$ μs (^{14}N , ^{17}O) and 8 μs (^{15}N) and an amplitude $\omega_1 = 12$ –16 $\times 10^6$ rad s^{-1} was used.



2.3 Spectral simulations

Spectra were fit assuming an effective spin $S_T = 1/2$ ground state (Section S4.2, ESI[†]). The basis set that describes the ^{55}Mn tetramer-single electron spin manifold (eqn (1)) and the ^{14}N , ^{15}N and ^{17}O single nucleus-single electron spin manifolds (eqn (2)) can be built from the product of the eigenstates of the interacting spins:

$$|\frac{1}{2}MI_1m_1I_2m_2I_3m_3I_4m_4\rangle \quad (1)$$

$$|\frac{1}{2}MIm\rangle \quad (2)$$

Here, M refers to the electronic magnetic sublevel, $\pm\frac{1}{2}$; I takes the values $5/2$ for ^{55}Mn , 1 for ^{14}N , $\frac{1}{2}$ for ^{15}N and $5/2$ for ^{17}O ; m_i takes the values $-I_i, 1 - I_i, \dots, I_i - 1, I_i$. The spin manifolds can be described by the following spin Hamiltonian:

$$\hat{H} = \beta_e \vec{B}_0 \cdot \hat{G} \cdot \vec{S} + \sum_i \left(-g_{n,i} \beta_n \vec{B}_0 \cdot \vec{I}_i + \vec{S} \cdot \hat{A}_i \cdot \vec{I}_i + \vec{I}_i \cdot \hat{Q}_i \cdot \vec{I}_i \right) \quad (3)$$

It contains (i) the Zeeman term for the total electronic spin, (ii) the hyperfine and (iii), except for the EPR spectra, nuclear Zeeman terms for either the metal ^{55}Mn nuclei, or the ligand ^{14}N , ^{15}N or ^{17}O nuclei and (iv), for the ^{14}N nuclei ($I = 1$), the nuclear quadrupole interaction (NQI) term; the NQI splitting is not resolved in the ^{55}Mn and ^{17}O spectra. Spectral simulations were performed numerically using MATLAB[®] (R2010a, The MathWorks, Natick, MA, USA), a vector-based linear algebra package, and the EasySpin toolbox.⁸² For further information on data processing, details of the simulations and theory, see Sections S2, S3 and S4 (ESI[†]), respectively.

2.4 DFT calculations

All calculations were performed with ORCA.⁸³ The DFT models of the OEC systems consist of 238 or 239 atoms (with H_2O or NH_3 at the W1 position, respectively) and were constructed as described in Pantazis *et al.*⁴⁰ Alternative ammonia binding modes, including terminal or bridging amido and imido substitution, can be rejected on energetic grounds alone (see Fig. S2, ESI[†]). Geometry optimizations of the cluster models used the BP86 density functional^{84,85} with the zeroth-order regular approximation (ZORA)^{86–88} and specially adapted segmented all-electron relativistically contracted basis sets⁸⁹ (ZORA-TZVP for Mn, O and N; ZORA-SVP for C and H). The conductor-like screening model (COSMO)⁹⁰ was used with a dielectric constant $\epsilon = 8.0$. D3 dispersion corrections⁹¹ were applied in all calculations. Exchange coupling constants, assuming an isotropic Heisenberg Hamiltonian of the form

$$\hat{H} = -2J_{ij} \sum_{i < j} \hat{S}_i \cdot \hat{S}_j, \quad (4)$$

and all EPR properties were computed with the TPSSH hybrid meta-GGA functional^{92,93} from BS-DFT calculations.^{35,94–98} The resolution of identity (RI)⁹⁹ approximation was used in the calculation of Coulomb integrals and the chain-of-spheres approximation (COSX)¹⁰⁰ was used for Hartree–Fock exchange, employing completely decontracted def2-TZVP/J auxiliary basis sets.¹⁰¹ Tight SCF

convergence criteria and increased integration grids (Grid6 and GridX6) were applied throughout.

For the calculation of the hyperfine tensors, triple-zeta ZORA-recontracted basis sets were used on all atoms, while locally dense radial grids were used for Mn, N and O atoms (integration accuracy of 11 for Mn and 9 for N and O as per ORCA nomenclature). Picture change effects were applied for the calculation of EPR parameters and the complete mean-field approach was used for the spin–orbit coupling operator. The results were transformed into on-site or spin-projected values as detailed previously.³⁶ To compare computed ^{55}Mn hyperfine coupling constants using the methods described above with experimental results, a scaling factor of 1.78 was calculated from a set of twelve $\text{Mn}^{\text{III}}\text{Mn}^{\text{IV}}$ mixed-valence dimers.¹⁰²

3 Results and discussion

3.1 DFT models of different OEC forms in the S_2 state

Geometric parameters of optimized DFT cluster models of the S_2 state of the OEC in the $S_T = 1/2$ configuration⁴⁰ are shown in Fig. 2 (for coordinates, see Section S5, ESI[†]). Four variants were considered in this study: (i) the native cofactor system ($\text{Mn}_4\text{O}_5\text{Ca}$, also see Fig. 1), (ii) the Sr^{2+} -substituted system obtained by replacing Ca^{2+} with Sr^{2+} ($\text{Mn}_4\text{O}_5\text{Sr}$), (iii) the NH_3 -modified system obtained by replacing the H_2O in the W1 position with NH_3 ($\text{Mn}_4\text{O}_5\text{Ca-NH}_3$), and (iv) the combined Sr^{2+} -substituted and NH_3 -modified system ($\text{Mn}_4\text{O}_5\text{Sr-NH}_3$). In all models, W2 was considered to be an OH^- ligand, as determined previously.¹² Mulliken spin population analysis of all four variants confirms that the only Mn^{III} ion of the tetramanganese complex is Mn_{D1} . The three Mn^{IV} ions (Mn_{A4} , Mn_{B3} and Mn_{C2}) represent coordinatively saturated, 6-coordinate octahedral sites, whereas the $\text{Mn}_{\text{D1}}^{\text{III}}$ is 5-coordinate square-pyramidal, with a Jahn–Teller elongation along the axis of the $\text{Mn}_{\text{D1}}\text{-Asp342}$ carboxylate ligand, opposite to its open coordination site.

In accordance with previous DFT and QM/MM structures,^{12,37,38,40–42,103–106} the optimized Mn–Mn and Mn–Ca distances of the $\text{Mn}_4\text{O}_5\text{Ca}$ model are consistent with those determined from EXAFS spectroscopy.^{107–110} Only minor changes are observed between the $\text{Mn}_4\text{O}_5\text{Ca}$ and the $\text{Mn}_4\text{O}_5\text{Sr}$ models (Fig. 2). As a result of the larger radius of Sr^{2+} , the O–Sr bond lengths increase by 0.04 Å, while the Mn–Sr distances also increase by 0.04 Å except for $\text{Mn}_{\text{D1}}\text{-Sr}$, which is 0.03 Å shorter than the $\text{Mn}_{\text{D1}}\text{-Ca}$ distance. On average, this is in line with observations from EXAFS spectroscopy¹⁰⁸ and with the recent 2.1 Å resolution crystallographic model of Sr^{2+} -substituted PSII.¹¹¹ The Mn–Mn distances are almost entirely unaffected, with the exception of $\text{Mn}_{\text{D1}}\text{-Mn}_{\text{C2}}$, which is shortened by 0.02 Å in the $\text{Mn}_4\text{O}_5\text{Sr}$ model.

Upon NH_3 substitution of W1 ($\text{Mn}_4\text{O}_5\text{Ca-NH}_3$), only the $\text{Mn}_{\text{D1}}\text{-Mn}_{\text{B3}}$ distance and the Ca^{2+} distance from the terminal Mn ions change notably, albeit by less than 0.05 Å (Fig. 2). Only one structural element is more significantly perturbed, *i.e.* the position of O5, the μ -oxo bridge *trans* to the binding position of NH_3 . The $\text{Mn}_{\text{A4}}\text{-O5}$ distance increases by 0.05 Å with concomitant



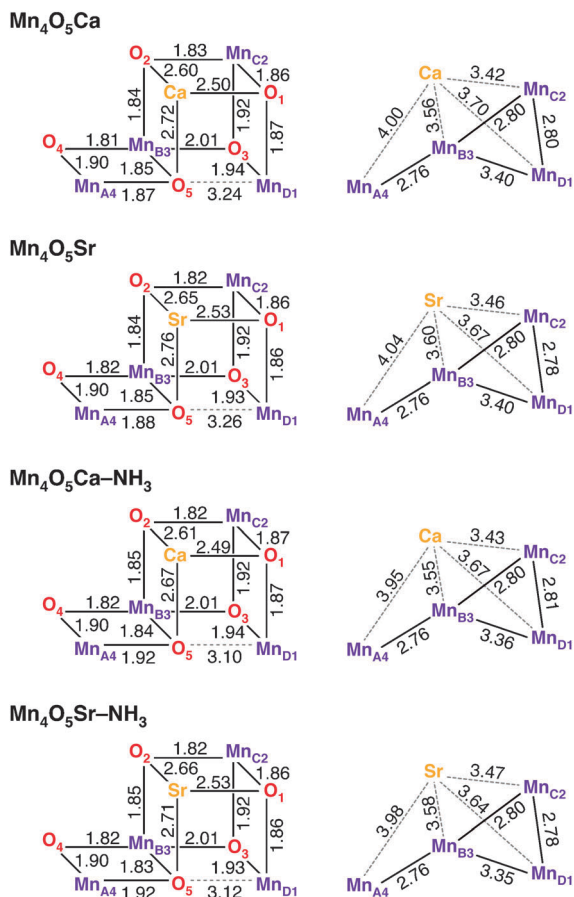


Fig. 2 Bond lengths and metal-metal distances in Å of the four geometry-optimized DFT models.

decrease of the Mn_{D1}-O5 distance by 0.14 Å. Other ligands of Mn_{A4}, such as the second water-derived ligand, W2, remain unaffected. A similar modification to the connectivity of the Mn₄O₅ core was seen for the smaller OEC models reported in our previous study.⁴⁴ We note that EXAFS data for the NH₃-modified OEC have only been reported for samples purified from spinach, not from the cyanobacterial model systems *T. elongatus/vulcanus*, and suggested an elongation of one of the short Mn-Mn distances of 0.02 Å.¹¹³ This type of perturbation is not observed in our optimized Mn₄O₅Ca-NH₃ model. The structural model including both Sr²⁺ and NH₃ (Mn₄O₅Sr-NH₃) is found to replicate both effects seen in the singly modified structures.

3.2 Multifrequency EPR and ⁵⁵Mn-ENDOR of the S₂ states of the OEC variants

Multifrequency EPR/⁵⁵Mn-ENDOR experiments spanning the microwave range from ≈9 to ≈90 GHz were employed to experimentally characterize the electronic structures of the different S₂ state forms described above. Fig. 3A (black solid traces) depicts X-band CW EPR spectra of the S₂ state of native PSII (Mn₄O₅Ca),³³ Sr²⁺-substituted PSII (Mn₄O₅Sr),³³ NH₃-modified (annealed) native PSII (Mn₄O₅Ca-NH₃)⁴⁴ and NH₃-modified Sr²⁺-substituted PSII (Mn₄O₅Sr-NH₃). Shown are light-minus-dark spectra, generated by taking the difference between the

illuminated spectrum (S₂) and the dark-state spectrum (S₁) in order to remove background signals, such as from the cytochromes *b*₅₅₉ and *c*₅₅₀. The modified multiline (Mn₄O₅Sr, Mn₄O₅Ca-NH₃) displays 26 lines of altered intensity as compared to the native multiline signal with 24 lines. The Mn₄O₅Sr-S₂ state yields essentially the same modified multiline signal; the simulation superimposing this data trace uses the parameters that fit the Mn₄O₅Sr dataset.

Fig. 3B shows the corresponding Q-band ESE-detected S₂ state multiline EPR signals of the Mn₄O₅Ca, Mn₄O₅Sr and Mn₄O₅Ca-NH₃ OEC forms. Pseudo-modulated (CW-like) spectra are shown in order to more clearly visualize differences in the hyperfine structures between the three forms. Compared to earlier published data by Cox *et al.*,³³ the spectra are essentially free of contaminating hexaquo-Mn²⁺ signals. Furthermore, there is a small difference of the centre positions of the multiline spectral envelopes, presumably due to inaccuracy in the microwave frequency calibration of this earlier study.

Fig. 3C shows the W-band ESE-detected multiline signals of the Mn₄O₅Ca, Mn₄O₅Sr, Mn₄O₅Ca-NH₃ and Mn₄O₅Ca-NH₃ S₂ state forms. These spectra do contain small hexaquo-Mn²⁺ contaminations. This contamination manifests itself as six inverted hyperfine lines centred at *g* ≈ 2, as the high-spin Mn²⁺ signal (*S* = 5/2) is over-rotated when using optimal instrumental settings to visualize the *S* = 1/2 multiline signal. No ⁵⁵Mn hyperfine structure is observable in the W-band multiline EPR spectra. Thus, these signals provide no additional information on the hyperfine matrices. The utility of these high-frequency data instead is to constrain the *G* tensor. While the spectra of the Mn₄O₅Ca and the Mn₄O₅Ca-NH₃ cluster show similar signals, centred at *g* = 1.975, the Mn₄O₅Sr spectrum is shifted to higher field and centred at *g* = 1.980, similar to the shift observed in W-band spectra from the Bittl laboratory.¹¹⁴ The NH₃-modified Sr²⁺-substituted S₂ state signal is centred at *g* = 1.979. The almost identical high-field shift, illustrated by the superimposed Mn₄O₅Sr simulation, indicates that the *G*-tensor shift is dependent only on the presence of Sr²⁺ but not NH₃. This is in contrast to the result at X-band, which showed that the hyperfine structure is approximately the same for both modifications.

Fig. 3D shows the Q-band Davies ⁵⁵Mn-ENDOR light-minus-dark spectra, measured at the central magnetic field position of the corresponding EPR spectra (Fig. 3B). The line shape of the ⁵⁵Mn-ENDOR signal shows only a small field dependence over the 1190 to 1260 mT range (not shown), consistent with its assignment to the tetranuclear Mn cluster.³¹ In contrast to the X-band CW EPR spectra described above (Fig. 3A), the S₂ states of the native, Sr²⁺-substituted, NH₃-annealed and doubly modified (not shown) OEC give rise to highly similar ⁵⁵Mn-ENDOR spectra. Five peaks are observed for all three sample types appearing at approximately the same frequency positions and of similar intensities. Small differences in the region of the largest peak (≈115 MHz) may represent residual Mn²⁺ contaminations. Importantly, no large difference is seen with regard to the total spectral breadth of the signal (≈55 to ≈195 MHz). For the NH₃-modified S₂ state, the results are nominally consistent with the earlier X-band ENDOR data of Peloquin *et al.*³⁰



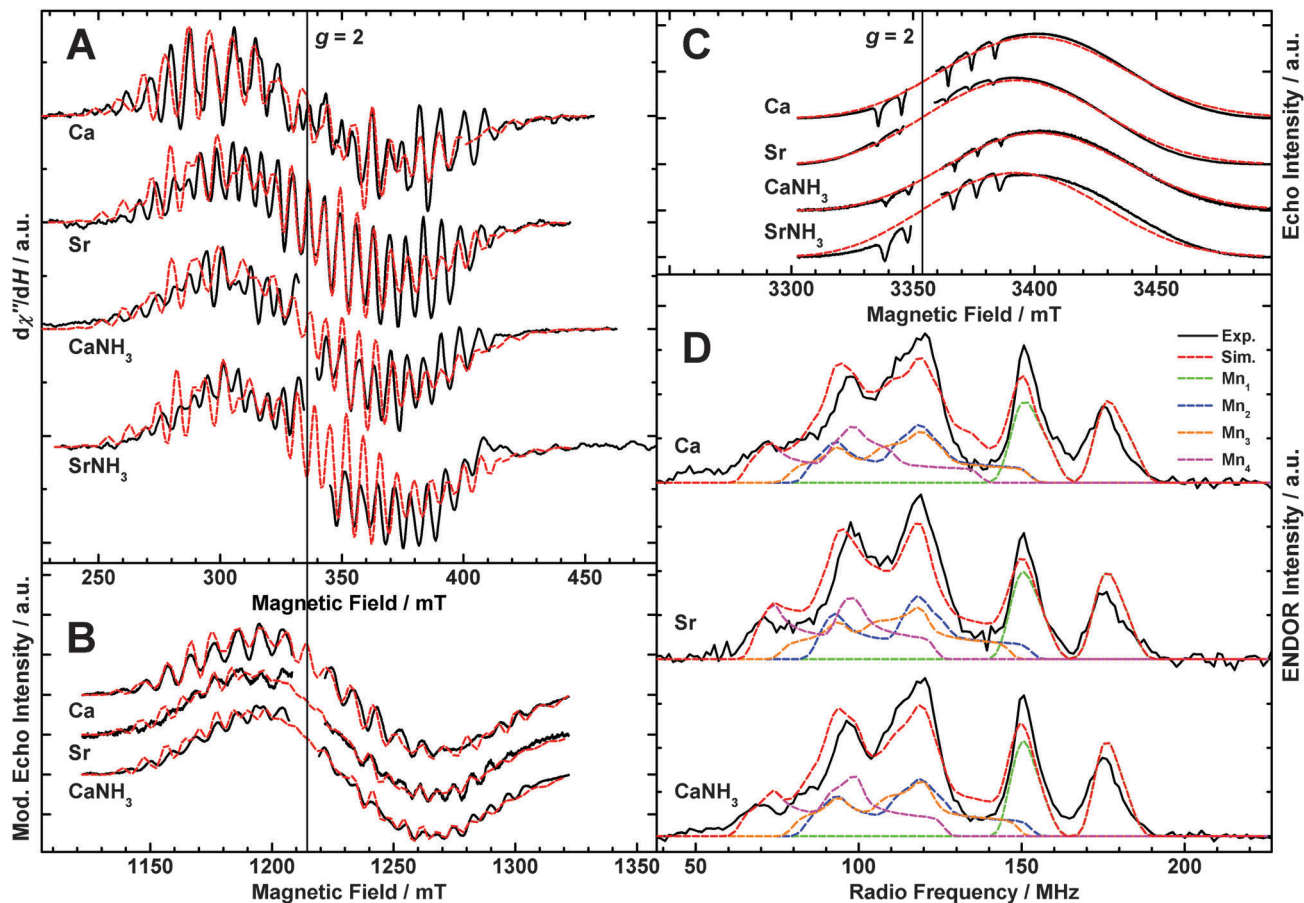


Fig. 3 EPR and ^{55}Mn -ENDOR spectra of the S_2 states of the native (Ca), Sr^{2+} -substituted (Sr), NH_3 -modified (CaNH $_3$) and NH_3 -modified Sr^{2+} -substituted (SrNH $_3$) OEC in PSII isolated from *T. elongatus*. In panels A, B and D, the black solid traces depict the light-minus-dark subtractions of the experimental spectra. If present, the $g \approx 2$ radical signal of Y_D^* (D2-Tyr160) was removed from the EPR spectra for clarity of presentation. Least-squares fittings to the EPR and ^{55}Mn -ENDOR datasets using a model based on the spin Hamiltonian formalism (see Section 2.3 and Sections S3 and S4, ESI †) are represented by superimposing red dashed lines. In panel D, coloured dashed lines represent a decomposition of the simulation showing contributions from the individual ^{55}Mn nuclei. Simulations superimposed on the SrNH $_3$ spectra are those fitted to the Sr dataset. The optimized parameter sets are listed in Table 1. (A) X-band CW EPR. In the Ca and Sr samples, Y_D had been replaced by a phenylalanine, removing the Y_D^* signal from the spectra,¹¹² which were taken from Cox *et al.*⁵³ The CaNH $_3$ spectrum was originally published in ref. 44. Experimental parameters: microwave frequencies: 9.4097 GHz (Ca), 9.4213 GHz (Sr), 9.4075 GHz (CaNH $_3$), 9.4970 GHz (SrNH $_3$); microwave power: 20 mW; modulation amplitude: 25 G; time constant: 82 ms; temperature: 8.6 K. (B) Q-band ESE-detected EPR. The experimental data are presented as pseudo-modulated, derivative-shaped spectra. Experimental parameters: microwave frequencies: 34.0368 GHz (Ca), 34.0430 GHz (Sr), 34.0162 GHz (CaNH $_3$); shot repetition time: 1 ms; microwave pulse length (π): 24 ns; τ : 260 ns; temperature: 5.2 K. (C) W-band ESE-detected EPR. Contaminating Mn^{2+} , present in the samples in varying concentrations, is evident as over-rotated hyperfine features of negative signal intensity. Experimental parameters: microwave frequencies: 93.9894 GHz (Ca), 93.9781 GHz (Sr), 94.0669 GHz (CaNH $_3$), 94.0615 GHz (SrNH $_3$); shot repetition time: 1 ms (Ca, Sr), 5 ms (CaNH $_3$, SrNH $_3$); microwave pulse length (π): 48 ns; τ : 300 ns; temperature: 4.8 K. (D) Q-band Davies ENDOR. Experimental parameters: microwave frequencies: 33.9678 GHz (Ca), 33.9950 GHz (Sr), 34.0053 GHz (CaNH $_3$); magnetic field: 1220 mT; shot repetition time: 1 ms; microwave pulse length (π): 32 ns; τ : 268 ns; RF pulse length (π_{RF}): 3.5 μs ; temperature: 4.8 K.

The Q-band ENDOR spectra presented here do slightly differ from those presented in ref. 33, 34, 44 and 115 with regard to line intensities, discussed in detail in the Section S6 (ESI †).

Spectral simulations of the complete EPR and ^{55}Mn -ENDOR datasets using the spin Hamiltonian formalism are also shown in Fig. 3 (red dashed lines); the fitted effective G and hyperfine tensors A of the Mn clusters in the low-spin S_2 state are listed in Table 1. The effective G tensors of all three spin systems are in the same range as inferred from EPR measurements on PSII single crystals at W-band, *i.e.* $G = [1.997, 1.970, 1.965]$ ¹¹⁶ and $G = [1.988, 1.981, 1.965]$.¹¹⁷ As found previously,^{30,31,33,34,44} the inclusion of four hyperfine tensors of approximately the

same magnitude and near-axial symmetry is required to simultaneously fit the X-, Q- and W-band EPR and Q-band ^{55}Mn -ENDOR line widths and shapes. The z component represents the principal component for the fitted G and all four hyperfine tensors. Comparison of the fitted parameters demonstrates that the three samples basically exhibit the same electronic structure. The sets of the four isotropic values $A_{i,\text{iso}}$ deviate only by $\leq 4\%$ between the three different systems and the signs and magnitudes of the anisotropies $A_{i,\text{aniso}}$ are broadly similar, suggesting that there are no significant differences in the electronic exchange coupling schemes of the $\text{Mn}_4\text{O}_5\text{Ca}/\text{Sr}(\text{NH}_3)$ clusters.



Table 1 Principal values of the effective G and ^{55}Mn hyperfine tensors A_i for the simulations of the S_2 state spectra of the $\text{Mn}_4\text{O}_5\text{Ca}$, $\text{Mn}_4\text{O}_5\text{Sr}$ and $\text{Mn}_4\text{O}_5\text{Ca-NH}_3$ clusters in PSII from *T. elongatus*^a

		G	A_i/MHz			
			A_1	A_2	A_3	A_4
Native	x	1.989	350	214	214	173
	y	1.978	329	195	184	157
	\perp^b	1.983	339	204	199	165
	z^b	1.956	321	282	282	251
	iso ^c	1.974	333	230	227	194
	aniso ^d	0.028	19	-78	-83	-87
Sr^{2+} -substituted	x	1.992	328	213	215	161
	y	1.981	347	201	180	175
	\perp^b	1.986	338	207	197	168
	z^b	1.963	320	283	270	224
	iso ^c	1.978	332	232	221	187
	aniso ^d	0.024	17	-76	-73	-56
NH_3 -modified	x	1.989	326	214	215	154
	y	1.978	345	195	187	175
	\perp^b	1.984	336	204	201	164
	z^b	1.956	322	283	275	229
	iso ^c	1.975	331	231	225	186
	aniso ^d	0.027	13	-79	-74	-65

^a All G and A tensors are collinear. ^b The equatorial and axial G and A_i values are defined as $G_{\perp} = (G_x + G_y)/2$, $G_{\parallel} = G_z$, and $A_{i,\perp} = (A_{i,x} + A_{i,y})/2$, $A_{i,\parallel} = A_{i,z}$. ^c The isotropic G and A_i ($i = 1-4$) values are the averages of the individual values: $G_{\text{iso}} = (G_x + G_y + G_z)/3$ and $A_{i,\text{iso}} = (A_{i,x} + A_{i,y} + A_{i,z})/3$. ^d The anisotropy in the G and A_i values is expressed as the difference $A_{i,\text{aniso}} = A_{i,\perp} - A_{i,\parallel}$.

3.3 Calculated magnetic properties for the native and modified S_2 states of the OEC

The electronic structure of the coupled OEC spin system is defined by the set of six pairwise Mn–Mn exchange interaction terms J_{ij} , which can be calculated using BS-DFT. For all four computational models describing the set of native and chemically perturbed S_2 state clusters, the calculations reveal that the $\alpha\beta\alpha$ spin configuration (Fig. 4A and B) is the lowest in energy. Sets of J_{ij} coupling constants are given in Table S1 of the ESI†. Diagonalization of the Heisenberg Hamiltonian to obtain the complete spin ladder confirms that all four models exhibit an effective total spin $S_T = 1/2$ ground state, as observed experimentally, and an $S_T = 3/2$ first excited state. The estimated energy differences between the two lowest states of the spin ladder are on the order of 24–26 cm^{-1} for the $\text{Mn}_4\text{O}_5\text{Ca/Sr}$ S_2 state structures, lowering by 7 cm^{-1} upon exchange of W1 for NH_3 (Table S1, ESI†). These values are in the range inferred from experiments.‡^{33,34,118,119}

For all four S_2 state OEC forms, the J -coupling topology consists of three main coupling pathways (Table S1, ESI† and Fig. 4B): (i) an antiferromagnetic coupling pathway between Mn_{D1} and Mn_{C2} (J_{CD}); (ii) a ferromagnetic coupling pathway between Mn_{C2} and Mn_{B3} (J_{BC}); (iii) and an antiferromagnetic

‡ Differences in the experimental numbers between the $\text{Mn}_4\text{O}_5\text{Ca-NH}_3$ ($\geq 30 \text{ cm}^{-1}$) and the $\text{Mn}_4\text{O}_5\text{Ca/Sr}$ ($\approx 25 \text{ cm}^{-1}$) S_2 states are likely due to different sample types, *i.e.* higher plant *vs.* cyanobacterial PSII with and without EtOH, respectively.

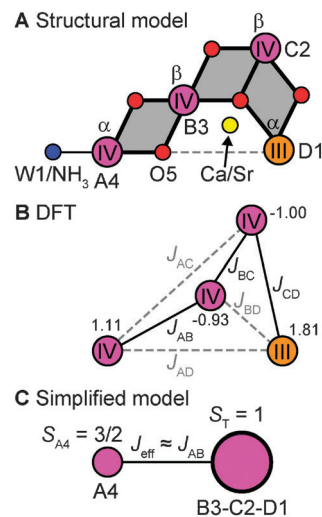


Fig. 4 The magnetism of the low-spin S_2 state. (A) Connectivity of the inorganic centres showing the three μ -oxo-bridged dimanganese units, defining the main electronic exchange pathways of the cluster. (B) Spin coupling scheme showing the main (black solid lines) and weak (grey dashed lines) exchange couplings J_{ij} within the OEC. The numbers next to the Mn ions represent their spin projection factors $\rho_{i,\text{iso}}$ for the native S_2 state BS-DFT model. (C) Simplified spin coupling model in which the trimer unit $\text{Mn}_{\text{B3}}\text{Mn}_{\text{C2}}\text{Mn}_{\text{D1}}$ interacts with the outer Mn_{A4} via an effective coupling J_{eff} that may be approximated as J_{AB} .

coupling pathway between Mn_{B3} and Mn_{A4} (J_{AB}). The ferromagnetic exchange pathway $J_{\text{BC}} = 19\text{--}28 \text{ cm}^{-1}$ is the largest in absolute magnitude, while the antiferromagnetic pathways $J_{\text{CD}} = -16$ to -18 cm^{-1} and $J_{\text{AB}} = -12$ to -16 cm^{-1} are slightly weaker. The remaining exchange coupling constants J_{AC} , J_{AD} and J_{BD} are small, as can be expected from geometric considerations (see Table S1, ESI†). J_{CD} and J_{BC} represent the two largest exchange interactions within the cuboidal trimer unit ($\text{Mn}_{\text{B3}}\text{Mn}_{\text{C2}}\text{Mn}_{\text{D1}}$) of the cluster, whereas J_{AB} can be considered to a good approximation as being representative of an effective exchange interaction between this cuboidal unit and the outer Mn_{A4} , as shown in Fig. 4C.

Systematic differences are observed for the exchange pathways upon the two chemical perturbations, replacement of Ca^{2+} by Sr^{2+} and NH_3 exchange at W1 (Table S1, ESI†). When comparing the structure pairs that differ in terms of the presence of Ca^{2+} or Sr^{2+} , *i.e.* $\text{Mn}_4\text{O}_5\text{Ca}$ *vs.* $\text{Mn}_4\text{O}_5\text{Sr}$ and $\text{Mn}_4\text{O}_5\text{Ca-NH}_3$ *vs.* $\text{Mn}_4\text{O}_5\text{Sr-NH}_3$, it is seen that only the major coupling pathways J_{CD} and J_{BC} are modified, decreasing by 2 cm^{-1} and 5 cm^{-1} , respectively. J_{AB} remains unchanged. By contrast, for the corresponding structure pairs where NH_3 is exchanged for W1, the J_{CD} pathway is unchanged, while J_{BC} and J_{AB} increase by 4 cm^{-1} . It is noted that the perturbation of the O5 position upon NH_3 substitution, as shown in Fig. 2, results also in an enhancement of J_{BD} by 3 cm^{-1} . In both cases, the changes in the magnetic interactions can be understood within the geometric changes discussed in Section 3.1 (see Fig. 2): Sr^{2+} substitution mostly affects the structure of the cuboidal unit, thus perturbing principally the exchange pathways within the Mn-trimer unit, whereas NH_3 binding perturbs mostly the connectivity between the trimeric moiety and the outer Mn_{A4} (Fig. 4C).



Table 2 Isotropic and anisotropic spin projection factors $\rho_{i,\text{iso}}^a$ and $\rho_{i,\text{aniso}}^b$, and calculated and experimental isotropic and anisotropic on-site hyperfine values $a_{i,\text{iso}}^a$ and $a_{i,\text{aniso}}^b$ in MHz for the Mn ions of the BS-DFT models of the $\text{Mn}_4\text{O}_5\text{Ca}$, $\text{Mn}_4\text{O}_5\text{Sr}$ and $\text{Mn}_4\text{O}_5\text{Ca-NH}_3$ clusters in the low-spin S_2 state configuration^c

Mn ion	Structure	Spin projections		BS-DFT		Experiment	
		$\rho_{i,\text{iso}}$	$\rho_{i,\text{aniso}}$	$a_{i,\text{iso}}$	$a_{i,\text{aniso}}$	$a_{i,\text{iso}}$	$a_{i,\text{aniso}}$
Mn_{A4} (Mn^{IV})	$\text{Mn}_4\text{O}_5\text{Ca}$	1.11	0.23	-247	-33	-206	25
	$\text{Mn}_4\text{O}_5\text{Sr}$	1.13	0.19	-247	-32	-204	31
	$\text{Mn}_4\text{O}_5\text{Ca-NH}_3$	0.94	0.36	-242	-30	-245	-9
Mn_{B3} (Mn^{IV})	$\text{Mn}_4\text{O}_5\text{Ca}$	-0.93	0.29	194	-22	207	26
	$\text{Mn}_4\text{O}_5\text{Sr}$	-0.92	0.24	194	-21	202	8
	$\text{Mn}_4\text{O}_5\text{Ca-NH}_3$	-0.86	0.44	193	-19	221	-33
Mn_{C2} (Mn^{IV})	$\text{Mn}_4\text{O}_5\text{Ca}$	-1.00	0.32	212	-17	226	9
	$\text{Mn}_4\text{O}_5\text{Sr}$	-0.99	0.27	212	-18	224	11
	$\text{Mn}_4\text{O}_5\text{Ca-NH}_3$	-1.01	0.46	213	-16	226	-26
Mn_{D1} (Mn^{III})	$\text{Mn}_4\text{O}_5\text{Ca}$	1.81	0.38	-128	-142	-186	-46
	$\text{Mn}_4\text{O}_5\text{Sr}$	1.78	0.32	-138	-144	-188	-41
	$\text{Mn}_4\text{O}_5\text{Ca-NH}_3$	1.92	0.54	-127	-142	-176	-52

^a The isotropic $\rho_{i,\text{iso}}$ and $a_{i,\text{iso}}$ values are the averages of the individual tensor components $\rho_{i,\text{iso}} = (2\rho_{i,\perp} + \rho_{i,\parallel})/3$ and $a_{i,\text{iso}} = (a_{i,x} + a_{i,y} + a_{i,z})/3$.

^b The anisotropies of the ρ_i and a_i tensors are expressed as the differences $\rho_{i,\text{aniso}} = \rho_{i,\perp} - \rho_{i,\parallel}$ and $a_{i,\text{aniso}} = a_{i,\perp} - a_{i,\parallel}$, *i.e.* between the perpendicular and parallel tensor components. ^c The intrinsic fine structure values of Mn^{IV} ions were assumed to be $d_{\text{A4}} = d_{\text{B3}} = d_{\text{C2}} = 0 \text{ cm}^{-1}$. For the $\text{Mn}_{\text{D1}}^{\text{III}}$ ion, a value of $d_{\text{D1}} = -1.43 \text{ cm}^{-1}$ was fitted, with $e_{\text{D1}}/d_{\text{D1}} = 0$.

Calculated ^{55}Mn on-site (intrinsic/not spin-projected) hyperfine tensors as in the full (non-effective) spin Hamiltonian based on the BS-DFT models are listed in Table 2 for the four S_2 state variants. The calculated isotropic hyperfine values $a_{i,\text{iso}}$ for the three Mn^{IV} ions fall within the range seen in Mn^{IV} model compounds experimentally, *i.e.* $|a_{\text{iso}}| = 187\text{--}253 \text{ MHz}$ (see ref. 30 and 33). The anisotropy of the calculated hyperfine tensors for these three sites is also small, of the order seen in octahedral Mn^{IV} model complexes, *i.e.* $|a_{\text{aniso}}| < 30 \text{ MHz}$.³³ For the $\text{Mn}_{\text{D1}}^{\text{III}}$ ion, the calculated isotropic hyperfine value ($\approx 130 \text{ MHz}$) is smaller than that for Mn^{IV} , as expected, and lies just outside the range seen in Mn^{III} compounds, *i.e.* $|a_{\text{iso}}| = 165\text{--}225 \text{ MHz}$.^{30,33} As typical for Mn^{III} , it exhibits a significant hyperfine anisotropy, more pronounced than for the Mn^{IV} ions. However, it is noted that the calculated values for the $\text{Mn}_{\text{D1}}^{\text{III}}$ site are unexpectedly large. Nevertheless, the computed parameters correlate with the inferred site geometry of Mn_{D1} , namely that of a square-pyramidal 5-coordinate Mn^{III} ion. Such a coordination environment generally yields a small isotropic ^{55}Mn on-site hyperfine coupling and a negative anisotropy (see Table 2), consistent with an effective local $^5\text{B}_1$ electronic ground state for the $\text{Mn}_{\text{D1}}^{\text{III}}$ ion.^{30,33,120}

The effective hyperfine couplings measured by EPR spectroscopy for oligonuclear metal complexes reflect the on-site hyperfine couplings of the individual metal ion nuclei scaled by the contribution of the electronic spin of each metal ion to the effective spin state: $A_i = \rho_i a_i$. The set of scaling factors ρ_i , termed spin projection coefficients, are primarily determined by the set of pairwise exchange couplings as detailed in ref. 18,

30, 31, 33, 34, 36, 37 and 63. However, additional terms must be included to correctly estimate such spin projections for the OEC, specifically the relevant on-site fine structure parameters d_i for the individual Mn_i ions,^{18,30,33,34,63} yielding what are more accurately described as spin projection tensors. As the coordination geometries of the three Mn^{IV} ions of the S_2 state are all octahedral, their local electronic structure should be of approximate spherical symmetry, their orbitals of t_{2g} origin (d_{xy} , d_{xz} and d_{yz}) being half-filled (local high-spin d^3 configuration). As such, the Mn^{IV} ions are expected to only display small fine structure parameters d_i ($< 0.3 \text{ cm}^{-1}$)¹²¹ and hence do not need to be explicitly considered. Thus, the set of parameters which define the spin projection tensors in the S_2 state are the six pairwise exchange interaction terms and the fine structure parameter of the Mn^{III} ion, d_{D1} .

Using these spin projection tensors, the fitted projected ^{55}Mn hyperfine tensors were scaled back to on-site hyperfine tensors to allow comparison to the BS-DFT values discussed above (Table 2). The only plausible assignment for all three forms of the OEC is that A_1 , A_2 , A_3 , and A_4 correspond to a_{D1} , a_{A4} , a_{C2} and a_{B3} , respectively. In our previous work,³³ using BS-DFT structural models predating the latest crystal structure,⁹ values of -1.2 to -1.3 cm^{-1} were estimated for a supposedly axially symmetric d_{D1} in the native and Sr^{2+} -substituted S_2 states. Using the same approach, d_{D1} was re-estimated. It was possible to obtain on-site hyperfine anisotropies in the ranges characteristic for Mn^{III} and Mn^{IV} ions employing a single value of -1.43 cm^{-1} for the three OEC systems, well within the range typically seen for Mn^{III} model complexes. As discussed above with regard to the hyperfine tensor anisotropy of $\text{Mn}_{\text{D1}}^{\text{III}}$, a negative d value requires an effective local $^5\text{B}_1$ state for the $\text{Mn}_{\text{D1}}^{\text{III}}$ ion and is thus consistent with the square-pyramidal 5-coordinate ligand geometry of $\text{Mn}_{\text{D1}}^{\text{III}}$, as present in all computational models. The experimental on-site hyperfine tensor values (Table 2) generally agree well with the BS-DFT estimates and Mn^{III} and Mn^{IV} model compounds, with smaller isotropic values $a_{i,\text{iso}}$ for the Mn^{III} ion than for the Mn^{IV} ions. In the native and Sr^{2+} -substituted models, Mn_{A4} displays a smaller $a_{\text{A4,iso}}$ than computed and in the NH_3 -modified system, where it exhibits the largest coupling of the Mn^{IV} ions. Compared to the calculations, the anisotropic components for the Mn^{IV} ions show a larger variance within $|a_{i,\text{aniso}}| \lesssim 30 \text{ MHz}$. For $\text{Mn}_{\text{D1}}^{\text{III}}$, $a_{\text{D1,aniso}} < -40 \text{ MHz}$ is less negative than calculated. Overall, the experimental results confirm that the computed spin coupling schemes serve as a valid description of the native and modified S_2 states.

3.4 The Mn_{D1} -His332-imino-N interaction

Three-pulse ESEEM measurements were performed to characterize the imino-N signal of His332 associated with the OEC variants in the S_2 state. Fig. S4 and S5 (ESI[†]), respectively, depict τ - and magnetic-field-dependent ($g \approx 2.10\text{--}1.90$) light-minus-dark- subtracted spectra and simulations of the native $\text{Mn}_4\text{O}_5\text{Ca}$ (A, B), Sr^{2+} -substituted $\text{Mn}_4\text{O}_5\text{Sr}$ (C, D) and NH_3 -modified $\text{Mn}_4\text{O}_5\text{Ca-NH}_3$ (E, F) S_2 state samples. As noted in Pérez Navarro *et al.*,⁴⁴ the ^{14}N nitrogen signal observed for the native S_2 state



from *T. elongatus* is very similar to that measured in PSII from both higher plants (spinach)¹²² and the mesophilic cyanobacteria *Synechocystis* sp. PCC 6803,¹²³ assigned to the imino-N of His332 *via* mutagenesis.^{123,124} The signals are essentially the same in the native, Sr²⁺-substituted and NH₃-modified OEC clusters with regard to both their τ and magnetic-field dependence. The His332 imino-¹⁴N signal at Q-band nearly fulfils the cancellation condition, where A_{iso} is twice the ¹⁴N nuclear Larmor frequency ($\nu_n = 3.75$ MHz at 1.22 T). The spectra are characterized by three features: the lines centred at frequencies below 2.5 MHz ($\nu_\alpha = \nu_n - |A_{\text{iso}}|/2$), single-quantum transitions around 7.5 MHz ($\nu_\beta = \nu_n + |A_{\text{iso}}|/2$) and smaller double-quantum resonances around 15 MHz ($\nu_{2\beta} = 2\nu_n + |A_{\text{iso}}|$). The line structuring is defined both by the ¹⁴N hyperfine anisotropy and the NQL.

HYSCORE spectroscopy (a two-dimensional ESEEM technique) was performed on the three S₂ state OECs at different magnetic-field positions ($g \approx 2.07$ – 1.93) of the corresponding Q-band EPR envelopes to further constrain the ¹⁴N hyperfine and quadrupolar interaction matrices. Panels A, C and E in Fig. 5 show the Fourier-transformed spectra and simulations at the centre field position; low- and high-field spectra and simulations are presented in Fig. S6 and S7 in the ESI.† As seen for the three-pulse ESEEM spectra, their appearance is highly similar for all three variants of the OEC in the S₂ state. In two dimensions, the three features that comprise the Q-band ESEEM spectra appear as cross peaks at corresponding frequencies both in the (–,+) and the (+,+) quadrants. As the ¹⁴N hyperfine coupling matches the cancellation condition, the cross peaks are shifted away from the diagonal, instead appearing near the

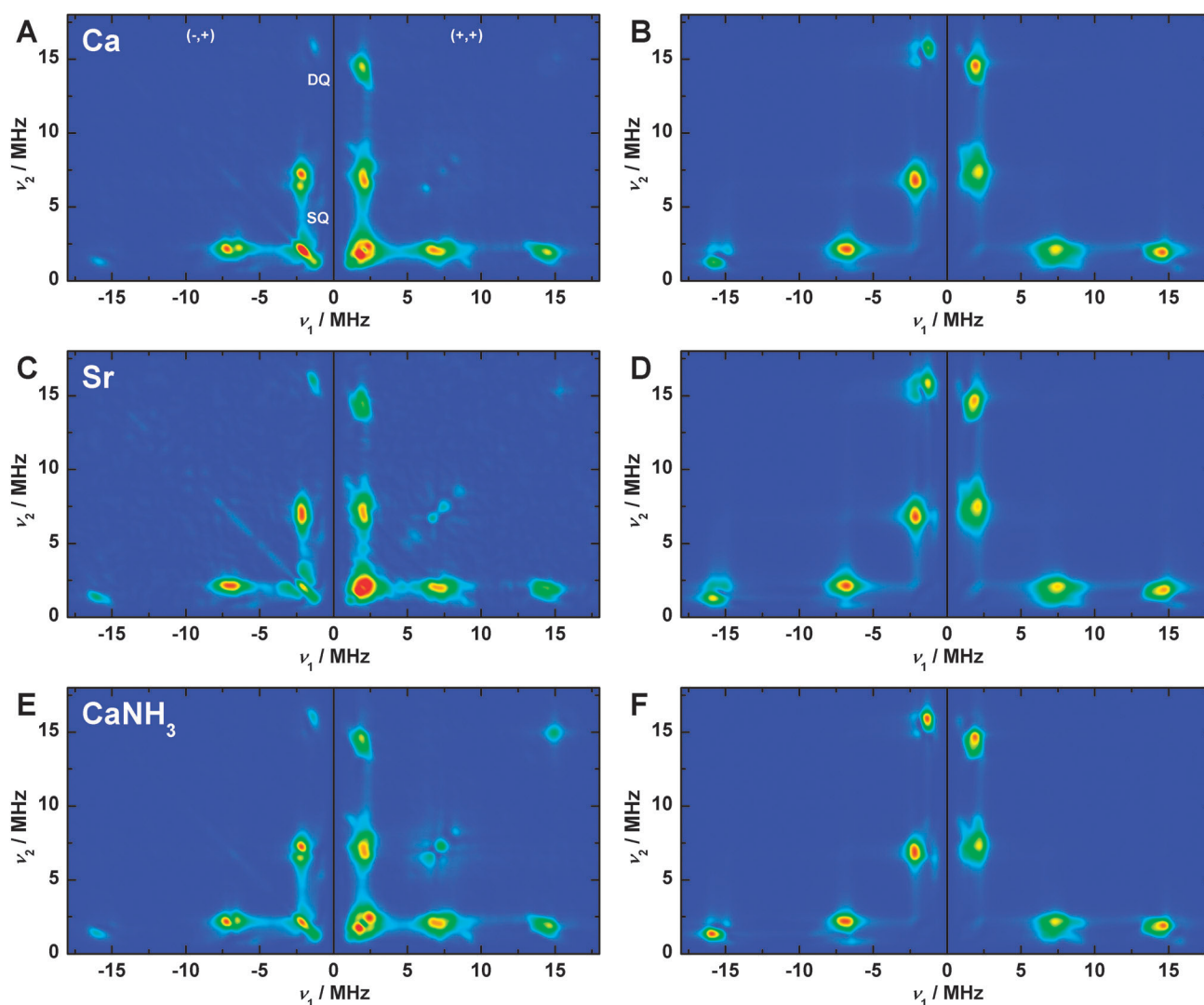


Fig. 5 (–,+) and (+,+) quadrants of the Fourier-transformed Q-band HYSCORE experimental spectra (A, C, E) and spin Hamiltonian-based simulations (B, D, F) of the S₂ state Mn₄O₅Ca (A, B), S₂ state Mn₄O₅Sr (C, D) and annealed S₂ state Mn₄O₅Ca–NH₃ (E, F) clusters in PSII samples isolated from *T. elongatus* at central magnetic field. SQ and DQ point out the regions of single- and double-quantum transitions, respectively. The optimized parameter sets for the simulations, as described in Section 2.3 and Sections S3, S4 and S8.4 (ESI†), are listed in Table 3 and, in detail, in Table S2 (ESI†). Experimental parameters: microwave frequencies: 34.0370 GHz (Ca), 34.0433 GHz (Sr), 34.0151 GHz (NH); magnetic fields: 1220 mT (Ca), 1222 mT (NH, Sr); shot repetition time: 1 ms; microwave pulse length ($\pi/2$): 12 ns; τ : 260 ns; ΔT : 100 ns; temperature: 5.2 K.



frequency axes. Overall, virtually no orientation dependence is seen comparing the spectra at the three different magnetic fields (Section S8.2, ESI[†]), consistent with the electron–nuclear interaction being dominated by the isotropic component of the hyperfine coupling as compared to the anisotropic part and the traceless NQI, as in ref. 122, 123 and 125. Thus, the orientation of the His332 imino-¹⁴N hyperfine tensor relative to the *G* tensor cannot be determined from this dataset.

Fitted spin Hamiltonian parameters derived from the simultaneous simulation of both the ESEEM and HYSOCORE datasets are given in Table 3 together with BS-DFT estimates. To directly compare DFT values with experiment, the calculated site hyperfine tensor for the His332 was multiplied by the axial Mn_{D1} spin projection tensor described in Section 3.3. All DFT models yield virtually the same hyperfine and quadrupole values. The calculated *A*_{iso} underestimates experimental results by <20%, but the dipolar component *A*_{dip} and the rhombicity *A*_η nominally agree with experiment. It is noted that the on-site ¹⁴N hyperfine tensor *a* is expected to be axial with its unique component *a*₁ aligned along the Mn_{D1}–N bond, as seen in our calculations (Table S2, ESI[†]). As such, the axial ¹⁴N hyperfine component *a*₁ is essentially rotated 90° relative to that of the Mn_{D1} spin projection tensor, which is expected to coincide with the Jahn–Teller axis of Mn_{D1}^{III}. This 90° rotation explains why the ¹⁴N hyperfine tensor *A* is rhombic in the projected (experimental) reference frame. For a more detailed description of the simulations, see Section S8.4 (ESI[†]). Importantly, the near-invariance of the imino-N spin Hamiltonian parameters for the three S₂ state forms requires the His332 ligation, the electronic structure of the Mn_{D1}^{III} ion and by extension the whole tetranuclear Mn cluster, to not be significantly perturbed by Ca²⁺/Sr²⁺ and NH₃/W1 exchange, in line with the EPR/⁵⁵Mn ENDOR results described in Section 3.2.

While the orientation of the hyperfine tensor relative to the *G* tensor cannot be determined using ESEEM/HYSOCORE at Q-band frequencies, it can be measured at W-band, *e.g.* using

EDNMR. In our earlier study,¹⁴ it was found that the hyperfine tensor is orientated such that its principal, *i.e.* the smallest component *A*₁ is aligned such that it is mid-way between *G*_x and *G*_z. Importantly though, it is noted that the set of spin Hamiltonian parameters deduced from Q-band ESEEM/HYSOCORE (Table 3) does not reproduce the W-band data sets (Section S8.3, ESI[†]). This is not due to the inclusion/exclusion of the NQI term, which, for the W-band EDNMR data, mainly contributes to the spectral line width. To reproduce the field dependence of the ¹⁴N- and ¹⁵N-EDNMR signals (Fig. S8 and S9, ESI[†]), the values determined from Q-band ESEEM/HYSOCORE needed to be scaled: *A*_{iso} was decreased by 10%, whereas *A*_{dip} was increased by a factor of two (Table S2, ESI[†]). The same results were observed for all three S₂ state forms, which basically exhibit the same ¹⁴N-EDNMR spectra. A possible reason for this difference comes from the observation that the ground spin state, an effective spin *S*_T = 1/2 state, is not very well separated energetically from higher spin states in the regime of the W-band excitation energy (≈3 cm⁻¹), consistent with DFT estimates for the ground-to-first excited state energy splitting Δ*E* (Section S7, ESI[†]). Excited-state mixing due to a small Δ*E* has the consequence of altering spin Hamiltonian observables such as effective ⁵⁵Mn and ¹⁴N hyperfine tensors. Alternatively, the rhombicity of the effective *G* tensor as inferred from the EPR/⁵⁵Mn-ENDOR simulations may be artificial, a consequence of using collinear *G* and ⁵⁵Mn hyperfine tensors. This latter suggestion would also explain why the *G* tensors inferred from W-band measurements on PSII single crystals^{116,117} differ from those inferred from our multifrequency measurements on frozen solution PSII samples.

The lack of agreement between the two ¹⁴N datasets brings into question whether the W-band ¹⁴N/¹⁵N-EDNMR signals can be used to assign the exchangeable μ-oxo bridge ¹⁷O signal based on the relative orientations of the ¹⁴N and ¹⁷O hyperfine tensors, as suggested by Rapatskiy *et al.*¹⁴ Thus, further experimental results, particularly from single crystals of PSII, are needed to test this proposal (see Section 3.6).

Table 3 Fitted and calculated effective/projected ¹⁴N hyperfine and NQI tensors in MHz for the electron–nuclear couplings of the His332 imino-N and of NH₃ with the various cluster forms studied in the S₂ state in PSII from *T. elongatus*

S ₂ state	¹⁴ N	Method	<i>A</i> _{iso} ^a	<i>A</i> _{dip} ^b	<i>A</i> _η ^c	<i>e</i> ² <i>Qq/h</i>	η ^c
Native	His332 ^d	Exp.	7.1	0.75	0.81	1.97	0.75
		DFT	5.8	0.59	0.74	1.65	0.91
Sr ²⁺ -substituted	His332 ^d	Exp.	7.3	0.69	0.83	1.98	0.79
		DFT	5.8	0.57	0.61	1.65	0.91
NH ₃ -modified	His332 ^d	Exp.	7.2	0.75	0.89	1.96	0.80
		DFT	6.1	0.71	0.99	1.68	0.88
	NH ₃	Exp.	2.36	0.33	0.22	1.52	0.47
		DFT	2.68	−0.65	0.02	0.94	0.87
NH ₃ -modified, Sr ²⁺ -substituted	NH ₃	Exp.	2.37	0.28	0.23	1.58	0.45
		DFT	2.68	−0.59	0.03	0.93	0.87

^a *A*_{iso} is defined as the average of the principal components of the hyperfine tensor: *A*_{iso} = (*A*₁ + *A*₂ + *A*₃)/3. ^b *A*_{dip} is defined in terms of *T*₁, *T*₂, and *T*₃ as *A*_{dip} = (*T*₁ + *T*₂)/2 = −*T*₃/2. ^c The rhombicity is defined by *A*_η or η = (*T*₁ − *T*₂)/*T*₃, respectively. *T*₁, *T*₂, and *T*₃ represent the three principal components of the hyperfine tensors minus *A*_{iso} and of the NQI tensors and are labelled such that |*T*₁| ≤ |*T*₂| ≤ |*T*₃|. ^d The Euler rotation angles [α, β, γ] of the NQI relative to the *A* tensors are [20, 12, 0]°, [18, 9, 0]° and [16, 16, 0]° for the Mn₄O₅Ca, Mn₄O₅Sr and Mn₄O₅Ca–NH₃ clusters, respectively.



3.5 NH₃ binding to the Ca²⁺- and the Sr²⁺-containing OEC

In the NH₃-modified S₂ state, a second nitrogen nucleus is bound to the Mn cluster as a terminal ligand, as described in Pérez Navarro *et al.*⁴⁴ Its binding can be observed using X-band (three-pulse) ESEEM, as shown in Fig. S11 (ESI[†]) for ¹⁴NH₃/¹⁵NH₃-bound, Ca²⁺- and Sr²⁺-containing PSII. The ¹⁴NH₃ resonances comprise three characteristic single-quantum lines at 0.5, 0.95 and 1.45 MHz split by the NQI and smaller double-quantum transitions centred at 4.9 MHz, highly similar to the higher plant data.⁷⁰ Due to the lack of the NQI, the ¹⁵NH₃ signal is clearly less complicated, consisting only of one single-quantum hyperfine peak centred at 0.3 MHz. As seen for the His332 imino-¹⁴N signal at Q-band, the NH₃ interaction at X-band fulfils the cancellation condition, leading to a narrow ν_α line while the ν_β line is broadened beyond detection.⁷⁰ Most importantly, the spectra of the ¹⁴NH₃-modified Ca²⁺- and Sr²⁺-containing ¹⁴N-PSII samples are essentially identical. Thus, NH₃ binding to the Sr²⁺-substituted S₂ state cluster is the same as in the native S₂ state.

In our first report on NH₃ binding to the OEC, only the ¹⁴NH₃ interaction was considered.⁴⁴ Here, we simultaneously fit the spectra of both the ¹⁴NH₃-modified ¹⁵N-PSII and the ¹⁵NH₃-modified ¹⁴N-PSII in the S₂ state (Table 3, Fig. S11 and Table S3, ESI[†]). This resulted in an optimized hyperfine tensor $A = [2.76 \ 2.62 \ 1.69]$ MHz for ¹⁴NH₃ (and for ¹⁵N scaled by the ratio of the nuclear g values of ¹⁵N and ¹⁴N) and ¹⁴N NQI parameters $e^2Qq/h = 1.52$ MHz and $\eta = 0.47$. Highly similar hyperfine and NQI values reproduce the NH₃ signal observed in the annealed S₂ state of Sr²⁺-containing ¹⁴N-PSII. The isotropic ¹⁴N hyperfine coupling $A_{\text{iso}} = 2.36$ MHz and $A_{\text{dip}} = 0.33$ MHz, e^2Qq/h and the asymmetry parameter η are the same as reported before for PSII from *T. elongatus*⁴⁴ and similar to the values from the analysis of higher plant X-band ESEEM spectra⁷⁰ (Table 3).

An axial projected ¹⁴NH₃ hyperfine tensor is obtained from BS-DFT calculations, as seen in the experiment. This is because (i) the on-site ¹⁴NH₃ hyperfine tensor is axial, and (ii) its axial and equatorial components are essentially coincident with those of the Mn_{A4} spin projection tensor (Table S3, ESI[†]), unlike the case for the His332 imino-¹⁴N a tensor (see Section 3.4). The BS-DFT calculations also reproduce the comparably large and rhombic NQI parameters (Table 3), although the sign of the hyperfine anisotropy is inverted compared to experiment. For more details, see Section S9 in the ESI[†].

3.6 Interactions with exchangeable ¹⁷O species

As we have recently shown,^{14,19} EDNMR spectroscopy at W-band, due to its comparatively high sensitivity, is the preferred method to measure the interactions of exchangeable ¹⁷O nuclei with fast-relaxing electronic species such as the S₂ state of the OEC. Fig. 6 shows these spectra and simulations (see Section 2.3 and Sections S3 and S4, ESI[†] for details) of the single-quantum region for the native, the Sr²⁺-substituted, the NH₃-annealed and the Sr²⁺- and NH₃-modified S₂ state variants after H₂¹⁷O buffer exchange in the S₁ state (see Fig. S12 (ESI[†]) for the double-quantum region). The spectrum of the native system exhibits the single- and double-quantum resonances of the

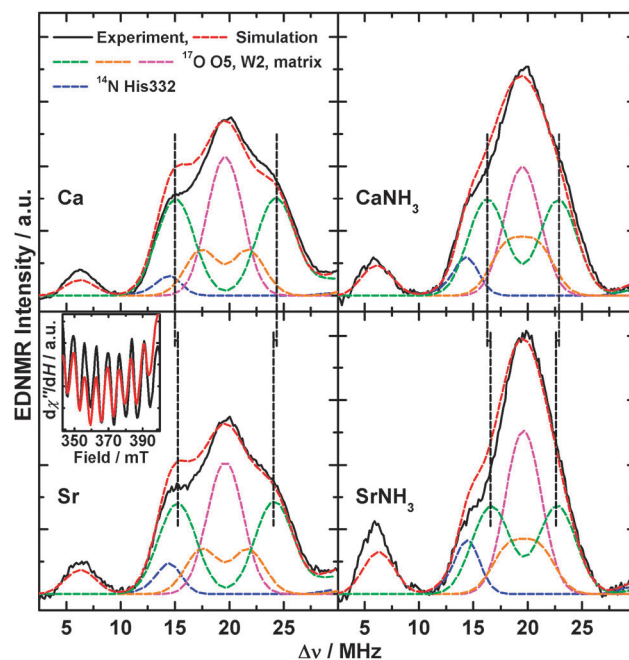


Fig. 6 ¹⁷O-EDNMR spectra of the native (Ca) the Sr²⁺-substituted (Sr), the NH₃-annealed (CaNH₃) and the Sr²⁺-substituted NH₃-annealed (SrNH₃) S₂ states in PSII samples isolated from *T. elongatus*. Black solid traces depict the single-quantum region of background-corrected experimental spectra; superimposing red dashed traces represent simulations based on the spin Hamiltonian formalism as outlined in Section 2.3 and Sections S3 and S4 (ESI[†]). Coloured dashed lines represent a decomposition of the simulation showing contributions from the individual ¹⁴N and ¹⁷O nuclei. Black dashed lines highlight the decrease of the strong ¹⁷O interaction upon Ca²⁺/Sr²⁺ exchange. The optimized parameter sets are listed in Table S4 (ESI[†]). Double-quantum regions are shown in Fig. S12 (ESI[†]). Inset: a section of the X-band CW EPR spectra of the Sr²⁺-substituted S₂ state in PSII samples in the absence (black) and presence (red) of H₂¹⁷O showing no line broadening upon ¹⁷O exchange. Experimental parameters: see Fig. S12 and for the inset Fig. S14 (ESI[†]).

imino-¹⁴N of His332 (blue) and of three different classes of ¹⁷O species,¹⁴ *i.e.* (i) a strongly coupled, bridging species (green), (ii) an intermediately coupled terminal O-ligand (orange), and (iii) a weakly coupled terminal class (cyan). These were assigned to the μ -oxo bridge O5, the hydroxide ion W2¹² and the H₂O matrix (comprising ligand W1 of Mn_{A4} and two H₂O ligands at the Ca²⁺ ion), respectively. NH₃ binding causes a narrowing of the ¹⁷O single- and double-quantum envelopes, reproduced by a decrease of the hyperfine couplings of O5 and W2 and concomitant reduction of the matrix line intensity, which was interpreted by NH₃ binding to Mn_{A4} in exchange for W1.⁴⁴ Comparing these two spectral forms to those of the corresponding Sr²⁺-substituted W1- and NH₃-containing clusters (Fig. S13, ESI[†]), we see a systematic narrowing of the single-quantum envelope by ≈ 0.5 MHz and a corresponding narrowing of the double-quantum envelope. This can be reproduced by spectral simulations in which the hyperfine couplings of the μ -oxo bridge are reduced accordingly (W1: 9.2 MHz *vs.* 9.7 MHz, NH₃: 6.5 *vs.* 7.0 MHz), while the other ¹⁷O interactions remain unaltered (for a complete set of hyperfine parameters, see Table S4, ESI[†]). Although weaker than the NH₃ effect, the



narrowing was found to be reproducible in all Sr²⁺-substituted PSII samples. It clearly shows that Ca²⁺/Sr²⁺ exchange perturbs the μ -oxo bridge, in addition to a simultaneous modification by NH₃ binding.

The inset in Fig. 6 depicts a section of the X-Band CW EPR spectra of the Sr²⁺-substituted S₂ state, which exhibits an intrinsically smaller average line width (≈ 3.6 mT peak-to-peak) than the native form (≈ 4 mT), in the presence and absence of ¹⁷O (see Fig. S14 (ESI[†]) for the entire spectra). No EPR line broadening is observed upon ¹⁷O exchange. This demonstrates that the largest ¹⁷O coupling represents only one exchangeable oxo bridge. In the case of two hyperfine interactions of ≈ 10 MHz, the effective line broadening due to the combined ¹⁷O couplings would be larger than 120 MHz or 4.3 mT, exceeding the actual line width.

4 Discussion

4.1 A common electronic structure of the S₂ state variants

Our DFT results show that the Sr²⁺-substituted, the NH₃-annealed and the Sr²⁺- and NH₃-modified low-spin S₂ states basically represent the same structure on both a geometric and electronic level. This result is not immediately obvious from their X-band EPR signals. Indeed historically, the Sr²⁺-substituted and NH₃-modified forms were explained in terms of a change of the valence state distribution within the Mn tetramer and thus of the coordination environment of the Mn^{III} ion.¹²⁶ The comprehensive approach pursued in this study conclusively rules out such a mechanism for electronic structure perturbation. Instead, as proposed by our group,^{33,34,63} multiline heterogeneity reflects rather subtle changes of the Mn-tetramer structure. The similarity of the perturbed multiline forms suggest a common mechanism for electronic perturbation, which probably also explains S₁ state heterogeneity. This is discussed below, with reference to solvent access, substrate binding and exchange.

4.1.1 The mechanism of structural perturbation. In Su *et al.*,³⁴ a qualitative model for multiline heterogeneity was proposed. In this model, the electronic structure of the S₂ state was considered in terms of a simplified model of two spin fragments: (i) a cuboidal trimer unit, made up of Mn_{D1}, Mn_{C2} and Mn_{B3}, and (ii) a 'monomeric' Mn unit, consisting of the outer Mn_{A4}. Therein, variation of the electronic structure in S₂ was attributed to changes in the connectivity of the outer Mn_{A4} to the cuboid, changing the properties of the electronic ground state by altering the mixing-in of excited spin state character. The physical rationale for this observation was that the outer Mn_{A4} represents the solvent accessible end of the cluster. It has two water-derived ligands and solvent channels that begin or terminate at this site.^{9,127} As such, it is this site and its connection to the rest of the cluster that is most likely to vary amongst different sample conditions and possibly different PSII species. In terms of this 'monomer-trimer' model with regard to the two modifications discussed here, Ca²⁺/Sr²⁺ forms part of the linkage between the cuboidal and outer fragments, as mediated by the μ -oxo bridge O5, whereas NH₃ binds to the

outer Mn_{A4}, also perturbing O5, the bridge *trans* to its binding position W1.⁴⁴

The magnetic observable that is altered upon Ca²⁺/Sr²⁺ replacement and/or W1/NH₃ exchange, leading to the perturbed multiline forms is the ⁵⁵Mn hyperfine anisotropy. Small perturbations of the four hyperfine tensors result in a change in the hyperfine peak superposition, altering the apparent structure of the X-band EPR signal (Fig. 3A). Importantly these changes are subtle, as demonstrated by the invariance of the ⁵⁵Mn-ENDOR spectra (Fig. 3D). The ⁵⁵Mn hyperfine anisotropy is not a site property, but instead an indirect measure of the fine structure splitting of the Mn^{III} ion^{30,33,34,63} or, in the 'monomer-trimer' model, the zero-field splitting of the whole trimer unit. Within this model, its contribution is modulated by the electronic connectivity between the two fragments, predominantly the exchange pathway *J*_{AB}, the coupling that mostly defines the energy splitting ΔE between the ground state and the first excited state (Fig. 4C). Our BS-DFT results support this basic mechanism for electronic structure perturbation and, for the first time, describe the changes on the molecular level that impart this variation, and which differ for the two modifications. Upon replacement of Ca²⁺ by Sr²⁺, the slight distortion of the cuboidal moiety leads to a perturbation of the intra-cuboidal exchange network and possibly the Mn_{D1}^{III} site fine structure splitting. It is noted that this, besides changing the ⁵⁵Mn hyperfine anisotropy, also manifests itself in terms of the *G* tensor, also contributing to the altered multiline appearance and the *g* shift of the W-band EPR signal. Exchange of W1 by NH₃ affects the connectivity of the outer Mn_{A4} to the cuboidal unit, as modulated by the μ -oxo bridge O5, perturbing the *J*_{AB} exchange pathway, thus changing the ⁵⁵Mn hyperfine anisotropy. In the case of the S₂ state variant that contains both these modifications, their effects on the electronic structure are additive. It is noted that it is the properties of the cuboidal unit that define the *G* tensor as opposed to the outer Mn_{A4}, which presumably has an isotropic on-site *g* value. This is expected, as it is the Mn_{D1}^{III} ion, which is part of the trimer fragment in the *S* = 1/2 configuration, that should form the dominant contribution to the anisotropy of the *G* tensor in all four systems.

4.1.2 The Mn_{D1}-His332-imino-N and Mn_{A4}-NH₃ interactions as local probes for the electronic structure

4.1.2a The Mn_{D1}-His332-imino-N interaction. As described by Stich *et al.*,¹²³ the magnitude of the Mn_{D1}-His332 imino-N hyperfine interaction, as compared against mixed-valence Mn^{III}Mn^{IV} model compounds and protein cofactors with imidazole ligands to Mn^{III} (*A*_{iso} ≤ 13 MHz) and Mn^{IV} ions (*A*_{iso} = 1.5–3.3 MHz),^{128–134} favours assigning Mn_{D1} as the only Mn^{III} ion of the S₂ state, consistent with the EPR/⁵⁵Mn-ENDOR/DFT results already reported in the literature and detailed above (Sections 3.1–3.3). The large hyperfine couplings seen for ligands coordinating to Mn^{III} in S₂ (and model systems) comes from the fact that the Mn^{III} ion carries the largest spin projection coefficient, *i.e.* in Mn dimers $\rho_{\text{iso}}(\text{Mn}^{\text{III}}) = 2$ and $\rho_{\text{iso}}(\text{Mn}^{\text{IV}}) = -1$. Interestingly, the hyperfine and quadrupole couplings of imidazole ligands of Mn^{III} ions differ depending on whether they represent axial (*A*_{iso} = 9–13 MHz, $e^2Qq/h = 2.1\text{--}3.0$ MHz)^{128–132} or equatorial ligands (*A*_{iso} = 1.5–6.6 MHz, $e^2Qq/h = 1.5\text{--}2.5$ MHz).^{131–134} The values seen for the His332



imino-N ($A_{\text{iso}} = 7.1$ MHz, $e^2Qq/h = 1.97$ MHz) fall closer to the equatorial range supporting its assignment as an equatorial ligand consistent with DFT structural models. In such models,^{12,37,40,103,106} the local Jahn–Teller axis of the $\text{Mn}_{\text{D1}}^{\text{III}}$ ion is aligned along the open coordination site, thus considered a pseudo-Jahn–Teller axis, perpendicular to the $\text{Mn}_{\text{D1}}\text{--N}$ bond. It is supposed that the reason why the ^{14}N couplings measured for the His332 do not exactly fall within the range seen in model complexes is that all model complexes measured thus far represent 6-coordinate Mn^{III} ions whereas the $\text{Mn}_{\text{D1}}^{\text{III}}$ ion in the S_2 state is 5-coordinate.

4.1.2b The $\text{Mn}_{\text{A4}}\text{--NH}_3$ interaction. As recently shown in Pérez Navarro *et al.*,⁴⁴ the binding site of NH_3 is likely the W1 site. The small effective isotropic ^{14}N hyperfine coupling ($A_{\text{iso}} = 2.36$ MHz) and the axially of the hyperfine tensor are both consistent with a terminal ligand to a Mn^{IV} (d^3) ion.^{44,70} The similar A_{iso} in the $\text{Mn}_4\text{O}_5\text{Sr--NH}_3$ cluster confirms that the oxidation state of the Mn_{A4} ion is not altered by Sr^{2+} substitution. Moreover, the binding mode and perturbation mechanism of NH_3 is the same in the Ca^{2+} - and Sr^{2+} -containing Mn clusters. The non-axiality of the electric field gradient ($\eta = 0.47$) is characteristic for this ligand. A large asymmetry parameter is uncommon for a terminal ligand of Mn^{IV} (although our value is already $\approx 20\%$ smaller than that reported earlier⁷⁰). The latest crystal structure⁹ suggests that such an asymmetric distortion could be present for the W1 site due to the charged residue D1-Asp61, in H-bonding distance to W1/ NH_3 , as seen for other protein systems.¹³⁵ Indeed, upon inclusion of the Asp61 residue, which was not included in our previous, smaller BS-DFT model,⁴⁴ the asymmetric quadrupole tensor is now reproduced, and the hyperfine coupling constant shows better agreement with experiment (Fig. 7 and Table 3). In contrast, such an asymmetric distortion is not seen for the W2 ligand as a similar charged amino-acid residue partner is not present to provide a H-bond.

4.2 The exchangeable μ -oxo bridge

Both modifications investigated, $\text{Ca}^{2+}/\text{Sr}^{2+}$ substitution and $\text{NH}_3/\text{W1}$ replacement, perturb the ^{17}O -EDNMR signals of

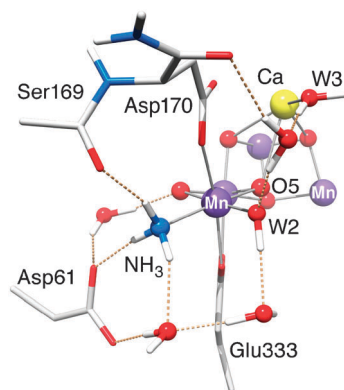


Fig. 7 Hydrogen bonding network in the vicinity of the Mn_{A4} -bound NH_3 , as observed in the optimized DFT structure of the $\text{Mn}_4\text{O}_5\text{Ca--NH}_3$ model. Mn ions are depicted in purple, O in red, Ca in yellow, C in light grey, N in blue and H in white. Only relevant residues, water molecules and protons are shown.

exchangeable oxygen species of the OEC, specifically the exchangeable μ -oxo bridge. It is this bridge that likely represents one of the substrate water sites of the Mn tetramer. As the electronic structure of the OEC is essentially invariant for all four OEC forms, the change in hyperfine coupling for this μ -oxo bridge must represent a site modification, near or at the oxygen nucleus. NH_3 binding primarily affects the connectivity of the outer Mn_{A4} to the cuboidal trimer, whereas Sr^{2+} substitution instead perturbs the exchange network within the cluster. Thus, it can be surmised that the exchangeable μ -oxo bridge must both coordinate to the outer Mn_{A4} and be associated with the $\text{Ca}^{2+}/\text{Sr}^{2+}$ ion itself as a structural element of the cuboidal trimer. Only the bridge O5 fulfils both these criteria. As a ligand to the $\text{Ca}^{2+}/\text{Sr}^{2+}$ ion, O5 is affected by the exchange of these ions of the same charge but different sizes. Similarly, as argued in Pérez Navarro *et al.*,⁴⁴ $\text{NH}_3/\text{W1}$ exchange perturbs O5 by binding *trans* to this bridge position, distorting the $\text{Mn}_{\text{A4}}\text{--O5}$ bond length.

It is noted that these results exclude the possibility that NH_3 displaces the exchangeable μ -oxo bridge as a bridging $\text{--NH}_2\text{--}$ species, an alternative rationale for the narrowing of the ^{17}O signal envelope in line with earlier suggestions.⁷⁰ $\text{Ca}^{2+}/\text{Sr}^{2+}$ and $\text{W1}/\text{NH}_3$ exchange are *additive* in terms of their effect on the width of the ^{17}O -EDNMR envelope, modelled here as defined by the μ -oxo bridge hyperfine coupling A_{iso} . This result mirrors the structural modifications observed for the doubly modified $\text{Mn}_4\text{O}_5\text{Sr--NH}_3$ OEC model; *i.e.*, the model contains *additive* structural modifications reflecting both singularly modified $\text{Mn}_4\text{O}_5\text{Sr}$ and $\text{Mn}_4\text{O}_5\text{Ca--NH}_3$ structures. If instead the NH_3 did indeed replace the bridge, the width of the ^{17}O -EDNMR envelope would be now defined by the W2 hyperfine coupling, and as such should be invariant to $\text{Ca}^{2+}/\text{Sr}^{2+}$ substitution. It is also noted that NH_3 replacement of the exchangeable bridge O5 cannot quantitatively explain the virtually unaltered $^{14}\text{NH}_3$ signal upon exchange of the O5-binding Ca^{2+} , and the ^{17}O hyperfine changes. Assuming an unaltered spin density on the bridge position, as follows from the similar spin projection factors for the four Mn ions, the measured ^{14}N hyperfine coupling for the bound ammonia at this position is far too small. On the other hand, the ^{17}O coupling of 6.5–7 MHz seen for the $\text{NH}_3/\text{W1}$ -exchanged system is in the range of those observed in Mn model complexes with a N-ligand *trans* to the oxo bridge.¹⁴

5 Conclusions

Time-dependent mass spectrometry experiments indicate that the early binding substrate (W_S) is associated with all intermediate states of the OEC.^{66,136} Furthermore, the relatively slow exchange and the S-state dependence of this bound substrate with bulk water suggests that it represents a ligand of (a) Mn ion(s). As $\text{Ca}^{2+}/\text{Sr}^{2+}$ substitution also perturbs its exchange rate, W_S is also supposed to coordinate to the Ca^{2+} ion.^{65,66} Of the exchangeable oxygen species identified here by ^{17}O -EDNMR, only O5 is a ligand to both Mn and Ca^{2+} . Similarly, only the O5 spectral signature is perturbed by $\text{Ca}^{2+}/\text{Sr}^{2+}$ exchange. Thus, O5 is the most likely candidate for W_S . This assignment limits the



possible reaction pathways for photosynthetic water splitting, and lays a foundation for studies of higher oxidized S states, which will serve to identify the second, fast exchanging substrate and eventually elucidate the mechanism of O–O bond formation. Currently two pathways are envisaged: O–O bond formation could proceed as a coupling between O5 and either (i) Mn_{A4}-bound W2 or Ca²⁺-bound W3, or (ii) a further oxygen not present yet in the S₂ state.

Acknowledgements

Financial support was provided by the Max-Planck-Gesellschaft, the “Bioénergie” program of the Commissariat à l’Énergie Atomique et aux Énergies Alternatives, the French Infrastructure for Integrated Structural Biology (FRISBI) ANR-10-INSB-05-01 program, and the EU/Energy Network project SOLAR-H2 (FP7 contract 212508). T.L. was supported by the Federal Ministry of Education and Research of Germany (BMBF) in the framework of the Bio-H2 project (03SF0355C). M.P.N. acknowledges support from the Spanish Ministerio de Economía y Competitividad (MAT 2008-03461).

Notes and references

- P. Joliot, G. Barbieri and R. Chabaud, *Photochem. Photobiol.*, 1969, **10**, 309–329.
- B. Kok, B. Forbush and M. McGloin, *Photochem. Photobiol.*, 1970, **11**, 457–475.
- J. P. McEvoy and G. W. Brudvig, *Chem. Rev.*, 2006, **106**, 4455–4483.
- W. Lubitz, E. J. Reijerse and J. Messinger, *Energy Environ. Sci.*, 2008, **1**, 15–31.
- J. Messinger, T. Noguchi and J. Yano, in *Molecular Solar Fuels*, ed. T. J. Wydrzynski and W. Hillier, Royal Society of Chemistry, Cambridge, 2012, pp. 163–207.
- N. Cox and W. Lubitz, in *Chemical Energy Storage*, ed. R. Schlögl, De Gruyter Publishers, Berlin, 2012, pp. 185–224.
- N. Cox and J. Messinger, *Biochim. Biophys. Acta, Bioenerg.*, 2013, **1827**, 1020–1030.
- N. Cox, D. A. Pantazis, F. Neese and W. Lubitz, *Acc. Chem. Res.*, 2013, **46**, 1588–1596.
- Y. Umena, K. Kawakami, J.-R. Shen and N. Kamiya, *Nature*, 2011, **473**, 55–60.
- C. P. Aznar and R. D. Britt, *Philos. Trans. R. Soc. London, Ser. B*, 2002, **357**, 1359–1365.
- K. A. Åhring, M. C. W. Evans, J. H. A. Nugent, R. J. Ball and R. J. Pace, *Biochemistry*, 2006, **45**, 7069–7082.
- W. Ames, D. A. Pantazis, V. Krewald, N. Cox, J. Messinger, W. Lubitz and F. Neese, *J. Am. Chem. Soc.*, 2011, **133**, 19743–19757.
- S. Milikisiyants, R. Chatterjee, C. S. Coates, F. H. M. Koua, J.-R. Shen and K. V. Lakshmi, *Energy Environ. Sci.*, 2012, **5**, 7747–7756.
- L. Rapatskiy, N. Cox, A. Savitsky, W. M. Ames, J. Sander, M. M. Nowaczyk, M. Rögner, A. Boussac, F. Neese, J. Messinger and W. Lubitz, *J. Am. Chem. Soc.*, 2012, **134**, 16619–16634.
- H. Nagashima and H. Mino, *Biochim. Biophys. Acta, Bioenerg.*, 2013, **1827**, 1165–1173.
- A. Haddy, *Photosynth. Res.*, 2007, **92**, 357–368.
- L. Kulik and W. Lubitz, *Photosynth. Res.*, 2009, **102**, 391–401.
- T. Lohmiller, W. Ames, W. Lubitz, N. Cox and S. K. Misra, *Appl. Magn. Reson.*, 2013, **44**, 691–720.
- N. Cox, W. Lubitz and A. Savitsky, *Mol. Phys.*, 2013, **111**, 2788–2808.
- J. L. Casey and K. Sauer, *Biochim. Biophys. Acta, Bioenerg.*, 1984, **767**, 21–28.
- J. C. de Paula and G. W. Brudvig, *J. Am. Chem. Soc.*, 1985, **107**, 2643–2648.
- K. A. Åhring, M. C. Evans, J. H. Nugent and R. J. Pace, *Biochim. Biophys. Acta, Bioenerg.*, 2004, **1656**, 66–77.
- G. C. Dismukes and Y. Siderer, *Proc. Natl. Acad. Sci. U. S. A.*, 1981, **78**, 274–278.
- A. Boussac, S. Un, O. Horner and A. W. Rutherford, *Biochemistry*, 1998, **37**, 4001–4007.
- A. Boussac, H. Kuhl, S. Un, M. Rögner and A. W. Rutherford, *Biochemistry*, 1998, **37**, 8995–9000.
- O. Horner, E. Rivière, G. Blondin, S. Un, A. W. Rutherford, J.-J. Girerd and A. Boussac, *J. Am. Chem. Soc.*, 1998, **120**, 7924–7928.
- A. Boussac and A. W. Rutherford, *Biochim. Biophys. Acta, Bioenerg.*, 2000, **1457**, 145–156.
- A. Haddy, K. V. Lakshmi, G. W. Brudvig and H. A. Frank, *Biophys. J.*, 2004, **87**, 2885–2896.
- A. Boussac, J. J. Girerd and A. W. Rutherford, *Biochemistry*, 1996, **35**, 6984–6989.
- J. M. Peloquin, K. A. Campbell, D. W. Randall, M. A. Evanchik, V. L. Pecoraro, W. H. Armstrong and R. D. Britt, *J. Am. Chem. Soc.*, 2000, **122**, 10926–10942.
- L. V. Kulik, B. Epel, W. Lubitz and J. Messinger, *J. Am. Chem. Soc.*, 2007, **129**, 13421–13435.
- C. Teutloff, S. Pudollek, S. Kessen, M. Broser, A. Zouni and R. Bittl, *Phys. Chem. Chem. Phys.*, 2009, **11**, 6715–6726.
- N. Cox, L. Rapatskiy, J.-H. Su, D. A. Pantazis, M. Sugiura, L. Kulik, P. Dorlet, A. W. Rutherford, F. Neese, A. Boussac, W. Lubitz and J. Messinger, *J. Am. Chem. Soc.*, 2011, **133**, 3635–3648.
- J.-H. Su, N. Cox, W. Ames, D. A. Pantazis, L. Rapatskiy, T. Lohmiller, L. V. Kulik, P. Dorlet, A. W. Rutherford, F. Neese, A. Boussac, W. Lubitz and J. Messinger, *Biochim. Biophys. Acta, Bioenerg.*, 2011, **1807**, 829–840.
- F. Neese, *Coord. Chem. Rev.*, 2009, **253**, 526–563.
- D. A. Pantazis, M. Orto, T. Petrenko, S. Zein, E. Bill, W. Lubitz, J. Messinger and F. Neese, *Chem.–Eur. J.*, 2009, **15**, 5108–5123.
- D. A. Pantazis, M. Orto, T. Petrenko, S. Zein, W. Lubitz, J. Messinger and F. Neese, *Phys. Chem. Chem. Phys.*, 2009, **11**, 6788–6798.
- S. Schinzel, J. Schraut, A. Arbuznikov, P. Siegbahn and M. Kaupp, *Chem.–Eur. J.*, 2010, **16**, 10424–10438.



- 39 N. Cox, W. Ames, B. Epel, L. V. Kulik, L. Rapatskiy, F. Neese, J. Messinger, K. Wieghardt and W. Lubitz, *Inorg. Chem.*, 2011, **50**, 8238–8251.
- 40 D. A. Pantazis, W. Ames, N. Cox, W. Lubitz and F. Neese, *Angew. Chem., Int. Ed.*, 2012, **51**, 9935–9940.
- 41 H. Isobe, M. Shoji, S. Yamanaka, Y. Umena, K. Kawakami, N. Kamiya, J.-R. Shen and K. Yamaguchi, *Dalton Trans.*, 2012, **41**, 13727–13740.
- 42 K. Yamaguchi, H. Isobe, S. Yamanaka, T. Saito, K. Kanda, M. Shoji, Y. Umena, K. Kawakami, J.-R. Shen, N. Kamiya and M. Okumura, *Int. J. Quantum Chem.*, 2013, **113**, 525–541.
- 43 V. Krewald, F. Neese and D. A. Pantazis, *J. Am. Chem. Soc.*, 2013, **135**, 5726–5739.
- 44 M. Pérez Navarro, W. M. Ames, H. Nilsson, T. Lohmiller, D. A. Pantazis, L. Rapatskiy, M. M. Nowaczyk, F. Neese, A. Boussac, J. Messinger, W. Lubitz and N. Cox, *Proc. Natl. Acad. Sci. U. S. A.*, 2013, **110**, 15561–15566.
- 45 A. Boussac and A. W. Rutherford, *Biochemistry*, 1988, **27**, 3476–3483.
- 46 T. A. Ono and Y. Inoue, *Arch. Biochem. Biophys.*, 1989, **275**, 440–448.
- 47 A. Boussac, F. Rappaport, P. Carrier, J. M. Verbavatz, R. Gobin, D. Kirilovsky, A. W. Rutherford and M. Sugiura, *J. Biol. Chem.*, 2004, **279**, 22809–22819.
- 48 W. F. Beck, J. C. de Paula and G. W. Brudvig, *J. Am. Chem. Soc.*, 1986, **108**, 4018–4022.
- 49 W. F. Beck and G. W. Brudvig, *Biochemistry*, 1986, **25**, 6479–6486.
- 50 L.-E. Andréasson, Ö. Hansson and K. von Schenck, *Biochim. Biophys. Acta, Bioenerg.*, 1988, **936**, 351–360.
- 51 A. Boussac, A. W. Rutherford and S. Styring, *Biochemistry*, 1990, **29**, 24–32.
- 52 D. H. Kim, R. D. Britt, M. P. Klein and K. Sauer, *J. Am. Chem. Soc.*, 1990, **112**, 9389–9391.
- 53 D. H. Kim, R. D. Britt, M. P. Klein and K. Sauer, *Biochemistry*, 1992, **31**, 541–547.
- 54 A. Boussac, M. Sugiura, Y. Inoue and A. W. Rutherford, *Biochemistry*, 2000, **39**, 13788–13799.
- 55 M. C. W. Evans, R. J. Ball and J. H. A. Nugent, *FEBS Lett.*, 2005, **579**, 3081–3084.
- 56 D. F. Ghanotakis, G. T. Babcock and C. F. Yocum, *FEBS Lett.*, 1984, **167**, 127–130.
- 57 P. O. Sandusky and C. F. Yocum, *Biochim. Biophys. Acta*, 1984, **766**, 603–611.
- 58 P. O. Sandusky and C. F. Yocum, *Biochim. Biophys. Acta*, 1986, **849**, 85–93.
- 59 T.-a. Ono and Y. Inoue, *FEBS Lett.*, 1988, **227**, 147–152.
- 60 A. Boussac, J. L. Zimmermann and A. W. Rutherford, *Biochemistry*, 1989, **28**, 8984–8989.
- 61 M. Sivaraja, J. Tso and G. C. Dismukes, *Biochemistry*, 1989, **28**, 9459–9464.
- 62 A. Boussac, J. L. Zimmermann, A. W. Rutherford and J. Lavergne, *Nature*, 1990, **347**, 303–306.
- 63 T. Lohmiller, N. Cox, J.-H. Su, J. Messinger and W. Lubitz, *J. Biol. Chem.*, 2012, **287**, 24721–24733.
- 64 J. S. Vrettos, D. A. Stone and G. W. Brudvig, *Biochemistry*, 2001, **40**, 7937–7945.
- 65 G. Hendry and T. Wydrzynski, *Biochemistry*, 2003, **42**, 6209–6217.
- 66 W. Hillier and T. Wydrzynski, *Coord. Chem. Rev.*, 2008, **252**, 306–317.
- 67 J. Messinger, M. Badger and T. Wydrzynski, *Proc. Natl. Acad. Sci. U. S. A.*, 1995, **92**, 3209–3213.
- 68 K. Beckmann, J. Messinger, M. R. Badger, T. Wydrzynski and W. Hillier, *Photosynth. Res.*, 2009, **102**, 511–522.
- 69 B. A. Diner and R. D. Britt, in *Photosystem II: The Light-Driven Water:Plastoquinone Oxidoreductase*, ed. T. Wydrzynski and K. Satoh, Springer, Dordrecht, 2005, vol. 1, pp. 207–233.
- 70 R. D. Britt, J. L. Zimmermann, K. Sauer and M. P. Klein, *J. Am. Chem. Soc.*, 1989, **111**, 3522–3532.
- 71 M. Tsuno, H. Suzuki, T. Kondo, H. Mino and T. Noguchi, *Biochemistry*, 2011, **50**, 2506–2514.
- 72 M. Sugiura, A. Boussac, T. Noguchi and F. Rappaport, *Biochim. Biophys. Acta, Bioenerg.*, 2008, **1777**, 331–342.
- 73 N. Ishida, M. Sugiura, F. Rappaport, T. L. Lai, A. W. Rutherford and A. Boussac, *J. Biol. Chem.*, 2008, **283**, 13330–13340.
- 74 J. Sander, M. Nowaczyk, J. Buchta, H. Dau, I. Vass, Z. Deák, M. Dorogi, M. Iwai and M. Rögner, *J. Biol. Chem.*, 2010, **285**, 29851–29856.
- 75 M. M. Nowaczyk, K. Krause, M. Mieseler, A. Sczibilanski, M. Ikeuchi and M. Rögner, *Biochim. Biophys. Acta, Bioenerg.*, 2012, **1817**, 1339–1345.
- 76 E. Reijerse, F. Lendzian, R. Isaacson and W. Lubitz, *J. Magn. Reson.*, 2012, **214**, 237–243.
- 77 E. L. Hahn, *Phys. Rev.*, 1950, **80**, 580–594.
- 78 L. G. Rowan, E. L. Hahn and W. B. Mims, *Phys. Rev.*, 1965, **137**, A61–A71.
- 79 P. Höfer, A. Grupp, H. Nebenführ and M. Mehring, *Chem. Phys. Lett.*, 1986, **132**, 279–282.
- 80 E. R. Davies, *Phys. Lett. A*, 1974, **A47**, 1–2.
- 81 P. Schosseler, T. Wacker and A. Schweiger, *Chem. Phys. Lett.*, 1994, **224**, 319–324.
- 82 S. Stoll and A. Schweiger, *J. Magn. Reson.*, 2006, **178**, 42–55.
- 83 F. Neese, *Wiley Interdiscip. Rev.: Comput. Mol. Sci.*, 2012, **2**, 73–78.
- 84 J. P. Perdew, *Phys. Rev. B: Condens. Matter Mater. Phys.*, 1986, **33**, 8822–8824.
- 85 A. D. Becke, *Phys. Rev. A: At., Mol., Opt. Phys.*, 1988, **38**, 3098–3100.
- 86 E. van Lenthe, E. J. Baerends and J. G. Snijders, *J. Chem. Phys.*, 1993, **99**, 4597–4610.
- 87 E. van Lenthe, E. J. Baerends and J. G. Snijders, *J. Chem. Phys.*, 1994, **101**, 9783–9792.
- 88 C. van Wüllen, *J. Chem. Phys.*, 1998, **109**, 392–399.
- 89 D. A. Pantazis, X. Y. Chen, C. R. Landis and F. Neese, *J. Chem. Theory Comput.*, 2008, **4**, 908–919.
- 90 A. Klamt and G. Schüürmann, *J. Chem. Soc., Perkin Trans. 2*, 1993, 799–805.
- 91 S. Grimme, J. Antony, S. Ehrlich and H. Krieg, *J. Chem. Phys.*, 2010, **132**, 154104–154119.

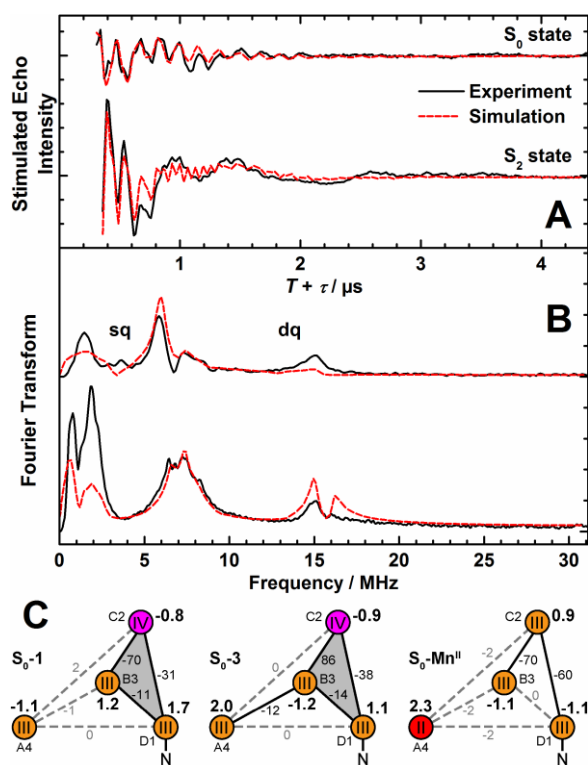


- 92 V. N. Staroverov, G. E. Scuseria, J. Tao and J. P. Perdew, *J. Chem. Phys.*, 2003, **119**, 12129–12137.
- 93 J. Tao, J. P. Perdew, V. N. Staroverov and G. E. Scuseria, *Phys. Rev. Lett.*, 2003, **91**, 146401.
- 94 L. Noodleman, *J. Chem. Phys.*, 1981, **74**, 5737–5743.
- 95 K. Yamaguchi, T. Tsunekawa, Y. Toyoda and T. Fueno, *Chem. Phys. Lett.*, 1988, **143**, 371–376.
- 96 S. Yamanaka, T. Kawakami, H. Nagao and K. Yamaguchi, *Chem. Phys. Lett.*, 1994, **231**, 25–33.
- 97 A. Bencini and F. Totti, *J. Chem. Theory Comput.*, 2009, **5**, 144–154.
- 98 M. Orio, D. A. Pantazis and F. Neese, *Photosynth. Res.*, 2009, **102**, 443–453.
- 99 F. Neese, *J. Comput. Chem.*, 2003, **24**, 1740–1747.
- 100 F. Neese, F. Wennmohs, A. Hansen and U. Becker, *Chem. Phys.*, 2009, **356**, 98–109.
- 101 F. Weigend, *Phys. Chem. Chem. Phys.*, 2006, **8**, 1057–1065.
- 102 M. Orio, D. A. Pantazis, T. Petrenko and F. Neese, *Inorg. Chem.*, 2009, **48**, 7251–7260.
- 103 P. E. M. Siegbahn, *Acc. Chem. Res.*, 2009, **42**, 1871–1880.
- 104 S. Luber, I. Rivalta, Y. Umena, K. Kawakami, J.-R. Shen, N. Kamiya, G. W. Brudvig and V. S. Batista, *Biochemistry*, 2011, **50**, 6308–6311.
- 105 X. Li, E. M. Sproviero, U. Ryde, V. S. Batista and G. Chen, *Int. J. Quantum Chem.*, 2013, **113**, 474–478.
- 106 M. Retegan, F. Neese and D. A. Pantazis, *J. Chem. Theory Comput.*, 2013, **9**, 3832–3842.
- 107 Y. Pushkar, J. Yano, P. Glatzel, J. Messinger, A. Lewis, K. Sauer, U. Bergmann and V. K. Yachandra, *J. Biol. Chem.*, 2007, **282**, 7198–7208.
- 108 Y. L. Pushkar, J. Yano, K. Sauer, A. Boussac and V. K. Yachandra, *Proc. Natl. Acad. Sci. U. S. A.*, 2008, **105**, 1879–1884.
- 109 H. Dau, A. Grundmeier, P. Loja and M. Haumann, *Philos. Trans. R. Soc. London, Ser. B*, 2008, **363**, 1237–1243.
- 110 A. Grundmeier and H. Dau, *Biochim. Biophys. Acta, Bioenerg.*, 2012, **1817**, 88–105.
- 111 F. H. Koua, Y. Umena, K. Kawakami and J.-R. Shen, *Proc. Natl. Acad. Sci. U. S. A.*, 2013, **110**, 3889–3894.
- 112 M. Sugiura, F. Rappaport, K. Brettel, T. Noguchi, A. W. Rutherford and A. Boussac, *Biochemistry*, 2004, **43**, 13549–13563.
- 113 H. Dau, J. C. Andrews, T. A. Roelofs, M. J. Latimer, W. Liang, V. K. Yachandra, K. Sauer and M. P. Klein, *Biochemistry*, 1995, **34**, 5274–5287.
- 114 S. Pudollek, *Doctoral Thesis*, Freie Universität Berlin, 2012.
- 115 S. Pudollek, F. Lendzian and R. Bittl, *Biochem. Soc. Trans.*, 2008, **36**, 1001–1004.
- 116 C. Teutloff, S. Kessen, J. Kern, A. Zouni and R. Bittl, *FEBS Lett.*, 2006, **580**, 3605–3609.
- 117 H. Matsuoka, K. Furukawa, T. Kato, H. Mino, J.-R. Shen and A. Kawamori, *J. Phys. Chem. B*, 2006, **110**, 13242–13247.
- 118 D. Koulougliotis, R. H. Schweitzer and G. W. Brudvig, *Biochemistry*, 1997, **36**, 9735–9746.
- 119 G. A. Lorigan and R. D. Britt, *Photosynth. Res.*, 2000, **66**, 189–198.
- 120 K. A. Campbell, D. A. Force, P. J. Nixon, F. Dole, B. A. Diner and R. D. Britt, *J. Am. Chem. Soc.*, 2000, **122**, 3754–3761.
- 121 M. Zheng, S. V. Khangulov, G. C. Dismukes and V. V. Barynin, *Inorg. Chem.*, 1994, **33**, 382–387.
- 122 G. J. Yeagle, M. L. Gilchrist, L. M. Walker, R. J. Debus and R. D. Britt, *Philos. Trans. R. Soc. London, Ser. B*, 2008, **363**, 1157–1166.
- 123 T. A. Stich, G. J. Yeagle, R. J. Service, R. J. Debus and R. D. Britt, *Biochemistry*, 2011, **50**, 7390–7404.
- 124 R. J. Debus, K. A. Campbell, W. Gregor, Z. L. Li, R. L. Burnap and R. D. Britt, *Biochemistry*, 2001, **40**, 3690–3699.
- 125 G. J. Yeagle, M. L. Gilchrist, R. M. McCarrick and R. D. Britt, *Inorg. Chem.*, 2008, **47**, 1803–1814.
- 126 M. Zheng and G. C. Dismukes, *Inorg. Chem.*, 1996, **35**, 3307–3319.
- 127 A. Guskov, J. Kern, A. Gabdulkhakov, M. Broser, A. Zouni and W. Saenger, *Nat. Struct. Mol. Biol.*, 2009, **16**, 334–342.
- 128 X. L. Tan, Y. Gultneh, J. E. Sarneski and C. P. Scholes, *J. Am. Chem. Soc.*, 1991, **113**, 7853–7858.
- 129 X. S. Tang, M. Sivaraja and G. C. Dismukes, *J. Am. Chem. Soc.*, 1993, **115**, 2382–2389.
- 130 S. Khangulov, M. Sivaraja, V. V. Barynin and G. C. Dismukes, *Biochemistry*, 1993, **32**, 4912–4924.
- 131 K.-O. Schäfer, R. Bittl, W. Zweggart, F. Lendzian, G. Haselhorst, T. Weyhermüller, K. Wieghardt and W. Lubitz, *J. Am. Chem. Soc.*, 1998, **120**, 13104–13120.
- 132 S. Sinnecker, F. Neese, L. Noodleman and W. Lubitz, *J. Am. Chem. Soc.*, 2004, **126**, 2613–2622.
- 133 S. Sinnecker, F. Neese and W. Lubitz, *J. Biol. Inorg. Chem.*, 2005, **10**, 231–238.
- 134 T. A. Stich, J. W. Whittaker and R. D. Britt, *J. Phys. Chem. B*, 2010, **114**, 14178–14188.
- 135 D. T. Edmonds, *Phys. Rep.*, 1977, **29**, 234–290.
- 136 W. Hillier and T. Wydrzynski, *Phys. Chem. Chem. Phys.*, 2004, **6**, 4882–4889.



Chapter 7

The First Substrate Water of Nature's Water-Oxidizing Cofactor Binds as a μ -Hydroxo Bridge during Catalyst Regeneration



Lohmiller, T.; Krewald, V.; Sedoud, A.; Rutherford, A. W.; Neese, F.; Lubitz, W.; Pantazis, D. A.; Cox, N.

in preparation.

The First Substrate Water of Nature's Water-Oxidizing Cofactor Binds as a μ -Hydroxo Bridge during Catalyst Regeneration

Thomas Lohmiller,[†] Vera Krewald,[†] Arezki Sedoud,[‡] A. William Rutherford,[§] Frank Neese,[†] Wolfgang Lubitz,[†] Dimitrios A. Pantazis,[†] and Nicholas Cox^{*,†}

[†]Max-Planck-Institut für Chemische Energiekonversion, Stiftstrasse 34-36, D-45470 Mülheim an der Ruhr, Germany

[‡]iBiTec-S, URA CNRS 2096, CEA Saclay, 91191 Gif-sur-Yvette, France

[§]Department of Life Sciences, Imperial College London, London SW7 2AZ, United Kingdom

ABSTRACT: Nature's water splitting catalyst, a penta-oxygen tetra-manganese calcium ($\text{Mn}_4\text{O}_5\text{Ca}$) complex, sequentially activates two substrate water molecules, forming an O_2 molecule during its catalytic cycle. Its reaction (S-state) cycle is composed of five intermediate S_i states, where the index i indicates the number of oxidizing equivalents stored by the cofactor. After formation of the S_4 state, the product dioxygen is released and the cofactor returns to its lowest oxidation state, S_0 . Fast membrane-inlet mass spectrometry measurements suggest that at least one substrate is bound in all catalytic (S-)states, as the rate of ^{18}O -labeled water incorporation into the product O_2 is slow (seconds timescale) in all S states. Here, we demonstrate that the $\text{Mn}_4\text{O}_5\text{Ca}$ complex poised in the S_0 state contains an exchangeable μ -hydroxo bridge. It is assigned to O5, the same exchangeable bridge identified in the S_2 state, where it represents a fully deprotonated μ -oxo bridge [Pérez Navarro *et al. Proc. Natl. Acad. Sci. U.S.A.* **2013** *110*, 15561]. It is this oxygen species that is the most probable candidate for the bound substrate in the S_0 (and S_2) state. The assignment of the μ -hydroxo bridge is based on multifrequency, multiresonance spectroscopies and comparison to theoretical models. DFT models were developed from the S_2 state [Pantazis *et al. Angew. Chem., Int. Ed.* **2012** *51*, 9935] and tested against magnetic resonance constraints (spin state multiplicity, ^{55}Mn and ^{14}N hyperfine couplings), as well as EXAFS distances and relative energies. An open-cubane structure is identified to be consistent with all spectroscopic observables and the protonation pattern and valence distribution of the S_0 state is resolved. These results refine the mechanism of binding and inclusion of the first substrate. Its incorporation and single deprotonation is required for regeneration of the catalyst. Subsequent formation of the S_1 state is then coupled to its further deprotonation, *i.e.* substrate activation.

1. INTRODUCTION

Nature's water splitting catalyst, a penta-oxygen tetra-manganese calcium cofactor ($\text{Mn}_4\text{O}_5\text{Ca}$), is found in the transmembrane protein super-complex photosystem II (PSII).¹⁻⁷ The water-splitting chemistry it performs is driven by a photosensitizer, a multi-chlorophyll assembly, found in the center of PSII. Visible light excitation generates a charge-separated state with the electron donor (P680) then acting as the chemical oxidant for the water splitting reaction. The $\text{Mn}_4\text{O}_5\text{Ca}$ oxygen-evolving complex (OEC) itself functions as an accumulator of the four oxidizing equivalents required for water oxidation.⁸ It is coupled to the photosensitizer via a redox-active tyrosine residue Y_Z (D1-Tyr161), which acts as a single electron relay.^{9,10} This requires that the cofactor moves through a cycle of five distinct redox states, the S_i states ($i = 0-4$, Figure 1).¹¹ The S_4 state spontaneously decays back to the S_0 state followed by the release of dioxygen and the rebinding of at least one substrate water.

The $\text{Mn}_4\text{O}_5\text{Ca}$ cofactor, as visualized using X-ray crystallography,^{3,4} adopts a distorted chair conformation in its resting state, with a $\text{Mn}_3\text{O}_4\text{Ca}$ cubane unit forming the base of the chair (Figure 1A). The fourth, outer Mn is attached via the oxo bridge O4 and possibly O5. The X-ray structure is however

not considered physiological¹² owing to the long Mn-Mn and Mn-O bond distances observed, significantly longer than those seen in simpler chemical models. These long distances suggest that the cofactor underwent photochemical reduction during data collection.¹³ Nevertheless, from this structure, chemical models for the cofactor have been developed from quantum chemical calculations, which are consistent with all available experimental data.¹⁴⁻²³ Such models have been validated for the cofactor poised in the S_2 state (Figure 1B), for which there are a number of spectroscopic constraints, including those from electron paramagnetic resonance (EPR).

In the S_2 state, the net oxidation state of the cofactor is generally considered to be $\text{Mn}^{\text{IV}}_3\text{Mn}^{\text{III}}$, however, see Refs. ^{24,25} for an alternative assignment. In this state, the cofactor can adopt two distinct conformations which differ in terms of their oxo-bridge connectivity (Figure 1D). In the open-cubane isomer, O5 represents an oxo bridge between Mn_{A4} and Mn_{B3} , rendering the cubane unit incomplete.^{14,17-19,21-23,26,27} In the second, closed-cubane isomer, the O5 instead represents the vertex of the cuboidal unit.¹⁸ Importantly, these two structures represent valence isomers, where the position of the unique, five-coordinate Mn^{III} ion shifts from Mn_{D1} (open) to Mn_{A4} (closed). This repositioning of the Mn^{III} ion entails that the two

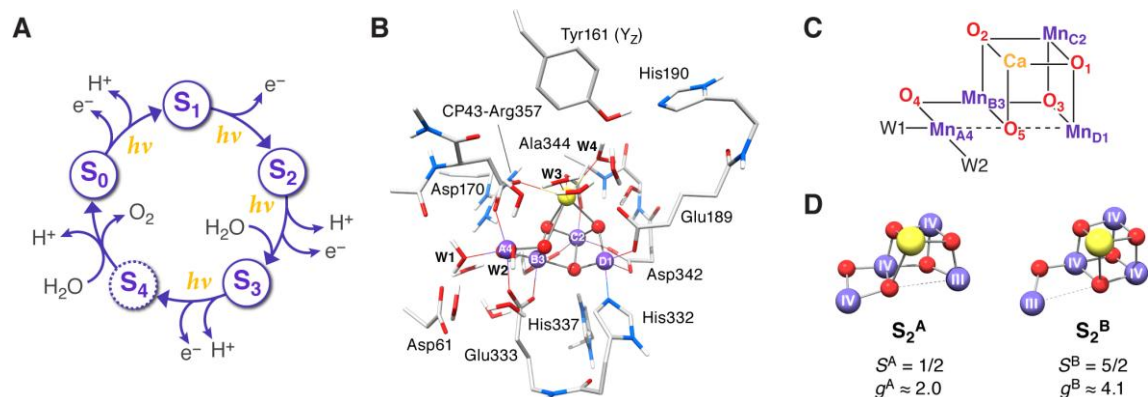


Figure 1. (A) Light ($h\nu$)-driven S-state cycle of the OEC indicating oxidation by Y_Z^* , proton release and substrate water binding. (B) DFT cluster model of the OEC in the $S_T = 1/2$ conformation of the S_2 state including its immediate surroundings.¹⁸ (C) Schematic representation of the inorganic Mn_4O_5Ca cluster core including the waters W1 and W2 bound to Mn_{A4} (W3 and W4 on the Ca^{2+} ion are omitted). (D) The two conformational isomers of the S_2 state Mn_4O_5Ca core, differing in the connectivity of oxygen O5, the Mn^{III} position, the total spin states and thus the g factors of their EPR signals.¹⁸ Mn ions are shown in purple, O in red, Ca in yellow, C in light grey, N in blue and H in white; most H atoms are omitted for clarity.

conformations display a different ground total spin state S_T . The open configuration exhibits an S_T of $1/2$,¹⁸ which gives rise to a distinct “multiline” EPR signature centered at $g \approx 2$.²⁸ The closed configuration instead adopts a high-spin ground state of $5/2$, which gives rise to broad EPR signatures centered at $g \geq 4.1$.²⁹⁻³⁵

The S_0 state represents the two-electron-reduced S_2 state cofactor. Depending on whether the S_0 -to- S_1 and S_1 -to- S_2 state transitions are both coupled to proton release, it is expected that the cofactor in the S_0 state should carry either the same overall charge, or differ by -1 . The S_0 state displays a single EPR signal similar to the S_2 multiline ($S_T = 1/2$) signal, associated with the open-cubane conformation.³⁶⁻⁴¹ Concomitant ⁵⁵Mn electron-nuclear double resonance (ENDOR) measurements demonstrate that the magnetic topologies/electronic structures of the S_2 (multiline) state and S_0 state are similar.⁴² While this suggests the cofactor in the S_0 state adopts an open-cubane conformation, this assignment is not straightforward as the different protonation states and site-Mn oxidation states may have a considerable effect on the magnetic coupling topology.⁴²

Here, we deduce the geometric structure of the S_0 state, constrain the local oxidation states of all four Mn ions, the bridging network (connectivity) of the cofactor and its protonation, with new ligand hyperfine data providing further support for these assignments. Using this model, we examine solvent-exchangeable oxygen sites of the cofactor, which represent potential substrates. Such sites were visualized by isotopic labelling $H_2^{17}O/2H_2O$ and high-field magnetic spectroscopies previously developed for the S_2 state¹⁹. The location of the first substrate binding site is assigned to a μ -hydroxo bridge (O5). Consequences for product release and catalyst regeneration are discussed.

2. EXPERIMENTAL SECTION

2.1 PSII sample preparation. PSII core complex preparations from wild-type *Thermosynechococcus elongatus* (*T. elongatus*)⁴³ and from a mutant in which D2-Tyr160 (Y_D) had been replaced by a phenylalanine⁴⁴ were isolated as described

earlier.^{45,46} PSII preparations were stored at $-80^\circ C$ or 77 K (liquid N_2) until use. All work was conducted in the dark or under dim green light. Frozen solution PSII samples were placed in X-, Q- or W-band quartz tubes with inner diameters of 3.0, 1.6 and 0.6 mm, respectively. If not used immediately, EPR samples were kept at 77 K. Saturating flash illumination was conducted at room temperature using a Nd:YAG laser (532 nm, 10 ns). EPR samples at a concentration of ≈ 1 mg chlorophyll/ml were synchronized to the S_1 state by equilibration in complete darkness at room temperature for ≈ 1 h, followed by one pre-flash and another dark-adaptation for at least 20 min. The two forms of the S_0 state were prepared as follows: (i) Photo-flash advancement: To S_1 state X- and Q-band EPR samples (not for W-band samples), the electron acceptor phenyl-*p*-benzoquinone (PPBQ) at 0.5 mM in either dimethyl sulfoxide (DMSO) or MeOH was added such that the final concentration of PPBQ was $\approx 10 \mu M$ and that of the organic solvent was $< 3\%$. The sample was illuminated by three light flashes at a rate of 1 Hz and frozen in the dark at 77 K. (ii) Chemical reduction: At room temperature, Na-dithionite was added from a freshly prepared buffer (0.4 M 2-(N-morpholino)ethanesulfonic acid (MES), pH 6.5, 0.3 M Na-dithionite) to give a final concentration of ≈ 50 mM to a dark-adapted (1 h) EPR sample at chlorophyll concentrations of 3 mg/ml (X-band) or 8–9 mg/ml (Q-band), followed by an incubation under resuspension for 45 s and immediate freezing at 77 K. Exchange of the solvent of PSII samples by resuspension in isotopically enriched $H_2^{17}O$ or $2H_2O$ was conducted as described in Ref.¹⁹.

2.2 EPR measurements. X-band (≈ 9 GHz) continuous wave (CW) EPR spectra were recorded at 4 K using a Bruker ELEXSYS E500 spectrometer equipped with an Oxford Instruments Ltd. ESR 900 liquid He flow cryostat and an ITC503 He flow temperature controller. Q-band (≈ 34 GHz) pulse EPR and ⁵⁵Mn-Davies ENDOR experiments were performed at 4.8 K on a Bruker ELEXSYS E580 spectrometer equipped with a homebuilt TE₀₁₁ microwave cavity,⁴⁷ a CF935 liquid He cryostat, an ITC503 He flow temperature controller (Oxford Instruments Ltd.) and an ENI 5100L radio frequency (RF) amplifier. W-band (≈ 94 GHz) measurements were per-

formed at 5 K using a Bruker ELEXSYS E680 EPR spectrometer. All experiments were carried out employing a homebuilt ENDOR microwave cavity, which comprised a solenoid of Teflon-coated silver wire integrated into a commercial W-band ENDOR probe head (Bruker). To ensure broadband microwave excitation and to minimize distortions, the loaded quality factor Q_L was lowered to 700 to obtain a microwave frequency bandwidth of 130 MHz. For further details on the EPR experiments, see Supporting Information section S4.

2.3 Spectral simulations. Spectra were fitted assuming an effective spin $S_T = 1/2$ ground state (Supporting Information section S3.2). The basis set that describes the spin manifolds consisting of one electron and n interacting nuclear spins can be built from the product of the eigenstates of the interacting spins:

$$|\frac{1}{2} M I_1 m_1 \dots I_n m_n \rangle \quad (1)$$

Here, M refers to the electronic magnetic sublevel, $\pm 1/2$; I takes the values $5/2$ for ^{55}Mn and 1 for ^{14}N and $5/2$ for ^{17}O ; m_i takes the values $-I_i, 1-I_i, \dots, I_i-1, I_i$. The spin manifolds can be described by the following spin Hamiltonian:

$$\hat{H} = \beta_e \vec{B}_0 \cdot \hat{G} \cdot \vec{S} + \sum_i \left(-g_{n,i} \beta_n \vec{B}_0 \cdot \vec{I}_i + \vec{S} \cdot \hat{A}_i \cdot \vec{I}_i + \vec{I}_i \cdot \hat{Q}_i \cdot \vec{I}_i \right) \quad (2)$$

It contains (i) the Zeeman term for the total electronic spin, (ii) the hyperfine and (iii), except for the EPR spectra, nuclear Zeeman terms for either the metal ^{55}Mn nuclei or the ligand ^{14}N or ^{17}O and (iv), for the ^{14}N nuclei ($I = 1$), the nuclear quadrupole interaction (NQI) term; the NQI splitting is not resolved in the EPR, ^{55}Mn -ENDOR and ^{17}O Electron-electron double resonance (ELDOR)-detected NMR (EDNMR) spectra. Spectral simulations were performed numerically using MATLAB® (R2010a, The MathWorks, Natick, MA, USA), a vector-based linear algebra package, and the EasySpin toolbox.⁴⁸ For further information on data processing, details of the simulations and theory, see Supporting Information sections S1, S2 and S3, respectively.

2.4 Density functional theory (DFT) calculations. The computational models consist of 239 or 240 atoms, depending on the total protonation state. All first-sphere amino acid residues that ligate the $\text{Mn}_4\text{O}_5\text{Ca}$ cluster (His332, Glu189, Asp342, Ala344, CP43-Glu354, Glu333 and Asp170), the two Mn4-coordinating and two Ca-coordinating water ligands, second sphere hydrogen-bonding residues (His337, Asp61 and CP43-Arg357), the redox-active tyrosine and its H-bonding partner (Tyr161 and His190), and eight additional water molecules are included in the simulation. Initial geometries were adapted from previously optimized S_2 state models¹⁸ by changing the protonation pattern appropriately, assuming the charge and multiplicity for the S_0 state. The geometry was fully relaxed while imposing α -CH backbone crystallographic³ constraints to maintain the overall shape of the folded protein. All calculations were carried out with the ORCA program package.⁴⁹ Geometries were optimized with the dispersion-corrected density functional BP86-D3,⁵⁰⁻⁵² in combination with the scalar relativistic zeroth order regular approximation (ZORA).^{53,54} ZORA-recontracted TZVP basis sets were used for all atoms except C and H, for which ZORA-SVP was used.^{55,56} The resolution of the identity (RI) approximation with the decontracted auxiliary basis set def2-TZVP/J was used.⁵⁷ Tight SCF convergence criteria in combination with

larger than standard integration grids and integration accuracy were used (Grid6 and IntAcc 6.0 in ORCA nomenclature). The electrostatic effect of the protein environment was modeled with a dielectric constant of 8.0 in the conductor-like screening model (COSMO).⁵⁸ Broken symmetry (BS) DFT calculations⁵⁹⁻⁶² were performed with the same settings as the geometry optimizations, except for the density functional that was chosen as the hybrid meta-GGA functional TPSSH,⁶³ in line with previous studies that have confirmed its good performance for magnetic and spectroscopic properties.⁶⁴⁻⁶⁸ For these calculations the RIJCOSX approximation with GridX6 was used.⁶⁹ BS solutions were obtained with the FlipSpin feature of ORCA, employing a level shift of $0.1 E_h$ to improve convergence. For models with the desired spin ground state of $S = 1/2$, ^{55}Mn and ^{14}N hyperfine coupling constants (HFCs) were calculated based on the lowest energy BS solution. For the ^{55}Mn HFC calculations, established methodologies for the calculation of spin projection coefficients were followed.^{14-18,21-23,68,70,71} Accordingly, the setup for the BS-DFT calculations was modified by introducing more dense radial integration grids for Mn, N and O of 11, 9 and 9, respectively (ORCA nomenclature). The one-center approximation was applied in all calculations. Spin-orbit coupling was evaluated with the effective potential/complete mean field approach. Picture change effects were taken into account in calculations of EPR parameters.

3. RESULTS

3.1 DFT models of the S_0 state. The interconvertible S_2 state models of Pantazis *et al.*,¹⁸ which to date are the only models that can structurally explain the two S_2 state EPR signals, are characterized by unprotonated μ -oxo bridges, H_2O in the W1 position and OH^- in the W2 position (Figure 1).¹⁷ In the S_1 -to- S_2 transition, one electron is lost, whereas in the S_0 -to- S_1 transition, one electron and one proton are lost from the catalytic center. Thus, any S_0 model that could lead to the interconvertible S_2 models must have one more proton and two more electrons. There are then three possible protonation sites: the μ -oxo bridges O4 and O5 and the terminal OH⁻ ligand W2. This yields three possible models, labeled here S_0 -1, S_0 -2 and S_0 -3, (Figure 2, Table 1). S_0 -1 has the same protonation pattern as a model proposed by Siegbahn^{26,72} (protonated O5, W1 = H_2O , W2 = OH^-), while S_0 -2 has the same protonation pattern as that suggested by Ichino *et al.*,⁷³ *i.e.* doubly protonated W1 and W2 and unprotonated μ -oxo bridges. Computational models for the S_0 state that contain a different total number of protons have also been proposed in the literature. Specifically, Yamaguchi and co-workers have suggested a model for S_0 where O5 is singly protonated and all waters W1–W4 are present as H_2O .^{74,75} A similar model is also favored by Batista and co-workers, who additionally tested an isomer that is singly protonated at O4 instead of O5.⁷⁶ To cover the above possibilities, we optimized and evaluated with our computational setup two additional models that correspond to the above protonation patterns, S_0 -4 and S_0 -5.

Despite extensive searches, no closed-cubane form, reminiscent of the interchangeable closed form of the S_2 state,¹⁸ was found for any of the protonation patterns. All models presented here have an oxidation state distribution of $\text{Mn}_{\text{D1}}^{\text{III}}\text{Mn}_{\text{C2}}^{\text{IV}}\text{Mn}_{\text{B3}}^{\text{III}}\text{Mn}_{\text{A4}}^{\text{III}}$, except for S_0 -2, where Mn_{B3} is the unique Mn^{IV} . This alternative oxidation state distribution was found for the other models, too, but it is consistently

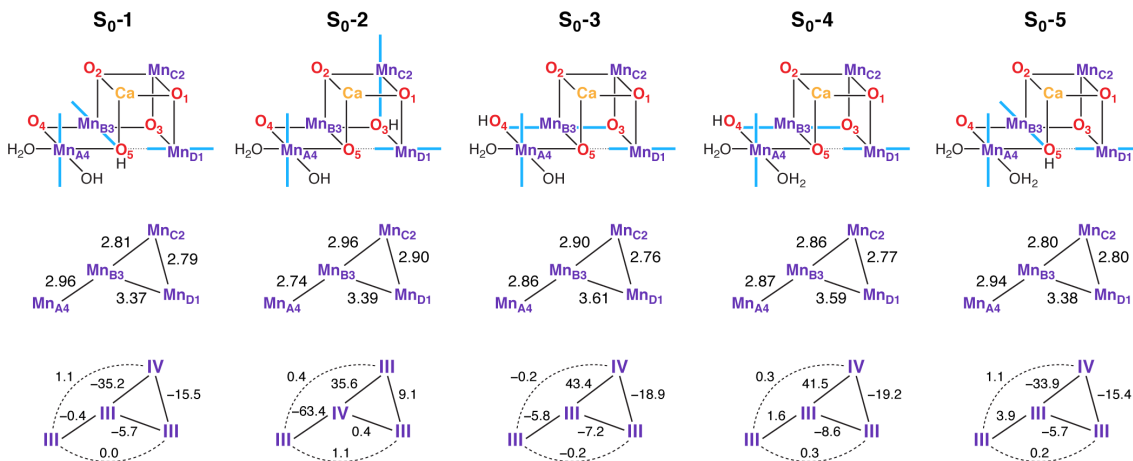


Figure 2. Schematic representation of five selected DFT models for the S_0 state. **Top row:** protonation patterns and orientations of the Jahn–Teller axes, indicated by blue bars. **Middle:** Mn–Mn distances in Å. **Bottom:** Mn oxidation state distributions and computed exchange-coupling constants in cm^{-1} .

higher in energy (by 1.1–3.1 kcal mol^{-1}) and produces high-spin states in all cases. The overall $\text{Mn}^{\text{III}}_3\text{Mn}^{\text{IV}}$ oxidation state pattern of the present models is in agreement with other literature models. Moreover, their individual Mn valence distributions are identical to those of corresponding models.^{72–74,76} We note that only in one case, that of the model $S_0\text{-3}$, a valence isomer that contained a Mn^{II} ion was located. However, this solution, characterized by the oxidation state pattern $\text{Mn}_{\text{D1}}^{\text{IV}}\text{Mn}_{\text{C2}}^{\text{III}}\text{Mn}_{\text{B3}}^{\text{IV}}\text{Mn}_{\text{A4}}^{\text{II}}$, was computed to be more than 18 kcal mol^{-1} higher in energy than the above alternative. Therefore, in line with the calculations of Ichino *et al.*⁷³ on more simplified models, we confirm that the presence of Mn^{II} in the S_0 state is highly unfavorable energetically and can thus be excluded. Models $S_0\text{-1}$ and $S_0\text{-2}$, where the protonated groups with respect to the S_1 state are O5 and W2, respectively, are practically isoenergetic ($< 1 \text{ kcal mol}^{-1}$ difference), while $S_0\text{-3}$ is predicted to be $\sim 5 \text{ kcal mol}^{-1}$ higher. Between the $S_0\text{-4}$ and $S_0\text{-5}$ isomers, the latter is favored by a little more than 3 kcal mol^{-1} .

Based on simulations of Mn extended X-ray absorption fine structure (EXAFS) spectra, two or three Mn–Mn distances between 2.7 and 2.86 Å were obtained for the OEC in the S_0 state.^{77–79} All presented models are consistent with this observation. We note that the Mn–Mn distances of $S_0\text{-4}$ and $S_0\text{-5}$ agree well with those of the optimized geometries in Pal *et al.*,⁷⁶ with mean absolute deviations for the short Mn–Mn distances of 0.04 Å and 0.05 Å compared with the QM/MM and the Monte-Carlo-refined QM/MM models of that study, respectively. Overall, all models, irrespective of their protonation state, contain three short (2.74–2.96 Å) Mn–Mn distances, while there exists one longer Mn–Mn distance at > 3.3 Å.

From the above, it appears that a screening of the models based only on agreement with EXAFS distances is not possible. However, the models can be differentiated by their electronic properties, since differences in the magnetic coupling of the Mn ions in each model results in different total spin states S_T . The exchange coupling constants and ground spin states were calculated for all models as in previous studies.^{14–18,21–23,68,71,80} Crucially, the only models for which the computed spin state agrees with the experimentally observed $S = 1/2$ are models $S_0\text{-1}$ and $S_0\text{-3}$ (Table 1). In combination with the above

observations regarding the energetics of the models, this supports $S_0\text{-1}$ as the best candidate for the S_0 state among the models considered here. The origin of the higher spin ground states of the other models can be traced back to the orientation of the Jahn–Teller axes of the Mn^{III} ions: ferromagnetic coupling is always observed between pairs of Mn ions where a Jahn–Teller axis is oriented in the direction of one of the μ -oxo units bridging these Mn ions (*i.e.* in-plane with respect to the Mn_2O_2 subunit, see Figure 2). In all such models, the remaining antiferromagnetic coupling constants are not strong enough to compensate for this ferromagnetic contribution.

Table 1. Protonation Patterns, Relative Energies E_{rel} in kcal mol^{-1} and Spin Ground and First Excited States with Their Energy Separation Δ in cm^{-1} of the DFT Models for the S_0 State.

model	O4, O5, W2	$E_{\text{rel}} / \text{kcal mol}^{-1}$	S_{GS}	S_{ES}	Δ / cm^{-1}
$S_0\text{-1}$	$\text{O}_2^-, \text{OH}^-, \text{OH}^-$	0.6	1/2	3/2	1.9
$S_0\text{-2}$	$\text{O}_2^-, \text{O}_2^-, \text{H}_2\text{O}$	0.0	7/2	5/2	68.8
$S_0\text{-3}$	$\text{OH}^-, \text{O}_2^-, \text{OH}^-$	5.5	1/2	3/2	15.6
$S_0\text{-4}$	$\text{OH}^-, \text{O}_2^-, \text{H}_2\text{O}$	3.3	7/2	5/2	11.4
$S_0\text{-5}$	$\text{O}_2^-, \text{OH}^-, \text{H}_2\text{O}$	0.0	9/2	7/2	9.7

3.2 Multifrequency EPR and ^{55}Mn -ENDOR. In order to determine the ^{55}Mn hyperfine couplings and obtain information about the effective/spin-projected G tensor of the tetranuclear Mn cluster in the S_0 state, multifrequency EPR and ^{55}Mn -ENDOR experiments were performed on PSII samples advanced to the S_0 state by three photo flashes. The CW EPR spectrum of a sample containing $\approx 3\%$ DMSO as the sole organic solvent is shown in Figure 3A. Besides the S_0 state multiline signal, it contains virtually no contributions from contaminating Mn^{2+} ions, however little signal intensity between 300–310 mT from the oxidized low-spin heme of the cofactor cytochrome c_{550} is seen.⁸¹ The multiline signal is centered at $g \approx 2$ and exhibits at least 24 peaks spread over the range from 235–455 mT. Its hyperfine pattern is almost

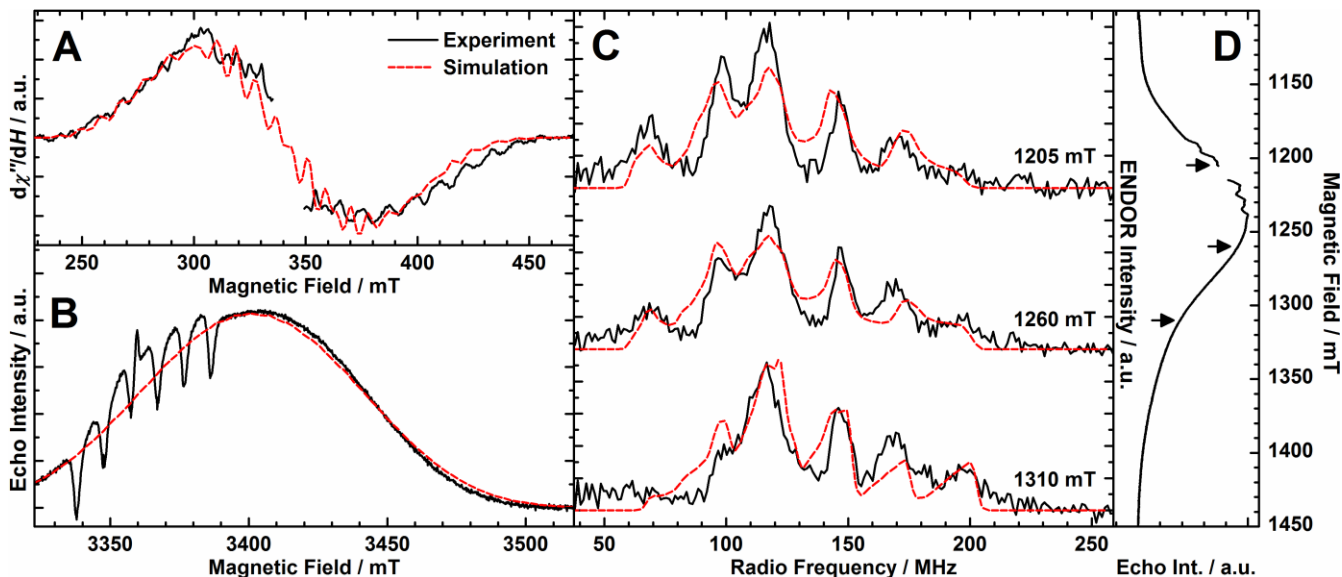


Figure 3. EPR and ^{55}Mn -ENDOR spectra (black solid traces) and spin Hamiltonian-based simulations (red dashed traces, see sections 2.3, S2 and S3) of the S_0 state of the OEC in 3-flash-advanced PSII isolated from *T. elongatus*. The optimized parameter set is given in Table 2. In panels A and D, the $g \approx 2$ radical signal of Y_D^* (D2-Tyr160) was excised for clarity of presentation. In C and D, the experimental spectra represent light-minus-dark differences. **(A)** X-band CW EPR. Experimental parameters: microwave frequency: 9.498 GHz; microwave power: 20 mW; modulation amplitude: 25 G; time constant: 82 ms; temperature: 4.0 K. **(B)** W-band electron spin echo (ESE)-detected EPR. Y_D had been replaced by a phenylalanine, removing the Y_D^* signal from the spectra.⁴⁴ Contaminating Mn^{2+} is evident as over-rotated hyperfine features of negative signal intensity. Experimental parameters: microwave frequency: 94.062 GHz; shot repetition time: 1 ms; microwave pulse length (π): 56 ns; τ : 280 ns; temperature: 4.8 K. **(C)** Q-band Davies ENDOR. A decomposition of the simulation depicting the contributions from the individual ^{55}Mn nuclei is shown in Figure S2C. Experimental parameters: microwave frequencies: 33.979 GHz, 33.971 GHz, 33.984 GHz; magnetic fields: 1205 mT, 1260 mT, 1310 mT (top to bottom); shot repetition time: 100 μs ; microwave pulse length (π): 24 ns; τ : 260 ns; RF pulse length (π_{RF}): 3.5 μs ; temperature: 4.8 K. **(D)** Q-band ESE-detected EPR. The arrows indicate the magnetic field positions of the ENDOR experiments in D. Experimental parameters: microwave frequency: 33.891 GHz; shot repetition time: 100 μs ; microwave pulse length (π): 24 ns; τ : 260 ns; temperature: 4.8 K.

identical to that presented earlier for 3-flash-advanced PSII samples from *T. elongatus* in the absence of MeOH⁴⁰, featuring a more pronounced hyperfine structure than the corresponding spectrum reported from spinach PSII in Ref. ³⁸ (however, other studies^{37,39,40,82} did not resolve any S_0 multiline in spinach PSII in the absence of MeOH). The spectral width, line shapes, prominence and positions differ clearly from the $S_T = 1/2$ multiline signal of the S_2 state (240-435 mT, 24 lines, see Figure S2A in the Supporting Information), of which the presented spectrum does not show any contribution. The fraction of Mn clusters in that state is thus negligibly small, demonstrating efficient S-state turnover by the laser flashes.

Figure 3B presents the ESE-detected EPR spectrum at W-band frequency of a Y_D -less PSII sample from a *T. elongatus* mutant. Contributions from contaminating Mn^{2+} are more intensely visible than in the X-band CW EPR spectrum as six inverted hyperfine lines of negative intensity centered at $g \approx 2$, since the high-spin Mn^{2+} signal ($S = 5/2$) is over-rotated when optimum $\pi/2$ pulse length and power to visualize the $S_T = 1/2$ signal are employed. Same as in the S_2 state (compare Figure S2B),²³ no ^{55}Mn hyperfine structure is resolved in the W-band EPR spectrum of the S_0 state. Hence, the spectrum does not provide additional information on the hyperfine matrices, but due to the increased Zeeman energy at higher field is most important to constrain the G tensor. Lacking the overlapping/background signals apparent in the X-band CW EPR spectrum, the center of the signal can be determined more

accurately as $g = 1.976$. The signal of the S_0 state spans approximately the same range (3310–3500 mT) as that of the S_2 state. As such, the greater width of the S_0 state in X-band spectra results from larger or more anisotropic ^{55}Mn hyperfine interactions as compared to S_2 , while the range of G tensor components should be similar.

Figure 3C shows magnetic-field-dependent Davies ENDOR light-minus-dark spectra at Q-band frequencies. They were measured at the low field (1205 mT), central (1260 mT) and high field (1310 mT) regions of the corresponding EPR spectrum (Figure 3D). The three-flashes-minus-zero-flashes subtraction removed minor ^{55}Mn resonances of Mn^{2+} ions (at ≈ 115 MHz and ≈ 155 MHz) to obtain pure ^{55}Mn -ENDOR signals of the cyanobacterial S_0 state. ^1H resonances are largely suppressed due to the short RF pulse of 3.5 μs . The spectra resolve six distinct peaks that cover the range from ≈ 55 to ≈ 215 MHz. This pattern is of the same general appearance as the spectra of the 3-flash-advanced S_0 state in PSII isolated from higher plants⁴². No ENDOR intensity is observed in the RF range from 215 to 400 MHz (not shown). Compared to Q-band spectra^{15,16,22,23,83} of the cyanobacterial S_2 state, their general appearance is also similar, with the majority of the ^{55}Mn -ENDOR intensity centered on the two peaks between 90 and 130 MHz. However, the signal is ≈ 20 MHz wider on the high RF frequency end, leading to the resolution of the additional sixth peak. In contrast to the S_2 state,^{15,23,42,84,85} the S_0 state signal of frozen-solution PSII samples exhibits a pronounced orientation dependence, in the form of a shift of

⁵⁵Mn-ENDOR intensity from the low- to the high-frequency features with increasing magnetic field B_0 .

Simultaneous powder-pattern spectral simulation of the S_0 state EPR and ⁵⁵Mn-ENDOR signals using a model based on the spin Hamiltonian formalism (see sections 2.3, S2 and S3 for details) were performed using a least-squares fitting routine. The simulated spectra are shown as red dashed lines in Figure 3, the corresponding parameter set of optimized effective G and ⁵⁵Mn hyperfine tensors A is listed in Table 2. Same as for previous concerted simulations of S_0 ⁴² (and S_2 , see Supporting Information Table S1)^{15,16,22,23,42,84-86} state EPR and ⁵⁵Mn-ENDOR signals, four ⁵⁵Mn hyperfine tensors, assumed to be collinear with the G tensor and numbered in order of their isotropic coupling strength, are required to simultaneously reproduce the spectra. The simulation matches position and width of the W-band EPR absorption, determining the G tensor components. At the same time, the features governing the ⁵⁵Mn A tensors, the X-band CW EPR hyperfine pattern in large part and the width of the Q-band ENDOR signal, its peak positions and its orientation selectivity are well reproduced.

The isotropic component of the G tensor of 1.976 corresponds to the central position of the W-band EPR absorption envelope, which is nearly identical to that of the low spin conformation of the S_2 state^{23,87,88} ($G_{\text{iso}} = 1.974$). The absolute G anisotropy of the quasi-axial tensor is slightly larger than in the S_2 state ($G_{\text{aniso}} = 0.040$ compared to 0.028 ²⁰), but its

Table 2. Effective G and ⁵⁵Mn Hyperfine Tensors A_i for the Simulations of the EPR and ENDOR Spectra^a (Figure 3) of the S_0 -State OEC in 3-flash-advanced PSII from *T. Elongatus* and BS-DFT-Computed ⁵⁵Mn Hyperfine Couplings A_{iso} ^b of Selected S_0 Models.

experimental	G	A_i / MHz			
		A_1	A_2	A_3	A_4
x	2.003	327	262	221	148
y	1.965	314	217	188	164
z	1.960	377	276	266	232
\perp^c	1.963	321	269	205	156
iso ^d	1.976	339	252	225	181
aniso ^e	-0.040	-56	52	-62	-76
model S_0 -1	$d_{\text{III}} / \text{cm}^{-1}$	A_{D1}	A_{B3}	A_{A4}	A_{C2}
iso	0	-417	-300	348	186
iso	-1	-384	-272	296	171
model S_0 -3	$d_{\text{III}} / \text{cm}^{-1}$	A_{A4}	A_{B3}	A_{D1}	A_{C2}
iso	0	-521	251	-164	173
iso	-1	-524	253	-166	173

^a All G and A_i ($i = 1-4$) tensors are collinear. ^b Calculated as $A_{i,\text{iso}} = a_{i,\text{iso}} \rho_{i,\text{iso}}$ employing the theoretical spin projection factors $\rho_{i,\text{iso}}$ (section 3.3, Supporting Information Table S2). ^c The axial/parallel and equatorial/perpendicular G and A_i values are defined as the unique tensor component and the average of the two non-unique components, respectively. ^d The isotropic components are the averages of the individual values: $G_{\text{iso}} = (G_x + G_y + G_z)/3$ and $A_{i,\text{iso}} = (A_{i,x} + A_{i,y} + A_{i,z})/3$. ^e The anisotropies of the G and A_i tensors are expressed as the differences $G_{\text{aniso}} = G_{\perp} - G_{\parallel}$ and $A_{i,\text{aniso}} = A_{i,\perp} - A_{i,\parallel}$.

relative contribution is still comparatively small (2 % of G_{iso}). In the present simulation, the x component corresponds to the unique direction of the G tensor. The optimized effective ⁵⁵Mn hyperfine tensors comprise isotropic components in the range from 181 to 339 MHz, which are highly similar to those fitted to the spinach S_0 state data⁴², as well as those of the cyanobacterial S_2 state.²³ Similarly, all of them are near-axial with varying degrees of rhombicity. Except for A_3 , their z components are their largest and unique components, resulting in negative anisotropies as defined in Table 2, identical to the higher plant S_0 simulations. In contrast, the unique axis of A_2 is the smallest component y , resulting in a positive anisotropy ($A_{2,\text{aniso}} = 52$ MHz), similarly seen for the S_0 state of higher-plant PSII. While their signs are the same, the absolute anisotropies reported for the spinach S_0 state are slightly larger.

3.3 Electronic structure of the S_0 state: Mn oxidation states and exchange couplings. When treating an exchange-coupled spin system by the effective spin Hamiltonian formalism, spin projection tensors ρ_i relate the effective hyperfine tensor A_i to the intrinsic (on-site) tensor $a_{i,\text{iso}}$ of each spin-bearing center as $A_{i,\text{iso}} = \rho_{i,\text{iso}} a_{i,\text{iso}}$. As such, its isotropic spin projection coefficient $\rho_{i,\text{iso}}$ can be considered a measure for the relative spin population and spin density on a Mn ion and thus for its contribution to the corresponding spin state. The expected spin projection factors can then be calculated from the isotropic hyperfine component $A_{i,\text{iso}}$ of the fitted, effective tensor and literature values for the isotropic intrinsic hyperfine couplings determined in monomeric Mn complexes in the respective oxidation state (see Table S2 and Refs. ^{15,86,89-91}). As there is considerable variation in Mn hyperfine values observed for model complexes, ranges of spin projections are to be calculated as opposed to definite values. On the other hand, from the electronic structure of a spin system, its valence state configuration and electronic exchange-coupling scheme, as obtained from theoretical computations on the system, numbers for $\rho_{i,\text{iso}}$ can be calculated by diagonalization of the Heisenberg-Dirac-van Vleck Hamiltonian (see Refs. ^{14,17,18,68,92}). Comparing “experimental” and “theoretical” values is a method to test the validity of models, as those that yield values that fall outside this range are very unlikely to represent plausible models for the electronic structure of the system. This has been successfully applied to the S_2 multiline state.^{15,16,23,86,93}

Table S2 contains the ranges of the isotropic spin projection factors expected from the simulated A tensors (Table 2) for the four Mn ions of the S_0 state in the possible oxidation states +II, +III and +IV. In the tetrameric spin system, a spin center of higher multiplicity S_i should exhibit larger spin projections than higher oxidized ions as, possessing more unpaired electrons, it is expected to carry a larger spin population. This is reproduced in computational OEC models in which the most reduced ion is either a Mn^{III}^{14,17,18} or a Mn^{II} ion⁹⁴. While this can vary with the actual J_{ij} -coupling scheme and with intrinsic fine structure interactions (Supporting Information section S7), for a single ion in the most reduced state, $|\rho_{i,\text{iso}}|$ is closer to 2 than 1 (Figure 4C). Considering that the largest possible $|\rho_{i,\text{iso}}|$ in case of a Mn^{II} ion is < 1.5 , our experimental effective ⁵⁵Mn^{II} hyperfine couplings together with the required large intrinsic couplings rule out the presence of a Mn^{II} ion in the S_0 state cluster. In other words, in the presence of a Mn^{II} ion, ⁵⁵Mn resonances would be expected in the ENDOR spectrum above the actual edge of ≈ 215 MHz, which is not the case (Figure 3C). Hence, it precludes the low-valent hypothesis, in which the mean Mn oxidation state is 2.75 in the S_0 state,

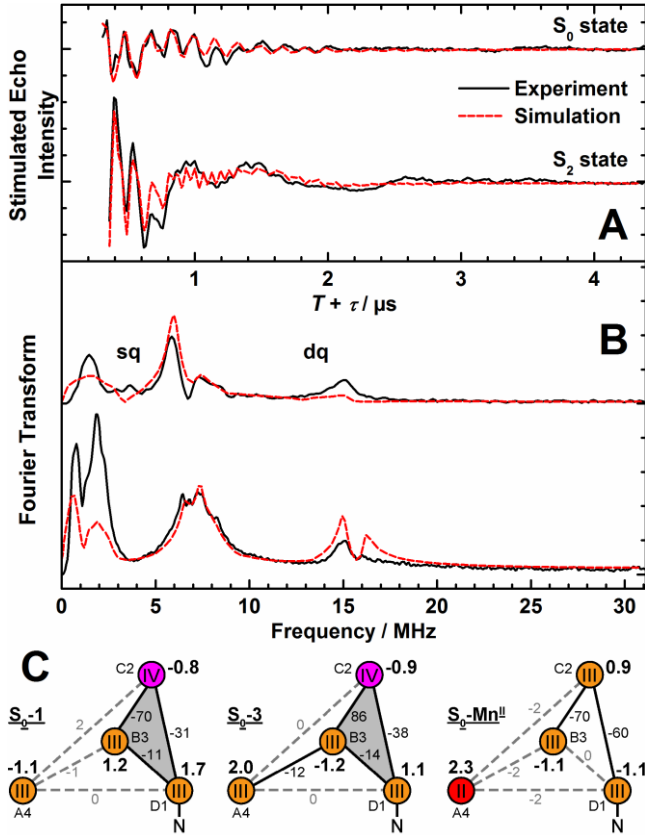


Figure 4. Q-band three-pulse ESEEM light-minus-dark spectra of PSII samples isolated from *T. elongatus* in the 3-flash-advanced S_0 (top) and in the S_2 (bottom) state and electronic structural models for S_0 . Black solid traces depict the baseline-corrected experimental spectra; superimposing red dashed traces represent simulations based on the spin Hamiltonian formalism as outlined in sections 2.3, S2 and S3. The optimized parameter sets are listed in Table 3. “sq” and “dq” refer to the position of single and double-quantum transitions, respectively. For a description of the baseline subtraction procedure, see section S1. The S_2 state traces were originally published in Ref. ²³. **(A)** Time-domain spectra and **(B)** corresponding Fourier transforms. Experimental parameters: microwave frequencies: 33.965 GHz (S_0), 34.037 GHz (S_2); magnetic fields: 1245 mT (S_0), 1250 mT (S_2); shot repetition times: 0.5 ms (S_0), 1 ms (S_2); microwave pulse lengths ($\pi/2$): 16 ns (S_0), 12 ns (S_2); τ : 260 ns; ΔT : 48 ns (S_0), 100 ns (S_2); temperatures: 4.8 K (S_0), 5.2 K (S_2). **(C)** Valence-state and exchange-interaction schemes of the models S_0 -1, S_0 -3 and S_0 -Mn^{II} showing the main (black solid lines) and weak (grey dashed lines) pair-wise exchange couplings J_{ij} given in cm^{-1} . The bold numbers next to the Mn ions represent their spin projection factors $\rho_{i,\text{iso}}$.

since this would require the presence of at least one Mn^{II} ion, e.g. Mn^{II}Mn^{III}₃. Such a model was recently proposed on the basis of time-dependent DFT computations and K-edge energies (exemplified by the hypothetical model S_0 -Mn^{II} in Figure 4C).⁹⁴ Similarly, considering the high-valent scheme,^{42,78,95-97} which exhibits a mean Mn oxidation state of 3.25, the variant that comprises a Mn^{II} ion, Mn^{II}Mn^{III}Mn^{IV}₂, is inconsistent. This leaves as the only Mn configuration possible the high oxidation state pattern variant Mn^{III}₃Mn^{IV}.^{42,76} The presence of three Mn^{III} ions in the cluster is supported by the greater ⁵⁵Mn-ENDOR width and field dependence, reflected by the larger

tensor anisotropies, than in the S_2 state (Tables 2 and S1), which comprises only one Mn^{III} ion. This is a consequence of the significant fine structure interaction of the Jahn-Teller ion Mn^{III}, negligible for Mn^{IV}.^{15,16,23,86,93}

The assignment of hyperfine tensors to specific Mn positions within the tetranuclear cluster in the +III and +IV oxidation states can be accomplished on the basis of electronic exchange-coupling schemes. At the same time, models such as those resulting from BS-DFT computations (Figure 4C) can be tested for consistency with experiment.^{15,16,23,86,93} Our experimental results and the spin projection factors confirm the Mn^{III}₃Mn^{IV} pattern for S_0 found for both our energy-minimized $S_T = 1/2$ models S_0 -1, and S_0 -3. Their “theoretical” spin projection factors $\rho_{i,\text{iso}}$ and resulting intrinsic hyperfine components $a_{i,\text{iso}}$ are listed in Table S2. Arranging them according to their magnitude, one can see clearly that the theoretical $\rho_{i,\text{iso}}$ match the ranges set by the experimental hyperfine tensors very well. At the same time, their calculated intrinsic hyperfine couplings $a_{i,\text{iso}}$ fall within the limits observed in Mn model compounds. We can assign the simulation parameters to the individual Mn ions in these S_0 state structures. We see that comparing the models, Mn_{A4} and Mn_{D1} are switched, because the largest spin projection factor $|\rho_{1,\text{iso}}|$ is associated with Mn_{D1} in model S_0 -1, same as in the S_2 state, but Mn_{A4} in model S_0 -3. This will be relevant with respect to the hyperfine coupling of the His332 nitrogen ligand to Mn_{D1} (section 3.4).

In conclusion, the spin projection approach demonstrates that our EPR/⁵⁵Mn ENDOR data are consistent with a Mn^{III}₃Mn^{IV} valence state configuration in which Mn_{C2} is the single Mn^{IV} ion, as in our models S_0 -1 and S_0 -3. For the effect of additional consideration of the intrinsic Mn fine structure splittings d on their spin projection factors in the models tested and on the intrinsic ⁵⁵Mn hyperfine couplings, see section S7. Theoretical effective ⁵⁵Mn hyperfine interactions can be calculated from the BS-DFT computations of the intrinsic couplings and spin projection factors (Table 2). Those based on model S_0 -1 reproduce the experimental magnitudes reasonably well when including an assumed $d_{\text{III}} = -1 \text{ cm}^{-1}$, as described in section S7, markedly better than those from S_0 -3.

3.4 The Mn_{D1}-His332-imino-N interaction: a local probe for the electronic structure. In order to characterize the interaction of the imino-N of His332 with the OEC in the S_0 state, we present the first ¹⁴N-three-pulse electron spin echo envelope modulation (ESEEM) and ¹⁴N Hyperfine sublevel correlation (HYSCORE) at Q-band and ¹⁴N-EDNMR experiments at W-band frequencies on 3-flash-advanced cyanobacterial PSII samples. In Figure 4, light-minus-dark subtracted three-pulse ESEEM spectra at central field positions of the multiline EPR spectra, displaying signals stemming from the interaction of the His332 imino-¹⁴N ligand with the S_0 and S_2 ²³ states, are compared. The Fourier-transformed spectra from both states similarly contain basically three features: the lines centered at frequencies below 2.5 MHz ($\nu_\alpha = \nu_n - |A_{\text{iso}}|/2$), single-quantum transitions between ≈ 5 and ≈ 9 MHz ($\nu_\beta = \nu_n + |A_{\text{iso}}|/2$) appearing as two split lines and smaller double-quantum resonances around 15 MHz ($\nu_{2\beta} = 2\nu_n + |A_{\text{iso}}|$). Comparison of their resonance positions shows that the strength of the effective ¹⁴N coupling is smaller in S_0 than in S_2 . The precise line structuring is defined both by the ¹⁴N hyperfine anisotropy and the NQI. A set of field- and τ -dependent three-pulse ESEEM spectra, depicted in Supporting Information Figures S4, S5 and S6,

Table 3. Fitted and Calculated Effective/Projected ^{14}N and ^{17}O Hyperfine and NQI Tensors in MHz for the Electron-nuclear Couplings of the His332 Imino-N and Exchangeable Oxygen Species with the OEC in the S_0 State and, for Comparison, the S_2 State^{19,23} in PSII from *T. Elongatus*.^a

		Method	$ A_1 ^b$	$ A_2 ^b$	$ A_3 ^b$	$ A_{\text{iso}} ^c$	A_{dip}^d	A_η^e	$ e^2Qq/h $	η^e
His332-imino- ^{14}N	S_0	Q-, W-band ^f	3.3	7.4	5.4	5.3	1.03	0.97	1.78	0.75
		BS-DFT, S₀₋₁				5.1			1.79	0.71
		BS-DFT, S₀₋₃				3.3			1.87	0.65
	S_2^{23}	Q-band ^f	5.6	8.4	7.2	7.1	0.75	0.81	1.97	0.75
		W-band ^f	3.2	9.2	6.7	6.3	1.59	0.80		
		BS-DFT				5.8			1.65	0.91
$^{17}\text{O}_5$	S_0	W-band	11	5.6	13.4	10.0	2.2	0.55		
	$S_2^{19,23}$		10.7	5.3	13.1	9.7	2.2	0.55		
W2 ^{17}O	S_0	W-band	4.3	4.4	2.5	3.7	0.6	0.08		
	$S_2^{19,23}$		5.1	5.1	3.3	4.5	0.6	0.08		
matrix ^{17}O	$S_0, S_2^{19,23}$	W-band	2.1	0.2	2	1.4	0.6	0.08		

^a The G tensors used were those fitted to the EPR/ ^{55}Mn ENDOR spectra (S_0 : Table 2, S_2 : Table S1). ^b A_1, A_2 and A_3 are the principal components of the hyperfine tensor, which are not assigned to the principal axes of the coordinate system defined by the G tensor. ^c A_{iso} is defined as the average of the principal components of the hyperfine tensor: $A_{\text{iso}} = (A_1 + A_2 + A_3)/3$. ^d A_{dip} is defined in terms of X_1, X_2 , and X_3 as $A_{\text{dip}} = (X_1 + X_2)/2 = -X_3/2$. ^e The rhombicity is defined by A_η or $\eta = (X_1 - X_2)/X_3$, respectively. X_1, X_2 , and X_3 represent the three principal components of the hyperfine tensors minus A_{iso} and of the NQI tensors and are labeled such that $|X_1| \leq |X_2| \leq |X_3|$. ^f The Euler rotation angles $[\alpha, \beta, \gamma]$ of the NQI relative to the A tensors are $[23, 111, 15]$ in the S_0 and $[20, 12, 0]$ for the S_2^{23} state simulations.

respectively, display the same general appearance of the His332 imino- ^{14}N signal. While it exhibits some variation in the intensities of the three features, hardly any orientation selectivity is observed upon changing the magnetic field. The field dependence present is mostly a result of the varying Zeeman energy.

For full characterization of the ^{14}N hyperfine and NQI matrices of the His332 imino- ^{14}N interaction in the S_0 state, we also measured Q-band HYSORE spectra at four magnetic field positions corresponding to $g = 2.032$ - 1.798 , shown in Supporting Information Figure S7. In the two dimensions of the Fourier transforms, the three features that comprise the Q-band ESEEM spectra appear as cross peaks at corresponding frequencies in the (+,+) quadrant. Since the smaller ^{14}N electron-nuclear coupling in S_0 than in S_2 is further away from cancellation conditions, mostly artifacts but hardly any real ^{14}N signal intensity is observed in the (-,+) quadrant (not shown, compare Ref. ²³). At the same time, the cross peaks stretch from the frequency axes inwards towards the diagonal. As opposed to the three-pulse ESEEM spectra (Figures S4, S5 and S6), a systematic variation of peak position, intensity and profile is clearly apparent as a function of the magnetic field. The ν_β feature dominates in the spectra over the two weaker lines.

The interaction of the imino- ^{14}N of His332 with Mn_{D1} can also be detected as a signal in EDNMR experiments at W-band (Supporting Information Figure S8). Therein, one can identify the feature comprising the superimposed single- and double quantum transitions ν_β and $\nu_{2\alpha}$ between 10.5 and 16 MHz and the $\nu_{2\beta}$ line centered at 27 MHz, while the ν_α line closer to the hole burned at $\Delta\nu = 0$ is not apparent in the spectra. By comparison with the corresponding spectra on S_2 state samples^{19,23}, it is again seen that in the S_0 state, the effective ^{14}N coupling is less strong than in the S_2 state.

Fitted hyperfine and NQI spin Hamiltonian parameters for the Mn_{D1} -His332-imino- ^{14}N interaction along with computed values from our BS-DFT models **S₀₋₁** and **S₀₋₃** are given in Table 3. In contrast to the S_2 state,²³ a single common parameter set could be employed for simultaneous orientation-selective simulations (see section 2.3, S2 and S3) of both the entire ESEEM and HYSORE dataset at Q-band and the EDNMR signal at W-band frequencies, only comprising a spectrum at a central field position though. The hyperfine magnitude is $A_{\text{iso}} = 5.3$ MHz and thus 15–25 % smaller than in the S_2 state, depending on the S_2 dataset used, reproducing what is seen visually in the spectra of all our experiments. In contrast, the anisotropic dipolar component A_{dip} is larger than in S_2 with a likewise pronounced rhombicity A_η . For direct comparison of theoretical and experimental numbers, the computed intrinsic imino- ^{14}N hyperfine tensors were multiplied by the Mn_{D1} spin projection coefficient given in Table S2 ($d_{\text{III}} = -1 \text{ cm}^{-1}$). The calculated value of 5.1 MHz for the BS-DFT model **S₀₋₁** is highly similar to the experimental A_{iso} , while that of model **S₀₋₃** is clearly too small. This results from their different $|\rho_{\text{D1,iso}}|$, while their intrinsic $a_{\text{iso}} \approx 2.9$ MHz are basically identical, lying in the empirical range for equatorial ^{14}N ligands (see below). Same as in the S_2 state,²³ the DFT computations confirm the expected alignment of the unique (smallest) component of the quasi-axial intrinsic hyperfine tensor a along the Mn_{D1} -N bond. Since also in S_0 , the pseudo-Jahn-Teller axis and thus the unique fine structure and spin projection component of the Mn_{D1} ion are aligned along its open coordination site (section 3.1), the rhombicity of the projected/effective A tensor can equally be rationalized by this perpendicularity. The NQI of the imino- ^{14}N in the S_0 state is similar to that in S_2 . While its magnitude $|e^2Qq/h| < 2$ is smaller, it exhibits the same pronounced rhombicity.

Comparison with the parameters of the His332 ligand in the S_2 state and of ^{14}N ligands in model complexes identifies the

imino- ^{14}N also in S_0 to be in an equatorial position of Mn_{D1} in the +III oxidation state (for details, see Supporting Information section S9.2), consistent with our DFT structures. Most importantly, the result clearly demonstrates that the $\text{Mn}_{\text{D1}}^{\text{III}}$ ion must carry a spin protection factor $|\rho_{\text{D1,iso}}| > 1.5$, in analogy to the dimeric $\text{Mn}^{\text{III}}\text{Mn}^{\text{IV}}$ complexes, were $|\rho_{\text{III,iso}}| = 2$.^{89,98-100} In the same way as described in section 3.3 with regards to the ^{55}Mn hyperfine couplings, a Mn^{II} ion present in the cluster would carry the largest $|\rho_{i,\text{iso}}|$, precluding the inferred magnitude for $|\rho_{\text{D1,iso}}|$ (Figure 4C, $S_0\text{-Mn}^{\text{II}}$). This is especially the case for a dimer-of-dimers model with $|\rho_{\text{D1,iso}}| \ll 1$. Thus, the data for the imino-N coupling rule out the presence of a Mn^{II} ion in the S_0 state and confirm the $\text{Mn}^{\text{III}}\text{Mn}^{\text{IV}}$ valence state configuration. Specifically, the determined hyperfine interaction is fully consistent with the S_0 state BS-DFT model $S_0\text{-1}$. The intrinsic ^{14}N hyperfine coupling $a_{\text{iso}} \approx 3.1$ MHz resulting from the large large $|\rho_{\text{D1,iso}}| = 1.7$ (Figure 4C) is below the maximum $a_{\text{iso}} = 3.3$ MHz measured in $\text{Mn}^{\text{III}}\text{Mn}^{\text{IV}}$ dimers.⁹⁸⁻¹⁰¹ In contrast, the a_{iso} of 4.6 MHz on basis of the smaller $|\rho_{\text{D1,iso}}| = 1.1$ in model $S_0\text{-3}$ is too large for an equatorial ^{14}N ligand, however would be at the lower limit of 4.5 MHz determined for axial ligands. Since His332 is in equatorial position in structure $S_0\text{-3}$ (and all others as well), model $S_0\text{-3}$ is inconsistent with our experimental data. Same as for the ^{55}Mn tensors, the larger hyperfine anisotropy A_{iso} compared to the S_0 state may well be a result of stronger contributions of fine structure interactions from an increased number of Mn^{III} ions.

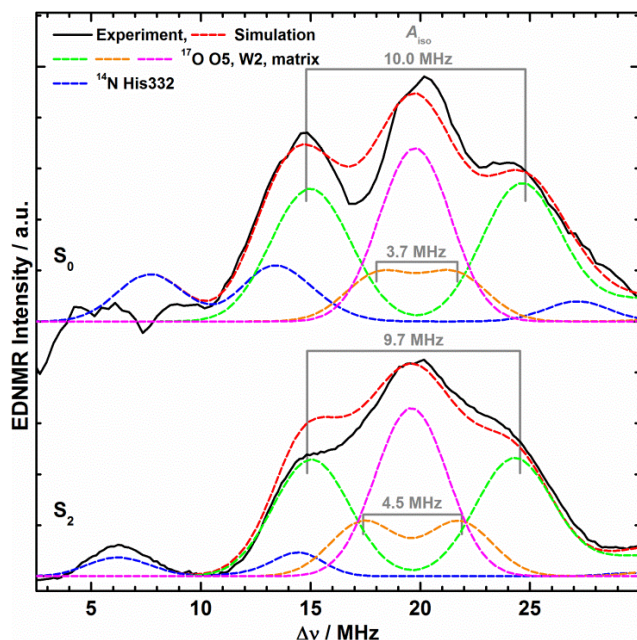


Figure 5. W-band EDNMR spectra of H_2^{17}O -exchanged PSII samples isolated from *T. elongatus* in the 3-flash-advanced S_0 (top) and in the S_2 (bottom) state. Black solid traces depict the single-quantum region of background-corrected experimental spectra; superimposing red dashed traces represent simulations based on the spin Hamiltonian formalism as outlined in sections 2.3, S2 and S3. Colored dashed lines represent a decomposition of the simulation showing contributions from the individual ^{14}N and ^{17}O nuclei. The optimized parameter sets are listed in Table 3. The S_2 state traces were originally published in Ref.²³. Double-quantum regions are shown in Figure S8. Experimental parameters: see Figure S8.

3.5 Interactions with water-derived ligands.

3.5.1 Interactions with exchangeable ^{17}O species. As recently demonstrated in our laboratory,^{19,102} the sensitive EDNMR experiment at W-band is superior to techniques suffering from fast T_1 relaxation, such as ENDOR, for measuring nuclei with a small gyromagnetic ratio. As such, we found it to be the method of choice to characterize interactions of ^{17}O with the Mn tetramer of the OEC,^{19,22,23} particularly in the fast relaxing S_0 state (Supporting Information section S8.2). Figure 5 shows spectra and simulations (see sections 2.3, S2 and S3) of the single-quantum region for the 3-flash-advanced S_0 and the S_2 state²³ after H_2^{17}O buffer exchange in the S_2 state (see Figure S8 for the double-quantum region) at central multiline field positions. The S_0 state spectral profile is similar in appearance to that of the S_2 state,^{19,22,23} yet slightly broader. Additionally, at frequencies ≥ 40 MHz,⁵⁵Mn resonances attributable to the smallest ^{55}Mn hyperfine coupling A_4 (Table 2, see also section 4.1) are present, superimposed on the ^{17}O double-quantum region. Thus, spectral simulations employing four different species of interacting nuclei, same as in S_2 , served to reproduce the single- (≈ 28 MHz) and double-quantum (≥ 25 MHz) envelopes. They represent the His332 imino- ^{14}N ligand and three classes of ^{17}O interactions of different strength. The simulation parameters for the imino- ^{14}N (blue) are those described in section 3.4. The ^{17}O hyperfine tensors as compared to the S_2 state are the same for the weakly coupling species (magenta); for the intermediate (orange) and strong (green) interaction, A_{dip} and A_{H} were kept the same, whereas A_{iso} was allowed to vary (Table 3). Smaller intermediate (S_0 : 3.7 MHz, S_2 : 4.5 MHz) and slightly larger strong (S_0 : 10.0 MHz, S_2 : 9.7 MHz) isotropic hyperfine components were obtained. Also their relative single-, as well as double-quantum intensities are similar to the S_2 state. Thus we can likewise assign them to (i) terminal and matrix waters (including ligand W1 of Mn_{A4} and two H_2O ligands at the Ca^{2+} ion), (ii) the hydroxide ion W2 bound terminally to Mn_{A4} (iii) and a bridging oxygen. The intermediately and weakly coupled species thus comprise the four first-coordination sphere $\text{H}_2\text{O}/\text{OH}^-$ ligands identified in the PSII crystal structure and present in our models $S_0\text{-1}$ and $S_0\text{-3}$ (Figure 2). The assignment of the bridging species can only be made on the basis of the specific S_0 state model (section 4.2). Considering the similar intensity, we can conclude that the signal originates from only one bridging ^{17}O species, as demonstrated for the S_2 state by the lack of a ^{17}O line broadening in X-band CW multiline spectra.²³

3.5.2 Interactions with exchangeable $^1\text{H}^2\text{H}$ species. Both S_0 state models consistent with our EPR/ ^{55}Mn ENDOR results, $S_0\text{-1}$ and $S_0\text{-3}$, (section 3.3) contain a μ -hydroxo bridge as part of the binding motif between $\text{Mn}_{\text{A4}}^{\text{III}}$ and $\text{Mn}_{\text{B3}}^{\text{III}}$ (Figure 2). Whether this is O5 ($S_0\text{-1}$) or O4 ($S_0\text{-3}$), the bound proton should exhibit a comparatively strong electron-nuclear interaction with the Mn tetramer. Since ^2H -spectroscopies reduce the number of nuclei contributing to our spectra to only the exchangeable H/D sites, we employed Q-band two-pulse and three-pulse ESEEM, three-pulse vs. two-pulse and HYSORE experiments on 3-flash-advanced S_0 state PSII samples after D_2O buffer exchange. Besides deuterons of potential substrates rebound upon illumination, all O- and N-bound ^2H , quantitatively exchanged in the PSII core preparations during incubation for least 2 h, will also be visible in the spectra.

Figure S9 in the Supporting Information depicts Q-band

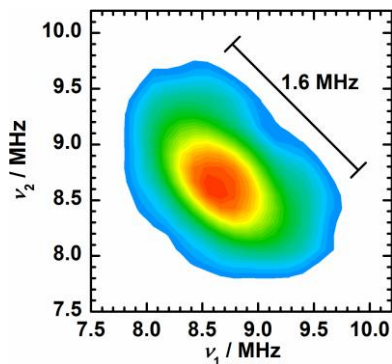


Figure 6. Section of the (+,+) quadrant of the Fourier-transformed Q-band HYSCORE spectrum of a $^2\text{H}_2\text{O}$ -exchanged PSII sample in the 3-flash-advanced S_0 state isolated from *T. elongatus*, measured at $g = 1.832$, the high field edge of the corresponding Q-band multiline EPR spectrum. The full frequency space of the (+,+) quadrant is depicted in Figure S10B. Experimental parameters: see Figure S10.

two-pulse and three-pulse ESEEM spectra at low (1194 mT, $g = 2.035$) and high (1326 mT, $g = 1.832$) field positions of the corresponding Q-band multiline EPR spectrum at optimum microwave pulse settings for the $S_T = 1/2$ S_0 state ($\pi/2 = 12$ ns, microwave power setting: 20 mW) and for high spin systems ($\pi/2 = 8$ ns, 3 mW). At high field, the Fourier-transform contain superimposed sharp ^2H and broader ^{14}N (His332) signals centered at their respective Larmor frequencies, while at low field, the ^2H peak is comparatively larger. However, as the comparison of the two pulse settings shows, it is dominated by resonances from the water ligands of Mn^{II} -hexaquo ($S_T = 5/2$) contaminants. The high-spin pulse settings demonstrate that at 1326 mT, in contrast, virtually no Mn^{II} -hexaquo signals are detected. Thus, experiments are preferentially performed at high field. By extension to two dimensions, the separation of ^2H from ^{14}N resonances is improved. While the two-pulse and three-pulse vs. two-pulse (Supporting Information Figure S10A) ESEEM spectra also display double-quantum resonances, these are largely suppressed in 3-pulse ESEEM and HYSCORE (Figure S10B) experiments.

Figure 6 shows the ^2H peak centered at the Larmor frequency $\nu_n = 8.67$ MHz in the Q-band HYSCORE spectrum. As the modulations of the time traces result from the entire interacting neighboring ^2H nuclei, their simulation is not straightforward for a highly complex system like the OEC. In the vicinity of the Mn tetramer, a large number of $^1\text{H}/^2\text{H}$ nuclei exhibit considerable dipolar coupling,¹⁹ dominantly contributing to the spectra, while our interest is directed at only one particular nucleus. In this case, visual inspection of the spectrum in frequency space can give us an estimate of the largest coupling present. As indicated in Figure 6, a ^2H hyperfine splitting as large as 1.6 MHz is apparent from the width of the superimposed peak. It corresponds to a ^1H hyperfine coupling of 10.4 MHz, which is slightly above the calculated through-space dipolar coupling of 8 MHz for a hypothetical proton on O5 in the S_2 state model.¹⁹ This larger splitting can also be discriminated from the “unsplit” central matrix line as it resolves a bipartite structure. This suggests the presence of a μ -hydroxo bridge in the S_0 state, based on models $\text{S}_0\text{-1}$ and $\text{S}_0\text{-3}$ between $\text{Mn}_{\text{A4}}^{\text{III}}$ and $\text{Mn}_{\text{B3}}^{\text{III}}$.

4. DISCUSSION

4.1 The S_0 state exhibits a tetrameric $\text{Mn}^{\text{III}}_3\text{Mn}^{\text{IV}}$ open-cubane core topology. Similar to the successful approach employed in our recent analysis of the S_2 state,²³ the techniques of EPR/ ^{55}Mn -ENDOR and ^{14}N -ESEEM/HYSCORE/EDNMR spectroscopy in combination with extensive theoretical calculations allowed us to test the feasibility of models for the S_0 state of the OEC. Of the two possible models identified, we favour $\text{S}_0\text{-1}$ (O5-H) over $\text{S}_0\text{-3}$ (O4-H) for the following reasons: (i) the 4.9 kcal mol $^{-1}$ lower relative energy, (ii) the determined hyperfine coupling of the equatorial His332-imino- ^{14}N ligand consistent with the large Mn_{D1} spin projection factor $\rho_{\text{D1,iso}} > 1.5$, and (iii) the mechanistic consideration that the proton of the μ -hydroxo bridge is associated with O5 from the same water molecule. Furthermore, its low ground-to-first excited state energy barrier $\Delta \approx 2$ cm $^{-1}$ is consistent with inversion recovery experiments (Supporting Information section S8).

Considering our previous work on the S_2 state of the OEC^{14,17,18} together with our new results on S_0 , as well as information from Mn model complexes,⁷¹ a general pattern emerges for the conditions for the formation of a total spin $S_T = 1/2$ ground state in the $\text{Mn}_4\text{O}_5\text{Ca}$ tetrameric clusters. Both with the $\text{Mn}^{\text{III}}_3\text{Mn}^{\text{IV}}$ and $\text{Mn}^{\text{III}}\text{Mn}^{\text{IV}}_3$ valence state patterns of S_0 and S_2 , respectively, our theoretical examinations find the experimental $S_T = 1/2$ to require an open-cubane motif to exhibit a corresponding exchange-coupling scheme. Spectroscopic and all our theoretical results^{14-18,23,42,86} evidence a tetramer spin projection model for these states, in which all four Mn ions contribute to the ground spin states. Since this is not a general property of all $S_T = 1/2$ models (compare *e.g.* the dimer of dimers), but specific to the $S_T = 1/2$ states of the OEC, this can be used as a criterion for the selection of plausible models for these states.

In contrast to ^{55}Mn -ENDOR signals of various S_0 and S_2 state forms between 55 and 215 MHz, entailing four effective ^{55}Mn A tensors of similar magnitude ($A_{\text{iso}} = 180\text{-}340$ MHz),^{15,16,22,23,42,85,93} the Pace group recently presented S_2 state spectra at 2.5 K, which showed sharp resonances up to 350 MHz.¹⁰³ Since our measurements on the cyanobacterial S_2 state at 2.5 K (not shown) reveal the same basic spectrum as at 4.8 K (Figure S2C), we conclude that also our S_0 state spectra do include the entire resonances from all four Mn ions. A dimer-of-dimers model comprising Mn ions with $|\rho_{\text{C2,iso}}| \ll 1$ and corresponding small effective hyperfine couplings can also be ruled out by our EDNMR experiments (Figures 5, S8), also on the S_2 state^{19,22,23}, as these spectra do not feature ^{55}Mn resonances close to the central hole, overlapping with the ^{14}N and ^{17}O single-quantum transitions. In S_0 , the ^{55}Mn peak of lowest frequency corresponds to a minimum $A_{4,\text{iso}} \approx 170$ MHz, consistent with our ^{55}Mn -ENDOR results (Table 2).

4.2 The slowly exchanging substrate W_s is the μ -hydroxo bridge O5 in S_0 . While ^2H ESEEM and HYSCORE experiments are not able to resolve the many smaller water interactions, in contrast to X-band matrix ENDOR on spinach PSII,¹⁰⁴ Q-band ^2H HYSCORE at the high field edge on cyanobacterial PSII reveals the presence of a large splitting of 1.6 MHz. As a result of the identification of model $\text{S}_0\text{-1}$ for the S_0 state OEC, we can assign it to the proton/deuteron bound to O5. Our novel W-band EDNMR ^{17}O signals (Figure 5) are the first experimental evidence for water-derived ligands interacting with the Mn tetramer of the OEC in the S_0 state. The as-

segment of the weakly and intermediately coupling species is relatively straightforward on basis of the S_0 state models (Figure 2) due to their similar spectral appearance and simulation parameters compared to the S_2 state (section 3.5.1). The experimental observation of an intermediate coupling, clearly identifiable by its large double-quantum intensity, demonstrates the presence of a terminal OH⁻ ligand (W2) of a Mn ion in S_0 , further supporting our S_0 state model (Figure 2). In contrast, to assign the strong coupling to one of the oxygen bridges, knowledge of the spatial and electronic OEC structure is necessary. On the basis of the identified S_0 structure **S₀-1**, we assign the strongly coupling ^{17}O to the μ -hydroxo bridge O5 between $\text{Mn}_{\text{A4}}^{\text{III}}$ and $\text{Mn}_{\text{B3}}^{\text{III}}$ for the following reasons: (i) The hyperfine splitting is nearly identical to the exchangeable O5 in the S_2 state, owing to the similar absolute spin projection factors in the two $S_T = 1/2$ states of Mn_{A4} (S_0 : 1.1, S_2 : 1.1) and Mn_{B3} (S_0 : 1.2, S_2 : 0.9). An increase in coupling strength as a ligand along the Jahn-Teller axis of $\text{Mn}_{\text{B3}}^{\text{III}}$ may be compensated by its protonation and increased Mn-O distances, 0.43 Å longer than in S_2 .¹⁸ In contrast, in the **S₀-3** model or if Mn_{A4} was in the +II oxidation state, $\rho_{\text{A4,iso}}$ (Figure 4C) and thus $A_{\text{O5,iso}}$ would be much larger. (ii) Its assignment in the S_2 state as the slowly exchanging substrate W_s ²³ requires O5 to rebind during the S_4 -to- S_0 transition, most probably representing W_s also in S_0 . Its origination from a substrate water molecule is further supported by the bound proton in the identified S_0 structure. (iii) The bound proton enables fast exchange of O5, shown to be exchangeable in S_1 and to be a μ -oxo bridge in S_2 ,^{22,23} consistent with the experimental higher W_s rate constants than in the S_1 and S_2 states (S_0 : 8-10 s⁻¹, S_1 : 0.02 s⁻¹, S_2 : 2 s⁻¹ in spinach thylakoid membranes at 10 °C).^{105,106} Furthermore, the significantly smaller exchange coupling J_{AB} between Mn_{A4} and Mn_{B3} in S_0 (Table S2) than in S_2 (Table S1), also concluded by Kulik *et al.*,⁴² is entirely consistent with the experimental detection of a strong ^2H coupling arising from a μ -hydroxo bridge in S_0 (section 3.5.2) but not in S_2 .^{19,107-109}

4.3 Mechanism of photosynthetic water oxidation catalysis in the low S states. The outcome of this work and of previous work on the S_2 state,¹⁴⁻²³ combined with further information, especially on substrate exchange rates,^{105,106,110} allow

us to draw a detailed picture of the first half of the catalytic cycle of light-driven water oxidation by the OEC. It is noted that this could only be achieved by the combination of theoretical model construction and experimental characterization to provide essential selection constraints. This way, BS-DFT computations and EPR spectroscopy together yield a detailed, consistent picture of Mn oxidation states and ligand interactions of the OEC in the S_0 and S_2 states, the requirement for any mechanistic considerations. This leads to the following reaction sequence (Figure 7): (i) During the spontaneous transition from the transient state S_4 to S_0 , the loss of four oxidation equivalents and release of O_2 are followed by the uptake of W_s , incorporated at the O5 position as a μ -hydroxo bridge. Thereby a proton is released, which is demonstrated by the inconsistency of all models containing an additional proton (sections 3.1-3.3). (ii) The light-driven transition to S_1 proceeds most probably via oxidation of $\text{Mn}_{\text{B3}}^{\text{III}}$ to $\text{Mn}_{\text{B3}}^{\text{IV}}$ and release of the proton bound to O5 (see Refs. ^{5,42,76,110}). The proton-coupled electron transfer results in shortening of the $\text{Mn}_{\text{A4}}^{\text{III}}$ - $\text{Mn}_{\text{B3}}^{\text{IV}}$ distance^{77,78} and the significant decrease of the W_s exchange rate. (iii) Upon light-induced oxidation of $\text{Mn}_{\text{A4}}^{\text{III}}$ to $\text{Mn}_{\text{A4}}^{\text{IV}}$ without release of a proton (see Refs. ^{5,72,110}), the $\text{Mn}_4\text{O}_5\text{Ca}$ arrives at the structurally flexible¹⁸ S_2 state, enabling W_s exchange at increased rate. For completing our knowledge of the catalytic cycle, lacking the transitions to S_3 and S_4 , which involve the most important process of O-O bond formation, the next step will be to extend our approach to obtain a precise picture of the S_3 state.

ASSOCIATED CONTENT

Data processing: baseline correction and light-minus-dark subtraction; spectral simulations; theoretical background; experimental details of the EPR measurements; multifrequency EPR and ^{55}Mn ENDOR spectra and simulations of the S_2 and S_0 states; the S_2 state: EPR/ ^{55}Mn ENDOR simulation parameters, Mn exchange couplings, fine structure interactions and spin projections; electronic structure of the S_0 state: spin projections, ^{55}Mn hyperfine couplings and Mn fine structure interactions; T_1 relaxation and

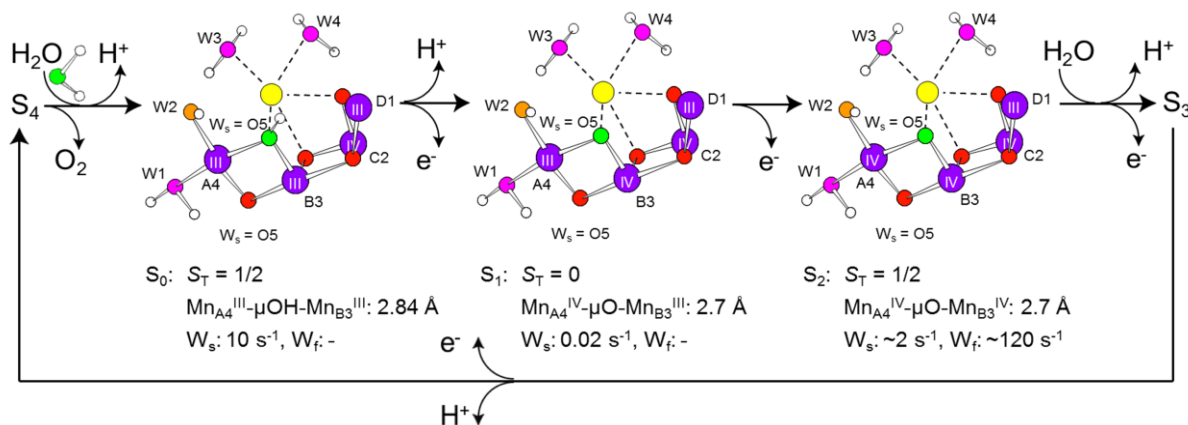


Figure 7. Catalytic mechanism of photosynthetic water oxidation in the low S states: schematic models of the $\text{Mn}_4\text{O}_5\text{Ca}$ clusters including directly bound $\text{H}_2\text{O}/\text{OH}^-$ ligands in the states S_0 , S_1 and S_2 of the Kok cycle, visualizing Mn oxidation state changes, substrate binding, deprotonation and oxygen release events as deduced from the results presented in this work. Furthermore, the corresponding total ground spin states S_T , $\text{Mn}_{\text{A4}}\text{-Mn}_{\text{B3}}$ distances as indicated by EXAFS^{77,78} and binding motifs, as well as exchange rates of the slowly (W_s) and fast (W_f) exchanging substrates^{105,106} are given. Mn ions are depicted in purple, Ca in yellow, non-exchangeable O in red, exchangeable O in green, orange and magenta as in Figure 5, and H in white and black.

spin state ladder: Q-band inversion recovery experiments and analysis; the Mn_{D1}-His332-imino-N interaction: field- and τ -dependent Q-band ¹⁴N-three-pulse ESEEM and ¹⁴N-HYSCORE experiments and interpretation of the simulation parameters; W-band ELDOR-detected NMR experiments; Interactions with exchangeable ¹H/²H species: Q-band ²H-two-pulse, ²H-three-pulse and ²H-three-pulse vs. two -pulse ESEEM and ²H-HYSCORE experiments; general considerations on the experimental approach. This material is available free of charge via the Internet at <http://pubs.acs.org>.

AUTHOR INFORMATION

Corresponding Author

* E-mail: nicholas.cox@cec.mpg.de, Phone: +49 208 306 3552, Fax: +49 208 306 3955.

Author Contributions

The manuscript was written through contributions of all authors. All authors have given approval to the final version of the manuscript.

Notes

The authors declare no competing financial interest.

ACKNOWLEDGMENT

Financial support was provided by The Max-Planck-Gesellschaft, the "Bioenergie" program of the Commissariat à l'Énergie Atomique et aux Énergies Alternatives, the program FRISBI, the EU SOLAR-H2 initiative (FP7 contract 212508). T. L. was supported by the Federal Ministry of Education and Research of Germany (BMBF) in the framework of the Bio-H2 project (03SF0355C).

ABBREVIATIONS

photosystem II; OEC, oxygen evolving complex; II, EPR, electron paramagnetic resonance; ENDOR, electron-nuclear double resonance; BS, broken-symmetry; *T.*, *Thermosynechococcus*; PPBQ, phenyl-*p*-benzoquinone; DMSO, dimethyl sulfoxide; CW, continuous wave; RF, radio frequency; NQI, nuclear quadrupole interaction; EDNMR, electron-electron double resonance-detected nuclear magnetic resonance; DFT, density functional theory; EXAFS, extended X-ray absorption fine structure; QM/MM, quantum mechanics/molecular mechanics; ESE, electron spin echo; ESEEM, electron spin echo envelope modulation; HYSCORE, hyperfine sublevel correlation.

REFERENCES

- (1) Ferreira, K. N.; Iverson, T. M.; Maghlaoui, K.; Barber, J.; Iwata, S. *Science* **2004**, *303*, 1831.
- (2) Guskov, A.; Kern, J.; Gabdulkhakov, A.; Broser, M.; Zouni, A.; Saenger, W. *Nat. Struct. Mol. Biol.* **2009**, *16*, 334.
- (3) Umena, Y.; Kawakami, K.; Shen, J.-R.; Kamiya, N. *Nature* **2011**, *473*, 55.
- (4) Suga, M.; Akita, F.; Hirata, K.; Ueno, G.; Murakami, H.; Nakajima, Y.; Shimizu, T.; Yamashita, K.; Yamamoto, M.; Ago, H.; Shen, J. R. *Nature* **2015**, *517*, 99.
- (5) McEvoy, J. P.; Brudvig, G. W. *Chem. Rev.* **2006**, *106*, 4455.
- (6) Cox, N.; Pantazis, D. A.; Neese, F.; Lubitz, W. *Acc. Chem. Res.* **2013**, *46*, 1588.
- (7) Yano, J.; Yachandra, V. *Chem. Rev.* **2014**, *114*, 4175.
- (8) Joliot, P.; Barbieri, G.; Chabaud, R. *Photochem. Photobiol.* **1969**, *10*, 309.
- (9) Diner, B. A.; Britt, R. D. In *Photosystem II: The Light-Driven Water:Plastoquinone Oxidoreductase*; Wydrzynski, T. J.,

Satoh, K., Freeman, J. A., Eds.; Springer: Dordrecht, 2005; Vol. 1, p 207.

- (10) Meyer, T. J.; Huynh, M. H. V.; Thorp, H. H. *Angew. Chem., Int. Ed.* **2007**, *46*, 5284.
- (11) Kok, B.; Forbush, B.; McGloin, M. *Photochem. Photobiol.* **1970**, *11*.
- (12) Galstyan, A.; Robertazzi, A.; Knapp, E. W. *J. Am. Chem. Soc.* **2012**, *134*, 7442.
- (13) Yano, J.; Kern, J.; Irrgang, K. D.; Latimer, M. J.; Bergmann, U.; Glatzel, P.; Pushkar, Y.; Biesiadka, J.; Loll, B.; Sauer, K.; Messinger, J.; Zouni, A.; Yachandra, V. K. *Proc. Natl. Acad. Sci. U. S. A.* **2005**, *102*, 12047.
- (14) Pantazis, D. A.; Orio, M.; Petrenko, T.; Zein, S.; Lubitz, W.; Messinger, J.; Neese, F. *Phys. Chem. Chem. Phys.* **2009**, *11*, 6788.
- (15) Cox, N.; Rapatskiy, L.; Su, J.-H.; Pantazis, D. A.; Sugiura, M.; Kulik, L.; Dorlet, P.; Rutherford, A. W.; Neese, F.; Boussac, A.; Lubitz, W.; Messinger, J. *J. Am. Chem. Soc.* **2011**, *133*, 3635.
- (16) Su, J. H.; Cox, N.; Ames, W.; Pantazis, D. A.; Rapatskiy, L.; Lohmiller, T.; Kulik, L. V.; Dorlet, P.; Rutherford, A. W.; Neese, F.; Boussac, A.; Lubitz, W.; Messinger, J. *Biochim. Biophys. Acta, Bioenerg.* **2011**, *1807*, 829.
- (17) Ames, W.; Pantazis, D. A.; Krewald, V.; Cox, N.; Messinger, J.; Lubitz, W.; Neese, F. *J. Am. Chem. Soc.* **2011**, *133*, 19743.
- (18) Pantazis, D. A.; Ames, W.; Cox, N.; Lubitz, W.; Neese, F. *Angew. Chem., Int. Ed.* **2012**, *51*, 9935.
- (19) Rapatskiy, L.; Cox, N.; Savitsky, A.; Ames, W. M.; Sander, J.; Nowaczyk, M. M.; Rögner, M.; Boussac, A.; Neese, F.; Messinger, J.; Lubitz, W. *J. Am. Chem. Soc.* **2012**, *134*, 16619.
- (20) Lohmiller, T.; Ames, W.; Lubitz, W.; Cox, N.; Misra, S. K. *Appl. Magn. Reson.* **2013**, *44*, 691.
- (21) Retegan, M.; Neese, F.; Pantazis, D. A. *J. Chem. Theory Comput.* **2013**, *9*, 3832.
- (22) Pérez Navarro, M.; Ames, W. M.; Nilsson, H.; Lohmiller, T.; Pantazis, D. A.; Rapatskiy, L.; Nowaczyk, M. M.; Neese, F.; Boussac, A.; Messinger, J.; Lubitz, W.; Cox, N. *Proc. Natl. Acad. Sci. U. S. A.* **2013**, *110*, 15561.
- (23) Lohmiller, T.; Krewald, V.; Pérez Navarro, M.; Retegan, M.; Rapatskiy, L.; Nowaczyk, M. M.; Boussac, A.; Neese, F.; Lubitz, W.; Pantazis, D. A.; Cox, N. *Phys. Chem. Chem. Phys.* **2014**, *16*, 11877.
- (24) Jaszewski, A. R.; Petrie, S.; Pace, R. J.; Stranger, R. *Chem.-Eur. J.* **2011**, *17*, 5699.
- (25) Pace, R. J.; Jin, L.; Stranger, R. *Dalton Trans.* **2012**, *41*, 11145.
- (26) Siegbahn, P. E. M. *Acc. Chem. Res.* **2009**, *42*, 1871.
- (27) Kurashige, Y.; Chan, G. K. L.; Yanai, T. *Nat. Chem.* **2013**, *5*, 660.
- (28) Dismukes, G. C.; Siderer, Y. *Proc. Natl. Acad. Sci. U. S. A.* **1981**, *78*, 274.
- (29) Casey, J. L.; Sauer, K. *Biochim. Biophys. Acta, Bioenerg.* **1984**, *767*, 21.
- (30) Zimmermann, J. L.; Rutherford, A. W. *Biochemistry* **1986**, *25*, 4609.
- (31) Pace, R. J.; Smith, P. J.; Bramley, R.; Stehlik, D. *Biochim. Biophys. Acta, Bioenerg.* **1991**, *1058*, 161.
- (32) Boussac, A. *J. Biol. Inorg. Chem.* **1997**, *2*, 580.
- (33) Horner, O.; Rivière, E.; Blondin, G.; Un, S.; Rutherford, A. W.; Girerd, J.-J.; Boussac, A. *J. Am. Chem. Soc.* **1998**, *120*, 7924.
- (34) Boussac, A.; Rutherford, A. W. *Biochim. Biophys. Acta, Bioenerg.* **2000**, *1457*, 145.
- (35) Haddy, A.; Lakshmi, K. V.; Brudvig, G. W.; Frank, H. A. *Biophys. J.* **2004**, *87*, 2885.
- (36) Messinger, J.; Nugent, J. H. A.; Evans, M. C. W. *Biochemistry* **1997**, *36*, 11055.
- (37) Åhring, K. A.; Peterson, S.; Styring, S. *Biochemistry* **1997**, *36*, 13148.
- (38) Messinger, J.; Robblee, J. H.; Yu, W. O.; Sauer, K.; Yachandra, V. K.; Klein, M. P. *J. Am. Chem. Soc.* **1997**, *119*, 11349.

- (39) Åhrling, K. A.; Peterson, S.; Styring, S. *Biochemistry* **1998**, *37*, 8115.
- (40) Boussac, A.; Kuhl, H.; Ghibaudi, E.; Rogner, M.; Rutherford, A. W. *Biochemistry* **1999**, *38*, 11942.
- (41) Boussac, A.; Sugiura, M.; Inoue, Y.; Rutherford, A. W. *Biochemistry* **2000**, *39*, 13788.
- (42) Kulik, L. V.; Epel, B.; Lubitz, W.; Messinger, J. *J. Am. Chem. Soc.* **2007**, *129*, 13421.
- (43) Sugiura, M.; Boussac, A.; Noguchi, T.; Rappaport, F. *Biochim. Biophys. Acta, Bioenerg.* **2008**, *1777*, 331.
- (44) Sugiura, M.; Rappaport, F.; Brettel, K.; Noguchi, T.; Rutherford, A. W.; Boussac, A. *Biochemistry* **2004**, *43*, 13549.
- (45) Boussac, A.; Rappaport, F.; Carrier, P.; Verbavatz, J. M.; Gobin, R.; Kirilovsky, D.; Rutherford, A. W.; Sugiura, M. *J. Biol. Chem.* **2004**, *279*, 22809.
- (46) Ishida, N.; Sugiura, M.; Rappaport, F.; Lai, T. L.; Rutherford, A. W.; Boussac, A. *J. Biol. Chem.* **2008**, *283*, 13330.
- (47) Reijerse, E.; Lendzian, F.; Isaacson, R.; Lubitz, W. *J. Magn. Reson.* **2012**, *214*, 237.
- (48) Stoll, S.; Schweiger, A. *J. Magn. Reson.* **2006**, *178*, 42.
- (49) Neese, F. *Wiley Interdiscip. Rev.: Comput. Mol. Sci.* **2012**, *2*, 73.
- (50) Perdew, J. P. *Physical Review B* **1986**, *33*, 8822.
- (51) Becke, A. D. *Phys. Rev. A* **1988**, *38*, 3098.
- (52) Grimme, S.; Antony, J.; Ehrlich, S.; Krieg, H. *Journal of Chemical Physics* **2010**, *132*, 154104.
- (53) van Lenthe, E.; Baerends, E. J.; Snijders, J. G. *Journal of Chemical Physics* **1993**, *99*, 4597.
- (54) van Lenthe, E.; Baerends, E. J.; Snijders, J. G. *J. Chem. Phys.* **1994**, *101*, 9783.
- (55) Pantazis, D. A.; Chen, X. Y.; Landis, C. R.; Neese, F. *Journal of Chemical Theory and Computation* **2008**, *4*, 908.
- (56) Schäfer, A.; Huber, C.; Ahlrichs, R. *J. Chem. Phys.* **1994**, *100*, 5829.
- (57) Weigend, F. *Physical Chemistry Chemical Physics* **2006**, *8*, 1057.
- (58) Klamt, A.; Schürman, D. *Journal of the Chemical Society, Perkin Transactions 2: Physical Organic Chemistry* **1993**, 799.
- (59) Bencini, A.; Totti, F. *Journal of Chemical Theory and Computation* **2009**, *5*, 144.
- (60) Orio, M.; Pantazis, D. A.; Neese, F. *Photosynthesis Research* **2009**, *102*, 443.
- (61) Neese, F.; Ames, W.; Christian, G.; Kampa, M.; Liakos, D. G.; Pantazis, D. A.; Roemelt, M.; Surawatanawong, P.; Ye, S. F. *Advances in Inorganic Chemistry* **2010**, *62*, 301.
- (62) Pantazis, D. A.; Krewald, V.; Orio, M.; Neese, F. *Dalton Transactions* **2010**, *39*, 4959.
- (63) Staroverov, V. N.; Scuseria, G. E.; Tao, J.; Perdew, J. P. *J. Chem. Phys.* **2003**, *119*, 12129.
- (64) Kossmann, S.; Kirchner, B.; Neese, F. *Mol. Phys.* **2007**, *105*, 2049.
- (65) Jensen, K. P. *Inorganic Chemistry* **2008**, *47*, 10357.
- (66) Röemelt, M.; Ye, S. F.; Neese, F. *Inorganic Chemistry* **2009**, *48*, 784.
- (67) Pantazis, D. A.; McGrady, J. E.; Maseras, F.; Etienne, M. *Journal of Chemical Theory and Computation* **2007**, *3*, 1329.
- (68) Pantazis, D. A.; Orio, M.; Petrenko, T.; Zein, S.; Bill, E.; Lubitz, W.; Messinger, J.; Neese, F. *Chem.-Eur. J.* **2009**, *15*, 5108.
- (69) Neese, F.; Wennmohs, F.; Hansen, A.; Becker, U. *Chemical Physics* **2009**, *356*, 98.
- (70) Orio, M.; Pantazis, D. A.; Petrenko, T.; Neese, F. *Inorganic Chemistry* **2009**, *48*, 7251.
- (71) Krewald, V.; Neese, F.; Pantazis, D. A. *J. Am. Chem. Soc.* **2013**, *135*, 5726.
- (72) Siegbahn, P. E. M. *Biochim. Biophys. Acta, Bioenerg.* **2013**, *1827*, 1003.
- (73) Ichino, T.; Yoshioka, Y. *Chem. Phys. Lett.* **2012**, *545*, 107.
- (74) Isobe, H.; Shoji, M.; Yamanaka, S.; Umena, Y.; Kawakami, K.; Kamiya, N.; Shen, J. R.; Yamaguchi, K. *Dalton Trans.* **2012**, *41*, 13727.
- (75) Yamaguchi, K.; Yamanaka, S.; Isobe, H.; Saito, T.; Kanda, K.; Umena, Y.; Kawakami, K.; Shen, J. R.; Kamiya, N.; Okumura, M.; Nakamura, H.; Shoji, M.; Yoshioka, Y. *Int. J. Quantum Chem.* **2013**, *113*, 453.
- (76) Pal, R.; Negre, C. F.; Vogt, L.; Pokhrel, R.; Ertem, M. Z.; Brudvig, G. W.; Batista, V. S. *Biochemistry* **2013**, *52*, 7703.
- (77) Robblee, J. H.; Messinger, J.; Cinco, R. M.; McFarlane, K. L.; Fernandez, C.; Pizarro, S. A.; Sauer, K.; Yachandra, V. K. *J. Am. Chem. Soc.* **2002**, *124*, 7459.
- (78) Haumann, M.; Müller, C.; Liebisch, P.; Iuzzolino, L.; Dittmer, J.; Grabolle, M.; Neisius, T.; Meyer-Klaucke, W.; Dau, H. *Biochemistry* **2005**, *44*, 1894.
- (79) Pushkar, Y. L.; Yano, J.; Sauer, K.; Boussac, A.; Yachandra, V. K. *Proc. Natl. Acad. Sci. U. S. A.* **2008**, *105*, 1879.
- (80) Baffert, C.; Orio, M.; Pantazis, D. A.; Duboc, C.; Blackman, A. G.; Blondin, G.; Neese, F.; Deronzier, A.; Collomb, M.-N. *Inorganic Chemistry* **2009**, *48*, 10281.
- (81) Boussac, A.; Kuhl, H.; Un, S.; Rögner, M.; Rutherford, A. W. *Biochemistry* **1998**, *37*, 8995.
- (82) Deák, Z.; Peterson, S.; Geijer, P.; Åhrling, K. A.; Styring, S. *Biochim. Biophys. Acta, Bioenerg.* **1999**, *1412*, 240.
- (83) Pudollek, S.; Lendzian, F.; Bittl, R. *Biochem. Soc. Trans.* **2008**, *36*, 1001.
- (84) Kulik, L.; Epel, B.; Messinger, J.; Lubitz, W. *Photosynth. Res.* **2005**, *84*, 347.
- (85) Pudollek, S., Doctoral Thesis, Freie Universität Berlin, 2012.
- (86) Peloquin, J. M.; Campbell, K. A.; Randall, D. W.; Evanchik, M. A.; Pecoraro, V. L.; Armstrong, W. H.; Britt, R. D. *J. Am. Chem. Soc.* **2000**, *122*, 10926.
- (87) Teutloff, C.; Kessen, S.; Kern, J.; Zouni, A.; Bittl, R. *FEBS Lett.* **2006**, *580*, 3605.
- (88) Matsuoka, H.; Furukawa, K.; Kato, T.; Mino, H.; Shen, J. R.; Kawamori, A. *J. Phys. Chem. B.* **2006**, *110*, 13242.
- (89) Zheng, M.; Khangulov, S. V.; Dismukes, G. C.; Barynin, V. V. *Inorg. Chem.* **1994**, *33*, 382.
- (90) Sturgeon, B. E.; Ball, J. A.; Randall, D. W.; Britt, R. D. *J. Phys. Chem.* **1994**, *98*, 12871.
- (91) Cox, N.; Ames, W.; Epel, B.; Kulik, L. V.; Rapatskiy, L.; Neese, F.; Messinger, J.; Wieghardt, K.; Lubitz, W. *Inorg. Chem.* **2011**, *50*, 8238.
- (92) Schinzel, S.; Schraut, J.; Arbuznikov, A.; Siegbahn, P.; Kaupp, M. *Chem.-Eur. J.* **2010**, *16*, 10424.
- (93) Lohmiller, T.; Cox, N.; Su, J. H.; Messinger, J.; Lubitz, W. *J. Biol. Chem.* **2012**, *287*, 24721.
- (94) Jaszewski, A. R.; Stranger, R.; Pace, R. J. *J. Phys. Chem. B* **2011**, *115*, 4484.
- (95) Roelofs, T. A.; Liang, W.; Latimer, M. J.; Cinco, R. M.; Rompel, A.; Andrews, J. C.; Sauer, K.; Yachandra, V. K.; Klein, M. P. *Proc. Natl. Acad. Sci. U. S. A.* **1996**, *93*, 3335.
- (96) Iuzzolino, L.; Dittmer, J.; Dorner, W.; Meyer-Klaucke, W.; Dau, H. *Biochemistry* **1998**, *37*, 17112.
- (97) Messinger, J.; Robblee, J. H.; Bergmann, U.; Fernandez, C.; Glatzel, P.; Visser, H.; Cinco, R. M.; McFarlane, K. L.; Bellacchio, E.; Pizarro, S. A.; Cramer, S. P.; Sauer, K.; Klein, M. P.; Yachandra, V. K. *J. Am. Chem. Soc.* **2001**, *123*, 7804.
- (98) Schäfer, K. O.; Bittl, R.; Zweggart, W.; Lendzian, F.; Haselhorst, G.; Weyhermüller, T.; Wieghardt, K.; Lubitz, W. *J. Am. Chem. Soc.* **1998**, *120*, 13104.
- (99) Sinnecker, S.; Neese, F.; Lubitz, W. *J. Biol. Inorg. Chem.* **2005**, *10*, 231.
- (100) Stich, T. A.; Whittaker, J. W.; Britt, R. D. *J. Phys. Chem. B* **2010**, *114*, 14178.
- (101) Sinnecker, S.; Neese, F.; Noodleman, L.; Lubitz, W. *J. Am. Chem. Soc.* **2004**, *126*, 2613.
- (102) Cox, N.; Lubitz, W.; Savitsky, A. *Mol. Phys.* **2013**, *111*, 2788.
- (103) Jin, L.; Smith, P.; Noble, C. J.; Stranger, R.; Hanson, G. R.; Pace, R. J. *J. Phys. Chem. Chem. Phys.* **2014**, *16*, 7799.
- (104) Yamada, H.; Mino, H.; Itoh, S. *Biochim. Biophys. Acta, Bioenerg.* **2007**, *1767*, 197.

- (105) Hillier, W.; Wydrzynski, T. *Biochemistry* **2000**, *39*, 4399.
- (106) Hillier, W.; Wydrzynski, T. *Coord. Chem. Rev.* **2008**, *252*, 306.
- (107) Åhrling, K. A.; Evans, M. C. W.; Nugent, J. H. A.; Ball, R. J.; Pace, R. J. *Biochemistry* **2006**, *45*, 7069.
- (108) Aznar, C. P.; Britt, R. D. *Phil. Trans. R. Soc., B* **2002**, *357*, 1359.
- (109) Milikisiyants, S.; Chatterjee, R.; Coates, C. S.; Koua, F. H. M.; Shen, J. R.; Lakshmi, K. V. *Energy Environ. Sci.* **2012**, *5*, 7747.
- (110) Cox, N.; Messinger, J. *Biochim. Biophys. Acta, Bioenerg.* **2013**, *1827*, 1020.

Chapter 8

Summary and Outlook

In the present work, a combined approach of spectroscopic techniques, supported by theoretical calculations, was employed to study different $S_T = 1/2$ states of the OEC in PSII. An array of EPR spectroscopic experiments was successfully applied to the systems. It is shown that these provide a toolbox at hand for addressing various questions, such as Mn oxidation states, spin coupling schemes, ligand interactions, substrate binding and protonation states. Isotopic labelling of the buffer solution ($H_2^{17}O$, D_2O) was key for the characterization of the water-derived ligands to identify possible substrates. Defined perturbations of the Mn_4O_5Ca cluster in the S_2 state served to obtain information about the unperturbed, native system: (i) By Ca^{2+} depletion, it could be shown that the presence of Ca^{2+} is not crucial for the OEC to adopt the correct electronic structure. Instead, it is supposed to play a key role for access of substrate water to the catalyst and electron-coupled proton translocation towards the protein surface. (ii) Exchange of the Ca^{2+} for a Sr^{2+} ion and binding of NH_3 to the OEC allowed the definite assignment of O5 to be the only exchangeable μ -oxo bridge in the cluster and most likely the early binding, slowly exchanging substrate W_s (Figure 8.1). This finding is consistent with a very similar signal of a bridging oxygen detected in the S_0 state, supposedly bound to the regenerated catalyst in the process of S_0 state formation in the form of a hydroxide. Altogether, the outcome of this work is a self-consistent description of the first half of the mechanism of photosynthetic water-oxidation catalysis comprising the early S states S_0 to S_2 , as summarized in detail in the Discussion section of Chapter 7.

An exchangeable μ -oxo bridge serving as one of the substrates in this reaction is a novel concept. It has previously been disfavored due to lack of evidence in model systems for the OEC for such bridging oxygens exchanging rapidly with bulk solvent,^{1,2} *i.e.* on a seconds time scale, as observed in the S_1 state.³ However, as compared to di-Mn model complexes, the

OEC exhibits structural flexibility that allows the position of the exchangeable μ -oxo bridge O5 to change between two almost isoenergetic structures, the open (fused-twist) and the closed (cubane-like) conformations (Figure 8.1), interconverting through a high-energy transition state.⁴ This isomerism has first been shown for the S_2 state by theoretical evaluation of the structural basis for its $S_T = 1/2$ and $S_T = 5/2$ EPR signals,⁵ and has been similarly proposed for the S_1 state of the OEC.⁶ As a consequence, O5 is less tightly bound to the coordinated Mn ions than in the fixed geometries of the model systems, enabling its fast exchange. Another factor in this respect may be the nearby Ca^{2+} ion, the presence of which is critical for the conformational interconversion. While it does not affect the electronic configuration of the low-spin $S_T = 1/2$ state significantly, lack of the Ca^{2+} ion stabilizes this conformation, preventing formation of a high-spin $S_T = 5/2$ isomer. Furthermore, as a strong Lewis acid, Ca^{2+} possibly provides for the specific coordination environment of O5, thus lowering its binding constant K_A . For support of this suggestion, the absence of a signal from exchangeable O5 would have to be probed for the S_2' state in Ca^{2+} -depleted PSII samples suspended in H_2^{17}O buffer.

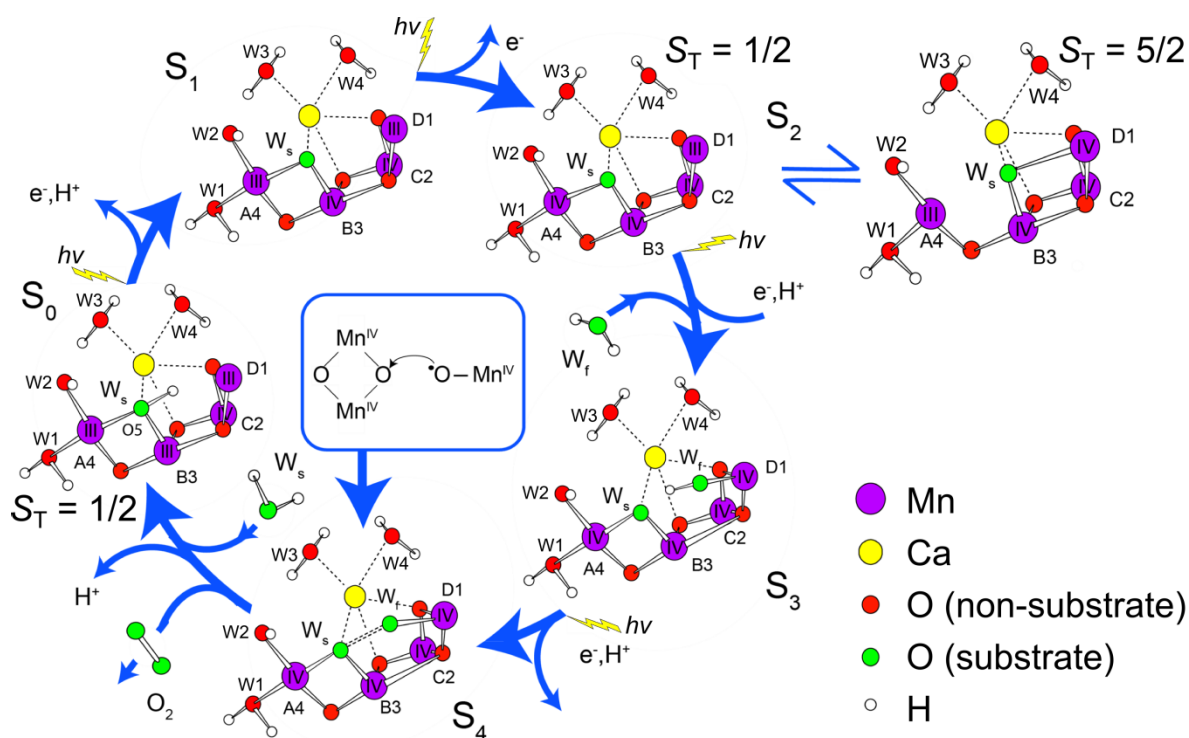


Figure 8.1. Possible reaction pathway for O-O bond formation in photosynthetic water oxidation by the $\text{Mn}_4\text{O}_5\text{Ca}$ cluster of PSII via a radical-coupling mechanism. The advancement of the catalyst is illustrated schematically by conformational changes of the cluster in the S_iY_Z ($i = 0-4$) states, which are interconnected by intermediate $S_{i-1}Y_Z^\bullet$ states not depicted.

An exchangeable, substrate-derived μ -oxo bridge actively taking part in the reaction cycle is however not a novel phenomenon in chemical catalysis or biocatalysis, but rather a prevalent concept of substrate activation, known from Mn and Fe bioinorganic chemistry. In the disproportion reaction of hydrogen peroxide catalyzed by Mn catalase⁷⁻⁹ for example, a labile μ -oxo bridge stemming from a H_2O_2 is transiently inserted into the di-Mn cofactor in a $\text{Mn}^{\text{II}}\text{Mn}^{\text{II}}$ state. Upon concerted two-electron oxidation to $\text{Mn}^{\text{III}}\text{Mn}^{\text{III}}$, the bridge is released as part of a H_2O molecule. Similarly, in class 1a¹⁰ and class 1b¹¹ ribonucleotide reductases, a H_2O_2 or O_2 substrate is inserted into a μ -oxo bridge in the non-catalytic formation of the active di-Fe and di-Mn cofactors, respectively. However, in these reactions the oxygens from the substrates are reduced, whereas the OEC catalyzes the oxidation of the oxygen atom from water, yielding O_2 . As such, the OEC is a unique biocatalyst performing this complex, light-energy-driven uphill oxidative Mn chemistry.

Based on the findings for the early reactions of the S-state cycle, further considerations can be made regarding the steps subsequent to the S_2 state up to O-O bond formation, reviewed in Ref. ¹². In this respect, the most important question is that of the binding site and identity of the second, fast exchanging substrate W_f . On basis of the identification of O5 being W_s (Chapter 6), steric considerations leave only two candidates for W_f among the exchangeable oxygen sites directly coordinating to the $\text{Mn}_4\text{O}_5\text{Ca}$ complex in the S_2 state; these are Mn_{A4} -bound W_2 and Ca^{2+} -bound W_3 (Figure 8.1). However, W_3 is rather unlikely in view of the exchange rates measured by membrane-inlet mass spectrometry. They are not considerably affected by $\text{Ca}^{2+}/\text{Sr}^{2+}$ exchange, but significantly S-state-dependent, indicating a W_f to be bound to Mn instead of Ca^{2+} . The S_3 -to- S_4 state transition might then be a ligand-centered oxidation of W_2 . The oxyl-radical would then attack O5, forming the product O_2 . Another option is the binding of an additional water molecule in the S_3 state to the open coordination site of the Mn^{III} ion in the S_2 state (Figure 8.1), *i.e.* Mn_{D1} in the low-spin conformation. In this mechanism proposed by Siegbahn based on theoretically calculated free energies,^{13,14} O-O bond formation occurs as well via a radical coupling between O5 and the terminal oxyl-radical on Mn_{D1} formed in the S_4 state. A unifying concept incorporating both these pathways into a common scheme has recently been presented by Cox and Messinger.¹² Thus, future research will be directed at the higher S states of the OEC, for which the EPR methods applied in this work will be very valuable, in order to provide strong experimental evidence for a specific mechanism.

8.1 References

- (1) Tagore, R.; Crabtree, R. H.; Brudvig, G. W. *Inorg. Chem.* **2007**, *46*, 2193.
- (2) McConnell, I. L.; Grigoryants, V. M.; Scholes, C. P.; Myers, W. K.; Chen, P. Y.; Whittaker, J. W.; Brudvig, G. W. *J. Am. Chem. Soc.* **2012**, *134*, 1504.
- (3) Rapatskiy, L.; Cox, N.; Savitsky, A.; Ames, W. M.; Sander, J.; Nowaczyk, M. M.; Rögner, M.; Boussac, A.; Neese, F.; Messinger, J.; Lubitz, W. *J. Am. Chem. Soc.* **2012**, *134*, 16619.
- (4) Bovi, D.; Narzi, D.; Guidoni, L. *Angew. Chem., Int. Ed.* **2013**, *52*, 11744.
- (5) Pantazis, D. A.; Ames, W.; Cox, N.; Lubitz, W.; Neese, F. *Angew. Chem., Int. Ed.* **2012**, *51*, 9935.
- (6) Kusunoki, M. *J. Photochem. Photobiol., B* **2011**, *104*, 100.
- (7) Dismukes, G. C. *Chem. Rev.* **1996**, *96*, 2909.
- (8) Boelrijk, A. E. M.; Dismukes, G. C. *Inorg. Chem.* **2000**, *39*, 3020.
- (9) Barynin, V. V.; Whittaker, M. M.; Antonyuk, S. V.; Lamzin, V. S.; Harrison, P. M.; Artymiuk, P. J.; Whittaker, J. W. *Structure* **2001**, *9*, 725.
- (10) Burdi, D.; Willems, J. P.; Riggs-Gelasco, P.; Antholine, W. E.; Stubbe, J.; Hoffman, B. M. *J. Am. Chem. Soc.* **1998**, *120*, 12910.
- (11) Cox, N.; Ogata, H.; Stolle, P.; Reijerse, E.; Auling, G.; Lubitz, W. *J. Am. Chem. Soc.* **2010**, *132*, 11197.
- (12) Cox, N.; Messinger, J. *Biochim. Biophys. Acta, Bioenerg.* **2013**, *1827*, 1020.
- (13) Siegbahn, P. E. M. *Acc. Chem. Res.* **2009**, *42*, 1871.
- (14) Siegbahn, P. E. M. *Biochim. Biophys. Acta, Bioenerg.* **2013**, *1827*, 1003.

Appendices

Appendices

Electronic Supplementary Material

EPR Spectroscopy and the Electronic Structure of the Oxygen-Evolving Complex of Photosystem II

Thomas Lohmiller, William Ames, Wolfgang Lubitz, Nicholas Cox

Max-Planck-Institut für Chemische Energiekonversion, Stiftstrasse 34-36, D-45470 Mülheim an der Ruhr, Germany

49-208-306-3552

49-208-306-3955

nicholas.cox@cec.mpg.de

Present Address:

William Ames

Department of Chemistry & Biochemistry, Middlebury College, McCardell Bicentennial Hall, 276 Bicentennial Way, Middlebury, VT 05753, USA

Sushil K. Misra

Physics Department, Concordia University, 1455 de Maisonneuve Boulevard West, Montreal, QC H3G 1M8, Canada

S1 Spin Hamiltonian Parameters of monomeric and heterodimeric Mn^{III} and Mn^{IV} complexes

Table S1 Monomeric Mn^{III} Complexes

Mn ^{III}		g _⊥		g	D / cm ⁻¹	E/D	a _⊥ / MHz	a / MHz	a _{iso} / MHz	a _{aniso} / MHz
		g _x	g _y	g _z						
Mn ^{III} in rutile (TiO ₂) [1]		2.00		1.99	-3.4	0.116	256	158	233	-98 (-33)
Mn(H ₂ O) ₆ ³⁺ [2]		2.000		1.984	-4.514	-0.162	261	159	197	-102 (-34)
[Mn(dbm) ₃] Octahedral/ tetrahedral elongated [3]		1.99		1.87	-4.35	0.26	-	-	-	-
[(terpy)Mn ^{III} (N ₃) ₃] Octahedral/ tetrahedral elongated [4]		2.00	1.98	2.01	-3.29	0.51	-	-	-	-
[Mn(cyclam)I ₂]I Octahedral/ tetrahedral elongated [5]		2.00		1.99	0.604	0.034	-	-	-	-
[Mn(bpia)(OAc)-(OCH ₃)]PF ₃ Octahedral/ tetragonally compressed [6]		1.981	1.952	1.978	3.526	0.589	-	-	-	-
Mn ^{III} -Porphyrins [7-9]	Mn(TPP)Cl	2.005		1.982	-2.29	0.00	-	-	-	-
	MnPcCl	2.005		2.00	-2.31	0.00	-	-	-	-
	Mn(ODMAP ₂)Cl	-	-	1.984	-2.33	~0	-	-	-	-
	Mn(ODMAP ₂)DTC	-	-	1.983	-2.61	~0	-	-	-	-
	Mn(DP-IX_DME)Cl	-	-	-	-2.53	~0	-	-	-	-
	Mn(DPDME)Cl	2	2	2	-2.53	~0.01	-	-	-	-
	Mn(DPDME)Br	2	2	2	-1.1	~0	-	-	-	-
Mn ^{III} -Corrole [10, 11]	(tpfc)Mn(OPPh ₃)	1.994		1.980	2.69	0.03	-	-	-	-
	Mn ^{III} C ³⁻	2.002		-	-2.66 - -2.78	0.13 - 0.15	-	-	-	-
Mn-Salen [12, 13]	+ NMO (CH ₂ Cl ₂)	2.0	1.98	1.98	-2.5	0.269	190	126	167	-64 (-21)
	+ 4-PPNO (CH ₂ Cl ₂)	2.0	1.98	1.98	-2.5	0.249	190	119	166	-71 (-24)
	HFEP (CH ₂ Cl ₂ /toluene 3:2 v/v)	2.00		-	-2.47	0.17	-	-	-	-
PS II Mn ^{III} bound to the high affinity site [14]		2.0		1.98	-2.5	0.269	190	123	168	-67 (-22)
MnSOD Trigonal-bipyramidal [15]		2.00	1.99	1.98	2.10	0.243	283	280	282	-2 (-1)

Table S2 Monomeric Mn^{IV} Complexes

Mn ^{IV}	g_{\perp}		g_{\parallel}	D / cm^{-1}	E/D	a_{\perp} / MHz		$a_{\parallel} / \text{MHz}$	$a_{\text{iso}} / \text{MHz}$	$a_{\text{aniso}} / \text{MHz}$
	g_x	g_y	g_z			a_x / MHz	a_y / MHz	a_z / MHz		
Mn ^{IV} in MgO (Octahedral) [16]	1.994			-	-	212			212	-
Mn ^{IV} in MgO (Tetragonal) [16]	1.9940		1.9931	0.5287	-	213			213	-
Mn ^{IV} in Al ₂ O ₃ (tetragonal distorted) [17]	1.993		-	-0.1957	-	209		211	210	2 (1)
Mn ^{IV} in SnO ₂ /TiO ₂ (octahedral, rhomically distorted) [18, 19]	1.9879	1.9870	1.9870	0.8818	0.2635	252	209	226	229	-26 (-1.5)
K ₂ MnCl ₆ (perfect octahedron) [20]	~2.00			0	0	-			-	-
[Mn(MePH) ₃]PF ₆ [21]	~2.00			<<0.31	-	266			-	-
Mn ^{IV} tridentate ONO ligands [22]	[Mn ^{IV} (azpSS) ₂] ⁻⁴		2.01	0.0115	-	272			-	-
	[Mn ^{IV} (3mps) ₂] ⁻⁴		2.00	0.0116	-	272			-	-
	[Mn ^{IV} (azpSa) ₂] ⁻⁴		2.03	0.0117	-	263			-	-
	[Mn ^{IV} (azpSb) ₂] ⁻⁴		2.02	0.0117	-	272			-	-
Schiff base (N ₂ O ₂ coordination environment) [23-25]	Mn(SALAHE) ₂ H ₂ O		$g_{\text{eff}} \approx 5.45$	>>0.31	(0.32)	-			-	-
	Mn(SALAH) ₂ 3H ₂ O		$g_{\text{eff}} \approx 5.91$	>>0.31	(0.07)	216			216	-
	Mn(SALAH) ₂ DMF		$g_{\text{eff}} \approx 5.15, 4.38, 1.96$	>>0.31	(0.22)	-			-	-
	Mn(SALATHM) ₂ H ₂ O		$g_{\text{eff}} \approx 4.32$	>>0.31	(0.06)	-			-	-
	Mn(SALAPDH) ₂ DMF		$g_{\text{eff}} \approx 4.98$	>>0.31	(0.19)	-			-	-
	Mn(L) ₂ 2THF (2 phenolic O)		$g_{\text{eff}} \approx 4.0$	>>0.31	~0	-			-	-
	Mn(als) ₂ (carbox ligand)		$g_{\text{eff}} \approx 3.86, 2.02$	>>0.31	~0	$a_{\text{av}} \approx 216$			216	-
Mn(salen) [26]	$g_{\text{eff}} \approx 5.02$			>>0.31	-	210			210	-
[Mn ^{IV} H ₃ burea(O)] ⁻ (terminal oxo) [27]	$g_{\text{eff}} \approx 5.15, 2.44, 1.63$			3.0	(0.26)	190			190	-
Mn ^{IV} (dbpip) ₂ (N ₂ O ₂ coordination environment) [28]	~2.00			<<0.31		-			-	-
[Mn ^{IV} (HIB) ₃] ²⁻ (hydroxyl acid ligands) [29]	$g_{\text{eff}} \approx 3.9$ (crossover)			>>0.31	0.05	198			198	-
[Mn ^{IV} Br(T _{piv} PP)] (Mn-porphyrins) [30]	$g_{\text{eff}} \approx 4.0$			>>0.31	~0	-			-	-

Table S3 Dimeric Mn^{III}Mn^{IV} mixed valance complexes

Mn ^{III} Mn ^{IV} complexes		g_{\perp}		g_{\parallel}	a_{\perp} / MHz		a_{\parallel} / MHz	a_{iso} / MHz	a_{aniso} / MHz
		g_x	g_y	g_z	a_x / MHz	a_y / MHz	a_z / MHz		
[(phen) ₂ Mn ^{III} O ₂ -Mn ^{IV} (phen) ₂](ClO ₄) ₃ ($J = -150 \text{ cm}^{-1}$) [31]	Mn ^{III}	-	-	-	245		189	227	-56 (-18.6)
	Mn ^{IV}	-	-	-	-	-	-	-	-
[Mn ^{III} Mn ^{IV} O ₂ (OAc)(HB(pz) ₃) ₂] ($J < -150 \text{ cm}^{-1}$) [31]	Mn ^{III}	-	-	-	228		163	206	65 (-21.7)
	Mn ^{IV}	-	-	-	-	-	-	-	-
[(phen) ₂ Mn ^{III} O ₂ -Mn ^{IV} (phen) ₂](ClO ₄) ₃ ($J = -150 \text{ cm}^{-1}$) [32] ^a	Mn ^{III}	-	-	-	237 - 249		178 - 187	220	-59 (-19.7) - -62 (-20.7)
	Mn ^{IV}	-	-	-	208 - 229		226 - 249	218	18 (6) - 20 (7)
Mn ^{III} Mn ^{IV} -[2-OH-3,5-Cl ₂ -salpn] ₂ (THF)(ClO ₄) ($J = -10 \text{ cm}^{-1}$) [32] ^a	Mn ^{III}	-	-	-	-	-	-	170 - 180	60 (20) - 30 (10)
	Mn ^{IV}	-	-	-	-	-	-	200 - 210	15 (5) - -27 (-9)
[Mn ^{III} Mn ^{IV} (μ -O) ₂ bipy ₄](ClO ₄) (BIPY) ($J = -144 \text{ to } -150 \text{ cm}^{-1}$) [33, 34] ^b	Mn ^{III}	1.991	1.988	1.984	253	242	183	226	-70 (-21.5)
	Mn ^{IV}	1.988	1.987	1.991	214	219	223	219	9 (2.2)
[Mn ^{III} Mn ^{IV} (μ -O) ₂ (μ -OAc)tacn ₂]BPh ₄ (TACN) ($J = -110 \text{ cm}^{-1}$) [33, 34] ^b	Mn ^{III}	1.995	1.994	1.988	209	233	143	195	-90 (-26.0)
	Mn ^{IV}	1.988	1.987	1.991	227	198	213	213	15 (0.2)
[Mn ^{III} Mn ^{IV} (μ -O) ₂ (μ -OAc)dtne]BPh ₄ (DTNE) ($J = -110 \text{ cm}^{-1}$) [33, 34] ^b	Mn ^{III}	1.995	1.992	1.987	212	238	144	198	-94 (-27.0)
	Mn ^{IV}	1.988	1.987	1.991	227	199	201	209	-26 (-4.0)
[Mn ^{III} Mn ^{IV} (μ -O) ₂ (μ -OAc)Me ₄ dtne]BPh ₄ (MDTN) ($J = -130 \text{ cm}^{-1}$) [33, 34] ^b	Mn ^{III}	1.995	1.992	1.987	212	244	153	203	-51 (-25.0)
	Mn ^{IV}	1.988	1.987	1.991	226	198	206	210	-20 (-2)
MnCat 1 ($J < -175 \text{ cm}^{-1}$) [31]	Mn ^{III}	-	-	-	245		157	192	-88 (-29.3)
	Mn ^{IV}	-	-	-	-	-	-	-	-
MnCat 2 ($J < -175 \text{ cm}^{-1}$) [33, 34] ^b	Mn ^{III}	1.996	1.995	1.989	215	208	147	190	-68 (21.5)
	Mn ^{IV}	1.988	1.987	1.991	228	237	245	237	17 (4.2)

^a Using the range of acceptable D values (see Fig. 4 in Peloquin *et al.* [32]); ^b Using the literature D values of Gerritsen *et al.* [1] and From *et al.* [19] (see table 4.4 in Ref. [33])

S2 Spin Projections

Spin projections can be calculated following the methodology outlined in Chapter 3 of Bencini and Gatteschi [35]. The coupling scheme for a tetramanganese system is expressed as $|S_1 S_2 S_{12} S_3 S_4 S_{34} S M\rangle$, or more succinctly $|S_{12} S_{34} S M\rangle$, where $|S_1 - S_2| \leq S_{12} \leq |S_1 + S_2|$, $|S_3 - S_4| \leq S_{34} \leq |S_3 + S_4|$, and $|S_{12} - S_{34}| \leq S \leq |S_{12} + S_{34}|$. The resultant basis set for the subset where $S = 1/2$, and assuming (S_1, S_2, S_3, S_4) is $(\frac{3}{2}, \frac{3}{2}, \frac{3}{2}, 2)$ or $(\frac{3}{2}, \frac{3}{2}, 2, \frac{3}{2})$, is:

$$\begin{array}{lll} |0 \frac{1}{2} \frac{1}{2} M\rangle & |2 \frac{3}{2} \frac{1}{2} M\rangle & |3 \frac{7}{2} \frac{1}{2} M\rangle \\ |1 \frac{1}{2} \frac{1}{2} M\rangle & |2 \frac{5}{2} \frac{1}{2} M\rangle & \\ |1 \frac{3}{2} \frac{1}{2} M\rangle & |3 \frac{5}{2} \frac{1}{2} M\rangle & \end{array}$$

where M takes all half-integer values $-\frac{1}{2} \leq M \leq \frac{1}{2}$.

The complete set of basis vectors is listed below in Supplementary Chapter S3.

S3 The Eigenstates $|S_{12} S_{34} S M\rangle$

Table S4 List of the eigenstates $|S_{12} S_{34} S M\rangle$. M takes all half-integer values $-S \leq M \leq S$, for each entry.

		S ₁₂			
		0	1	2	3
S ₃₄	$\frac{1}{2}$	$\frac{1}{2}$	$\frac{1}{2} \frac{3}{2}$	$\frac{3}{2} \frac{5}{2}$	$\frac{5}{2} \frac{7}{2}$
	$\frac{3}{2}$	$\frac{3}{2}$	$\frac{1}{2} \frac{3}{2} \frac{5}{2}$	$\frac{1}{2} \frac{3}{2} \frac{5}{2} \frac{7}{2}$	$\frac{3}{2} \frac{5}{2} \frac{7}{2} \frac{9}{2}$
	$\frac{5}{2}$	$\frac{5}{2}$	$\frac{3}{2} \frac{5}{2} \frac{7}{2}$	$\frac{1}{2} \frac{3}{2} \frac{5}{2} \frac{7}{2} \frac{9}{2}$	$\frac{1}{2} \frac{3}{2} \frac{5}{2} \frac{7}{2} \frac{9}{2}$
	$\frac{7}{2}$	$\frac{7}{2}$	$\frac{5}{2} \frac{7}{2} \frac{9}{2}$	$\frac{3}{2} \frac{5}{2} \frac{7}{2} \frac{9}{2} \frac{11}{2}$	$\frac{11}{2} \frac{3}{2} \frac{5}{2} \frac{7}{2} \frac{9}{2}$

The Spin Hamiltonian for the system takes the form of a series of pairwise interactions i.e.

$$H = -2 \sum_{i < j} J_{ij} S_i S_j$$

which can be reexpressed in generalized operator form:

$$H = \sum_k \sqrt{2k+1} \cdot O_k(k_1 k_2 k_{12} k_3 k_4 k_{34} k) \cdot \left\{ \{T_{k_1}(S_1) \otimes T_{k_2}(S_2)\}_{k_{12}} \otimes \{T_{k_3}(S_3) \otimes T_{k_4}(S_4)\}_{k_{34}} \right\}_k \\ = \sum_k \sqrt{2k+1} \cdot O_k(k_1 k_2 k_{12} k_3 k_4 k_{34} k) \cdot X_k(k_1 k_2 k_{12} k_3 k_4 k_{34} k),$$

where O_k corresponds to the scalar exchange coupling term J , i.e.

$$O_k(k_1 k_2 k_{12} k_3 k_4 k_{34} k) = -\frac{\sqrt{3}}{2} J_{ij};$$

$$\text{i.e. } O_0(110000) = -\frac{\sqrt{3}}{2} J_{12}, O_0(1011010) = -\frac{\sqrt{3}}{2} J_{12}, \text{ etc;}$$

and the matrix elements X_k correspond to:

$$\langle S_1 S_2 S_{12} S_3 S_{34} S_M | X_k | S_1 S_2 S'_{12} S_3 S'_{34} S_M \rangle = (-1)^{S-M} \begin{pmatrix} S & k & S \\ -M & q & M \end{pmatrix} \cdot \langle S_1 S_2 S_{12} S_3 S_{34} S | X_k | S_1 S_2 S'_{12} S_3 S'_{34} S \rangle$$

The reduced matrix elements can be calculated using:

$$\langle S_1 S_2 S_{12} S_3 S_{34} S | X_k | S_1 S_2 S'_{12} S_3 S'_{34} S \rangle = (2S+1) \sqrt{(2k_{12}+1)(2S_{12}+1)(2S'_{12}+1)(2k_{34}+1)(2S_{34}+1)(2S'_{34}+1)} \\ \cdot \begin{Bmatrix} S_{12} & S'_{12} & k_{12} \\ S_{34} & S'_{34} & k_{34} \\ S & S & k \end{Bmatrix} \cdot \begin{Bmatrix} S_1 & S_1 & k_1 \\ S_2 & S_2 & k_2 \\ S_{12} & S'_{12} & k_{12} \end{Bmatrix} \begin{Bmatrix} S_3 & S_3 & k_3 \\ S_4 & S_4 & k_4 \\ S_{34} & S'_{34} & k_{34} \end{Bmatrix} \\ \langle S_1 || T_{k_1} || S_1 \rangle \cdot \langle S_2 || T_{k_2} || S_2 \rangle \cdot \langle S_3 || T_{k_3} || S_3 \rangle \cdot \langle S_4 || T_{k_4} || S_4 \rangle$$

Thus, the six reduced matrix elements corresponding to the six pair-wise interactions that they form are:

$$\langle S_1 S_2 S_{12} S_3 S_{34} S | X_0(110000) | S_1 S_2 S'_{12} S_3 S'_{34} S \rangle = \frac{\delta_{S_{12} S'_{12}} \delta_{S_{34} S'_{34}}}{2} \\ \sqrt{\frac{(2S+1)}{3}} [S_1(S_1+1) + S_2(S_2+1) - S_{12}(S_{12}+1)]$$

$$\langle S_1 S_2 S_{12} S_3 S_{34} S | X_0(1011010) | S_1 S_2 S'_{12} S_3 S'_{34} S \rangle = \frac{(-1)^{\left(3(S_1+S_2+S_3+S_4+S_{34})+2(S_{12}+S'_{12})+S'_{34}+S\right)}}{\sqrt{3}} \\ \sqrt{(2S+1)(2S_{12}+1)(2S'_{12}+1)(2S_{34}+1)(2S'_{34}+1)} \cdot \sqrt{(2S_1+1)S_1(S_1+1)(2S_3+1)S_3(S_3+1)} \\ \cdot \begin{Bmatrix} S_{12} & S'_{12} & 1 \\ S_{34} & S'_{34} & S \end{Bmatrix} \cdot \begin{Bmatrix} S_1 & S_1 & 1 \\ S'_{12} & S_{12} & S_2 \end{Bmatrix} \cdot \begin{Bmatrix} S_3 & S_3 & 1 \\ S'_{34} & S_{34} & S_4 \end{Bmatrix}$$

$$\left\langle S_1 S_2 S_{12} S_3 S_{34} S \parallel X_0 (1010110) \parallel S_1 S_2 S'_{12} S_3 S'_{34} S \right\rangle = \frac{(-1)^{\left(3(S_1+S_2+S_3+S_4)+2(S_{12}+S'_{12}+S_{34}+S'_{34})+S\right)}}{\sqrt{3}}$$

$$\sqrt{(2S+1)(2S_{12}+1)(2S'_{12}+1)(2S_{34}+1)(2S'_{34}+1)} \cdot \sqrt{(2S_1+1)S_1(S_1+1)(2S_4+1)S_4(S_4+1)} \cdot$$

$$\begin{Bmatrix} S_{12} & S'_{12} & 1 \\ S_{34} & S'_{34} & S \end{Bmatrix} \cdot \begin{Bmatrix} S_1 & S_1 & 1 \\ S'_{12} & S_{12} & S_2 \end{Bmatrix} \cdot \begin{Bmatrix} S_4 & S_4 & 1 \\ S'_{34} & S_{34} & S_3 \end{Bmatrix}$$

$$\left\langle S_1 S_2 S_{12} S_3 S_{34} S \parallel X_0 (0111010) \parallel S_1 S_2 S'_{12} S_3 S'_{34} S \right\rangle = \frac{(-1)^{\left(3(S_1+S_2+S_3+S_4+S_{12}+S'_{34})+S'_{12}+S_{34}+S\right)}}{\sqrt{3}}$$

$$\sqrt{(2S+1)(2S_{12}+1)(2S'_{12}+1)(2S_{34}+1)(2S'_{34}+1)} \cdot \sqrt{(2S_2+1)S_2(S_2+1)(2S_3+1)S_3(S_3+1)} \cdot$$

$$\begin{Bmatrix} S_{12} & S'_{12} & 1 \\ S_{34} & S'_{34} & S \end{Bmatrix} \cdot \begin{Bmatrix} S_2 & S_2 & 1 \\ S'_{12} & S_{12} & S_1 \end{Bmatrix} \cdot \begin{Bmatrix} S_3 & S_3 & 1 \\ S'_{34} & S_{34} & S_4 \end{Bmatrix}$$

$$\left\langle S_1 S_2 S_{12} S_3 S_{34} S \parallel X_0 (0111010) \parallel S_1 S_2 S'_{12} S_3 S'_{34} S \right\rangle = \frac{(-1)^{\left(3(S_1+S_2+S_3+S_4+S_{12}+S'_{34})+S'_{12}+S_{34}+S\right)}}{\sqrt{3}}$$

$$\sqrt{(2S+1)(2S_{12}+1)(2S'_{12}+1)(2S_{34}+1)(2S'_{34}+1)} \cdot \sqrt{(2S_2+1)S_2(S_2+1)(2S_4+1)S_4(S_4+1)} \cdot$$

$$\begin{Bmatrix} S_{12} & S'_{12} & 1 \\ S_{34} & S'_{34} & S \end{Bmatrix} \cdot \begin{Bmatrix} S_2 & S_2 & 1 \\ S'_{12} & S_{12} & S_1 \end{Bmatrix} \cdot \begin{Bmatrix} S_3 & S_3 & 1 \\ S'_{34} & S_{34} & S_4 \end{Bmatrix}$$

$$\left\langle S_1 S_2 S_{12} S_3 S_{34} S \parallel X_0 (0001100) \parallel S_1 S_2 S'_{12} S_3 S'_{34} S \right\rangle = \frac{\delta_{S_{12} S'_{12}} \delta_{S_{34} S'_{34}}}{2}$$

$$\sqrt{\frac{(2S+1)}{3}} [S_3(S_3+1) + S_4(S_4+1) - S_{34}(S_{34}+1)]$$

The resulting matrix is block diagonal, wherein only terms with the same total spin mix.

The projection of the total spin onto the individual Mn ions can be calculated in a similar manner using the Wigner-Eckart theorem. This problem reduces to calculating the matrix elements X_k , where X_k now refers to the spin operators S_x ($x = 1, 2, 3$ or 4). For instance, for $X_k = T_1(S_1)$:

$$\left\langle S_1 S_2 S_{12} S_3 S_{34} S \parallel T_1(S_1) \parallel S_1 S_2 S'_{12} S_3 S'_{34} S \right\rangle = (-1)^{(S_1 + S_2 + S_{12} + S'_{12} + S_{34} + S)}$$

$$\delta_{S_{34} S'_{34}} (2S+1) \sqrt{(2S_{12}+1)(2S'_{12}+1)(2S_1+1)S_1(S_1+1)} \cdot \begin{Bmatrix} S_{12} & S'_{12} & 1 \\ S & S & S_{34} \end{Bmatrix} \cdot \begin{Bmatrix} S_1 & S_1 & 1 \\ S'_{12} & S_{12} & S_2 \end{Bmatrix}$$

The ratio of the matrix element $\langle \dots \| X_k \| \dots \rangle$ to the expectation value of the total spin $\langle \dots \| S \| \dots \rangle$ then yields the spin projection number (c_k) for each Mn center.

$$c_1 = \frac{\left\langle S_1 S_2 S_{12} S_3 S_{34} S \parallel T_1(S_1) \parallel S_1 S_2 S'_{12} S_3 S'_{34} S \right\rangle}{\left\langle S_1 S_2 S_{12} S_3 S_{34} S \parallel T_1(S) \parallel S_1 S_2 S'_{12} S_3 S'_{34} S \right\rangle} = (-1)^{(S_1 + S_2 + S_{12} + S'_{12} + S_{34} + S)}$$

$$\delta_{S_{34} S'_{34}} \frac{\sqrt{(2S+1)(2S_{12}+1)(2S'_{12}+1)(2S_1+1)S_1(S_1+1)}}{\sqrt{S(S+1)}} \cdot \begin{Bmatrix} S_{12} & S'_{12} & 1 \\ S & S & S_{34} \end{Bmatrix} \cdot \begin{Bmatrix} S_1 & S_1 & 1 \\ S'_{12} & S_{12} & S_2 \end{Bmatrix}$$

$$c_2 = \frac{\left\langle S_1 S_2 S_{12} S_3 S_{34} S \parallel T_1(S_2) \parallel S_1 S_2 S'_{12} S_3 S'_{34} S \right\rangle}{\left\langle S_1 S_2 S_{12} S_3 S_{34} S \parallel T_1(S) \parallel S_1 S_2 S'_{12} S_3 S'_{34} S \right\rangle} = (-1)^{(S_1 + S_2 + 2S_{12} + 2S'_{12} + S_{34} + S)}$$

$$\delta_{S_{34} S'_{34}} \frac{\sqrt{(2S+1)(2S_{12}+1)(2S'_{12}+1)(2S_2+1)S_2(S_2+1)}}{\sqrt{S(S+1)}} \cdot \begin{Bmatrix} S_{12} & S'_{12} & 1 \\ S & S & S_{34} \end{Bmatrix} \cdot \begin{Bmatrix} S_2 & S_2 & 1 \\ S'_{12} & S_{12} & S_1 \end{Bmatrix}$$

$$c_3 = \frac{\left\langle S_1 S_2 S_{12} S_3 S_{34} S \parallel T_1(S_3) \parallel S_1 S_2 S'_{12} S_3 S'_{34} S \right\rangle}{\left\langle S_1 S_2 S_{12} S_3 S_{34} S \parallel T_1(S) \parallel S_1 S_2 S'_{12} S_3 S'_{34} S \right\rangle} = (-1)^{(S_3 + S_4 + S_{12} + 2S'_{34} + 2S_{34} + S)}$$

$$\delta_{S_{12} S'_{12}} \frac{\sqrt{(2S+1)(2S_{34}+1)(2S'_{34}+1)(2S_3+1)S_3(S_3+1)}}{\sqrt{S(S+1)}} \cdot \begin{Bmatrix} S_{34} & S'_{34} & 1 \\ S & S & S_{12} \end{Bmatrix} \cdot \begin{Bmatrix} S_3 & S_3 & 1 \\ S'_{34} & S_{34} & S_4 \end{Bmatrix}$$

$$c_4 = \frac{\left\langle S_1 S_2 S_{12} S_3 S_{34} S \parallel T_1(S_4) \parallel S_1 S_2 S'_{12} S_3 S'_{34} S \right\rangle}{\left\langle S_1 S_2 S_{12} S_3 S_{34} S \parallel T_1(S) \parallel S_1 S_2 S'_{12} S_3 S'_{34} S \right\rangle} = (-1)^{(S_3 + S_4 + S_{12} + 2S'_{34} + S_{34} + S)}$$

$$\delta_{S_{12} S'_{12}} \frac{\sqrt{(2S+1)(2S_{34}+1)(2S'_{34}+1)(2S_4+1)S_4(S_4+1)}}{\sqrt{S(S+1)}} \cdot \begin{Bmatrix} S_{34} & S'_{34} & 1 \\ S & S & S_{12} \end{Bmatrix} \cdot \begin{Bmatrix} S_4 & S_4 & 1 \\ S'_{34} & S_{34} & S_3 \end{Bmatrix}$$

For an arbitrary coupling scheme, the basis eigenstates have the form:

$$\Psi_a = \sum_{S_{12}} \sum_{S_{34}} C_{S_{12} S_{34}} |S_1 S_2 S_{12} S_3 S_{34} S\rangle$$

Thus, the calculation of the spin projection value requires the weighted sum over all matrix elements:

$$c_k = \sum_{S_{12}} \sum_{S_{34}} C_{S_{12} S_{34}} C_{S'_{12} S'_{34}} \frac{\langle S_1 S_2 S'_{12} S_3 S'_{34} S \| X_k \| S_1 S_2 S_{12} S_3 S_{34} S \rangle}{\langle S_1 S_2 S'_{12} S_3 S'_{34} S \| S \| S_1 S_2 S_{12} S_3 S_{34} S \rangle}$$

S4 Jahn-Teller distortion of the Mn^{III} ion

Normally, no Kramers degeneracy is exhibited by the Mn^{III} ion ($S = 2$), a d^4 ion, in zero-field [31, 36-38]. Its inherent asymmetry of the valence electron configuration makes it undergo a considerable Jahn-Teller distortion, due to coupling of the electronic and nuclear motions. Spin-orbit coupling removes the degeneracy of the 5E_g levels giving rise to either an ${}^5A_{1g}$ or ${}^5B_{1g}$ ground state [1, 38]. As illustrated in Ref. [39], with regards to coordination sphere geometries and the resulting fine structure parameters, it was demonstrated that [1, 32]: (i) A ${}^5A_{1g}$ ground state results from a trigonal bipyramidal (5-coordinate) or a tetragonally compressed octahedral (6-coordinate) ligand geometry, the vacant electron orbital then being the d_{z^2} orbital, which yields a positive ZFS parameter D ; and (ii) A ${}^5B_{1g}$ ground state results from a square-pyramidal (5-coordinate) or a tetragonally elongated (6-coordinate) ligand geometry, the vacant electron orbital being the $d_{x^2-y^2}$ orbital. This yields a negative ZFS parameter D .

References

- [1] H.J. Gerritsen, E.S. Sabisky, Phys. Rev. 132(4), 1507-1512 (1963)
- [2] I. Krivokapic, C. Noble, S. Klitgaard, P. Tregenna-Piggott, H. Weihe, A.-L. Barra, Angew. Chem., Int. Ed. 44(23), 3613-3616 (2005)
- [3] A.-L. Barra, D. Gatteschi, R. Sessoli, G.L. Abbati, A. Cornia, A.C. Fabretti, M.G. Uytterhoeven, Angew. Chem., Int. Ed. 36(21), 2329-2331 (1997)
- [4] J. Limburg, J.S. Vrettos, R.H. Crabtree, G.W. Brudvig, J.C. de Paula, A. Hassan, A.-L. Barra, C. Duboc-Toia, M.-N. Collomb, Inorg. Chem. 40(7), 1698-1703 (2001)
- [5] S. Mossin, H. Weihe, A.-L. Barra, J. Am. Chem. Soc. 124(30), 8764-8765 (2002)

- [6] Q. Scheifele, C. Riplinger, F. Neese, H. Weihe, A.-L. Barra, F. Juranyi, A. Podlesnyak, P.L.W. Tregenna-Piggott, *Inorg. Chem.* 47(2), 439-447 (2007)
- [7] D.P. Goldberg, J. Telser, J. Krzystek, A.G. Montalban, L.-C. Brunel, A.G.M. Barrett, B.M. Hoffman, *J. Am. Chem. Soc.* 119(37), 8722-8723 (1997)
- [8] J. Krzystek, J. Telser, L.A. Pardi, D.P. Goldberg, B.M. Hoffman, L.-C. Brunel, *Inorg. Chem.* 38(26), 6121-6129 (1999)
- [9] G.C. Brackett, P.L. Richards, W.S. Caughey, *J. Chem. Phys.* 54(10), 4383-4401 (1971)
- [10] J. Bendix, H.B. Gray, G. Golubkov, Z. Gross, *Chem. Commun.* 19), 1957-1958 (2000)
- [11] J. Krzystek, J. Telser, B.M. Hoffman, L.-C. Brunel, S. Licocchia, *J. Am. Chem. Soc.* 123(32), 7890-7897 (2001)
- [12] K.A. Campbell, M.R. Lashley, J.K. Wyatt, M.H. Nantz, R.D. Britt, *J. Am. Chem. Soc.* 123(24), 5710-5719 (2001)
- [13] J. Krzystek, J. Telser, *J. Magn. Reson.* 162(2), 454-465 (2003)
- [14] K.A. Campbell, D.A. Force, P.J. Nixon, F. Dole, B.A. Diner, R.D. Britt, *J. Am. Chem. Soc.* 122(15), 3754-3761 (2000)
- [15] K.A. Campbell, E. Yikilmaz, C.V. Grant, W. Gregor, A.-F. Miller, R.D. Britt, *J. Am. Chem. Soc.* 121(19), 4714-4715 (1999)
- [16] J.J. Davies, S.R.P. Smith, J.E. Wertz, *Phys. Rev.* 178(2), 608-612 (1969)
- [17] N. Laurance, J. Lambe, *Phys. Rev.* 132(3), 1029-1036 (1963)
- [18] H.G. Andresen, *Phys. Rev.* 120(5), 1606-1611 (1960)
- [19] W.H. From, P.B. Dorain, C. Kikuchi, *Phys. Rev.* 135(3A), A710-A714 (1964)
- [20] D.T. Richens, D.T. Sawyer, *J. Am. Chem. Soc.* 101(13), 3681-3683 (1979)
- [21] S. Pal, P. Ghosh, A. Chakravorty, *Inorg. Chem.* 24(22), 3704-3706 (1985)
- [22] S. Dutta, A. Chakravorty, *Polyhedron* 13(12), 1811-1816 (1994)
- [23] S.K. Chandra, P. Basu, D. Ray, S. Pal, A. Chakravorty, *Inorg. Chem.* 29(13), 2423-2428 (1990)
- [24] D.P. Kessissoglou, X. Li, W.M. Butler, V.L. Pecoraro, *Inorg. Chem.* 26(15), 2487-2492 (1987)
- [25] M. Mikuriya, S. Shigematsu, K. Kawano, T. Tokii, H. Oshio, *Chem. Lett.* 19(5), 729-732 (1990)
- [26] K.P. Bryliakov, O.A. Kholdeeva, M.P. Vanina, E.P. Talsi, *J. Mol. Catal. A: Chem.* 178(1-2), 47-53 (2002)
- [27] T.H. Parsell, R.K. Behan, M.T. Green, M.P. Hendrich, A.S. Borovik, *J. Am. Chem. Soc.* 128(27), 8728-8729 (2006)

- [28] T.M. Rajendiran, J.W. Kampf, V.L. Pecoraro, *Inorg. Chim. Acta* 339(497-502 (2002)
- [29] S.M. Saadeh, M.S. Lah, V.L. Pecoraro, *Inorg. Chem.* 30(1), 8-15 (1991)
- [30] K. Ayougou, E. Bill, J.M. Charnock, C.D. Garner, D. Mandon, A.X. Trautwein, R. Weiss, H. Winkler, *Angew. Chem.* 107(3), 370-373 (1995)
- [31] M. Zheng, S.V. Khangulov, G.C. Dismukes, V.V. Barynin, *Inorg. Chem.* 33(2), 382-387 (1994)
- [32] J.M. Peloquin, K.A. Campbell, D.W. Randall, M.A. Evanchik, V.L. Pecoraro, W.H. Armstrong, R.D. Britt, *J. Am. Chem. Soc.* 122(44), 10926-10942 (2000)
- [33] K.O. Schäfer, Exchange Coupled Manganese Complexes: Model Systems for the Active Centres of Redoxproteins Investigated with EPR Techniques, Doctoral Thesis, Technische Universität Berlin, 2002
- [34] K.O. Schäfer, R. Bittl, W. Zweggart, F. Lenzian, G. Haselhorst, T. Weyhermuller, K. Wieghardt, W. Lubitz, *J. Am. Chem. Soc.* 120(50), 13104-13120 (1998)
- [35] A. Bencini, D. Gatteschi, *EPR of Exchange Coupled Systems*, (Springer-Verlag, Berlin, 1990),
- [36] A. Abragam, B. Bleaney, *Electron Paramagnetic Resonance of Transition Metal Ions*, (Clarendon Press, Oxford, 1970),
- [37] A. Carrington, A.D. McLachlan, *Introduction to Magnetic Resonance*, 1 (Harper and Row, New York, 1967),
- [38] J.S. Griffith, *The theory of Transition-Metal Ions* (Cambridge University Press, London, 1971),
- [39] N. Cox, L. Rapatskiy, J.-H. Su, D.A. Pantazis, M. Sugiura, L. Kulik, P. Dorlet, A.W. Rutherford, F. Neese, A. Boussac, W. Lubitz, J. Messinger, *J. Am. Chem. Soc.* 133(10), 3635-3648 (2011)

Appendices

SUPPLEMENTAL DATA

The Basic Properties of the Electronic Structure of the
Oxygen-Evolving Complex of Photosystem II are not
Perturbed by Ca²⁺ Removal

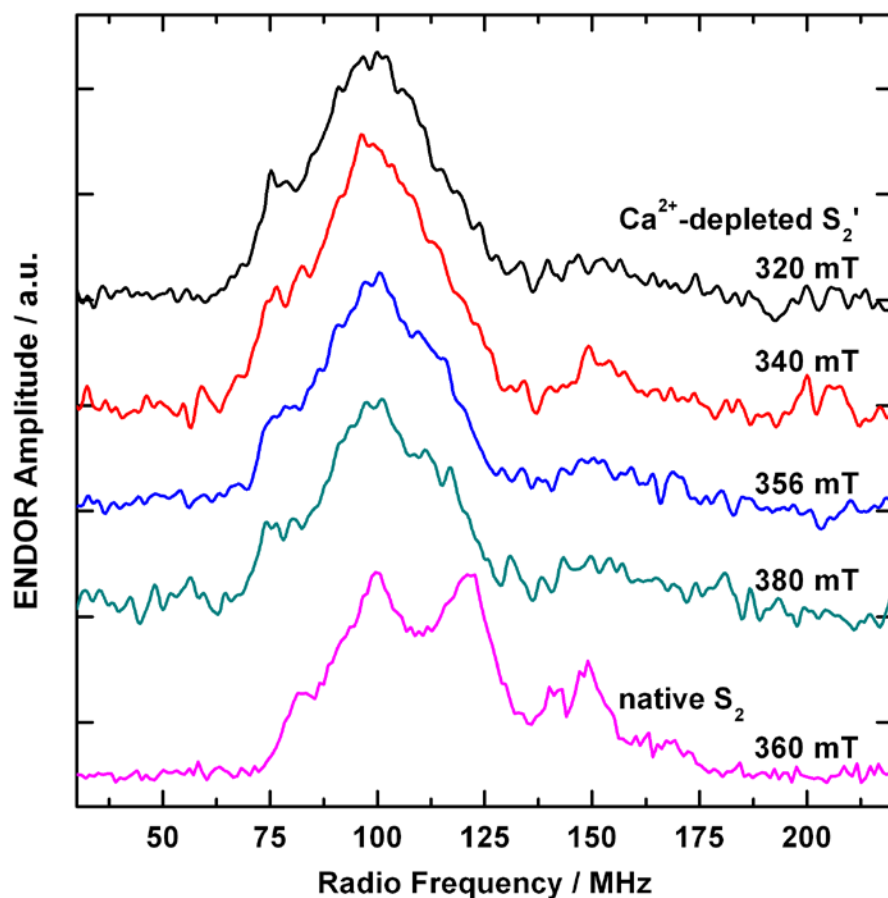
Thomas Lohmiller,[‡] Nicholas Cox,[‡] Ji-Hu Su,^{‡,§} Johannes Messinger,^{||} Wolfgang Lubitz^{‡,1}

[‡]Max-Planck-Institut für Bioanorganische Chemie, Stiftstrasse 34-36, 45470 Mülheim an der Ruhr,
Germany.

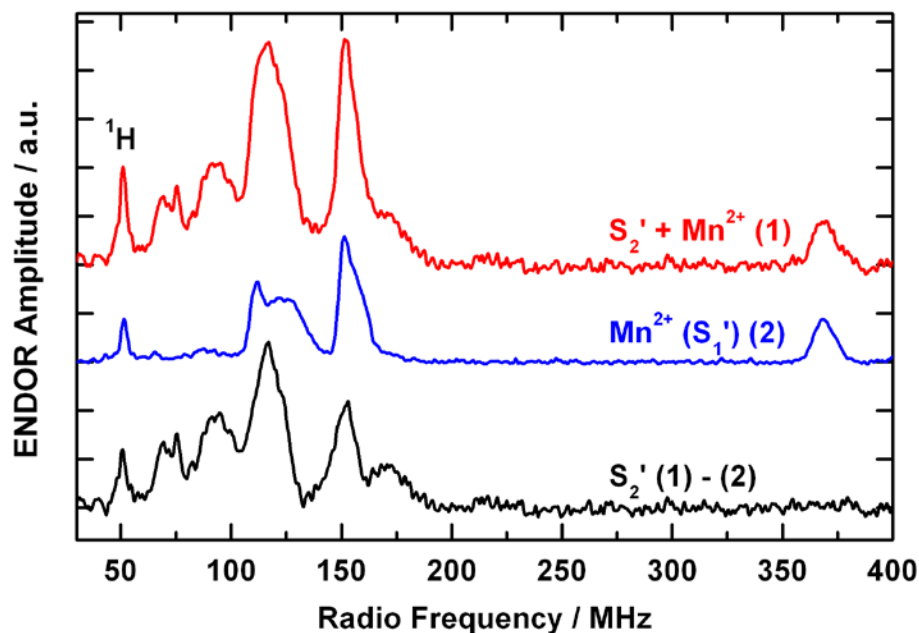
[§]Present address: Department of Modern Physics, University of Science and Technology of China,
Hefei, Anhui 230026, China.

^{||}Department of Chemistry, Chemical Biological Centre (KBC), Umeå University, S-90187 Umeå,
Sweden.

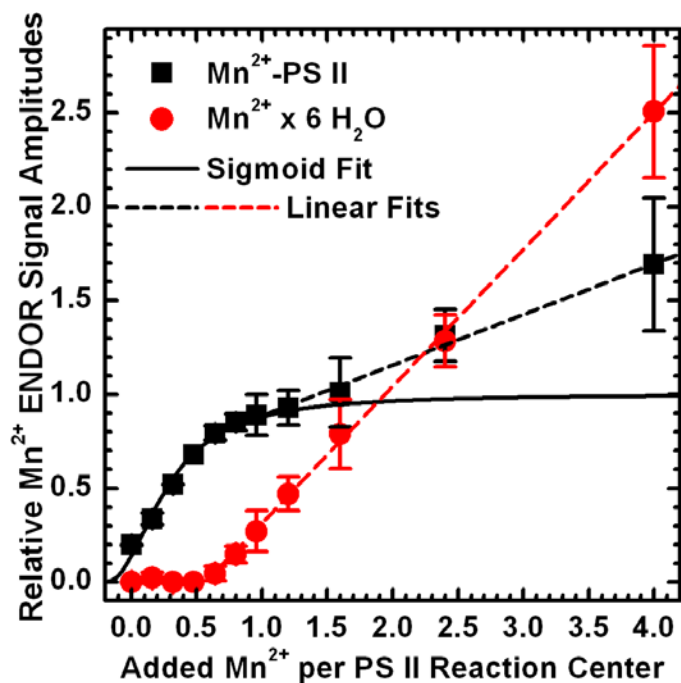
¹To whom correspondence should be addressed: Prof. Dr. Wolfgang Lubitz, Max-Planck-Institut für
Bioanorganische Chemie, Stiftstrasse 34-36, 45470 Mülheim an der Ruhr, Germany, Tel: +49 208 306
3614. Fax: +49 208 306 3955. E-mail: wolfgang.lubitz@mpi-mail.mpg.de.



SUPPLEMENTAL FIGURE S1. X-band Davies ENDOR spectra of the Ca^{2+} -depleted OEC poised in the S_2' state in PS II isolated from spinach at various magnetic fields and, for comparison, of the native OEC in the S_2 state in the presence of 3 % MeOH at $B_0 = 360$ mT (bottom trace), as published in Refs. (1, 2). The S_2' state spectra were smoothed using a 9-point moving average. Experimental parameters (S_2' state): MW frequency: 9.717 GHz; shot repetition rate: 5 μs ; MW pulse length π : 12 ns; τ : 200 ns; magnetic fields B_0 : 320 mT, 340 mT, 356 mT, 380 mT (from the top); RF pulse length π_{RF} : 4 μs ; temperature: 5 K; accumulations/time: 460/355 min, 166/149 min, 160/144 min, 339/305 min (from the top).



SUPPLEMENTAL FIGURE S2. Q-band Davies ENDOR spectra of Ca^{2+} -depleted PS II isolated from spinach illustrating the subtraction of the contaminating Mn^{2+} signal from the raw data obtained from the sample poised in the S_2' state, which yields the pure spectrum of the Ca^{2+} -depleted Mn_4O_5 cluster in the S_2' state. Top trace (1): Spectrum of an illuminated sample poised in the S_2' state containing both the S_2' state signal and contributions from residual Mn^{2+} ions. Middle trace (2): Spectrum of a dark-adapted sample poised in the S_1' state before illumination showing only the Mn^{2+} signal. For the subtraction, both spectra (1) and (2) were normalized with respect to the signal around 370 MHz, to which only the Mn^{2+} ion contributes. Bottom trace (1 – 2): difference of the spectra from samples in the S_2' and the S_1' states, the result of which is the spectrum of the OEC in the S_2' state. Experimental settings: MW frequency: 34.033 GHz; shot repetition rate: 5 μs ; MW pulse length π : 72 ns; τ : 480 ns; magnetic field B_0 : 1208 mT; RF pulse length π_{RF} : 4 μs ; temperature: 5 K; accumulations/time: 202/218 min (1), 358/387 min (2).



SUPPLEMENTAL FIGURE S3. Titration of dark-adapted Ca^{2+} -depleted PS II samples (S_1' state) with Mn^{2+} . The relative Q-band ^{55}Mn Davies ENDOR signal intensities of Mn^{2+} ions bound to the PS II protein complex (black squares) and hexaquo- Mn^{2+} in solution (red circles), quantified as described in the Experimental Procedures section 2.6 (main text), are plotted against the equivalents of Mn^{2+} ions added to the samples. The concentration of the defined PS II-bound Mn^{2+} species as a function of added Mn^{2+} was reproduced by means of a sigmoid curve fitted to the determined intensities up to 1.2 equivalents of Mn^{2+} in which the zero crossing of the x-axis was shifted to -0.2 equivalents with a half-binding value of 0.47 equivalents (solid line). The increase of hexaquo- Mn^{2+} , as well as additionally unspecifically bound hexaquo- Mn^{2+} ions was reproduced by linear fits to the measured intensities above 0.64 equivalents of added Mn^{2+} ions (dashed lines). The concentration of reaction centers in the samples was $25 \pm 3 \mu\text{M}$. For the experimental parameters of the ^{55}Mn Davies ENDOR measurements see Fig. 4A (main text).

<i>T. vulcanus</i>	1	-----	0
<i>T. elongatus</i>	1	-----MKYRILMATLLAV	13
<i>Spinacea oleracea</i>	1	MAASLQASTTFLQPTKVASRNTLQLRSTQNVCKAFGVESASSGGRLSLSLQSDLKELANK	60
<i>T. vulcanus</i>	1	-----TLTYDDIVGTGLANKCPTLDDTAR	24
<i>T. elongatus</i>	14	CLGTFSL-----SAPAFAAKQTLTYDDIVGTGLANKCPTLDDTAR	53
<i>Spinacea oleracea</i>	61	CVDATKLAGLALATSALIASGANAEGGKRLTYDEIQSKTYLEVKGGTANQCPTVEGGVD	120
<i>T. vulcanus</i>	25	GAYPIDSSQTYRIARLCLQPTTFLVKEE PKNKRQEAEFVPTKLVTRETTSLDQIQGELKV	84
<i>T. elongatus</i>	54	GAYPIDSSQTYRIARLCLQPTTFLVKEE PKNKRQEAEFVPTKLVTRETTSLDQIQGELKV	113
<i>Spinacea oleracea</i>	121	SF-A-FKPGKYTAKKFLEPTKFAVKA E GISKNSGPDFQNTKLMTRLTYTLDEIEGPFV	178
<i>T. vulcanus</i>	85	NSDGSLTFVEEDGIDFQPVTVQMAGGE RIPLLFTVKNLVASTQPNVTSIT I STDFKGEFN	144
<i>T. elongatus</i>	114	NSDGSLTFVEEDGIDFQPVTVQMAGGE RIPLLFTVKNLVASTQPNVTSIT I STDFKGEFN	173
<i>Spinacea oleracea</i>	179	SSDGTVKFEEKDGIDYAAVTVQLPGGE RVPFLLFTIKQLVASGKPE-----SFSGDFL	230
<i>T. vulcanus</i>	145	VPSYRTANFLDPKGRGLASGYDSAIALPQA---KEEELARANVKRFSLT KGQISL NVAKV	201
<i>T. elongatus</i>	174	VPSYRTANFLDPKGRGLASGYDSAIALPQA---KEEELARANVKRFSLT KGQISL NVAKV	230
<i>Spinacea oleracea</i>	231	VPSYRGSSFLDPKGRGGSTGYDNAVALPAGGRGDEEELQKENNKVASSKGTITL SVTSS	290
<i>T. vulcanus</i>	202	DGRTGEIAGTFE SEQLSDDDMGA HEPHEVKIQGVFYASIEP-	242
<i>T. elongatus</i>	231	DGRTGEIAGTFE SEQLSDDDMGA HEPHEVKIQGVFYASIEPA	272
<i>Spinacea oleracea</i>	291	KPETGEVIGVFQSLQPSDTDLGAKV PKDVKIEGWYQAQLEQQ	332

SUPPLEMENTAL FIGURE S4. Amino acid sequence alignment of the PsbO proteins from the cyanobacteria *T. vulcanus* and *T. elongatus* and the higher plant spinach (*Spinacea oleracea*). Residues ligating the Ca²⁺ ions at the sites identified in the PS II crystal structures from *T. vulcanus* and *T. elongatus* are highlighted in red and blue, respectively. The protein sequence alignment was performed using the BLAST search engine provided by UniProt (3).

SUPPLEMENTAL TABLE S1. Principal Values^a and Isotropic^b and Anisotropic^c Values of the Effective G and ^{55}Mn HFI Tensors A_i ($i = 1-4$) for the Simulations of the X- and Q-Band EPR and ENDOR Spectra of the Ca^{2+} -depleted PS II from Spinach in the S_2' State (Fig. 2, Main Text) and for the S_2 States of Native Spinach PS II (2) and Native and Sr^{2+} -substituted PS II from *T. elongatus* (4).

			G	A_1 / MHz	A_2 / MHz	A_3 / MHz	A_4 / MHz
Spinach	- Ca^{2+} S_2'	x	1.979	342	212	173	139
		y	1.986	328	199	205	164
		\perp^a	1.983	335	206	189	152
		$z(\parallel)^a$	1.979	263	290	227	211
		<i>iso</i> ^b	1.981	311	234	202	171
		<i>aniso</i> ^c	0.004	72	-84	-38	-59
	Ca^{2+} S_2	x	1.997	310	235	185	170
		y	1.970	310	235	185	170
		\perp^a	1.984	310	235	185	170
		$z(\parallel)$	1.965	275	275	245	240
		<i>iso</i>	1.977	298	248	205	193
		<i>aniso</i>	0.019	35	-40	-60	-70
<i>T. elongatus</i>	Ca^{2+} S_2	x	1.971	350	249	202	148
		y	1.948	310	227	182	162
		\perp^a	1.960	330	238	192	155
		$z(\parallel)$	1.985	275	278	240	263
		<i>iso</i>	1.968	312	251	208	191
		<i>aniso</i>	-0.025	55	-40	-48	-108
	Sr^{2+} S_2	x	1.995	343	244	200	156
		y	1.968	361	217	185	152
		\perp^a	1.982	352	231	193	154
		$z(\parallel)$	1.957	293	268	223	210
		<i>iso</i>	1.973	332	243	203	173
		<i>aniso</i>	0.025	59	-37	-30	-56

^a The equatorial and axial G and A_i values are defined as $G_{\perp} = (G_x + G_y)/2$, $G_{\parallel} = G_z$ and $A_{i,\perp} = (A_{i,x} + A_{i,y})/2$, $A_{i,\parallel} = A_{i,z}$. ^b The isotropic G_{iso} and $A_{i,\text{iso}}$ ($i = 1-4$) values are the averages of the principal values: $G_{\text{iso}} = (G_x + G_y + G_z)/3$ and $A_{i,\text{iso}} = (A_{i,x} + A_{i,y} + A_{i,z})/3$. ^c The anisotropy in the G and A_i values is expressed as the differences $G_{\text{aniso}} = G_{\perp} - G_{\parallel}$ and $A_{i,\text{aniso}} = A_{\perp} - A_{\parallel}$ between the perpendicular and parallel components of the tensors.

Correlation between the ground-to-first excited state energy difference Δ and the temperature dependence of the intensity I_1 of the ground spin state EPR signal. The relative intensity I_1 of the ground spin state signal I_1 depends on the inverse temperature weighted by the Boltzmann factor:

$$I_1 = \frac{C}{T} \frac{(2S_1 + 1)\exp(-E_1/kT)}{\sum_i (2S_i + 1)\exp(-E_i/kT)} \quad (\text{S1})$$

where C is a proportionality constant, S_i represents the total spin of the coupled states of the spin manifold ($S = 1/2, 3/2, \dots$) and E_i are the respective energies. Here, a two spin model is used to describe the energy ladder in terms of a single effective coupling constant, J_{eff} between two fragments of the Mn tetramer: monomeric Mn_{A4} (Mn^{IV} , $S_{\text{A4}} = 3/2$), and the coupled trimer $\text{Mn}_{\text{B3}}\text{Mn}_{\text{C2}}\text{Mn}_{\text{D1}}$ ($\text{Mn}^{\text{III}}(\text{Mn}^{\text{IV}})_2$, spin ground state $S_{\text{B3-C2-D1}} = 1$ or 2), see (5). The corresponding simplified Hamiltonian $H = -J_{\text{eff}}S_{\text{A4}}S_{\text{B3-C2-D1}}$ gives spin state energies $E_i = (S_{\text{A4}}(S_{\text{A4}} + 1) + S_{\text{B3-C2-D1}}(S_{\text{B3-C2-D1}} + 1) - S_i(S_i + 1))J_{\text{eff}}$, where the total spin $S_i = (S_{\text{A4}} - S_{\text{B3-C2-D1}}) \dots (S_{\text{A4}} + S_{\text{B3-C2-D1}}) = 1/2 \dots 5/2$. Equation S1 can thus be used to estimate J_{eff} and $\Delta = E_2 - E_1 = -3J_{\text{eff}}$.

Effect of the Zero-Field Splitting Interaction on the Spin States and EPR and ^{55}Mn ENDOR Signals of Mn^{2+} Complexes (see also (6)). The EPR and ^{55}Mn ENDOR signals originating from the Mn^{2+} ions bound to Ca^{2+} -depleted PS II differ substantially from those typically associated with mononuclear Mn^{2+} species in that they appear significantly broadened by the large and strongly rhombic ZFS (Figs. 3 and 4A in the main text). The characteristic EPR spectrum of high-spin $S = 5/2$ Mn^{2+} complexes is the six-line signal with a HFI splitting of ~ 9 mT. For the ^{55}Mn nucleus of nuclear spin $I = 5/2$, each of these lines can be assigned to one nuclear spin sublevel m_I ranging from $-5/2$ to $+5/2$. The corresponding ^{55}Mn ENDOR signal contains 3 orientation-selective doublets centered roughly around ~ 125 , ~ 375 and ~ 625 MHz, which originate from nuclear transitions within the $m_S = |1/2|$, $|3/2|$ and $|5/2|$ electronic submanifolds, respectively.

In the absence of a ZFS interaction, a $^{55}\text{Mn}^{2+}$ EPR spectrum consist of six separate lines associated with one m_I sublevel, to each of which the five $\Delta m_S = \pm 1$ transitions contribute. The ZFS leads to an anisotropic broadening of these transitions, especially those involving manifolds of electronic spin substates $|m_S| > 1/2$. Additionally, the symmetry of the ZFS tensor has a considerable effect on the orientation-dependence and thus on the line width. A large rhombicity of this interaction enhances the broadening of the powder patterns. As the ZFS becomes more relevant, the transitions associated with a certain m_I are increasingly overlapping, such that it comes to a spreading of the entire spectrum. To some extent, the broadening may additionally be attributed to small site-to-site inhomogeneities of the Mn^{2+} environment, which have an immediate effect on the spin Hamiltonian parameters and are especially found in large and dynamic biological systems like proteins. These effects add up to result in the very broad, featureless spectrum, in which the six-line hyperfine structure from $|m_S| = 1/2$ transitions is not resolved.

The pulse ENDOR spectra are directly affected by this spread. In the absence of a ZFS, the transitions involving a particular m_I can be probed individually by selective irradiation at frequency and field of one of the six EPR lines. Therefore, six different ^{55}Mn ENDOR spectra can be measured, each of them only comprising the transitions corresponding to the selected nuclear spin m_I , associated with all six m_S

sublevels. In case of a ZFS-induced anisotropic spread of the m_S substate energies, the relative intensities of the ENDOR lines from the six m_S substates for a particular m_I become orientation-selective. In Fig. 4 (main text), the high-frequency $m_S = -3/2$ signal intensities relative to those of the low-frequency $m_S = -1/2$ and $m_S = +1/2$ signals are clearly smaller at the more central field positions in the EPR spectrum, the spectra at 1208 mT and 1224 mT, compared to the outer ones. At 1195 mT and 1260 mT, there is a stronger relative contribution from the $m_S = -3/2$ transitions due to their larger spread by the ZFS. Furthermore, the overlapping transition energies of the different m_I manifolds result in spectra comprising the ENDOR transitions of more than one m_I value, which leads to a broadening and concomitant lowering of the structural resolution of ENDOR lines. This reduced m_I selectivity can be clearly seen in these very broad ^{55}Mn ENDOR spectra where no spectral structure of single m_I transitions is resolved. Due to the large energetic spread in the case of the high-spin $m_S = -3/2$ sublevels, even all five corresponding m_I transitions are excited at the same time.

The Electronic Structure of an Effective $S = 1/2$ Spin State System: Relation of Effective Tensor Properties and Non-Explicitly Treated Interaction Terms. For evaluation of the intrinsic ZFS values d_i of the Mn ions resulting from the obtained electronic exchange coupling scheme (Fig. 7 in the main text) and whether these are within the reasonable ranges for the individual Mn oxidation states, a short overview is given on how they are calculated based on the inferred coupling topology and experimental effective spin Hamiltonian parameters:

Same as for the Ca^{2+} - and Sr^{2+} -containing S_2 states, the coupled Mn electronic spin system of the Ca^{2+} -depleted S_2' state can be described by an effective spin Hamiltonian (see the Experimental Procedures section 2.5), which does not include any pair-wise interaction terms such as the Heisenberg-Dirac-Van Vleck operator for the electronic exchange interaction and the ZFS term. Thus, the fitted G and HFI tensors A_i (Table 2 in the main text, supplemental Table S1) also represent effective tensors. However instead, the corresponding intrinsic (on-site) HFI tensors a_i need to be considered for comparison to values reported for other Mn systems, assignment of oxidation states and conclusions about coordination geometries of individual Mn ions. Effective and intrinsic properties of each Mn_i ion are related by a spin projection coefficient ρ_i , a measure of the contribution of Mn_i to a particular spin state. The tensor components of this scaling factor are the ratio of the corresponding effective and intrinsic values, i.e. $\rho_i = A_i / a_i$ for the HFI. The effective G tensor, as a property of the effective electron spin S of the Mn cluster, is a weighted linear sum of the intrinsic g tensors of the individual Mn ions $G = \sum \rho_i g_i$. As they map the subspace of the effective spin state to the entire configuration space, the ρ_i tensors for oligomeric spin systems can be computed based on the spin coupling scheme in the form of pair-wise electronic exchange interaction terms between all of the four Mn ions. Therein, the ZFS interaction, not considered explicitly as a term of the spin Hamiltonian, can be taken into account such that it affects the ρ_i tensors in an orientation-dependent manner. Through the exchange coupling between the electronic spins, the intrinsic ZFS value d_i of one Mn ion influences the ρ_j tensors of the others, too, which thus can be envisaged as a transfer of anisotropy to the other Mn ions in the cluster (for more detailed information see Refs. (4, 7, 8)).

REFERENCES

1. Kulik, L., Epel, B., Messinger, J., and Lubitz, W. (2005) *Photosynth. Res.* **84**, 347–353
2. Kulik, L. V., Epel, B., Lubitz, W., and Messinger, J. (2007) *J. Am. Chem. Soc.* **129**, 13421–13435
3. The UniProt Consortium (2011) *Nucleic Acids Res.* **40**, D71–D75
4. Cox, N., Rapatskiy, L., Su, J.-H., Pantazis, D. A., Sugiura, M., Kulik, L., Dorlet, P., Rutherford, A. W., Neese, F., Boussac, A., Lubitz, W., and Messinger, J. (2011) *J. Am. Chem. Soc.* **133**, 3635–3648
5. Su, J.-H., Cox, N., Ames, W., Pantazis, D. A., Rapatskiy, L., Lohmiller, T., Kulik, L. V., Dorlet, P., Rutherford, A. W., Neese, F., Boussac, A., Lubitz, W., and Messinger, J. (2011) *Biochim. Biophys. Acta, Bioenerg.* **1807**, 829–840
6. Sturgeon, B. E., Ball, J. A., Randall, D. W., and Britt, R. D. (1994) *J. Phys. Chem.* **98**, 12871–12883
7. Peloquin, J. M., Campbell, K. A., Randall, D. W., Evanchik, M. A., Pecoraro, V. L., Armstrong, W. H., and Britt, R. D. (2000) *J. Am. Chem. Soc.* **122**, 10926–10942
8. Schäfer, K.-O., Bittl, R., Zweggart, W., Lendzian, F., Haselhorst, G., Weyhermüller, T., Wieghardt, K., and Lubitz, W. (1998) *J. Am. Chem. Soc.* **120**, 13104–13120

Appendices

Electronic Supporting Information

Structure, ligands and substrate coordination of the oxygen-evolving complex of photosystem II in the S₂ state: a combined EPR and DFT study

Thomas Lohmiller,^a Vera Krewald,^a Montserrat Pérez Navarro,^a Marius Retegan,^a Leonid Rapatskiy,^a Mark Nowaczyk,^b Alain Boussac,^c Frank Neese,^a Wolfgang Lubitz,^a Dimitrios A. Pantazis^{*a} and Nicholas Cox^{*a}

^aMax-Planck-Institut für Chemische Energiekonversion, Stiftstrasse 34-36, D-45470 Mülheim an der Ruhr, Germany. Fax: +49 208 306 3955; Tel: +49 208 306 3552; E-mail: dimitrios.pantazis@cec.mpg.de; nicholas.cox@cec.mpg.de

^bRuhr-University Bochum, Universitätsstrasse 150, D-44780 Bochum, Germany.

^ciBiTec-S, URA CNRS 2096, CEA Saclay, 91191 Gif-sur-Yvette, France.

Table of contents

- S1 PSII sample preparation
- S2 Data processing: baseline correction and light-minus-dark subtraction
- S3 Spectral simulations
- S4 Theoretical background
- S5 DFT calculations: NH₃ binding modes and spatial coordinates of the S₂ state models
- S6 Q-band ⁵⁵Mn-ENDOR: comparison of instrumental settings
- S7 Electronic structures: exchange couplings and spin states of the BS-DFT models
- S8 The Mn_{D1}-His332-imino-N interaction: Q-band three-pulse ESEEM, Q-band HYSCORE, W-band EDNMR and simulations
- S9 X-band ¹⁴N- and ¹⁵N-three pulse ESEEM experiments on the NH₃-modified S₂ state
- S10 Exchangeable ¹⁷O species: W-band EDNMR and X-band EPR
- S11 References

S1 PSII sample preparation

In native and Sr^{2+} substituted samples, the S_2 state was generated by short white-light illumination (5 s) with a tungsten lamp at 200 K, using an ethanol bath cooled with dry ice.

Ammonia was added to the samples as follows. A stock solution of 1 M ammonium chloride ($^{14}\text{NH}_4\text{Cl}$) in 1 M HEPES buffer set to a pH of 7.5 was made. For Q- and W-band samples, this solution was then added to the photosystem II (PSII) sample at a ratio of 1:10 (v/v), yielding a concentration of the free base NH_3 of 2 mM. The samples were reconcentrated using Millipore microcentrifuge filters to the desired concentration. Afterwards, the sample was placed in a Q- or W-band tube, left in complete darkness for ≈ 10 min and frozen for experiments in the S_1 state. To generate the NH_3 -modified S_2 state, the sample was first illuminated at 200 K for 5 s and then subsequently annealed at ≈ 260 K (ethanol/dry ice) for 20-30 s before freezing to 77 K (liquid N_2). A similar procedure was used for X-band samples. Here though, the PSII sample was placed in the X-band tube and given two saturating light flashes prior to the addition of $^{14}\text{NH}_4\text{Cl}$ solution. There was a one-hour delay between the two light flashes and the addition of NH_3 , during which the sample was kept in complete darkness. Phenyl-p-benzoquinone (PPBQ) dissolved in dimethyl sulfoxide (DMSO) was added to the sample immediately prior to the addition of $^{14}\text{NH}_4\text{Cl}$ solution. After incubation for 2-3 min, the sample was frozen to first record spectra in the dark-adapted state. Subsequent illumination at 180 K (ethanol/liquid N_2) followed by an annealing step at 0 °C (ice/water) for 10-20 s generated the NH_3 -modified S_2 state.

S2 Data processing: baseline correction and light-minus-dark subtraction

To minimize possible contributions from underlying signals from other paramagnetic species in the sample, such as hexaquo-Mn^{II}, oxidized cytochrome b₅₅₉ and c₅₅₀ and Fe^{II}/Q_A⁻, S₂-minus-S₁ (light-minus-dark) subtractions were performed for X- and Q-band pulse EPR and electron nuclear double resonance (ENDOR) spectra. From derivative-shaped, *i.e.* continuous wave (CW) or pseudo-modulated, EPR spectra a fitted baseline was subtracted.

Three-pulse electron spin echo envelope modulation (ESEEM) data were also baseline-corrected after light-minus-dark subtraction of the normalized time-domain traces. (Fig. S1), in order to obtain spectra containing only resonances from the oxygen-evolving complex (OEC) in the S₂ state, excluding modulations from other paramagnetic species, foremost the background cytochrome (¹⁴N) signals. The (T₁) decay was modeled and removed by subtracting a third (X-band), a fifth (Q-band Mn₄O₅Ca, Mn₄O₅Sr) or seventh (Q-band Mn₄O₅Ca-NH₃) order polynomial fit function from the light-minus-dark difference.

Hyperfine sublevel correlation (HYSCORE)-spectroscopic data were baseline corrected using polynomial fit curves in both dimensions. Before Fourier transformation, a hamming apodization window and zero-filling were applied to the individual ESEEM and HYSCORE spectra. Experimental and simulated X-band ESEEM spectra were normalized with respect to the time domain spectra. Frequency-domain HYSCORE spectra and simulations were normalized with respect to the height of the single-quantum ¹⁴N peaks.

Electron electron double resonance (ELDOR)-detected NMR (EDNMR) spectra were baseline-subtracted and further processed to obtain an ENDOR-like representation of the spectra as described in Ref.¹.

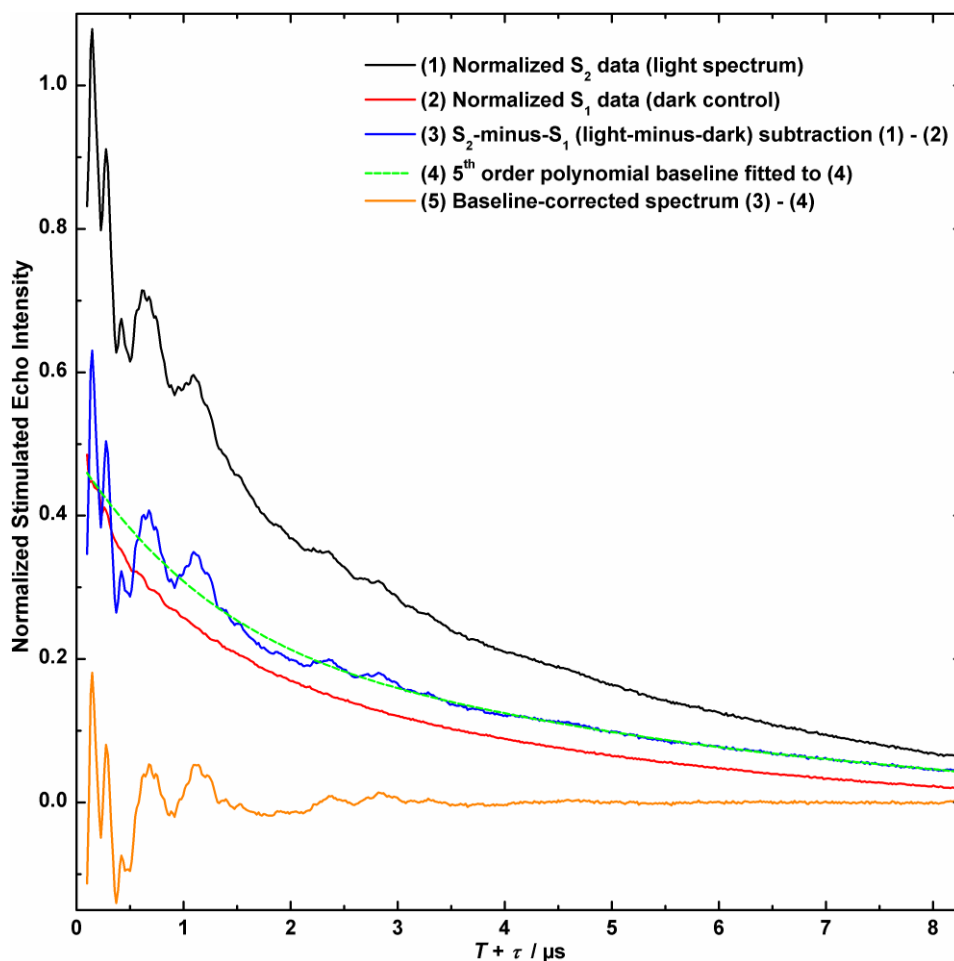


Fig. S1 Example for the light-minus-dark subtraction and baseline correction of three-pulse ESEEM spectra. The solid black and red lines depict ESEEM spectra of a PS II sample in the S_2 (1) and S_1 states (2), after subtraction of the y-axis offset and normalization. The blue solid line shows the spectrum resulting from the S_2 -minus- S_1 subtraction (3). The superimposing green dashed line (4) represents a fifth order polynomial fit curves to (3). The solid orange line (5) is the baseline-corrected resulting ESEEM spectrum after background subtraction. Experimental parameters: magnetic field: 1220 mT, τ : 260 ns; other settings were those given in Fig. S4.

S3 Spectral simulations

The EasySpin^{2,3} function ‘pepper’ was used to calculate EPR spectra, ‘salt’ for ENDOR, ‘saffron’ for three-pulse ESEEM and HYSCORE and a home-written script involving EasySpin functions for EDNMR spectra.

For calculation of the spin Hamiltonians of the ⁵⁵Mn tetramer-single electron spin manifolds that describe the EPR and ⁵⁵Mn-ENDOR spectra, the electron Zeeman term was treated exactly. The ⁵⁵Mn hyperfine terms were treated using second order perturbation theory. ⁵⁵Mn nuclear quadrupole interactions (NQI) are not resolved in both the EPR and ENDOR spectra and thus omitted in their simulations. The ⁵⁵Mn nuclear Zeeman terms were not included in the EPR simulations (see sections S4.2 and S4.3). The G and the four effective ⁵⁵Mn hyperfine tensors A_i were assumed to be collinear. First-derivative X- and Q-band EPR, and absorption-line W-band EPR and Q-band ⁵⁵Mn-ENDOR data were simultaneously fit using a least squares routine.

For simulation of the (orientation-selective) ESEEM, HYSCORE and EDNMR spectra, ¹⁴N, ¹⁵N and ¹⁷O single nucleus-single electron spin Hamiltonians were used. The ⁵⁵Mn nuclear interactions were not considered explicitly, but accounted for by employing hyperfine strain, *i.e.* an isotropic broadening due to unresolved hyperfine couplings, to compute the excitation window. All other spin Hamiltonian terms were treated exactly. In the simulations of the ¹⁷O-EDNMR spectra, the NQI term was omitted as it is not resolved within the line width.

ESEEM simulation traces were fitted to the time-domain spectra. The X-band ESEEM spectra were fitted including two nitrogen nuclei and contributions from ¹H nuclei simulated by a hyperfine interaction $A_i = [-0.44 \ -0.44 \ 1.44]$ MHz.

EDNMR transition intensities were calculated assuming small angle excitation by the high turning angle (HTA) pulse, as described in Cox *et al.*⁴. As in Refs.^{1,5}, the contributions from different nuclear species, as well as their individual single- and double-quantum transition envelopes, were calculated and normalized separately. Specifically, for the ¹⁷O signal envelopes, which are made up of multiple species,

the fitting was constrained such that the relative intensities of the different contributions were scaled according to the magnitude of the anisotropic component of the hyperfine interaction.

S4 Theoretical background

S4.1 The spin Hamiltonian formalism. Here, we consider a single ligand ^{14}N , ^{15}N or ^{17}O nucleus magnetically interacting with an exchange-coupled Mn tetramer. The current assignment for the oxidation states of the four Mn ions when poised in the S_2 state is $\text{Mn}^{\text{III}}\text{Mn}^{\text{IV}}\text{Mn}^{\text{IV}}\text{Mn}^{\text{IV}}$.⁶⁻¹³ This net oxidation state is assumed throughout the text. A basis set that describes the ^{14}N -, ^{15}N - or ^{17}O -Mn-tetramer spin manifold can be built from the product of the eigenstates of the interacting spins:

$$|S_1 S_2 S_3 S_4 M_1 M_2 M_3 M_4 I_1 I_2 I_3 I_4 m_1 m_2 m_3 m_4 L k\rangle, \quad (\text{Eq. S1})$$

Here, S_i (with $i = 1 - 4$) refers to the electronic spin state of Mn_i , M_i refers to the electronic magnetic sublevel of Mn_i , I_i refers to the nuclear spin state of Mn_i , and m_i refers to the nuclear magnetic sublevels of Mn_i . S_i takes the value 2 for Mn^{III} and $3/2$ for Mn^{IV} ; M_i takes the values: $S_i, S_i-1, \dots, 1-S_i, -S_i$; I_i takes the value $5/2$ for ^{55}Mn , m_i takes the values $-I_i, 1-I_i, \dots, I_i-1, I_i$, L takes the values 1 for ^{14}N , $1/2$ for ^{15}N and $5/2$ for ^{17}O , and k takes the values $-L, 1-L, \dots, L-1, L$.

The spin Hamiltonian that describes the spin manifold of the ^{14}N -, ^{15}N - or ^{17}O -Mn tetramer is:

$$H = \sum_i \beta_e \vec{B}_0 \cdot \hat{g}_i \cdot \vec{S}_i + \sum_i \vec{S}_i \cdot \hat{d}_i \cdot \vec{S}_i + \sum_{i<j} \vec{S}_i \cdot \hat{J}_{ij} \cdot \vec{S}_j - \sum_i g_{\text{Mn}} \beta_n \vec{B}_0 \cdot \vec{I}_i + \sum_i \vec{S}_i \cdot \hat{a}_{\text{Mn},i} \cdot \vec{I}_i \\ + \sum_i \vec{I}_i \cdot \hat{q}_{\text{Mn},i} \cdot \vec{I}_i - g_L \beta_n \vec{B}_0 \cdot \vec{L} + \vec{S}_L \cdot \hat{a}_L \cdot \vec{L} + \vec{L} \cdot q_L \cdot \vec{L} \quad (\text{Eq. S2})$$

It contains (i) an electronic Zeeman term for each Mn (g_i) ion, (ii) a fine structure term for each Mn (d_i) ion, and (iii) pair-wise electronic exchange terms for each Mn-Mn (J_{ij}) interaction, (iv) a nuclear Zeeman term for each ^{55}Mn (g_{Mn}) nucleus and the ligand (g_L) nucleus, (v) an electron-nuclear hyperfine term for each ^{55}Mn ($a_{\text{Mn},i}$) nucleus and the ligand (a_L) nucleus (vi) an NQI term for each ^{55}Mn ($q_{\text{Mn},i}$) and the ligand (q_L) nucleus.

S4.2 An effective spin $S_T = \frac{1}{2}$ ground state. A basis set that describes the entire spin manifold of the coupled four ^{55}Mn ions of the OEC requires 414720 vectors, too many to be readily handled by current numerical techniques. The problem can be greatly simplified by assuming that all Mn-Mn couplings are large, *i.e.* within the strong exchange limit. For this to apply, the exchange interactions between the Mn ions have to be significantly larger than any other term of the spin Hamiltonian. The resultant electronic spin states of the manifold are then adequately described by a single quantum number, the total spin (S_T). The multiline EPR signal observed for the S_2 state of the OEC is derived from only one total spin state, the ground state of the spin manifold with total spin $S_T = \frac{1}{2}$. The basis set that describes this subspace requires only 15552 vectors in the case that models the coupling of the effective electronic spin ($S_T = \frac{1}{2}$) to the nuclear spin of each ^{55}Mn ($I = 5/2$) and a single ligand (L) nucleus:

$$\left| \frac{1}{2} \quad M \quad I_1 \quad I_2 \quad I_3 \quad I_4 \quad m_1 \quad m_2 \quad m_3 \quad m_4 \quad L \quad k \right\rangle \quad (\text{Eq. S3})$$

Where M takes all half-integer values $-\frac{1}{2} \leq M \leq \frac{1}{2}$, m_i takes all half-integer values $-\frac{5}{2} \leq m_i \leq \frac{5}{2}$, and k takes values $-L \leq k \leq L$.

The effective spin Hamiltonian that describes the ground state of the spin manifold ($S_T = \frac{1}{2}$) is:

$$H = \beta_e \vec{B}_0 \cdot \hat{G} \cdot \vec{S} + \sum_i \left(-g_{\text{Mn}} \beta_n \vec{B}_0 \cdot \vec{I}_i + \vec{S} \cdot \hat{A}_{\text{Mn},i} \cdot \vec{I}_i \right) - g_L \beta_n \vec{B}_0 \cdot \vec{L} + \vec{S}_L \cdot \hat{A}_L \cdot \vec{L} + \vec{L} \cdot q_L \cdot \vec{L} \quad (\text{Eq. S4})$$

It contains, (i) the Zeeman term for the total electronic spin, (ii) Zeeman terms for each ^{55}Mn and the ligand nucleus, (iii) hyperfine terms for each ^{55}Mn and the ligand nucleus and (iv) a quadrupole term for the ligand nucleus. Quadrupole terms are neglected for the ^{55}Mn nuclei as their size is smaller than the fitted line width.

S4.3 Application to the different spectroscopic experiments. The simulation of spectra from EPR and related experiments probing electronic spin transitions of the OEC can be further simplified. As the ligand couplings are comparatively small, they do not significantly contribute to the inhomogeneous line width of the S_2 state EPR spectrum. Thus, for simulation of the EPR spectrum, the terms in Eq. S4 relating to the ligand nucleus can be excluded (Eq. S5).

$$H_{\text{EPR}} = \beta_e \vec{B}_0 \cdot \hat{G} \cdot \vec{S} + \sum_i \vec{S} \cdot \hat{A}_{\text{Mn},i} \cdot \vec{I}_i \quad (\text{Eq. S5})$$

Also, a simplified effective spin Hamiltonian can be used for the simulation of the spectra from experiments probing nuclear magnetic interactions, as the various nuclei do not significantly couple to each other. Thus, for the simulation of the ^{55}Mn -ENDOR resonances, terms in Eq. 4 associated with the ligand nucleus can be excluded:

$$H_{\text{MnENDOR}} = \beta_e \vec{B}_0 \cdot \hat{G} \cdot \vec{S} + \sum_i \left(-g_{\text{Mn}} \beta_n \vec{B}_0 \cdot \vec{I}_i + \vec{S} \cdot \hat{A}_{\text{Mn},i} \cdot \vec{I}_i \right) \quad (\text{Eq. S6})$$

Similarly, for describing the nuclear interactions of a ligand ^{14}N , ^{15}N or ^{17}O nucleus in the various experiments (ESEEM, HYSCORE, EDNMR), the terms relating to the ^{55}Mn nuclei in Eq. 4 can be omitted:

$$H_{\text{Ligand}} = \beta_e \vec{B}_0 \cdot \hat{G} \cdot \vec{S} - g_L \beta_n \vec{B}_0 \cdot \vec{L} + \vec{S}_L \cdot \hat{A}_L \cdot \vec{L} + \vec{L} \cdot q_L \cdot \vec{L} \quad (\text{Eq. S7})$$

In practice, however, the spin Hamiltonian in Eq. S7 is only valid when an ESEEM, ENDOR or EDNMR spectrum is collected at the center field of the S_2 state multiline spectrum as at this position all powder pattern orientations are sampled uniformly. Especially at W-band, spectra collected on the high- and low-field edges of the multiline spectrum must also take into account the sampling of the powder pattern orientations, which for the S_2 state ^{55}Mn tetramer is defined by the hyperfine coupling of the ^{55}Mn nuclei along with the G tensor. Eq. S7 can still be used (*i.e.*, terms associated with the ^{55}Mn nuclei can be excluded), but each orientation must include a weighting derived from simulation of the EPR line shape, for which the ^{55}Mn hyperfine interactions are taken account by hyperfine strain.

S5 DFT calculations: NH₃ binding modes and spatial coordinates of the S₂ state models

S5.1 Different coordination modes for the NH₃-annealed S₂ state and corresponding energies

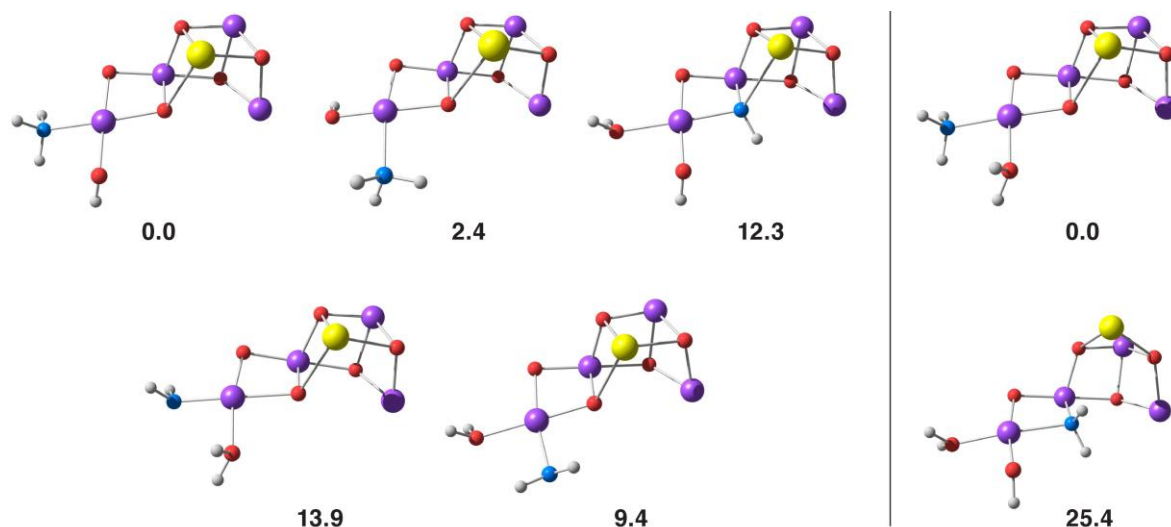


Fig. S2 Optimized structures (only the inorganic core framework and the terminal Mn_{A4} ligands are shown) and relative energies in kcal/mol of alternative models for NH₃, NH₂ and NH binding. The five structures on the left and the two structures on the right form two isomer sets. Although the complexity of the OEC structure and the extensive hydrogen bonding between terminal ligands and the surrounding residues and H₂O molecules make it difficult to isolate the structural origin of all energy differences, the results demonstrate unambiguously that terminal NH₃ coordination by W1 displacement (top left) is the energetically preferred interaction mode of ammonia with the OEC cluster.

S5.2 Cartesian coordinates of the optimized DFT structures

Mn ₄ O ₅ Ca							
				C	-24.184294	-29.659284	202.927390
				C	-24.721999	-30.234810	201.610409
				C	-25.721730	-31.373018	201.743287
				O	-26.013183	-31.839215	202.892913
Mn	-24.848563	-35.523079	203.967881	O	-26.200648	-31.819686	200.639196
Mn	-27.334886	-35.213752	205.224408	H	-24.820614	-28.955951	209.209804
Mn	-27.324954	-33.347594	203.139609	C	-25.289739	-29.704836	209.874338
Mn	-27.586920	-33.190450	200.400671	H	-25.215628	-29.314217	210.902923
Ca	-27.866960	-36.744419	202.214036	C	-24.609120	-31.083522	209.710893
O	-26.417337	-36.501815	204.230462	C	-24.555063	-31.562096	208.286908
O	-28.351166	-34.735051	203.786382	C	-25.355784	-32.430055	207.562703
O	-26.000441	-34.050081	204.476435	C	-23.592938	-31.124472	207.378052
O	-28.501367	-32.618552	201.966909	C	-23.785244	-31.692405	206.168990
O	-26.773447	-34.313956	201.661037	N	-24.861039	-32.482961	206.269039
O	-28.452549	-31.704459	199.310367	C	-24.708982	-37.374838	210.156821
O	-26.673182	-33.801897	198.916579	H	-24.708982	-37.374838	210.156821
O	-27.535444	-37.283560	199.908060	C	-25.333665	-37.110846	209.273415
O	-28.039762	-39.149284	202.493992	C	-26.302066	-38.223140	208.875615
H	-30.449048	-26.810280	200.178402	O	-26.045971	-39.056800	207.985385
C	-30.241434	-27.113395	201.222163	C	-24.390518	-36.709013	208.141123
H	-30.724377	-26.361921	201.871645	C	-24.995314	-36.021256	206.922435
C	-28.735963	-27.341748	201.414363	O	-26.247447	-35.729512	206.899027
C	-28.199732	-28.497414	200.548849	O	-24.176239	-35.777058	205.979846
O	-28.978095	-29.534053	200.450413	N	-27.489289	-38.237933	209.552060
O	-27.065544	-28.401467	200.005515	C	-28.420988	-39.357108	209.469748
C	-32.924381	-41.850903	196.489835	C	-29.302576	-39.449882	208.216351
C	-31.571913	-41.351348	195.946748	O	-29.919350	-40.500558	207.967913
C	-30.565368	-41.203392	197.075929	N	-29.381138	-38.331183	207.462795
C	-30.005378	-42.352283	197.678852	C	-30.071767	-38.285876	206.178140
C	-30.219133	-39.945803	197.617817	C	-29.365555	-37.278820	205.263257
C	-29.142594	-42.263841	198.782163	O	-29.557519	-37.302203	204.036093
C	-29.355473	-39.836453	198.721946	O	-28.618993	-36.427231	205.917796
C	-28.815969	-40.996556	199.313115	O	-25.189563	-37.830945	197.327508
O	-27.951563	-40.860113	200.380987	O	-27.362976	-35.979546	197.623234
H	-33.785375	-32.318034	197.913159	O	-26.499610	-30.205345	198.030232
C	-32.844739	-31.791422	197.688620	O	-24.648447	-32.100460	198.143353
C	-31.633691	-32.698381	197.678058	O	-29.820167	-30.416904	202.822043
O	-30.479771	-32.238554	197.548579	O	-25.769334	-39.372428	199.682432
H	-32.684897	-30.983928	198.422799	O	-26.808162	-39.050579	205.080655
N	-31.875152	-34.044975	197.757512	H	-30.315328	-30.632298	208.999280
C	-30.825021	-35.049751	197.612821	C	-30.997751	-31.051074	208.236197
C	-30.888736	-35.854848	196.310427	H	-31.843803	-31.521736	208.767318
O	-30.009176	-36.709569	196.081062	C	-30.280438	-32.094002	207.365998
C	-30.640197	-35.902739	198.882726	C	-29.002550	-31.542167	206.704535
C	-29.824344	-35.261129	200.019523	C	-28.324785	-32.556191	205.806489
O	-29.870659	-35.777979	201.169788	O	-28.076520	-33.718646	206.300284
O	-29.067769	-34.275626	199.682792	O	-28.029510	-32.191613	204.620538
N	-31.870257	-35.507945	195.452069	H	-36.639768	-31.792575	206.865042
C	-31.935591	-35.967611	194.072817	C	-36.971479	-32.276075	205.926511
H	-31.190723	-35.442656	193.449429	C	-35.764944	-32.788933	205.115057
H	-21.516057	-41.187718	202.032943	C	-34.832529	-33.697006	205.940910
C	-22.352883	-41.458335	202.717392	C	-33.756434	-34.444822	205.142553
C	-22.781191	-42.906955	202.604719	N	-32.759739	-33.538384	204.548528
O	-23.563034	-43.422685	203.424699	C	-31.817337	-33.925669	203.659223
C	-23.549150	-40.504733	202.473898	N	-31.645432	-35.231088	203.388681
C	-23.066676	-39.045303	202.457023	O	-31.087087	-33.019146	202.995109
C	-24.154409	-37.985608	202.560664	N	-27.626729	-29.307939	204.155135
O	-25.245648	-38.054524	201.948944	H	-32.788273	-42.803281	197.036192
O	-23.811291	-36.982100	203.323874	H	-33.336860	-41.123350	197.214330
N	-22.260513	-43.593061	201.547319	H	-33.700323	-42.030393	195.723193
C	-22.629343	-44.962153	201.252063	H	-31.702054	-40.382213	195.428906
H	-21.726399	-45.520632	200.924621	H	-31.186938	-42.064851	195.191736
C	-23.730290	-45.086017	200.172457	H	-30.251674	-43.345312	197.277293
C	-24.993767	-44.407864	200.583663	H	-28.718529	-43.170884	199.228945
C	-25.537884	-43.184397	200.232720	H	-29.068205	-38.858894	199.129846
N	-25.837688	-44.902174	201.568679	H	-30.611394	-39.027180	197.158676
C	-26.833926	-44.005179	201.787416	H	-27.492399	-41.807672	200.683751
N	-26.676843	-42.954433	200.984287	H	-25.186432	-42.463282	199.492006
H	-19.262626	-31.517297	202.779917	H	-27.637869	-44.150683	202.510626
C	-20.112713	-31.328697	202.090235	H	-28.777126	-37.534390	207.680920
C	-21.154324	-30.545460	202.872811	H	-27.643151	-37.538128	210.276277
O	-21.427294	-30.809815	204.064559	H	-21.526504	-29.397911	201.211747
C	-20.718700	-32.621528	201.484318	H	-21.667892	-43.094004	200.886496
C	-21.588166	-33.370625	202.438984	H	-22.974272	-45.418365	202.196465
C	-22.935559	-33.687611	202.415622	H	-23.906301	-46.160356	199.971989
N	-21.124735	-33.845842	203.657796	H	-23.378923	-44.635507	199.227014
C	-22.142018	-34.418977	204.333486	H	-22.513535	-38.839070	201.518066
N	-23.257629	-34.340485	203.596833	H	-24.047081	-40.756192	201.518478
N	-21.804706	-29.583301	202.173241	H	-21.977561	-41.306868	203.747367
C	-22.896307	-28.815019	202.759171	H	-22.355106	-38.865609	203.281935
H	-22.557559	-28.453986	203.752878				

H	-24.301734	-40.652867	203.270025
H	-26.358938	-29.763781	209.603411
H	-26.220428	-33.025771	207.856890
H	-23.147269	-31.534392	205.291984
H	-23.684622	-33.524182	201.638740
H	-22.065252	-34.899474	205.308562
H	-19.698085	-30.721961	201.264657
H	-23.076603	-27.937895	202.115324
H	-29.896088	-34.453597	197.496858
H	-32.820024	-34.354703	197.987338
H	-32.925528	-31.321758	196.691941
H	-32.460763	-34.722495	195.722132
H	-30.793684	-28.056205	201.384572
H	-19.901235	-33.268438	201.113909
H	-21.333568	-32.360309	200.605086
H	-25.923588	-36.230796	209.594643
H	-29.975762	-39.276336	205.695988
C	-31.564156	-37.928824	206.319346
H	-32.056613	-37.947667	205.331092
H	-32.062519	-38.671730	206.964277
H	-31.683667	-36.929700	206.775884
H	-29.094151	-39.310299	210.342798
H	-27.858742	-40.306732	209.536504
H	-23.602073	-36.034103	208.523038
H	-23.863239	-37.598136	207.748470
H	-30.066168	-36.812345	198.617400
H	-31.604854	-36.250281	199.292797
H	-31.385034	-30.210658	207.631826
H	-30.012169	-32.979335	207.971720
H	-28.269901	-31.258293	207.487263
H	-30.964891	-32.463056	206.575770
H	-29.201153	-30.638741	206.102238
H	-28.146833	-26.437556	201.181531
H	-28.500420	-27.615428	202.462237
H	-25.144131	-31.845570	210.304896
H	-23.576835	-31.046545	210.107853
H	-25.292301	-33.078319	205.481826
H	-37.548238	-31.526089	205.357493
H	-35.195683	-31.924827	204.717232
H	-35.436315	-34.474000	206.447865
H	-33.241171	-35.157342	205.817396
H	-37.650410	-33.104948	206.199040
H	-36.124111	-33.349679	204.228833
H	-34.351902	-33.112827	206.752078
H	-32.865338	-32.538412	204.705951
H	-34.232131	-35.033777	204.332879
H	-31.176326	-32.010814	203.158206
H	-31.976367	-35.949226	204.024923
H	-30.185561	-33.276123	202.558204
H	-30.914049	-35.512208	202.722443
H	-23.963557	-30.489480	203.618139
H	-25.216470	-29.463496	200.987817
H	-24.964386	-29.042215	203.409363
H	-23.890613	-30.637385	200.996140
H	-20.181078	-33.721257	204.021679
H	-25.897909	-33.224088	198.636671
H	-29.229519	-31.978237	198.744838
H	-28.667106	-30.776279	199.810498
H	-29.746630	-29.955121	201.936280
H	-29.241466	-31.207596	202.619636
H	-27.124877	-30.143312	204.225955
H	-28.475420	-29.634975	203.745033
H	-32.944446	-35.777473	193.676544
H	-31.725742	-37.049193	194.029264
H	-26.526019	-39.991045	199.877758
H	-25.481143	-39.036931	200.581548
H	-27.666916	-39.512951	203.330178
H	-27.537049	-36.751815	199.051621
H	-28.150279	-35.989060	197.036010
H	-27.193430	-35.042548	197.983106
H	-25.915461	-37.162327	197.336238
H	-25.390599	-38.411921	198.098016
H	-28.026489	-39.851553	201.791278
H	-26.878137	-38.012918	199.728867
H	-24.159252	-32.008798	198.980640
H	-25.260919	-31.287325	198.135510
H	-27.198052	-30.860903	198.286344
H	-26.609590	-29.529442	198.767862
H	-26.711950	-39.118824	206.056089
H	-26.544572	-38.112857	204.868630
H	-25.708383	-45.772595	202.082114
H	-22.831876	-30.479081	207.591768

Mn₄O₅Sr

Mn	-24.847522	-35.543564	204.005634
Mn	-27.322350	-35.221215	205.230987
Mn	-27.301408	-33.360082	203.133939
Mn	-27.570266	-33.190878	200.392937
Sr	-27.773969	-36.800711	202.185621
O	-26.395326	-36.530518	204.290632
O	-28.321095	-34.754475	203.778882
O	-25.984947	-34.062982	204.480107
O	-28.486683	-32.638832	201.963392
O	-26.729380	-34.301589	201.650723
O	-28.449881	-31.709891	199.309648
O	-26.642620	-33.791854	198.911122
O	-27.542861	-37.310450	199.773045
O	-28.067271	-39.274216	202.556052
H	-30.439098	-26.804571	200.178143
C	-30.241434	-27.113395	201.222163
H	-30.724377	-26.361921	201.871645
C	-28.738557	-27.350408	201.425078
C	-28.201955	-28.501402	200.553636
O	-28.977496	-29.540167	200.454472
O	-27.070837	-28.399496	200.005085
C	-32.924381	-41.850903	196.489835
C	-31.566967	-41.374251	195.939213
C	-30.558975	-41.227474	197.066268
C	-29.993014	-42.376462	197.663037
C	-30.222136	-39.970778	197.615746
C	-29.130223	-42.288611	198.766457
C	-29.360164	-39.862043	198.720908
C	-28.811541	-41.021967	199.303372
O	-27.943455	-40.884295	200.368763
H	-33.785375	-32.318034	197.913159
C	-32.844739	-31.791422	197.688620
C	-31.634108	-32.699247	197.680281
O	-30.480148	-32.239400	197.550866
H	-32.683822	-30.983826	198.422430
N	-31.875544	-34.045737	197.760638
C	-30.825021	-35.049751	197.612821
C	-30.891053	-35.854242	196.309656
O	-30.013559	-36.709922	196.077987
C	-30.630723	-35.903544	198.879125
C	-29.814141	-35.259888	200.014235
O	-29.875467	-35.762381	201.168485
O	-29.036385	-34.291453	199.668418
N	-31.872723	-35.506021	195.451452
C	-31.935591	-35.967611	194.072817
H	-31.190723	-35.442656	193.449429
H	-21.516057	-41.187718	202.032943
C	-22.352883	-41.458335	202.717392
C	-22.777025	-42.908578	202.607857
O	-23.549134	-43.427645	203.434844
C	-23.557907	-40.511524	202.471638
C	-23.084493	-39.047997	202.402297
C	-24.168388	-37.987059	202.549207
O	-25.264811	-38.035469	201.936834
O	-23.824841	-37.010368	203.340884
N	-22.265032	-43.591309	201.543887
C	-22.629343	-44.962153	201.252063
H	-21.726399	-45.520632	200.924621
C	-23.729143	-45.095444	200.172928
C	-24.996925	-44.427297	200.585019
C	-25.548238	-43.206738	200.236361
N	-25.836503	-44.927692	201.570687
C	-26.838027	-44.036674	201.791173
N	-26.687631	-42.984336	200.989178
H	-19.262626	-31.517297	202.779917
C	-20.112713	-31.328697	202.090235
C	-21.148504	-30.538340	202.872859
O	-21.414636	-30.796357	204.067668
C	-20.734300	-32.622151	201.497733
C	-21.603451	-33.368201	202.457635
C	-22.946290	-33.707963	202.429191
N	-21.137532	-33.838032	203.677440
C	-22.148150	-34.428194	204.348756
N	-23.262770	-34.367262	203.608879
N	-21.803538	-29.580554	202.172049
C	-22.896307	-28.815019	202.759171
H	-22.557559	-28.453986	203.752878
C	-24.181716	-29.660126	202.928755
C	-24.722407	-30.227121	201.610337
C	-25.718949	-31.367117	201.740658

O	-26.002379	-31.842055	202.889037	H	-23.078141	-27.937489	202.116223
O	-26.202553	-31.805270	200.635606	H	-29.897362	-34.451898	197.493798
H	-24.809359	-28.960819	209.212244	H	-32.820543	-34.355979	197.989244
C	-25.289739	-29.704836	209.874338	H	-32.924671	-31.323090	196.691292
H	-25.215628	-29.314217	210.902923	H	-32.462081	-34.719217	195.719947
C	-24.624893	-31.091091	209.712480	H	-30.799119	-28.054470	201.376360
C	-24.560543	-31.562523	208.286764	H	-19.923868	-33.276165	201.124087
C	-25.349798	-32.434305	207.554921	H	-21.352685	-32.360734	200.620986
N	-23.595543	-31.114786	207.385870	H	-25.922558	-36.229605	209.592752
C	-23.774996	-31.680275	206.174006	H	-29.994641	-39.266225	205.716684
N	-24.844970	-32.480241	206.264675	C	-31.576011	-37.907338	206.331053
H	-24.708982	-37.374838	210.156821	H	-32.067356	-37.932300	205.342274
C	-25.333665	-37.110846	209.273415	H	-32.079669	-38.642684	206.980616
C	-26.300933	-38.224773	208.878926	H	-31.691811	-36.904409	206.780181
O	-26.040335	-39.063990	207.994690	H	-29.091703	-39.310203	210.344813
C	-24.386912	-36.712850	208.142561	H	-27.858742	-40.306732	209.536504
C	-24.992459	-36.022343	206.927704	H	-23.596107	-36.041001	208.525313
O	-26.238003	-35.710160	206.916372	H	-23.862657	-37.603793	207.749980
O	-24.180164	-35.793742	205.972439	H	-30.050373	-36.807660	198.607772
N	-27.489437	-38.237473	209.551622	H	-31.591393	-36.257878	199.292352
C	-28.420988	-39.357108	209.469748	H	-31.385678	-30.212245	207.629892
C	-29.305038	-39.447628	208.219771	H	-29.997571	-32.973704	207.980342
O	-29.913924	-40.500987	207.963740	H	-28.275550	-31.242364	207.455690
N	-29.398341	-38.320876	207.480263	H	-30.970870	-32.481000	206.591322
C	-30.085454	-38.273385	206.194923	H	-29.225496	-30.652409	206.071063
C	-29.369811	-37.276449	205.276851	H	-28.143299	-26.447157	201.204788
O	-29.564530	-37.306122	204.050969	H	-28.515263	-27.633724	202.472907
O	-28.612781	-36.428849	205.927101	H	-25.176840	-31.849150	210.295893
O	-25.151856	-37.834078	197.301915	H	-23.596685	-31.069489	210.121075
O	-27.316256	-35.932702	197.549365	H	-25.263958	-33.079645	205.475862
O	-26.508973	-30.194245	198.024114	H	-37.548238	-31.526089	205.357493
O	-24.637913	-32.066365	198.138137	H	-35.192968	-31.924153	204.720225
O	-29.799381	-30.430228	202.827438	H	-35.439101	-34.477597	206.443308
O	-25.767207	-39.391760	199.664435	H	-33.246866	-35.164547	205.815492
O	-26.825769	-39.097706	205.138143	H	-37.650169	-33.105545	206.197916
H	-30.315733	-30.628829	208.997803	H	-36.123233	-33.346500	204.227348
C	-30.997751	-31.051074	208.236197	H	-34.353989	-33.118344	206.753344
H	-31.843803	-31.521736	208.767318	H	-32.855061	-32.542337	204.716747
C	-30.279499	-32.096912	207.368279	H	-34.229824	-35.030561	204.326920
C	-29.013025	-31.545151	206.684315	H	-31.151166	-32.017954	203.176466
C	-28.327552	-32.563676	205.795194	H	-31.961562	-35.953099	204.042903
O	-28.080955	-33.723607	206.294970	H	-30.166465	-33.291444	202.577663
O	-28.019919	-32.203459	204.611063	H	-30.904473	-35.519002	202.735048
H	-36.640291	-31.793756	206.865827	H	-23.957359	-30.494506	203.613336
C	-36.971479	-32.276075	205.926511	H	-25.219372	-29.452700	200.993647
C	-35.763832	-32.788497	205.115190	H	-24.960906	-29.046996	203.417023
C	-34.833474	-33.699931	205.939590	H	-23.892524	-30.625725	200.991398
C	-33.756307	-34.446956	205.141711	H	-20.197134	-33.699832	204.044862
N	-32.752267	-33.542214	204.556972	H	-25.877474	-33.200854	198.630977
C	-31.804334	-33.931414	203.673704	H	-29.228123	-31.984420	198.745683
N	-31.636098	-35.237271	203.401154	H	-28.665148	-30.783519	199.810884
N	-31.063395	-33.027386	203.019445	H	-29.730725	-29.966661	201.941859
O	-27.601196	-29.322117	204.155150	H	-29.223680	-31.221872	202.621833
H	-32.799026	-42.798213	197.047485	H	-27.099379	-30.157492	204.225445
H	-33.328280	-41.109535	197.204990	H	-28.451184	-29.648882	203.747647
H	-33.700323	-42.030393	195.723193	H	-32.944167	-35.779525	193.674748
H	-31.686363	-40.408931	195.411657	H	-31.724175	-37.048948	194.031317
H	-31.191800	-42.100324	195.191443	H	-26.524888	-40.007743	199.869361
H	-30.234818	-43.368675	197.256731	H	-25.495558	-39.036622	200.559927
H	-28.698804	-43.195183	199.207076	H	-27.694527	-39.630438	203.395105
H	-29.076401	-38.884424	199.130778	H	-27.524991	-36.745460	198.935755
H	-30.622065	-39.052237	197.162989	H	-28.113528	-35.928027	196.976887
H	-27.496965	-41.832812	200.676915	H	-27.152045	-35.006961	197.941725
H	-25.201723	-42.482824	199.495993	H	-25.869508	-37.157570	197.302270
H	-27.640563	-44.188034	202.514743	H	-25.364133	-38.418680	198.065646
H	-28.796871	-37.523202	207.702171	H	-28.051327	-39.973546	201.850653
H	-27.646985	-37.533196	210.270738	H	-26.872156	-38.027902	199.595628
H	-21.530663	-29.399200	201.208242	H	-24.148642	-31.969282	198.974769
H	-21.677238	-43.090484	200.880086	H	-25.258600	-31.259100	198.130512
H	-22.972298	-45.416804	202.197911	H	-27.201408	-30.855776	198.280424
H	-23.896325	-46.171435	199.973817	H	-26.621270	-29.520602	198.763778
H	-23.381788	-44.643190	199.226835	H	-26.729391	-39.161847	206.114547
H	-22.586096	-38.858679	201.430002	H	-26.556287	-38.163670	204.926956
H	-24.075507	-40.790807	201.534579	H	-25.702708	-45.799042	202.081429
H	-21.978856	-41.301263	203.746797	H	-22.841190	-30.463954	207.606809
H	-22.329213	-38.853074	203.183342				
H	-24.292487	-40.641882	203.287421				
H	-26.358163	-29.750767	209.597917				
H	-26.212428	-33.037018	207.840907				
H	-23.131951	-31.515173	205.301802				
H	-23.694957	-33.556265	201.649320				
H	-22.064848	-34.903542	205.325894				
H	-19.698989	-30.731536	201.257490				

Mn₄O₅Ca-NH₃

Mn	-24.864710	-35.521490	203.948726
Mn	-27.347645	-35.219577	205.222273
Mn	-27.313570	-33.383873	203.115499
Mn	-27.485767	-33.299034	200.363131
Ca	-27.838367	-36.773504	202.206296
O	-26.419856	-36.511777	204.238424
O	-28.356161	-34.755712	203.776060
O	-26.010801	-34.055338	204.486200
O	-28.448732	-32.678016	201.884329
O	-26.703765	-34.406807	201.716902
N	-28.266943	-31.835150	199.178604
O	-26.543687	-33.978771	198.919068
O	-27.544064	-37.346947	199.899022
O	-28.049725	-39.175016	202.519122
H	-30.509875	-26.860957	200.179093
C	-30.241434	-27.113395	201.222163
H	-30.724377	-26.361921	201.871645
C	-28.717362	-27.230848	201.366941
C	-28.147217	-28.372668	200.506754
O	-28.870316	-29.423316	200.397733
O	-27.003468	-28.225793	199.960457
C	-32.924381	-41.850903	196.489835
C	-31.581764	-41.318185	195.953559
C	-30.575680	-41.184853	197.084755
C	-29.977795	-42.339072	197.638888
C	-30.272636	-39.941171	197.681704
C	-29.119791	-42.269259	198.747269
C	-29.417002	-39.850281	198.793484
C	-28.839295	-41.016158	199.335137
O	-27.983212	-40.897097	200.411499
H	-33.785375	-32.318034	197.913159
C	-32.844739	-31.791422	197.688620
C	-31.653286	-32.714935	197.543999
O	-30.531221	-32.285140	197.217641
H	-32.633097	-31.060938	198.489041
N	-31.878803	-34.052802	197.766510
C	-30.825021	-35.049751	197.612821
C	-30.865287	-35.835399	196.298584
O	-29.945790	-36.642644	196.044494
C	-30.640852	-35.918810	198.872564
C	-29.789680	-35.310628	200.005116
O	-29.858555	-35.815521	201.157932
O	-28.981276	-34.372779	199.649010
N	-31.868631	-35.521649	195.456113
C	-31.935591	-35.967611	194.072817
H	-31.190723	-35.442656	193.449429
H	-21.516057	-41.187718	202.032943
C	-22.352883	-41.458335	202.717392
C	-22.776249	-42.908782	202.608354
O	-23.551661	-43.427050	203.432828
C	-23.552784	-40.510643	202.469132
C	-23.078230	-39.048869	202.449119
C	-24.171642	-37.994255	202.549317
O	-25.270984	-38.083792	201.953885
O	-23.825599	-36.975682	203.289600
N	-22.262672	-43.592225	201.545640
C	-22.629343	-44.962153	201.252063
H	-21.726399	-45.520632	200.924621
C	-23.731479	-45.089627	200.174408
C	-25.000266	-44.424899	200.591243
C	-25.559161	-43.206908	200.244674
N	-25.837340	-44.932188	201.575658
C	-26.844140	-44.047669	201.797756
N	-26.700283	-42.992700	200.997890
H	-19.262626	-31.517297	202.779917
C	-20.112713	-31.328697	202.090235
C	-21.149552	-30.539290	202.873280
O	-21.419003	-30.799420	204.066784
C	-20.723298	-32.618867	201.484204
C	-21.599273	-33.363171	202.436715
C	-22.944254	-33.689736	202.401952
N	-21.145202	-33.824906	203.664228
C	-22.166165	-34.398156	204.334587
N	-23.274161	-34.333814	203.585587
N	-21.799095	-29.576638	202.173515
C	-22.896307	-28.815019	202.759171
H	-22.557559	-28.453986	203.752878
C	-24.176837	-29.674212	202.924814
C	-24.722648	-30.242942	201.605811
C	-25.673598	-31.425442	201.731344

O	-26.018756	-31.851735	202.879987
O	-26.065736	-31.942535	200.620999
H	-24.801515	-28.965028	209.213262
C	-25.289739	-29.704836	209.874338
H	-25.215628	-29.314217	210.902923
C	-24.636080	-31.096445	209.714297
C	-24.578059	-31.571248	208.289346
C	-25.376593	-32.437107	207.560279
N	-23.611024	-31.133702	207.385609
C	-23.798680	-31.700932	206.175302
N	-24.875693	-32.490146	206.269295
H	-24.708982	-37.374838	210.156821
C	-25.333665	-37.110846	209.273415
C	-26.300738	-38.224866	208.877256
O	-26.041287	-39.063182	207.992233
C	-24.393954	-36.706939	208.139308
C	-25.002102	-36.019488	206.920698
O	-26.255457	-35.728630	206.900664
O	-24.183671	-35.775666	205.978534
N	-27.490167	-38.237322	209.549699
C	-28.420988	-39.357108	209.469748
C	-29.304581	-39.454352	208.217565
O	-29.921032	-40.506669	207.974643
N	-29.384204	-38.339404	207.458988
C	-30.071968	-38.300480	206.172216
C	-29.369738	-37.289425	205.258738
O	-29.561109	-37.312856	204.031272
O	-28.631097	-36.432971	205.915409
O	-25.256753	-37.985027	197.283490
O	-27.394488	-36.098233	197.572737
O	-26.252701	-29.970572	198.146402
O	-24.619668	-32.110776	198.117885
O	-29.701492	-30.390722	202.699176
O	-25.776766	-39.443943	199.703356
O	-26.817106	-39.052364	205.097592
H	-30.304360	-30.649272	208.998605
C	-30.997751	-31.051074	208.236197
H	-31.843803	-31.521736	208.767318
C	-30.299242	-32.089135	207.343432
C	-29.032035	-31.540173	206.658983
C	-28.353578	-32.561403	205.766910
O	-28.097633	-33.716666	206.279018
O	-28.062835	-32.210782	204.577261
H	-36.663406	-31.800759	206.877175
C	-36.971479	-32.276075	205.926511
C	-35.741686	-32.750576	205.123250
C	-34.772092	-33.611907	205.957189
C	-33.683948	-34.348734	205.163635
N	-32.719724	-33.434895	204.528030
C	-31.757597	-33.834930	203.664614
N	-31.543259	-35.145308	203.457803
N	-31.047224	-32.940683	202.962512
O	-27.559854	-29.319219	204.115328
H	-32.769260	-42.810763	197.017851
H	-33.346737	-41.144690	197.229596
H	-33.700323	-42.030393	195.723193
H	-31.728017	-40.338448	195.460444
H	-31.188644	-42.007082	195.180287
H	-30.190114	-43.321384	197.193914
H	-28.664658	-43.179784	199.154699
H	-29.160345	-38.882656	199.243123
H	-30.698698	-39.019225	197.260996
H	-27.525101	-41.846717	200.701984
H	-25.216575	-42.478730	199.506654
H	-27.645591	-44.204989	202.521261
H	-28.778547	-37.542060	207.671113
H	-27.647817	-37.533001	210.268672
H	-21.528970	-29.399498	201.208202
H	-21.676553	-43.090833	200.880790
H	-22.972246	-45.417617	202.197588
H	-23.899004	-46.164471	199.969225
H	-23.385908	-44.631971	199.230247
H	-22.524127	-38.841811	201.510847
H	-24.048025	-40.767550	201.513805
H	-21.979358	-41.302339	203.747290
H	-22.368586	-38.862857	203.274418
H	-24.306083	-40.660102	203.264364
H	-26.357875	-29.742211	209.595398
H	-26.245354	-33.029860	207.848221
H	-23.157158	-31.543306	205.301225
H	-23.687705	-33.541102	201.616471
H	-22.097321	-34.868618	205.315170
H	-19.696150	-30.723618	201.264263

H	-23.082995	-27.938595	202.116242
H	-29.896528	-34.451444	197.506025
H	-32.788477	-34.346718	198.122451
H	-32.960763	-31.226009	196.747974
H	-32.508765	-34.789033	195.760399
H	-30.726095	-28.079307	201.446514
H	-19.907851	-33.269977	201.116471
H	-21.334421	-32.355232	200.603054
H	-25.924836	-36.232018	209.595770
H	-29.968921	-39.290797	205.691356
C	-31.566606	-37.950180	206.306780
H	-32.053587	-37.969970	205.315712
H	-32.065376	-38.694688	206.949586
H	-31.692411	-36.951538	206.763000
H	-29.093141	-39.309782	210.343565
H	-27.858742	-40.306732	209.536504
H	-23.606290	-36.030492	208.520086
H	-23.865768	-37.595129	207.745866
H	-30.091398	-36.837912	198.589096
H	-31.606074	-36.249832	199.294797
H	-31.383088	-30.198805	207.647171
H	-30.022455	-32.978919	207.938924
H	-28.291208	-31.242267	207.429080
H	-31.000414	-32.449630	206.564168
H	-29.241508	-30.645701	206.047098
H	-28.201164	-26.291361	201.100794
H	-28.433679	-27.467158	202.412584
H	-25.192552	-31.849316	210.300155
H	-23.607107	-31.081871	210.121448
H	-25.301826	-33.092668	205.481387
H	-37.548238	-31.526089	205.357493
H	-35.206812	-31.867903	204.718424
H	-35.346282	-34.395013	206.488669
H	-33.137664	-35.023617	205.852756
H	-37.638922	-33.121520	206.174438
H	-36.077468	-33.332731	204.241646
H	-34.299288	-32.994667	206.747906
H	-32.881960	-32.433240	204.607462
H	-34.154886	-34.977513	204.381055
H	-31.127673	-31.930556	203.116276
H	-31.894146	-35.848399	204.099494
H	-30.148132	-33.204508	202.521251
H	-30.781219	-35.435485	202.834111
H	-23.940373	-30.509478	203.604410
H	-25.272365	-29.475630	201.023353
H	-24.960097	-29.072100	203.419980
H	-23.895851	-30.584811	200.951486
H	-20.207291	-33.687520	204.038040
H	-25.850528	-33.350448	198.562721
H	-29.051411	-32.169779	198.597391
H	-28.561419	-30.986686	199.723501
H	-29.591533	-29.909901	201.820146
H	-29.150648	-31.199882	202.502410
H	-27.071636	-30.162627	204.186895
H	-28.390706	-29.627465	203.654027
H	-32.944161	-35.768869	193.680452
H	-31.732285	-37.050323	194.016067
H	-26.538760	-40.048751	199.918316
H	-25.486437	-39.080015	200.590800
H	-27.678024	-39.530650	203.359394
H	-27.556708	-36.833499	199.032423
H	-28.208271	-36.093374	197.015818
H	-27.192198	-35.172672	197.931551
H	-25.976613	-37.309574	197.292913
H	-25.433830	-38.534189	198.082737
H	-28.042027	-39.884749	201.824854
H	-26.893567	-38.081659	199.722400
H	-24.238397	-32.158521	199.013738
H	-25.182206	-31.277130	198.165728
H	-27.534839	-31.466199	198.547559
H	-26.560745	-29.326508	198.890050
H	-26.714168	-39.115546	206.072735
H	-26.543578	-38.118929	204.876642
H	-25.698492	-45.803642	202.084843
H	-22.850254	-30.489410	207.603340
H	-26.357141	-29.474536	197.313611

Mn₄O₅Sr-NH₃

Mn	-24.870509	-35.539329	203.989923
Mn	-27.340841	-35.222259	205.228375
Mn	-27.292163	-33.392297	203.110512
Mn	-27.476682	-33.295887	200.355604
Sr	-27.752982	-36.822127	202.179576
O	-26.406325	-36.535667	204.295951
O	-28.332329	-34.768821	203.768907
O	-26.001418	-34.064573	204.491932
O	-28.436041	-32.690994	201.881801
O	-26.663437	-34.389934	201.707436
N	-28.270236	-31.836664	199.173019
O	-26.530811	-33.968438	198.908871
O	-27.559152	-37.383758	199.770505
O	-28.082822	-39.294418	202.579115
H	-30.511930	-26.862077	200.179348
C	-30.241434	-27.113395	201.222163
H	-30.724377	-26.361921	201.871645
C	-28.716820	-27.229948	201.363685
C	-28.147090	-28.369839	200.500231
O	-28.870145	-29.420590	200.389066
O	-27.003767	-28.221983	199.953847
C	-32.924381	-41.850903	196.489835
C	-31.591286	-41.295157	195.953669
C	-30.580898	-41.171873	197.081378
C	-29.937040	-42.324334	197.584858
C	-30.322810	-39.943417	197.728551
C	-29.074501	-42.266780	198.690600
C	-29.465369	-39.865292	198.839427
C	-28.838579	-41.028995	199.328269
O	-27.975519	-40.919512	200.400304
H	-33.785375	-32.318034	197.913159
C	-32.844739	-31.791422	197.688620
C	-31.655305	-32.717606	197.543642
O	-30.533492	-32.289763	197.213592
H	-32.632048	-31.061552	198.489283
N	-31.880706	-34.055156	197.770125
C	-30.825021	-35.049751	197.612821
C	-30.858404	-35.825563	196.292943
O	-29.923667	-36.611134	196.026084
C	-30.631803	-35.922702	198.866495
C	-29.786836	-35.308747	200.001542
O	-29.874668	-35.798116	201.157354
O	-28.960611	-34.385092	199.639541
N	-31.870492	-35.524436	195.456880
C	-31.935591	-35.967611	194.072817
H	-31.190723	-35.442656	193.449429
H	-21.516057	-41.187718	202.032943
C	-22.352883	-41.458335	202.717392
C	-22.774231	-42.909619	202.609580
O	-23.543294	-43.430115	203.438550
C	-23.558783	-40.515366	202.468346
C	-23.092230	-39.049970	202.420715
C	-24.186159	-37.997152	202.545792
O	-25.286445	-38.077515	201.942668
O	-23.847022	-36.996896	203.307240
N	-22.266811	-43.590684	201.542341
C	-22.629343	-44.962153	201.252063
H	-21.726399	-45.520632	200.924621
C	-23.728796	-45.098880	200.173284
C	-25.002428	-44.443408	200.587577
C	-25.567040	-43.228574	200.240535
N	-25.837911	-44.955603	201.570800
C	-26.850857	-44.077366	201.790468
N	-26.711062	-43.021754	200.990983
H	-19.262626	-31.517297	202.779917
C	-20.112713	-31.328697	202.090235
C	-21.142051	-30.529960	202.873739
O	-21.404472	-30.782789	204.070537
C	-20.743469	-32.618576	201.499916
C	-21.620941	-33.357372	202.458280
C	-22.961443	-33.706184	202.418193
N	-21.165378	-33.813624	203.687212
C	-22.180107	-34.404189	204.352655
N	-23.286237	-34.357118	203.599989
N	-21.797752	-29.573286	202.171792
C	-22.896307	-28.815019	202.759171
H	-22.557559	-28.453986	203.752878
C	-24.173579	-29.676573	202.925769
C	-24.726314	-30.232580	201.605000
C	-25.672560	-31.418409	201.727008

O	-26.007616	-31.854330	202.875286	H	-23.085872	-27.938089	202.117665
O	-26.070516	-31.926253	200.614765	H	-29.899221	-34.446364	197.508854
H	-24.800910	-28.965208	209.213497	H	-32.788640	-34.349051	198.130461
C	-25.289739	-29.704836	209.874338	H	-32.960159	-31.226065	196.747923
H	-25.215628	-29.314217	210.902923	H	-32.523787	-34.806491	195.767831
C	-24.636445	-31.096368	209.714303	H	-30.724448	-28.079858	201.447803
C	-24.576420	-31.568127	208.288617	H	-19.937574	-33.279712	201.128633
C	-25.374814	-32.430712	207.555672	H	-21.357895	-32.353404	200.621460
N	-23.608563	-31.127262	207.387445	H	-25.924889	-36.231881	209.594840
C	-23.793881	-31.690942	206.175362	H	-29.998700	-39.276550	205.713370
N	-24.871308	-32.480384	206.265462	C	-31.579953	-37.916363	206.329213
H	-24.708982	-37.374838	210.156821	H	-32.070147	-37.933457	205.339639
C	-25.333665	-37.110846	209.273415	H	-32.085942	-38.653299	206.975163
C	-26.298825	-38.227273	208.880875	H	-31.693250	-36.915262	206.783374
O	-26.034080	-39.071731	208.002795	H	-29.090655	-39.309697	210.345652
C	-24.393359	-36.707916	208.138466	H	-27.858742	-40.306732	209.536504
C	-25.006546	-36.019809	206.923738	H	-36.605484	-36.031269	208.518876
O	-26.253416	-35.709714	206.918387	H	-23.865326	-37.595870	207.744462
O	-24.198206	-35.792488	205.965740	H	-30.070251	-36.832955	198.577586
N	-27.490164	-38.237102	209.548700	H	-31.592955	-36.265769	199.287937
C	-28.420988	-39.357108	209.469748	H	-31.383226	-30.197413	207.649203
C	-29.308363	-39.451177	208.221618	H	-30.018359	-32.976667	207.935066
O	-29.920824	-40.504489	207.973385	H	-28.299911	-31.227380	207.403633
N	-29.400647	-38.328308	207.476552	H	-31.010014	-32.453694	206.567346
C	-30.089803	-38.284032	206.191723	H	-29.261543	-30.653567	206.020910
C	-29.377355	-37.284825	205.273604	H	-28.202025	-26.289602	201.097828
O	-29.567899	-37.318561	204.046801	H	-28.431085	-27.467010	202.408612
O	-28.632910	-36.427974	205.925130	H	-25.194296	-31.849900	210.297998
O	-25.228282	-37.982119	197.252603	H	-23.608113	-31.082826	210.123077
O	-27.361477	-36.060418	197.497938	H	-25.294782	-33.083804	205.478370
O	-26.258547	-29.970485	198.136556	H	-37.548238	-31.526089	205.357493
O	-24.600782	-32.092006	198.129105	H	-35.206991	-31.855823	204.723199
O	-29.683302	-30.396811	202.691263	H	-35.328758	-34.369673	206.513045
O	-25.777111	-39.465538	199.678778	H	-33.110723	-34.984187	205.885955
O	-26.856479	-39.088755	205.162419	H	-37.636458	-33.125324	206.167805
H	-30.302318	-30.651418	208.997851	H	-36.059929	-33.332342	204.250509
C	-30.997751	-31.051074	208.236197	H	-34.291166	-32.959631	206.758337
H	-31.843803	-31.521736	208.767318	H	-32.905350	-32.413718	204.569143
C	-30.302753	-32.089436	207.339341	H	-34.134988	-34.971931	204.417980
C	-29.042886	-31.540018	206.641231	H	-31.102868	-31.924680	203.127769
C	-28.356810	-32.563938	205.756527	H	-31.883470	-35.831315	204.150365
O	-28.102777	-33.717484	206.273217	H	-30.134069	-33.206742	202.533270
O	-28.053840	-32.216833	204.569059	H	-30.719044	-35.428700	202.928366
H	-36.671474	-31.802446	206.880663	H	-23.931230	-30.518094	203.595585
C	-36.971479	-32.276075	205.926511	H	-25.282088	-29.461133	201.033746
C	-35.734039	-32.742129	205.130412	H	-24.954717	-29.080727	203.431699
C	-34.759290	-33.588323	205.973971	H	-23.903268	-30.565599	200.941418
C	-33.666355	-34.326064	205.188288	H	-20.231362	-33.661954	204.065249
N	-32.712478	-33.412744	204.537143	H	-25.833108	-33.341442	198.560188
C	-31.736449	-33.821997	203.692888	H	-29.057201	-32.174546	198.597216
N	-31.499991	-35.132709	203.523249	H	-28.561046	-30.985814	199.716156
N	-31.029268	-32.935795	202.977734	H	-29.577497	-29.914867	201.812199
O	-27.549622	-29.324547	204.113995	H	-29.133717	-31.206666	202.492959
H	-32.754117	-42.815413	197.004591	H	-27.065176	-30.169600	204.191299
H	-33.352280	-41.159588	197.240309	H	-28.378077	-29.631591	203.647289
H	-33.700323	-42.030393	195.723193	H	-32.943857	-35.767843	193.680253
H	-31.751372	-40.308558	195.478760	H	-31.733037	-37.050448	194.013505
H	-31.195976	-41.966346	195.166283	H	-26.540648	-40.065914	199.905515
H	-30.116214	-43.295029	197.101498	H	-25.491279	-39.084972	200.559008
H	-28.579777	-43.174588	199.055748	H	-27.702034	-39.639150	203.419397
H	-29.240217	-38.906858	199.323388	H	-27.551924	-36.843399	198.918497
H	-30.788422	-39.023181	197.348285	H	-28.191208	-36.056123	196.964152
H	-27.526386	-41.873942	200.688637	H	-27.174080	-35.146680	197.893762
H	-25.226807	-42.497666	199.504098	H	-25.944154	-37.303079	197.254847
H	-27.653126	-44.239576	202.511964	H	-25.414702	-38.536933	198.044855
H	-28.794171	-37.532057	207.690460	H	-28.058535	-39.999244	201.880339
H	-27.651806	-37.527846	210.261959	H	-26.908205	-38.117800	199.592769
H	-21.534419	-29.401559	201.203616	H	-24.237337	-32.138510	199.032375
H	-21.682603	-43.088648	200.876292	H	-25.173977	-31.264988	198.168586
H	-22.971258	-45.416172	202.198599	H	-27.541448	-31.471562	198.536193
H	-23.887777	-46.175282	199.969547	H	-26.558768	-29.329519	198.885066
H	-23.385288	-44.640150	199.228886	H	-26.729472	-39.161264	206.134768
H	-22.568865	-38.850613	201.463442	H	-26.569953	-38.160553	204.945723
H	-24.064555	-40.787839	201.522850	H	-25.695765	-45.827136	202.078993
H	-21.980193	-41.299354	203.747011	H	-22.848922	-30.482577	207.608098
H	-22.359002	-38.854140	203.222528	H	-26.345265	-29.460304	197.310298
H	-24.301835	-40.657508	203.274482				
H	-26.357774	-29.741578	209.595036				
H	-26.245096	-33.023157	207.839884				
H	-23.151367	-31.529694	205.302659				
H	-23.704583	-33.568333	201.630201				
H	-22.105384	-34.870781	205.334646				
H	-19.697250	-30.734625	201.256062				

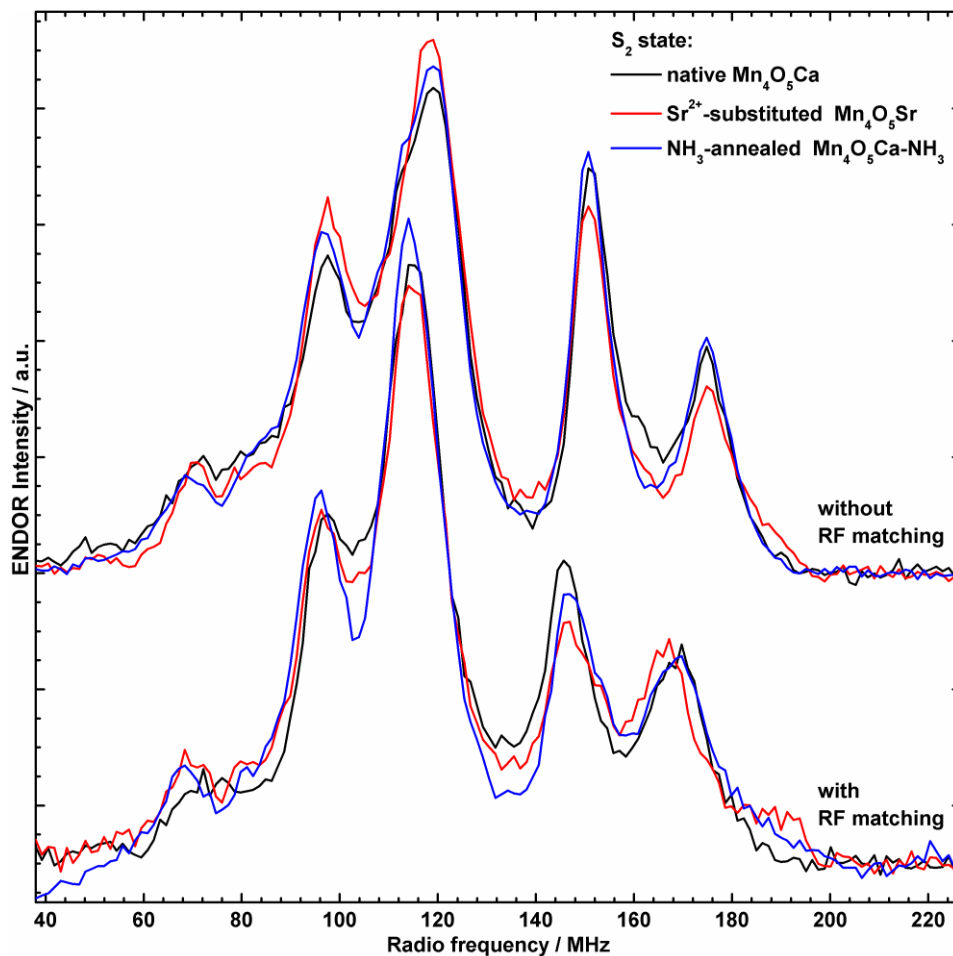


Fig. S3 Comparison of Q-band ^{55}Mn -ENDOR spectra of PSII samples isolated from *T. elongatus* in the native ($\text{Mn}_4\text{O}_5\text{Ca}$, black), Sr^{2+} -substituted ($\text{Mn}_4\text{O}_5\text{Ca}$, red) and NH_3 -annealed ($\text{Mn}_4\text{O}_5\text{Ca-NH}_3$, blue) S_2 states recorded without (top traces) and with (bottom traces)⁵ radio frequency (RF) matching employed. Shown are the spectra of illuminated samples without light-minus-dark subtraction. Experimental parameters: microwave frequencies: 33.9678 GHz (top, black), 33.9950 GHz (top, red), 34.0053 GHz (top, blue), 34.0368 GHz (bottom, black), 34.0435 GHz (bottom, red), 34.0159 GHz (bottom, blue); magnetic field: 1220 mT; shot repetition time: 1 ms; microwave pulse length (π): 32 ns (top), 24 ns (bottom); τ : 268 ns; RF pulse length (π_{RF}): 3.5 μs ; temperature: 4.8 K (top), 5.2 K (bottom).

In order to overcome variations of the spectral shape, especially at higher frequencies (>150 MHz), the ^{55}Mn -ENDOR experiments presented here were performed under instrumental settings that allowed for the best reproducibility. To obtain cleaner spectra, a radio frequency (RF) matching network, usually employed for producing a more uniform, frequency-independent RF amplitude to suppress artifacts and distortions of the spectral baseline, was omitted. Our optimization of the experimental conditions rationalizes spectral differences from earlier published Q-band data^{5, 12, 13}, in which the higher frequency resonances (> \approx 140 MHz) were comparatively suppressed, their maxima appearing shifted to somewhat lower frequencies (Fig. S3).^{*} This is reflected in the fitted hyperfine tensor components reproducing these spectra. While the magnitudes $A_{i,\text{iso}}$ of the four ^{55}Mn hyperfine tensors are approximately the same as those determined in PSII from higher plants and cyanobacteria,^{5, 9, 10, 12, 13} the size of the effective anisotropic components $A_{i,\text{aniso}}$ differ. This can be rationalized spectrally by the intensity profiles of the actual ^{55}Mn -ENDOR signals, specifically the relative enhancement of the two peaks at highest radio frequencies, yielding a more isotropic largest hyperfine tensor A_1 . This in turn requires the other three tensors A_2 , A_3 and A_4 to be less isotropic. Furthermore, reduced orientation selectivity, by employing harder, *i.e.* shorter microwave pulses (π : 32 ns vs. 80 ns in Ref.¹²) with a broader excitation width, and a more central field position (1220 mT vs. 1260 mT)¹² led to more similar spectra of the native and Sr^{2+} -substituted S_2 state (Fig. 3D in the main text), as also observed for the native and NH_3 -modified S_2 state⁵. This pronounced similarity confirms the structural homogeneity among all three cluster types.

Similar to the high RF region, the RF power may be not entirely uniform also at smaller frequencies such that the ENDOR intensities are not quantitative. This may be the reason why the edge of the ^{55}Mn -ENDOR feature ranging from \approx 85 to \approx 95 MHz cannot be correctly reproduced by the simulations (main text Fig. 3).

^{*} It is noted that this behaviour stands in contrast to the effect of RF matching on ^{55}Mn -ENDOR resonances observed at a commercial Bruker W-band ENDOR setup in the laboratory of the Bittl group. It is reported that, in the RF range >180 MHz, the peaks intensities are suppressed with increasing radio frequencies and the maxima shifted to lower radio frequencies in the absence of a RF matching network.¹⁴ S. Pudollek, Doctoral Thesis, Freie Universität Berlin, 2012.

S7 Electronic structures: exchange couplings and spin states of the BS-DFT models

Table S1 Calculated magnetic parameters for the broken-symmetry (BS) density functional theory (DFT) models of the for S₂ state variants described in the main text (sections 3.1 and 3.3), including total spins *S* of the ground state (GS) and the first excited state (ES) and the energy difference ΔE between these spin states. Listed are also the differences of the electronic exchange coupling constants J_{ij} and energy gaps between the Sr²⁺- and Ca²⁺-containing models $\Delta(\text{Sr-Ca})$ and the NH₃- and W1-containing models $\Delta(\text{NH}_3\text{-W1})$. J_{ij} and ΔE are given in wavenumbers (cm⁻¹).

	Ca	Sr	CaNH ₃	SrNH ₃	$\Delta(\text{Sr-Ca})$		$\Delta(\text{NH}_3\text{-W1})$	
					W1	NH ₃	Ca	Sr
$J_{\text{CD}} (J_{12})$	-15.7	-17.6	-15.5	-17.4	-1.9	-2.0	-15.7	-17.6
$J_{\text{BD}} (J_{13})$	2.0	1.5	5.0	4.7	-0.5	-0.3	2.0	1.5
$J_{\text{AD}} (J_{14})$	0.8	0.9	0.2	0.3	0.1	0.1	0.8	0.9
$J_{\text{BC}} (J_{23})$	23.8	19.3	27.5	22.6	-4.6	-5.0	23.8	19.3
$J_{\text{AC}} (J_{24})$	1.9	1.9	1.3	1.4	0.0	0.2	1.9	1.9
$J_{\text{AB}} (J_{34})$	-15.9	-16.0	-11.9	-11.9	-0.2	0.1	-15.9	-16.0
S_{GS}	1/2	1/2	1/2	1/2			1/2	1/2
S_{ES}	3/2	3/2	3/2	3/2			3/2	3/2
ΔE_{DFT}	23.5	26.3	16.8	19.0	+2.8	+2.2	23.5	26.3
ΔE_{exp}	23.5 ¹²	26.5 ¹²	30-34 ^{15, 16 a}		+3.0		— ^a	

^a For the CaNH₃ form of the S₂ state, ΔE was determined on PSII preparations isolated from higher plants (spinach), in contrast to the samples of the Ca and Sr forms, which were isolated from cyanobacterial PSII (*T. elongatus*). Thus, their values are not suited for direct comparison and no difference was calculated.

S8 The $\text{Mn}_{\text{D1}}\text{-His332-imino-N}$ interaction: Q-band three-pulse ESEEM, Q-band HYSCORE, W-band EDNMR and simulations

S8.1 τ - and field-dependent Q-Band three-pulse ESEEM spectra

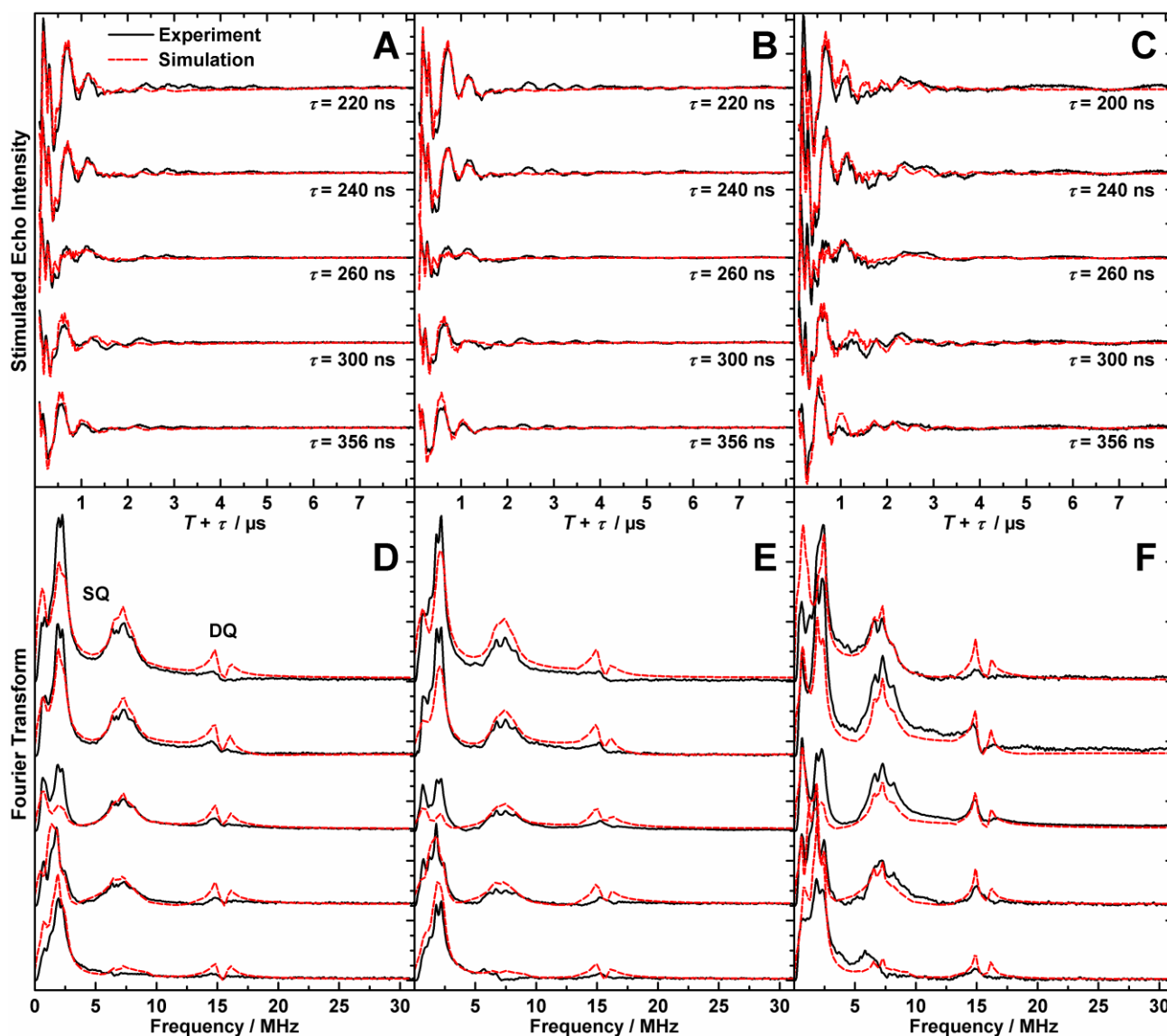


Fig. S4 Q-band three-pulse ESEEM light-minus-dark spectra of the S_2 state $\text{Mn}_4\text{O}_5\text{Ca}$ (A, D), S_2 state $\text{Mn}_4\text{O}_5\text{Sr}$ (B, E) and annealed S_2 state $\text{Mn}_4\text{O}_5\text{Ca-NH}_3$ (C, F) clusters in PSII isolated from *T. elongatus* at various τ values. (A–C) Time-domain spectra and (D–F) corresponding Fourier transforms. Black solid traces depict the baseline-corrected experimental spectra; superimposing red dashed traces represent simulations based on the spin Hamiltonian formalism as outlined in sections 2.3 in the main text, S3, S4 and S8.4. The optimized parameter sets are listed in Table 3 of the main text and in detail in

Table S2. ‘SQ’ and ‘DQ’ refer to the position of single and double-quantum transitions, respectively. For a description of the background subtraction procedure, see section S2. The data from the $\text{Mn}_4\text{O}_5\text{Ca}$ and $\text{Mn}_4\text{O}_5\text{Ca-NH}_3$ samples at $\tau = 240\text{-}300$ ns were originally reported in Ref.⁵ and reprocessed for this work. Experimental parameters: microwave frequencies: 34.0368 GHz (Ca^{2+}), 34.0433 GHz (Sr^{2+}), 34.0151 GHz (NH_3); magnetic fields: 1220, 1222 mT; shot repetition time: 1 ms; microwave pulse length ($\pi/2$): 12 ns; τ : 220–356 ns (Ca^{2+} , Sr^{2+}), 200–356 ns (NH_3); ΔT : 100 ns; temperature: 5.2 K.

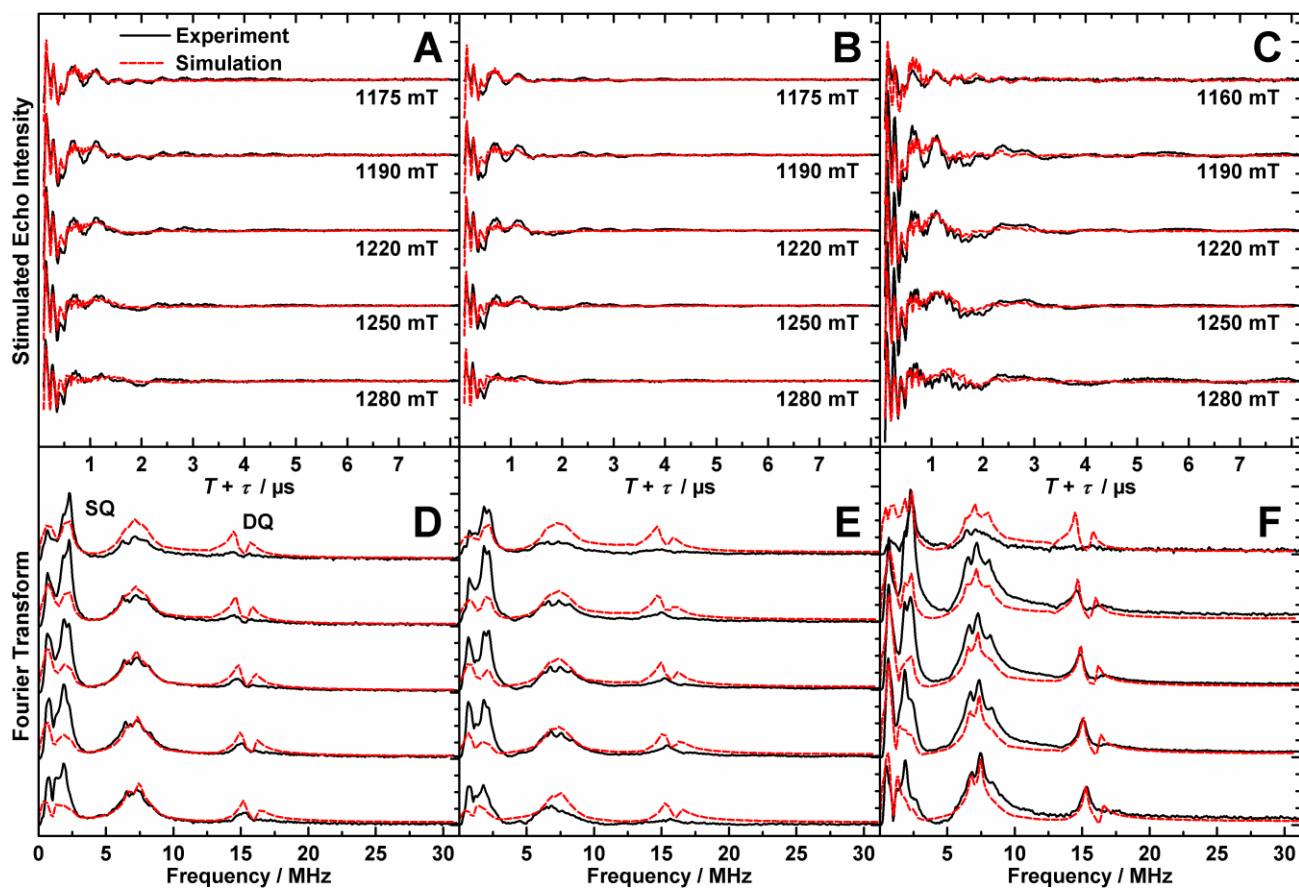


Fig. S5 Q-band three-pulse ESEEM light-minus-dark spectra of the S_2 state Mn_4O_5Ca (A, D), S_2 state Mn_4O_5Sr (B, E) and annealed S_2 state $Mn_4O_5Ca-NH_3$ (C, F) clusters in PSII isolated from *T. elongatus* at selected magnetic-field positions across the multiline spectrum. (A–C) Time-domain spectra and (D–F) corresponding Fourier transforms. Black solid traces depict the baseline-corrected experimental spectra; superimposing red dashed traces represent simulations based on the spin Hamiltonian formalism as outlined in sections 2.3 in the main text, S3, S4 and S8.4. The optimized parameter sets are listed in Table 3 of the main text and in detail in Table S2. The labels ‘SQ’ and ‘DQ’ refer to the position of single and double-quantum transitions, respectively. For a description of the background subtraction procedure, see section S2. Experimental parameters: microwave frequencies: 34.0368 GHz (Ca^{2+}), 34.0433 GHz (Sr^{2+}), 34.0151 GHz (NH_3); magnetic fields: 1175–1280 mT (Ca^{2+} , Sr^{2+}), 1160–1280 mT (NH_3); shot repetition time: 1 ms; microwave pulse length ($\pi/2$): 12 ns; τ : 260 ns; ΔT : 100 ns; temperature: 5.2 K.

S8.2 Q-band HYSCORE spectra at low and high magnetic-field positions

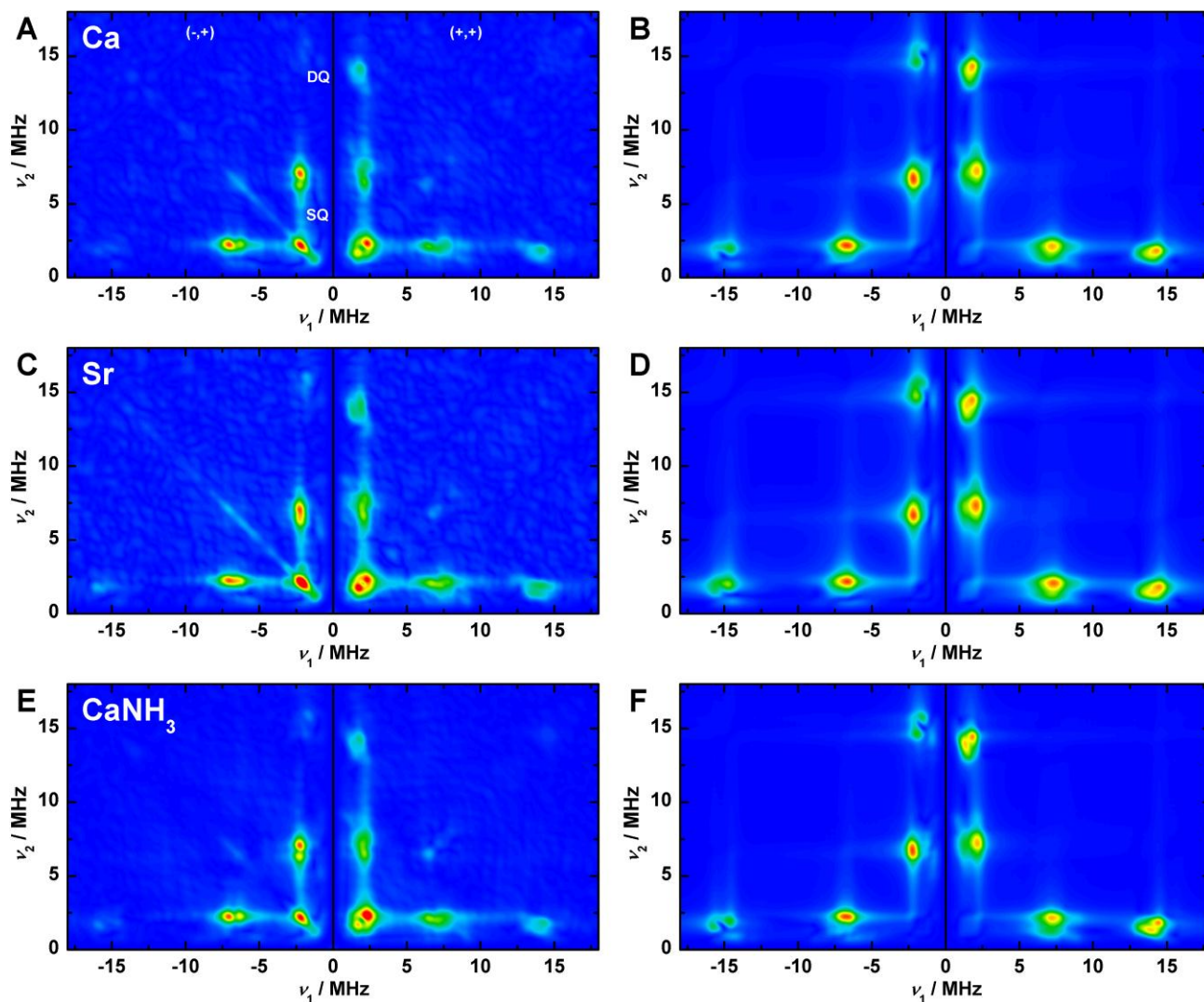


Fig. S6 (-,+) and (+,+) quadrants of the Fourier-transformed Q-band HYSCORE experimental spectra (A, C, E) and simulations (B, D, F) of the S_2 state Mn_4O_5Ca (A, B), S_2 state Mn_4O_5Sr (C, D) and annealed S_2 state $Mn_4O_5Ca-NH_3$ (E, F) clusters in PSII isolated from *T. elongatus*, measured at the low field edge of the corresponding Q-band multiline spectra. The labels ‘SQ’ and ‘DQ’ indicate the regions of single and double quantum transitions, respectively. The optimized parameter sets for the simulations, as described in sections 2.3 in the main text, S3, S4 and S8.4, are listed in Table 3 of the main text and in detail in Table S2. Experimental parameters: microwave frequencies: 34.0222 GHz (Ca^{2+}), 34.0425 GHz (Sr^{2+}), 34.0153 GHz (NH_3); magnetic field: 1175 mT; other settings were those given in Fig. 5 in the main article.

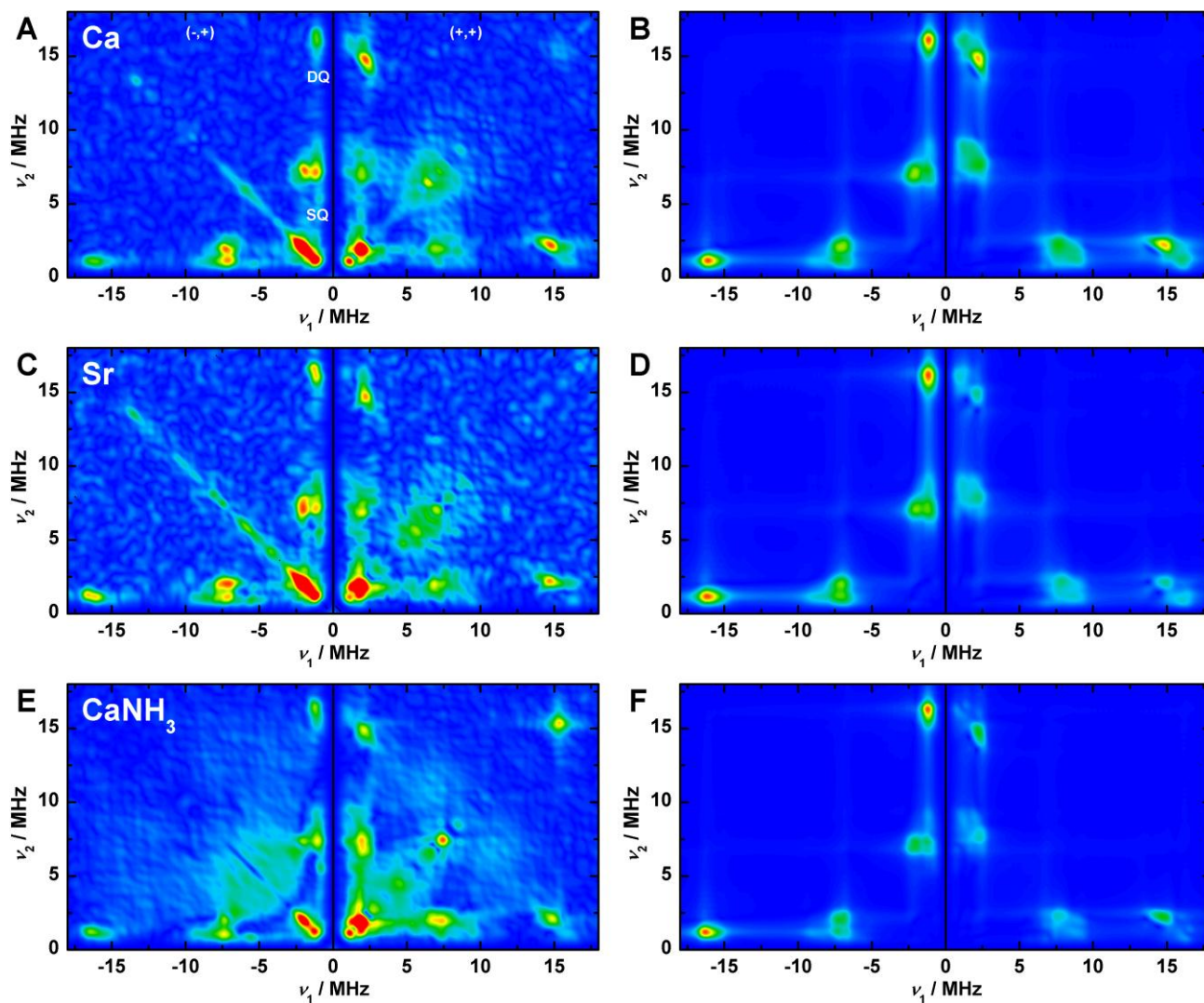


Fig. S7 (-,+) and (+,+) quadrants of the Fourier-transformed Q-band HSCORE experimental spectra (A, C, E) and simulations (B, D, F) of the S_2 state Mn_4O_5Ca (A, B), S_2 state Mn_4O_5Sr (C, D) and annealed S_2 state $Mn_4O_5Ca-NH_3$ (E, F) clusters in PSII isolated from *T. elongatus*, measured at the high field edge of the corresponding Q-band multiline spectra. The labels ‘SQ’ and ‘DQ’ indicate the regions of single and double quantum transitions, respectively. The optimized parameter sets for the simulations, as described in sections 2.3 in the main text, S3, S4 and S8.4, are listed in Table 3 of the main text and in detail in Table S2. Experimental parameters: microwave frequencies: 34.0227 GHz (Ca^{2+}), 34.0428 GHz (Sr^{2+}), 34.0153 GHz (NH_3); magnetic field: 1260 mT; other settings were those given in Fig. 5 in the main article.

S8.3 W-band ^{14}N - and ^{15}N -ELDOR-detected NMR experiments

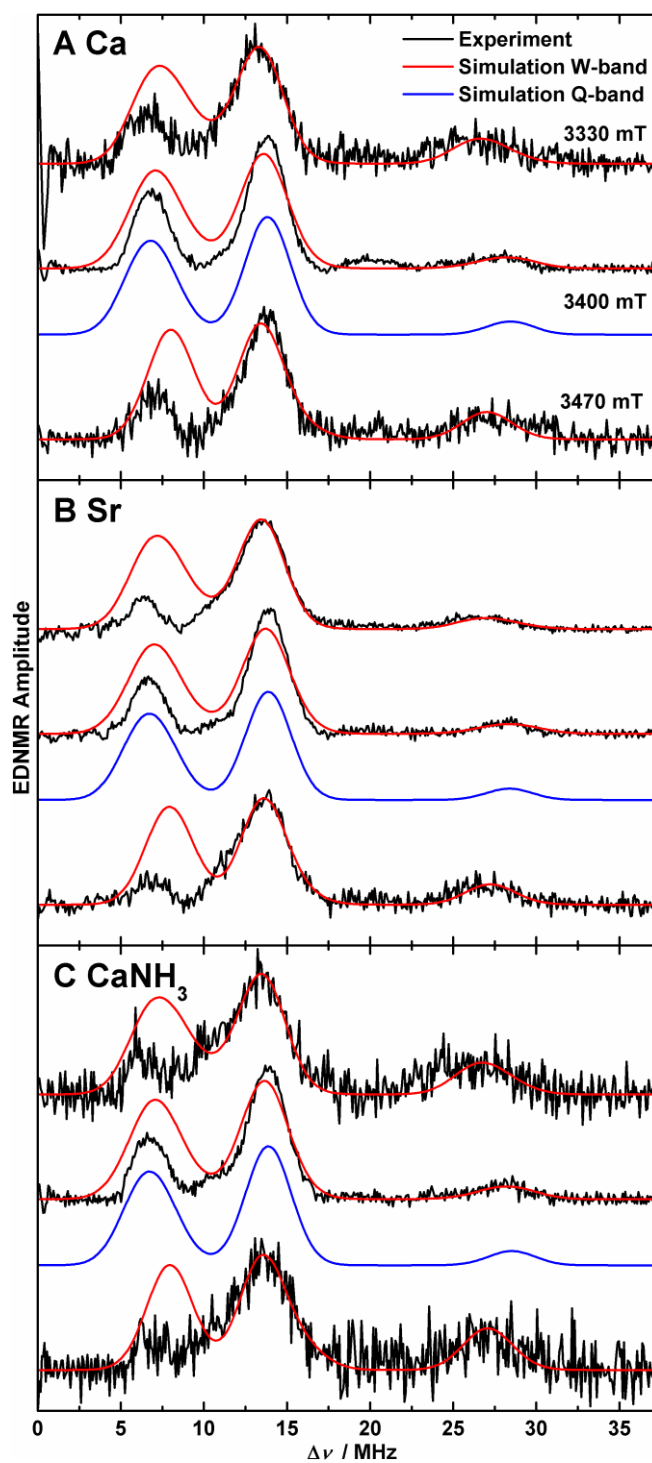


Fig. S8 W-band EDNMR spectra of illuminated **A**) native ^{14}N -PSII ($\text{Mn}_4\text{O}_5\text{Ca S}_2$), **B**) Sr^{2+} -substituted ^{14}N -PSII ($\text{Mn}_4\text{O}_5\text{Sr S}_2$) and **C**) NH_3 -modified ^{14}N -PSII ($\text{Mn}_4\text{O}_5\text{Ca-NH}_3 \text{ S}_2$) samples isolated from *T. elongatus*. Black solid traces depict the baseline-corrected experimental spectra, red and blue solid traces represent simulations based on the spin Hamiltonian formalism (see sections 2.3 in the main text, S3 and S4). The optimized parameter sets are listed in Table S2. The spectra displayed in each panel

S25

were measured or simulated at the low field edge, the center field and the high field edge (top to bottom) of the corresponding W-band multiline EPR spectra (Fig. 3C in the main text). The data from the native S₂ state were originally published in Ref.¹ and were reprocessed to allow comparison to the two chemically modified samples. Experimental parameters: microwave frequencies: 94.011 (A), 93.978 GHz (B), 94.066 GHz (C); magnetic fields: 3.33 T (top), 3.4 T (center), 3.47 T (bottom); shot repetition time: 1.5 ms; microwave pulse length (π): 400 ns; high turning angle pulse length t_{HTA} : 14 μ s; τ : 500 ns; temperature: 4.8 K.

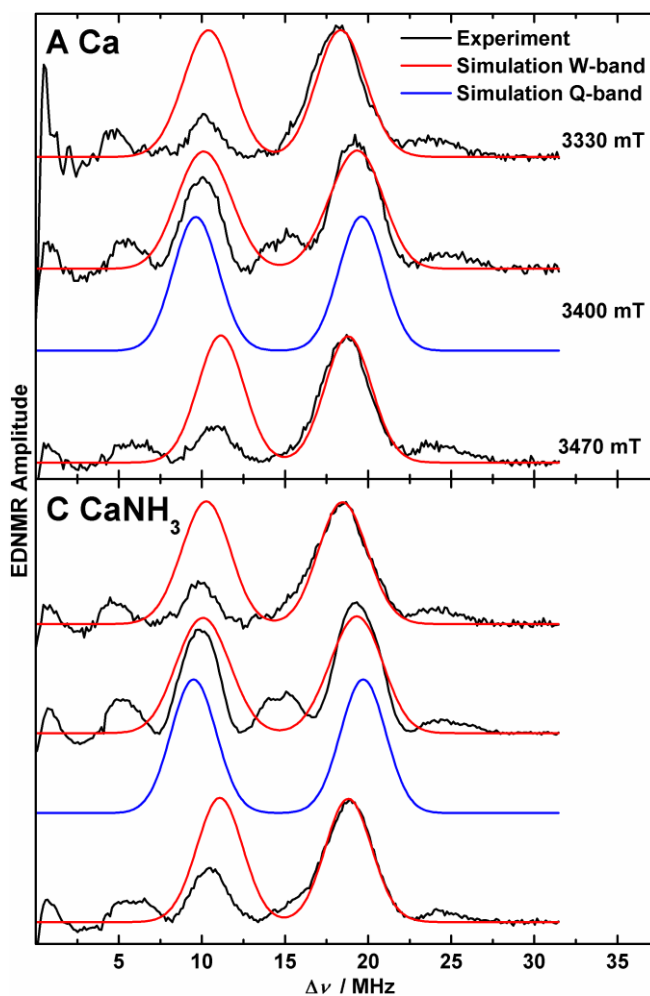


Fig. S9 Field-dependent W-band EDNMR spectra of illuminated **A**) native ^{15}N -PSII ($\text{Mn}_4\text{O}_5\text{Ca S}_2$), **B**) NH_3 -modified ^{15}N -PSII ($\text{Mn}_4\text{O}_5\text{Ca-NH}_3 \text{ S}_2$) samples isolated from *T. elongatus*. Black solid traces depict the baseline-corrected experimental spectra, red and blue solid traces represent simulations based on the spin Hamiltonian formalism (see sections 2.3 in the main text, S3 and S4). The optimized parameter sets are listed in Table S2. The spectra displayed in each panel were measured or simulated at the low field edge, the center field and the high field edge (top to bottom) of the corresponding W-band multiline EPR spectra (Fig. 3C in the main text). Experimental parameters: microwave frequencies: 94.022 GHz (A), 93.996 GHz (B); magnetic fields: 3.33 T (top), 3.4 T (center), 3.47 T (bottom); shot repetition time: 0.5 ms; microwave pulse length (π): 160 ns; t_{HTA} : 8 μs ; τ : 500 ns; temperature: 4.8 K.

Both the ^{14}N and ^{15}N spectra are highly similar for the native, Sr^{2+} -substituted and NH_3 -modified S_2 states. The three systems exhibit identical orientation dependencies, with the clearly largest splitting at the central field position ($g \approx 1.98$) and smaller splittings at the low- and high-field edges ($g \approx 2.02$ and $g \approx 1.94$, respectively). This behaviour is shown by both the ^{14}N and ^{15}N signals of the His332 imino-N. At the outer magnetic-field positions, the hyperfine splittings are approximately of the same size. The general similarity of the ^{14}N orientation selectivity to that of the ^{15}N signals results from the fact that the hyperfine coupling is the dominant electron-nuclear interaction and the magnitude of the NQI is considerably smaller. Despite the similar overall field-dependence, there are differences in the exact positions of the peaks, most prominent for the double-quantum transitions, at a certain magnetic field between the three variants of the S_2 state.

S8.4 Magnetic parameters of the His332 imino-¹⁴N interactions with the S₂ state OEC forms

Table S2 Effective/projected ¹⁴N hyperfine and NQI tensors in MHz for the interaction of the His332 imino-N with the Mn₄O₅Ca, Mn₄O₅Sr and annealed Mn₄O₅Ca–NH₃ clusters in the S₂ state in PSII from *T. elongatus* and parameters from previous studies on various species. The Q-band ESEEM/HYSCORE (Figs. 5 in the main text, S4, S5, S6 and S7) and the W-band EDNMR (Figs. S8, S9) simulations employed two different *A* tensors for a given spin system, while the NQI tensor and the Euler angle rotations of the hyperfine and NQI tensor were identical for the two frequencies.

S ₂ state	Method	A ₁	A ₂	A ₃	A _{iso} ^a	A _{dip} ^b	A _η ^c	e ² Qq/h	η ^c
Native	Q-Band ^d	5.6	8.4	7.2	7.1	0.75	0.81	1.97	0.75
	W-band ^d	3.2	9.2	6.7	6.3	1.59	0.80		
	BS-DFT ^e	4.6	5.9	6.8	5.8	0.59	0.74		
Sr ²⁺ -substituted	Q-Band ^d	5.9	8.5	7.4	7.3	0.69	0.83	1.98	0.79
	W-band ^d	3.4	9.6	6.8	6.6	1.58	0.87		
	BS-DFT ^e	4.7	6.1	6.8	5.8	0.57	0.61		
NH ₃ -modified	Q-Band ^d	5.7	8.6	7.3	7.2	0.75	0.89	1.96	0.80
	W-band ^d	3.5	9.1	6.6	6.4	1.45	0.86		
	BS-DFT ^e	4.7	6.1	7.5	6.1	0.71	0.99		
Native, spinach ¹⁷	X-, P-, K _a -band	6.3, 7.8, 7.8			7.3	0.5	0	1.98	0.84
Native, <i>Synechocystis</i> sp. PCC 6803 ¹⁸	K _a -, Q-band ^f	5.45, 7.15, 8.25			6.95	0.75	0.73	1.98	0.82
Native ¹	W-band ^g	3.8	7.7	6.2	5.9	1.1	0.71	0	0

^a A_{iso} is defined as the average of the principal components of the hyperfine tensor: $A_{\text{iso}} = (A_1 + A_2 + A_3)/3$. ^b A_{dip} is defined in terms of T_1 , T_2 , and T_3 as $A_{\text{dip}} = (T_1 + T_2)/2 = -T_3/2$. ^c The rhombicity is defined by A_η or $\eta = (T_1 - T_2)/T_3$, respectively. T_1 , T_2 , and T_3 represent the three principal components of the hyperfine tensors minus A_{iso} and of the NQI tensors and are labeled such that $|T_1| \leq |T_2| \leq |T_3|$. ^d The Euler rotation angles $[\alpha, \beta, \gamma]$ are $[0, 45, 0]^\circ$, $[0, 45, 0]^\circ$ and $[0, 44, 0]^\circ$ for the *A* tensors and $[20, -57, 0]^\circ$, $[18, -54, 0]^\circ$ and $[16, -60, 0]^\circ$ for the NQI tensors of the Mn₄O₅Ca, Mn₄O₅Sr and Mn₄O₅Ca–NH₃ clusters,

respectively. ^e Their calculated orientations are such that the smallest, medium and large effective components are aligned approximately (angular deviation $< 6^\circ$) along the Mn_{D1}-His332, the Mn_{D1}-O3 and the Mn_{D1}-Asp342, respectively (Fig. S10, main text Fig. 1). By definition, the large components along the Jahn-Teller axis were assigned to A_3 and, by inspection, the others to A_1 and A_2 . ^f The Euler rotation angles $[\alpha, \beta, \gamma]$ of the NQI tensor are $[-30, 0, 40]^\circ$. ^g Euler rotation angles $[\alpha, \beta, \gamma]$ of the hyperfine tensor were $[0, 30, 0]^\circ$.

A simultaneous fitting of all Q-band three-pulse ESEEM (Figs. S4, S5) and HYSCORE (Figs. 5 in the main text, S6 and S7) spectra and W-band ¹⁴N- and, if available, ¹⁵N-EDNMR spectra (Figs. S8 and S9) of the native, the Sr²⁺-substituted and the NH₃-modified S₂ state was performed using the spin Hamiltonian formalism (see Materials and Methods section 2.3 and sections S3 and S4). Only one nitrogen nucleus was included representing the coordinating imino-N in the imidazole ring of His332. Non-coordinating nitrogens do not contribute significantly to the ESEEM and HYSCORE modulations and the EDNMR spectra (see also Figs. S8 and S9).^{1, 17, 19} As the relative intensities of single- and double-quantum transition lines in EDNMR experiments are highly dependent on an experimental parameter, namely the high turning angle (HTA) pulse, single- and double-quantum transitions were calculated and normalized separately in the simulations, as in Rapatskiy *et al.*¹ and Pérez Navarro *et al.*⁵. The fitted effective ¹⁴N A and NQI tensors are listed in Table S2. In case of the ¹⁵N EDNMR spectra, the A tensor components were scaled by the ratio of the nuclear g values of ¹⁴N and ¹⁵N (and no NQI is effective). The effective G tensors used were the same as those determined by the EPR and ⁵⁵Mn-ENDOR simulations (Table 1 in the main text).

In simulations where the entire Q-band ESEEM/HYSCORE dataset was included, a single, consistent parameter set could be obtained. The fitted hyperfine and NQI parameters of all three S₂ state variants are very similar to those reported in higher plant and mesophilic cyanobacterial (*Synechocystis* sp. PCC 6803) PSII by the Britt laboratory^{17, 18} (Table S2). These simulations though do not constrain the orientation of the hyperfine tensor orientations relative to the G matrix. The inclusion of the high-

S30

frequency W-band EDNMR data allows the relative tensor orientations to be ascertained. However, the hyperfine tensors found to reproduce the field dependence of the W-band EDNMR dataset do not reproduce the Q-band ESEEM and HYSCORE data but instead comprise a smaller isotropic and a larger dipolar component. As the blue solid traces in Figs. S8 and S9 show, the splitting of the peaks in the W-band EDNMR spectra is overestimated when employing the hyperfine tensors fitted to the Q-band ESEEM and HYSCORE data, already to a smaller extent at the center field and more drastically at the edge position. Since our simulations of the W-band EDNMR signals now explicitly include the NQI term, the omission of this term cannot be the reason for this apparent mismatch. A rationale for this difference is given in the main text section 3.4. Despite the differences of the size of the dipolar component A_{dip} of the nitrogen hyperfine interaction between the Q- and W-band simulations, for all three S_2 state variants, their rhombicities A_{η} are very similar.

For the three forms of the S_2 state, the hyperfine tensors were required to be rotated about -45° around the y axis, relative to the orientation of the effective G tensors, which resulted to be rhombic from the simulations of the EPR/ ^{55}Mn ENDOR spectra in this work (main text section 3.2). This is similar to the simulation of the ^{14}N -EDNMR spectra at W-band of the native S_2 state in Ref.¹. This rotation results from the fact that approximately the same peak splittings are present in the W-band EDNMR spectra recorded at the edge positions of the S_2 multiline, corresponding to the x and z axes in the G tensor frame. Thus, the hyperfine coupling is expected to be small along G_x and G_z and large along G_y . However, the effective $^{14}\text{N}/^{15}\text{N}$ hyperfine tensor cannot be axial, as inferred from the ESEEM and HYSCORE spectra. Hence, it is supposed that the A tensor of the imino- $^{14}\text{N}/^{15}\text{N}$ and the molecular G tensor are not collinear. A β angle rotation in the xz plane (Fig. S10) allows the EDNMR data to be fit employing a rhombic hyperfine tensor, as noted earlier in Ref.¹. The simulations also afforded rotations of the NQI tensor around the z axis ($\alpha = 16$ to 20°) and the y' axis ($\beta = -54$ to -60°). Upon a switch of the values of A_1 and A_3 and use of $\beta = 45^\circ - 90^\circ = -45^\circ$, generating the same simulation traces, it becomes obvious that the orientations of NQI and hyperfine tensors are relatively similar, as observed in previous simulations of K_a - and Q-band three-pulse ^{14}N and ^{15}N -ESEEM data of this His332 imino-N.¹⁸

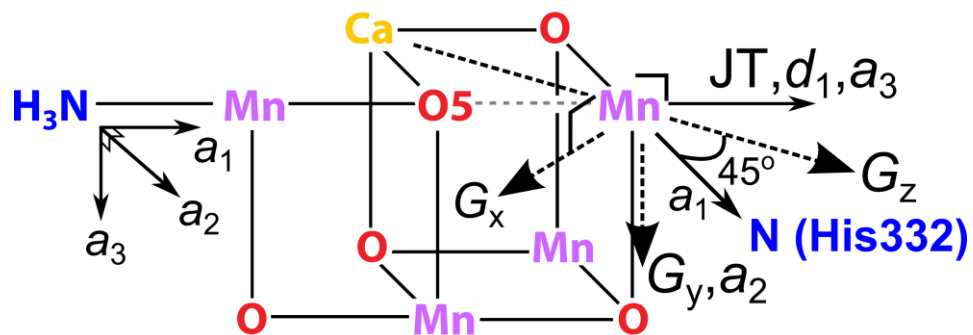


Fig. S10 Proposed orientations of the His332 imino- $^{14}\text{N}/^{15}\text{N}$ and $^{14}\text{NH}_3$ hyperfine tensors relative to the fine structure tensor of the $\text{Mn}_{\text{D1}}^{\text{III}}$ ion d and the molecular G frame in a schematic model of the $\text{Mn}_4\text{O}_5\text{Ca-NH}_3$ cluster. a_1 , d_1 and G_z define the unique tensor axis, ‘JT’ denotes the Jahn-Teller axis of $\text{Mn}_{\text{D1}}^{\text{III}}$.

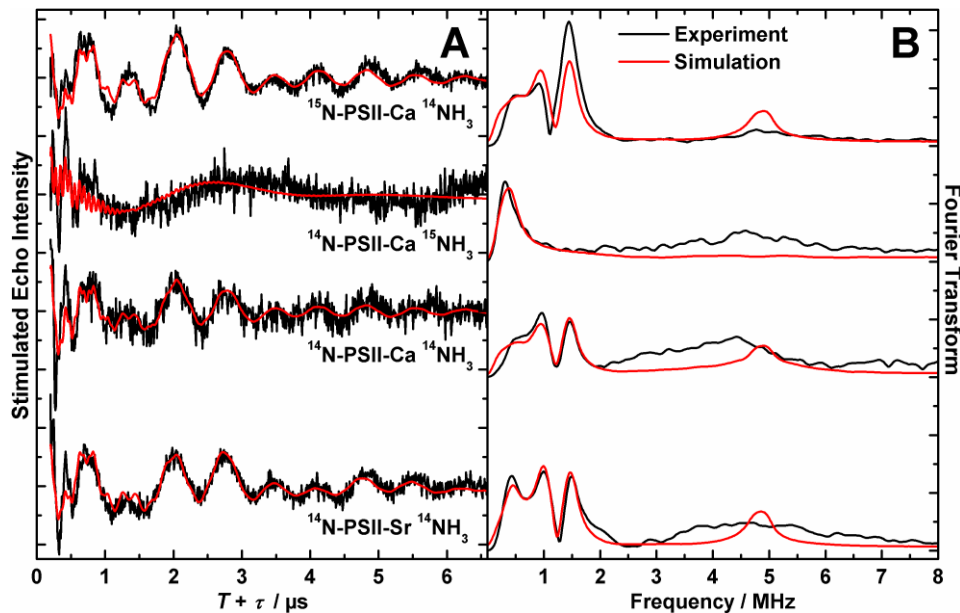


Fig. S11 X-band three-pulse ESEEM light-minus-dark spectra of $^{14}\text{NH}_3$ -modified native ^{15}N -PSII, $^{15}\text{NH}_3$ -modified native ^{14}N -PSII, $^{14}\text{NH}_3$ -modified native ^{14}N -PSII and $^{14}\text{NH}_3$ -modified Sr^{2+} -substituted ^{14}N -PSII (top to bottom) samples isolated from *T. elongatus* in the annealed S_2 state. **A)** Time-domain spectra and **B)** corresponding Fourier transforms. Black traces depict the baseline-corrected experimental spectra (see section S2); superimposing red traces represent simulations based on the spin Hamiltonian formalism (see sections 2.3 in the main text, S3 and S4). The optimized parameter sets are listed in Table S3. The ^{15}N -PSII-Ca $^{14}\text{NH}_3$ and ^{14}N -PSII-Ca $^{14}\text{NH}_3$ data were originally presented in Pérez Navarro *et al.*⁵ and reprocessed for this work. Experimental parameters: microwave frequencies: 9.680 GHz, 9.674 GHz, 9.684 GHz, 9.681 GHz (top to bottom); magnetic field: 333 mT; shot repetition time: 8.16 ms; microwave pulse length ($\pi/2$): 8 ns; τ : 136 ns (A), average of experiments with 136, 152, 168, 184 ns (B); ΔT : 64 ns; temperature: 4.3 K.

Table S3 Fitted (X-band three-pulse ESEEM, Fig. S11) and calculated effective/projected ^{14}N hyperfine and NQI tensors, listed as absolute values in MHz, for the electron-nuclear coupling of the NH_3 bound in the annealed $\text{Mn}_4\text{O}_5\text{Ca-NH}_3$ and $\text{Mn}_4\text{O}_5\text{Sr-NH}_3$ S_2 state clusters in PSII from *T. elongatus* and, from earlier studies, higher plant spinach.

S_2 state	Method	$ A_1 $	$ A_2 $	$ A_3 $	$ A_{\text{iso}} ^a$	A_{dip}^b	A_η^c	$ e^2Qq/h $	η^c
$\text{Mn}_4\text{O}_5\text{Ca-NH}_3$	ESEEM	1.69	2.76	2.62	2.36	0.33	0.22	1.52	0.47
	BS-DFT	3.97	2.01	2.04	2.68	-0.65	0.02	0.94	0.87
$\text{Mn}_4\text{O}_5\text{Sr-NH}_3$	ESEEM	1.81	2.72	2.59	2.37	0.28	0.23	1.58	0.45
	BS-DFT	3.87	2.07	2.10	2.68	-0.59	0.03	0.93	0.87
$\text{Mn}_4\text{O}_5\text{Ca-NH}_3$, spinach ²⁰	ESEEM	1.89	2.49	2.49	2.29	0.20	0.0	1.61	0.59

^a A_{iso} is defined as the average of the principal components of the hyperfine tensor: $A_{\text{iso}} = (A_1 + A_2 + A_3)/3$. ^b A_{dip} is defined in terms of T_1 , T_2 , and T_3 as $A_{\text{dip}} = (T_1 + T_2)/2 = -T_3/2$. ^c The rhombicity is defined by A_η or $\eta = (T_1 - T_2)/T_3$, respectively. T_1 , T_2 , and T_3 represent the three principal components of the hyperfine tensors minus A_{iso} and of the NQI tensors and are labeled such that $|T_1| \leq |T_2| \leq |T_3|$.

Three-pulse ESEEM experiments were performed at X-band on $^{14}\text{NH}_3/^{15}\text{NH}_3$ -modified (annealed), Ca^{2+} - and Sr^{2+} -containing, wild-type and all- ^{15}N -labeled PSII samples in the NH_3 -treated S_2 state. Fig. S11 depicts light-minus-dark-corrected time-domain (Fig. S11A) and, to minimize spectral artifacts, τ -averaged frequency-domain (Fig. S11B) spectra at 4.8 K of $^{14}\text{NH}_3$ -modified native ^{15}N -PSII, $^{15}\text{NH}_3$ -modified native ^{14}N -PSII, $^{14}\text{NH}_3$ -modified native ^{14}N -PSII and $^{14}\text{NH}_3$ -modified Sr^{2+} -substituted ^{14}N -PSII (top to bottom). At X-band frequencies, the echo modulations are dominated by the nitrogen hyperfine interaction of the bound NH_3 as it meets the cancellation condition ($A = 2\nu_n$). Importantly, the His332 imino-N interaction is suppressed as at X-band. Resonances from ^{14}N nuclei ($I = 1$), which exhibit significant NQI contributions in contrast to the ^{15}N nucleus ($I = 1/2$), appear more prominent in the three-pulse ESEEM data than those from ^{15}N ligands. Thus, the $^{14}\text{NH}_3$ -modified native ^{15}N -PSII data are dominated by the $^{14}\text{NH}_3$ interactions as compared to the ^{15}N His332 resonances, while all ^{14}N -PSII spectra show a broad His332 imino- ^{14}N resonance centered at ≈ 4.6 MHz in the Fourier-transformed spectrum.⁵

Spectral simulations of the X-band time-domain data were performed as described in the Materials and Methods section 2.3 and sections S3 and S4. They also included the ligating imino- ^{14}N or ^{15}N nucleus of His332, represented by the fitted Q-band parameters, and contributions from ^1H nuclei. The ^1H resonances, not displayed in the Fourier transforms, are centered at ≈ 14.2 MHz and were largely suppressed at a τ length of 136 ns.

The presented BS-DFT calculations confirm the small hyperfine rhombicity, however, yielding a negative dipolar hyperfine component with the unique component being the largest. The non-axiality of the electric field gradient, inferred from the large asymmetry parameter $\eta = 0.47$ of the NQI and reproduced by the BS-DFT computations, is attributed to a non-axial H-bonding geometry (main text section 4.1.2b, Fig. 7). In the original work by Britt *et al.*²⁰, the large η was proposed not to arise from a terminal NH_3 but rather from a less symmetric amido (NH_2) bridge between two Mn and/or the Ca^{2+} ion.

S10 Exchangeable ^{17}O species

S10.1 W-band ^{17}O -ELDOR-detected NMR experiments

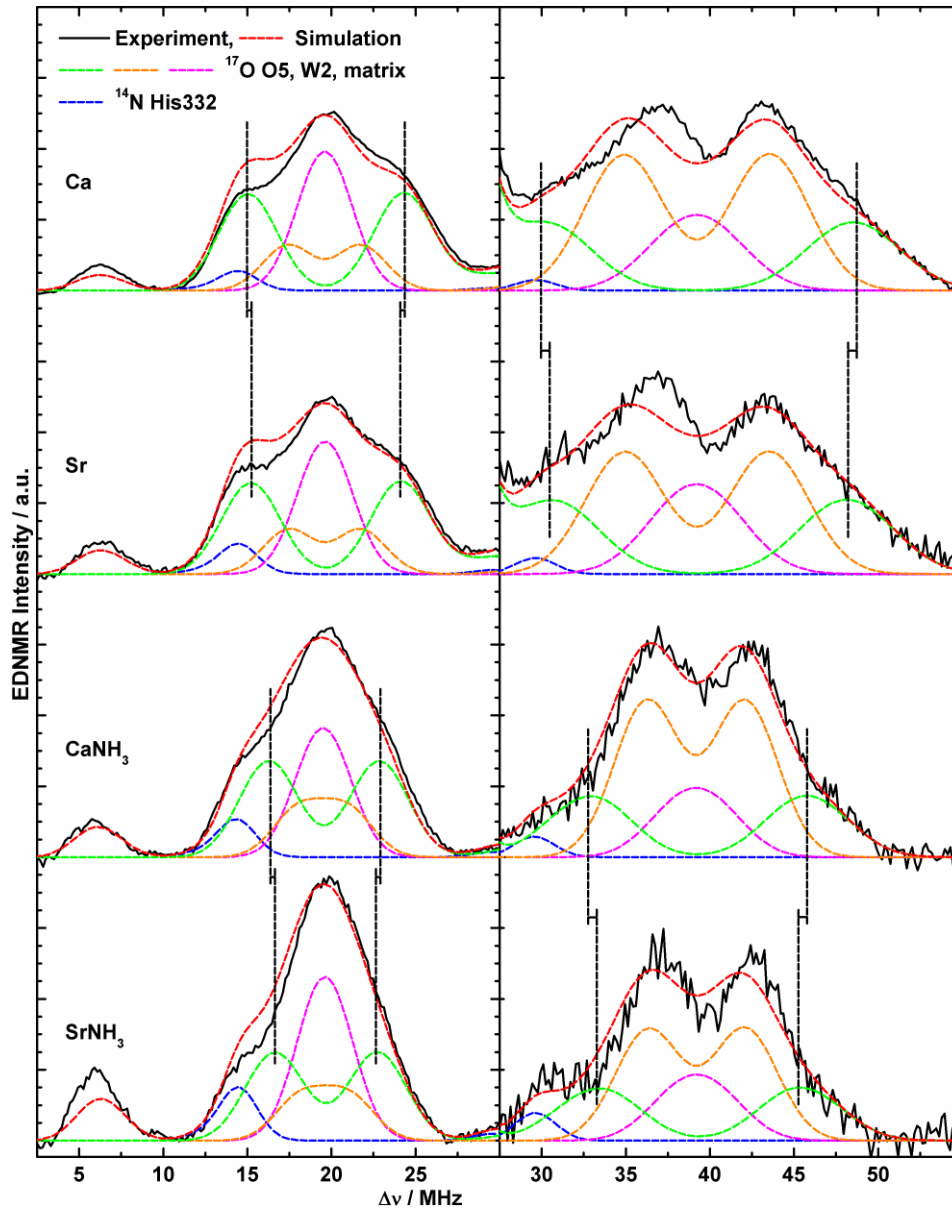


Fig. S12 Single-quantum (left) and double-quantum (right) regions of the ^{17}O -EDNMR spectra of the native (Ca) the Sr^{2+} -substituted (Sr), the NH_3 -annealed (CaNH_3) and the Sr^{2+} -substituted NH_3 -annealed (SrNH_3) S_2 states in PSII samples isolated from *T. elongatus*. The double-quantum envelopes are presented on a 4 times expanded vertical scale as compared to the single quantum resonances. Black solid traces show the background-corrected experimental spectra; superimposing red dashed traces represent simulations based on the spin Hamiltonian formalism as outlined in sections 2.3 in the main text, S3, S4. Coloured dashed lines represent a decomposition of the simulation showing contributions

from the individual ^{14}N and ^{17}O nuclei. Black dashed lines, visualizing the shift of the fitted single- and double-quantum transition peaks, highlight the decrease of the strong ^{17}O interaction, assigned to the μ -oxo bridge O5, upon substitution of the Ca^{2+} for a Sr^{2+} ion. The optimized parameter sets are listed in Table S4. Same as for the ^{14}N - and ^{15}N -EDNMR signals, the single- and double-quantum resonances of each ^{17}O species were weighted and normalized individually. In the simulations, the double-quantum peaks ν_α and ν_β of the individual ^{17}O species were required to be equal, unlike in Refs.^{1, 5}, where an intensity imbalance was allowed for. The data from the NH_3 -treated S_2 state were originally published in Ref.¹ and were reprocessed to allow comparison to the other S_2 state forms. Experimental parameters: microwave frequencies: 93.988 (Ca), 94.033 GHz (Sr), 94.069 GHz (CaNH_3), 93.964 GHz (SrNH_3); magnetic field: 3.4 T; shot repetition time: 1.5 ms; microwave pulse length (π): 400 ns; t_{HTA} : 14 μs ; τ : 500 ns; temperature: 4.8 K..

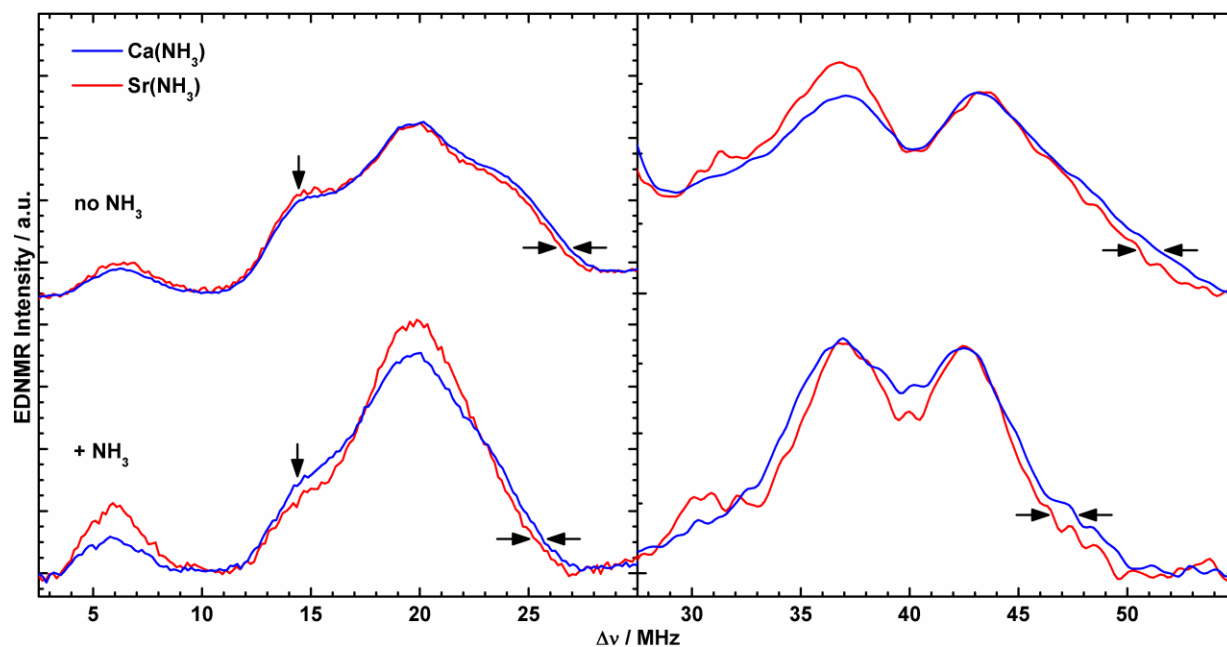


Fig. S13 Effect of $\text{Ca}^{2+}/\text{Sr}^{2+}$ exchange on the single-quantum (left) and double-quantum (right) envelopes of the ^{17}O -EDNMR spectra of the not NH_3 -treated (top) and NH_3 -annealed (bottom) S_2 states in PSII samples isolated from *T. elongatus*. The blue traces depict the Ca^{2+} -containing $\text{Mn}_4\text{O}_5\text{Ca}$ and $\text{Mn}_4\text{O}_5\text{Ca-NH}_3$ clusters, red traces represent the Sr^{2+} -containing $\text{Mn}_4\text{O}_5\text{Sr}$ and $\text{Mn}_4\text{O}_5\text{Sr-NH}_3$ clusters. The double-quantum envelopes are presented on a 4.5 times expanded vertical scale as compared to the single quantum resonances. They were smoothed using a 9-point moving average and normalized with respect to the high-frequency doublet peak around 43 MHz for better comparability. As pointed out by the horizontal arrows, Sr^{2+} substitution results in a systematic narrowing of the single- and double quantum envelopes in both the S_2 states without and with NH_3 bound to the Mn cluster. The vertical arrows mark the maximum of the underlying ν_β peaks of the His332 imino- ^{14}N , which prevent the low-frequency edges of the ^{17}O single-quantum envelopes and thus their differences from being resolved. Experimental parameters: see Fig. S12.

Table S4 Fitted effective ^{17}O hyperfine tensors, listed as absolute values in MHz, from W-band EDNMR experiments (Fig. 6 in the main text and Fig. S12) for the electron-nuclear coupling of the oxygen species exchangeable in the S_1 state with the $\text{Mn}_4\text{O}_5\text{Ca}$, $\text{Mn}_4\text{O}_5\text{Sr}$, $\text{Mn}_4\text{O}_5\text{Ca-NH}_3$ and $\text{Mn}_4\text{O}_5\text{Sr-NH}_3$ S_2 state clusters in PSII from *T. elongatus*. A_1 , A_2 and A_3 are the principal components of the hyperfine tensor, which are not assigned to the principal axes of the coordinate system defined by the G tensor.

S_2 state	Oxygen	$ A_1 , A_2 , A_3 $	$ A_{\text{iso}} ^a$	A_{dip}^b	A_η^c
all	matrix	2.1, 0.2, 2	1.4	0.6	0.08
$\text{Mn}_4\text{O}_5\text{Ca}$	W2	5.1, 5.1, 3.3	4.5	0.6	0.08
	O5	10.7, 5.3, 13.1	9.7	2.2	0.55
$\text{Mn}_4\text{O}_5\text{Sr}$	W2	5.1, 5.1, 3.3	4.5	0.6	0.08
	O5	10.2, 4.8, 12.6	9.2	2.2	0.55
$\text{Mn}_4\text{O}_5\text{Ca-NH}_3$	W2	3.7, 3.7, 1.9	3.1	0.6	0.08
	O5	8.0, 2.6, 10.4	7.0	2.2	0.55
$\text{Mn}_4\text{O}_5\text{Sr-NH}_3$	W2	3.7, 3.7, 1.9	3.1	0.6	0.08
	O5	7.5, 2.1, 9.9	6.5	2.2	0.55

^a A_{iso} is defined as the average of the principal components of the hyperfine tensor: $A_{\text{iso}} = (A_1 + A_2 + A_3)/3$. ^b A_{dip} is defined in terms of T_1 , T_2 , and T_3 as $A_{\text{dip}} = (T_1 + T_2)/2 = -T_3/2$. ^c The rhombicity is defined by A_η or $\eta = (T_1 - T_2)/T_3$, respectively. T_1 , T_2 , and T_3 represent the three principal components of the hyperfine tensors minus A_{iso} and of the NQI tensors and are labeled such that $|T_1| \leq |T_2| \leq |T_3|$.

S10.2 X-band CW EPR experiments in the absence and presence of H₂¹⁷O

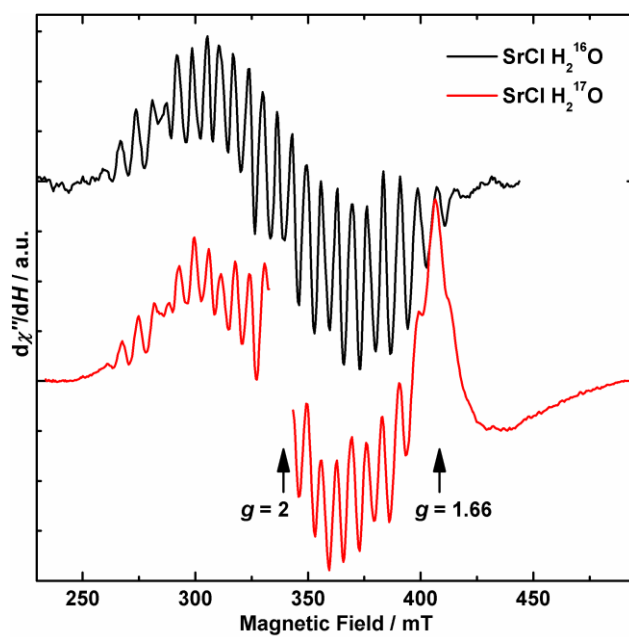


Fig. S14 X-band CW EPR spectra of the Sr²⁺-substituted S₂ state in PSII samples in the absence (black) and presence (red) of H₂¹⁷O showing no line broadening upon ¹⁷O exchange. The spectrum in the not H₂¹⁷O -enriched buffer was taken from Cox *et al.*¹². In the spectrum of the H₂¹⁷O-exchanged PSII sample, the Y_D[•] signal centered at about $g \approx 2$ was removed for clarity of presentation; the underlying comparatively narrow signal centered at $g \approx 1.66$ originates from the semiquinone-iron in the Q_A⁻Fe²⁺Q_B⁻ state.^{21, 22} Experimental parameters: microwave frequencies: 9.4213 GHz (no ¹⁷O); 9.4989 GHz (with ¹⁷O); microwave power: 20 mW; modulation amplitude: 25 G; time constant: 82 ms; temperature: 8.6 K.

S11 References

1. L. Rapatskiy, N. Cox, A. Savitsky, W. M. Ames, J. Sander, M. M. Nowaczyk, M. Rögner, A. Boussac, F. Neese, J. Messinger and W. Lubitz, *J. Am. Chem. Soc.*, 2012, **134**, 16619-16634.
2. S. Stoll and A. Schweiger, *J. Magn. Reson.*, 2006, **178**, 42-55.
3. S. Stoll and R. D. Britt, *Phys. Chem. Chem. Phys.*, 2009, **11**, 6614-6625.
4. N. Cox, W. Lubitz and A. Savitsky, *Mol. Phys.*, 2013, **111**, 2788-2808.
5. M. Pérez Navarro, W. M. Ames, H. Nilsson, T. Lohmiller, D. A. Pantazis, L. Rapatskiy, M. M. Nowaczyk, F. Neese, A. Boussac, J. Messinger, W. Lubitz and N. Cox, *Proc. Natl. Acad. Sci. U. S. A.*, 2013, **110**, 15561-15566.
6. V. K. Yachandra, K. Sauer and M. P. Klein, *Chem. Rev.*, 1996, **96**, 2927-2950.
7. J. Messinger, J. H. Robblee, U. Bergmann, C. Fernandez, P. Glatzel, H. Visser, R. M. Cinco, K. L. McFarlane, E. Bellacchio, S. A. Pizarro, S. P. Cramer, K. Sauer, M. P. Klein and V. K. Yachandra, *J. Am. Chem. Soc.*, 2001, **123**, 7804-7820.
8. M. Haumann, C. Müller, P. Liebisch, L. Iuzzolino, J. Dittmer, M. Grabolle, T. Neisius, W. Meyer-Klaucke and H. Dau, *Biochemistry*, 2005, **44**, 1894-1908.
9. J. M. Peloquin, K. A. Campbell, D. W. Randall, M. A. Evanchik, V. L. Pecoraro, W. H. Armstrong and R. D. Britt, *J. Am. Chem. Soc.*, 2000, **122**, 10926-10942.
10. L. V. Kulik, B. Epel, W. Lubitz and J. Messinger, *J. Am. Chem. Soc.*, 2007, **129**, 13421-13435.
11. C. Teutloff, S. Pudollek, S. Kessen, M. Broser, A. Zouni and R. Bittl, *Phys. Chem. Chem. Phys.*, 2009, **11**, 6715-6726.
12. N. Cox, L. Rapatskiy, J.-H. Su, D. A. Pantazis, M. Sugiura, L. Kulik, P. Dorlet, A. W. Rutherford, F. Neese, A. Boussac, W. Lubitz and J. Messinger, *J. Am. Chem. Soc.*, 2011, **133**, 3635-3648.
13. J. H. Su, N. Cox, W. Ames, D. A. Pantazis, L. Rapatskiy, T. Lohmiller, L. V. Kulik, P. Dorlet, A. W. Rutherford, F. Neese, A. Boussac, W. Lubitz and J. Messinger, *Biochim. Biophys. Acta, Bioenerg.*, 2011, **1807**, 829-840.

14. S. Pudollek, Doctoral Thesis, Freie Universität Berlin, 2012.
15. D. Koulougliotis, R. H. Schweitzer and G. W. Brudvig, *Biochemistry*, 1997, **36**, 9735-9746.
16. G. A. Lorigan and R. D. Britt, *Photosynth. Res.*, 2000, **66**, 189-198.
17. G. J. Yeagle, M. L. Gilchrist, R. M. McCarrick and R. D. Britt, *Inorg. Chem.*, 2008, **47**, 1803-1814.
18. T. A. Stich, G. J. Yeagle, R. J. Service, R. J. Debus and R. D. Britt, *Biochemistry*, 2011, **50**, 7390-7404.
19. S. Milikisiyants, R. Chatterjee, A. Weyers, A. Meenaghan, C. Coates and K. V. Lakshmi, *J. Phys. Chem. B*, 2010, **114**, 10905-10911.
20. R. D. Britt, J. L. Zimmermann, K. Sauer and M. P. Klein, *J. Am. Chem. Soc.*, 1989, **111**, 3522-3532.
21. A. R. Corrie, J. H. A. Nugent and M. C. W. Evans, *Biochimica Et Biophysica Acta*, 1991, **1057**, 384-390.
22. C. Fufezan, C. X. Zhang, A. Krieger-Liszkay and A. W. Rutherford, *Biochemistry*, 2005, **44**, 12780-12789.

Electronic Supporting Information

The First Substrate Water of Nature's Water-Oxidizing Cofactor Binds as a μ -Hydroxo Bridge during Catalyst Regeneration

**Thomas Lohmiller,[†] Vera Krewald,[†] Arezki Sedoud,[‡] A. William Rutherford,[§] Frank Neese,[†]
Wolfgang Lubitz,[†] Dimitrios A. Pantazis,[†] and Nicholas Cox^{*,†}**

[†] *Max-Planck-Institut für Chemische Energiekonversion, Stiftstrasse 34-36, D-45470 Mülheim an der Ruhr, Germany*

[‡] *iBiTec-S, URA CNRS 2096, CEA Saclay, 91191 Gif-sur-Yvette, France*

[§] *Department of Life Sciences, Imperial College London, London SW7 2AZ, United Kingdom*

** Corresponding Author: E-mail: nicholas.cox@cec.mpg.de, Phone: +49 208 306 3552, Fax: +49 208 306 3955*

Table of contents

- S1 Data processing: baseline correction and light-minus-dark subtraction
- S2 Spectral simulations
- S3 Theoretical background
- S4 Experimental details of the EPR measurements
- S5 Multifrequency EPR and ^{55}Mn ENDOR spectra and simulations of the S_2 and S_0 states
- S6 The S_2 state: EPR/ ^{55}Mn ENDOR simulation parameters, Mn exchange couplings, fine structure interactions and spin projection factors
- S7 Electronic structure of the S_0 state: spin projections, intrinsic ^{55}Mn hyperfine couplings and Mn fine structure interactions
- S8 T_1 relaxation and spin state ladder: Q-band inversion recovery experiments and analysis
- S9 The $\text{Mn}_{\text{D1}}\text{-His332-imino-N}$ interaction: field- and τ -dependent Q-band ^{14}N -three-pulse ESEEM and ^{14}N -HYSCORE experiments and interpretation of the simulation parameters
- S10 W-band ELDOR-detected NMR experiments
- S11 Interactions with exchangeable $^1\text{H}/^2\text{H}$ species: Q-band ^2H -two-pulse, ^2H -three-pulse and ^2H -three-pulse vs. two-pulse ESEEM and ^2H -HYSCORE experiments
- S12 General considerations on the experimental approach
- S13 References

S1 Data processing: baseline correction and light-minus-dark subtraction

To minimize possible contributions from underlying signals from other paramagnetic species in the sample, such as hexaquo-Mn^{II}, oxidized cytochrome b₅₅₉ and c₅₅₀ and Fe^{II}/Q_A⁻, a fitted polynomial baseline was subtracted from derivative-shaped continuous wave (CW) EPR spectra, and S₀-minus-S₁ (three-flashes-minus-zero-flashes or light-minus-dark) subtractions were performed for ⁵⁵Mn electron-nuclear double resonance (ENDOR) spectra.

Three-pulse electron spin echo envelope modulation (ESEEM) data were also baseline-corrected after light-minus-dark subtraction of the normalized time-domain traces. (Figure S1), in order to obtain spectra containing only resonances from the oxygen-evolving complex (OEC) of photosystem II (PSII) in the S₀ state, excluding modulations from other paramagnetic species, foremost the background cytochrome (¹⁴N) signals. The (*T*₁) decay was modeled and removed by subtracting a seventh order polynomial fit function from the light-minus-dark difference for ¹⁴N-ESEEM experiments. For ²H-two-pulse and ²H-three-pulse ESEEM experiments, instead of a light-minus-dark, a ²H-minus-¹H subtraction was employed, *i.e.* the difference of spectra from a ²H₂O-exchanged sample and a non-isotopically enriched sample. The (*T*₁) decay was then subtracted using a ninth order polynomial fit.

Hyperfine sublevel correlation (HYSCORE) and three-pulse *vs.* two-pulse spectroscopic data were baseline-corrected using polynomial fit curves in both dimensions. Before Fourier transformation, a hamming apodization window and zero-filling were applied to the individual ESEEM and HYSCORE spectra. Frequency-domain ¹⁴N-HYSCORE spectra and simulations were normalized with respect to the height of the single-quantum ¹⁴N peaks.

Electron-electron double resonance (ELDOR)-detected NMR (EDNMR) spectra were baseline-subtracted and further processed to obtain an ENDOR-like representation of the spectra as described in Ref. ¹.

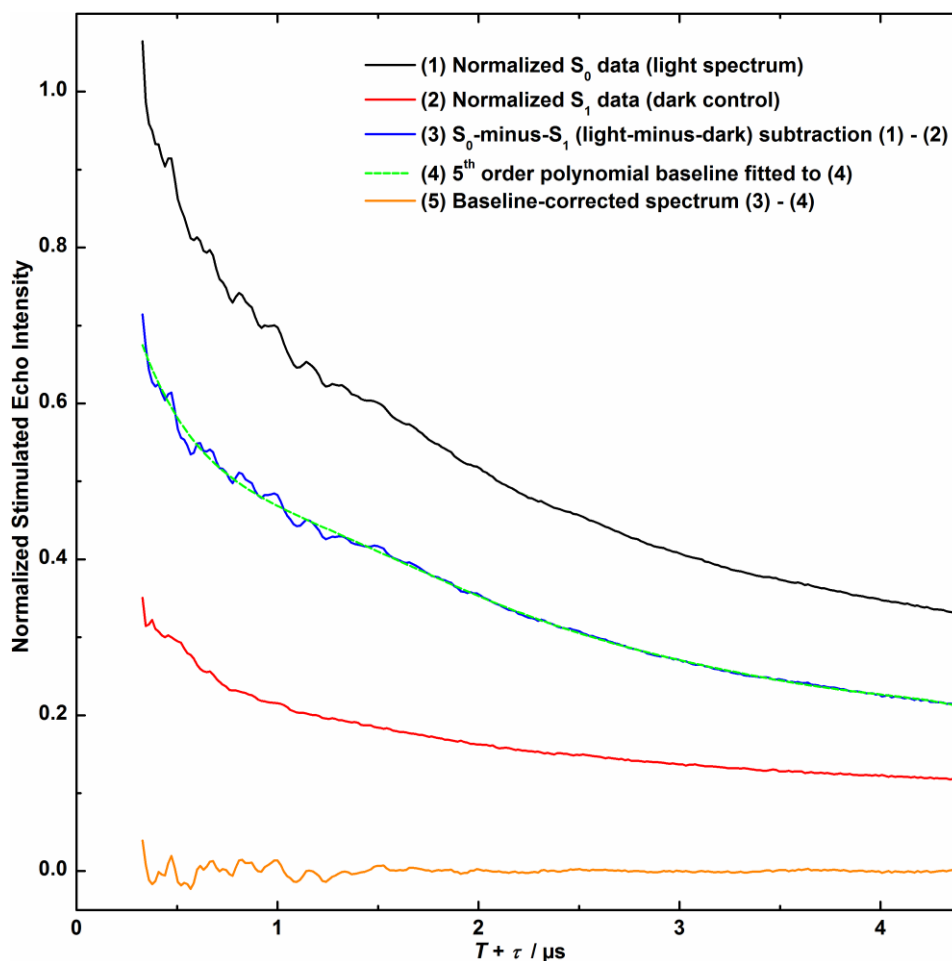


Figure S1. Example for the light-minus-dark subtraction and baseline correction of three-pulse ESEEM spectra. The solid black and red lines depict ESEEM spectra of a PSII sample in the 3-flash-advanced S_0 (1) and S_1 states (2), after subtraction of the y -axis offset and normalization. The blue solid line shows the spectrum resulting from the S_0 -minus- S_1 subtraction (3). The superimposing green dashed line (4) represents a fifth order polynomial fit curves to (3). The solid orange line (5) is the baseline-corrected resulting ESEEM spectrum after background subtraction. Experimental parameters: microwave frequency: 33.965 GHz; magnetic field: 1245 mT; shot repetition time: 0.5 ms; microwave pulse lengths ($\pi/2$): 16 ns; τ : 280 ns; ΔT : 48 ns; temperature: 4.8 K.

S2 Spectral simulations

The EasySpin^{2,3} function “pepper” was used to calculate powder-pattern spectra for the EPR experiment, “salt” for ENDOR, “saffron” for three-pulse ESEEM and HYSCORE and a home-written script involving EasySpin functions for powder-pattern EDNMR spectra.

For calculation of the spin Hamiltonians of the ⁵⁵Mn tetramer-single electron spin manifolds that describe the EPR and ⁵⁵Mn-ENDOR spectra, the electron Zeeman term was treated exactly. The ⁵⁵Mn hyperfine terms were treated using second order perturbation theory. ⁵⁵Mn nuclear quadrupole interactions (NQI) are not resolved in both the EPR and ENDOR spectra and thus omitted in their simulations. The ⁵⁵Mn nuclear Zeeman terms were not included in the EPR simulations (see sections S3.2 and S3.3). The G and the four effective ⁵⁵Mn hyperfine tensors A_i were assumed to be collinear. First-derivative X-band EPR, absorption-line W-band EPR and Q-band ⁵⁵Mn-ENDOR data were simultaneously fit using a least squares routine.

For simulation of the (orientation-selective) ESEEM, HYSCORE and EDNMR spectra, respective ¹⁴N and ¹⁷O single ligand nucleus-single electron spin Hamiltonians were used. The ⁵⁵Mn nuclear interactions were not considered explicitly, but accounted for by employing hyperfine strain, *i.e.* an isotropic broadening due to unresolved hyperfine couplings, to compute the excitation window. All other spin Hamiltonian terms were treated exactly. In the simulations of the ¹⁷O-EDNMR spectra, the NQI term was omitted as it is not resolved within the line width. For ¹⁴N/¹⁷O-EDNMR simulations, the nuclear resonances were calculated separately.

EDNMR transition intensities were calculated assuming small angle excitation by the high turning angle (HTA) pulse, as described in Cox *et al.*⁴. As in Refs.^{1,5,6}, the contributions from different nuclear species, as well as their individual single- and double-quantum transition envelopes, were calculated and normalized separately. Specifically, for the ¹⁷O signal envelopes, which are made up of multiple species, the fitting was constrained such that the relative intensities of the different contributions were scaled according to the magnitude of the anisotropic component of the hyperfine interaction.

ESEEM simulation traces were fitted to the time-domain spectra.

S3 Theoretical background

S3.1 The spin Hamiltonian formalism. Here, we consider a spin system consisting of an exchange-coupled Mn tetramer including the respective ^{55}Mn nuclei and a number of ligands with n magnetically interacting ^{14}N or ^{17}O nuclei. The assignment for the oxidation states of the four Mn ions when poised in the S_0 state is $\text{Mn}^{\text{III}}\text{Mn}^{\text{III}}\text{Mn}^{\text{III}}\text{Mn}^{\text{IV}}$, as analyzed in the Results and Discussion sections (see also Refs. ^{7,8}) This net oxidation state is assumed throughout the text. A basis set that describes the ^{14}N - or ^{17}O -Mn-tetramer spin manifold can be built from the product of the eigenstates of the interacting spins:

$$|S_1 S_2 S_3 S_4 M_1 M_2 M_3 M_4 I_1 I_2 I_3 I_4 m_1 m_2 m_3 m_4 L_1 k_1 \dots L_i k_i \dots L_n k_n\rangle, \quad (\text{S1})$$

Here, S_i (with $i = 1 - 4$) refers to the electronic spin state of Mn_i , M_i refers to the electronic magnetic sublevel of Mn_i , I_i refers to the nuclear spin state of Mn_i , and m_i refers to the nuclear magnetic sublevels of Mn_i . S_i takes the value 2 for Mn^{III} and 3/2 for Mn^{IV} ; M_i takes the values: $S_i, S_i-1, \dots, 1-S_i, -S_i$; I_i takes the value 5/2 for ^{55}Mn , m_i takes the values $-I_i, 1-I_i, \dots, I_i-1, I_i$, L_i takes the values 1 for ^{14}N and 5/2 for ^{17}O , and k_i takes the values $-L_i, 1-L_i, \dots, L_i-1, L_i$.

The spin Hamiltonian that describes the spin manifold of the ^{14}N -, ^{15}N - or ^{17}O -Mn tetramer is:

$$\begin{aligned} \hat{H} = & \sum_{i=1}^4 \beta_e \vec{B}_0 \cdot \hat{g}_i \cdot \vec{S}_i + \sum_{i=1}^4 \vec{S}_i \cdot \hat{d}_i \cdot \vec{S}_i + \sum_{i<j} \vec{S}_i \cdot \hat{J}_{ij} \cdot \vec{S}_j - \sum_{i=1}^4 g_{\text{Mn}} \beta_n \vec{B}_0 \cdot \vec{I}_i + \sum_{j=1}^4 \sum_{i=1}^4 \vec{S}_j \cdot \hat{a}_{\text{Mn},i} \cdot \vec{I}_i \\ & + \sum_{i=1}^4 \vec{I}_i \cdot \hat{q}_{\text{Mn},i} \cdot \vec{I}_i - \sum_{i=1}^n g_{\text{L},i} \beta_n \vec{B}_0 \cdot \vec{L}_i + \sum_{j=1}^4 \sum_{i=1}^n \vec{S}_j \cdot \hat{a}_{\text{L},i} \cdot \vec{L}_i + \sum_{i=1}^n \vec{L}_i \cdot \hat{q}_{\text{L},i} \cdot \vec{L}_i \end{aligned} \quad (\text{S2})$$

It contains (i) an electronic Zeeman term for each Mn ion (g_i), (ii) a fine structure term for each Mn ion (d_i), and (iii) pair-wise electronic exchange terms for each Mn-Mn interaction (J_{ij}), (iv) a nuclear Zeeman term for each ^{55}Mn (g_{Mn}) nucleus and ligand (g_{L}) nucleus, (v) an electron-nuclear hyperfine term for each ^{55}Mn ($a_{\text{Mn},i}$) nucleus and ligand (a_{L}) nucleus, and (vi) an NQI term for each ^{55}Mn ($q_{\text{Mn},i}$) and ligand (q_{L}) nucleus. Inter-nuclear interactions are comparatively small and as such are not considered for the description of spectra from any of the experiments.

S3.2 An effective spin $S_T = 1/2$ ground state. A basis set that describes the entire spin manifold of the coupled four ^{55}Mn ions of the OEC, without considering any cluster-ligand interactions, requires 414720 vectors - too many to be readily handled by current numerical techniques. The problem can be greatly simplified by assuming that all Mn-Mn couplings are large, *i.e.* within the strong exchange limit. For this to apply, the exchange interactions between the Mn ions have to be significantly larger than any other term of the spin Hamiltonian. The resultant electronic spin states of the manifold are then adequately described by a single quantum number, the total spin (S_T). The multiline EPR signal observed for the S_0 state (same as in the S_2 state) of the OEC is derived from only one total spin state, the ground state of the spin manifold with total spin $S_T = 1/2$. The basis set that describes this subspace requires only 2592 vectors in the case that models the coupling of the effective electronic spin ($S_T = 1/2$) to the nuclear spin of each ^{55}Mn ($I = 5/2$). Considering additional n ligand nuclei (L_i), the basis set is the following:

$$|\frac{1}{2} M I_1 I_2 I_3 I_4 m_1 m_2 m_3 m_4 L_1 k_1 \dots L_i k_i \dots L_n k_n\rangle \quad (\text{S3})$$

where M takes all half-integer values $-\frac{1}{2}$ and $\frac{1}{2}$, m_i takes all half-integer values $-\frac{5}{2} \leq m_i \leq \frac{5}{2}$, and k_i takes values $-L_i \leq k_i \leq L_i$.

The effective spin Hamiltonian that describes the ground state of the spin manifold ($S_T = 1/2$) is:

$$\begin{aligned} \hat{H} = & \beta_e \bar{B}_0 \cdot \hat{G} \cdot \bar{S} + \sum_{i=1}^4 \left(-g_{\text{Mn}} \beta_n \bar{B}_0 \cdot \bar{I}_i + \bar{S} \cdot \hat{A}_{\text{Mn},i} \cdot \bar{I}_i \right) \\ & + \sum_{i=1}^n \left(-g_{L,i} \beta_n \bar{B}_0 \cdot \bar{L}_i + \bar{S} \cdot \hat{A}_{L,i} \cdot \bar{L}_i + \bar{L}_i \cdot \hat{q}_{L,i} \cdot \bar{L}_i \right) \end{aligned} \quad (\text{S4})$$

It contains, (i) the Zeeman term for the total electronic spin, (ii) Zeeman terms for each ^{55}Mn and ligand nucleus, (iii) hyperfine terms for each ^{55}Mn and ligand nucleus and (iv) a quadrupole term for each ligand nucleus. Quadrupole terms are neglected for the ^{55}Mn nuclei as their size is smaller than the fitted line width.

S3.3 Application to the different spectroscopic experiments. The simulation of spectra from EPR and related experiments probing electronic spin transitions of the OEC can be further simplified.

Nuclear Zeeman terms do not affect the EPR transition energies and thus can be omitted. As the ligand couplings are comparatively small, they are not resolved and also do not contribute significantly to the inhomogeneous line width of the S_0 state EPR spectrum. Hence, for simulation of the EPR spectrum, the terms in Eq. S4 relating to the ligand nuclei can be excluded (Eq. S5).

$$\hat{H}_{\text{EPR}} = \beta_e \bar{B}_0 \cdot \hat{G} \cdot \bar{S} + \sum_{i=1}^4 \bar{S} \cdot \hat{A}_{\text{Mn},i} \cdot \bar{I}_i \quad (\text{S5})$$

Also, a simplified effective spin Hamiltonian can be used for the simulation of the spectra from experiments probing nuclear magnetic interactions, as the various nuclei do not significantly couple to each other. Thus, for the simulation of the ^{55}Mn -ENDOR resonances, terms in Eq. 4 associated with the ligand nuclei can be excluded:

$$\hat{H}_{\text{MnENDOR}} = \beta_e \bar{B}_0 \cdot \hat{G} \cdot \bar{S} + \sum_{i=1}^4 \left(-g_{\text{Mn}} \beta_n \bar{B}_0 \cdot \bar{I}_i + \bar{S} \cdot \hat{A}_{\text{Mn},i} \cdot \bar{I}_i \right) \quad (\text{S6})$$

Similarly, for describing the nuclear interactions of n ligand ^{14}N , ^{15}N or ^{17}O nuclei in the various experiments (ESEEM, HYSCORE, EDNMR), the terms relating to the ^{55}Mn nuclei in Eq. 4 can be omitted:

$$\hat{H}_{\text{Ligand}} = \beta_e \bar{B}_0 \cdot \hat{G} \cdot \bar{S} + \sum_{i=1}^n \left(-g_{\text{L},i} \beta_n \bar{B}_0 \cdot \bar{L}_i + \bar{S} \cdot \hat{A}_{\text{L},i} \cdot \bar{L}_i + \bar{L}_i \cdot \hat{q}_{\text{L},i} \cdot \bar{L}_i \right) \quad (\text{S7})$$

In practice, however, the spin Hamiltonians in Eqs. S6 and S7 is only valid when an ENDOR, ESEEM, HYSCORE or EDNMR spectrum is collected at the center field of the S_0 state multiline spectrum as at this position all powder pattern orientations are sampled uniformly. Especially at high magnetic B_0 fields, spectra collected on the high- and low-field edges of the respective multiline EPR spectrum must also take into account the sampling of the powder pattern orientations, which for the ^{55}Mn tetramer in the S_0 state (same as in the S_2 state) is defined by the hyperfine coupling of the ^{55}Mn nuclei along with the G tensor. Eqs. S6 and S7 can still be used (*i.e.*, terms associated with the nuclei not

considered can be excluded), but each orientation must include a weighting derived from simulation of the EPR line shape, for which the ^{55}Mn hyperfine interactions are taken account by hyperfine strain.

S4 Experimental details of the EPR measurements

Electron spin echo (ESE)-detected field-swept spectra were measured by use of the pulse sequence $\pi/2-\tau-\pi-\tau$ -echo⁹, electron spin echo-detected inversion recovery traces using the 3-pulse sequence: $\pi_{\text{inv}}-T-\pi/2-\tau-\pi-\tau$ -echo, two-pulse ESEEM spectra employing the sequence $\pi/2-\tau+T-\pi-\tau+T$ -echo¹⁰, three-pulse ESEEM spectra employing $\pi/2-\tau-\pi/2-T-\pi/2-\tau$ -echo¹¹, three-pulse vs. two-pulse ESEEM spectra using $\pi/2-T_1-\pi/2-T_2-\pi/2-T_1$ -echo¹² and HYSCORE spectra using $\pi/2-\tau-\pi/2-T_1-\pi-T_2-\pi/2-\tau$ -echo¹³. The lengths of the microwave pulses were generally set such that $\pi/2 = 12$ ns, 16 ns or 36 ns at Q-band and 28 ns at W-band. For ESE-detected EPR experiments, inter-pulse distances were $\tau = 260$ ns, 320 ns or 348 ns at Q-band and 280 ns at W-band. For the three-pulse ESEEM measurements, six τ values in steps of 20 ns in the range $\tau = 200$ –300 ns to account for blind-spotting artifacts and an optimum $\tau = 260$ ns for the HYSCORE experiments were chosen. Q-band ⁵⁵Mn-ENDOR spectra were collected by using the Davies-type pulse sequence $\pi_{\text{inv}}-\pi_{\text{RF}}-T-\pi/2-\tau-\pi-\tau$ -echo¹⁴ with a length $\pi_{\text{inv}} = 24$ ns for the inversion microwave pulse, a RF pulse length $\pi_{\text{RF}} = 3.5$ μs , an inter-pulse delay of $T = 1.5$ μs and $\pi/2 = 12$ ns and $\tau = 260$ ns. EDNMR measurements were collected using the pulse sequence $\pi_{\text{HTA}}-T-\pi/2-\tau-\pi-\tau$ -echo¹⁵. The high turning angle (HTA) microwave pulse was applied at microwave frequencies ν_{mw} . The Hahn echo detection pulse sequence $\pi/2-\tau-\pi-\tau$ -echo at a microwave frequency $\nu_{\text{mw}}^{(0)}$ matched to the cavity resonance was set at a sufficient time T after the HTA pulse to ensure near-complete decay of the electron spin coherencies. The pulse length used for detection was $\pi/2 = 80$ ns and an inter-pulse separation of $\tau = 500$ ns was used. The echo was integrated over a window of 500 ns. The spectra were acquired via continuously sweeping the HTA frequency ν_{mw} at a fixed magnetic field in steps of ≈ 31 kHz. A HTA microwave pulse of length $\pi_{\text{HTA}} = 8$ μs and an amplitude $\omega_1 = 14$ – 18×10^6 rad s⁻¹ was used to minimize the width of the central blind spot¹ to improve resolution of the low-frequency ¹⁴N spectral lines. Shot repetition times employed varied in the range of 0.1–5 ms for the different experiments.

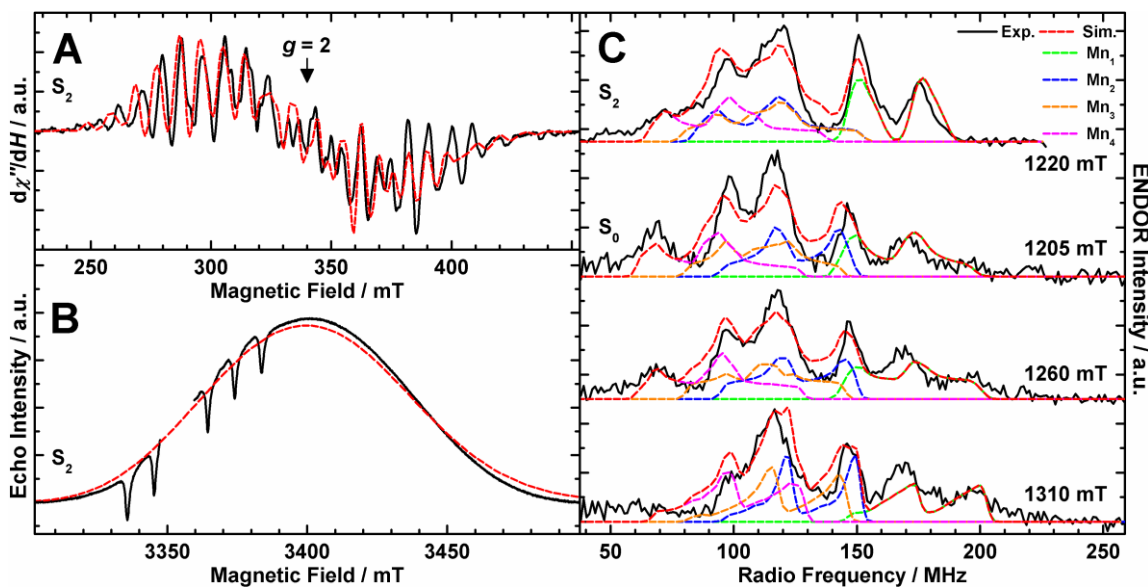


Figure S2. EPR and ^{55}Mn -ENDOR spectra (black solid traces) and spin Hamiltonian-based simulations (red dashed traces) of the S_2 state (originally published in Ref. ⁶) and the 3-flash-advanced S_0 state of the OEC in PSII isolated from *T. elongatus*. The optimized parameter sets are given in Table S1 and main text Table 2, respectively. **(A)** S_2 state X-band CW EPR. Y_D had been replaced by a phenylalanine, removing the Y_D^\bullet signal from the spectra.¹⁶ Experimental parameters: microwave frequency: 9.410 GHz; microwave power: 20 mW; modulation amplitude: 25 G; time constant: 82 ms; temperature: 8.6 K. **(B)** S_2 state W-band ESE-detected EPR. The $g \approx 2$ radical signal of Y_D^\bullet (D2-Tyr160) was excised for clarity of presentation. Experimental parameters: microwave frequency: 93.989 GHz; shot repetition time: 1 ms; microwave pulse length (π): 48 ns; τ : 300 ns; temperature: 4.8 K. **(C)** S_2 and S_0 states Q-band Davies ENDOR. The experimental spectra represent light-minus-dark differences. Colored dashed lines depict a decomposition of the simulation showing resonances from the individual ^{55}Mn nuclei. The simulations of the S_0 state spectra are those in main text Figure 1 resulting from simultaneous fits of the EPR and ^{55}Mn ENDOR signals (see sections 2.3 in the main text, S2 and S3). Experimental parameters: S_2 : microwave frequencies: 33.968 GHz; magnetic field: 1220 mT; shot repetition time: 1 ms; microwave pulse length (π): 32 ns; τ : 268 ns; RF pulse length ($\pi\tau_{\text{RF}}$): 3.5 μs ; temperature: 4.8 K; S_0 : see Figure 1.

S6 The S₂ state: EPR/⁵⁵Mn ENDOR simulation parameters, Mn exchange couplings, fine structure interactions and spin projection factors

Table S1. Principal Values of the Effective G and ⁵⁵Mn Hyperfine Tensors A_i / MHz for the Simulations of the multifrequency EPR and ENDOR Spectra (Figure S2),^a “Experimental”^b and “Theoretical”^c Isotropic Spin Projections $\rho_{i,\text{iso}}$, as Well as Intrinsic Isotropic Hyperfine Components $a_{i,\text{iso}}$ / MHz^d for the Individual Mn Ions of the S₂ State of the OEC in PSII from *T. Elongatus*, as reported in Ref. ⁶.

	G^a	A_1^a	A_2^a	A_3^a	A_4^a
x	1.989	350	214	214	173
y	1.978	329	195	184	157
\perp^e	1.983	339	204	199	165
z^e	1.956	321	282	282	251
iso ^f	1.974	333	230	227	194
aniso ^g	0.028	25	-78	-83	-87
experimental ^b		$ \rho_{1,\text{iso}} $ (Mn ^{III})	$ \rho_{2,\text{iso}} $ (Mn ^{IV})	$ \rho_{3,\text{iso}} $ (Mn ^{IV})	$ \rho_{4,\text{iso}} $ (Mn ^{IV})
		1.48-2.02	0.91-1.23	0.90-1.21	0.77-1.04
theoretical ^{c,f}		$\rho_{\text{D1,iso}}$	$\rho_{\text{A4,iso}}$	$\rho_{\text{C2,iso}}$	$\rho_{\text{B3,iso}}$
		1.81	1.11	-1.00	-0.93
d,f		$a_{\text{D1,iso}}$	$a_{\text{A4,iso}}$	$a_{\text{C2,iso}}$	$a_{\text{B3,iso}}$
		-186	-206	226	207

^a All G and A_i ($i = 1-4$) tensors are collinear. ^b Calculated as $|\rho_{i,\text{iso}}| = A_{i,\text{iso}}/|a_{\text{iso}}|$ from the fitted $A_{i,\text{iso}}$ and the ranges of literature $|a_{\text{iso}}|$ values for monomeric Mn ions, Mn^{III}: 165-225 MHz, Mn^{IV}: 187-253 MHz (see Refs. ^{17,18}). ^c Calculated via matrix diagonalization from the exchange couplings $J_{\text{AB}}, J_{\text{AC}}, J_{\text{AD}}, J_{\text{BC}}, J_{\text{BD}}, J_{\text{CD}} = -15.9, 1.9, 0.8, 23.8, 2.0, -15.7 \text{ cm}^{-1}$ and intrinsic fine structure values of the Mn^{III} and Mn^{IV} ions $d_{\text{D1},z} = -1.43 \text{ cm}^{-1}$, with $e_{\text{D1}}/d_{\text{D1}} = 0$, and $d_{\text{IV}} = 0 \text{ cm}^{-1}$. ^d Calculated as $a_{i,\text{iso}} = -A_{i,\text{iso}}/\rho_{i,\text{iso}}$ employing the theoretical spin projection factors $\rho_{i,\text{iso}}$ above. ^e The axial/parallel and equatorial/perpendicular G and A_i values are defined as the unique tensor component and the average of the two non-unique components, respectively. ^f The isotropic $G_{\text{iso}}, A_{i,\text{iso}}, \rho_{i,\text{iso}}$ and $a_{i,\text{iso}}$ values are the averages of the

individual values: $Y_{\text{iso}} = (Y_x + Y_y + Y_z)/3$.⁸ The anisotropies of the G and A_i tensors are expressed as the differences $G_{\text{aniso}} = G_{\perp} - G_{\parallel}$ and $A_{i,\text{aniso}} = A_{i,\perp} - A_{i,\parallel}$.

S7 Electronic structure of the S_0 state: spin projections, intrinsic ^{55}Mn hyperfine couplings and Mn fine structure interactions

As mentioned in the main text section 3.3, in contrast to Mn^{IV} ions, fine structure interactions of Mn^{III} ions are of significant size ($|d(\text{Mn}^{\text{III}})| = 1\text{-}4 \text{ cm}^{-1}$) relative to the exchange couplings J_{ij} to perturb the spin projections ρ_i , now tensor instead of scalar quantities, and thus the hyperfine tensors considerably.^{6,17-20} In Table S2, we test if the exchange-coupling schemes of the BS-DFT models **S₀-1** and **S₀-3** (Figure 4C in the main text) can be principally valid for the S_0 state when taking into account fine structure terms for the Mn^{III} ions. An outcome of these structural models of the S_0 state, we employed fine structure tensors with unique components aligned along the canonical directions of the Jahn-Teller axes of the respective Mn^{III} ions (section 3.1), yielding rhombic ρ_i tensors, and chose an axial $d_{\text{III}} = -1 \text{ cm}^{-1}$ ($e_{\text{III}}/d_{\text{III}} = 0$). For model **S₀-3**, the resulting values of $\rho_{i,\text{iso}}$ and $a_{i,\text{iso}}$ are affected only to a very small degree by the fine structure tensors used. For model **S₀-1**, the only one with the unique fine structure tensor components of the three Mn^{III} ions aligned along the three different canonical axes, $\rho_{i,\text{iso}}$ and $a_{i,\text{iso}}$ are more strongly affected. Nevertheless, they all fall within the empirical ranges, only $a_{\text{A4},\text{iso}}$ being slightly too negative. In conclusion, the implementation of the fine structure terms does not change the result that models **S₀-1** and **S₀-3** are consistent with experimental and literature constraints. We note that these fine structure tensors are not final and their determination taking into account the anisotropic ^{55}Mn hyperfine components $a_{i,\text{iso}}$ forms ongoing work in our group.

Table S2. Possible “Experimental”^a and “Theoretical”^b Isotropic Spin Projection Factors $\rho_{i,\text{iso}}$, as Well as Intrinsic Isotropic Hyperfine Components $|a_{i,\text{iso}}|$ / MHz for the Individual ⁵⁵Mn Ions of the 3-flash-advanced S₀ State in PSII from *T. Elongatus* Based on the DFT Models **S₀-1** and **S₀-3**.^c

experimental ^a	$ \rho_{1,\text{iso}} $	$ \rho_{2,\text{iso}} $	$ \rho_{3,\text{iso}} $	$ \rho_{4,\text{iso}} $
Mn ^{II}	1.29-1.44	0.96-1.07	0.86-0.95	0.69-0.77
Mn ^{III}	1.51-2.06	1.12-1.53	1.00-1.36	0.81-1.10
Mn ^{IV}	1.34-1.81	0.99-1.35	0.89-1.20	0.72-0.97
model S₀-1 ^b	$\rho_{\text{D1,iso}}$	$\rho_{\text{B3,iso}}$	$\rho_{\text{A4,iso}}$	$\rho_{\text{C2,iso}}$
$d_{\text{III}} = 0 \text{ cm}^{-1}$	1.87	1.32	-1.32	-0.87
$d_{\text{III}} = -1 \text{ cm}^{-1}$	1.72	1.20	-1.12	-0.80
	$ a_{\text{D1,iso}} $	$ a_{\text{B3,iso}} $	$ a_{\text{A4,iso}} $	$ a_{\text{C2,iso}} $
$d_{\text{III}} = 0 \text{ cm}^{-1}$ ^d	181	190	170	208
$d_{\text{III}} = -1 \text{ cm}^{-1}$ ^d	205	218	230	232
model S₀-3 ^b	$\rho_{\text{A4,iso}}$	$\rho_{\text{B3,iso}}$	$\rho_{\text{D1,iso}}$	$\rho_{\text{C2,iso}}$
$d_{\text{III}} = 0 \text{ cm}^{-1}$	1.96	-1.23	1.14	-0.87
$d_{\text{III}} = -1 \text{ cm}^{-1}$	1.97	-1.24	1.15	-0.87
	$ a_{\text{A4,iso}} $	$ a_{\text{B3,iso}} $	$ a_{\text{D1,iso}} $	$ a_{\text{C2,iso}} $
$d_{\text{III}} = 0 \text{ cm}^{-1}$ ^d	173	204	197	209
$d_{\text{III}} = -1 \text{ cm}^{-1}$ ^d	174	206	197	213

^a Calculated as $|\rho_{i,\text{iso}}| = A_{i,\text{iso}}/|a_{i,\text{iso}}|$ from the fitted $A_{i,\text{iso}}$ values in Table 2 and the ranges of literature $|a_{i,\text{iso}}|$ values for monomeric Mn ions, Mn^{II}: 236-263 MHz, Mn^{III}: 165-225 MHz, Mn^{IV}: 187-253 MHz (see Refs. ^{17,18,20-23}). ^b Calculated via matrix diagonalization from the exchange couplings J_{ij} of the respective model (Figure 4C) and the given fine structure interactions d_{III} of the three Mn^{III} ions with their axial components aligned along the canonical directions of their Jahn–Teller axes (section 3.1). ^c The values of the only feasible Mn valence states and the most likely BS-DFT model, as elaborated in the text, are shaded green. ^d Calculated as $|a_{i,\text{iso}}| = A_{i,\text{iso}}/|\rho_{i,\text{iso}}|$ employing the theoretical spin projection factors $\rho_{i,\text{iso}}$ above.

S8 T_1 relaxation and spin state ladder: Q-band inversion recovery experiments and analysis

S8.1 Spin-lattice relaxation processes, signal intensities and their temperature dependences

Spin-lattice relaxation proceeds via processes that involve energy exchange between the magnetic transitions and its surroundings, *i.e.* in the solid state one or multiple phonon vibrational modes, depending on the phonon density spectrum and the accesibility of excited spin states. At very low temperatures $< \approx 2$ K, the only process relevant is the direct, one-phonon mechanism, in which the excited electron spin relaxes to the ground state by exciting a lattice vibration mode, necessarily of the same energy.²⁴ In the higher temperature range employed in our experiments, the two-phonon relaxation pathways occur with increased probabilities, such that the dominant mechanisms for spin-lattice relaxation pathways are either Raman processes²⁴ or, in the case of the presence of (a) low-lying excited spin state(s), Orbach processes.²⁵ Both of them involve two phonons with an energy difference equal to the EPR microwave energy. While for the Raman-type, this involves a scattering process via a “virtual excited state”, the Orbach-type proceeds via resonant phonon absorption and emission involving excitation to an actual higher quantum level of the spin system. The phonon resonance process occurs with higher probability than a scattering process. The corresponding temperature dependences of the T_1 times are $1/T_1 \propto T^n$ for Raman processes and $1/T_1 \propto e^{-\Delta/kT}$ for Orbach processes, thus depending on the ratio between the ground-to-first excited state energy difference Δ and the thermal energy kT . Which of the two is the dominating one in a certain temperature range can be determined by fits of the respective functions to the T -dependent T_1 times. For better visualizability, the fit functions are linearized, such that $\ln(T_1^{-1}) = A + n \ln T$ for the Raman and $\ln(T_1^{-1}) = A + \frac{-\Delta}{k} T$ for the Orbach process with $\ln(T_1^{-1})$ as the ordinate and $\ln(T)$ and T^{-1} as the respective abscissae. In case of a dominant Raman-type relaxation, the exponent n , the slope in the linear plot, typically ranges between 3 and 9. For a dominant Orbach-type mechanism, the temperature dependence of T_1 can be utilized to determine Δ in order to characterize the spin state ladder of a oligonuclear spin system, which results from the inter-spin electronic exchange couplings.

Besides the T_1 relaxation times in case of an Orbach process, also the relative intensities I_1 of the ground spin state signal can be utilized to gain information about the ground-to-first state energy splitting Δ . I_1 corresponds to the maximum spin echo amplitudes obtained from the inversion recovery fits as the parameter representing the asymptote of the exponential curve. It depends on the inverse temperature weighted by the Boltzmann factor as (see Ref. ²⁶):

$$I_1 = \frac{C}{T} \frac{(2S_1 + 1)\exp(-E_1/kT)}{\sum_i (2S_i + 1)\exp(-E_i/kT)} \quad (\text{S1})$$

where C is a proportionality constant, S_i represents the total spin of the coupled states of the spin manifold ($S_i = 1/2, 3/2, \dots$) and E_i are the respective energies. Here, a simplified two spin model derived from the computational exchange-coupling scheme of the form $\alpha\beta\alpha\beta$ of S_0 state model **S₀-1** (Figure 4C) is used to describe the energy ladder in terms of a single effective coupling constant, J_{eff} between two fragments of the Mn tetramer: monomeric $\text{Mn}_{\text{A4}}^{\text{III}}$ ($S_{\text{A4}} = 2$), and the $\beta\alpha\beta$ -coupled trimer $\text{Mn}_{\text{B3}}^{\text{III}}\text{Mn}_{\text{C2}}^{\text{IV}}\text{Mn}_{\text{D1}}^{\text{III}}$ (spin ground state $S_{\text{B3-C2-D1}} = 5/2$). The corresponding simplified Hamiltonian $\hat{H} = -J_{\text{eff}}\vec{S}_{\text{A4}}\vec{S}_{\text{B3-C2-D1}}$ gives spin state energies $E_i = (S_{\text{A4}}(S_{\text{A4}} + 1) + S_{\text{B3-C2-D1}}(S_{\text{B3-C2-D1}} + 1) - S_i(S_i + 1))J_{\text{eff}}$, where the total spin $S_i = (S_{\text{B3-C2-D1}} - S_{\text{A4}}) \dots (S_{\text{B3-C2-D1}} + S_{\text{A4}}) = 1/2 \dots 9/2$. Equation S1 can thus be employed to estimate J_{eff} and $\Delta = E_2 - E_1 = -3J_{\text{eff}}$.

S8.2 Q-band inversion recovery experiments

Previous studies of higher plant spinach and cyanobacterial PSII indicated that the OEC in the low spin $S_2^{18,19,26-28}$ state predominantly displays an Orbach-type spin relaxation²⁵ over the 4.2 – 11 K temperature range. As the rate of the longitudinal relaxation via an Orbach process is also dependent on the energy separation Δ between the ground and the first excited spin state, this temperature dependence of T_1 can thus be utilized to assess Δ in a coupled spin system such as the S_0 state OEC (see above). However, the relaxation process in the S_0 state at these temperatures so far remained ambiguous. For the 3-flash-induced S_0 state from spinach PSII in the presence of MeOH (3 %), Kulik *et al.*²⁹ favor an

Orbach process with a Δ of 21.7 cm^{-1} . However, the temperature dependence could also be described by Raman behavior²⁴, such that the calculated Δ may not represent a real value. Based on microwave saturation experiments, the group of Styring came to the conclusion that relaxation under these conditions proceeds mainly via the Raman process³⁰ and that the lower limit for Δ was 30 cm^{-1} .³¹ This

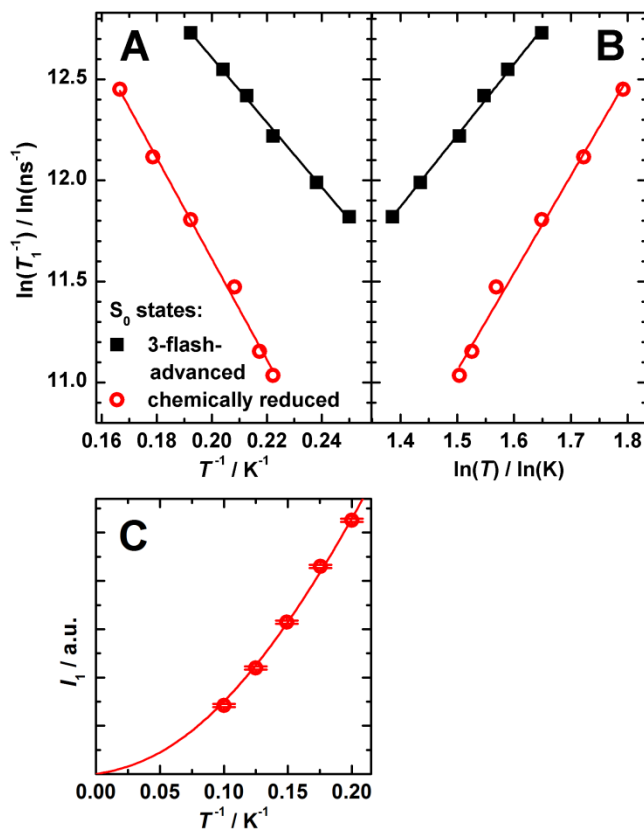


Figure S3. Temperature dependences of monoexponential fit parameters from inversion recovery experiments of the $\text{Mn}_4\text{O}_5\text{Ca}$ cluster in the 3-flash-advanced (black) and the chemically reduced (red) form of the S_0 state OEC in PSII isolated from *T. elongatus*. (A) Orbach and (B) Raman plots of the fitted T_1 relaxation times. (C) Curie plot of the fitted maximum spin echo intensities of the fully relaxed magnetization vectors. The solid lines represent fits to the data points, as described in detail in section S8.1. Experimental parameters: microwave frequencies: 33.879 GHz (A, B red), 34.02-34.05 GHz (C); magnetic field: 1260 mT; shot repetition times: 552 μs (A, B red), 5 ms (C); microwave pulse lengths (π): 32 ns (A, B red), 72 ns (C); τ : 320 ns (A, B red), 348 (C); temperatures: 4.0-5.2 K (A, B black), 4.4-6.0 (A, B red), 5.0-10.0 K (C).

was mainly based on the finding of a Curie behavior in S_0 , not consistent with the lower energy gap fitted for the case of an Orbach relaxation mechanism ($\Delta = 17 \text{ cm}^{-1}$).

We have performed inversion recovery experiments at Q-band on PSII samples from *T. elongatus* in both S_0 states at a central field position of the corresponding multiline EPR signals over various temperatures T . For this, the inter-pulse delays T (see Experimental Section 2.2) were varied over the range from 0.5 μs or 1 μs up to a maximum of 2000 μs or 99 μs for the PSII samples in the 3-flash-advanced and the chemically induced S_0 states, respectively. The time traces were reproduced by fitting a monoexponential decay function to the data in order to determine the T_1 relaxation times according to the Bloch equation for the z component of the magnetization vector³².

At liquid He temperatures, both the 3-flash-advanced and chemically reduced cyanobacterial S_0 states exhibit faster T_1 relaxation (5 μs and 16 μs , respectively, at 4.5 K) than the S_2 state multiline ($\approx 100 \mu\text{s}$ at 4.5 K¹⁹), similar to previous reports on plantal PSII.^{19,27-30} Due to the shorter T_1 times and resulting faster decrease of spin echo intensities and thus signal-to-noise ratios with increasing temperatures, the maximum temperatures to be used are smaller for the S_0 state (6 K) than the S_2 state ($\approx 8 \text{ K}$)^{18,19} in PSII core preparations from *T. elongatus*. The temperature dependences of the resultant T_1 relaxation times were modeled by linear fits on the basis of both an Orbach-type (Figure S3A) and a Raman-type (Figure S3B) correlation for $T = 4.0\text{-}5.0 \text{ K}$ (3-flash-advanced) and $4.5\text{-}6.0 \text{ K}$ (chemically reduced). They showed that these dependences can be described equally well ($R^2 \geq 0.99$) by either relaxation mechanism for both S_0 state variants, consistent with findings for the 3-flash-advanced S_0 state in spinach PSII.^{29,30} The Orbach fits yielded values for Δ of $11.1 \pm 0.3 \text{ cm}^{-1}$ for the 3-flash-advanced and $17.3 \pm 0.6 \text{ cm}^{-1}$ for the chemically reduced S_0 state, which is in the range observed for spinach PSII.^{29,30} For the Raman fits, temperature dependences of $T^{3.5}$ and $T^{4.8}$ reproduce the data, with exponents in the theoretically predicted range between 3 and 9.

Besides via the T_1 times, our experiments can also be utilized to gain information about the spin state ladder via the temperature dependence of the electron spin echoes upon complete relaxation (see section S8.1).²⁷ In Figure S3C, their relative intensities I/I for a chemically reduced S_0 state sample are plotted

versus the inverse experimental temperatures. In case of an energetically well separated first excited spin state, it would show Curie law behavior, *i.e.* an (almost) linear extrapolation of the determined data points towards the origin for infinite temperature. In contrast, we observe a clear deviation from linear, Curie behavior, in contrast to the multiline, $S = 1/2$ signal of the S_2 state.^{26,27,33} The data can be reproduced by a curve fitted to the function describing the relation between I_1 and T on the basis of a simplified exchange-coupling model of the Mn tetramer (section S8.1). The fit yields a Δ of 2.8 ± 1.7 cm^{-1} , significantly smaller than the apparent energy difference suggested by the Orbach fit of the T_1 times. This alleged inconsistency is analyzed in detail in the following section.

S8.3 The ground-to first excited state energy difference Δ in the cyanobacterial S_0 state

At first glance, the result from the temperature-dependent inversion recovery experiments to assess the T_1 relaxation properties may seem ambiguous. The datasets may well be reproduced both by Orbach and Raman fits (Figure S3A, B). The fact that the fit of the Curie plot of the maximum spin echo amplitudes (Figure S3C) does yield a ground-to-first excited state energy splitting Δ of 2.8 ± 1.7 cm^{-1} indicates that the Orbach fit does not provide the actual value of Δ . However, a low-lying excited spin state should enable resonant Orbach processes, rendering them the main relaxation mechanism in the temperature range investigated (see section S8.1).²⁵ The rationale for this seeming discrepancy is that, owing to the comparatively low Δ , the larger numbers obtained from the Orbach fits are effective values that represent energy spacings between the ground and several (higher) excited states. These offer multiple relaxation pathways, resulting in the fitted energy difference significantly larger than Δ . Via them, relaxation processes of the excited $S = 1/2$ electronic spin of the S_0 state occur with higher probabilities than via the Raman mechanism. The multiple excited spin states available for efficient Orbach relaxation at the same time provide a rationale for the higher T_1 relaxation rates in S_0 than in S_2 below 8°K . Furthermore, it may explain the finding that above 8°K , the situation changes³⁰ due to excited spin states in S_2 becoming increasingly available to promote faster Orbach relaxation. Hence in contrast, the Raman plots in Figure S3B reproduce the data by coincidence, as Raman processes occur with

significantly lower probabilities. The fitted Δ of 2.8 cm^{-1} agrees well with the comparably small energy difference $\Delta = 1.9 \text{ cm}^{-1}$ of model **S₀-1** (sections 3.1 and 3.3 in the main text) and provides strong support for its computational pair-wise electronic exchange interactions J_{ij} (Figure 4C) and the corresponding structure for the S_0 state (Figure 2 in the main text). The previous finding of the S_0 state showing Curie behavior with $\Delta \leq 30 \text{ cm}^{-1}$ in a plant PSII sample³¹ can probably be attributed to species differences and the presence of a small alcohol. The effect of MeOH binding³⁴⁻³⁶ leading to an increase of Δ in PSII from spinach is a phenomenology observed in the same way for the S_2 state.^{19,26,31}

On basis of the simplified exchange-coupling model involving only two interacting spin entities and not considering other terms such as the fine structure, as outlined in section S8.1, the energy separation relates to the effective exchange coupling as $\Delta = -3J_{\text{eff}} = 0.9 \text{ cm}^{-1}$. Thus, J_{eff} is on the order of both the Zeeman energy ($\approx 1 \text{ cm}^{-1}$ at Q-band) and the fine structure splitting of the Mn^{III} ions (typically $|d(\text{Mn}^{\text{III}})| = 1\text{-}4 \text{ cm}^{-1}$ ^{17,18}). It is not the dominant interaction or term in the spin Hamiltonian, as opposed to the assumptions made for the spectral simulations (section S3.2). The integration of the significantly less strongly interacting Mn_{A4} with the cuboidal trimer unit to result in an effective $S_{\text{T}} = 1/2$ ground state could be a reason that the orientation selectivity of the ^{55}Mn -ENDOR dataset is underestimated by the simulations (Figure 1C in the main text). The validity of the above rationale is further supported by comparison to the well-characterized situation in the low spin conformation of the cyanobacterial S_2 state. Its considerably larger Δ corresponds to a respectively larger J_{eff} , which represents the dominant magnetic interaction.^{6,18,19} As the relative contribution of the fine structure term of a single Mn^{III} ion to Δ is significantly smaller, the S_2 state ^{55}Mn -ENDOR signal of frozen solution PSII samples exhibits only little field dependence.^{6,7,18,37,38}

S9 The Mn_{D1} -His332-imino-N interaction: field- and τ -dependent Q-band ^{14}N -three-pulse ESEEM and ^{14}N -HYSCORE experiments and interpretation of the simulation parameters

S9.1 Field- and τ -dependent Q-band ^{14}N -three-pulse ESEEM and ^{14}N -HYSCORE experiments

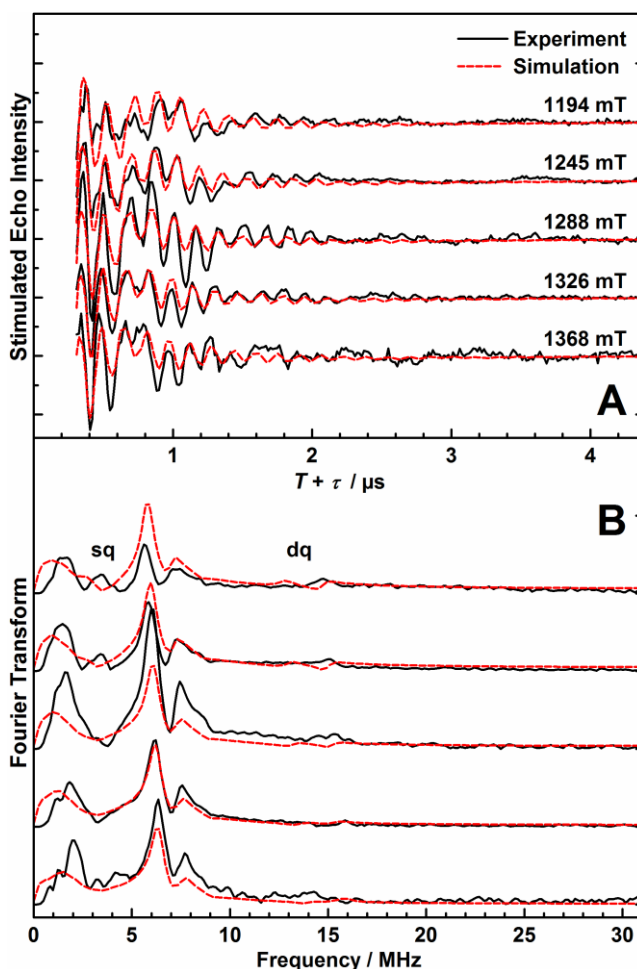


Figure S4. Q-band three-pulse ESEEM light-minus-dark spectra of PSII samples from *T. elongatus* in the 3-flash-advanced S_0 state at varying magnetic-field positions, as indicated, corresponding to $g = 2.032$ - 1.774 with $\tau = 220$ ns. **(A)** Time-domain spectra and **(B)** corresponding Fourier transforms. Black solid traces depict experimental spectra; superimposing red dashed traces represent simulations based on the spin Hamiltonian formalism as outlined in sections 2.3, S2 and S3. The optimized parameter set is listed in Table 3 in the main text. “sq” and “dq” indicate single- and double-quantum transition regions, respectively. For a description of the baseline-subtraction procedure, see section S1. Experimental parameters: microwave frequency: 33.965 GHz; magnetic fields: 1194-1368 mT; shot repetition time: 0.5 ms; microwave pulse length ($\pi/2$): 16 ns; τ : 220 ns; ΔT : 48 ns; temperature: 4.8 K.

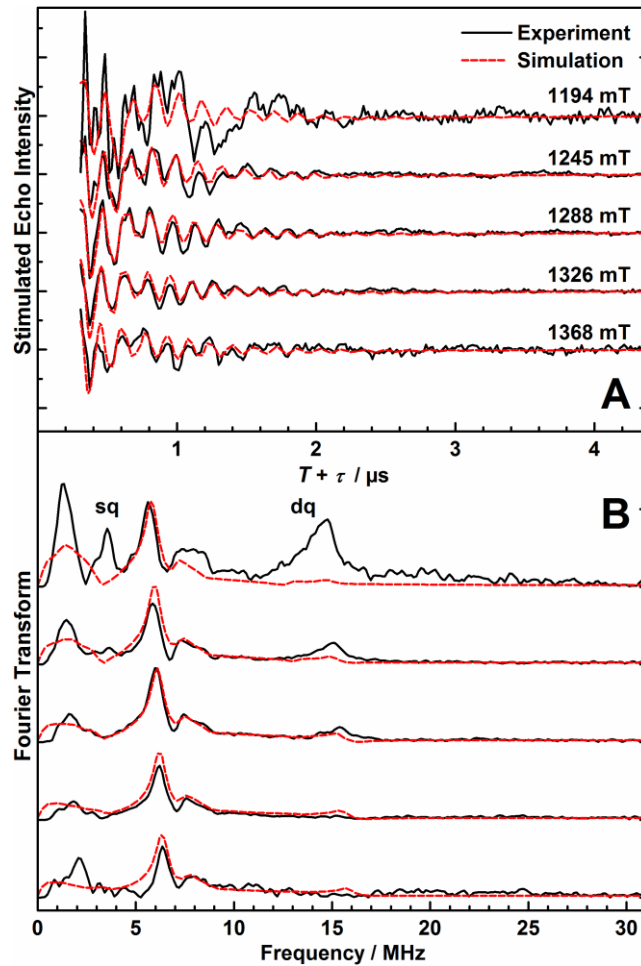


Figure S5. Q-band three-pulse ESEEM light-minus-dark spectra of PSII samples from *T. elongatus* in the 3-flash-advanced S_0 state at varying magnetic-field positions, as indicated, corresponding to $g = 2.032$ - 1.774 with $\tau = 260$ ns. **(A)** Time-domain spectra and **(B)** corresponding Fourier transforms. Black solid traces depict experimental spectra; superimposing red dashed traces represent simulations based on the spin Hamiltonian formalism as outlined in sections 2.3, S2 and S3. The optimized parameter set is listed in Table 3. “sq” and “dq” indicate single- and double-quantum transition regions, respectively. For a description of the baseline-subtraction procedure, see section S1. Experimental parameters: microwave frequency: 33.965 GHz; magnetic fields: 1194-1368 mT; shot repetition time: 0.5 ms; microwave pulse length ($\pi/2$): 16 ns; τ : 260 ns; ΔT : 48 ns; temperature: 4.8 K.

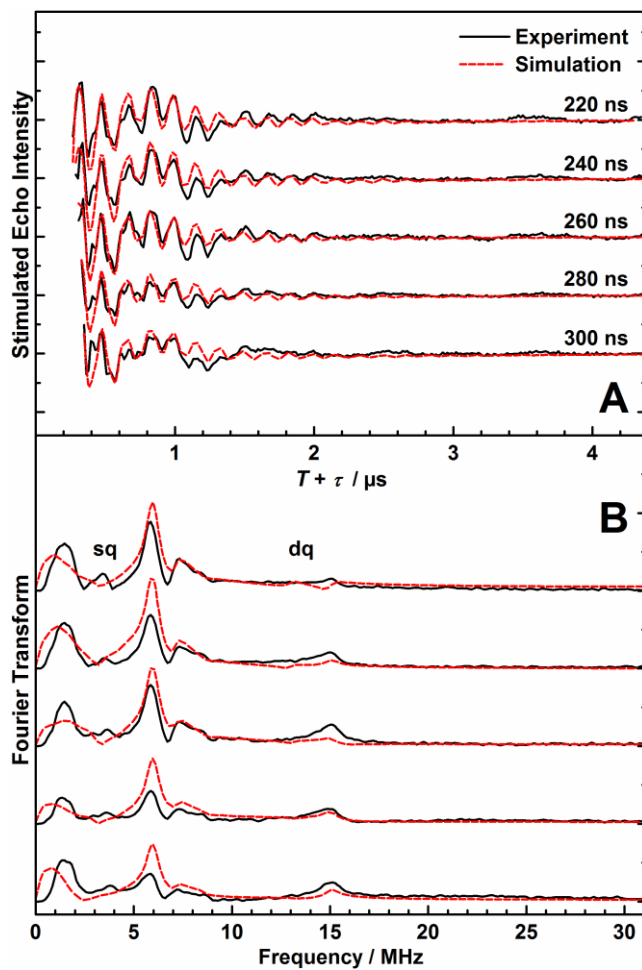


Figure S6. Q-band three-pulse ESEEM light-minus-dark spectra of PSII samples from *T. elongatus* in the 3-flash-advanced S_0 state at varying τ values, as indicated. **(A)** Time-domain spectra and **(B)** corresponding Fourier transforms. Black solid traces depict experimental spectra; superimposing red dashed traces represent simulations based on the spin Hamiltonian formalism as outlined in sections 2.3, S2 and S3. The optimized parameter set is listed in Table 3. “sq” and “dq” indicate single- and double-quantum transition regions, respectively. For a description of the baseline-subtraction procedure, see section S1. Experimental parameters: microwave frequency: 33.965 GHz; magnetic field: 1245 mT; shot repetition time: 0.5 ms; microwave pulse length ($\pi/2$): 16 ns; τ : 220-300 ns; ΔT : 48 ns; temperature: 4.8 K.

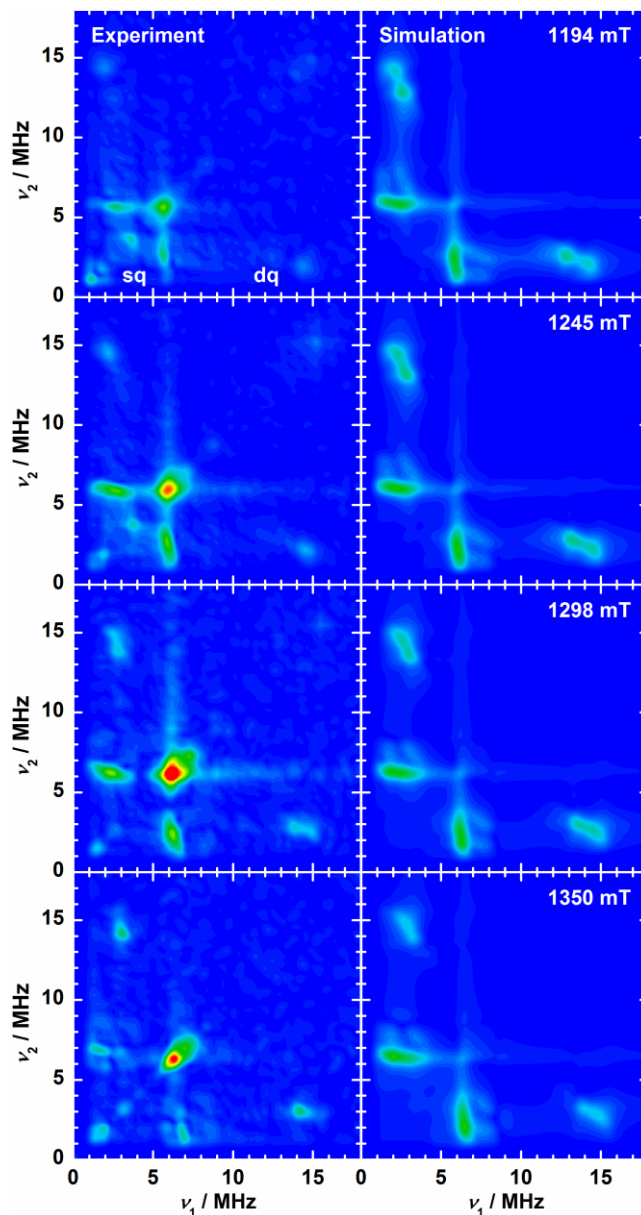


Figure S7. (+,+) quadrants of the Fourier-transformed Q-band HYSCORE experimental spectra (left) and spin Hamiltonian-based simulations (right) of PSII samples from *T. elongatus* in the 3-flash-advanced S_0 state at varying magnetic-field positions, as indicated, corresponding to $g = 2.032$ - 1.798 . “sq” and “dq” point out regions of single- and double-quantum transitions, respectively. The optimized parameter set for the simulations, as described in sections 2.3, S2 and S3, is listed in Table 3. For a description of the background-correction procedure, see section S1. Experimental parameters: microwave frequencies: 33.966 GHz (1194 mT, 1245 mT), 33.964 GHz (1298 mT, 1350 mT); magnetic fields: 1194-1350 mT; shot repetition time: 0.5 ms; microwave pulse length ($\pi/2$): 16 ns; τ : 260 ns; ΔT : 96 ns; temperature: 4.8 K.

S9.2 Interpretation of the His332 imino-¹⁴N simulation parameters

Our comprehensive characterization of the interaction between the His332 ligand and the tetra-Mn cluster represents the first report of these signals in the S₀ state of the PSII enzyme. While the spectroscopic signature of the S₀ state ¹⁴N signal appears relatively different in the Q-band three-pulse ESEEM and especially the HYSCORE experiments from that in the corresponding S₂ state spectra, this can be attributed to a considerable degree to the smaller A_{iso} and the noncompliance with the cancellation condition. Altogether, their fitted hyperfine and NQI parameters are sufficiently similar to unambiguously identify His332 as an equatorial ligand of a Mn ion in the oxidation state +III, *i.e.* Mn_{D1} (Figure 2, see also Ref. ³⁹). On the one hand, the effective hyperfine coupling A_{iso} is smaller than in the S₂ state by 15-25 %. Nonetheless, it is substantially larger than the values for imidazole ligands of Mn^{IV} ions in mixed-valence Mn^{III}Mn^{IV} model complexes and protein cofactors ($A_{\text{iso}} = 1.5\text{-}3.3$ MHz), but consistent with those of Mn^{III} ions ($A_{\text{iso}} \leq 13$ MHz).⁴⁰⁻⁴⁶ More precisely, both the isotropic hyperfine and NQI components match the ranges found in the literature for equatorial imidazole ligands of Mn^{III} ions ($A_{\text{iso}} = 1.5\text{-}6.6$ MHz, $e^2Qq/h = 1.5\text{-}2.5$ MHz)⁴³⁻⁴⁶, but are outside those for axial ones ($A_{\text{iso}} = 9\text{-}13$ MHz, $e^2Qq/h = 2.1\text{-}3.0$ MHz)⁴⁰⁻⁴⁴. Expected hyperfine couplings from spin projecting measured ¹⁴N couplings $a_{\text{iso}} = 2.1\text{-}3.3$ MHz⁴⁷⁻⁵² of histidine, imidazole and guanine ligands of monomeric Mn^{II} do not preclude a +II oxidation state of Mn_{D1}. However, apart from the fact that no such model has been proposed, the inconsistency with typical NQI couplings for these complexes ($e^2Qq/h = 2.6\text{-}3.1$ MHz)⁴⁸⁻⁵² rule out this possibility. This is consistent with the BS-DFT and EPR/⁵⁵Mn ENDOR results (sections 3.1-3.3) and the Jahn-Teller axis of Mn_{D1}, as its unique axis, being aligned along the Mn_{D1}-Asp342 direction also in the S₀ state.

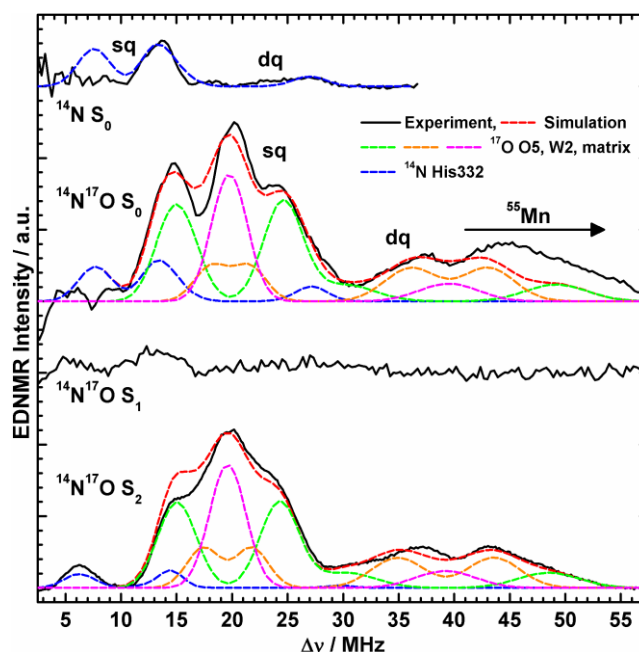


Figure S8. W-band EDNMR spectra of 3-flash-advanced non-isotopically enriched and H_2^{17}O -exchanged S_0 , H_2^{17}O -exchanged S_1 and H_2^{17}O -exchanged S_2 state PSII samples (top to bottom) isolated from *T. elongatus* including single-quantum (sq) and double-quantum (dq) regions. Black solid traces depict background-corrected experimental spectra; superimposing red dashed traces represent simulations based on the spin Hamiltonian formalism as outlined in sections 2.3, S2 and S3. Coloured dashed lines represent a decomposition of the simulation showing contributions from the individual ^{14}N and ^{17}O nuclei. The optimized parameter sets are listed in Table 3. The S_2 state traces were originally published in Ref. ⁶. The ^{14}N S_0 state spectrum shows resonances from the His332 imino- ^{14}N . The $^{14}\text{N}^{17}\text{O}$ S_0 state spectrum shows additional signals from the three exchangeable ^{17}O species, similar to the $^{14}\text{N}^{17}\text{O}$ S_2 state spectrum. Furthermore, ^{55}Mn resonances are present $> \approx 40$ MHz, superimposing the ^{17}O double-quantum region. The $^{14}\text{N}^{17}\text{O}$ S_1 state spectrum shows only residual ^{14}N resonances not attributable to the OEC, but no ^{17}O signals. Experimental parameters: microwave frequencies: 94.002 (^{14}N S_0), 94.062 GHz ($^{14}\text{N}^{17}\text{O}$ S_0), 94.040 GHz ($^{14}\text{N}^{17}\text{O}$ S_1), 93.988 GHz ($^{14}\text{N}^{17}\text{O}$ S_2); magnetic fields: 3.43 T (S_0), 3.4 T (S_1 , S_2); shot repetition times: 0.1 ms (S_0), 0.5 ms (S_1), 1.5 ms (S_2); microwave pulse lengths (π): 160 ns (S_0 , S_1), 400 ns (S_2); t_{HTA} : 8 μs (S_0 , S_1), 14 μs (S_2); τ : 500 ns; temperature: 4.8 K.

S11 Interactions with exchangeable $^1\text{H}/^2\text{H}$ species: Q-band ^2H -two-pulse, ^2H -three-pulse and ^2H -three-pulse vs. two-pulse ESEEM and ^2H -HYSCORE experiments

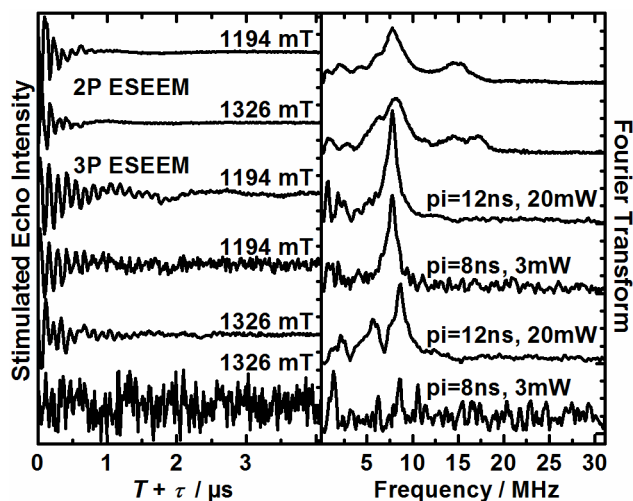


Figure S9. Q-band two-pulse and three-pulse ESEEM ^2H -minus- ^1H spectra of PSII samples in the 3-flash-advanced S_0 state isolated from *T. elongatus*, measured at low ($g = 2.035$) and high ($g = 1.832$) field regions of the corresponding Q-band multiline EPR spectrum. Experimental parameters: microwave frequency: 34.008 GHz; magnetic fields: 1194 mT, 1326 mT; shot repetition time: 0.5 ms; microwave pulse length ($\pi/2$): 12 ns, 8 ns (3 mW); τ : 300 ns; ΔT : 48 ns; temperature: 4.8 K.

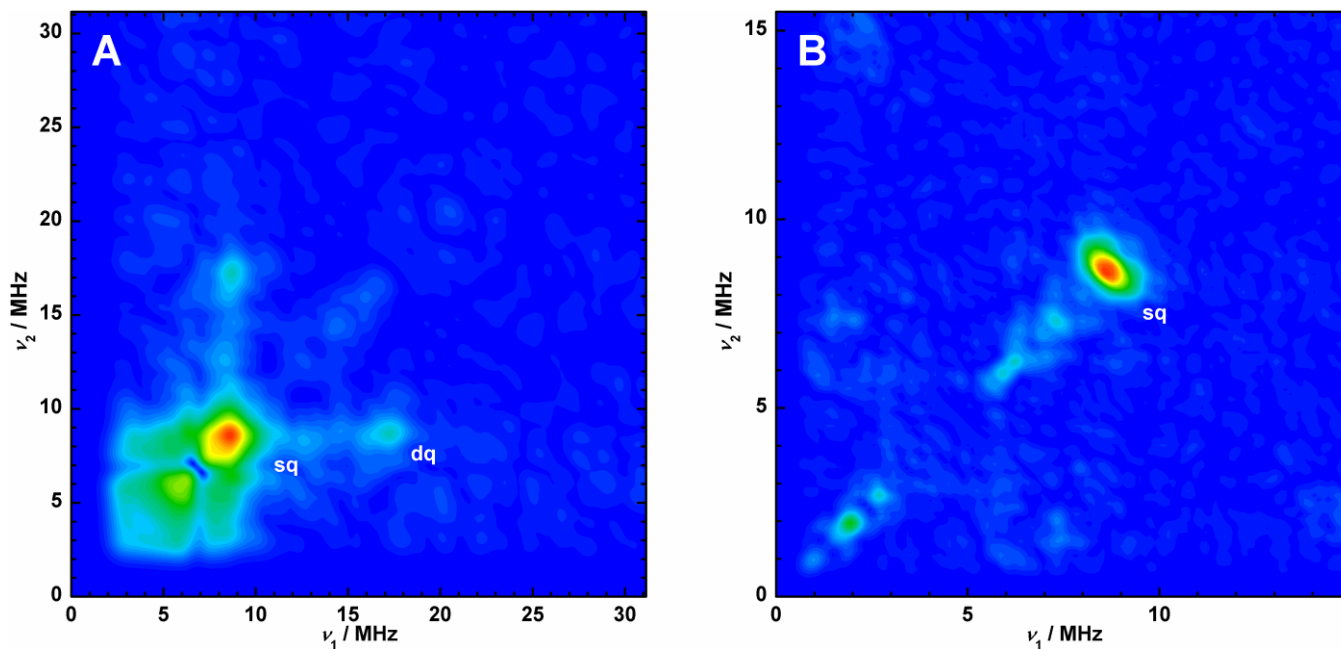


Figure S10. (+,+) quadrants of **(A)** the Fourier-transformed Q-band three-pulse vs. two-pulse spectrum and **(B)** the Q-band HYSCORE spectrum of a $^2\text{H}_2\text{O}$ -exchanged PSII sample in the 3-flash-advanced S_0 state isolated from *T. elongatus*, measured at $g = 1.832$, the high field edge of the corresponding Q-band multiline EPR spectrum. “sq” and “dq” point out regions of single- and double-quantum transitions, respectively. Experimental parameters: microwave frequency: 34.003 GHz; magnetic field: 1326 mT; shot repetition time: 0.5 ms; microwave pulse length ($\pi/2$): 12 ns; τ (B): 300 ns; ΔT : 48 ns (A), 96 ns (B); temperature: 4.8 K.

S12 General considerations on the experimental approach

Besides the differences in the lineshapes of the X-band CW EPR and Q-band ^{55}Mn -ENDOR signals of the S_0 compared to the S_2 state, they exhibit general similarities, especially with respect to their spectral positions ($g \approx 2$ and $\nu_{\text{RF}} \leq 215$ MHz, respectively). Thus, the approach of treating the S_0 state as an effective $S_T = 1/2$ spin state for their analysis (section S3.2) is valid, confirmed by the reasonably good simulation quality (Figure 3 in the main text). A most apparent difference of the ^{55}Mn -ENDOR signals to the S_2 state is their considerably more pronounced field dependence in S_0 . Despite the possibility that the effective $S_T = 1/2$ spin Hamiltonian approach may not be able to account quantitatively for it, as outlined in section S8.3, the overall trends are correctly reproduced. By application of multiple microwave frequencies up to ~ 90 GHz (W-band) an experimental requirement to obtain reasonable field-dependent (Zeeman) and field-independent (hyperfine) spin Hamiltonian parameters is fulfilled.⁶ It is seen that even without considering the fine structure terms of the Mn ions explicitly, the S_0 state EPR/ ^{55}Mn -ENDOR signals are reproduced. Moreover, the approximation of using collinear hyperfine tensors for all ^{55}Mn ions appears reasonable. For the S_2 state, this was deduced in analogy from Mn dimer complexes.^{1818,43,53} Collinear ^{55}Mn A tensors result from near-collinear ligand geometries enforced by the μ -oxo bridges, the dominant structural motif of Mn connectivity common for the synthetic compounds and the OEC. In the same way, our DFT-based structures of the $\text{Mn}_4\text{O}_5\text{Ca}$ complex in the S_0 state, display a high degree of collinearity of the individual Mn coordination geometries (Figure 2), thus employed also for their ^{55}Mn A tensors. However, accounting for small deviations from collinearity, as well as the inclusion of ^{55}Mn NQI terms, could potentially improve the simulation quality, at the same time leading to underdetermination of the system.

Since the ^{14}N and ^{17}O datasets both lack spectra that display the orientation dependence of the signals explicitly enough, the orientation of the His332 imino- ^{14}N and μ -oxo ^{17}O hyperfine tensors relative to the G tensor cannot be determined unequivocally from this dataset. Orientation-dependent high-frequency experiments and the use of PSII crystal samples will be a means to solve this issue.

S13 References

- (1) Rapatskiy, L.; Cox, N.; Savitsky, A.; Ames, W. M.; Sander, J.; Nowaczyk, M. M.; Rögner, M.; Boussac, A.; Neese, F.; Messinger, J.; Lubitz, W. *J. Am. Chem. Soc.* **2012**, *134*, 16619.
- (2) Stoll, S.; Schweiger, A. *J. Magn. Reson.* **2006**, *178*, 42.
- (3) Stoll, S.; Britt, R. D. *Phys. Chem. Chem. Phys.* **2009**, *11*, 6614.
- (4) Cox, N.; Lubitz, W.; Savitsky, A. *Mol. Phys.* **2013**, *111*, 2788.
- (5) Pérez Navarro, M.; Ames, W. M.; Nilsson, H.; Lohmiller, T.; Pantazis, D. A.; Rapatskiy, L.; Nowaczyk, M. M.; Neese, F.; Boussac, A.; Messinger, J.; Lubitz, W.; Cox, N. *Proc. Natl. Acad. Sci. U. S. A.* **2013**, *110*, 15561.
- (6) Lohmiller, T.; Krewald, V.; Pérez Navarro, M.; Retegan, M.; Rapatskiy, L.; Nowaczyk, M. M.; Boussac, A.; Neese, F.; Lubitz, W.; Pantazis, D. A.; Cox, N. *Phys. Chem. Chem. Phys.* **2014**, *16*, 11877.
- (7) Kulik, L. V.; Epel, B.; Lubitz, W.; Messinger, J. *J. Am. Chem. Soc.* **2007**, *129*, 13421.
- (8) Pal, R.; Negre, C. F.; Vogt, L.; Pokhrel, R.; Ertem, M. Z.; Brudvig, G. W.; Batista, V. S. *Biochemistry* **2013**, *52*, 7703.
- (9) Hahn, E. L. *Phys. Rev.* **1950**, *80*, 580.
- (10) Rowan, L. G.; Hahn, E. L.; Mims, W. B. *Phys. Rev.* **1965**, *137*, A61.
- (11) Mims, W. B. *Phys. Rev. B: Solid State* **1972**, *5*, 2409.
- (12) Merks, R. P. J.; Beer, R. D. *J. Phys. Chem.* **1979**, *83*, 3319.
- (13) Höfer, P.; Grupp, A.; Nebenführ, H.; Mehring, M. *Chem. Phys. Lett.* **1986**, *132*, 279.
- (14) Davies, E. R. *Phys. Lett. A* **1974**, *A 47*, 1.
- (15) Schosseler, P.; Wacker, T.; Schweiger, A. *Chem. Phys. Lett.* **1994**, *224*, 319.
- (16) Sugiura, M.; Rappaport, F.; Brettel, K.; Noguchi, T.; Rutherford, A. W.; Boussac, A. *Biochemistry* **2004**, *43*, 13549.
- (17) Peloquin, J. M.; Campbell, K. A.; Randall, D. W.; Evanchik, M. A.; Pecoraro, V. L.; Armstrong, W. H.; Britt, R. D. *J. Am. Chem. Soc.* **2000**, *122*, 10926.

- (18) Cox, N.; Rapatskiy, L.; Su, J.-H.; Pantazis, D. A.; Sugiura, M.; Kulik, L.; Dorlet, P.; Rutherford, A. W.; Neese, F.; Boussac, A.; Lubitz, W.; Messinger, J. *J. Am. Chem. Soc.* **2011**, *133*, 3635.
- (19) Su, J. H.; Cox, N.; Ames, W.; Pantazis, D. A.; Rapatskiy, L.; Lohmiller, T.; Kulik, L. V.; Dorlet, P.; Rutherford, A. W.; Neese, F.; Boussac, A.; Lubitz, W.; Messinger, J. *Biochim. Biophys. Acta, Bioenerg.* **2011**, *1807*, 829.
- (20) Lohmiller, T.; Cox, N.; Su, J. H.; Messinger, J.; Lubitz, W. *J. Biol. Chem.* **2012**, *287*, 24721.
- (21) Zheng, M.; Khangulov, S. V.; Dismukes, G. C.; Barynin, V. V. *Inorg. Chem.* **1994**, *33*, 382.
- (22) Sturgeon, B. E.; Ball, J. A.; Randall, D. W.; Britt, R. D. *J. Phys. Chem.* **1994**, *98*, 12871.
- (23) Cox, N.; Ames, W.; Epel, B.; Kulik, L. V.; Rapatskiy, L.; Neese, F.; Messinger, J.; Wieghardt, K.; Lubitz, W. *Inorg. Chem.* **2011**, *50*, 8238.
- (24) Van Vleck, J. H. *Phys. Rev.* **1940**, *57*, 426.
- (25) Orbach, R. *Proc. R. Soc. Lond. A* **1961**, *264*, 458.
- (26) Pace, R. J.; Smith, P. J.; Bramley, R.; Stehlik, D. *Biochim. Biophys. Acta, Bioenerg.* **1991**, *1058*, 161.
- (27) Lorigan, G. A.; Britt, R. D. *Biochemistry* **1994**, *33*, 12072.
- (28) Lorigan, G. A.; Britt, R. D. *Photosynth. Res.* **2000**, *66*, 189.
- (29) Kulik, L. V.; Lubitz, W.; Messinger, J. *Biochemistry* **2005**, *44*, 9368.
- (30) Peterson, S.; Ahrling, K. A.; Styring, S. *Biochemistry* **1999**, *38*, 15223.
- (31) Åhrling, K. A.; Peterson, S.; Styring, S. *Biochemistry* **1998**, *37*, 8115.
- (32) Bloch, F. *Phys. Rev.* **1946**, *70*, 460.
- (33) Britt, R. D.; Lorigan, G. A.; Sauer, K.; Klein, M. P.; Zimmermann, J. L. *Biochim. Biophys. Acta, Bioenerg.* **1992**, *1140*, 95.
- (34) Britt, R. D.; Zimmermann, J. L.; Sauer, K.; Klein, M. P. *J. Am. Chem. Soc.* **1989**, *111*, 3522.
- (35) Force, D. A.; Randall, D. W.; Lorigan, G. A.; Clemens, K. L.; Britt, R. D. *J. Am. Chem. Soc.* **1998**, *120*, 13321.

- (36) Åhrling, K. A.; Evans, M. C. W.; Nugent, J. H. A.; Ball, R. J.; Pace, R. J. *Biochemistry* **2006**, *45*, 7069.
- (37) Kulik, L.; Epel, B.; Messinger, J.; Lubitz, W. *Photosynth. Res.* **2005**, *84*, 347.
- (38) Pudollek, S., Doctoral Thesis, Freie Universität Berlin, 2012.
- (39) Umena, Y.; Kawakami, K.; Shen, J.-R.; Kamiya, N. *Nature* **2011**, *473*, 55.
- (40) Tan, X. L.; Gultneh, Y.; Sarneski, J. E.; Scholes, C. P. *J. Am. Chem. Soc.* **1991**, *113*, 7853.
- (41) Tang, X. S.; Sivaraja, M.; Dismukes, G. C. *J. Am. Chem. Soc.* **1993**, *115*, 2382.
- (42) Khangulov, S.; Sivaraja, M.; Barynin, V. V.; Dismukes, G. C. *Biochemistry* **1993**, *32*, 4912.
- (43) Schäfer, K. O.; Bittl, R.; Zwegart, W.; Lenzian, F.; Haselhorst, G.; Weyhermüller, T.; Wieghardt, K.; Lubitz, W. *J. Am. Chem. Soc.* **1998**, *120*, 13104.
- (44) Sinnecker, S.; Neese, F.; Noodleman, L.; Lubitz, W. *J. Am. Chem. Soc.* **2004**, *126*, 2613.
- (45) Sinnecker, S.; Neese, F.; Lubitz, W. *J. Biol. Inorg. Chem.* **2005**, *10*, 231.
- (46) Stich, T. A.; Whittaker, J. W.; Britt, R. D. *J. Phys. Chem. B* **2010**, *114*, 14178.
- (47) Lobrutto, R.; Smithers, G. W.; Reed, G. H.; Ormejohnson, W. H.; Tan, S. L.; Leigh, J. S. *Biochemistry* **1986**, *25*, 5654.
- (48) Morrissey, S. R.; Horton, T. E.; Grant, C. V.; Hoogstraten, C. G.; Britt, R. D.; DeRose, V. J. *J. Am. Chem. Soc.* **1999**, *121*, 9215.
- (49) Hoogstraten, C. G.; Grant, C. V.; Horton, T. E.; DeRose, V. J.; Britt, R. D. *J. Am. Chem. Soc.* **2002**, *124*, 834.
- (50) Schiemann, O.; Fritscher, J.; Kisseleva, N.; Sigurdsson, S. T.; Prisner, T. F. *ChemBioChem* **2003**, *4*, 1057.
- (51) García-Rubio, I.; Angerhofer, A.; Schweiger, A. *J. Magn. Reson.* **2007**, *184*, 130.
- (52) Astashkin, A. V.; Nesselov, Y. E. *J. Phys. Chem. B* **2012**, *116*, 13655.
- (53) Randall, D. W.; Sturgeon, B. E.; Ball, J. A.; Lorigan, G. A.; Chan, M. K.; Klein, M. P.; Armstrong, W. H.; Britt, R. D. *J. Am. Chem. Soc.* **1995**, *117*, 11780.

Abbreviations

ADP	adenosine diphosphate
ATP	adenosine triphosphate
BS	broken-symmetry
Chl	chlorophyll
cyt	cytochrome
DCMU	3-(3,4-dichlorophenyl)-1,1-dimethylurea
DFT	density functional theory
EDNMR	electron-electron double resonance-detected nuclear magnetic resonance
EE	electron exchange
ELDOR	electron-electron double resonance
ENDOR	electron-nuclear double resonance
EPR	electron paramagnetic resonance
ESE	electron spin echo
ESEEM	electron spin echo envelope modulation
EZ	electron Zeeman
FID	free induction decay
FS	field-swept
FTIR	Fourier transform infrared
HF	hyperfine
HYSCORE	hyperfine sublevel correlation
LHCII	light-harvesting complex II
mw	microwave
NADPH	nicotinamide adenine dinucleotide phosphate
NMR	nuclear magnetic resonance
NQ	nuclear quadrupole
NZ	nuclear Zeeman
OEC	oxygen-evolving complex
PC	plastocyanin
PCET	proton-coupled electron transport
Pheo	pheophytin
P _i	inorganic phosphate
PSI	photosystem I

Abbreviations

PSII	photosystem II
psb	photosystem b (photosystem II)
Q	plastoquinone or plastoquinol
rf	radio frequency
ROS	reactive oxygen species
TOF	turnover frequency
TON	turnover number
W	water
ZFS	zero-field splitting / fine structure

Acknowledgments

I would like to express my sincerest gratitude to the following people who were involved in my work conducted in the context of this thesis:

- Prof. Dr. Wolfgang Lubitz for giving me the opportunity to carry out research under his supervision at the Max-Planck-Institut für Chemische Energiekonversion (MPI CEC) in Mülheim. I appreciate very much receiving his immediate feedback and helpful response whenever requested, as well as his encouragement and support of conference travels.
- Prof. Dr. Peter Hildebrandt for acting as co-examiner of this work at the Technische Universität Berlin.
- Dr. Nicholas ‘Nick’ Cox for his committed supervision throughout the work on my thesis, for both teaching me an enormous amount of practical skills and hands-on knowledge in the lab, and advancing my theoretical understanding of techniques and subject. I am greatly thankful for having been able to benefit from his broad knowledge and scientific expertise.
- Dr. Leonid Rapatskiy and Montserrat Pérez Navarro, who were constantly available for discussions and assistance, and who provided a great working atmosphere, which sparked excellent collaboration on various projects. I got to know them both as excellent coworkers, as well as supportive friends to share numerous fun events and memories with.
- Dr. Ji-Hu Su for initial supervision and introducing me into the EPR facilities at the institute.
- Dr. Dimitrios A. Pantazis, Vera Krewald, Dr. Marius Retegan, who performed all DFT computations in this work, and Prof. Dr. Frank Neese for a highly fruitful and inspiring collaboration joining spectroscopy and theory.
- Ethel Steenbergen, who was invaluable with respect to all organizational matters and far beyond.
- Gudrun Klihm and Frank Reikowski for outstanding technical support in the EPR laboratory.
- Birgit Deckers for instantaneous assistance regarding all graphical requests, and Rita Gröver, who always had a helping hand.
- All further coworkers and collaborators, in particular Dr. William Ames, Prof. Dr. Sushil K. Misra, Prof. Dr. Johannes Messinger, Prof. Dr. A. William ‘Bill’ Rutherford,

Acknowledgments

for helpful discussions and general support, and Dr. Alain Boussac, Dr. Arezki Sedoud and Dr. Marc M. Nowaczyk in addition for providing high-quality cyanobacterial PSII samples.

- Dr. Edward J. Reijerse for offering a PhD position in the framework of the Bio-H2 project (03SF0355C) of the Federal Ministry of Education and Research of Germany (BMBF).

I would like to thank all other current and former coworkers at the institute with whom I was able to undertake various activities. Willi Schlamann is especially acknowledged for his efforts with regards to Monday's football game.

People who were not immediately involved in this work, but whose contribution to its successful completion cannot be underestimated, are my friends and family, especially my parents and most of all Marta. I am deeply thankful for your continuous love, support and inspiration.

Publications

Parts of this work have been published:

Chapter 4:

Lohmiller, T.; Ames, W.; Lubitz, W.; Cox, N.; Misra, S. K.

“EPR Spectroscopy and the Electronic Structure of the Oxygen-Evolving Complex of Photosystem II”

Appl. Magn. Reson. **2013**, *44* (6), 691-720.

© Springer-Verlag Wien 2013; with kind permission from Springer Science and Business Media. The final publication is available at Springer via <http://dx.doi.org/10.1007/s00723-012-0437-3>.

Chapter 5:

Lohmiller, T.; Cox, N.; Su, J.-H.; Messinger, J.; Lubitz, W.

“The Basic Properties of the Electronic Structure of the Oxygen-evolving Complex of Photosystem II Are Not Perturbed by Ca²⁺ Removal”

J. Biol. Chem. **2012**, *287* (29), 24721-24733.

<http://dx.doi.org/10.1074/jbc.M112.365288>

This research was originally published in The Journal of Biological Chemistry. © the American Society for Biochemistry and Molecular Biology.

Chapter 6:

Lohmiller, T.; Krewald, V.; Pérez Navarro, M.; Retegan, M.; Rapatskiy, L.; Nowaczyk, M. M.; Boussac, A.; Neese, F.; Lubitz, W.; Pantazis, D. A.; Cox, N.

“Structure, ligands and substrate coordination of the oxygen-evolving complex of photosystem II in the S_2 state: a combined EPR and DFT study”

Phys. Chem. Chem. Phys. **2014**, *16* (24), 11877-11892.

<http://dx.doi.org/10.1039/c3cp55017f>

Reproduced by permission of the PCCP Owner Societies.

Chapter 7:

Lohmiller, T.; Krewald, V.; Sedoud, A.; Rutherford, A. W.; Neese, F.; Lubitz, W.; Pantazis, D. A.; Cox, N.

“The First Substrate Water of Nature’s Water-Oxidizing Cofactor Binds as a μ -Hydroxo Bridge during Catalyst Regeneration”

in preparation.

Further publications:

Su, J.-H.; Cox, N.; Ames, W.; Pantazis, D. A.; Rapatskiy, L.; Lohmiller, T.; Kulik, L. V.; Dorlet, P.; Rutherford, A. W.; Neese, F.; Boussac, A.; Lubitz, W.; Messinger, J.

“The electronic structures of the S_2 states of the oxygen-evolving complexes of photosystem II in plants and cyanobacteria in the presence and absence of methanol”

Biochim. Biophys. Acta, Bioenerg. **2011**, *1807* (7), 829-840.

<http://dx.doi.org/10.1016/j.bbabi.2011.03.002>

Publications

Lohmiller, T.; Cox, N.; Su, J.-H.; Messinger, J.; Lubitz, W.

“An EPR and ENDOR Spectroscopic Investigation of the Ca²⁺-Depleted Oxygen-Evolving Complex of Photosystem II”

In *Photosynthesis Research for Food, Fuel and Future: 15th International Conference on Photosynthesis*; Kuang, T.; Lu, C.; Zhang, L., Eds.; Zhejiang University Press: Huangzhou and Springer-Verlag: Berlin Heidelberg, 2013, pp 239–243.

http://dx.doi.org/10.1007/978-3-642-32034-7_50

Pérez Navarro, M.; Ames, W. M.; Nilsson, H.; Lohmiller, T.; Pantazis, D. A.; Rapatskiy, L.; Nowaczyk, M. M.; Neese, F.; Boussac, A.; Messinger, J.; Lubitz, W.; Cox, N.

“Ammonia binding to the oxygen-evolving complex of photosystem II identifies the solvent-exchangeable oxygen bridge (μ -oxo) of the manganese tetramer”

Proc. Natl. Acad. Sci. U. S. A. **2013**, *110* (39), 15561-15566.

<http://dx.doi.org/10.1073/pnas.1304334110>